
Structural Characterisation of Diverse Supramolecular Systems Using Mass Spectrometry

Inaugural-Dissertation
to obtain the academic degree
Doctor rerum naturalium (Dr. rer. nat.)

submitted to the Department of Biology, Chemistry, Pharmacy
of Freie Universität Berlin

by

Daniel Lloyd Stares

Berlin, 2023

The present research was carried out under the supervision of Prof. Dr. Christoph A. Schalley from September 2019 until November 2023.

Herewith I certify that I have prepared and written my thesis independently and that I have not used any sources and aids other than those indicated by me. I also declare that I have not submitted the dissertation in this or any other form to any other institution as a dissertation.

-Daniel Lloyd Stares

1st reviewer: Prof. Dr. Christoph Schalley

2nd reviewer: Prof. Dr. Kevin Pagel

Date of Defense: 21.03.2024

Acknowledgements

Firstly, thank you to Christoph for the supervision over the years. I certainly learnt a lot under your tutelage, and I appreciate your input and expertise in improving my work and knowledge. I wish you all the best for your future endeavours.

Kevin Pagel, thank you for taking the time to act as second reviewer.

Thank you to the members of the group who made the environment fun and enjoyable to work in. Good luck with your future projects and theses, I hope it goes well for you all with a smooth writing process and reasonable editors and-reviewers. Just remember that there will be good days and bad days, but you will get there eventually.

A special thank you to Henrik, Marius and Tuğrul for their help and advice with writing this monstrosity and getting it submitted.

Silke, I appreciate your help in navigating the maddening combination of FU, German and EU bureaucracy.

Thank you to Andreas Springer, Fabian Klautzsch and everyone within the core facility for the help with the MS measurements especially for taming, as much as possible, the mood swings of the FTICR.

I was fortunate enough to collaborate on a number of wonderful projects and I am grateful to all those I worked with throughout the years. Even though COVID tried to intervene, it was especially nice to be able to work in person with Cristina Mozaceanu and Michael Kathan.

Thank you to the NOAH network, particularly to Agnieszka Szumna for hosting my research stay, it was a pleasure to work with you all.

I appreciate the EU and FU Berlin for the funding for this project.

Finally, I want to say a major thank you to my friends, family and partner for the support during the PhD. COVID made for some difficult times, but there are brighter days ahead.

Abstract

The field of supramolecular chemistry is conceptually very broad, encompassing diverse classes of compounds with different functions and uses. Robust characterisation of the systems is one of the most important steps in building the knowledge necessary for the further development and eventual use in numerous potential applications. Establishing additional methods to characterize supramolecular complexes would be beneficial as it is currently dominated by NMR and X-ray crystallography. Further use of mass spectrometry (MS) would be useful for supramolecular chemistry as it is highly versatile and able to provide detailed structural information.

Throughout this thesis, MS was used to structurally characterise a diverse range of supramolecular systems including several different types of host-guest systems, a photoswitchable pseudorotaxane, a light driven molecular motor, and a bioderived rotaxane. Structural insights into the different complexes could be obtained by using various combinations of the tandem MS techniques collision induced dissociation (CID), ion-mobility mass spectrometry (IMS), and hydrogen deuterium exchange.

The general results show the ability of MS to build on other characterisation methods to gain further insights into the system under investigation. More specifically, it shows how MS can be used to follow dynamic processes of photoswitchable systems. For this, IMS is particularly useful as the different conformations can be separated and then assigned based on their collision cross section values. In addition, IMS can be combined with CID to investigate thermal relaxation processes.

There are also situations where the complexes may only be observed via MS. Here guest binding was seen via MS that was not observed via other techniques and the binding mode elucidated via IMS and CID measurements. The results show how the ionisation process can be used to generate complexes that will not form otherwise. This is particularly prevalent for host systems binding charged guests as the charged droplets enable interaction between the naked ion and the host.

Overall, the results show that MS is a powerful tool in the structural characterisation of supramolecular systems and can provide information not possible by other methods.

Kurzzusammenfassung

Das Gebiet der supramolekularen Chemie ist konzeptionell sehr breit gefächert und umfasst verschiedene Klassen von Verbindungen mit unterschiedlichen Funktionen und Verwendungszwecken. Eine robuste Charakterisierung der Systeme ist einer der wichtigsten Schritte beim Aufbau des Wissens, das für die Weiterentwicklung und den Einsatz in potenziellen Anwendungen erforderlich ist. Die Einführung zusätzlicher Methoden zur Charakterisierung supramolekularer Komplexe bietet Vorteile, da diese derzeit von Kernspinresonanz und Röntgenkristallographie dominiert werden. Der zusätzliche Einsatz von Massenspektrometrie (MS) für supramolekulare Chemie kann nützlich sein, da MS äußerst vielseitig ist und detaillierte Strukturinformationen über supramolekulare Komplexe liefern kann.

In dieser Arbeit wurde MS zur strukturellen Charakterisierung einer Vielzahl supramolekularer Systeme eingesetzt, darunter verschiedene Arten von Wirt-Gast-Systemen, ein photoschaltbares Pseudorotaxan, ein lichtgetriebener molekularer Motor und ein biologisch gewonnenes Rotaxan. Es konnten strukturelle Einblicke in die verschiedenen Komplexe durch den Einsatz verschiedener Kombinationen der Tandem-MS-Techniken der kollisionsinduzierten Dissoziation (CID), der Ionenmobilitäts-Massenspektrometrie (IMS) und des Wasserstoff-Deuterium-Austauschs gewonnen werden.

Die allgemeinen Ergebnisse zeigen die Fähigkeit von MS, auf anderen Charakterisierungsmethoden aufzubauen, um tiefere Einblicke in das untersuchte System zu gewinnen. Insbesondere wird gezeigt, wie IMS eingesetzt werden kann, um dynamische Prozesse in photoschaltbaren Systemen zu verfolgen. IMS ist besonders nützlich, da die verschiedenen Konformationen zunächst getrennt und dann auf der Grundlage der Kollisionsquerschnittswerte zugeordnet werden können. Darüber hinaus kann IMS mit CID kombiniert werden, um thermische Relaxationsprozesse zu untersuchen.

Es gibt auch Situationen, in denen Komplexe nur via MS beobachtet werden können. In einem Fall wurde mit MS eine Gastbindung festgestellt, die mit anderen Techniken nicht beobachtet werden konnte. Der Bindungsmodus wurde mit IMS- und CID-Messungen weiter aufgeklärt. Die Ergebnisse zeigen auch, wie der Ionisierungsprozess zur Bildung von Komplexen genutzt werden kann, die sich sonst nicht bilden würden. Dies gilt insbesondere für Wirtssysteme, die

geladene Gäste binden, da die geladenen Tröpfchen eine Wechselwirkung zwischen dem nackten Ion und dem Wirt ermöglichen.

Insgesamt zeigen die Ergebnisse, dass die MS ein leistungsfähiges Instrument für die strukturelle Charakterisierung supramolekularer Systeme ist und Informationen liefern kann, die mit anderen Methoden nicht gewonnen werden können.

Abbreviations

3c-4e.....	Three centre four electron bond
AAP.....	Arylazopyrazole
AMMs.....	Artificial molecular machines
ATD.....	Arrival time distribution
BIPY2+.....	Bipyridinium
BIRD.....	Blackbody infrared radiative dissociation
CBPQT.....	Cyclobis(paraquat-p-phenylene)
CCS.....	Collision cross section
CDs.....	Cyclodextrins
CID.....	Collision induced dissociation
CRM.....	Charge residue model
CUD.....	Cycloundecanone
DC.....	[c2]daisy chain
DnD.....	α,ω -alkylbisDABCOonium
DNP.....	1,5-dioxynaphthalene
DT-IMS.....	Drift-Tube Ion Mobility
<i>e/m</i>	Charge-to-Mass ratio
ECD.....	Electron capture dissociation
EI.....	Electron ionisation
ESI.....	Electrospray ionisation
ETD.....	Electron transfer dissociation
FID.....	Free induction decay
FT.....	Fourier-transform
FTICR.....	Fourier-transform ion cyclotron resonance
HDX.....	Hydrogen-deuterium exchange
HRMS.....	High resolution mass spectrometry
ICR.....	Ion cyclotron resonance
ID.....	indane-1,3-dione
IEM.....	Ion evaporation model
IMS.....	Ion-mobility mass spectrometry
IRMPD.....	Infrared multiple photon dissociation

<i>m/z</i>	Mass-to-charge ratio
MAC.....	7-amino-4-methylcoumarin
MALDI.....	Matrix-assisted laser desorption/ionisation
MC.....	4-methylcoumarin
MIMs.....	Mechanically interlocked molecules
MS.....	Mass spectrometry
MS/MS.....	Tandem mass spectrometry
NMR.....	Nuclear magnetic resonance
PES.....	Potential energy surface
PSS.....	Photostationary state
PY+.....	2,6-dimethylpyridinium
RCM.....	Ring closing metathesis
RF.....	Radio Frequency
SID.....	Surface induced dissociation
SLD.....	soft laser desorption
SY.....	Survival yield
SY50%.....	Inflection point of sigmoidal curve
TEA+.....	Tetraethylammonium
THI.....	Thermal helical inversion
TOF.....	Time-of-flight
TW-IMS.....	Travelling-wave ion mobility
UFF.....	Universal force field

Table of Contents

Acknowledgements.....	ii
Abstract.....	iii
Kurzzusammenfassung	iv
Abbreviations	vi
1. Introduction	1
Thesis Outline.....	4
2. Theoretical Background	5
2.1 Supramolecular Chemistry: An Introduction	5
2.1.1 Non-Covalent interactions	5
2.1.2 General Comments and Concepts	7
2.1.3 Host-Guest Chemistry	8
2.1.4 Self-Assembled Capsules	11
2.1.5 Metal-Organic cages	15
2.1.6 Rotaxanes, Pseudorotaxanes and Mechanically Interlocked Molecules.....	18
2.1.7 Stimuli Controlled Motion	20
2.1.8 Photoswitches	23
2.1.9 Molecular Motors	25
2.2 Mass Spectrometry	27
2.2.1 Brief History	27
2.2.2 Ionisation.....	28
2.2.3 Mass Analysers.....	30
2.2.4 Mass Spectrometry Techniques for Structural Characterisation	33
2.2.5 Instruments Used.....	41
2.3 MS as a Tool to Study Supramolecular Systems	43

3. Results.....	48
Preamble	48
3.1 Light-Controlled Interconversion Between a [c2]daisy Chain and a Lasso-Type Pseudo[1]rotaxane.....	48
3.2 A Light-Fuelled Nanoratchet Shifts a Coupled Chemical Equilibrium.....	52
3.3 Dimeric Iodine(I) and Silver(I) Cages From Tripodal N-Donor Ligands Via the [N–Ag–N] ⁺ to [N–I–N] ⁺ Cation Exchange Reaction	55
3.4 Binding Modes of High Stoichiometry Guest Complexes with a Co ₈ L ₁₂ Cage Uncovered by Mass Spectrometry	58
3.5 Encapsulation in Charged Droplets Generates Distorted Host-Guest Complexes	62
3.6 Bioderived Rotaxanes via Dynamic Covalent Boron Chemistry	66
4. Conclusions and Perspectives.....	70
5. References.....	74
6. Appendix	82
6.1 Manuscripts not Included in the thesis.....	82
6.2 Manuscripts Included in the Thesis	82
6.3 Prints of Manuscripts Included in the Thesis.....	82
Light-Controlled Interconversion Between a [c2]daisy Chain and a Lasso-Type Pseudo[1]Rotaxane	83
A Light-Fuelled Nanoratchet Shifts a Coupled Chemical Equilibrium.....	124
Dimeric Iodine(I) and Silver(I) Cages From Tripodal N-Donor Ligands Via the [N–Ag–N] ⁺ to [N–I–N] ⁺ Cation Exchange Reaction	221
Binding Modes of High Stoichiometry Guest Complexes with a Co ₈ L ₁₂ Cage Uncovered by Mass Spectrometry	311
Encapsulation in Charged Droplets Generates Distorted Host-Guest Complexes	326
Bioderived Rotaxanes via Dynamic Covalent Boron Chemistry	365

1. Introduction

The field of supramolecular chemistry covers a huge range of compounds with a wide variety of function and uses. The unifying feature of these supramolecular complexes is that they involve multiple components held together by non-covalent interactions.¹ The scope of the complexes that fall within this definition is enormous. Firstly, there are various types of non-covalent interactions which all have different impacts on the type of assemblies that forms. The number of components involved can also vary greatly with systems comprising just two components through to systems of effectively infinite size. Furthermore, there is also a plethora of different compound classes which all have distinct goals and aims. Some systems will have obvious overlap in their structure and function, but others will be so distinct from one another that it may be unclear that there is any relationship between them at all.

The possible applications of supramolecular chemistry are as broad as the systems themselves with potential uses for drug delivery,² sensing,³ separation,⁴ catalysis,⁵ electronics,⁶ and materials.⁷ The realisation of any application such as these requires the knowledge attained through foundational research. One of the most important components in building this knowledge is rigorous study and characterisation of the different complexes. For supramolecular chemistry, characterisation is dominated by nuclear magnetic resonance (NMR) and X-ray crystallography. The success and widespread use of these techniques has created somewhat of a dogma where other techniques are comparatively neglected. Such a situation is short sighted as no single method can address all systems or research inquiries. For instance, while NMR is a mainstay of chemistry, it also suffers from low sensitivity and signal overlap making analysing mixtures problematic.⁸ For X-ray crystallography, although crystal structures are perhaps the most esteemed of all analytical results, generating diffraction quality crystals is challenging and certain elements e.g. hydrogen are difficult to identify due to weak interactions with X-rays.⁹

Incorporating additional methods into the characterisation workflow would make for a more robust understanding of supramolecular chemistry and aid development of potential applications. This does not require the invention of entirely new methods, but rather utilising insightful methods that are currently underexploited. One such method is mass spectrometry (MS). MS has many desirable general features such as high sensitivity, quick data acquisition,

and the ability to analyse mixtures and impure samples. Furthermore, the fact that MS occurs in the gas-phase is beneficial for analysing supramolecular complexes. For example, non-covalent interactions are strengthened in the gas-phase, and dynamic exchange processes, which complicate analysis in solution, do not occur. It also means that interference from solvent is not present and computational structures need not consider solvation, reducing cost.¹⁰ Like any method, MS of course also has disadvantages such as being dependent on generating gaseous ions which may disrupt certain systems, however, there are far more situations where MS is useful than not.

Although high resolution MS (HRMS) is a requirement for all new compounds, this is regularly where the use of MS ends (and even this may be confined to a zoom of an isotopic pattern buried in the supplementary material). The lack of MS within supramolecular chemistry seems to stem from the pervasive notion that MS is only useful for HRMS and cannot be used for structural characterisation. While this may have been true at one-point, tandem MS (MS/MS) techniques have been developed which provide remarkable structural insight into an ion. For example, fragmentation techniques such as collision induced dissociation can infer the stability of ions and can also be used to follow structurally informative fragmentation. It is also possible to determine reactivity information via gas-phase ion-molecule reactions such as hydrogen/deuterium exchange experiments. Furthermore, ion-mobility mass spectrometry separates ions by their mobility through a buffer gas allowing separation of isomers and direct structural characterisation through calculation of collision cross section values.

Such measurements have great potential value to supramolecular chemistry, but they mostly go unused. The general aim of the thesis is thus to boost the appeal of MS to supramolecular chemists. The goal is not to replace existing characterisation methods but to simply demonstrate the advantages of MS and hopefully provide another tool to better understand supramolecular chemistry. More specific aims are as follows:

- Demonstrate the utility of complementary MS use for structural characterisation of supramolecular systems.

The general goal of the thesis is to show how MS can be used to structurally characterise different supramolecular systems. For the greatest scope, the systems should comprise diverse classes of supramolecular systems with different uses and research aims.

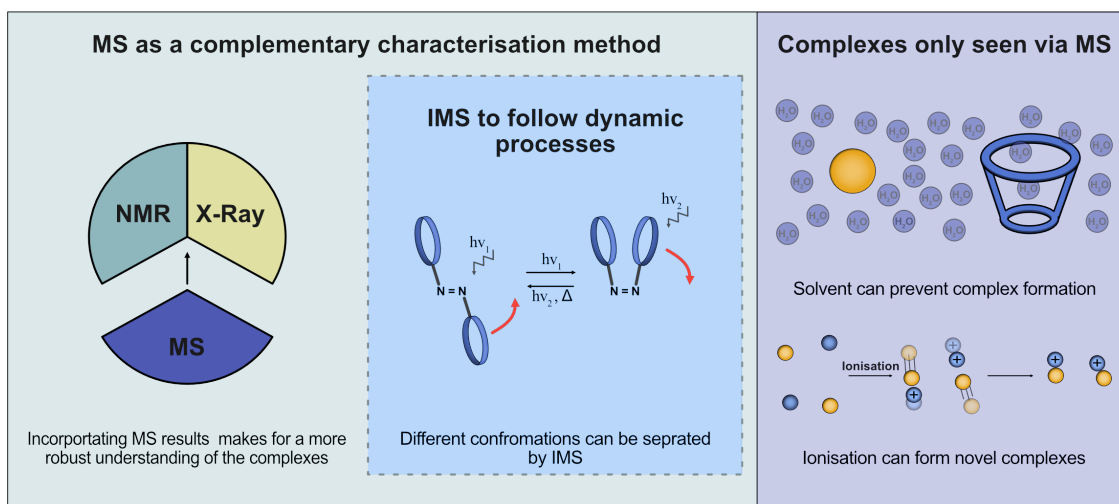


Figure 1.1: Graphical representation of the aims of the thesis.

Furthermore, the results show how different MS/MS techniques can provide different insights showcasing the versatility of MS. These results should serve to make MS a more attractive characterisation method for supramolecular chemists.

- Use IMS to follow dynamic processes of switchable systems.

Molecular machines and motors are major research areas within supramolecular chemistry. Switching and dynamic processes exist in equilibrium meaning that signal overlap can make characterisation via NMR challenging. Instead, IMS can be used to separate the different conformations and used to quickly follow dynamic processes. While several photoswitchable systems have been studied by MS, the use of MS to study molecular motors is currently underexplored. This represents a gap that MS could fill and would demonstrate the use of MS even with highly complex systems while extending the characterisation methods of molecular machines and motors.

- Structurally characterise complexes which cannot be observed by other methods.

There are several reasons why a certain complex may only be observed via MS. There is also the possibility of using the ionisation process to generate complexes that cannot be formed otherwise. These situations best represent the need for MS. If something can be studied using conventional characterisation methods, then people will opt to use them as that is what they know and feel comfortable with. The true test comes from MS 'going alone' and seeing if it can be used to structurally characterise something without input from other techniques. This not only demonstrates the capabilities of MS but also showcases the need of expanding the number of methods used for characterisation.

Thesis Outline

The thesis starts with a discussion of non-covalent interactions and supramolecular chemistry before certain classes of supramolecular systems are discussed in more detail. The different concepts of MS and various techniques will then be described with some contemporary examples of use of MS in supramolecular chemistry before the results obtained within the thesis will be presented and discussed. The systems studied during this work include a photoswitchable pseudorotaxane, a light driven molecular motor, halogen bonded capsules, hydrogen bonded capsules, a metal organic cage and a bioderived rotaxane.

2. Theoretical Background

2.1 Supramolecular Chemistry: An Introduction

2.1.1 Non-Covalent Interactions

As mentioned in the introduction, there are a number of distinct non-covalent interactions which can be used to form supramolecular complexes. With this in mind, before considering the different classes of supramolecular complexes which can be formed, it is important to define and discuss non-covalent interactions. Firstly, non-covalent interactions differ from covalent bonds as they do not involve shared electrons between atoms.¹¹ Instead, most non-covalent interactions are instead electrostatic in nature, but, as can be seen in figure 2.1, there are numerous ways this may manifest with a wide range of interaction energies.

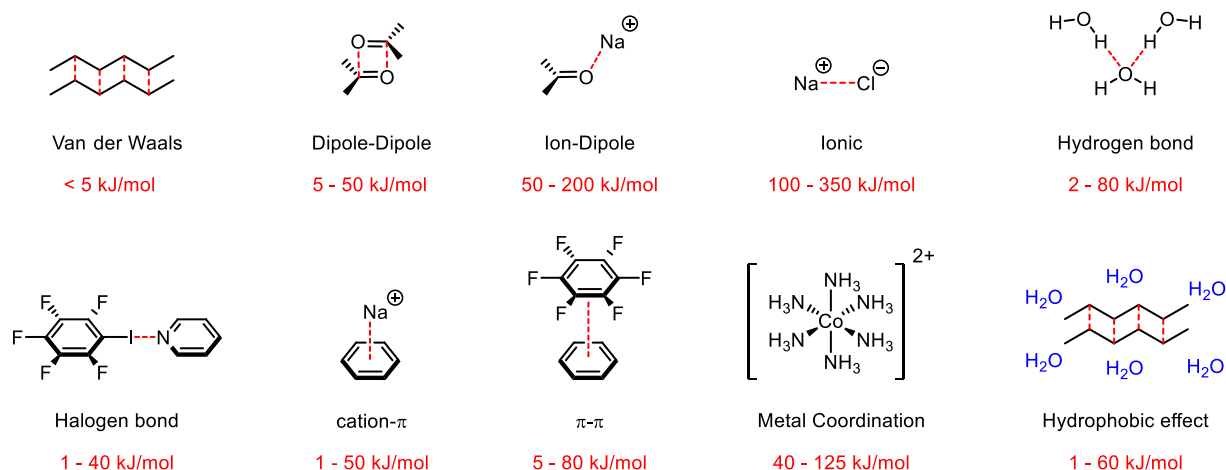


Figure 2.1: Some of the different non-covalent interactions with a general range of their respective binding strength shown in red.¹²⁻¹⁴

In general, interaction strength can be said to increase as the charges become more discrete. *Van der Waals* interactions are on the weaker side of the spectrum and arise when the electron cloud of one molecule causes a temporary dipole in another leading to a weak electrostatic interaction between them. These interactions are most commonly seen for non-polar molecules and are also referred to as dispersion interactions.¹⁵ *Dipole-dipole* interactions occur between entities possessing permanent dipoles and have greater binding strength than *Van der Waals* interactions. Interaction strength increases again for *ion-dipole* interactions and *ionic* interactions between two oppositely charged entities can form some of the strongest bonds in supramolecular chemistry.¹⁶ Most other types of non-covalent interactions can be considered as types of *dipole-dipole*, *ion-dipole* or *ionic* interactions.

Of all non-covalent interactions, *hydrogen bonds* deserve special attention as they are ubiquitous in nature and are utilised in many diverse applications. Hydrogen bonds are a type of dipole-dipole interaction that occur when an electropositive hydrogen interacts with a more electronegative atom.¹⁴ This is classically seen in H₂O where the electronegative oxygen induces a partial positive dipole on its hydrogens which then interacts with an oxygen of another H₂O molecule. Depending on the constituents involved, and the medium, the interaction strength of hydrogen bonds varies widely. Weak interactions of around 1 kJ/mol exist whilst bond strengths up to 160 kJ/mol have been observed for ionic hydrogen bonds (e.g. F-H...F) in the gas-phase.^{14, 17}

Although less commonly encountered, *halogen bonds* are conceptually similar to hydrogen bonds and also possess comparable binding strengths. Classic halogen bonds rely on an attractive interaction between an electron poor region of a halogen atom and the nucleophilic region of another entity, typically a Lewis base.¹⁸ Due to its polarizability, iodine covalently bound to perfluorinated aromatics is a popular halogen bond donor.¹⁹ It is also possible to form linear three-centre four-electron (3c-4e) bonds with halogens in a +1 oxidation state, X⁺, interacting with two Lewis bases to form [N-X-N]⁺ bonds.^{20, 21} These [N-X-N]⁺ bonds are known to be stronger than classical halogen bonds, but are also more reactive and difficult to work with.²²

There are several distinct interactions available to π -systems. *Cations- π* interactions are a type of ion-dipole interaction between a cation and the electron cloud in π -systems and commonly occur with aromatic systems. Aromatic systems possess an electronic system which resembles a quadrupole with an electropositive σ -system sandwiched between two π -clouds.²³ Because of this, most *Cations- π* interactions are more appropriately classified as *ion-quadrupole* interaction. The quadrupole electronic system can also justify the edge-to-face or face-shifted arrangement in π - π interactions of aromatic complexes as a means to avoid unfavourable π - π repulsion.^{24, 25} Face-to-Face arrangements are seen in situations where one face is sufficiently electron deficient e.g. due to electron withdrawing groups, allowing true *π - π stacking* interactions such as that seen between hexafluorobenzene and benzene.^{26, 27}

Metal coordination bonds with ligands are one of the most common types of interaction utilised in supramolecular chemistry. The interaction strength will vary broadly depending on the metal, oxidation state and type of ligand making metal coordination bonds highly

versatile.²⁸

The *hydrophobic effect* is somewhat of an exception to the other interactions discussed above as it is not driven by electrostatic interactions *per se*. Rather it is a system wide effect to avoid unfavourable interactions between water and non-polar molecules. Instead of being separately solvated by water, non-polar molecules will aggregate allowing for Van der Waals interactions between the non-polar molecules.²⁹ Aggregation also has the effect of releasing the solvating water into the bulk solution enabling the water to form a greater number of hydrogen bonds. This is not only favourable enthalpically but also has a positive entropic contribution as well.²⁹⁻³¹ Similar effects are also possible with other solvent and are known simply as *solvophobic effects* and demonstrates the major influence environment has on non-covalent interactions (discussed further in section 2.3).

2.1.2 General Concepts and Comments

The general aim of supramolecular chemists is to construct systems with multiple components using the different non-covalent interactions discussed in section 2.1.1. Other than in a few instances, these non-covalent interactions are weaker than covalent bonds. This may make non-covalent interactions seem less useful, but it is precisely their weak nature that is valuable as it makes the interactions reversible. Bond *reversibility* is one of the most important aspects of supramolecular chemistry and is even important for life itself. An example of this is in DNA where hydrogen bonding is responsible for base pairing and reversibility permits the unwinding required for DNA replication.³² Reversibility also allows for error correction where different components can dissociation and re-associate in another orientation until they find the thermodynamic minimum, assuming they can move freely (figure 2.2).^{33, 34} This process is known as *self-assembly* and is a crucial concept in supramolecular chemistry.

If there is a mixture of different components, then it is possible to have a *self-sorting* phenomenon where, out of a library of possible complexes, a smaller number of discrete assemblies are formed.^{35, 36} Self-sorting can either be narcissistic where the different components will only form complexes with other copies of themselves or social where mixed component assemblies are formed.³⁷ A related concept to self-assembly and self-sorting is *self-organisation*, where the complex is maintained out of thermodynamic equilibrium by

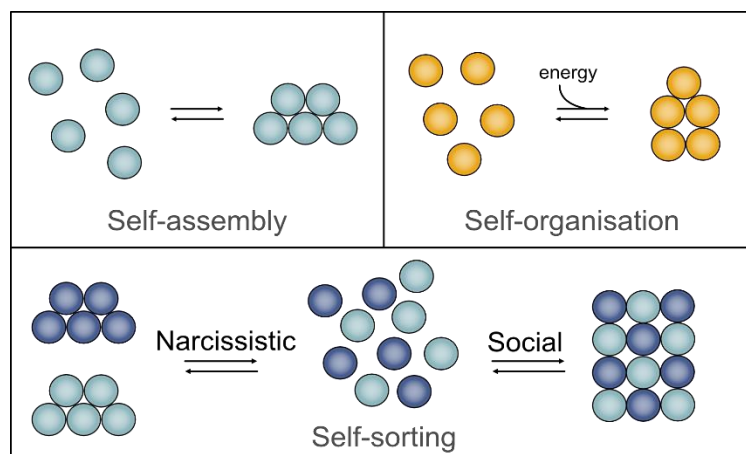


Figure 2.2: The three ‘selves’ of supramolecular chemistry. Self-assembly is the spontaneous assembly of the components into a thermodynamic minimum. Self-organisation is an out of equilibrium assembly requiring the input of energy to maintain the complex. Self-sorting involves mixture of components assembling into a discrete number of assemblies rather than a library of complexes. Self-sorting can be either social or narcissistic.

input of energy. Self-organisation is seen in biological systems where a flow of chemical fuel powers cellular functions and is also pursued in the context of artificial molecular machines (section 2.1.7-9).³⁸

Another important aspect of non-covalent interactions that enables them to be used to construct larger systems is the *directionality* of the bonds. With bond directionality appropriately designed building blocks can be programmed to spontaneously assemble into specific ordered structures of higher complexity.³⁹ For instance, hydrogen bonds are strongest with a bond angle of 180° between donor and acceptor and it is recommended to not even be considered a hydrogen bond if this angle is less than 110° .^{19, 40-42} The directionality of hydrogen bonds is one reason for their widespread adoption throughout supramolecular chemistry. The less commonly encountered halogen bonds offer even greater directionality with bonding angles that do not significantly deviate from 180° .¹⁸ Furthermore, metal coordination bonds have great directionality due to well-defined coordination geometries dependent on the type of metal, and its oxidation and spin states.⁴³

With the different attributes of non-covalent interactions, it is possible to form large supramolecular systems which would be impossible to form via covalent synthesis.

2.1.3 Host-Guest Chemistry

As mentioned above, supramolecular chemistry is ubiquitous in nature and the goals of supramolecular chemists were, and still are, largely inspired by this. More specifically, the

initial goal was to mimic the highly specific binding between an enzyme and its substrate.⁴⁴ For their work in this area, Jean-Marie Lehn, Donald J. Cram and Charles J. Pedersen jointly received the 1987 Nobel chemistry prize for the ‘development and use of molecules with structure-specific interactions of high selectivity’. This was primarily for selectively binding alkali metal ions in synthetic macrocyclic receptors such as crown ethers and cryptands.⁴⁵⁻⁴⁸ These compounds helped to define the concept of *molecular recognition* where two or more components selectively bind together via non-covalent interaction.^{49, 50} With this, they were able to realise the goal of mimicking the recognition processes seen with enzymes.^{13, 51}

Molecular recognition would further develop into the field of *host-guest chemistry* which is concerned with the development of host molecules which can be used to selectively bind guests via non-covalent interactions (figure 2.3).⁵² Guest binding with a host will generally be enthalpically driven by forming favourable interactions between host and guest but entropic contributions can also play a role. Although guest binding with a host can be considered to bring order to a system, there is also the possibility of liberating several solvent molecules from within the cavity of the host which can result in favourable entropic contributions.⁵³ However, the host adopts a more rigid structure with a decreased number of degrees of freedom, incurring an entropic penalty. Entropic penalties can be mitigated by *pre-organisation* of the system such that large changes in the conformation of the host are not required to bind the guest.⁵³

Upon binding with the host, the guest’s local environment changes which has potential applications for catalysis,⁵⁴⁻⁵⁷ stabilising reactive intermediates,⁵⁸⁻⁶⁰ sensing & recognition,⁶¹ as well as drug delivery.⁶² With such potential applications, it is not surprising that developing new hosts is a major research area. Crown ethers were the first synthetic host developed, serendipitously, by PEDERSEN in 1967.⁴⁶ The nomenclature of crown ethers provides the total number of atoms in the macrocycle along with the number of oxygens. For example, 21-

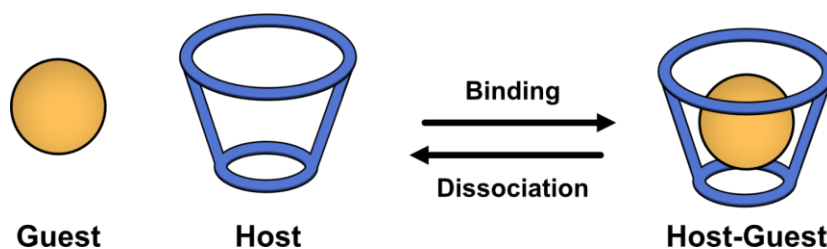


Figure 2.3: General principle of a host-guest system with reversible guest binding.

crown-7 has twenty-one atoms in the macrocycle, seven of which are oxygens. Pedersen was attempting to synthesis catechol based ligands for vanadium and inadvertently formed a small amount of what was later determined to be dibenzo-21-crown-6 (figure 2.4).⁴⁸ He found that the crown ether would bind Na^+ and synthesised several other crown ethers of various size. Shortly after the publication of crown ethers, LEHN developed the analogous three-dimensional cryptand molecules (figure 2.4).⁴⁹ With cryptands, the number of repeating $(\text{CH}_2\text{CH}_2\text{O})$ units per strand are stated in square brackets e.g. [2.2.2]. Both crown ethers and cryptands bind alkali metals through ion-dipole interactions with the oxygens and it is possible to selective bind different alkali metals by using crown ethers and cryptands of different sizes.⁶³ For example, K^+ will preferentially bind with 18-crown-6 but Cs^+ is too large to fit inside this crown ether and instead binds in the larger 21-crown-7.⁶⁴ This is a simple demonstration of molecular recognition based on size complementarity.⁶⁵

In addition to alkali metals, crown ethers also bind other cations such as ammonium ions. Whilst they will only form side on complexes with primary ammonium ions, crown ethers of a certain size can thread onto secondary ammonium ions.⁶⁶ Threading is favoured over the side on complex due to additional $\text{C-H}\cdots\text{O}$ hydrogen bonds and has been exploited to form the classes of compounds known as rotaxanes and pseudorotaxanes which will be discussed further in section 2.1.6.⁶⁷

Cyclodextrins (CDs) are naturally occurring host macrocycles with either 6 (α), 7 (β) or 8 (γ) repeating glucopyranoside units which forms an internal hydrophobic cavity (figure 2.4). CDs are water soluble due to the hydroxy groups at the openings and include guests into their cavity via the hydrophobic effect. These properties and the fact that they are naturally occurring have made CDs highly attractive for use in drug delivery with over 130 cyclodextrin-

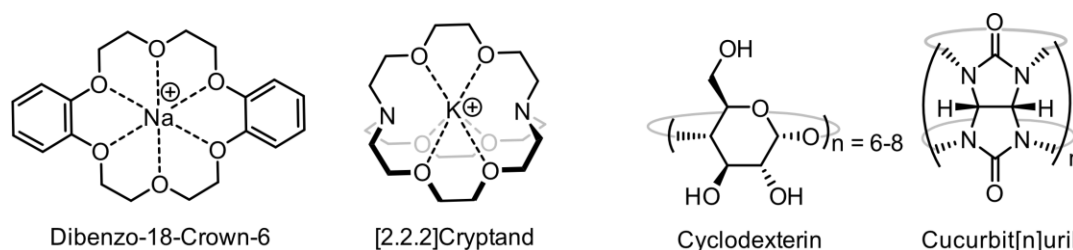


Figure 2.4: Examples of popular host systems. Crown ethers were the first synthetic host made by Pedersen in 1967 and were further developed into the three-dimensional cryptands by Lehn. Cyclodextrins are naturally occurring hosts formed from repeating glucopyranoside units. Cucurbit[n]urils are considered a synthetic analogue to the cyclodextrins formed from repeating glycoluril units.

drug formulations currently marketed.⁶⁸ As a result of this and other potential applications, CDs are some of the most widely studied hosts.^{69, 70} Cucurbit[n]urils are somewhat of a synthetic analogue of CDs and are formed from repeating glycoluril units.⁷¹ Like CDs, cucurbit[n]urils are water soluble and possess a hydrophobic interior for binding neutral guests but can also bind cationic guests via ion-dipole interactions with the carbonyls of the openings.^{72, 73} CDs and cucurbit[n]urils typify host molecules forming rigid structures with a well-defined cavity which can more precisely be classified as cavitands.⁷⁴

2.1.4 Self-Assembled Capsules

The hosts discussed so far are formed purely from covalent bonds, but it is also possible to form larger capsules via self-assembly. The following discussion will mostly be focused on resorcin[4]arenes as they are a prominent example of self-assembled capsules and were used within the thesis. Resorcinarenes are macrocycles comprising repeating resorcinol units formed from the condensation of resorcinol and an aldehyde with the resorcin[4]arene the thermodynamically favoured product (figure 2.5a).⁷⁵ Resorcin[4]arene are a bowl shaped cavitand with a wider upper rim with hydroxy groups and a narrower lower rim usually containing alkyl chains. Resorcin[4]arenes are able to bind cations via cation- π interactions with the aromatic walls of the cavity or neutral guests via the hydrophobic effect with further interactions possible via the hydroxy groups.^{76, 77} Resorcin[4]arene can self-assemble into dimers⁷⁸ and hexameric capsules⁷⁹⁻⁸⁴ by intermolecular hydrogen bonds via the hydroxyl groups on the upper rims. Self-assembly into these larger capsules increases the cavity size

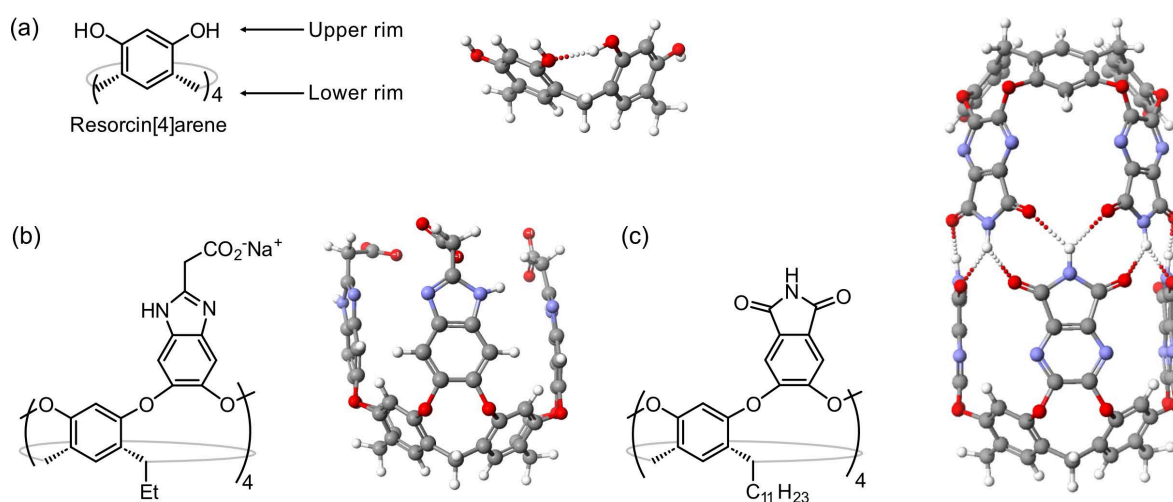


Figure 2.5: Different types of resorcin[4]arene based cavitands and capsules: The un modified resorcin[4]arene (a) can form dimers and hexamers via intermolecular hydrogen bonds; functionalisation of the hydroxy groups enables the formation of deeper cavitands (b); and larger hydrogen bonded dimers (c).

which permits binding of guests not possible by the monomeric cavitands.

Resorcin[4]arenes have great versatility owing to potential modifications at both their upper and lower rims. Lower rim modifications typically do not alter complexation or self-assembly but offers the ability to control the solubility of the cavitands.⁸⁵ Upper rim modification, on the other hand, can dramatically alter the function and self-assembly of the resorcin[4]arene. REBEK and co-workers have made several aryl-extended cavitands through functionalising the hydroxy groups which extended the size of the non-polar guest which could be encapsulated (figure 2.5b).⁸⁶ It is also possible to form resorcin[4]arene which bind anions by bridging the hydroxy groups with CH_2 allowing $\text{C-H}\cdots\text{anion}$ bonds.⁸⁷ Furthermore, by designing the resorcin[4]arene in a complementary way, it is also possible to form larger assemblies via intermolecular hydrogen bonds.⁸⁸⁻⁹⁰ For example, imide containing resorcin[4]arenes self-assemble into cylindrical dimers by the formation of $\text{N-H}\cdots\text{O=}$ hydrogen bonds (figure 2.5c). Here the cavity size and hence the size of the guests which could be encapsulated was increased dramatically.^{91, 92}

Further functionality can also be introduced by the addition of metal binding moieties into the upper rim. With this, the resorcin[4]arene can bind a substrate in a certain arrangement that is then activated by the metal centre.^{93, 94} One example is a resorcin[4]arene with a Zn(II) salen wall which could catalyse the hydrolysis of a carbonate providing a 10-fold rate increase due to the arrangement of the carbonate in the cavity.⁹⁵ More recently, phosphine groups have also be installed in the upper rim forming bis-gold complexes which can then be used for the catalytic dimerisation of terminal alkyne compounds.⁹⁶ These types of systems closely mimic the activity of metalloenzymes by binding a substrate in a certain arrangement which is then activated by the metal.

Modifications at the upper rim are also possible by derivatisation of the carbon between the hydroxyl groups. Such modifications were utilised by CRAM when developing the carcerands, molecules in 1985 (figure 2.6a).⁷⁴ Carcerands are formed from by disulfide bonding of methylthiol and methylchloride components. Such complexes are statistically unlikely to form and require either a solvent molecule or a suitable guest to act as a templating agent to bring the two components together in the correct arrangement. Once the disulfide bonds are formed and the shell closed, the templating agent is trapped indefinitely within the cage hence the name carcerands.⁹⁷

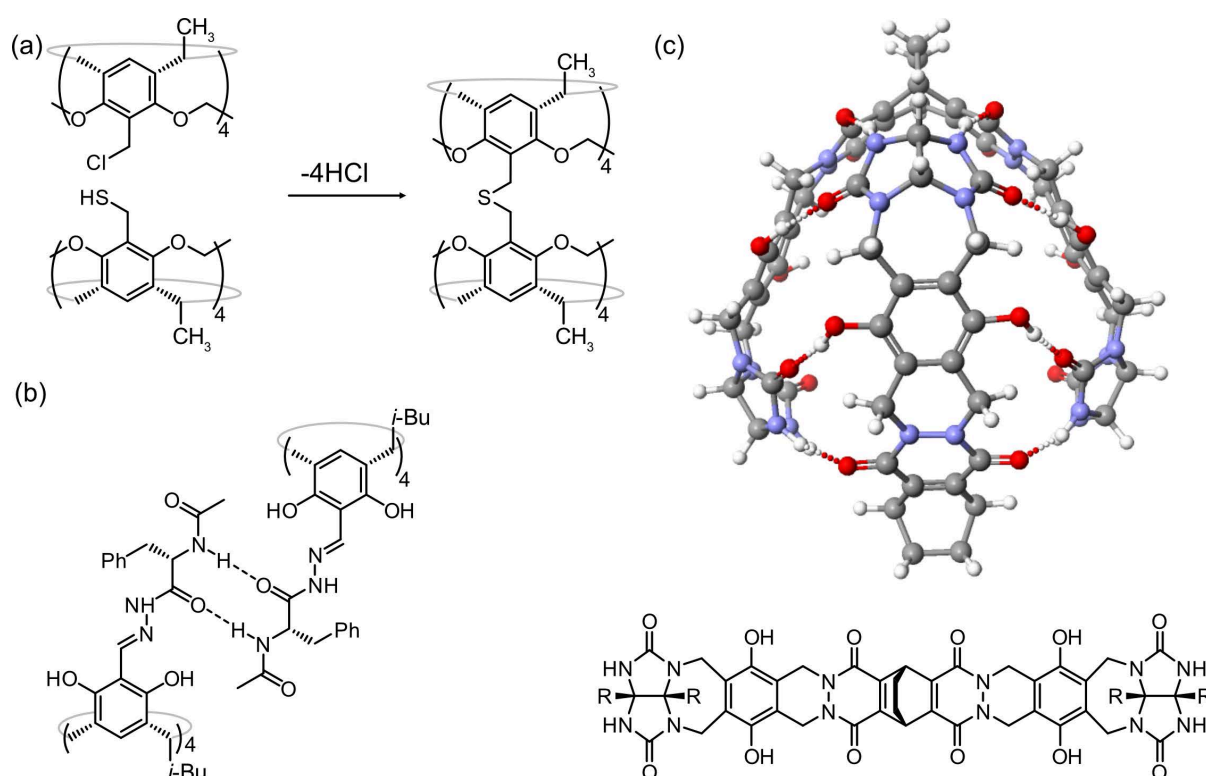


Figure 2.6: (a) Resorcin[4]arenes can be functionalised at the upper rim carbon which was utilised to form the carcerands via disulfide bonds. (b) Peptide based resorcin[4]arenes have also been formed which dimerised via N-H \cdots O hydrogen bonds. (c) The self-complementary hydrogen bonding motif which forms a dimer with a seam of hydrogen bonds resembling that of a softball.

Another example of upper ring modification comes from the SZUMNA group who installed aldehyde groups at these positions which could then be used to attach hydrazine strands via acylhydrazone chemistry.⁹⁸ With this strategy, peptide strands consisting of varying phenylalanine and glycine moieties of mono, di, tri and tetra length were attached to the upper rim of the resorcin[4]arene (figure 2.6b). Monomers self-assemble into hydrogen bonded dimers via N-H \cdots O hydrogen bonds of the interlaced strands. Attachment of the strands to the resorcin[4]arene pre-organises the system which facilitates the subsequent hydrogen bond formation.⁹⁹ It was expected that the longer chains would result in larger cavities when dimerising. However, it was found that the binding motif remains the same for all strands, engaging only the first amino acid in the sequence and leaving the terminal end of peptide chains unbound. Therefore, increasing the strand length did not modulate cavity size.¹⁰⁰

Another prominent example of a hydrogen bonded capsules is the molecular ‘softball’, again, from REBEK and co-workers.^{101, 102} These intricately designed monomers will self-assemble into a dimeric structure with the hydrogen bonding pattern resembling the seam of a softball

ball (figure 2.6c). As the cavity of this structure is large, it is possible for it to encapsulate multiple guests at the same time. This was used to encapsulate p-quinone and cyclohexadiene; two components capable of a Diels-Alder reaction. The reaction between the two will be slow at room temperature but encapsulation into the cavity of the softball accelerates the reaction due to a large increase in the local concentration of the components.^{103, 104}

Hydrogen bonds are popular choice to design complexes as they offer good directionality and reversibility.¹⁰⁵ Another bond which is gaining popularity for these purposes are halogen bonds which possess an even greater degree of directionality.^{18, 106} To utilise halogen bonds, it generally requires the synthesis of both a halogen bond donor and acceptor component which can form capsules analogous to the hydrogen bonded capsules. DIEDERICH group used such an approach with a perfluorinated iodophenyl resorcin[4]arene and an analogous pyridyl resorcin[4]arene to form a halogen bonded capsule (figure 2.7a).¹⁰⁷ It is also possible to form capsules using linear 3c-4e bonds with a cationic halogen in a +1 oxidation state, X^+ , interacting with two Lewis bases.²⁰ The Lewis bases can be the same meaning that a single

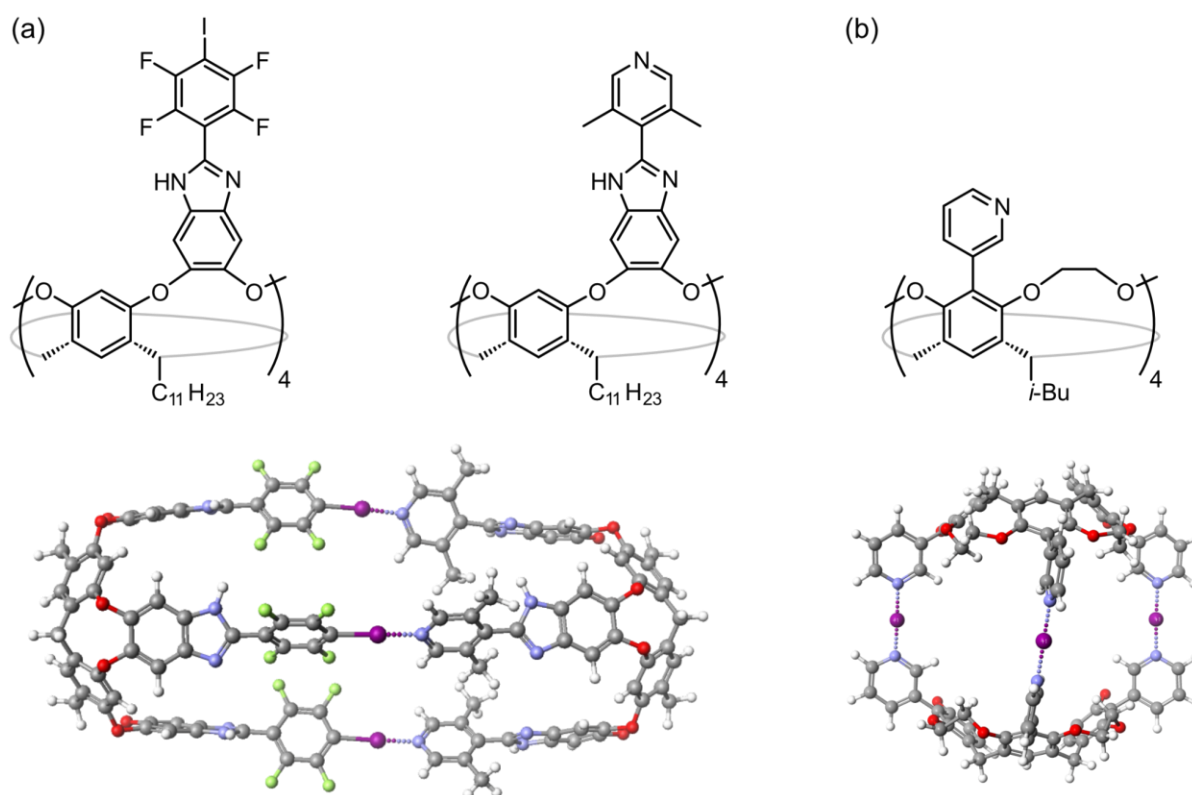


Figure 2.7: (a) Dimeric capsules can be formed from distinct halogen bond donor and acceptor components. (b) 3c-4e bonds with iodine(I) cations can also be used to form capsules via the $[N-I-N]^+$ bonds. In this approach, the two components of the dimer can be the same.

component can be used to generate larger structures via $[L-X-L]^+$ bonds which was used by RISSANEN to form capsules via four $[N-I-N]^+$ bonds (figure 2.7b).¹⁰⁸

2.1.5 Metal-Organic Cages

Metal-organic cages are another class of host which receive significant research focus.¹⁰⁹ The well-defined metal geometries allow the construction of diverse complexes through the rational design of ligands.¹¹⁰ The ligands themselves can be quite simple but can be combined with the metal to form different shaped polyhedra. The shapes which can be formed with metal-organic complexes are essentially endless due to the tunability of the systems but squares,^{111, 112} tetrahedrons,¹¹³ and cubes are commonly seen.^{43, 114} Typically, the systems will be described with M_xL_n nomenclature with M representing the metal, L the ligand with x and n their respective amounts. Although this description does not actually provide the structure, certain stoichiometry will generally be synonymous with a specific shape.³⁴

The principles of using simple ligands to generate complex architecture is elegantly demonstrated by FUJITA and co-workers in their work using Pd(II) metals and bipyridine

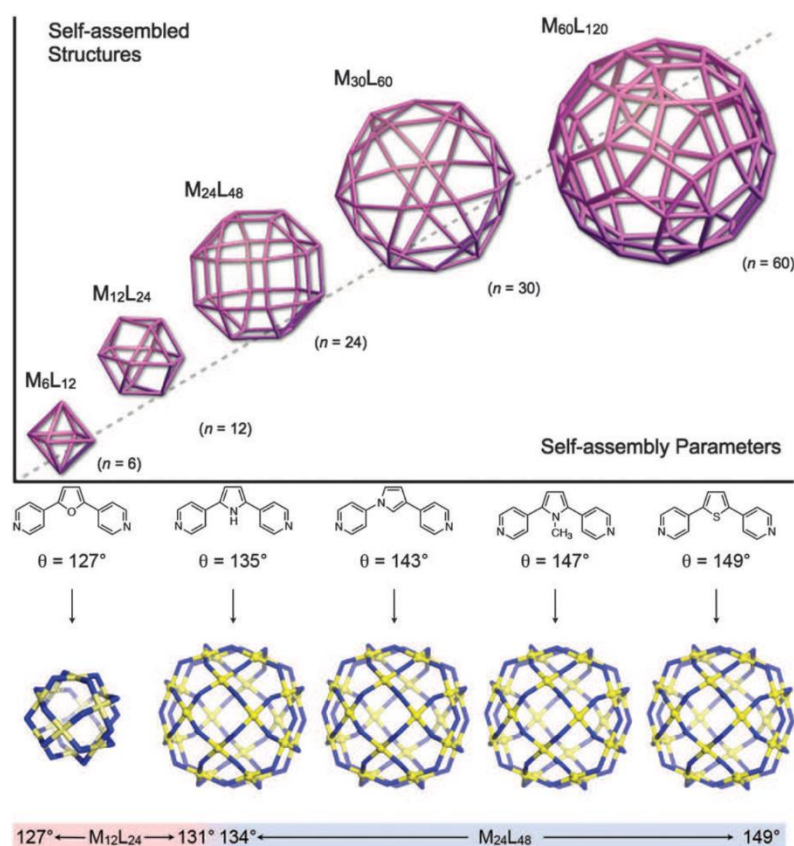


Figure 2.8: Progressively larger Pd(II) metal sphere shaped polyhedra formed from ligands with slight variations in their dihedral angle. Used with permission from the Royal Society of Chemistry.¹¹⁵

ligands. When the 4,4'-bipyridine ligand is combined with ethylenediamine Pd(II), it forms a molecular square with M_4L_4 stoichiometry.¹¹¹ Modification of the ligand via a spacer group between the pyridines could be used to construct progressively larger spheres (figure 2.8).¹¹⁵ The key to generating the larger structures is the dihedral angle of the ligand where minor changes have a large impact on the self-assembled structure. Currently, the largest complex formed to date is a $M_{48}L_{96}$ sphere, but it is predicted that an even larger $M_{60}L_{120}$ complex can be made. These giant cages can potentially bind proteins bringing a number of possible applications.¹¹⁶

Another classic metal-organic cage is the M_4L_6 tetrahedron formed with octahedral geometry metals with bis-catechol ligands.¹¹⁷ M_2L_3 helicates can also form from these building blocks so in order to form the M_4L_6 , it is necessary to design the ligand so formation of the tetrahedron is favoured. RAYMOND group achieved this by including a naphthalene spacer in the ligand which led to the catechol binding moieties being offset which prevents helicate formation. Thus, the M_4L_6 tetrahedron could be formed with the naphthalene spaced ligand and Ga(III), Ge(IV) or Ti(III) metal centres (figure 2.9a). The M_4L_6 tetrahedra are capable of encapsulating a range of cationic guests from small quaternary ammonium ions through to metal complexes.¹¹⁸ By encapsulating a Rh(I) complex it was possible to selectively isomerise alcohols as only certain alcohols could be co-encapsulated with the Rh(I) catalyst (figure 2.9b).¹¹⁹ It is also possible to form M_4L_4 tetrahedron cages by using a tris-bidentate ligand instead of bis-bidentate ligands with the ligands acting as a panel of the face rather than spanning the edge like in the M_4L_6 cages.¹²⁰ Furthermore, octahedral shaped cages with M_6L_4 stoichiometries could be formed by utilising tritopic, monodentate ligands with Pd(II) complexes.¹²¹

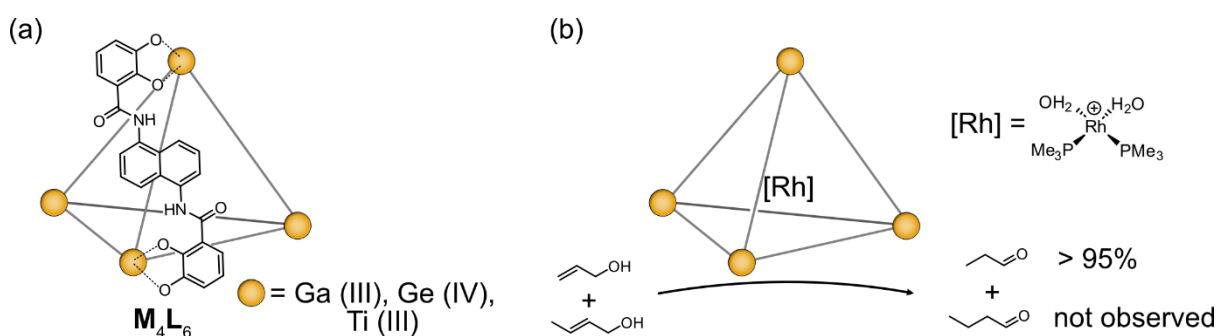


Figure 2.9: (a) M_4L_6 tetrahedra. (b) Substrate specific oxidation of alcohols within the cavity of the cage.

WARD group developed a M_8L_{12} cubic cage using octahedral metals with bis-bidentate bridging ligands (figure 2.10a). Here the central connecting moiety of the ligand also plays a key role in the structure of the cage. If meta-phenyl or pyridine spacer are used, the cage will form a distorted cube with corner angles that deviate significantly from 90° .¹²² When a 1,5-naphthalene moiety is used as spacer a more stable, cubic structure is formed.¹¹⁴ The stability enhancement comes from five π - π stacks composed of three electron deficient pyridyl pyrazole metal coordination components intercalated with two of the more electron rich 1,5-naphthalene moieties.¹¹⁴ The ligands can also be endowed with methylhydroxy groups (L^W) making the cage water soluble and enabling it to bind guests via hydrogen bonding with the hydroxy group or in its cavity via the hydrophobic effect.^{56, 123} Due to ion pairing with the metal centres, the cage will also accumulate anions in the portals of the faces. By accumulating hydroxide ions, the cage can catalyse the Kemp reaction of an encapsulated benzisoxazole to 2-cyano-phenolate. The 2-cyano-phenolate is hydrophilic which means it is expelled from the hydrophobic cavity permitting catalytic turnover (figure 2.10b).¹²³ The cage also catalyses the aldol condensation of indane-1,3-dione (ID) by binding two IDs within the cavity which accelerates the intermolecular reactions due to an increased local concentrations of reactants.⁵⁶

Given the different binding modes available to the M_8L_{12} cubic cage, it should be capable of binding a high number of guests simultaneously which would have potential uses for additional catalysis reactions. However, to date, high stoichiometry guest binding has not

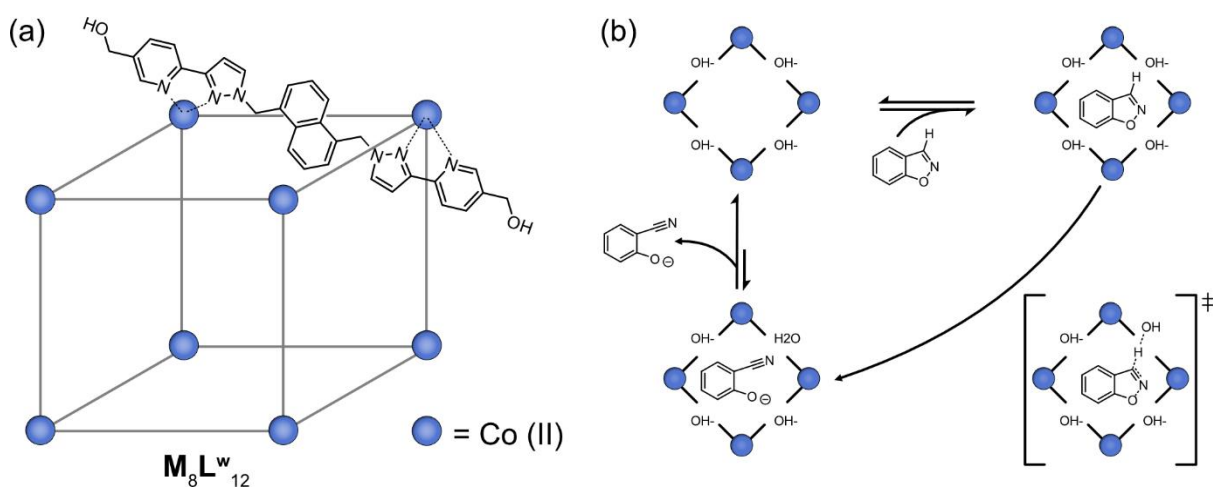


Figure 2.10: (a) M_8L_{12} cubic cage with methylhydroxy containing ligand (L^W). (b) Catalysis of benzisoxazole to 2-cyano-phenolate via the accumulation of hydroxide anions around the encapsulated benzisoxazole. The 2-cyano-phenolate is hydrophilic and expelled from the hydrophobic cavity.

been observed via NMR or X-ray crystallography.^{56, 124, 125}

2.1.6 Rotaxanes, Pseudorotaxanes and Mechanically Interlocked Molecules

As mentioned in section 2.1.3, rather than forming side on complex, 21-crown-7 and larger crown ethers will thread onto secondary ammonium stations to form pseudorotaxanes and rotaxanes.⁶⁷ Pseudorotaxanes and rotaxanes can be composed of more than just crown ethers and ammonium stations so the general terms 'macrocycle' and 'axle' will be used henceforth. The distinction between pseudorotaxanes and rotaxanes is that in pseudorotaxanes the macrocycle can de-thread again whereas in rotaxanes dethreading is blocked by stopper groups (figure 2.11a).¹²⁶ For rotaxanes, the macrocycle can be said to be kinetically trapped on the axle but how big the dethreading barrier needs to definitively be classed as a rotaxane is undefined. Temperature, solvent and the counterion(s) all play a role but the main determinate of barrier height will be the size of the macrocycle relative to the stopper groups.¹²⁶ For instance, a 21-crown-7 can move over an alkyl chain but is too small to move over a phenyl moiety, whereas the larger 24-crown-8 is able to move over phenyl groups requiring even larger stoppers to trap it on the axle.

Rotaxanes can be formed by several different methods (figure 2.11b).¹²⁷ One method is 'capping' where the macrocycle threads onto the axle with at least one open end to form a pseudorotaxane before subsequent attachment of the stopper group(s) to form the rotaxane. Capping reactions needs to be highly efficient and quick, with click chemistry a popular reaction to use. 'Clipping' is another strategy for rotaxane formation, where the macrocycle is formed around an axle which already possesses stopper groups. One way of employing this strategy is to use a ring-closing metathesis (RCM) of a bis-alkene moiety. 'Slipping' is the final

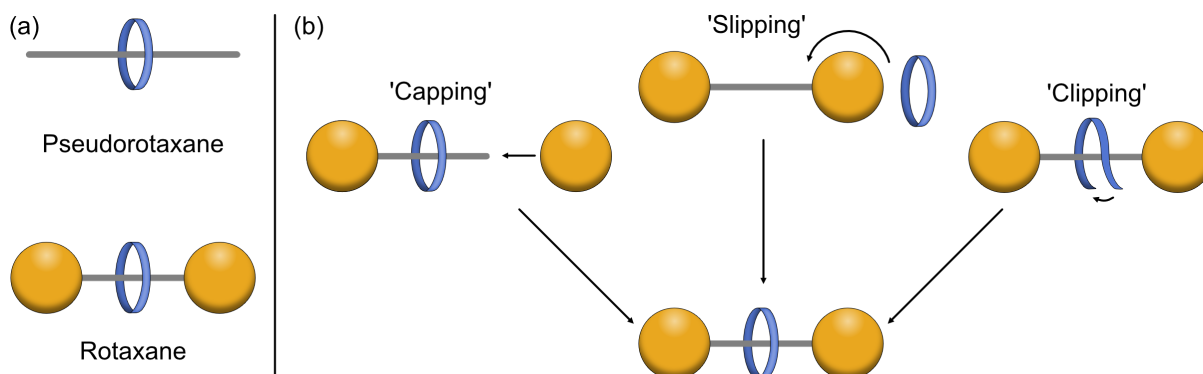


Figure 2.11: (a) Principle of pseudorotaxanes and rotaxanes. In pseudorotaxanes the macrocycle is able to de-thread from the axle compared to a true rotaxane where the macrocycle is blocked from dethreading by the bulky stopper groups. (b) The different strategies to form rotaxanes.

strategy that will be discussed and is somewhat cruder than the other methods as it simply involves the macrocycle slipping over the stopper at elevated temperatures. The very existence of such a strategy demonstrates that the line between pseudorotaxane and rotaxane can be blurry.

Rotaxanes along with catenanes and knots form the class of compounds known as mechanically interlocked molecules (MIMs) (figure 2.12).^{126, 128} MIMs bear a mechanical bond which prevents the dissociation of the different components, or unravelling of the structure in the case of knots, due to an "entanglement in three-dimensional space."¹²⁹ In other words, the different components cannot dissociate from each other without breaking a covalent bond.¹³⁰ In this way, the different components are not covalently linked together but are trapped together by the mechanical bond.

This is clearly seen with catenanes which consist of multiple interlocked rings where the number of components is enclosed within square brackets. ¹³¹ The first [2]catenane was synthesised by WASSERMAN in 1960 using a 'statistical approach' where some ring closure of a macrocycle will occur within another macrocycle to form the [2]catenane.¹³² However, the likelihood of this happening is extremely low meaning that the final product was only formed in infinitesimally low yields and could not be directly characterised. In 1983, SAUVAGE and DIETRICH-BUCHECKER improved the synthesis dramatically by employing a template approach. They used Cu(I) to position phenanthroline containing phenol groups before double cyclisation to form the [2]catenane (figure 2.13).¹³³ Such template approaches are still the primary method of forming MIMs.¹³⁴

Knots on the other hand are entangled molecules which cross over themselves. Knots can be described in the Alexander-Briggs, X_Z^Y , where X describes the number of crossings in the system, Y denotes the number of discrete components and Z is an arbitrary notation to distinguish knots with the same number of crossings. The concept of topological isomers is



Figure 2.12: The different types of MIMs: Catenanes consist of multiple interlocked rings whilst knots are molecules with entangled conformations.

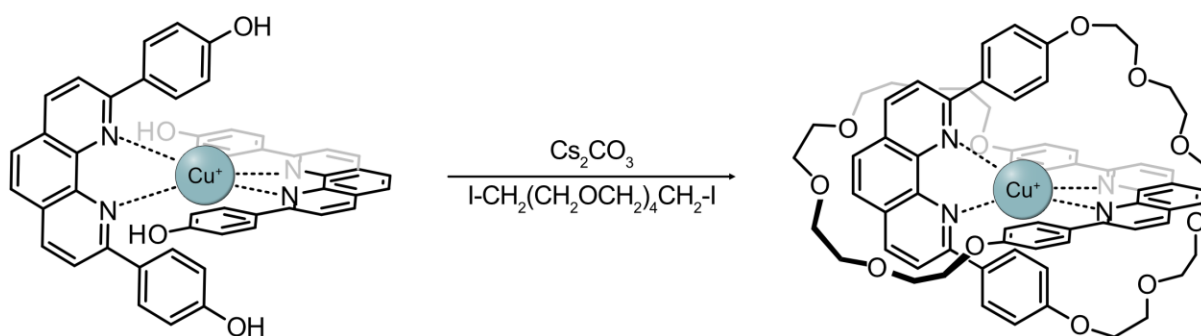


Figure 2.13: Template synthesis of a [2]catenane from Dietrich-Buchecker and Sauvage. The [2]catenane was formed in a yield of 27%.

important where their composition is the same but they differ in their topology.¹³⁵ For instance, SAUVAGE was able to form a molecular trefoil knot (3_1^1) by employing a similar Cu(I) template strategy used to form the [2]catenane but this time with two phenanthroline binding units per component.¹³⁴ In addition to the trefoil knot, a small amount of the macrocycle with no crossing, mathematically considered to be a unknot (0_1^1), was also formed (figure 2.12) which is the topological isomers of the trefoil knot. Extremely complex topologies have subsequently been formed with several 8_2^1 knots synthesised and also [2]catenanes where the interlocked structures are themselves trefoil knots.^{135, 136}

2.1.7 Stimuli Controlled Motion

The interlocked nature of MIMS means that the components can move relative to one another.¹³⁷ For instance, with rotaxanes, it is possible for the macrocycle to *pirouette* around the axle; *rock* back and forth; and also *shuttle* along the axle when there are multiple binding stations.¹³⁸ If the stations are degenerate, the macrocycle will have the same affinity for all stations so will shuttle between them if no barrier prevents its movement. If the stations are non-degenerate, the macrocycle will have different affinity for the stations and will hence reside at one station preferentially over the other(s). It is possible to influence the affinity between macrocycle and the stations by the input of different stimuli and in this way control the motion of the macrocycle between the different stations.¹³⁹ With controlled motion, the systems act as artificial molecular machines (AMMs). AMMs are one of the most active research areas and were the basis of the 2016 Nobel Prize in Chemistry which was awarded to Jean-Pierre Sauvage, J. Fraser Stoddart and Bernard L. Feringa.

One way to control shuttling is by protonation/deprotonation. GIUSEPPONE group used this

principle to design a 'sliding' [c2]daisy chain rotaxane (figure 2.14).¹⁴⁰ A [c2]daisy chain is a rotaxane dimer where the component monomer contains both a macrocycle and binding station on the same unit which then forms a double threaded, symmetric dimer.^{141, 142} In this work, the axle contained ammonium and triazolium stations. The dibenzo-24-crown-8 has higher affinity for the ammonium station but the triazolium becomes preferred upon deprotonation of the ammonium leading to shuttling of the macrocycle. Both monomers shuttle and thus the two slide over one another leading to an overall expansion of the system. The process is reversed upon protonation back to the ammonium leading to contraction back to the original state. With this mechanism, the pH can be used to control the contraction and expansion of the system and make [c2]daisy chain interesting for their ability to act as artificial muscles.^{141, 143}

Another popular method of inducing motion is via redox switching. This was recently utilised by STODDART in the construction of a rotaxane based artificial molecular pump (figure 2.15a).¹⁴⁴ These compounds use a delicate interplay of steric and Coulombic barriers to pump macrocycles onto the axle out of the chemical equilibrium. The macrocycle in this case is the redox switchable cyclobis(paraquat-p-phenylene) (CBPQT) known colloquially as the 'blue box'. The axle consists of a cationic 2,6-dimethylpyridinium (PY⁺) stopper attached to a redox-

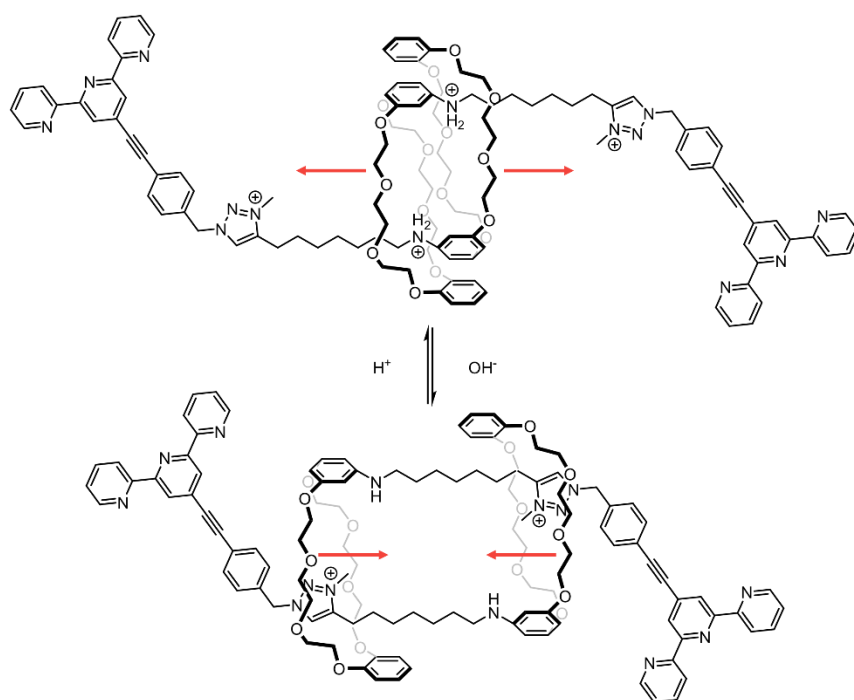


Figure 2.14: Contraction and expansion of the [c2]daisy chain can be controlled by the protonation/deprotonation of the ammonium station.

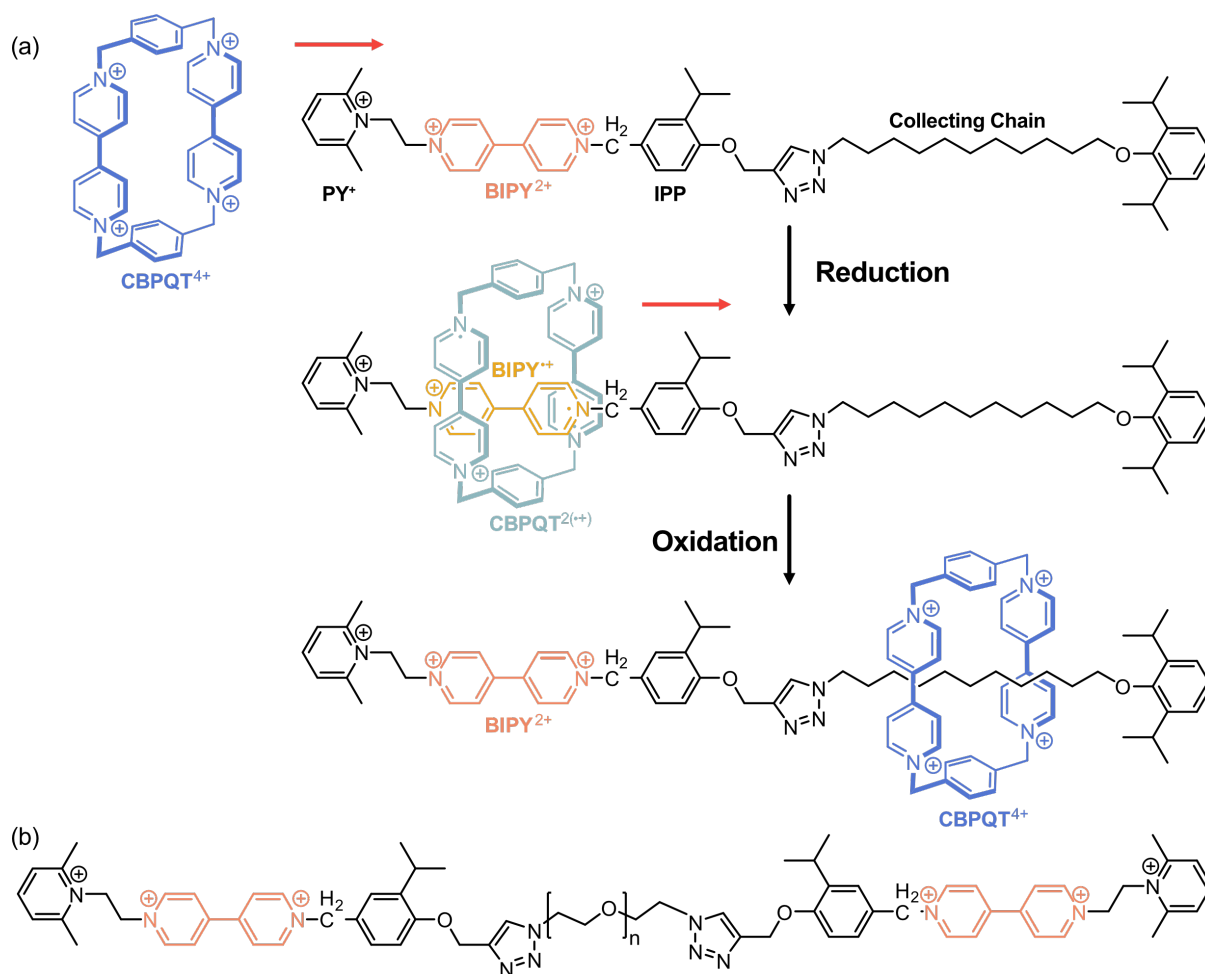


Figure 2.15: (a) Operation of the molecular pump from Stoddart and co-workers. The CBPQT²⁽⁺⁾ can move over the PY⁺. Subsequent oxidation to CBPQT⁴⁺ increases the charge repulsion such that the macrocycle is pumped over the IPP unit to the collecting chain. (b) Double pumping cassette tethered by a polyethylene glycol collecting unit that can collect up to 10 macrocycles.

active bipyridinium (BIPY²⁺) unit. An isopropylphenylene (IPP) barrier is connected to an alkyl collecting chain with a sterically bulky 2,6-diisopropylphenyl stopper at the end.¹⁴⁵ The coulomb barrier between CBPQT⁴⁺ and PY⁺ is initially too high for CBPQT⁴⁺ to be able to thread onto the axle. Reduction of the systems forms CBPQT²⁽⁺⁾ and BIPY⁺, respectively, and the Coulomb barrier between CBPQT²⁽⁺⁾ and PY⁺ is low enough that CBPQT²⁽⁺⁾ can thread onto the axle driven by trisradical tricationic interactions with BIPY⁺. Oxidation back to CBPQT⁴⁺ and BIPY²⁺ leads to significant charge repulsion that forces CBPQT⁴⁺ to shuttle away. However, as in the initial state, the barrier to pass back over PY⁺ is too high and thus the CBPQT⁴⁺ is pumped over the IPP barrier to the alkyl collecting chain. The macrocycle residing on the collecting chain, cannot move back over the IPP, even when reduced, as it cannot overcome the steric barrier trapping it on the collecting ring. This allows the process to be repeated and pump a second ring onto the pumping station in the same manner.¹⁴⁶ The number of

macrocycles threaded onto the axle was able to be increased to ten by tethering two pumping cassettes with a polyethylene glycol linker which serves as the central collecting chain (figure 2.14b).¹⁴⁷ In these systems the reducing and oxidising agents (Zn dust and NOPF₆, respectively) fuel the pumping of the cassettes onto the axle.

2.1.8 Photoswitches

Light is one of the most popular stimuli to induce switching as it has high spatiotemporal control, operates without waste, is highly efficient and accesses metastable states which cannot be accessed thermally.^{148,149} This can be understood by looking at the potential energy surface (PES) between a thermodynamically more stable state, I, and a metastable state, II, separated by a barrier (figure 2.16a). In a thermal equilibrium, the population will predominantly reside in the global minimum, I, as governed by the Boltzmann distribution. Excitation with light instead leads to a temporary population of an excited state which then relaxes back to the ground state via the top of the barrier where it can fall into either I or II. If the wavelength of light aligns better with the excitation wavelength from I, then more molecules will be excited from I than II and thus under constant irradiation, the system is pushed towards II.

State I can be repopulated in a thermal process by surmounting the barrier with the half-life dependent on the barrier height and the temperature of the system. For some systems, thermal relaxation will occur spontaneously when not under irradiation forming a so-called

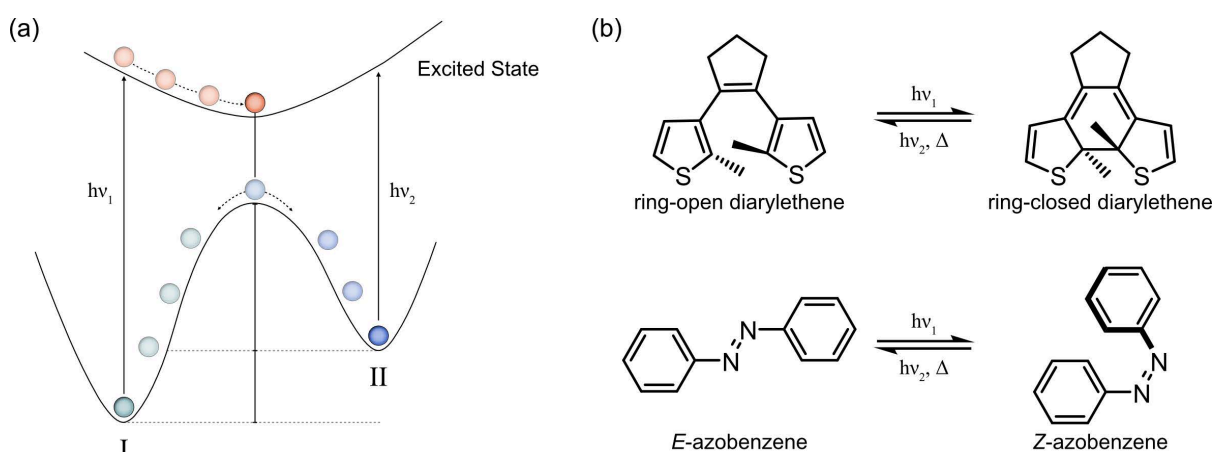


Figure 2.16: (a) Archetypal PES of a photoswitch. An electron is promoted from the ground state, I, to a an excited state by a certain wavelength of light. Relaxation to the ground state via the top of the barrier allows it to fall into metastable state, II. The reverse process is also possible by light or via heating. (b) Structure of common photoswitches, diarylethene (top) and azobenzene (bottom).

T-type switch.¹⁵⁰ The opposite are P-type switches where the barrier is high enough to permit survival of the metastable state for an extended period of time at reasonable temperatures. Transition from II to I can also be achieved photochemically by irradiation with a wavelength of light that better matches the excitation wavelength from II.

Complete population of the metastable state is not practically achievable as some amount of excitation from II will inevitably occur at the excitation wavelength of I leading to population of both I and II. The ratio between the occupancy of these two states at a certain wavelength is the so called photostationary state (PSS) of the system and is a dynamic process akin to a photochemical equilibrium between the two states. The PSS and the thermal lifetime of a photoswitch are important parameters when considering the utility of a photoswitch. Photofatigue is another factor which relates loss of switching under prolonged irradiation due to the formation of by-products, switch breakdown etc.¹⁵¹

Perhaps the most important parameter of a photoswitch is the actual change that the switching can induce. There are two main mechanisms by which photoswitching can occur: either by 6π -electrocyclisation or via double-bond isomerisation.¹⁵¹ For 6π -electrocyclisation, e.g. diarylethenes (figure 2.16b), switching mostly alters the electronic properties of the material whilst double bond isomerisation generally produces structural changes.^{152, 153} The most widely utilised double-bond isomerisation type switches are azobenzenes derivatives which typically have a thermodynamically stable *E*-state and a metastable *Z*-state (figure 2.16b).¹⁵⁴ The reason for their popularity is that they have excellent photophysical properties such as high PSSs, relatively long thermal lifetimes, and switching brings about pronounced structural changes. A popular azobenzene derivative is the arylazopyrazoles which possess excellent switching abilities such as higher PSS and thermal lifetimes.^{155, 156}

Photoswitches have been used in a number of ways in supramolecular chemistry such as to control the assembly of supramolecular polymers or to trigger guest uptake or release.^{157, 158} For instance, SHINKAI created a so-called 'butterfly crown ether' consisting of two 15-crown-5 bridged by an azobenzene (figure 2.17).¹⁵⁹ The crown ethers are too small for a K^+ to fit so there is only low affinity for the *E*-state. In the *Z*-state, the two crown ethers are close enough that they can sandwich the K^+ ion producing a 42-fold increase in affinity compared to the *E*-state. It was possible for the system to transport K^+ from an aqueous source across chloroform interphase to an aqueous receiving phase by binding the K^+ in the *Z*-state and releasing in the

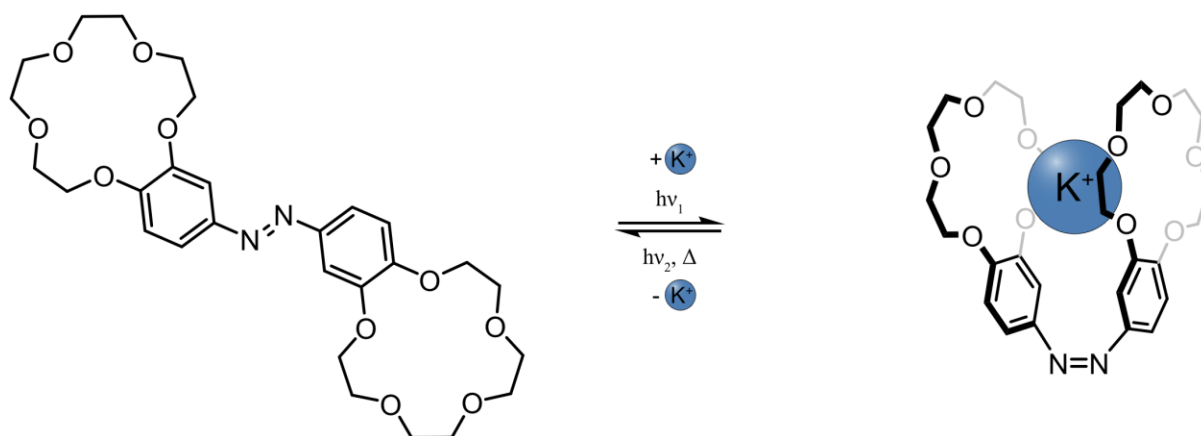


Figure 2.17: Butterfly crown ether. In the *E*-state, there is only low affinity for K^+ ions as it is too large to fit in either of the crown ethers. When switched to the *Z*-state, the K^+ can be bound between the crown ethers acting as tweezers and increases the affinity 42-fold.

E-state.¹⁶⁰

2.1.9 Molecular Motors

An extension of photoswitches are light driven molecular motors. Whereas photoswitches can interconvert between, normally, two states, motors generate continual unidirectional motion. This allows the motor to perform work by consuming energy and potentially drive reactions out of equilibrium, similar to what is seen in biology.¹⁴⁴

FERINGA achieved unidirectional motion around a double bond by incorporating helical and point chirality into the motor.¹⁶¹ In the so-called first generation motor, the double bond connects two identical, chiral, components where steric clashes between the two leads to out of plane bending introducing helicity (figure 2.17a). The helical chirality in addition to the double bond isomerism means there are 4 distinct isomers which can be sequentially formed via successive photochemical and thermal helical inversions (THI) (figure 2.17b).^{162, 163} Irradiation produces $E \rightarrow Z$ isomerisation which also leads to inversion of helicity forcing the methyl group to adopt the less stable pseudo-equatorial position. The methyl can adopt the favoured axial position by a THI where the halves slide over one another. The THI has a lower barrier than the $Z \rightarrow E$ relaxation and hence the forward process is favoured (figure 2.18c). The THI is an equilibrium process, but the reverse barrier is high enough that the process can be considered irreversible providing directionality to the whole process. These two steps result in a 180° rotation of one component in relation to the other and the two processes are repeated to complete the 360° rotation to reform the initial isomer which can undergo

2.2 Mass Spectrometry

2.2.1 Brief History

MS has a long history dating back to the late 19th century and the physicist J. J. Thomson. In 1897, he discovered that a cathode ray is deflected by an electric field if the system is held under reduced pressure. With these experiments, he was able to determine the mass-to-charge ratio (m/z) (referred to by physicists as charge-to-mass (e/m)) of particles he referred to as corpuscles that he postulated must have a mass much lower than hydrogen.¹⁶⁹ Although further measurements were needed, these measurements eventually led to the discovery of electrons and their mass. For his work, Thomson received the 1906 Physics Nobel prize for ‘theoretical and experimental investigations on the conduction of electricity by gases’.¹⁷⁰

The work was later taken up by Thomson’s student Francis Aston who developed the method into one which more closely resembles the MS instruments used today. A gas discharge tube generated the ions and then a sector field like section with sequential electric and magnetic fields deflects the ions based on their m/z which could then be determined by resolution on photographic plates.¹⁷¹ The method was hence termed mass spectrograph and was used to determine the existence of isotopes for various elements such as Neon and Chlorine (figure 2.19).^{172, 173} For this work, Aston received the 1922 Chemistry Nobel prize.

MS was mainly used in physics until instruments became commercially available in the 1940s

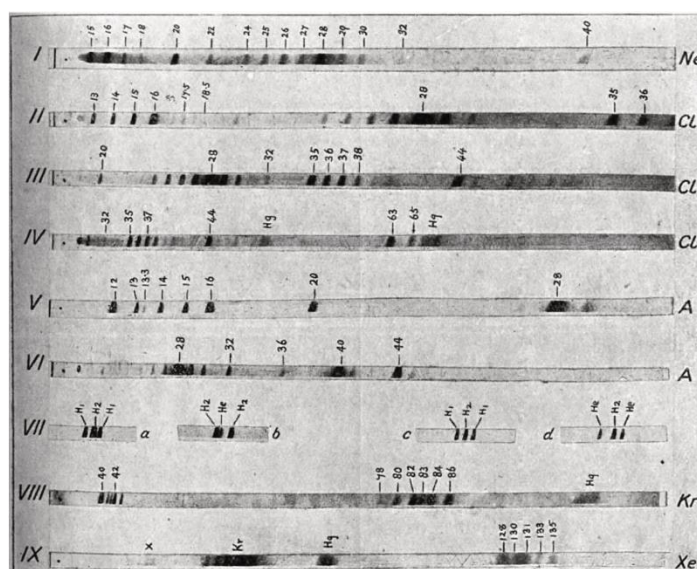


Figure 2.19: Some of the earliest mass spectra from Aston’s mass spectrograph which proved the existence of isotopes. Used with permission from Springer Nature.¹⁷²

where it was adopted for use in other areas.¹⁷⁰ Since then, of course, numerous developments have made major improvements in all aspects of the MS that have allowed it to become so widely utilised today. Some of the improvements which are relevant to the work performed within the thesis are discussed below.

2.2.2 Ionisation

The first step in the MS workflow is to produce gaseous ions and thus ionisation techniques are crucially important. The classic ionisation method is electron ionisation (EI) where samples are vaporised and subsequently bombarded with an electron beam to produce a radical cation by electron ejection from the analyte.¹⁷⁴ This produces predictable ionisation products which aids interpretation of the spectra. However, samples need to be sufficiently volatile, and EI is very harsh producing a large amount of fragment ions. This not only complicates analysis but makes investigation of some systems impossible.¹⁷⁵ Therefore, one of the most important developments for MS was soft-ionisation techniques which can introduce ions into the gas-phase with minimal fragmentation.

The goal in developing soft ionisation techniques was to study large intact biomolecules, e.g. proteins, which were either being destroyed completely or losing their conformation when ionised via harsher methods. For their work in this area, John B. Fenn and Koichi Tanaka shared half of the 2002 Nobel prize for using electrospray ionisation (ESI)¹⁷⁶ and soft laser desorption (SLD)¹⁷⁷, respectively, to ionise biomolecules. A widely utilised soft-ionisation technique is matrix assisted laser desorption/ionisation (MALDI) which is closely related to SLD.¹⁷⁸ Although MALDI was actually developed before SLD, and is much more widely utilised, it was not used to ionise a protein until after SLD. This was enough to mean that MALDI's inventors, Franz Hillenkamp and Michael Karas, were overlooked for the Nobel prize in favour of Tanaka. Amongst these soft-ionisation techniques, ESI is the mostly widely utilised ionisation technique and was used exclusively in this work so it will be discussed in more detail below.¹⁷⁹

Electrospray Ionisation (ESI)

ESI was initially utilised by the working group of Malcolm Dole in 1968 to study polystyrene.¹⁸⁰ It wasn't until some 15 years later that it was adopted by Fenn, coupled to MS, and applied to the study of large biomolecules.¹⁸¹ The working principle of ESI is that it generates charged

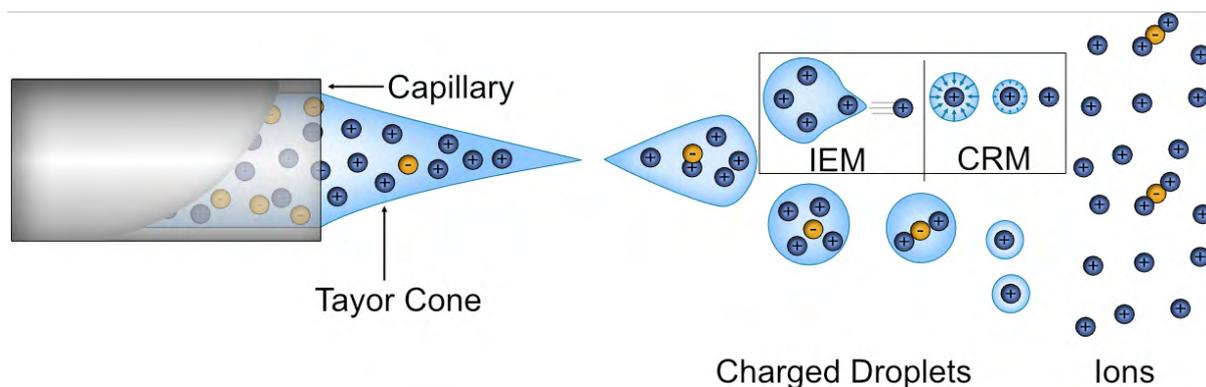


Figure 2.20: ESI process operating in positive mode. A voltage is applied to the capillary which forms a Taylor cone which ejects the charged droplets. The droplets undergo desolvation to produce gaseous ions via either the IEM or CRM.

droplets which undergo desolvation to generate gaseous ions (figure 2.20). This is achieved by pushing a solution through a capillary which has a voltage applied to it resulting in the formation of a so called ‘Taylor cone’ at the capillary tip. The Taylor cone ejects charged droplets which undergo desolvation which pushes the droplets beyond their Rayleigh limit (the point where charge repulsion exceeds the surface tension). At this point, the charged droplets undergo multiple coulombic fissions producing smaller and smaller droplets before free analyte ions are eventually generated.¹⁸²

There are two proposed mechanisms explaining how ions are eventually produced from the charged droplet, the ion evaporation model (IEM) and charge residue model (CRM).¹⁸³ In the IEM, the larger droplets emit ions directly whilst the CRM assumes the droplet undergoes so many coulombic fissions that the droplet eventually contains a single ion which undergoes further desolvation to generate the final gaseous ion.^{184,185} It is thought that smaller ions form via the IEM whilst larger molecules form with the CRM.¹⁸⁶

There are several advantages to ESI that make it so widely adopted. One is that it proceeds directly from solution without the need for matrix preparation and makes it suitable to combine with liquid chromatography.¹⁸⁷ ESI also provides very soft ionisation conditions as the solvent acts as a heat sink with very little residual energy being taken up by the ions themselves. In addition, ESI can be operated in both positive and negative mode and generates multiply charged ions. This effectively increases the mass range of instruments and permits the analysis of high mass molecules and provides ‘wings for molecular elephants’.^{188,189} Another potential benefit of ESI is that the charge imbalance in these droplets could possibly be used to generate novel supramolecular complexes that do not form in solution,

but this has currently not been explored extensively.

2.2.3 Mass Analysers

After ions are generated, their m/z needs to be determined by a mass analyser. Many types of mass analysers exist offering different advantages and disadvantages over one another. Those which were utilised in this work: quadrupoles; time-of-flight (TOF); and Fourier transform ion cyclotron resonance (FTICR), will be discussed below.

Quadrupoles

A quadrupole consists of 4 cylindrical rods equally spaced around a central axis (figure 2.21). A rod operates in a pair with the rod opposite and have static DC and alternating radio frequency (RF) potentials applied to them.^{190,191} The two rod pairings have the opposite polarity and the potential on them fluctuates in time equal to $(+ \text{ or } -)(U+V\cos(\omega t))$ where U is the DC potential, and V and ω the amplitude and frequency of the RF, respectively. This generates a fluctuating electric field between the rods which dictates an ions motion through the quadrupole.^{192, 193} Depending on the ratio between U and V , only ions with a certain m/z will have a stable trajectory through the quadrupole with higher and lower m/z ions being ejected in the different axis. By alternating the voltages, a sweep of all m/z can be performed enabling the quadrupole to act as a mass analyser. As mass analysers, quadrupoles have the advantages that they are simple to implement, robust and cheap but they suffer from relatively low resolving power and mass range. Quadrupoles are commonly employed in tandem MS instrument (section 2.2.4) as mass filters by maintaining voltages that only allow a certain m/z to pass through or to transfer a narrow m/z range.¹⁹⁴

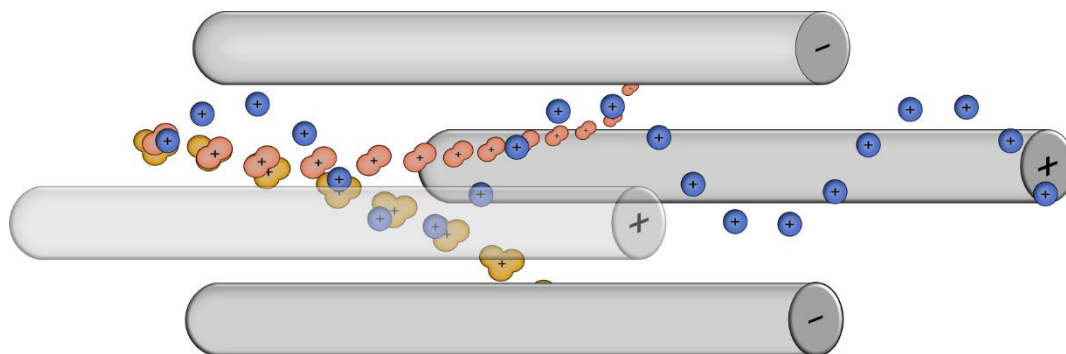


Figure 2.21: Simplified representation of a quadrupole. The voltages of the rod pairing follow $\pm(U+V\cos(\omega t))$ and are set such that only ions of a certain m/z will have a stable trajectory through the quadrupole. A sweep of voltages enables quadrupoles to act as mass analysers. In reality, ion motion will be more complicated than depicted.

Time of Flight (TOF)

TOFs are perhaps the simplest of all the mass analysers to understand as they operate according to fairly rudimentary physics. In TOFs the ions are pulsed by an electric field which leads to the ions taking up a certain amount of energy, E_{el} , depending on ion charge, z , the elementary charge, e , and the applied voltage, U (equation (1)). The E_{el} is converted into kinetic energy, E_{kin} , which enables the ions to travel the field free drift region of set length, l , to the detector (figure 2.22). The time it takes the ions to travel the field free drift region, t , depends on the ion's velocity, v (equation (2)). By substituting (2) into (1), the m/z can be calculated by equation (3).^{195, 196}

$$E_{el} = ezU = \frac{1}{2}mv^2 = E_{kin}(1)$$

$$\therefore m/z = \frac{2eU}{v^2}$$

$$t = \frac{l}{v}(2)$$

$$m/z = \frac{2eU}{l^2}t^2(3)$$

In reality, the ions don't all receive the same energy from the pulse and will instead have an energy distribution which decreases resolution due to incoherent arrival at the detector. This can be partially overcome by a reflectron which uses a constant electric field to reflect the ion towards the detector. Reflectrons correct for kinetic energy differences as higher energy ions will penetrate further into the reflectron and thus take a longer path to the detector, bringing the arrival time into phase with the less energetic ions.^{197, 198} Resolution can be increased

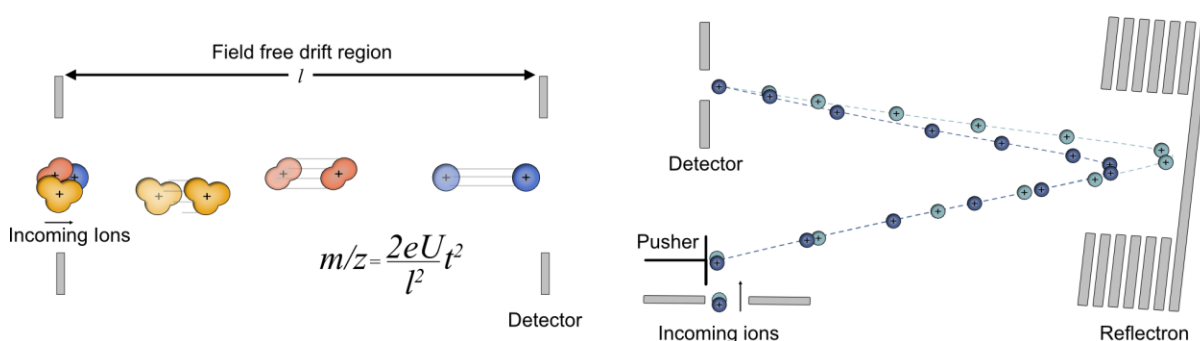


Figure 2.22: Principles of a TOF mass analyser. (a) A linear drift free region is where m/z can be determined by the equation shown where e is the elemental charge, U acceleration voltage and t and l the time and distance, respectively. (b) Resolution can be increased by using orthogonal extraction, increasing the length of the flight tube or incorporating a reflectron.

further by incorporating an ion mirror which reflects the ions back into the reflectron a second time before reaching the detector resulting in a 'W-shaped' trajectory. In addition, orthogonal extraction can also be used to increase resolution by pulsing the ions perpendicular to their initial direction making the starting point of flight equivalent.¹⁹⁹ TOFs offer reasonably high resolution and mass range with fast scan rates while also being cheap and robust.²⁰⁰

Fourier Transform Ion Cyclotron Resonance (FTICR)

Compared to the other mass analysers, FTICRs are perhaps the least conceptually intuitive to understand. In FTICRs, the ions are first trapped axially within a Penning trap using end-cap electrodes (figure 2.23).²⁰¹ A strong, uniform, magnetic field results in the ions orbiting perpendicular to the magnetic field in a circular motion due to the Lorentz force, F , equation (4) where v is the incident velocity of the ion and B is the magnetic field strength.

$$F = zvB \quad (4)$$

The frequency of the cyclic motion, the ion cyclotron frequency, ω_c , is dependent on the m/z of the ion by equation (5).

$$m/z = \frac{eB}{2\pi\omega_c} \quad (5)$$

As can be seen, the relationship is independent of ion velocity, meaning higher resolutions can be obtained as it is not influenced by ion kinetic energy spread as seen with TOFs.²⁰² The

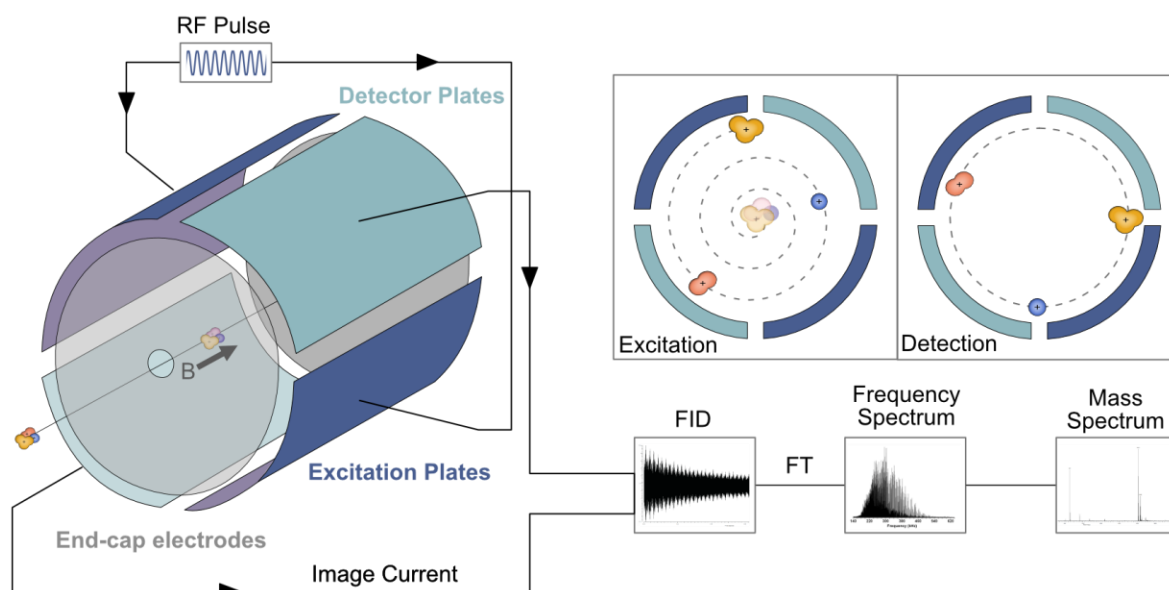


Figure 2.23: Principles of FTICR. The ICRs of excited ions orbiting circularly can be registered by detection plates. A FT can extract individual ion frequencies from the FID and convert them to a frequency domain which can then be converted to a conventional mass spectrum.

ω_c can be registered by two detection plates positioned opposite one another.²⁰³ However, the radius of the ions' orbit is initially too small to be detectable so excitation plates are required to excite the ions by a RF pulse. If the RF pulse matches the ion cyclotron resonance (ICR), the ion will be excited to a larger orbit where their motion induces an image current in the detector plates. A RF sweep excites ions of different m/z and the sum of all ions' image current is known as the free induction decay (FID) or simply transient signal. A Fourier transformation (FT) can extract individual ω_c from the FID and transform them into a frequency domain which can then be converted to a conventional mass spectrum by equation (6).^{204, 205}

$$m/z = \frac{kB}{f} \quad (6)$$

This enables the detection of all ions simultaneously and enables the FTICR to act as a mass analyser and detector without destroying the ions.

FTICRs require higher vacuum ($\sim 10^{-10}$ Torr) to prevent ion activation during their orbit as well as a superconducting magnet, necessitating cooling with liquid nitrogen and helium. This makes FTICRs operationally expensive, however, they are able to achieve extremely high resolution making them useful for highly charged species and/or compounds which are very close in mass.²⁰⁶ In addition, the RF excitation can be used to expel ions from orbit enabling high resolution mass selection and additionally double resonance experiments which can provide information about reaction/fragmentation pathways.²⁰⁷ FTICRs also allow longer ion lifetimes than other instruments allowing uni- and bimolecular gas-phase reactions to be performed (section **2.2.4**) making FTICRs highly versatile and valuable instruments.²⁰²

2.2.4 Mass Spectrometry Techniques for Structural Characterisation

The determination of m/z by MS is a crucial step in characterisation of any compound. However, it is important to recognise that m/z alone is not structurally informative, so additional techniques are required to provide such information. Thankfully, there are a several techniques which allow further investigation of an ion to determine information about structure, energetics, and reactivity, which will be discussed below.

Tandem Mass spectrometry (MS/MS)

MS/MS is the combination of multiple mass analysers into a single instrument where the first mass analyser mass selects an ion of interest with the second used for conventional mass analysis.²⁰⁸⁻²¹⁰ There have been a number of different combinations of mass analysers used over the years for this purpose. These days, hybrid instruments are popular with a combination of a quadrupole and TOF commonly used.²¹¹

With MS/MS, it is possible isolate and study an ion of interest in greater detail using different MS techniques. One typical use of MS/MS is to study the fragmentation of an ion after its activation by one of several methods. While it is possible to achieve in-source fragmentation during the ionisation process, MS/MS is distinct in that it occurs after ionisation with mass selected ions so the daughter ions which form can be unambiguously assigned to the parent ion. This eases analysis and also enables mixtures and impure samples to be studied and is particularly useful for ESI which produces multiply and differently charged ions.²¹²

Several methods exist which can be used to activate the ions with a large component of these using the absorption of photons to induce fragmentation e.g. Infrared multiple photon dissociation (IRMPD), blackbody infrared dissociation (BIRD). They require extended irradiation times and so rely on an ion trap instrument of some description e.g. FTICRs. One downside of activation via photons is that the ion may not absorb at that wavelength, which is more likely to occur with smaller compounds.¹⁶

Electron capture dissociation (ECD) and electron transfer dissociation (ETD) are other activation methods and work, as the name suggest, by introducing electrons to gaseous ions. ECD & ETD are commonly utilised in the study of peptides as they produce predictable cleavage patterns which can be used for peptide sequencing and can also be used to probe gas-phase reduction processes.²¹³

The most common method of ion activation comes via collisions. The collisions can either be with a surface as in surface induced dissociation (SID), or more popularly with an inert gas in collision induced dissociation (CID). CID was used extensively throughout the thesis and will be discussed in more detail below.

Collision Induced Dissociation (CID)

CID is the most widely used fragmentation technique as it is non-selective, meaning that it can be used to analysis all ions, whilst being simple and cheap. CID is conceptually straightforward and operates by accelerating the ions with an electric field and then colliding them with a static inert collision gas (figure 2.24).²¹² The collision converts some of the ions' kinetic energy into internal energy in the form of vibrations which results in potential rearrangement at low energies or fragmentation if this energy is sufficiently high.²¹⁴ CID can be utilised to investigate fragmentation pathways of ions which can be used to determine structural information e.g. sequence information of multithreaded pseudorotaxanes²¹⁵ or guest binding modes.²¹⁶

In addition to the fragmentation pathways, it is also possible to determine the relative stability of different ions through the construction of survival yield (SY) curves. SY curves can be generated by determining parent ion relative intensity at a series of increasing collision voltages. If a single fragmentation pathway is followed, a plot of the parent ion relative intensity versus collision voltage should produce a sigmoidal shaped curve (figure 2.25). The inflection point of the curve represents the collision voltage at which the parent ion is 50% of the total intensity ($SY_{50\%}$) and is commonly used to provide a relative ranking of gas-phase stabilities. If multiple sigmoidal slopes are observed, this is evidence of multiple fragmentation pathways or the presence of different isomers/conformation.²¹⁷ For a valid comparison, it is important to correct for the kinetic shift of the ions by using one of the ions as a reference and applying the correction based on the relative degrees of freedom.²¹⁸ If this is not completed, a larger ion with more DOF will appear to be more stable due to its ability to vibrate more.

Determination of absolute bond dissociation energy using CID is unfortunately quite challenging as it is necessary to precisely account for all the different energies. The internal

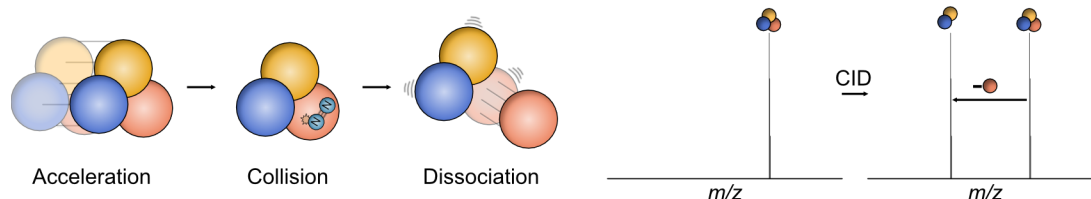


Figure 2.24: Principles of the MS/MS technique of CID. The ion is accelerated into an inert collision gas which converts some of the ion's kinetic energy into internal energy. Fragmentation follows if this energy is sufficiently high.

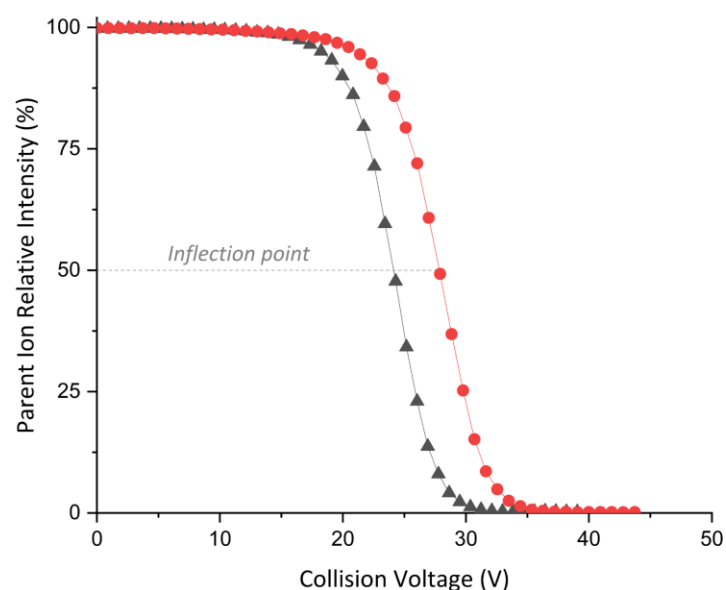


Figure 2.25: Representative SY curves demonstrating the sigmoidal curve expected. In this instance, the red curve is rightward shifted indicating greater stability as higher voltages are required to induce dissociation.

energy of the ions after ionisation is difficult to ascertain as the ions cannot thermalise and hence will not represent a Boltzmann distribution of energies.^{219, 220} Furthermore, it is necessary to accurately determine the kinetic energy of the ions with both of these requirements necessitating the use of specialised instruments such as guided ion beam tandem mass spectrometers.²²¹

It is however possible to convert the collision voltage to a centre of mass energy (E_{com}) as the maximum energy transfer is limited by the conservation of linear momentum which for a stationary target gas is equal to:

$$E_{com} = \frac{zVm_n}{m_n + m_{ion}}$$

Where z is the charge on the ion, V the collision voltage and m_n and m_{ion} the mass of the collision gas and ion, respectively. After undergoing a collision, it is impossible to determine an ion's kinetic energy, so the above relationship is only true in instances of a single collision.²²⁰

Ion-Mobility Mass Spectrometry (IMS)

Out of all the MS/MS techniques, IMS offers the most direct structural information as it determines the mobility of the ion in a buffer gas which can be related to an ion's size and shape.²²² Ion mobility has widespread applications, for example being utilised in screening

and sensing of explosive and other compound.^{223, 224} When coupled with MS the potential utility is huge and is employed in many fields of research. Effectively, IMS can be thought of as analogous to gel electrophoresis in the gas-phase where ions move through a cell filled with an inert buffer gas under the influence of an electric field and are separated based on their mobility.²²⁵ Although the mechanism of transmission will depend on the exact technique employed, the ions arrival time through the cell will be dependent on its size, shape, and charge. An arrival time distribution (ATD) of the ions can thus resolve ions based on size with, in most instruments, larger ions having a longer arrival time than smaller, more compact ions.¹⁰ With this, IMS adds a new dimension to MS by enabling separation of isomers and conformers.

IMS has a surprisingly long history dating back to instruments as far back as the 1950s.²²⁶ Recently, IMS has become more mainstream as a number of commercially available instruments employing various methods of IMS have been developed. One major benefit of IMS is its ability to calculate ions' collision cross section (CCS). CCS is a property of the ion buffer gas pairing and describes the area of the ion that will undergo a collision with the buffer gas and is typically reported in \AA^2 .²²⁷ Importantly, CCS is instrument independent and, if the measurements are done correctly, can be used to compare across different laboratories and instruments. Furthermore, theoretical CCS values of computational models can be calculated and compared to the experimental value providing a direct link between the experimental results and computational structures. Such structural assignment is particularly powerful when traditional methods e.g. crystal structures or NMR are not feasible.²²⁸

There are several methods of calculating theoretical CCS values which differ in accuracy and computational time. The simplest is the projection approximation (PA) which projects the buffer gas onto the ion and the CCS is calculated as the rotationally averaged 'shadow' of the ion.²²⁹ For these calculations, they consider the Van der Waals radii of both the buffer gas and ion and while the PA calculation is quick, it is also lacks accuracy. The exact hard-sphere (EHS) method models the ion and buffer gas molecules as hard sphere and simulates their trajectories and calculates the collision between them. Upon collisions, the gas-molecules are re-emitted which allows for grazing and secondary collisions.²³⁰ Furthermore, the momentum transfer between the two collision partner is taken into account and makes the EHS more accurate than the PA. The trajectory method is similar to the EHS but considers additional

interactions such as ion-induced dipoles between the ion and buffer gas.²³¹ The collisions are modelled using Lennart-Jones potentials and are overall the most accurate but can be computationally expensive. The convention for reporting theoretical CCS values is to provide the method in superscript and the buffer gas as subscript e.g. TMCCS_{N₂} for CCS values calculated in N₂ with the trajectory method. The experimental values are similar but instead provide the instrument used in the superscript.²³²

The two IMS methods, which were employed in this work, drift tube IMS (DT-IMS) and travelling wave IMS (TW-IMS),²³³ will be discussed below.

DT-IMS: DT-IMS is the simplest method to describe and basically acts as a wind tunnel for ions by transmitting them through a cell filled with an inert drift gas under the influence of a weak electric field (figure 2.26). As the ions travel through this cell, they undergo low energy collisions with the drift gas which slows the ions down and hence a smaller ion which has fewer collisions will have a shorter drift time through this cell than a larger ion undergoing more collisions.²³⁴ The simplicity of the technique is not just beneficial when trying to describe its function but it also enables the direct determination of CCS values.²³⁵ This is because it uses a uniform electric field which can be precisely controlled and modelled and hence it is possible to calculate CCS values directly from arrival times. Ion velocity, v_d , can be determined by equation (7), where K is the ion mobility, E the electric field, d path length and t_d the arrival time.

$$v_d = KE = \frac{d}{t_d} \quad (7)$$

The t_d will typically be measured at a series of different values of E and then the two plotted against each other which should produce a linear curve where the slope is equal to K .²³⁶ A reduced mobility K_0 , which is temperature (T) and pressure (P) independent, can then be

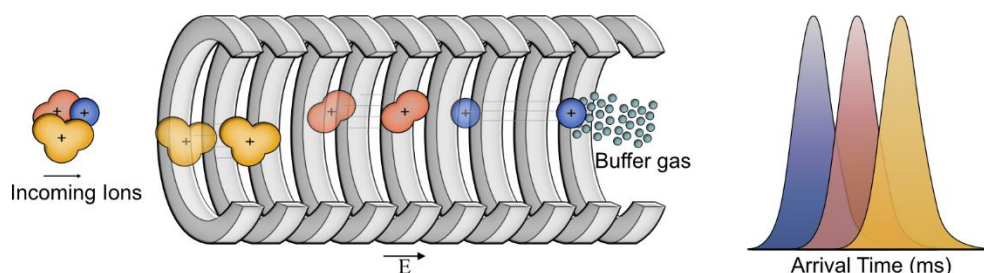


Figure 2.26: Principles of DT-IMS where ions are drawn through a drift cell, filled with a buffer gas, via a weak electric field.

determined by equation (8). With K_0 , CCS can then be calculated using the Mason-Schamp equation (9) where μ is the reduced mass of the ion and buffer gas, k_B is Boltzmann's constant, and N is the number density of the buffer gas.

$$K_0 = K \left(\frac{p}{1013} \frac{273}{T} \right) \quad (8)$$

$$CCS = \frac{3}{16} \sqrt{\frac{2\pi}{\mu k_B T}} \frac{z}{N K_0} \quad (9)$$

The direct determination of CCS values not only simplifies workflow and saves time but also reduces a potential source of error and enables assessment of analytes without suitable calibrants.²³⁷ The resolution ($t/\Delta t$) which a DT-IMS can achieve is dependent on the length of the drift cell but drift gas and pressure are also important parameters. The resolution will generally be lower than for other methods as practical considerations limit cell size. Typically, DT-IMS also have low duty cycle as the ions are injected in a pulse without ion accumulation which is one drawback of them as instruments.²³⁸

TW-IMS: The travelling wave design by Waters corporation was incorporated into the commercially available Synapt HDMS which helped to kick-start the development of commercially available IMS instruments. The cell in TW-IMS instruments is similar to those in DT-IMS but rather than a static electric field, TW-IMS utilises an oscillating one.²³⁶ This is achieved by applying opposite phases of RF voltages to adjacent electrodes to radial confine ions. A superimposing pattern of DC voltages is applied which results in a propagating wave which pushes the ions through the cell (figure 2.27).²³⁹ The velocity that the ions are propelled depends on their mobility with smaller ions being more effectively pushed resulting in shorter arrival times than larger ions. It is possible to control both the wave height and velocity which can influence the ions drift time as ions which cannot keep up with the wave will 'roll over' to the next wave increasing their arrival time.²⁴⁰

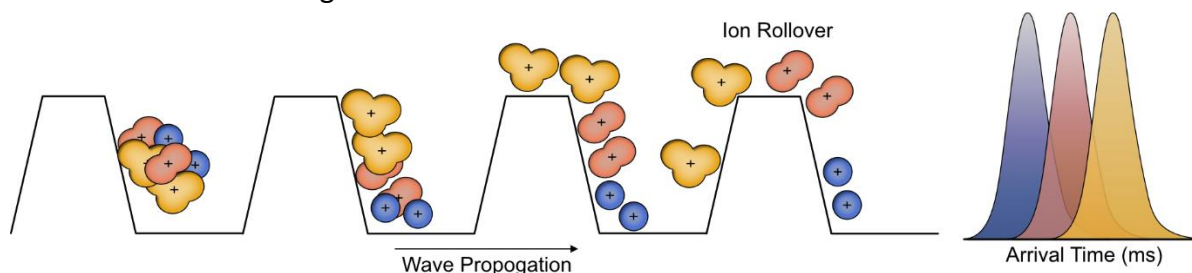


Figure 2.27: Principles of TW-IMS where a propagating wave pushes the ions through the cell. More mobile ions can ride the wave more effectively and will hence travel through the cell more quickly.

Unlike DT-IMS, a direct relationship between arrival time and mobility has not been established due to the continually changing electric field being difficult to model. For this reason, a calibrant of known CCS is required to be able to determine CCS values.²³⁹ To achieve reliable results, the calibrant should be chemically similar to the analyte which is not always possible.²⁴¹ Alternatively, for ions of the same charge state, arrival time can be used to obtain relative size information which can still be informative.

Hydrogen Deuterium Exchange (HDX)

The final MS/MS technique which will be discussed is gas-phase HDX. HDX is a class of bimolecular ion-molecule reaction where labile hydrogens are exchanged for the deuterium(s) of a deuterating agent (e.g. MeOD).²⁴² Although it is possible to use other modified instruments for these measurements, ideally HDX will be performed in an ion-trap instrument where ions storage over longer intervals is possible.²⁴³ Amongst these, FTICRs offer the best performance due to the long ion storage possibilities and the ability to precisely control reaction times.²⁴⁴ FTICRs can perform the reaction in the cell, where exchange is slower but allows for monoisotopic mass selection, or in the hexapole collision cells of certain instruments e.g. Ionspec QFT-7. Here pressure and hence exchange rates are faster and occurs with all ions simultaneously.

The general mechanism of gas-phase HDX initially involves the formation of an encounter complex (figure 2.28a). Proton transfer, isotope scrambling, deuterium back transfer and subsequent reagent dissociation has the net effect of a HDX on the ion. Exchange number can

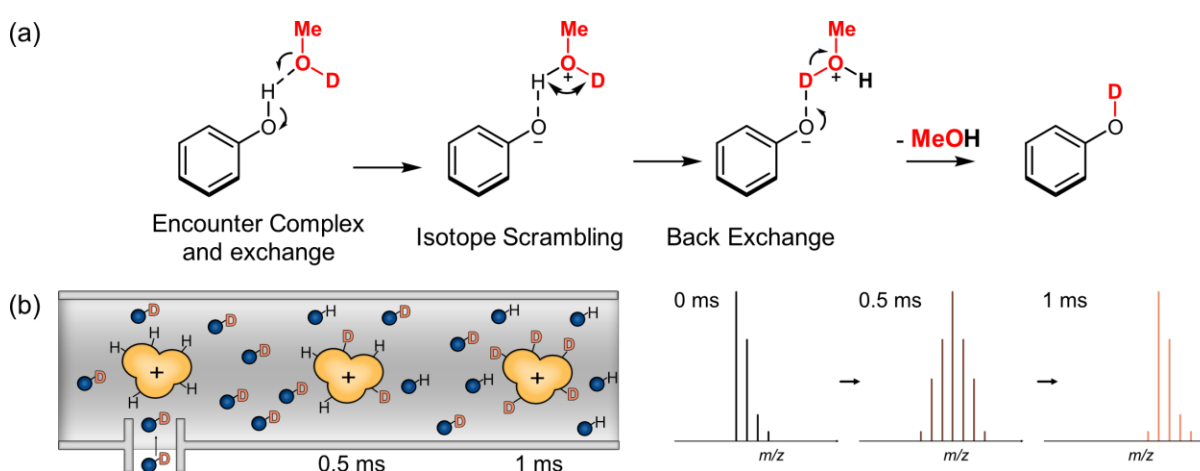


Figure 2.28: (a) General HDX mechanism. (b) HDX setup. Deuterating reagent introduced to chamber containing ions. Reaction interval can be modified, and the exchange followed over time.

easily be followed due to the mass difference between hydrogen and deuterium (figure 2.28b). The rate of the exchange can also be informative as it is dictated by the proton affinity differences between the deuterating agent and the ion. Exchange is prevented if the proton affinity difference is greater than around 85 kJ/mol.²⁴⁵

HDX experiments are more specialised than IMS and CID providing information on hydrogen bonded complexes, which nonetheless represents a large portion of complexes, including proteins and peptides. Indeed, HDX was mostly developed with these biomolecules in mind as it is possible to discriminate between hydrogens which are conformationally buried from those which are exposed and able to exchange. It should be noted that for the analysis of most biomolecules, exchange is typically completed in solution and MS is then used to determine the number of exchanges.²⁴⁶ True gas-phase HDX have been used in the study of synthetic supramolecular systems (section 2.3).²⁴⁷ Here, HDX can distinguish between different hydrogen bonding motifs by the number and rate of exchange. If there is a continuous hydrogen bonding network, the MeOD can be incorporated into the network and the exchange can proceed via a concerted, 1D Grotthuss mechanism. Such exchange is efficient and will hence occur quickly. If there is no continuous network, the exchange may proceed via a relay mechanism which occurs much slower due to the formation of a charge separated species (figure 2.29).^{245, 248}

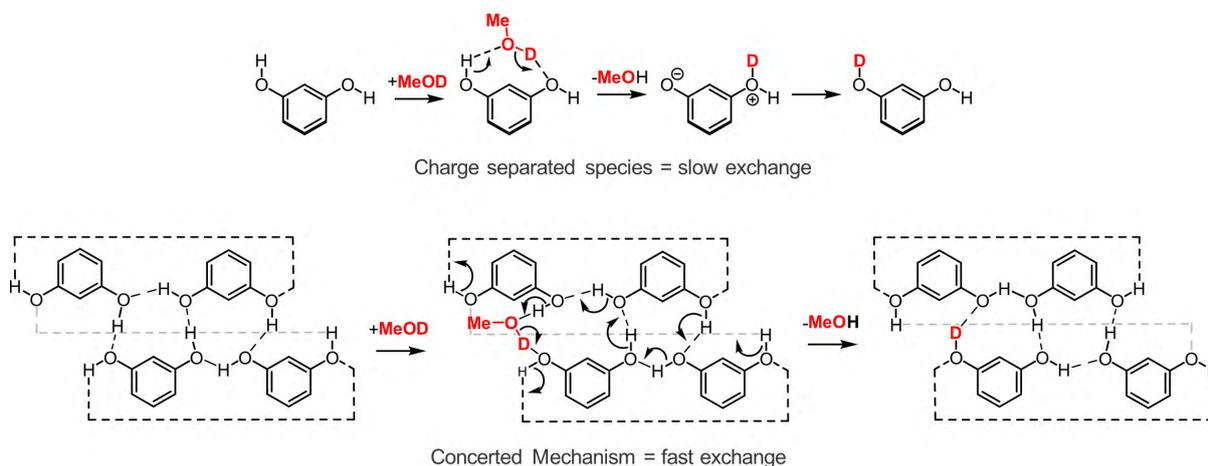


Figure 2.29: HDX mechanisms with a non-continuous relay mechanism (top) and a continuous mechanism in a seam of hydrogen bonds via 1D Grotthuss mechanism (bottom).

2.2.5 Instruments Used

Measurements for the thesis were primarily performed on a Waters Synapt G2-S Q-TOF with the basic schematic shown in figure 2.30. The Synapt G2-S possesses a quadrupole for mass

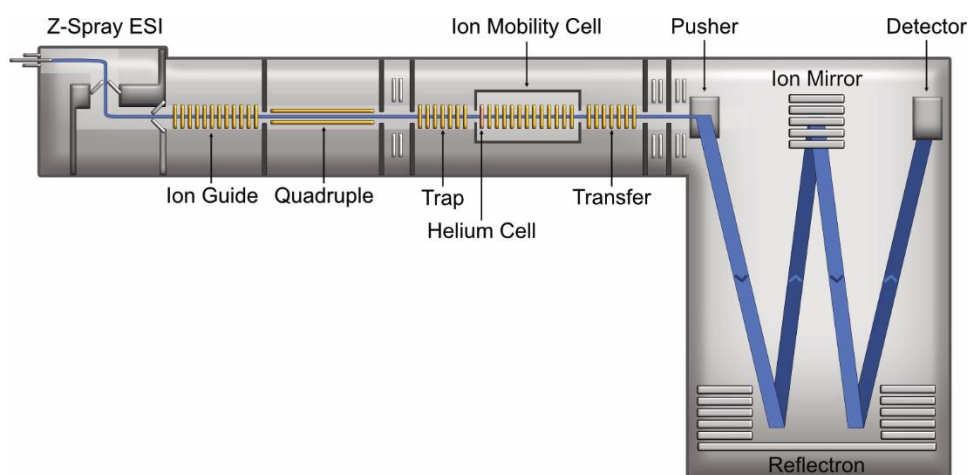


Figure 2.30: Schematic of the Synapt G2-S. The instrument possesses a quadrupole for mass selection, a TW-IMS cell with trap and collision cells either side with a TOF mass analyser.

selection and a TOF for mass analysis. The TOF contains a dual stage reflectron and ion mirror enabling high resolution measurements. The instrument includes a TW-IMS cell with CID cells (trap and transfer) flanking it on either side making it a highly versatile instrument capable of performing CID prior to entrance to the IMS cell or on IMS separated ions. A helium cell prior to TW-IMS cell allows for higher N_2 pressures in the IMS cell, improving resolution. This is because the He balances the N_2 pressure so that leaking is reduced. The He also softens transmission of the ions as they are more mobile in He and scattering is reduced.^{239, 249} This also come with drawbacks as high IMS resolution leads to ion activation and potential conformational changes/fragmentation.²⁵⁰

Other measurements including HDX were performed on a Varian Ionspec FTICR with a 7-tesla superconducting magnet (figure 2.31). The second hexapole can store the ions and be used as a chamber for gas-phase reactions (e.g. HDX) with the quadrupole preventing ions from entering the hexapole. Ions are then transferred to the FTICR cell for mass analysis. In addition, the instrument has an IRMPD laser for ion activation.

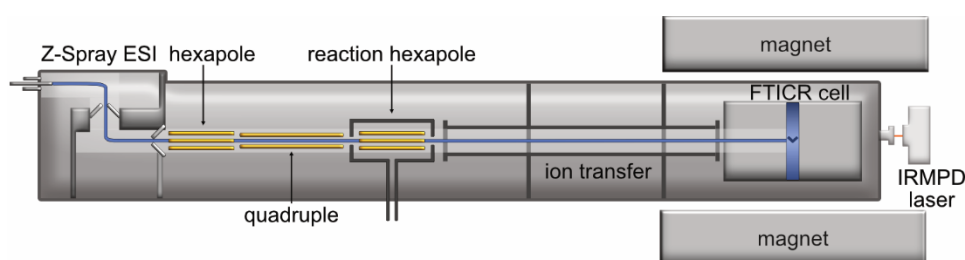


Figure 2.31: Schematic of the Varian Ionspec FTICR. HDX can be performed in the hexapole or in the FTICR cell.

2.3 MS as a Tool to Study Supramolecular Systems

The general benefits of MS are succinctly stated by McLAFFERTY as the three “S” advantages: specificity; sensitivity; and speed.²⁰⁸ There are also several additional benefits that make MS a valuable technique for supramolecular chemistry. Firstly, MS deals with isolated ions so dynamic exchange processes, which complicates analysis in solution, or interference from solvent are not present.^{16, 251, 252} This makes it relatively straightforward to determine a system’s stoichiometry which is one of the most fundamental pieces of information for a supramolecular complex. Another advantage of the gas-phase is that non-covalent interactions, including repulsive ones, significantly strengthen in the absence of solvent. This is clearly demonstrated by the binding strength of NaCl in the different phases with a binding strength of 697 kJ/mol in the gas-phase versus only 9 kJ/mol when the ions are solvated in water.¹⁶ The exception to this is the hydrophobic effect which is not present in the gas-phase as there is simply no longer any water/solvent to fear. Thus, systems binding by the hydrophobic effect may not survive in the gas-phase as they will instead rely on the weaker Van der Waals interactions, in most situations (*vide infra*).²⁵³

Actually generating the assemblies as gaseous ions is another matter. To minimise the chance of the system fragmenting, it is necessary to use soft ionisation methods such as ESI (section **2.2.2**). Sometimes, even when using ESI there will still be difficulties. For example, the resorcin[4]arene hexamer could not be observed via ESI due, at least in part, to the assembly being disrupted by the charge adduct during ionisation.²⁵⁴ However, when a mixture of the resorcin[4]arene and a suitably sized cationic guest were measured, the hexamer was observed and in much higher intensities than other stoichiometries.⁸¹ Here, ionisation aided self-assembly as the charged guest facilitates hexamer formation and harmlessly provides the charge needed for it to be observed via MS.

It is also possible that the intact assembly may be seen but with a different interaction than what is responsible for binding in solution.²⁵⁵ For instance, cyclodextrins bind guests primarily through the hydrophobic effect but protonation during ionisation can enable a proton bridge to form between the guest and the hydroxyl groups of the host. This illustrates the importance of considering the ‘where’ & ‘how’ of ionisation and to recognise that the gas-phase and condensed phase are fundamentally different. Therefore, one must always be

careful when generalising results from the gas-phase to other phases and vice versa. All of this is to say that ionisation can introduce some difficulties in certain situations but can be beneficial in others.

There are of course examples where MS has been used to study supramolecular complexes. Some contemporary examples based on the MS/MS technique used will be presented below and along with the results obtained in the thesis, they should demonstrate the broad applicability of MS for the structural characterisation of supramolecular systems.

CID could be used to follow the kinetics of pseudo[2]rotaxane formation where the macrocycle initially forms a side-on complex before threading onto the axle. The side-on complex undergoes dissociation at lower collision voltages than the threaded structure and thus the threading kinetics could be followed by constructing SY curves at different time points (figure 2.32a).²¹⁷ When both conformations are present, the SY curve resembles a double sigmoidal shape where the plateau region represents the ratio between the thread and non-threaded structures.

CID can also be used in a similar fashion to distinguish inclusion and exclusion complexes formed with cucurbiturils.²⁵⁶ The externally bound guest dissociates more easily than an encapsulated guest so CID could be used to quickly determine the influence of guest size on encapsulation. As a final example, CID can also be used to determine sequence information

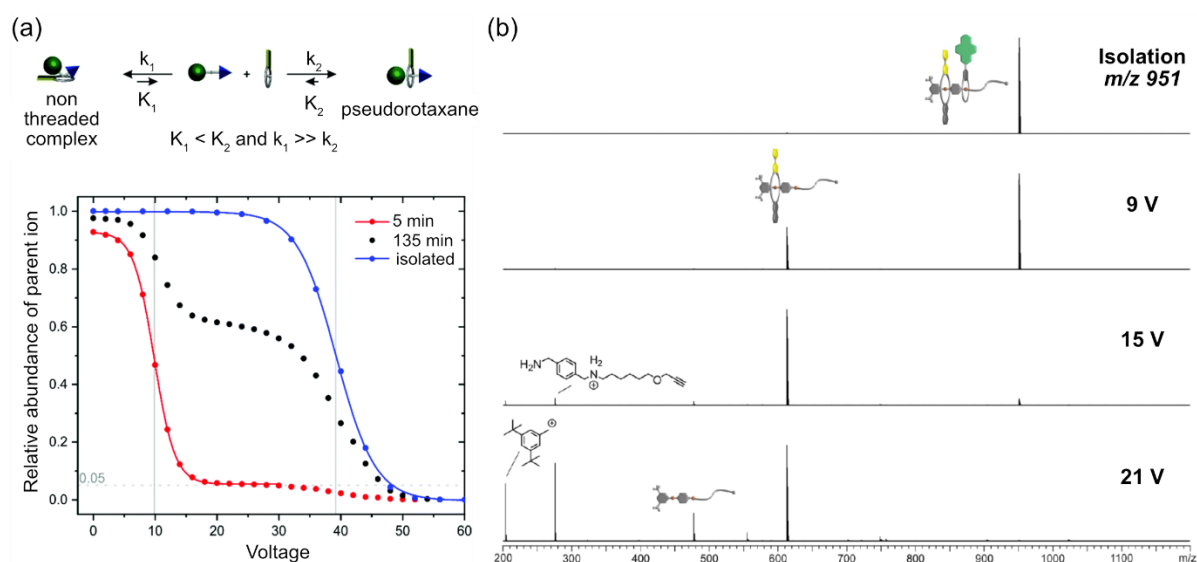


Figure 2.32: (a) The kinetics of threading can be followed by CID as the non-threaded complex dissociated more easily than the threaded structure. (b) CID spectra of a multi-threaded pseudo rotaxane. The rings can only de-thread over the open end of the axle thus CID can be used to determine sequence information of the macrocycle on the axle. Both used under respective open access agreements.^{217, 215}

such as with a pseudo[3]rotaxane binding different macrocycles. Macrocycles can thread and de-threaded via the open end of the axle and if different macrocycles are used, it is possible to generate pseudo[3]rotaxanes with a different sequence of macrocycles. CID was used to easily distinguish the sequence of the macrocycles on the axle by observing which macrocycle was initially lost from the pseudo[3]rotaxanes (figure 2.32b).²¹⁵

HDX is more specialised than CID and is mostly employed to study hydrogen bonded assemblies such as resorcin[4]arenes.²⁴⁸ Resorcin[4]arene dimers encapsulating Cs^+ undergo relatively fast, concerted exchange via a 1D-Grotthus mechanism. The exchange rate slows when the larger tetraethylammonium (TEA^+) is encapsulated as it disrupts the intermolecular hydrogen bonds to produce a PacMan like structure where efficient exchange is prevented. Pyrogall[4]arenes are similar to resorcin[4]arenes but possess an additional hydroxy group at the 2-position of the upper rims. When dimerising, pyrogall[4]arenes produce a hydrogen bonding pattern with 8, separate, three-hydrogen bond 'cells' (figure 2.33a). For the pyrogall[4]arene dimer, the PacMan arrangement can still undergo efficient exchange within the individual hydrogen bond cells (figure 2.33b). Thus, the pyrogall[4]arenes dimer with TEA^+ undergoes faster exchange than the corresponding resorcin[4]arene complex. For the exchange to occur for all the hydrogen bonded cells, the PacMan like structure would need to undergo a rearrangement providing insight into dynamic gas-phase rearrangements.²⁴⁸

Compared to CID and HDX, IMS has seen more widespread use within supramolecular chemistry. One reason is that IMS and the calculation of CCS values can be especially useful for structural assignment in situations where traditional methods e.g. crystal structures and NMR are challenging. For example, pyridyl-substituted resorcin[4]arene cavitands can form a hexameric capsule via twelve $[\text{N} \cdots \text{I} \cdots \text{N}]^+$ halogen bonds. In dichloromethane, the hexamer

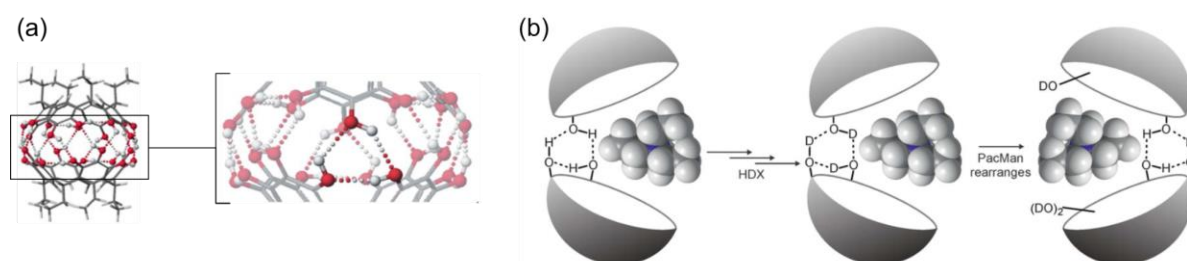


Figure 2.33: (a) structure of the pyrogall[4]arenes dimer with a zoom showing the three-hydrogen bonded 'cells'. (b) Pac-man structure in response to binding TEA^+ . The separate hydrogen bonded cells can still undergo efficient exchange. The structure can undergo a rearrangement to allow exchange of the other cells. Used with permission from the Royal Society of Chemistry.²⁴⁸

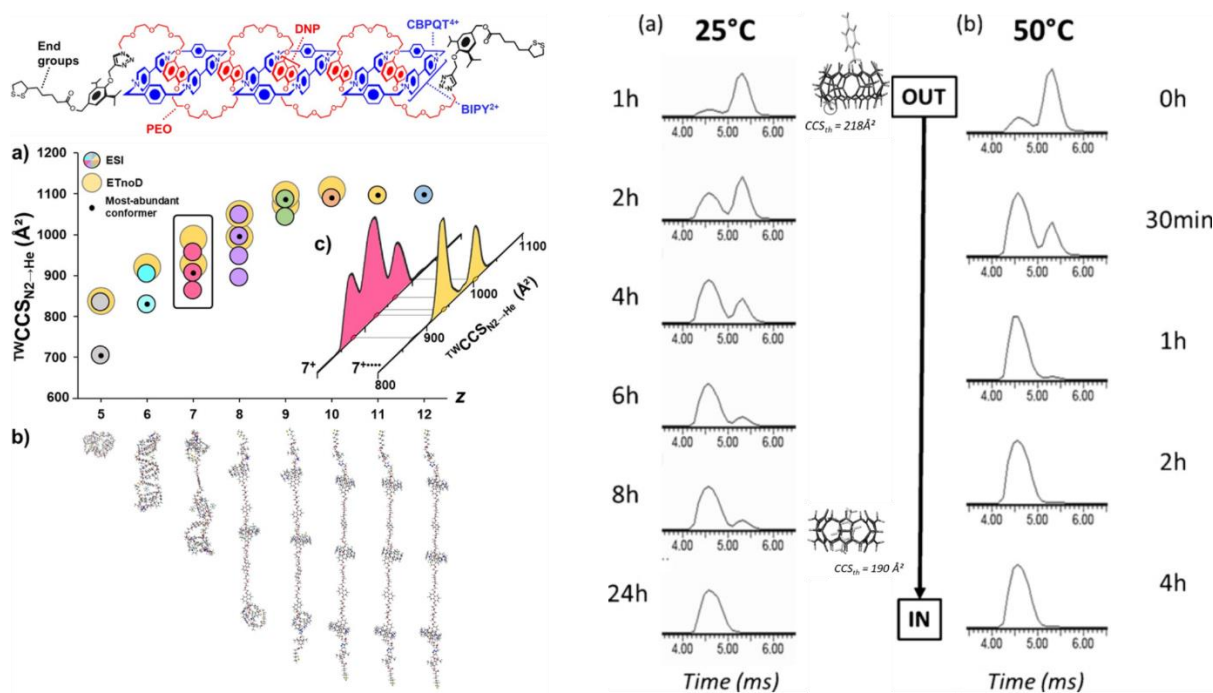


Figure 2.34: (a) ATD of the different charge states. The charge state can be achieved directly by removal of the counterion or by reduction of the +12 charge state via ETD. The structure is more compact at lower charge states. Used under the open access agreement.²⁵⁷ (b) ATDs of cucurbituril binding 1,4-phenylenediamine. The exclusion and inclusion complex can be seen and be used to follow the inclusion kinetics. Used with permission from John Wiley and Sons.²⁵⁸

rearranges into a different structure which could not be identified via either NMR or X-ray crystallography. Instead, the structure was assigned as a pentamer based on DT-IMS by the comparison of experimental and theoretical CCS values. The pentameric capsule had an unusual structure with an overall pseudo-trigonal bipyramidal geometry with two pyridyl units left unoccupied.²²⁸

IMS was used in the investigation of an [4]rotaxane with three CBPQT⁴⁺ 'Blue Box' macrocycles threaded onto an axle containing multiple 1,5-dioxynaphthalene (DNP) units. The DNP will π - π stack with the CBPQT which means that at low charge states, the complex will adopt a compact structure (figure 2.34a). Upon removal of the PF₆⁻ counterions, charge repulsion leads to an expansion of the system which can be observed by the changing CCS values. For the high charge state species, the CBPQT⁴⁺ units were reduced in the gas-phase by ETD and IMS showed the reduced species assumed a more compact conformation. As the counterions are gone, there are no favourable ionic interactions possible but additional radical pairing interactions could help to overcome the charge repulsion. Here IMS could be used to follow the interplay of the different interactions and their effect on the conformation of the structure.²⁵⁷

As the last example, IMS can also be used to assess internal versus external binding of host-guest systems. This was demonstrated with cucurbit[6]uril binding 1,4-phenylenediamine. The exclusion complex has a larger CCS so can be separated from the inclusion complex by IMS (figure 2.34b). Although CCS values were calculated, a straightforward assessment can be used to infer the identity of the contributions directly from the ATD. IMS could then be used to monitor the kinetics of guest inclusion which occurred over 24 hrs when the sample was maintained at 25 °C and 4 hrs at 50 °C.²⁵⁸

3. Results

Preamble

Throughout the work, there have been contributions to several published works, in collaboration with external groups and via a research secondment abroad. The systems studied during this work include a photoswitchable pseudorotaxane, a light driven molecular motor, halogen bonded capsules, hydrogen bonded capsules, a metal organic cage and a bioderived rotaxane. The compounds were all investigated via MS but are largely distinct from one another so each publication will be presented separately before a unified discussion of all results and their impact in the conclusion. The manuscripts were all published 'open access' and thus all figures are used and adapted in-line with the licensing agreement.

3.1 Light-Controlled Interconversion Between a [c2]daisy Chain and a Lasso-Type Pseudo[1]rotaxane

Chih-Wei Chu, Daniel L. Stares, and Christoph A. Schalley*.

Chem. Commun. **2021**, 57 (92), 12317-12320.

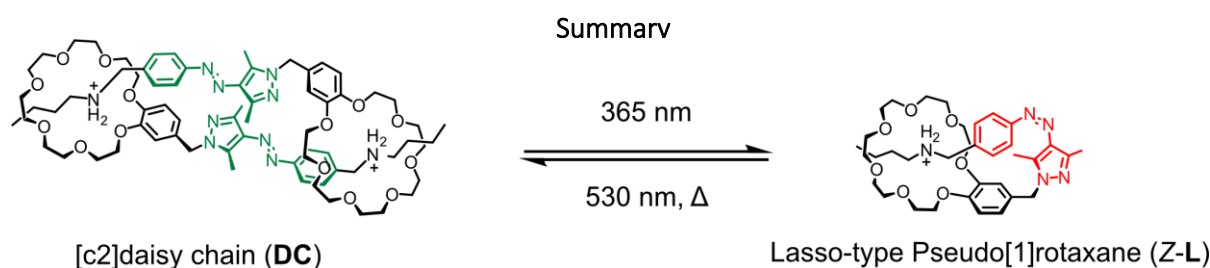


Figure 3.1: Isomerisation of the AAP photoswitch leads to interconversion between *E,E*-**DC** and **Z-L**.

This work involved the design, synthesis and characterisation of a photoswitchable [c2]daisy chain (**DC**). The monomer consists of a benzo-21-crown-7 and secondary ammonium station spaced via an aryazopyrazole (AAP) photo switch (section 2.1.8). The system was designed so that its self-assembly would be dictated by the state of the AAP (figure 3.1). In the thermodynamically favoured *E*-state, the system will self-assemble into **DC** as the ammonium station and crown ether are far enough apart that they cannot self-include. Contrarily, in the *Z*-state, they will be in a position that favours self-inclusion to form the lasso-type pseudo[1]rotaxane (**L**). *E* → *Z* isomerisation can be achieved with irradiation with 365 nm light,

whilst $Z \rightarrow E$ isomerisation is possible thermally or via irradiation with 530 nm light. UV/Vis and NMR spectroscopy showed the system possesses excellent photo switching with $PSS_{365\text{nm}}$ of > 98% and a $PSS_{530\text{nm}}$ of > 95% with the Z -state possessing a thermal half-life of up to 16 days. NMR measurements revealed the predominant formation of E,E -DC in the purified sample which could be converted to Z -L by irradiation with 365 nm light.

The switching and assembly processes were also investigated with IMS. Measurements with a non-irradiated 10 μM sample in DCM had a major contribution at an arrival time of around 8.5 ms in addition to a minor contribution at around 11 ms. These were assigned as E,E -DC and Z -L, respectively (Figure 3.2). Upon irradiation with 365 nm light, E,E -DC decreased with a subsequent increase, and eventual exclusive formation of Z -L. An intermediate contribution at earlier drift times than E,E -DC was also observed and tentatively, as it was not observed via NMR, assigned as the E,Z -DC. The back-switching was then studied by irradiating with 530 nm after 10 mins of irradiation with 365 nm light. In this process, it should not be possible to form the E,Z -DC as dimerization should only occur with the E -monomer where a strong enthalpic driving force leads to the formation of the E,E -DC. The E,E -DC was completely

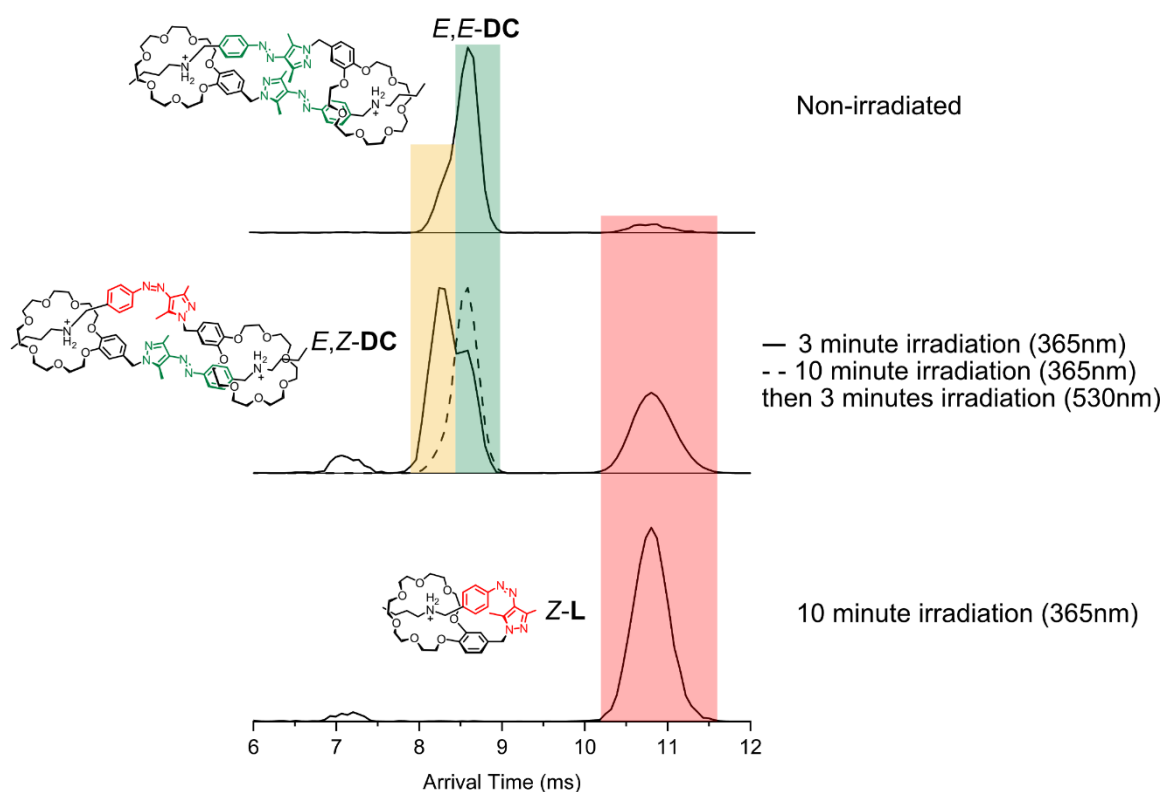


Figure 3.2: ATDs upon irradiation with 365 nm light and subsequently 530 nm light to follow the assembly and disassembly processes which occur in response to switching of the AAP. An intermediate E,Z -DC which was not seen via NMR was formed before exclusive formation of the Z -L with longer irradiation. E,E -DC could be recovered by irradiation with 530 nm light.

recovered and notably, no contribution was seen from the *E,Z*-DC which strengthens the assignment of this isomer.

Energy-resolved IMS was also undertaken by performing CID in the trap cell prior to IMS to investigate gas-phase thermal relaxation. CID of a sample irradiated for 3 minutes with 365 nm light showed relaxation of the *E,Z*-DC to reform the *E,E*-DC whereas a slight increase of arrival time was seen for *Z*-L (figure 3.3). This could result from the formation of an *E*-monomer which cannot associate to *E,E*-DC as it is isolated in the gas-phase allowing it to be observed. Fragmentation of the systems occurs at a similar collision voltage to this via cleavage of the C-N bond to form a radical cation.

The results show the ability to control the assembly of a pseudorotaxane by light. The work builds towards the eventual goal of functional photoswitchable materials with this type of architecture mostly useful for artificial muscles. IMS could be used to follow the isomerisation of the AAP and the resulting assembly and disassembly of the pseudorotaxane. These

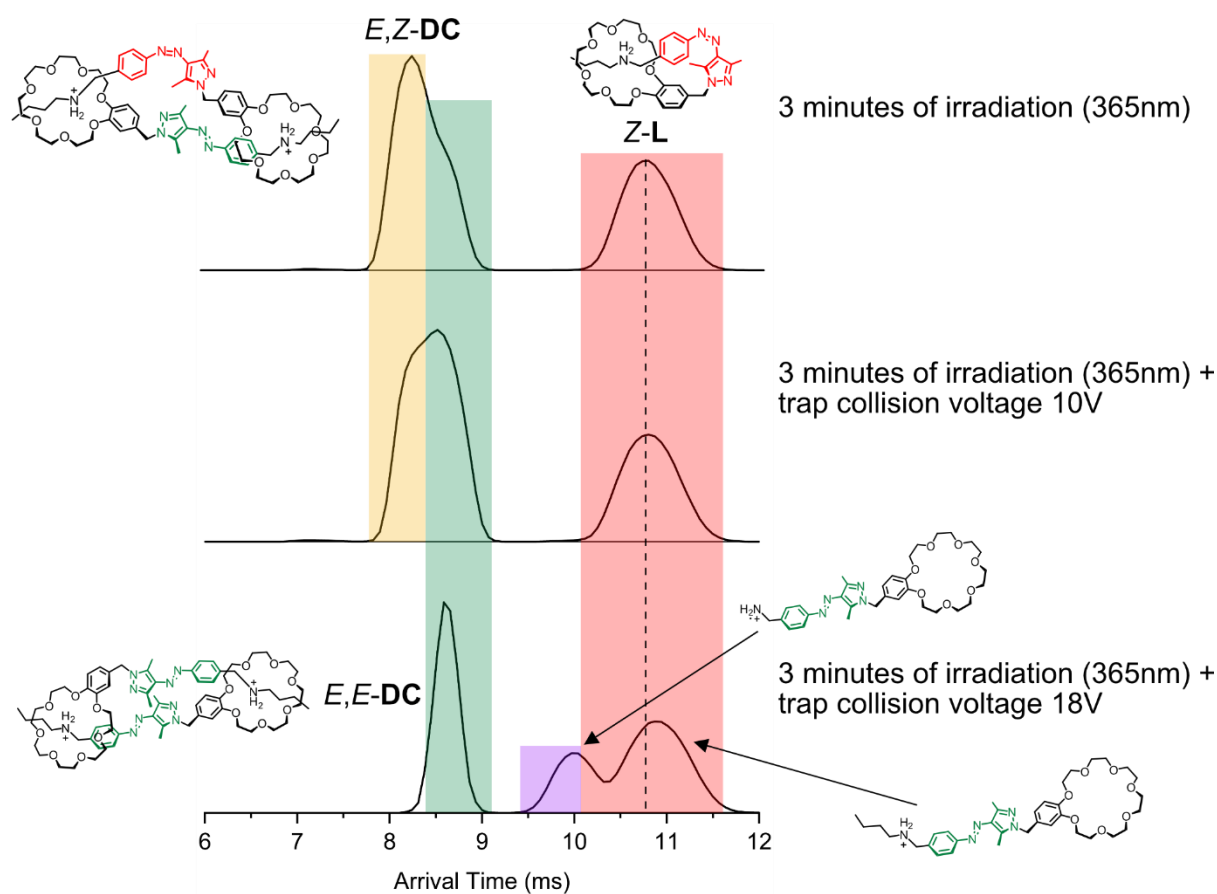


Figure 3.3: Energy resolved IMS with CID in the trap cell prior to IMS. *E,Z*-DC relaxes back to *E,E*-DC while *Z*-L has an increase in arrival time which would be consistent with formation of the *E*-monomer. Cleavage of the alkyl chain is also observed at a similar collision voltage.

measurements identified the intermediate *E,Z*-**DC** which was difficult to see via NMR. Further insight was gained from energy-resolved IMS and photo driven back switching measurements. The results demonstrate how IMS can be used to quickly visualise dynamic process of a photo responsive system.

Contribution

C-W.C. designed and synthesised the system and performed NMR and UV/Vis measurements. D.L.S. performed MS measurements, computational & CCS calculations. C.A.S. supervised the project. All authors contributed to manuscript preparation and revision.

3.2 A Light-Fuelled Nanoratchet Shifts a Coupled Chemical Equilibrium

Michael Kathan*, Stefano Crespi, Niklas O. Thiel, Daniel L. Stares, Denis Morsa, John de Boer, Gianni Pacella, Tobias van den Enk, Piermichele Kobauri, Giuseppe Portale, Christoph A. Schalley*, and Ben L. Feringa*.

Nat. Nanotechnol. **2022**, *17* (2), 159-165.

Summary

Work was completed as a collaboration with the Feringa group based at Stratingh Institute for Chemistry in Groningen. In this work, the stator and rotator portion of a second-generation Feringa motor (section 2.1.9) were tethered by Aza-Wittig reactions to form a motor with two imine macrocycles (figure 3.4). The macrocycles are large enough that they can cross over one another to form distinct topological isomers with different numbers of crossings. The maximum number of crossings is limited by strain in the system and was experimentally determined to be three crossings. The distribution of isomers at thermal equilibrium is governed by the principles of microscopic reversibility with -1, 0 and +1 crossing as determined via ^1H NMR measurements. In response to irradiation with 365 nm light, the motor will rotate unidirectionally and every 180° of rotation induces a positive crossing of the macrocycles forming new isomers not present in the thermal equilibrium. The distribution the isomers is thus coupled to the rotation of the motor, and hence the motor can perform

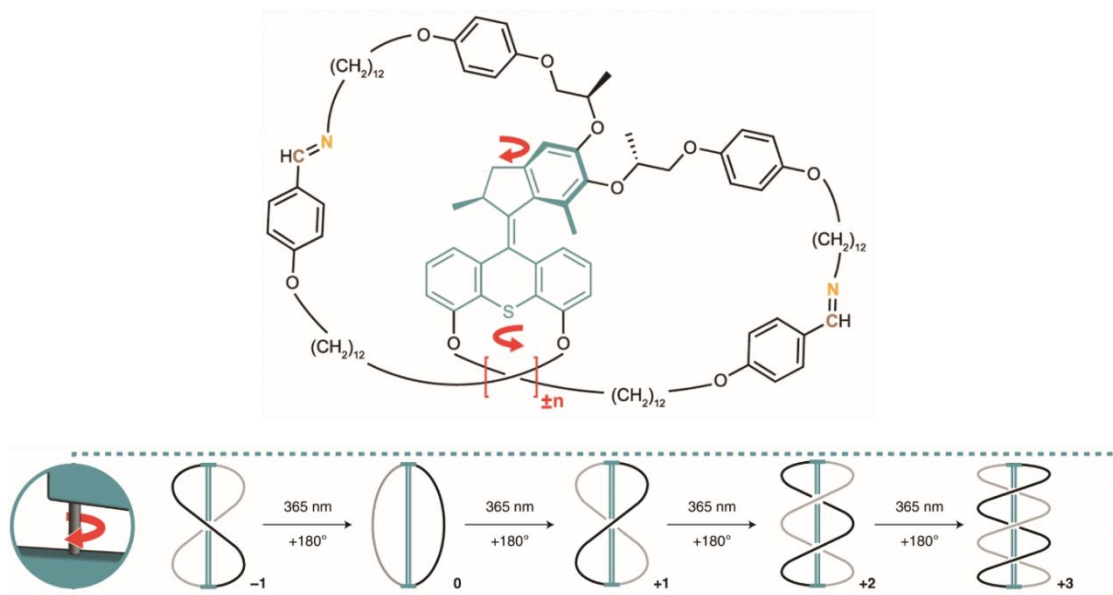


Figure 3.4: A light driven molecular motor constrained by two imine macrocycles, allowing the formation of various topologies by forming crossings in the strands of the bicyclic molecule.

work to shift the systems out of the initial equilibrium. Operating out of equilibrium is a crucial component of biological systems and is a major focus of the AMM community.

The system was initially assessed using ^1H NMR spectroscopy which revealed a roughly 1:2:1 ratio of the -1, 0, +1 isomers, respectively, at thermal equilibrium (figure 3.5a). Upon irradiation with 365 nm light, the +3 isomer was formed which was stable for several weeks at room temperature. The winding of the motor could also be followed by DT-IMS. The ATD of a sample at thermal equilibrium showed three contributions which converged to a single contribution at a different arrival time upon irradiation (figure 3.5b). The different contributions could be assigned as the -1, 0, +1 and +3, isomers respectively by comparing the $^{\text{DT}}\text{CCS}_{\text{He}}$ and $^{\text{TM}}\text{CCS}_{\text{He}}$ values. The $^{\text{TM}}\text{CCS}_{\text{He}}$ calculations sampled 500 structures generated from molecular dynamics of M06-2X/def-SVP//GFN-xTB structures. For this motor, X-ray crystallography was not possible due to polymerisation, so IMS and computational structures were important for the structural assignment of the different topologies.

There are two mechanisms by which the system can unwind: A purely thermal mechanism and through dynamic covalent chemistry of the imines in the macrocycles. In the latter, a competing nucleophile (e.g. H_2O , amine) can induce temporary ring opening and allowing recovery of the initial equilibrium of isomers as shown by ^1H NMR (figure 3.5c). The purely thermal pathway cannot proceed via ring opening and requires higher temperatures to recover the initial state than when the competing nucleophile was present. Purely thermal relaxation could also be followed by IMS and as the ions are isolated in the gas-phase, it allows a purely thermal process to be investigated without the possibility of hydrolysis. It showed

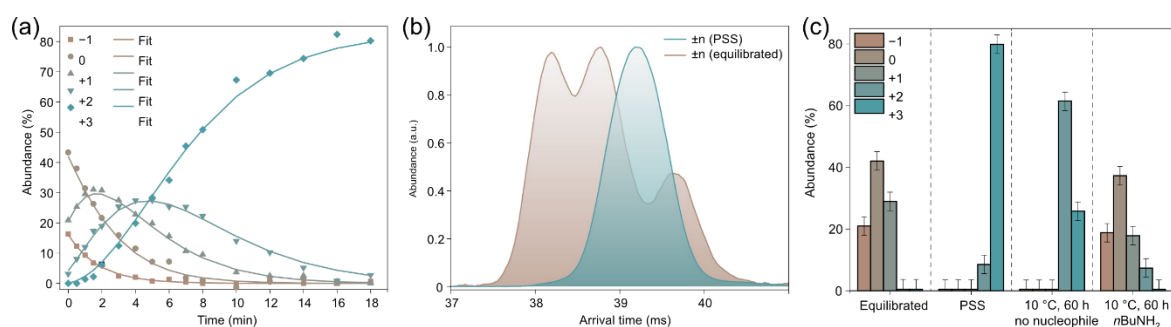


Figure 3.5: (a) Population of the different isomers upon irradiation with 365 nm light. Determined via ^1H NMR of a 1 mM sample in C_6D_6 (b) ATD of equilibrated sample (brown) showing three contributions assigned based on CCS values as -1, 0, +1 and after irradiation with 365 nm light (blue) showing a single contribution assigned as the +3 isomer. (c) Isomer population of an equilibrated sample (left), a sample at PSS (middle left), without addition of external nucleophile (middle right) and after relaxation at 10 °C for 60 h with 20 mol% of $n\text{BuNH}_2$ (right). Full relaxation at 10 °C only occurs in presence of $n\text{BuNH}_2$.

that the initial isomer distribution could be recovered after irradiation by ion activation through increasing the injection voltage into the IMS cell.

The results show the ability of the motor to perform work and demonstrates how a topological transformation can be coupled to the continuous motion of a molecular motor. Again, it also shows how IMS can be used to follow the dynamic light driven process even in a highly complex system. DT-IMS could be used to assign the different topological isomers and energy resolved DT-IMS could be used to follow the thermal relaxation process. It is also one of the first examples of a molecular motor studied by MS and potentially open a new avenue for their characterisation.

Contribution

M.K. conceived the idea and designed the study. B.L.F. guided and supervised the research. M.K., N.O.T., S.C., D.L.S., D.M., G. Pacella, G. Portale and C.A.S. planned experiments. M.K., N.O.T., J.d.B. and T.v.d.E. synthesized molecules. S.C. and P.K. conducted computations. M.K., D.L.S., D.M. and C.A.S. performed mass spectrometric measurements. M.K., G. Pacella and G. Portale carried out SAXS measurements. M.K. and N.O.T. measured CD spectra. M.K. performed NMR measurements. M.K. and S.C. analysed kinetics. M.K. and B.L.F. prepared the manuscript with help from N.O.T. and S.C. All authors discussed the results and edited the manuscript.

3.3 Dimeric Iodine(I) and Silver(I) Cages From Tripodal N-Donor Ligands Via the $[N-Ag-N]^+$ to $[N-I-N]^+$ Cation Exchange Reaction

Essi Taipale, Jas S. Ward, Giorgia Fiorini, Daniel L. Stares, Christoph A. Schalley, and Kari Rissanen*.

Inorg. Chem. Front. **2022**, 9 (10), 2231-2239.

Summary

Work was completed as a collaboration with the Rissanen group based at the University of Jyväskylä. The basis for the work was utilising halogen bonding to form self-assembled dimeric cages using imidazole-derived N-donor tripodal ligands (**L**). With these ligands, it is possible to form 3c-4e bonds with iodine(I) cations (section 2.1.1). Iodine(I) is extremely polarised and is also highly reactive but results in some of the strongest halogen bonds when forming $[N-I-N]^+$ 3c-4e bonds. Such bonds can be accessed by the $[N-Ag-N]^+$ to $[N-I-N]^+$ cation exchange reaction and this work was to characterise different L_2I_3 cages formed in this manner (figure 3.6).

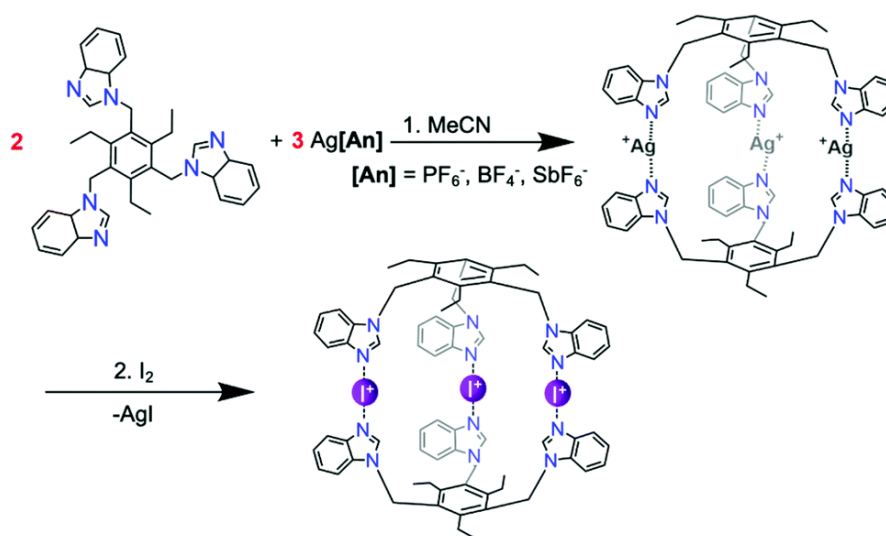


Figure 3.6: Formation of the iodine(I) cage with tripodal ligands from the analogous silver(I) cage via $[N-Ag-N]^+$ to $[N-I-N]^+$ cation exchange.

The ligands consist of different imidazole moieties attached to a trialkylbenzene via methylene linkers which provides flexibility to the ligands (figure 3.7). The ligands were mixed in a 2:3 ratio with $AgPF_6$ (other salts are also feasible) to form the $L_2Ag_3(PF_6)_3$ cage via three $[N-Ag-N]^+$ bonds. Addition of I_2 results in $[N-Ag-N]^+$ to $[N-I-N]^+$ cation exchange leading to the formation of the $L_2I_3(PF_6)_3$ cages. X-ray crystal structures of the L_2Ag_3 cages generally

showed encapsulation of one of the counterions, but unfortunately diffraction quality crystals of the iodine(I) cages could not be obtained. NMR spectra showed the assembly of the $L_2Ag_3(PF_6)_3$ and $L_2I_3(PF_6)_3$ cage by the downfield shifts of the 1H NMR signals of **L**. However, the decreased solubility of the $L_2I_3(PF_6)_3$ species resulted in their precipitation at the concentrations required for NMR meaning that full characterisation by 1H - ^{15}N HMBC was not possible.

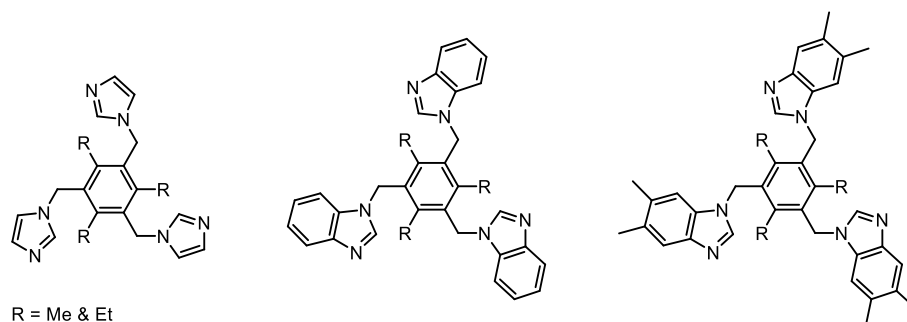


Figure 3.7: Structures of N-donor tripodal ligands (**L**) used in the formation of the iodine(I) cages.

The $[N-Ag-N]^+$ to $[N-I-N]^+$ cation exchange can easily be followed by MS due to the mass differences and the lower concentration requirements meant precipitation was not an issue. The measurements showed the formation of the L_2I_3 cages but for some ligands, there was only partial conversion with some L_2Ag_3 still present. For both L_2Ag_3 and L_2I_3 cages, there was also partial hydrolysis of the PF_6^- counterion to $PF_2O_2^-$ as well as counterion exchange with I^- . In most cases, the complexes retained a single counterion forming $L_2(Ag_3/I_3)X^{2+}$ ions with no higher charge states present. This ionisation pattern would be consistent with encapsulation

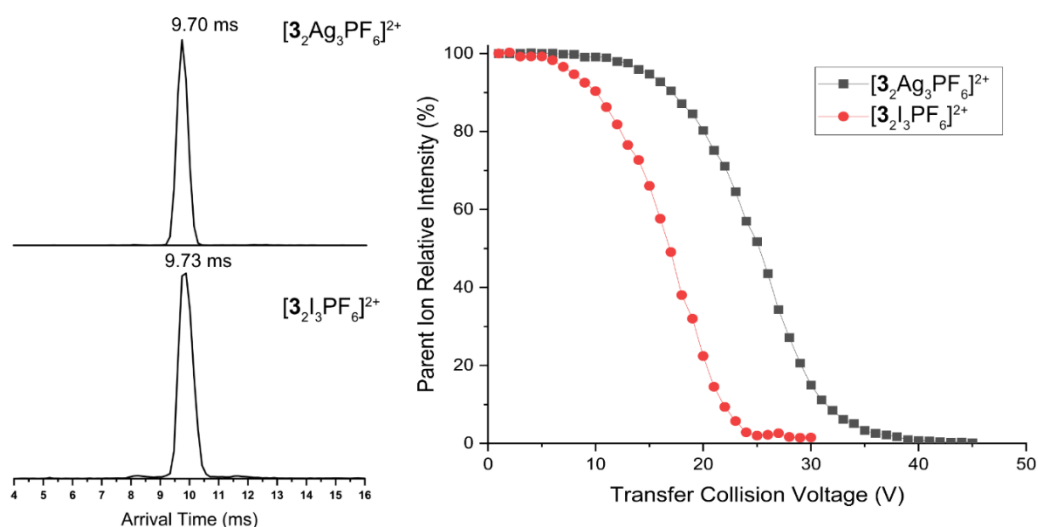


Figure 3.8: Comparison of ATD (left) and SY (right) of $L_2Ag_3PF_6^{2+}$ and $L_2I_3PF_6^{2+}$. Analogous results i.e., similar arrival time and decreased stability of the iodine(I) cages were seen for all ligands.

of one counterion which is more difficult to remove during ionisation.

Structural analysis came via IMS with very similar ATDs for the $[\text{L}_2\text{Ag}_3\text{PF}_6]^{2+}$ and $[\text{L}_2\text{I}_3\text{PF}_6]^{2+}$ ions indicating the complexes maintain their structure upon $[\text{N}-\text{Ag}-\text{N}]^+$ to $[\text{N}-\text{I}-\text{N}]^+$ exchange (Figure 3.8). The CID fragmentation pathways were also similar with the mass selected $[\text{L}_2(\text{Ag}_3/\text{I}_3)\text{PF}_6]^{2+}$ ions fragmenting to the $[\text{LAg}]^+$ and $[\text{LI}]^+$ ions, respectively. The corresponding $[\text{LAg}_2\text{PF}_6]^+$ and $[\text{LI}_2\text{PF}_6]^+$ ions were not observed during fragmentation which indicates a subsequent rapid loss of AgPF_6 and IPF_6 ion pairs to generate the $[\text{LAg}]^+$ and $[\text{LI}]^+$ ions. SY curves were constructed to assess the relative gas-phase stabilities of $[\text{L}_2(\text{Ag}_3/\text{I}_3)\text{PF}_6]^{2+}$ which showed $[\text{L}_2\text{I}_3\text{PF}_6]^{2+}$ to be considerably less stable than $[\text{L}_2\text{Ag}_3\text{PF}_6]^{2+}$ (Figure 3.8).

This work further demonstrates the utility of MS in the structural assignment of self-assembled systems. It is especially pertinent given the issues when attempting to study the iodine(I) systems by NMR and X-ray crystallography. The CID and IMS verified the structural similarities of the silver(I) and iodine(I) cages. SY curves showed the gas-phase stability of all iodine(I) cages to be clearly less stable than their silver(I) counterparts which can possibly justify some of the difficulties in the condensed phase measurements. Overall, the work demonstrates the use of the $[\text{N}-\text{Ag}-\text{N}]^+$ to $[\text{N}-\text{I}-\text{N}]^+$ cation exchange reaction to form host structures.

Contribution

E.T., J.W., and G.F. performed synthesis, X-ray crystallography and NMR spectroscopy measurements. D.L.S performed all MS measurements. K.R. and C.A.S. supervised the project. E.T. prepared the initial manuscript. All authors contributed to revision and final manuscript preparation.

3.4 Binding Modes of High Stoichiometry Guest Complexes with a Co_8L_{12} Cage Uncovered by Mass Spectrometry

Daniel L. Stares, Cristina Mozaceanu, Michael D. Ward, Christoph A. Schalley*.

Chem. Commun. **2023**, 59 (79), 12317-12320.

Summary

The work was conducted as part of a secondment agreement within the 'NOAH' Marie Curie innovative training network (ITN) by hosting Cristina Mozaceanu from the Ward group based at Warwick University. The basis of the work was to use MS to study a Co_8L_{12} ($\text{H}^{\text{W}}\text{Co}$) cubic cage with methylhydroxy containing ligands (L^{W}) (figure 3.9, & section 2.1.5). $\text{H}^{\text{W}}\text{Co}$ is a well established

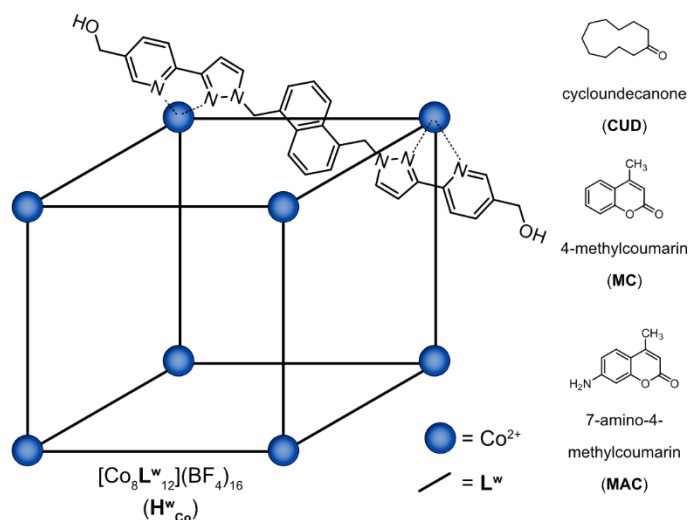


Figure 3.9: Structure of $\text{H}^{\text{W}}\text{Co}$ and the guests used in this work.

metal-organic cage which can bind guests both internally in its cavity or peripherally with the hydroxy groups of L^{W} , theoretically enabling high stoichiometry host-guest complexes. Characterisation to date, mostly via NMR or X-ray crystallography, has only shown binding of a maximum of two guests even under forcing conditions with very large excess of guests. In this work, a detailed MS study of $\text{H}^{\text{W}}\text{Co}$ was conducted to study its host-guest properties, particularly to investigate the ability to bind multiple guests.

The host-guest properties were explored with three guests: cycloundecanone (**CUD**); 4-methylcoumarin (**MC**); and 7-amino-4-methylcoumarin (**MAC**); all of which have been studied in solution and the solid state (Figure 3.9). When assessing via ESI-MS, the number of bound guests differed depending on the guest: **CUD** formed a 1:1 complex with $\text{H}^{\text{W}}\text{Co}$ with no evidence of multiple guest binding whereas **MC** was mostly observed as $\text{H}^{\text{W}}\text{Co}/\text{MC}$ with smaller amounts of $\text{H}^{\text{W}}\text{Co}/2\text{MC}$ also seen. In contrast, much higher guest stoichiometries were observed with **MAC** where strong signals for $\text{H}^{\text{W}}\text{Co}/4\text{MAC}$ (Figure 3.10a) with even higher stoichiometries with up to 8 **MAC** bound albeit at lower intensities. The results of **CUD** and

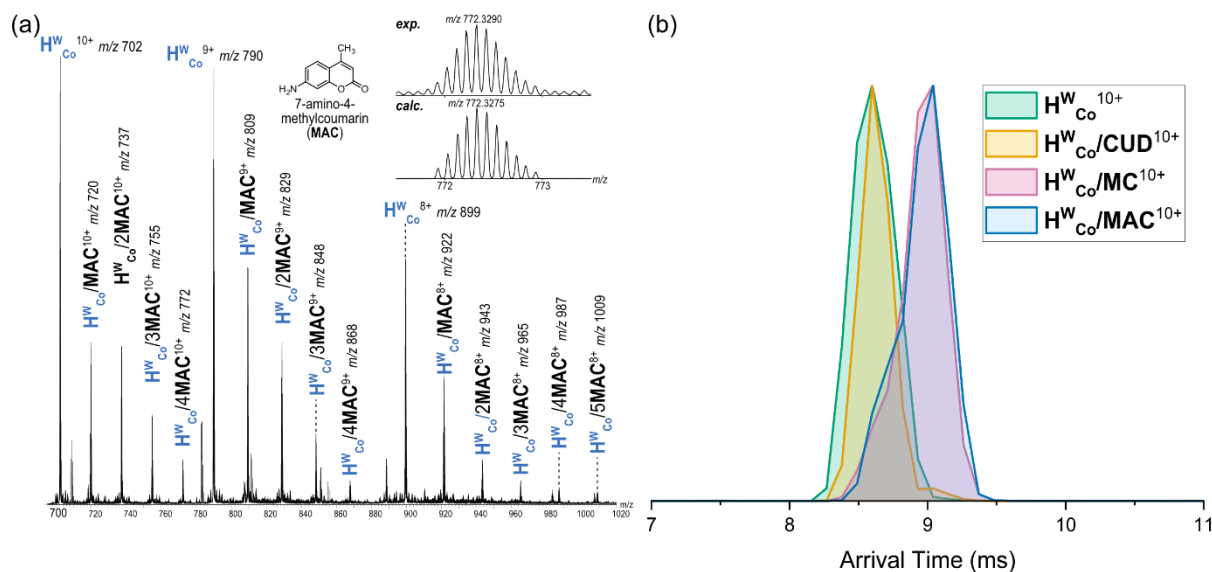


Figure 3.10: (a) ESI-MS spectrum of H^W_{Co} with **MAC** (10 μ M & 50 μ M, respectively) in 5% CH_3OH/H_2O . Multiple guest binding stoichiometries with up to 5 **MAC**s bound are observed. The experimental vs calculated m/z values for the $H^W_{Co}/4MAC^{10+}$ is shown in the inset (b) ATDs of $H^W_{Co}^{10+}$, H^W_{Co}/CUD^{10+} , H^W_{Co}/MC^{10+} , H^W_{Co}/MAC^{10+} . The ATDs of $H^W_{Co}^{10+}$ and H^W_{Co}/CUD^{10+} overlap indicating encapsulation whilst H^W_{Co}/MC^{10+} and H^W_{Co}/MAC^{10+} have longer arrival times consistent with external binding.

MC mostly match what is seen in the condensed phase but the higher stoichiometries with **MAC** were observed for the first time. Mass-selection of the respective 1:1 H^W_{Co} :**Guest (G)** ions resulted in a portion of free H^W_{Co} even when mass selecting a lower charge state and softening instrument conditions. This means facile guest loss which can occur just from transmission through the instrument. The relative intensities of H^W_{Co}/CUD^{8+} and H^W_{Co}/MAC^{8+} (71 and 77 %, respectively) after mass selection are considerably higher than that for H^W_{Co}/MC^{8+} (47 %) with complete guest loss for all guests at low collision voltages.

A clear difference was seen between the different H^W_{Co}/G when measuring IMS. The ATDs of H^W_{Co} and H^W_{Co}/CUD^{10+} overlapped, whereas H^W_{Co}/MC^{10+} and H^W_{Co}/MAC^{10+} were shifted to longer arrival times (Figure 3.10b). A straightforward explanation is that **CUD** is encapsulated in the cavity and hence not contributing significantly to the CCS of H^W_{Co} whilst **MC** and **MAC** are both bound externally increasing CCS and hence arrival times. Calculation of $^{TM}CCS_{N2}$ values of universal force field (UFF) structures with these binding modes showed the expected results with the encapsulated H^W_{Co}/CUD^{10+} complex having the same $^{TM}CCS_{N2}$ value as $H^W_{Co}^{10+}$. Both H^W_{Co}/MC^{10+} and H^W_{Co}/MAC^{10+} with guests bound externally with the hydroxy groups of L^W had higher $^{TM}CCS_{N2}$ values, qualitatively matching the IMS results.

External binding of **MC** and **MAC** likely occurs via hydrogen bonding with the hydroxy groups of L^W . This binding mode can justify the difficulty of observing high stoichiometry guest

complexes in solution as these measurements are performed in highly competitive solvents such as H₂O where encapsulation dominates due to the hydrophobic effect. The aniline group of **MAC** would potentially enable it to form an additional hydrogen bond with a second **L^w** in the corner of **H^wCo** which was supported by computational models at the B97-3c level of theory (figure 3.11a). The additional interactions available to **MAC** can explain why it is able to form the higher stoichiometry complexes not seen with the other guests.

The ATDs of the **H^wCo/MAC** complexes showed increasing arrival times with more **MACs** bound but also showed the appearance of a shoulder region at earlier arrival times that increased in magnitude until clear double peaks were seen in the ATDs of **H^wCo/3MAC** and **H^wCo/4MAC**. This is consistent with two binding modes: one where all **MAC** are bound externally and another where a single **MAC** has been encapsulated with the others bound externally. As the amount of the encapsulated **MAC** increases with the number of guests, it suggest **MAC** preferentially binds externally but is encapsulated with high enough guest loading.

The work shows that **H^wCo** can bind more guests than previously determined using other methods, likely as a result of the competitive solvent used in those measurements. There were different preferences for external versus internal binding and also number of guests bound depending on the guest used. The different preferences for external and internal binding could be determined via IMS and were rationalised on the basis of the different interactions between host and guests. **H^wCo** has been shown to catalyse different reactions via external binding of guests (section 2.1.5) so this could be useful knowledge for such applications.

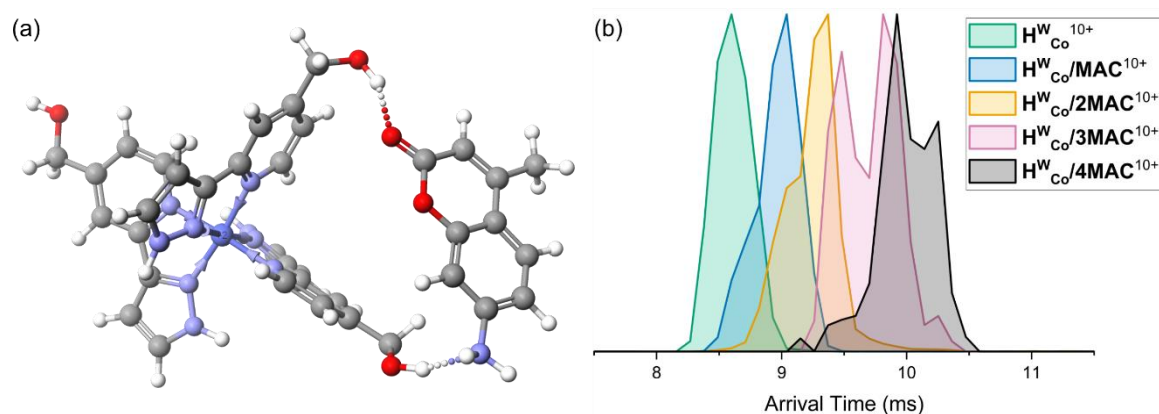


Figure 3.11: (a) Binding mode of **MAC** with two **L^w** in a mer corner of **H^wCo**. Structure was optimised at the B97-3c level of theory. (b) ATDs of **H^wCo/nMAC¹⁰⁺** with n=1 – 4.

Contribution

D.L.S. and C.M. performed the MS measurements and data evaluation. Ligand was synthesised by C.M. Computational work was carried out by D.L.S. Both M.W. and C.A.S. supervised the project. Both D.L.S and C.M. prepared the initial manuscript and all authors contributing to revision and final manuscript preparation.

3.5 Encapsulation in Charged Droplets Generates Distorted Host-Guest Complexes

Daniel L. Stares, Agnieszka Szumna* and Christoph A. Schalley*

Chem. Eur. J. **2023**, early view, DOI: 10.1002/chem.202302112.

Summary

The work was performed as part of the secondment agreement within the 'NOAH' Marie Curie ITN including a 3-month internship in the Szumna group based at the Institute of Organic Chemistry-Polish Academy of Science (IChO-PAN).

The work focused on generating new resorcinarene capsules and cavitands using acylhydrazone chemistry from tetraformylated resorcinarene precursors (section 2.1.4). Here, the strand was shortened to an acetyl moiety to form an acetylhydrazoneresorcinarene (**1**). **1** dimerises to form the capsule, **1₂**, with a series of 8 N-H...O= hydrogen bonds propagating around the capsule (figure 3.12a). The host-guest properties were investigated with different length α,ω -alkylbisDABCONium (**DnD**) ($n = 2 - 12$) guests (figure 3.12b). The double charge of the **DnD** means it will be fully extended and can form cation- π interactions with the resorcinarene cores of both hemispheres of **1₂**. However, no interaction between **1₂** and various **DnD**(PF₆)₂ salts was observed via ¹H NMR even with different counterions, solvents or when remeasuring after several days. In contrast, strong signals were seen via ESI-MS for [**1₂**+**DnD**]²⁺ with all **DnD** guests, even those which are far longer than the cavity. As these complexes are not detected in solution it indicates that they are formed in the shrinking charged droplets during the ESI process where concentration increases and ion pairing is obviated. CID, IMS and HDX along with computational modelling were used to elucidate the conformation of these unusual complexes.

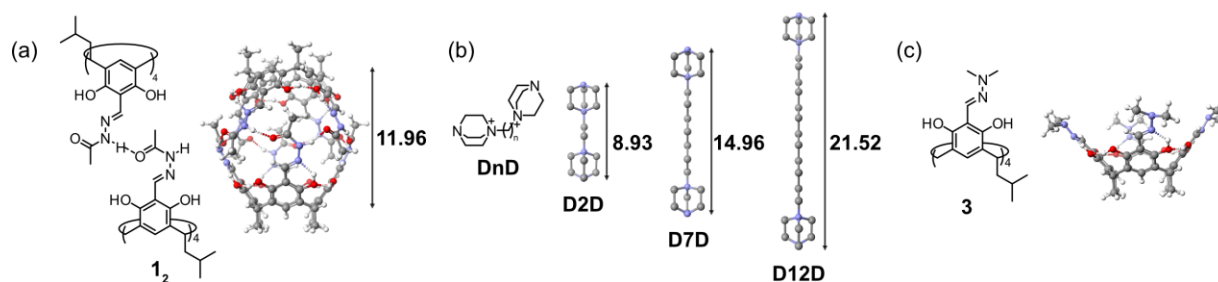


Figure 3.12: (a) Acetylhydrazoneresorcinarene capsule (**1₂**). The distances from lower rim to lower rim are marked in Å. (b) **DnD**²⁺ guests which should be fully extended due to charge repulsion. The (CH₂)₃N-N(CH₂)₃ distance is marked in Å. All models were optimised at the HF-3c level of theory. (c) N,N-dimethyl resorcinarene cavitand (**3**).

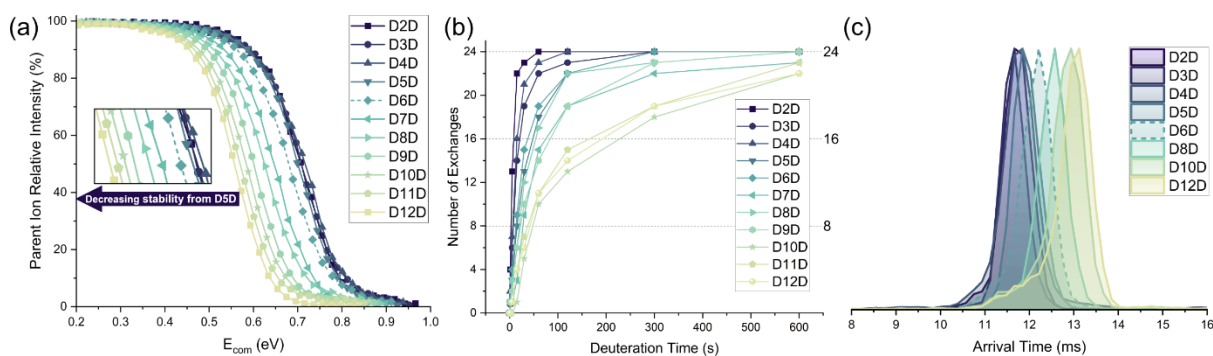


Figure 3.13: (a) SY curves of $[1_2\text{C}\text{DnD}]^{2+}$ with a zoom of the $\text{SY}_{50\%}$ region shown in the inset. Note that the collision voltage was converted to the centre of mass energy (E_{com}). (b) HDX for $[1_2\text{C}\text{DnD}]^{2+}$. The dashed lines represent the 8 NH and 16 OH hydrogens which are exchangeable. The number of exchanges is consistent, but the rate decreases for longer guests. (c) ATDs of $[1_2\text{C}\text{DnD}]^{2+}$ for $n=2-6,8,10,12$ ($n=7,9,11$ omitted for clarity).

The simplest explanation for the $[1_2+\text{DnD}]^{2+}$ ions would be non-specific binding during ESI where the guests bind externally rather than truly being encapsulated. Mass-selected $[1_2+\text{DnD}]^{2+}$ ions dissociated by loss of one cavitand to $[1+\text{DnD}]^{2+}$ before the free DnD^{2+} ion was observed. The fragmentation pathway, along with the relatively high collision voltage required to induce dissociation, speaks against non-specific binding as direct guest loss would dominate and require less collision voltage if the guest is bound externally. Additionally, SY analysis showed similar stability of **D2D-D5D** with a gradual *decrease* of stability from $n \geq 5$ onwards (figure 3.13a).

Instead of binding externally, the guest could be bridging two partially or full separated cavitands. A N,N-dimethylhydrazone cavitand, **3** (figure 3.12c), was prepared to serve as a control to investigate this as it cannot dimerise via hydrogen bonding and can only do so via a bridging guest. $[3_2+\text{DnD}]^{2+}$ ions were only observed for $n \geq 5$ indicating the complexes with shorter guests are not very stable and SY curves of the $[3_2+\text{DnD}]^{2+}$ ions revealed *increasing* stability when the guest length increased. The fact that **1₂** and **3₂** have the opposite stability trend, suggest that **1₂** is maintaining hydrogen bonding between the cavitands in some manner. HDX was then used with $[1+\text{DnD}]^{2+}$ which showed that the number of exchanges remained constant (24) but the rate decreased from **D5D** onwards (figure 3.13b). Furthermore, this also marked the point of a continual increase in arrival time seen via IMS (figure 3.13c). These results indicate that the **D2D-D5D** are encapsulated in the cavity, but longer guests partially disrupt the hydrogen bonding of **1₂** and begins to expand outside of the cavity.

The experimental results were validated by computational modelling at the HF-3c level of

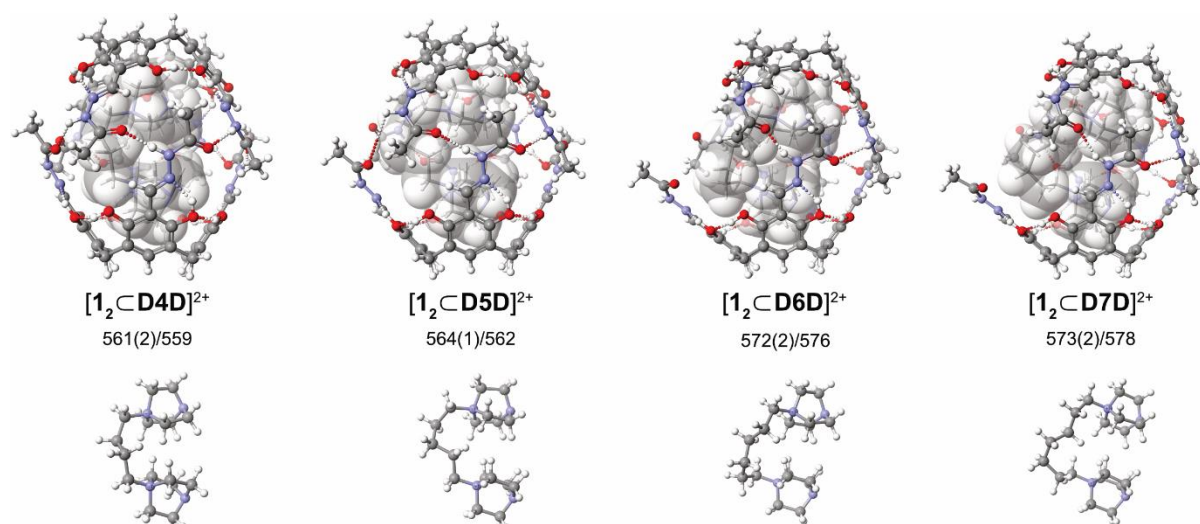


Figure 3.14: HF-3c optimised structures of $[1_2 \subset D_nD]^{2+}$ with $n = 4, 5, 6, 7$ (left to right), experimental ${}^{\text{TM}}\text{CCS}_{\text{N}_2}$ values from CCS calibration (with standard deviation in parentheses) and theoretical ${}^{\text{TM}}\text{CCS}_{\text{N}_2}$ values are given below the $[1_2 \subset D_nD]^{2+}$ structures. The bound guest is shown in space-filling mode in the host-guest structures and shown without host underneath the respective host-guest structures. The *i*-Bu groups of the hosts have been omitted for clarity.

theory. These showed the guests pointing their inner nitrogens into the resorcinarene core to maximise cation- π interactions. $[3_2 + D_nD]^{2+}$ becomes more stable with longer guests due to any potential steric clashes between the cavitands and charge repulsion being reduced. The hydrogen bonding of **1**₂ prevent translation of the cavitands as seen with **3** so the DABCONium moieties are effectively locked in position. The alkyl chain loops into a horse-shoe arrangement which grows with the longer guest and eventually pushes against the strands, weakening the hydrogen bonding, and leading to a shift in the cavitand position (figure 3.14). This process can explain the experimental results where the weakening hydrogen bonding leads to the stability decreases seen via the SY curves as well as the HDX rate decrease as a rearrangement is required to allow efficient exchange. Furthermore, as the guest expands outside of the cavity, the CCS of the complex increases which leads to the gradual increase in arrival times. ${}^{\text{TM}}\text{CCS}_{\text{N}_2}$ and ${}^{\text{TM}}\text{CCS}_{\text{N}_2}$ values of **1**₂ were also in close agreement with one another and thus there is strong evidence for the proposed binding modes.

This work shows how charged droplets formed during ESI can generate unusual host-guest complexes and binding modes not observed in solution. This highlights the different factors at play in solution, the charged droplets, and the gas-phase. It also shows how MS alone can be used to elucidate conformations that would be hard to predict. The work utilised a unison of CID, IMS, HDX and computational modelling with no single technique providing a clear structural picture but the unusual structures could be uncovered when the techniques were

combined.

Contribution

D.L.S. performed synthesis of hosts and most guests; NMR analysis; MS measurements; data processing; computational modelling; initial manuscript preparation. A.S. and C.A.S. supervised the project. All authors contributed to revision and final manuscript preparation.

3.6 Bioderived Rotaxanes via Dynamic Covalent Boron Chemistry

Jingjing Yu, Marius Gaedke, Satyajit Das, [Daniel L. Stares](#), Christoph A. Schalley, Fredrik Schaufelberger*.

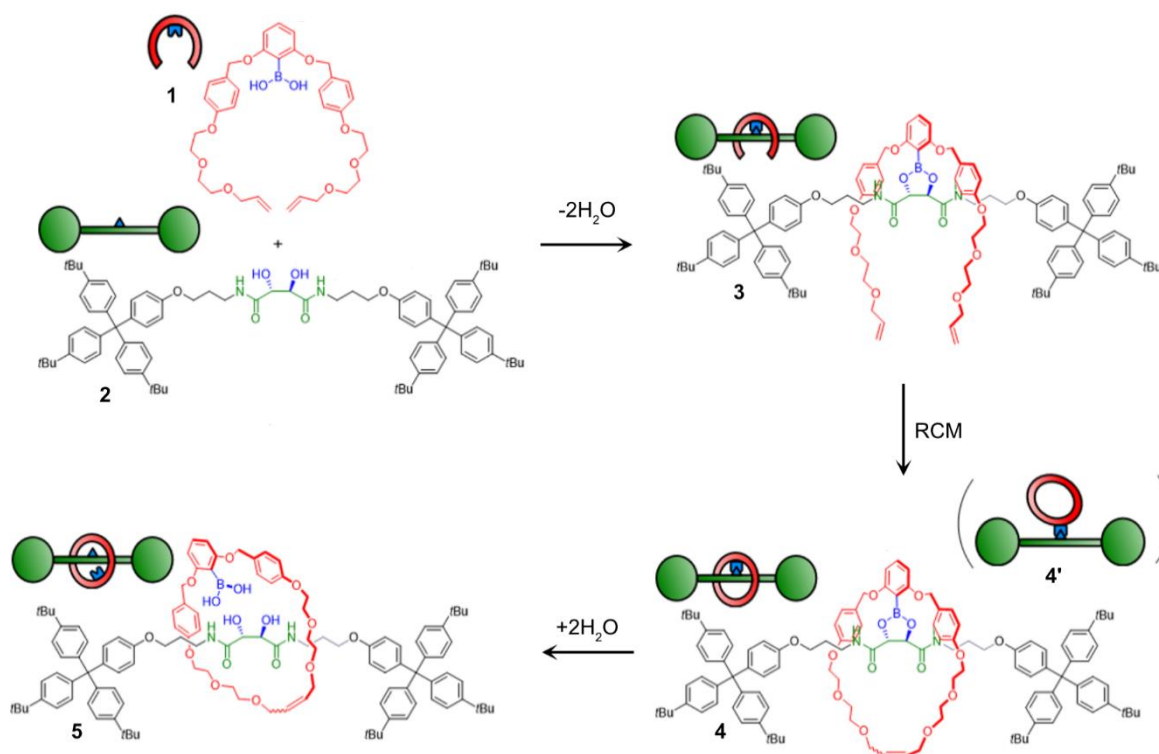
Pre-print: 10.26434/chemrxiv-2023-v95p8.

Summary

Work was completed as a collaboration with the Schaufelberger group based at the KTH Royal Institute of Technology in Stockholm. The goal of the work was to establish a proof-of-principle of generating MIMs from bioderived components. MIMs would have many potential biological applications due to their switchable nature and their ability to sterically protect functional groups. However, making water soluble and biocompatible MIMs is synthetically difficult with very few successful examples. One issue is that most MIM syntheses relies on non-covalent interactions e.g. metal coordination which require additional, non-biological functional groups. One option to avoid this is by building the MIMs from biogenic precursors, but their water-solubility means that most pre-organisation strategies are interfered with by the solvent. In this work, the MIM was formed using the dynamic covalent chemistry of boronic esters.

At the core of the axle, **2**, is a L-tartaric acid unit which is attached to stopper groups via amide coupling. A boronic acid 'pincer', **1**, can undergo condensation with the tartaric acid to form the boronic ester structure **3** (Scheme 3.1). The pincer has two terminal alkenes which can be used to form a macrocycle by RCM and analysis by ¹H-NMR revealed two major products in a roughly 2:1 ratio. As determined by HRMS, both products had the same molecular mass and were thus assigned as the structural isomers where the ring closure occurred around the axle, **4**, and where the ring closure occurred outside the axle, **4'**. Isolation of **4** and **4'** was possible via column chromatography and silica gel flash-chromatography, respectively, and through ¹H-NMR analysis, it was determined that **4'** was the major product of the RCM.

¹H-NMR was also used to follow the hydrolysis of the **4** and **4'** by dissolving both in wet CDCl₃. **4'** hydrolysed to form **2** and free macrocycle, **6**, over the course of 24 hrs with 95% conversion after 48 hrs. The interlocked nature of **4** protects the boronic ester such that hydrolysis occurs over several days but eventually forms the [2]rotaxane, **5** with 70% conversion. Formation of



Scheme 3.1: Synthesis of [2]rotaxane, **5**, via a boronic ester dynamic covalent chemistry. The boronic acid pincer, **1**, can undergo condensation with the L-tartaric acid axle, **2**. Subsequent RCM forms the non-threaded structure **4'** as the major product and the threaded structure **4**. Hydrolysis of **4** forms the MIM, **5**.

5 demonstrates that the reversible nature of the boronic ester bond can be used as a template to form a MIM and how the mechanical bond influences its hydrolysis.

4 and **4'** also showed a clear difference in size when analysed by IMS. The results were somewhat counterintuitive with the threaded **4** having a longer arrival time than the non-threaded **4'** (figure 3.15a). Comparison of the ^{TW}CCS_{N2} and TMCCS_{N2} values of HF-3c optimised structures had good agreement with one another (figure 3.15c & d). The structures suggest that the macrocycle in **4'** is more flexible and can form greater dispersion interactions with the stoppers of the axle resulting in an overall more compact structure. Hydrolysis of **4** & **4'** for MS analysis was induced by preparing samples in 4:1 acetonitrile:water and the products assessed via CID. Hydrolysis of **4'** forms **2** and **6** and the non-covalent complex between the two ([**2+6+Na**]⁺) was still observed by ESI-MS and dissociated at ~20 V to the free macrocycle **6**. In contrast, fragmentation of [**5+Na**]⁺ required much higher voltages (>70 V) and proceeded via a completely different pathway than [**2+6+Na**]⁺. Interestingly, **5** could undergo a double condensation to reform **4** which is only possible as the mechanical prevents dissociation enabling it to reach the internal energies necessary for condensation (figure 3.15b). At around 90 V, separate competing dissociation pathway was also observed by loss of wheel and axle

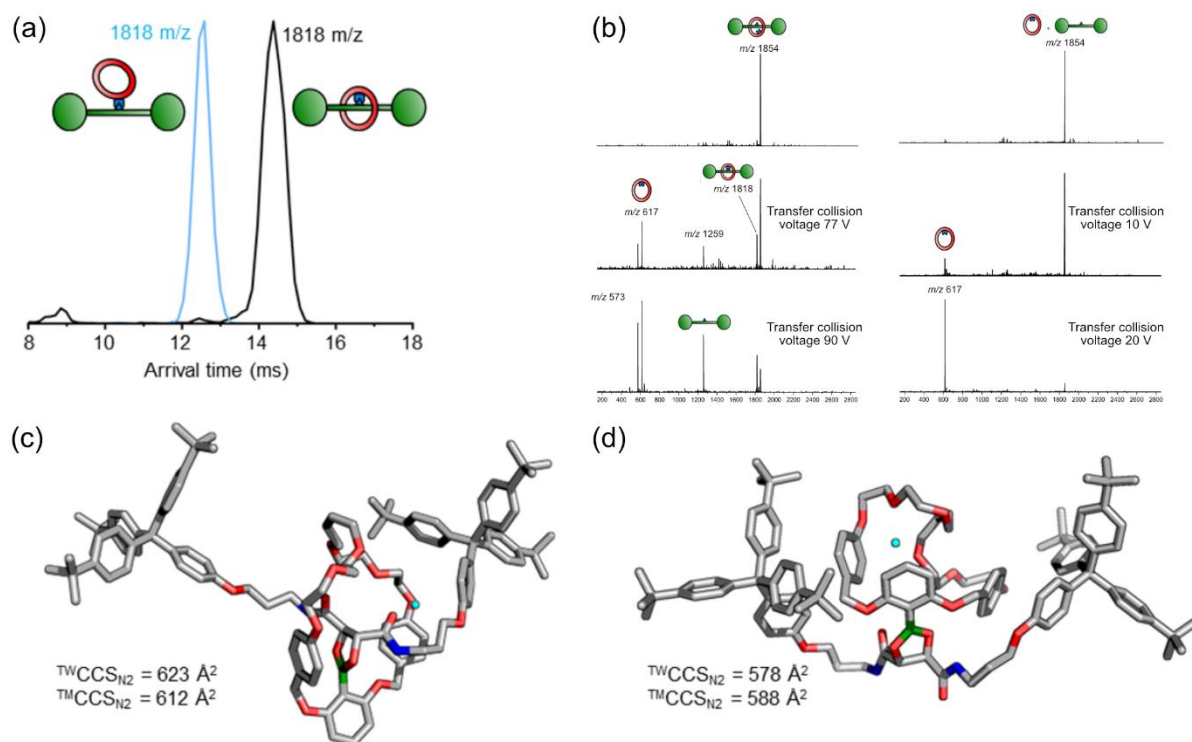


Figure 3.15: (a) ATDs of **4** and **4'** showing **4'** to be overall smaller than **4**. (b) CID of the hydrolysis products $[5+Na]^+$ and $[2+6+Na]^+$. The CID is distinctly different for both reflecting the different interlocked nature of the ions. (c) HF-3c optimised structure of $[5+Na]^+$ (left) and $[2+6+Na]^+$ (right). The $^{TW}CCS_{N_2}$ and $^{TM}CCS_{N_2}$ are shown below both structures.

likely by opening the macrocycle via cleavage of a benzylic ether bond.

The boronic ester moiety of **4** is also useful for other transformations. For instance, the phenol rotaxane could be formed by treatment of **4** with H_2O_2 . Other transformations lead to cleavage of the macrocycle liberating the free axle.

The work shows how the dynamic covalent bond of boronic esters can be used to template rotaxane formation. It shows a proof of concept for generating MIMs using biologically relevant materials and is a starting point for rotaxanes derived entirely from biomolecules. Characterisation came in the form of complementary use of NMR and MS. NMR could identify the reaction products and follow the kinetics of hydrolysis and MS could be used to clearly distinguish the outside from the inside product by IMS and CID. CID was particularly useful as the ability to condense and the high collision voltages required to induce dissociation clearly result from the mechanical bond in **4**.

Contribution

J.Y., M.G., and S.D. synthesised the complexes and performed NMR. ESI-HRMS was performed by M.G. while D.L.S. performed MS/MS measurements and computational calculations. F.S.

and C.A.S. supervised the project. F.S. prepared the initial manuscript and all authors contributed to revision and final manuscript preparation.

4. Conclusions and Perspectives

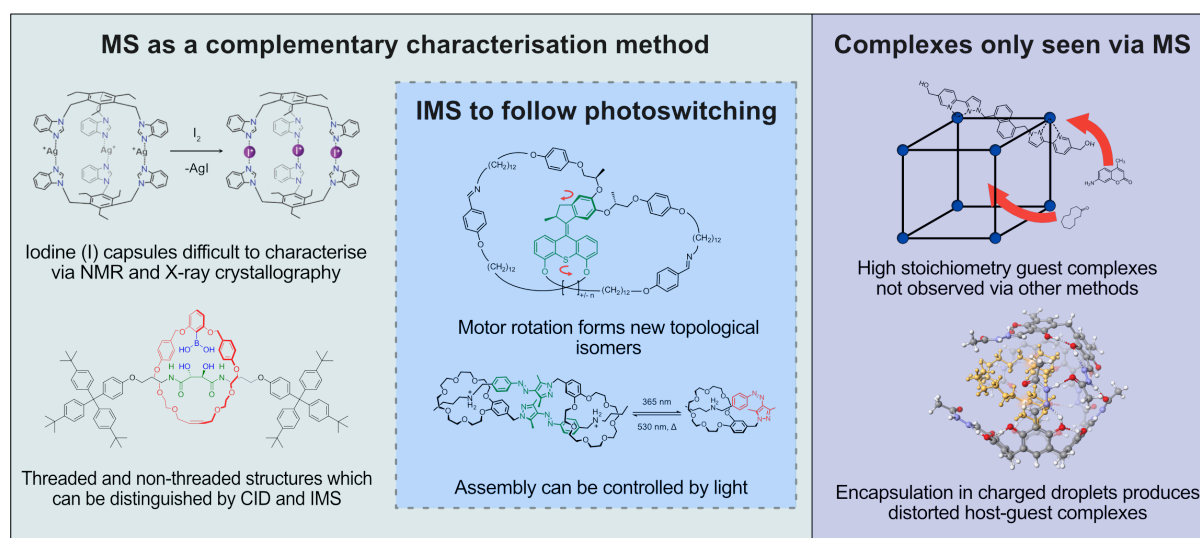


Figure 4.1: Summary of the different projects studied throughout the thesis.

The complexes which were studied within this thesis span a diverse range of supramolecular systems. In general, this demonstrates the versatility and broad applicability of MS to the field of supramolecular chemistry where it can nicely complement existing techniques such as NMR and X-ray crystallography. The study into the silver(I) and iodine(I) cages shows the benefit of combining these characterisation methods. The silver(I) cages were fully characterised by NMR and X-ray crystallography, but there were difficulties studying the iodine(I) cages due to precipitation and reactivity issues. Instead, MS was used to follow the $[N-Ag-N]^+$ to $[N-I-N]^+$ cation exchange reaction and showed the structural similarity of the iodine(I) the silver(I) cages by IMS and CID. The size and fragmentation pathway of both were similar but the iodine(I) cages were far less stable than the analogous silver(I) cages which can rationalise some of the difficulties in studying the iodine(I) cages in the condensed phase. The project represents what should be ‘conventional’ use of MS where it complements and, fills the gaps, of the more common characterisation methods to increase understanding of the system under investigation.

The boron rotaxane work also shows the benefits of the complementary use of MS/MS for structural assignment. Two structures formed from the RCM, one where ring closure occurs outside the axle and the other where it occurs around the axle to generate the quasi[1]rotaxane. IMS showed a clear size difference between the two with the non-threaded structure being smaller. Experimental and theoretical CCS values were in good agreement and

the computational structures revealed the non-threaded structure was more flexible and adopts a more compact structure. Hydrolysis to the boronic acid species was possible for both structures forming the [2]rotaxane and the free macrocycle-axle complex. CID showed a clear difference between the two with the macrocycle-axle complex undergoing facile dissociation as expected for a non-covalent complex while the [2]rotaxane required much higher collision voltages to induce dissociation due to the mechanical bond. The [2]rotaxane was even able to re-condense to form the boronic ester with other fragmentation products likely forming by opening the macrocycle. CID (or other fragmentation techniques) are particularly useful for studying MIMs as the interlocked nature of the complexes is reflected in the fragmentation pathways and the energy required to induce dissociation.

Of all the MS/MS techniques used throughout the work, IMS is the one which is most likely to be adopted in the field of supramolecular chemistry. One reason is that instruments capable of IMS are becoming more abundant but more importantly is the utility of IMS as a technique. IMS was used throughout the thesis in different ways, but a specific use is to follow dynamic processes in switchable systems as clearly showcased by the different photoswitchable systems investigated within this work. For the AAP pseudorotaxane, the ratio between *E,E*-**DC** and *Z-L* was clearly visualised by IMS as they are easily separated from one another due to their different charge states. IMS could then be used to follow the assembly and disassembly upon photoswitching by measuring a sample irradiated by the different wavelengths of light. With this, the *E,Z*-**DC** isomer was observed as an intermediate before disassembly of the **DC** and exclusive formation of the *Z-L* with the direct reformation of the *E,E*-**DC** in the reverse process. Here IMS could visualise the process more easily than NMR where the different assemblies caused signal overlap meaning the *E,Z*-**DC** isomer could not be observed. When coupled with CID, IMS also enables the gas-phase thermal relaxation processes to be investigated providing further insight into the systems. IMS also makes it possible to separate individual isomers and then study them using other techniques e.g CID or gas-phase action spectroscopy. In this way, IMS is highly versatile and should have widespread appeal within supramolecular chemistry.

Another major benefit of IMS is the direct structural assignment of complexes by comparing experimental and theoretical CCS values. For the molecular motor, this was particularly important as the system would polymerise at elevated concentrations, so crystal structures

were not possible. Instead, IMS could be used to follow the winding and unwinding of the motor and the different topological isomers were assigned based on their CCS values. The system is highly complex, and IMS helped to visualise the motor's operation and to validate the computational structures. Determining structural features and following the operation of molecular motors via MS is currently unexplored and these results serve to demonstrate the ability of IMS to untangle structural details of a highly complex system. It should be noted that most commercially available IMS instruments rely on a calibrant to determine experimental CCS values. For some systems (e.g. metal-organic), this is a potential pitfall as suitable calibrants may not exist. Care needs to be taken when evaluating such systems so that the correct conclusions are drawn. Ideally, a series of suitable calibrants for different types of supramolecular systems should be developed to aid the uptake of IMS in the supramolecular community.

The aforementioned examples were studied in conjunction with other characterisation methods but there are also situations where MS is not just merely complementary but becomes a necessity to use. This is clearly demonstrated by the study of the metal-organic cage where the high stoichiometry guest complexes were not observed by other methods e.g. NMR either due to the competitive solvents preventing their formation or a lack of sensitivity of the method. MS could overcome these issues and once transferred to the gas-phase, the binding modes of the guests could be determined by IMS and CID. Guests had different preferences for internal versus external binding and differed in the number of guests bound. These differences could be rationalised by the different binding modes of the guest and showed that high stoichiometry guests had a preference for external binding but were encapsulated at high enough guest loading. Although binding mode determination by IMS has been demonstrated previously, here it was extended to show how it can quickly be used for systems binding a high number of guests and visualise different binding modes simultaneously.

In addition to being able to see complexes which cannot be observed by other techniques is the possibility of the ESI process playing an active role in complex formation. During ESI, the charge imbalance of the droplets coupled with the increasing concentration can lead to self-assembly/binding not present in the solvent prior to ionisation. In this work, this allowed encapsulation of different cationic guests into hydrogen bonded resorcinarene dimers. To

form favourable cation- π interactions with the resorcinarene cores of the capsules, the guest distorted into a horse-shoe arrangement. This arrangement led to expansion of the guest outside the cavity and disruption of the hydrogen bonding of the capsule forcing the cavitands to adjust their positions. The binding modes could be determined with a synergistic use of CID, IMS and HDX which provided different insights into the relative stability, size, and integrity of intermolecular hydrogen bonds. When the results were combined with computational structures, they were able to shed light on the unusual structures. Here the charged droplets formed during ESI were able to generate highly unusual structures and there is likely other intriguing chemistry that can occur in the environment where charge neutrality is violated. An interesting direction for this type of chemistry would be to combine it with ion-soft landing which has been utilised in several recent publications.²⁵⁹⁻²⁶¹

Overall, the work showcases some of the benefits of MS for understanding supramolecular chemistry. All of this is not to say that MS can be used to study everything, or that other characterisation methods are obsolete, but MS certainly has a greater role to play in supramolecular chemistry than it currently holds. MS seems to occupy a space where there are numerous potential applications but the adoption by the community does not reflect this. Further implementation of MS can expedite characterisation and help build a more robust understanding of supramolecular chemistry. As a greater number of commercially available instruments become available, there is the opportunity for greater MS use within supramolecular chemistry. The work within the thesis can serve as a potential workflow for characterisation and help to build the fundamental knowledge on the pathway to the realisation of some of the goals of supramolecular chemistry.

5. References

1. J.-M. Lehn, *Science*, 1993, **260**, 1762-1763.
2. M. J. Webber and R. Langer, *Chem. Soc. Rev.*, 2017, **46**, 6600-6620.
3. I. V. Kolesnichenko and E. V. Anslyn, *Chem. Soc. Rev.*, 2017, **46**, 2385-2390.
4. G. Zhang, W. Lin, F. Huang, J. Sessler and N. M. Khashab, *J. Am. Chem. Soc.*, 2023, **145**, 19143-19163.
5. G. Olivo, G. Capocasa, D. Del Giudice, O. Lanzalunga and S. Di Stefano, *Chem. Soc. Rev.*, 2021, **50**, 7681-7724.
6. H. Chen and J. Fraser Stoddart, *Nat. Rev. Mater.*, 2021, **6**, 804-828.
7. D. B. Amabilino, D. K. Smith and J. W. Steed, *Chem. Soc. Rev.*, 2017, **46**, 2404-2420.
8. N. Geue, R. E. P. Winpenny and P. E. Barran, *Chem. Soc. Rev.*, 2022, **51**, 8-27.
9. A. L. Thompson and N. G. White, *Chem. Soc. Rev.*, 2023, **52**, 6254-6269.
10. Z. Qi, T. Heinrich, S. Moorthy and C. A. Schalley, *Chem. Soc. Rev.*, 2015, **44**, 515-531.
11. P. A. Kollman, *Acc. Chem. Res.*, 1977, **10**, 365-371.
12. F. Biedermann and H. J. Schneider, *Chem. Rev.*, 2016, **116**, 5216-5300.
13. C. A. Schalley, *Analytical methods in supramolecular chemistry*, John Wiley & Sons, 2012.
14. T. Steiner, *Angew. Chem. Int. Ed.*, 2002, **41**, 48-76.
15. J. Hermann, R. A. DiStasio, Jr. and A. Tkatchenko, *Chem. Rev.*, 2017, **117**, 4714-4758.
16. L. Cera and C. A. Schalley, *Chem. Soc. Rev.*, 2014, **43**, 1800-1812.
17. J. W. Larson and T. B. McMahon, *Inorg. Chem.*, 1984, **23**, 2029-2033.
18. L. C. Gilday, S. W. Robinson, T. A. Barendt, M. J. Langton, B. R. Mullaney and P. D. Beer, *Chem. Rev.*, 2015, **115**, 7118-7195.
19. P. Metrangolo, F. Meyer, T. Pilati, G. Resnati and G. Terraneo, *Angew. Chem. Int. Ed.*, 2008, **47**, 6114-6127.
20. L. Turunen and M. Erdélyi, *Chem. Soc. Rev.*, 2020, **49**, 2688-2700.
21. A.-C. C. Carlsson, J. Gräfenstein, A. Budnjo, J. L. Laurila, J. Bergquist, A. Karim, R. Kleinmaier, U. Brath and M. Erdélyi, *J. Am. Chem. Soc.*, 2012, **134**, 5706-5715.
22. E. Taipale, J. S. Ward, G. Fiorini, D. L. Stares, C. A. Schalley and K. Rissanen, *Inorg. Chem. Front.*, 2022, **9**, 2231-2239.
23. E. G. Hohenstein and C. D. Sherrill, *J. Phys. Chem. A*, 2009, **113**, 878-886.
24. S. Grimme, *Angew. Chem. Int. Ed.*, 2008, **47**, 3430-3434.
25. C. R. Martinez and B. L. Iverson, *Chem. Sci.*, 2012, **3**, 2191-2201.
26. C. A. Hunter and J. K. M. Sanders, *J. Am. Chem. Soc.*, 1990, **112**, 5525-5534.
27. H. Adams, C. A. Hunter, K. R. Lawson, J. Perkins, S. E. Spey, C. J. Urch and J. M. Sanderson, *Chem. Eur. J.*, 2001, **7**, 4863-4877.
28. T. K. Piskorz, V. Martí-Centelles, R. L. Spicer, F. Duarte and P. J. Lusby, *Chem. Sci.*, 2023, DOI: 10.1039/D3SC02586A.
29. B. Kronberg, *Curr. Opin. Colloid Interface Sci.*, 2016, **22**, 14-22.
30. N. T. Southall, K. A. Dill and A. D. J. Haymet, *J. Phys. Chem. B*, 2002, **106**, 2812-2812.
31. W. Blokzijl and J. B. F. N. Engberts, *Angew. Chem., Int. Ed. Engl.*, 1993, **32**, 1545-1579.
32. J. Černý and P. Hobza, *Phys. Chem. Chem. Phys.*, 2007, **9**, 5291-5303.
33. A. Langner, S. L. Tait, N. Lin, C. Rajadurai, M. Ruben and K. Kern, *Proc. Natl. Acad. Sci. U.S.A.*, 2007, **104**, 17927-17930.
34. A. Tarzia and K. E. Jelfs, *Chem. Commun.*, 2022, **58**, 3717-3730.
35. A. Wu and L. Isaacs, *J. Am. Chem. Soc.*, 2003, **125**, 4831-4835.
36. P. Mukhopadhyay, A. Wu and L. Isaacs, *J. Org. Chem.*, 2004, **69**, 6157-6164.
37. M. M. Safont-Sempere, G. Fernández and F. Würthner, *Chem. Rev.*, 2011, **111**, 5784-5814.
38. M. Weißenfels, J. Gemen and R. Klajn, *Chem*, 2021, **7**, 23-37.
39. G. M. Whitesides and M. Boncheva, *Proc. Natl. Acad. Sci. U.S.A.*, 2002, **99**, 4769-4774.
40. E. Arunan, G. R. Desiraju, R. A. Klein, J. Sadlej, S. Scheiner, I. Alkorta, D. C. Clary, R. H. Crabtree,

- J. J. Dannenberg, P. Hobza, H. G. Kjaergaard, A. C. Legon, B. Mennucci and D. J. Nesbitt, *Pure Appl. Chem.*, 2011, **83**, 1619-1636.
41. E. Arunan, G. R. Desiraju, R. A. Klein, J. Sadlej, S. Scheiner, I. Alkorta, D. C. Clary, R. H. Crabtree, J. J. Dannenberg, P. Hobza, H. G. Kjaergaard, A. C. Legon, B. Mennucci and D. J. Nesbitt, *Pure Appl. Chem.*, 2011, **83**, 1637-1641.
42. G. R. Desiraju, P. S. Ho, L. Kloo, A. C. Legon, R. Marquardt, P. Metrangolo, P. Politzer, G. Resnati and K. Rissanen, *Pure Appl. Chem.*, 2013, **85**, 1711-1713.
43. B. S. Pilgrim and N. R. Champness, *ChemPlusChem*, 2020, **85**, 1842-1856.
44. J. Meeuwissen and J. N. H. Reek, *Nat. Chem.*, 2010, **2**, 615-621.
45. J.-M. Lehn, *Pure Appl. Chem.*, 1978, **50**, 871-892.
46. C. J. Pedersen, *Angew. Chem., Int. Ed. Engl.*, 1988, **27**, 1021-1027.
47. D. J. Cram and J. M. Cram, *Acc. Chem. Res.*, 1978, **11**, 8-14.
48. C. J. Pedersen, *J. Am. Chem. Soc.*, 1967, **89**, 7017-7036.
49. J.-M. Lehn, *Angew. Chem., Int. Ed. Engl.*, 1988, **27**, 89-112.
50. E. Persch, O. Dumele and F. Diederich, *Angew. Chem. Int. Ed.*, 2015, **54**, 3290-3327.
51. A. R. Fersht, *Trends Biochem. Sci.*, 1987, **12**, 301-304.
52. D. J. Cram, *Angew. Chem., Int. Ed. Engl.*, 1988, **27**, 1009-1020.
53. D. J. Cram, *Angew. Chem., Int. Ed. Engl.*, 1986, **25**, 1039-1057.
54. Q. Zhang and K. Tiefenbacher, *Nat. Chem.*, 2015, **7**, 197-202.
55. T. M. Bräuer, Q. Zhang and K. Tiefenbacher, *Angew. Chem. Int. Ed.*, 2016, **55**, 7698-7701.
56. C. Mozaceanu, C. G. Taylor, J. R. Piper, S. P. Argent and M. D. Ward, *Chemistry*, 2020, **2**, 22-32.
57. H. Takezawa, K. Shitozawa and M. Fujita, *Nat. Chem.*, 2020, **12**, 574-578.
58. P. Mal, B. Breiner, K. Rissanen and J. R. Nitschke, *Science*, 2009, **324**, 1697-1699.
59. D. Fiedler, R. G. Bergman and K. N. Raymond, *Angew. Chem. Int. Ed.*, 2006, **45**, 745-748.
60. D. J. Cram, M. E. Tanner and R. Thomas, *Angew. Chem., Int. Ed. Engl.*, 1991, **30**, 1024-1027.
61. M. Quan, X.-Y. Pang and W. Jiang, *Angew. Chem. Int. Ed.*, 2022, **61**, e202201258.
62. J. Wankar, N. G. Kotla, S. Gera, S. Rasala, A. Pandit and Y. A. Rochev, *Adv. Funct. Mater.*, 2020, **30**, 1909049.
63. B. Dietrich, J. Lehn and J. Sauvage, *Tetrahedron Lett.*, 1969, **10**, 2889-2892.
64. R. M. Izatt, K. Pawlak, J. S. Bradshaw and R. L. Bruening, *Chem. Rev.*, 1995, **95**, 2529-2586.
65. J. M. Lehn and J. P. Sauvage, *J. Am. Chem. Soc.*, 1975, **97**, 6700-6707.
66. O. A. Raevsky, V. P. Solovev, A. F. Solotnov, H. J. Schneider and V. Rudiger, *J. Org. Chem.*, 1996, **61**, 8113-8116.
67. P. R. Ashton, P. J. Campbell, P. T. Glink, D. Philp, N. Spencer, J. F. Stoddart, E. J. T. Chrystal, S. Menzer, D. J. Williams and P. A. Tasker, *Angew. Chem., Int. Ed. Engl.*, 1995, **34**, 1865-1869.
68. I. Puskás, L. Szente, L. Szőcs and É. Fenyvesi, *Period. Polytech. Chem. Eng.*, 2023, **67**, 11-17.
69. S. Wüpper, K. Lüersen and G. Rimbach, *Biomolecules*, 2021, **11**, 401-422.
70. Q.-D. Hu, G.-P. Tang and P. K. Chu, *Acc. Chem. Res.*, 2014, **47**, 2017-2025.
71. W. A. Freeman, W. L. Mock and N. Y. Shih, *J. Am. Chem. Soc.*, 1981, **103**, 7367-7368.
72. K. Kim, N. Selvapalam and D. H. Oh, *J. Inclusion Phenom. Macrocyclic Chem.*, 2004, **50**, 31-36.
73. K. Kim, N. Selvapalam, Y. H. Ko, K. M. Park, D. Kim and J. Kim, *Chem. Soc. Rev.*, 2007, **36**, 267-279.
74. D. J. Cram, S. Karbach, Y. H. Kim, L. Baczynskyj and G. W. Kallemeyn, *J. Am. Chem. Soc.*, 1985, **107**, 2575-2576.
75. A. S. Hoegberg, *J. Org. Chem.*, 1980, **45**, 4498-4500.
76. H.-J. Schneider and U. Schneider, *J. Incl. Phenomena Mol. Rec.*, 1994, **19**, 67-83.
77. K. Kobayashi and M. Yamanaka, *Chem. Soc. Rev.*, 2015, **44**, 449-466.
78. K. N. Rose, L. J. Barbour, G. W. Orr and J. L. Atwood, *Chem. Commun.*, 1998, DOI: 10.1039/A707802A, 407-408.
79. C. Gaeta, C. Talotta, M. De Rosa, P. La Manna, A. Soriente and P. Neri, *Chem. Eur. J.*, 2019, **25**, 4899-4913.

80. M. Yamanaka, A. Shivanyuk and J. Rebek, Jr., *J. Am. Chem. Soc.*, 2004, **126**, 2939-2943.
81. N. K. Beyeh, M. Kogej, A. Åhman, K. Rissanen and C. A. Schalley, *Angew. Chem. Int. Ed.*, 2006, **45**, 5214-5218.
82. S. Gambaro, M. De Rosa, A. Soriente, C. Talotta, G. Floresta, A. Rescifina, C. Gaeta and P. Neri, *Org. Chem. Front.*, 2019, **6**, 2339-2347.
83. A. Shivanyuk and J. Rebek, Jr., *Proc. Natl. Acad. Sci. U.S.A.*, 2001, **98**, 7662-7665.
84. L. R. MacGillivray and J. L. Atwood, *Nature*, 1997, **389**, 469-472.
85. S. Saito, D. M. Rudkevich and J. Rebek, Jr., *Org. Lett.*, 1999, **1**, 1241-1244.
86. L. Trembleau and J. Rebek, Jr., *Science*, 2003, **301**, 1219-1220.
87. S. S. Zhu, H. Staats, K. Brandhorst, J. Grunenber, F. Gruppi, E. Dalcanale, A. Lützen, K. Rissanen and C. A. Schalley, *Angew. Chem. Int. Ed.*, 2008, **47**, 788-792.
88. S. K. Körner, F. C. Tucci, D. M. Rudkevich, T. Heinz and J. Rebek, Jr., *Chem. Eur. J.*, 2000, **6**, 187-195.
89. T. Heinz, D. M. Rudkevich and J. Rebek, Jr., *Nature*, 1998, **394**, 764-766.
90. H. Mansikkamäki, M. Nissinen and K. Rissanen, *Chem. Commun.*, 2002, 1902-1903.
91. D. Ajami and J. Rebek, Jr., *J. Am. Chem. Soc.*, 2006, **128**, 5314-5315.
92. D. Ajami and J. Rebek, Jr., *Angew. Chem. Int. Ed.*, 2007, **46**, 9283-9286.
93. T. Iwasawa, *Tetrahedron Lett.*, 2017, **58**, 4217-4226.
94. N. Natarajan, E. Brenner, D. Sémeril, D. Matt and J. Harrowfield, *Eur. J. Org. Chem.*, 2017, **2017**, 6100-6113.
95. S. Richeter and J. Rebek, Jr., *J. Am. Chem. Soc.*, 2004, **126**, 16280-16281.
96. M. Kanaura, N. Endo, M. P. Schramm and T. Iwasawa, *Eur. J. Org. Chem.*, 2016, **2016**, 4970-4975.
97. D. J. Cram, *Nature*, 1992, **356**, 29-36.
98. M. Grajda, M. Wierzbicki, P. Cmoch and A. Szumna, *J. Org. Chem.*, 2013, **78**, 11597-11601.
99. M. Szymanski, M. Wierzbicki, M. Gilski, H. Jedrzejewska, M. Sztylko, P. Cmoch, A. Shkurenko, M. Jaskolski and A. Szumna, *Chemistry*, 2016, **22**, 3148-3155.
100. M. P. Szymański, J. S. Czajka, P. Cmoch, W. Iwanek and A. Szumna, *Supramol. Chem.*, 2018, **30**, 430-437.
101. R. S. Meissner, J. Rebek, Jr. and J. de Mendoza, *Science*, 1995, **270**, 1485-1488.
102. J. M. Kang and J. Rebek, Jr., *Nature*, 1996, **382**, 239-241.
103. J. M. Kang, G. Hilmersson, J. Santamaría and J. Rebek, Jr., *J. Am. Chem. Soc.*, 1998, **120**, 3650-3656.
104. J. Kang and J. Rebek, Jr., *Nature*, 1997, **385**, 50-52.
105. F. Hof, S. L. Craig, C. Nuckolls and J. Rebek, Jr., *Angew. Chem. Int. Ed.*, 2002, **41**, 1488-1508.
106. G. Cavallo, P. Metrangolo, R. Milani, T. Pilati, A. Priimagi, G. Resnati and G. Terraneo, *Chem. Rev.*, 2016, **116**, 2478-2601.
107. O. Dumele, N. Trapp and F. Diederich, *Angew. Chem. Int. Ed.*, 2015, **54**, 12339-12344.
108. L. Turunen, U. Warzok, R. Puttreddy, N. K. Beyeh, C. A. Schalley and K. Rissanen, *Angew. Chem. Int. Ed.*, 2016, **55**, 14033-14036.
109. M. Fujita, D. Oguro, M. Miyazawa, H. Oka, K. Yamaguchi and K. Ogura, *Nature*, 1995, **378**, 469-471.
110. M. D. Ward, *Chem. Commun.*, 2009, DOI: 10.1039/B906726B, 4487-4499.
111. M. Fujita, J. Yazaki and K. Ogura, *J. Am. Chem. Soc.*, 1990, **112**, 5645-5647.
112. M. Fujita, M. Tominaga, A. Hori and B. Therrien, *Acc. Chem. Res.*, 2005, **38**, 369-378.
113. D. Fiedler, D. H. Leung, R. G. Bergman and K. N. Raymond, *Acc. Chem. Res.*, 2004, **38**, 349-358.
114. I. S. Tidmarsh, T. B. Faust, H. Adams, L. P. Harding, L. Russo, W. Clegg and M. D. Ward, *J. Am. Chem. Soc.*, 2008, **130**, 15167-15175.
115. K. Harris, D. Fujita and M. Fujita, *Chem. Commun.*, 2013, **49**, 6703-6712.
116. D. Fujita, Y. Ueda, S. Sato, N. Mizuno, T. Kumasaka and M. Fujita, *Nature*, 2016, **540**, 563-566.
117. D. L. Caulder, R. E. Powers, T. N. Parac and K. N. Raymond, *Angew. Chem. Int. Ed.*, 1998, **37**,

- 1840-1843.
118. A. V. Davis and K. N. Raymond, *J. Am. Chem. Soc.*, 2005, **127**, 7912-7919.
119. D. H. Leung, R. G. Bergman and K. N. Raymond, *J. Am. Chem. Soc.*, 2007, **129**, 2746-2747.
120. D. L. Caulder, C. Brückner, R. E. Powers, S. König, T. N. Parac, J. A. Leary and K. N. Raymond, *J. Am. Chem. Soc.*, 2001, **123**, 8923-8938.
121. M. Fujita, S.-Y. Yu, T. Kusukawa, H. Funaki, K. Ogura and K. Yamaguchi, *Angew. Chem. Int. Ed.*, 1998, **37**, 2082-2085.
122. Z. R. Bell, L. P. Harding and M. D. Ward, *Chem. Commun.*, 2003, DOI: 10.1039/B307172N, 2432-2433.
123. W. Cullen, M. C. Misuraca, C. A. Hunter, N. H. Williams and M. D. Ward, *Nat. Chem.*, 2016, **8**, 231-236.
124. C. G. P. Taylor, S. P. Argent, M. D. Ludden, J. R. Piper, C. Mozaceanu, S. A. Barnett and M. D. Ward, *Chem. Eur. J.*, 2020, **26**, 3054-3064.
125. C. G. Taylor, J. S. Train and M. D. Ward, *Chemistry*, 2020, **2**, 510-524.
126. P. R. Ashton, I. Baxter, M. C. T. Fyfe, F. M. Raymo, N. Spencer, J. F. Stoddart, A. J. P. White and D. J. Williams, *J. Am. Chem. Soc.*, 1998, **120**, 2297-2307.
127. M. Xue, Y. Yang, X. Chi, X. Yan and F. Huang, *Chem. Rev.*, 2015, **115**, 7398-7501.
128. J. F. Stoddart, *Chem. Soc. Rev.*, 2009, **38**, 1802-1820.
129. C. J. Brunns and J. F. Stoddart, *The nature of the mechanical bond: from molecules to machines*, John Wiley & Sons, 2016.
130. S. R. Beeren, C. T. McTernan and F. Schaufelberger, *Chem*, 2023, **9**, 1378-1412.
131. R. S. Forgan, J.-P. Sauvage and J. F. Stoddart, *Chem. Rev.*, 2011, **111**, 5434-5464.
132. E. Wasserman, *J. Am. Chem. Soc.*, 1960, **82**, 4433-4434.
133. C. O. Dietrich-Buchecker, J. P. Sauvage and J. P. Kintzinger, *Tetrahedron Lett.*, 1983, **24**, 5095-5098.
134. C. O. Dietrich-Buchecker and J.-P. Sauvage, *Angew. Chem., Int. Ed. Engl.*, 1989, **28**, 189-192.
135. F. Schaufelberger, *Commun. Chem.*, 2020, **3**, 182.
136. Z. Cui and G.-X. Jin, *Nat. Synth.*, 2022, **1**, 635-640.
137. S. Kassem, T. van Leeuwen, A. S. Lubbe, M. R. Wilson, B. L. Feringa and D. A. Leigh, *Chem. Soc. Rev.*, 2017, **46**, 2592.
138. A. Saura-Sanmartin, J. S. Martinez-Espin, A. Martinez-Cuezva, M. Alajarin and J. Berna, *Molecules*, 2017, **22**.
139. P. L. Anelli, N. Spencer and J. F. Stoddart, *J. Am. Chem. Soc.*, 1991, **113**, 5131-5133.
140. G. Du, E. Moulin, N. Jouault, E. Buhler and N. Giuseppone, *Angew. Chem. Int. Ed.*, 2012, **51**, 12504-12508.
141. A. Goujon, E. Moulin, G. Fuks and N. Giuseppone, *CCS Chem.*, 2019, **1**, 83-96.
142. M. C. Jiménez, C. Dietrich-Buchecker, J.-P. Sauvage and A. De Cian, *Angew. Chem. Int. Ed.*, 2000, **39**, 1295-1298.
143. M. C. Jiménez, C. Dietrich-Buchecker and J.-P. Sauvage, *Angew. Chem. Int. Ed.*, 2000, **39**, 3284-3287.
144. Y. Feng, M. Ovalle, J. S. W. Seale, C. K. Lee, D. J. Kim, R. D. Astumian and J. F. Stoddart, *J. Am. Chem. Soc.*, 2021, **143**, 5569-5591.
145. C. Cheng, P. R. McGonigal, S. T. Schneebeli, H. Li, N. A. Vermeulen, C. Ke and J. F. Stoddart, *Nat. Nanotechnol.*, 2015, **10**, 547.
146. C. Pezzato, M. T. Nguyen, C. Cheng, D. J. Kim, M. T. Otley and J. F. Stoddart, *Tetrahedron*, 2017, **73**, 4849.
147. Y. Qiu, B. Song, C. Pezzato, D. Shen, W. Liu, L. Zhang, Y. Feng, Q. H. Guo, K. Cai, W. Li, H. Chen, M. T. Nguyen, Y. Shi, C. Cheng, R. D. Astumian, X. Li and J. F. Stoddart, *Science*, 2020, **368**, 1247.
148. A. A. Beharry and G. A. Woolley, *Chem. Soc. Rev.*, 2011, **40**, 4422-4437.
149. M. Baroncini, S. Silvi and A. Credi, *Chem. Rev.*, 2020, **120**, 200-268.

150. H. Lee, J. Tessarolo, D. Langbehn, A. Baksi, R. Herges and G. H. Clever, *J. Am. Chem. Soc.*, 2022, **144**, 3099-3105.
151. J. Volarić, W. Szymanski, N. A. Simeth and B. L. Feringa, *Chem. Soc. Rev.*, 2021, **50**, 12377-12449.
152. M. Irie, *Chem. Rev.*, 2000, **100**, 1685-1716.
153. K. Matsuda and M. Irie, *J. Photochem. Photobiol. C*, 2004, **5**, 169-182.
154. H. M. D. Bandara and S. C. Burdette, *Chem. Soc. Rev.*, 2012, **41**, 1809-1825.
155. L. Stricker, E. C. Fritz, M. Peterlechner, N. L. Doltsinis and B. J. Ravoo, *J. Am. Chem. Soc.*, 2016, **138**, 4547-4554.
156. C. E. Weston, R. D. Richardson, P. R. Haycock, A. J. P. White and M. J. Fuchter, *J. Am. Chem. Soc.*, 2014, **136**, 11878-11881.
157. A. Díaz-Moscoso and P. Ballester, *Chem. Commun.*, 2017, **53**, 4635-4652.
158. E. Fuentes, M. Gerth, J. A. Berrocal, C. Matera, P. Gorostiza, I. K. Voets, S. Pujals and L. Albertazzi, *J. Am. Chem. Soc.*, 2020, **142**, 10069-10078.
159. S. Shinkai, T. Nakaji, T. Ogawa, K. Shigematsu and O. Manabe, *J. Am. Chem. Soc.*, 1981, **103**, 111-115.
160. S. Shinkai, K. Shigematsu, M. Sato and O. Manabe, *J. Chem. Soc., Perkin trans. 1*, 1982, DOI: 10.1039/P19820002735, 2735-2739.
161. N. Koumura, R. W. J. Zijlstra, R. A. van Delden, N. Harada and B. L. Feringa, *Nature*, 1999, **401**, 152-155.
162. D. Roke, S. J. Wezenberg and B. L. Feringa, *Proc. Natl. Acad. Sci. U.S.A.*, 2018, **115**, 9423-9431.
163. M. Klok, M. Walko, E. M. Geertsema, N. Ruangsapapichat, J. C. M. Kistemaker, A. Meetsma and B. L. Feringa, *Chem. Eur. J.*, 2008, **14**, 11183-11193.
164. D. R. S. Pooler, A. S. Lubbe, S. Crespi and B. L. Feringa, *Chem. Sci.*, 2021, **12**, 14964-14986.
165. G. S. Kottas, L. I. Clarke, D. Horinek and J. Michl, *Chem. Rev.*, 2005, **105**, 1281-1376.
166. V. García-López, D. Liu and J. M. Tour, *Chem. Rev.*, 2020, **120**, 79.
167. Q. Li, G. Fuks, E. Moulin, M. Maaloum, M. Rawiso, I. Kulic, J. T. Foy and N. Giuseppone, *Nat. Nanotechnol.*, 2015, **10**, 161.
168. T. Kudernac, N. Ruangsapapichat, M. Parschau, B. Maciá, N. Katsonis, S. R. Harutyunyan, K. -H. Ernst and B. L. Feringa, *Nature*, 2011, **479**, 208-211.
169. J. J. Thomson, *Lond. Edinb. Dublin philos. mag. j. sci.*, 1897, **44**, 293-316.
170. J. Griffiths, *Anal. Chem.*, 2008, **80**, 5678-5683.
171. F. W. Aston, *Lond. Edinb. Dublin philos. mag. j. sci.*, 1919, **38**, 707-714.
172. F. W. Aston, *Nature*, 1920, **105**, 617-619.
173. F. W. Aston, *Lond. Edinb. Dublin philos. mag. j. sci.*, 1920, **39**, 611-625.
174. W. Bleakney, *Phys. Rev.*, 1929, **34**, 157-160.
175. D. J. Pappin, P. Hojrup and A. J. Bleasby, *Curr. Biol.*, 1993, **3**, 327-332.
176. M. Yamashita and J. B. Fenn, *J. Phys. Chem.*, 1984, **88**, 4451-4459.
177. K. Tanaka, H. Waki, Y. Ido, S. Akita, Y. Yoshida, T. Yoshida and T. Matsuo, *Rapid Commun. Mass Spectrom.*, 1988, **2**, 151-153.
178. M. Karas and F. Hillenkamp, *Anal. Chem.*, 1988, **60**, 2299-2301.
179. M. Wilm, *Mol. Cell. Proteomics*, 2011, **10**.
180. M. Dole, L. L. Mack, R. L. Hines, R. C. Mobley, L. D. Ferguson and M. B. Alice, *J. Chem. Phys.*, 1968, **49**, 2240-2249.
181. J. B. Fenn, M. Mann, C. K. Meng, S. F. Wong and C. M. Whitehouse, *Science*, 1989, **246**, 64-71.
182. P. Kebarle and U. H. Verkerk, *Mass Spectrom. Rev.*, 2009, **28**, 898-917.
183. L. Konermann, E. Ahadi, A. D. Rodriguez and S. Vahidi, *Anal. Chem.*, 2013.
184. G. Wang and R. B. Cole, *Anal. Chim. Acta*, 2000, **406**, 53-65.
185. E. A. C. Spencer, T. Ly and R. R. Julian, *Int. J. Mass Spectrom.*, 2008, **270**, 166-172.
186. J. F. de la Mora, *Anal. Chim. Acta*, 2000, **406**, 93-104.
187. P. Kebarle and L. Tang, *Anal. Chem.*, 1993, **65**, A972-A986.

-
188. G. L. Glish and R. W. Vachet, *Nat. Rev. Drug Discov.*, 2003, **2**, 140-150.
189. J. B. Fenn, *Angew. Chem. Int. Ed.*, 2003, **42**, 3871-3894.
190. W. Paul and H. Steinwedel, *Z. Naturforsch. A*, 1953, **8**, 448-450.
191. P. H. Dawson, *Mass Spectrom. Rev.*, 1986, **5**, 1-37.
192. R. E. March, *J. Mass Spectrom.*, 1997, **32**, 351-369.
193. D. J. Douglas, *Mass Spectrom. Rev.*, 2009, **28**, 937-960.
194. P. H. Dawson, *Quadrupole mass spectrometry and its applications*, Elsevier, 2013.
195. M. Guilhaus, *J. Mass Spectrom.*, 1995, **30**, 1519-1532.
196. W. Wiley and I. H. McLaren, *Rev. Sci. Instrum.*, 1955, **26**, 1150-1157.
197. B. Mamyurin, V. Karataev, D. Shmikk and V. Zagulin, *Zh. Eksp. Teor. Fiz*, 1973, **64**, 82-89.
198. H. Wollnik, *Mass Spectrom. Rev.*, 1993, **12**, 89-114.
199. M. Guilhaus, D. Selby and V. Mlynski, *Mass Spectrom. Rev.*, 2000, **19**, 65-107.
200. C. Weickhardt, F. Moritz and J. Grotemeyer, *Mass Spectrom. Rev.*, 1996, **15**, 139-162.
201. A. G. Marshall and C. L. Hendrickson, *Int. J. Mass Spectrom.*, 2002, **215**, 59-75.
202. A. G. Marshall, C. L. Hendrickson and G. S. Jackson, *Mass Spectrom. Rev.*, 1998, **17**, 1-35.
203. A. G. Marshall, *Acc. Chem. Res.*, 1985, **18**, 316-322.
204. M. B. Comisarow and A. G. Marshall, *Chem. Phys. Lett.*, 1974, **26**, 489-490.
205. M. B. Comisarow and A. G. Marshall, *Chem. Phys. Lett.*, 1974, **25**, 282-283.
206. D. F. Smith, D. C. Podgorski, R. P. Rodgers, G. T. Blakney and C. L. Hendrickson, *Anal. Chem.*, 2018, **90**, 2041-2047.
207. M. B. Comisarow, V. Grassi and G. Parisod, *Chem. Phys. Lett.*, 1978, **57**, 413-416.
208. F. W. McLafferty, *Science*, 1981, **214**, 280-287.
209. L. Sleno and D. A. Volmer, *J. Mass Spectrom.*, 2004, **39**, 1091-1112.
210. E. de Hoffmann, *J. Mass Spectrom.*, 1996, **31**, 129-137.
211. G. L. Glish and D. J. Burinsky, *J. Am. Soc. Mass Spectrom.*, 2008, **19**, 161-172.
212. K. R. Jennings, *Int. J. Mass Spectrom.*, 2000, **200**, 479-493.
213. R. A. Zubarev, *Curr. Opin. Biotechnol.*, 2004, **15**, 12-16.
214. J. Mitchell Wells and S. A. McLuckey, in *Methods Enzymol.*, Academic Press, 2005, vol. 402, pp. 148-185.
215. M. Gaedke, H. Hupatz, F. Witte, S. M. Rupf, C. Douglas, H. V. Schröder, L. Fischer, M. Malischewski, B. Paulus and C. A. Schalley, *Org. Chem. Front.*, 2022, **9**, 64-74.
216. F. McLafferty, P. Bente, R. Kornfeld, S.-C. Tsai and I. Howe, *J. Am. Chem. Soc.*, 1973, **95**, 2120-2129.
217. M. Gaedke, H. Hupatz, H. V. Schröder, S. Suhr, K. F. Hoffmann, A. Valkonen, B. Sarkar, S. Riedel, K. Rissanen and C. A. Schalley, *Org. Chem. Front.*, 2021, **8**, 3659-3667.
218. M. W. Forbes, D. A. Volmer, G. J. Francis and D. K. Böhme, *J. Am. Soc. Mass Spectrom.*, 2005, **16**, 779-791.
219. M. T. Rodgers and P. B. Armentrout, *Mass Spectrom. Rev.*, 2000, **19**, 215-247.
220. K. M. Ervin and P. B. Armentrout, *J. Chem. Phys.*, 1985, **83**, 166-189.
221. F. Muntean and P. Armentrout, *J. Chem. Phys.*, 2001, **115**, 1213-1228.
222. J. Hofmann and K. Pagel, *Angew. Chem. Int. Ed.*, 2017, **56**, 8342-8349.
223. G. A. Eiceman and J. A. Stone, *Anal. Chem.*, 2004, **76**, 390A-397A.
224. R. G. Ewing, D. A. Atkinson, G. A. Eiceman and G. J. Ewing, *Talanta*, 2001, **54**, 515-529.
225. T. Wyttenbach, P. R. Kemper and M. T. Bowers, *Int. J. Mass Spectrom.*, 2001, **212**, 13-23.
226. A. B. Kanu, P. Dwivedi, M. Tam, L. Matz and H. H. Hill, *J. Mass Spectrom.*, 2008, **43**, 1-22.
227. V. Gabelica and E. Marklund, *Curr. Opin. Chem. Biol.*, 2018, **42**, 51-59.
228. U. Warzok, M. Marianski, W. Hoffmann, L. Turunen, K. Rissanen, K. Pagel and C. A. Schalley, *Chem. Sci.*, 2018, **9**, 8343-8351.
229. J. Coots, V. Gandhi, T. Onakoya, X. Chen and C. Larriba-Andaluz, *J. Aerosol Sci.*, 2020, **147**, 105570.
230. A. A. Shvartsburg and M. F. Jarrold, *Chem. Phys. Lett.*, 1996, **261**, 86-91.
-

-
231. M. F. Mesleh, J. M. Hunter, A. A. Shvartsburg, G. C. Schatz and M. F. Jarrold, *The Journal of Physical Chemistry*, 1996, **100**, 16082-16086.
232. V. Gabelica, A. A. Shvartsburg, C. Afonso, P. Barran, J. L. P. Benesch, C. Bleiholder, M. T. Bowers, A. Bilbao, M. F. Bush, J. L. Campbell, I. D. G. Campuzano, T. Causon, B. H. Clowers, C. S. Creaser, E. De Pauw, J. Far, F. Fernandez-Lima, J. C. Fjeldsted, K. Giles, M. Groessl, C. J. Hogan Jr, S. Hann, H. I. Kim, R. T. Kurulugama, J. C. May, J. A. McLean, K. Pagel, K. Richardson, M. E. Ridgeway, F. Rosu, F. Sobott, K. Thalassinou, S. J. Valentine and T. Wytttenbach, *Mass Spectrom. Rev.*, 2019, **38**, 291-320.
233. S. D. Pringle, K. Giles, J. L. Wildgoose, J. P. Williams, S. E. Slade, K. Thalassinou, R. H. Bateman, M. T. Bowers and J. H. Scrivens, *Int. J. Mass Spectrom.*, 2007, **261**, 1-12.
234. M. Göth and K. Pagel, *Anal. Bioanal. Chem.*, 2017, **409**, 4305-4310.
235. X. Zheng, N. A. Aly, Y. Zhou, K. T. Dupuis, A. Bilbao, Vanessa L. Paurus, D. J. Orton, R. Wilson, S. H. Payne, R. D. Smith and E. S. Baker, *Chem. Sci.*, 2017, **8**, 7724-7736.
236. M. F. Bush, Z. Hall, K. Giles, J. Hoyes, C. V. Robinson and B. T. Ruotolo, *Anal. Chem.*, 2010, **82**, 9557-9565.
237. M. F. Bush, I. D. G. Campuzano and C. V. Robinson, *Anal. Chem.*, 2012, **84**, 7124-7130.
238. T. Reinecke, A. L. Davis and B. H. Clowers, *J. Am. Soc. Mass Spectrom.*, 2019, **30**, 977-986.
239. K. Giles, J. P. Williams and I. Campuzano, *Rapid Commun. Mass Spectrom.*, 2011, **25**, 1559-1566.
240. A. A. Shvartsburg and R. D. Smith, *Anal. Chem.*, 2008, **80**, 9689-9699.
241. J. Hofmann, W. B. Struwe, C. A. Scarff, J. H. Scrivens, D. J. Harvey and K. Pagel, *Anal. Chem.*, 2014, **86**, 10789-10795.
242. M. E. Hemling, J. J. Conboy, M. F. Bean, M. Mentzer and S. A. Carr, *J. Am. Soc. Mass Spectrom.*, 1994, **5**, 434-442.
243. K. D. Rand, S. D. Pringle, J. P. Murphy, III, K. E. Fadgen, J. Brown and J. R. Engen, *Anal. Chem.*, 2009, **81**, 10019-10028.
244. M. A. Freitas, C. L. Hendrickson, M. R. Emmett and A. G. Marshall, *J. Am. Soc. Mass Spectrom.*, 1998, **9**, 1012-1019.
245. H. D. F. Winkler, E. V. Dzyuba and C. A. Schalley, *New J. Chem.*, 2011, **35**, 529-541.
246. S. Marcisin and J. Engen, *Anal. Bioanal. Chem.*, 2010, **397**, 967-972.
247. E. Kalenius, D. Moiani, E. Dalcanale and P. Vainiotalo, *Chem. Commun.*, 2007, DOI: 10.1039/b707842k, 3865-3867.
248. H. D. F. Winkler, E. V. Dzyuba, J. A. W. Sklorz, N. K. Beyeh, K. Rissanen and C. A. Schalley, *Chem. Sci.*, 2011, **2**, 615-624.
249. I. D. G. Campuzano and K. Giles, *TrAC, Trends Anal. Chem.*, 2019, **120**, 115620.
250. D. Morsa, V. Gabelica and E. De Pauw, *Anal. Chem.*, 2011, **83**, 5775-5782.
251. B. Baytekin, H. T. Baytekin and C. A. Schalley, *Org. Biomol. Chem.*, 2006, **4**, 2825-2841.
252. J. S. McIndoe, *Angew. Chem. Int. Ed.*, 2010, **49**, 3717.
253. K. Barylyuk, R. M. Balabin, D. Grünstein, R. Kikkeri, V. Frankevich, P. H. Seeberger and R. Zenobi, *J. Am. Soc. Mass Spectrom.*, 2011, **22**, 1167-1177.
254. T. Gerkensmeier, W. Iwanek, C. Agena, R. Fröhlich, S. Kotila, C. Näther and J. Mattay, *Eur. J. Org. Chem.*, 1999, 2257-2262.
255. C. Bich, S. Baer, M. C. Jecklin and R. Zenobi, *J. Am. Soc. Mass Spectrom.*, 2010, **21**, 286-289.
256. T. Heravi, J. Shen, S. Johnson, M. C. Asplund and D. V. Dearden, *J. Phys. Chem. A*, 2021, **125**, 7803-7812.
257. E. Hanozin, B. Mignolet, J. Martens, G. Berden, D. Sluysmans, A. S. Duwez, J. F. Stoddart, G. Eppe, J. Oomens, E. De Pauw and D. Morsa, *Angew. Chem. Int. Ed.*, 2021, **60**, 10049-10055.
258. G. Carroy, C. Daxhelet, V. Lemaur, J. De Winter, E. De Pauw, J. Cornil and P. Gerbaux, *Chemistry*, 2016, **22**, 4528-4534.
259. B. Gologan, J. R. Green, J. Alvarez, J. Laskin and R. Graham Cooks, *Phys. Chem. Chem. Phys.*, 2005, **7**, 1490-1500.
-

-
260. M. Rohdenburg, Z. Warneke, H. Knorke, M. Icker and J. Warneke, *Angew. Chem. Int. Ed.*, 2023, **62**, e202308600.
261. K. Anggara, L. Sršan, T. Jaroentomeechai, X. Wu, S. Rauschenbach, Y. Narimatsu, H. Clausen, T. Ziegler, R. L. Miller and K. Kern, *Science*, 2023, **382**, 219-223.

6. Appendix

6.1 Manuscripts not Included in the thesis

1. S. F. Lim, B. L. Harris, G. N. Khairallah, E. J. Bieske, P. Maitre, G. da Silva, B. D. Adamson, M. S. Scholz, N. J. A. Coughlan, R. A. J. O'Hair, M. Rathjen, D. Stares and J. M. White, *J. Org. Chem.*, 2017, **82**, 6289-6297.
2. R. García-Vázquez, U. M. Battisti, J. T. Jørgensen, V. Shalgunov, L. Hvass, D. L. Stares, I. N. Petersen, F. Crestey, A. Löffler, D. Svatunek, J. L. Kristensen, H. Mikula, A. Kjaer and M. M. Herth, *Chem. Sci.*, 2021, **12**, 11668-11675.
3. A. Kondinski, M. Rasmussen, S. Mangelsen, N. Pienack, V. Simjanoski, C. Näther, D. L. Stares, C. A. Schalley and W. Bensch, *Chem. Sci.*, 2022, **13**, 6397-6412.
4. M. Gaschard, D. L. Stares, M. Gallardo-Villagrán, D. Y. Leger, B. Liagre, C. A. Schalley and B. Therrien, *preprint-ChemRxiv*, 2022. DOI: 10.26434/chemrxiv-2022-2gqfs

6.2 Manuscripts Included in the Thesis

5. C.-W. Chu, D. L. Stares and C. A. Schalley, *Chem. Commun.*, 2021, **57**, 12317-12320. DOI: [10.1039/D1CC04419B](https://doi.org/10.1039/D1CC04419B).

This is an open access article under the terms of the [Creative Commons Attribution License](#), which permits use, distribution and reproduction in any medium, provided the original work is properly cited.

6. M. Kathan, S. Crespi, N. O. Thiel, D. L. Stares, D. Morsa, J. de Boer, G. Pacella, T. van den Enk, P. Kobauri, G. Portale, C. A. Schalley and B. L. Feringa, *Nat. Nanotechnol.*, 2022, **17**, 159-165. DOI: [10.1038/s41565-021-01021-z](https://doi.org/10.1038/s41565-021-01021-z).

This is an open access article under the terms of the [Creative Commons Attribution License](#), which permits use, distribution and reproduction in any medium, provided the original work is properly cited.

7. E. Taipale, J. S. Ward, G. Fiorini, D. L. Stares, C. A. Schalley and K. Rissanen, *Inorg. Chem. Front.*, 2022, **9**, 2231-2239. DOI: [10.1039/D1QI01532J](https://doi.org/10.1039/D1QI01532J).

This is an open access article under the terms of the [Creative Commons Attribution License](#), which permits use, distribution and reproduction in any medium, provided the original work is properly cited.

8. D. L. Stares, C. Mozaceanu, M. D. Ward and C. A. Schalley, *Chem. Commun.*, 2023, **59**, 11811-11814. DOI: [10.1039/D3CC04291J](https://doi.org/10.1039/D3CC04291J).

This is an open access article under the terms of the [Creative Commons Attribution-NonCommercial License](#), which permits use, distribution and reproduction in any medium, provided the original work is properly cited and is not used for commercial purposes.

9. D. L. Stares, A. Szumna and C. A. Schalley, *Chem. Eur. J.*, 2023, early view, DOI: [10.1002/chem.202302112](https://doi.org/10.1002/chem.202302112).

This is an open access article under the terms of the [Creative Commons Attribution-NonCommercial License](#), which permits use, distribution and reproduction in any medium, provided the original work is properly cited and is not used for commercial purposes.

10. J. Yu, M. Gaedke, S. Das, D. L. Stares, C. A. Schalley and F. Schaufelberger, *preprint-ChemRxiv*, 2023. [DOI:10.26434/chemrxiv-2023-v95p8](https://doi.org/10.26434/chemrxiv-2023-v95p8).

This is an open access article under the terms of the [Creative Commons Attribution-NonCommercial License](https://creativecommons.org/licenses/by-nc/4.0/), which permits use, distribution and reproduction in any medium, provided the original work is properly cited and is not used for commercial purposes.

6.3 Prints of Manuscripts Included in the Thesis


 Cite this: *Chem. Commun.*, 2021, 57, 12317

 Received 11th August 2021,
 Accepted 22nd October 2021

DOI: 10.1039/d1cc04419b

rsc.li/chemcomm

Light-controlled interconversion between a [c2]daisy chain and a lasso-type pseudo[1]rotaxane†

 Chih-Wei Chu,  Daniel L. Stares  and Christoph A. Schalley *

A light-responsive self-complementary crown ether/ammonium conjugate bearing an arylazopyrazole photoswitch as a spacer can be switched between a [c2]daisy chain (*E*-isomer) and a lasso-type pseudo[1]rotaxane (*Z*-isomer) by light.

Molecular daisy chains¹ and supramolecular polymers made by them² represent a special class in mechanically interlocked molecules (MIMs). [c2]Daisy chains have gained much attention due to their potential as molecular muscles.^{3,4} The self-complementary building blocks of [c2]daisy chains consist of a wheel and an axle as the binding units, and several examples have been reported using crown ethers,^{5–8} cyclodextrins,^{9,10} pillararenes^{11,12} and cucurbiturils¹³ as the wheels together with the corresponding axles. The introduction of stimuli-responsive units in the molecular design provides access to [c2]daisy chains that can be stimulated by pH,^{7,14,15} light^{9,10} and redox reactions.¹⁶ Recently, these stimuli-responsive motifs have been coupled to polymers, so that the shuttling of the macrocycle and thus the expansion/contraction can be observed at a macroscopic level.^{9,10,14,15}

Pseudo[1]rotaxanes stand for another interesting category of MIMs. Similar to the precursors of [c2]daisy chains, they comprise a macrocycle and a threaded axle, in which the components are linked covalently. Though they exist in nature, *i.e.* as lasso peptides,^{17,18} synthetic pseudo[1]rotaxanes have been less frequently investigated compared to [c2]daisy chains.^{19–21} Synthetic chemists have engineered the molecular design to control the self-inclusion behaviour and the mechanical motion by external stimuli, such as pH,^{21,22} light²³ and redox.^{24–26}

Usually, the molecular design of a self-complementary monomer is different for making a [c2]daisy chain and a lasso-type pseudo[1]rotaxane. The “spacer” between the axle site and the

wheel part should be short and rigid for making a [c2]daisy chain;⁸ whereas it is often longer and more flexible in the case of a lasso-type pseudo[1]rotaxane in order to allow for the back-folding of the axle into the wheel.²⁵ Since Shinkai and coworkers presented a photoresponsive “tail-biting”, but non-threading crown ether by taking advantage of the configurational difference between *E*- and *Z*-isomers of azobenzene in 1985,²⁷ further studies aiming at photoresponsive pseudo[1]rotaxane are rare. Using azobenzene, a light-driven molecular pump²⁸ and gated photochromism²⁹ have been reported.

Herein, we demonstrate the possibility of forming both a [c2]daisy chain and a lasso-type pseudo[1]rotaxane from the same building block in a controlled way. In our design, we synthesise a heteroditopic monomer **1** that bears an arylazopyrazole (AAP) to bridge a threadable macrocycle, benzo-21-crown-7, and a secondary ammonium ion (Fig. 1a). AAP is a photoswitch that isomerises reversely under UV and green light irradiation with almost quantitative photoswitching and can be easily modified to tune its photophysical properties.^{30–34} In this work, the rigid AAP plays an essential role in the molecular design. Firstly, the *E*-AAP provides sufficient distance between the crown ether and the ammonium station, so that the self-inclusion conformation is unfavourable in this state. Instead, a dimeric daisy chain (*E,E*-DC) is likely more preferred due to its thermodynamic stability.^{6,8} Secondly, the metastable *Z*-AAP brings the two recognition sites closer, thus a self-included lasso-type pseudo[1]rotaxane (*Z*-L) is expected. The formation of *E,E*-DC and *Z*-L and the light-controlled transformation are investigated by NMR, UV/vis and tandem mass spectrometry.

Heteroditopic monomer **1** was synthesised from the aldehyde precursor containing the AAP unit attached to benzo-21-crown-7, and *n*-butylamine *via* reductive amination, followed by protonation with HCl and counterion exchange with NH₄PF₆ (for synthetic procedures and characterisation data, see ESI†). NMR and UV/vis experiments were carried out to determine the photoswitching properties of **1**.

In the UV/vis spectra (Fig. 2a), the characteristic absorption bands of AAP appear, namely a π - π^* transition at *ca.* 350 nm

Institut für Chemie und Biochemie, Freie Universität Berlin, Arnimallee 20, Berlin 14195, Germany. E-mail: c.schalley@fu-berlin.de

† Electronic supplementary information (ESI) available: Synthetic procedures, characterization data and original NMR and mass spectra for new compounds, additional NMR and UV/Vis spectroscopic experiments and ion mobility mass spectrometric data. See DOI: 10.1039/d1cc04419b



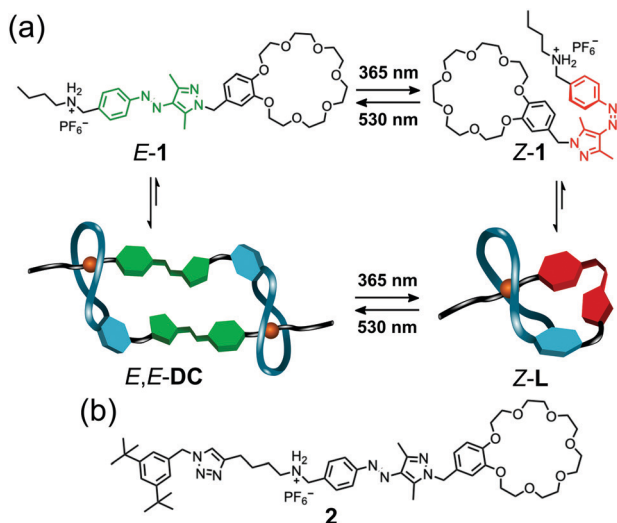


Fig. 1 (a) Molecular structure and light-responsiveness of **1** and the corresponding [c2]daisy chain *E,E*-DC and pseudo[1]rotaxane *Z-L*. (b) Molecular structure of control compound **2**.

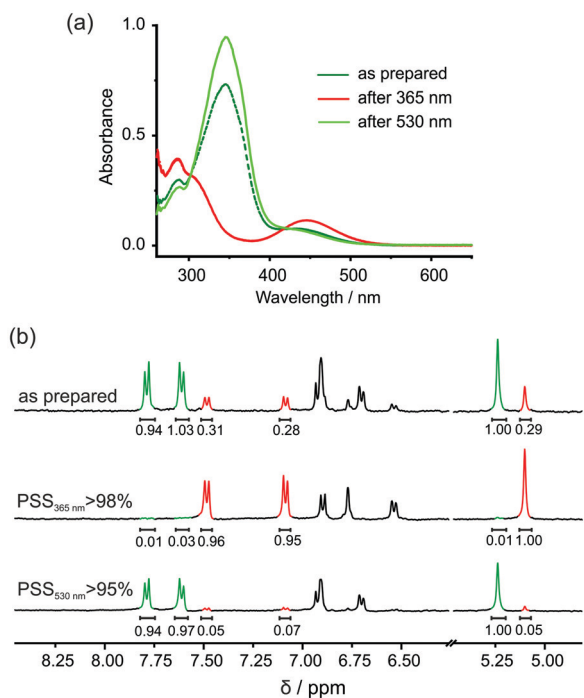


Fig. 2 (a) UV/vis spectra of **1** upon irradiation of UV and green light. (b) PSSs (at 365 and 530 nm) of **1** determined by ¹H NMR (400 MHz, 0.5 mM, DMSO-*d*₆).

and an *n*- π^* transition at *ca.* 450 nm.^{30,31} When irradiating at 365 nm for 15 min, the π - π^* band diminished and blue-shifted, and the *n*- π^* band increased and red-shifted, suggesting effective *E*- to *Z*-isomerisation of **1**. After 15 min of green light irradiation, not only the original spectrum was retrieved, but the absorbance at *ca.* 350 nm was further increased, implying the coexistence of the *E*- with some *Z*-isomer in the as-prepared

sample. This feature is also observed in the ¹H NMR experiments. The aromatic protons of AAP and the methylene protons between the AAP and the benzo-21-crown-7 moieties can be integrated to determine the photostationary state (PSS) at different wavelength (Fig. 2b). In the as-prepared sample, the ratio between *E*- and *Z*-isomer is approximately 7:3, which resonates with the UV/vis experiments. Irradiation of **1** at 365 nm for 15 min led to almost quantitative photoswitching (>98%) to the *Z*-isomer. Excitation of the *n*- π^* transition of **1** led to a PSS containing >95% of *E*-isomer. These results indicate that **1** possesses excellent photoswitching properties comparable to literature-known AAP derivatives.^{32–34}

Formation of *E,E*-DC from *E*-**1** is investigated by ¹H NMR spectroscopy. In competitive DMSO, **1** exists as an *E*-monomer (Fig. 3a). In CD₃CN, the equilibrium between monomer and dimer shifts almost completely towards *E,E*-DC, as indicated by the much more complex spectrum revealing a diastereotopic splitting of the crown ether CH₂ groups and of proton H_e (Fig. 3b) which is indicative of threading. In addition, aromatic protons at the phenyl ring of the AAP (H_c and H_d) shift upfield, and the adjacent methylene protons to the ammonium group H_a and H_b downfield. These observations can be easily understood: firstly, due to the self-complementary threading of *E,E*-DC, the phenyl group of the AAP is positioned atop the pyrazole group of the other and thus experiences its aromatic ring current. Secondly, the deshielding of the N-CH₂ protons is due to the hydrogen bonding to the crown ether's oxygen atoms. The assignment of protons in *E,E*-DC is further confirmed by ¹H-¹H COSY NMR spectroscopy (Fig. S1, ESI[†]) as well as concentration scanning (Fig. S2, ESI[†]) and a variable temperature NMR experiment (Fig. S3, ESI[†]). The ratios between non-threaded *E*-**1** and *E,E*-DC in CD₃CN range from *ca.* 4:6 (1 mM) up to 8:2 (20 mM). At elevated temperatures, *E,E*-DC dissociates to a non-threaded *E*-**1** due to a favourable entropy.

Irradiating *E*-**1** with UV light at a concentration of 5 mM in CD₃CN resulted in a mixture of *Z*-**1** and *Z-L* (Fig. 4b). Unfortunately, the concentration cannot go beyond 5 mM, otherwise *E*-**1** as well as *E,E*-DC were detected (Fig. S4, ESI[†]). We attribute this finding to an acid-mediated *Z*- to *E*-isomerisation of AAP, which has been discussed earlier in the literature^{35,36} and will be discussed below. Similar to *E,E*-DC, the CH₂ signals of *Z-L*

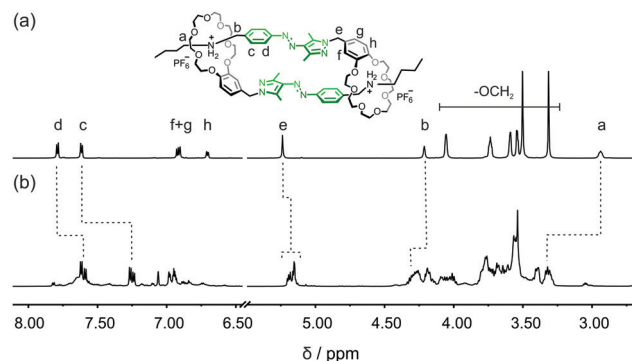


Fig. 3 Partial ¹H NMR spectra of *E*-**1** in (a) DMSO-*d*₆ (700 MHz, 298 K) and (b) CD₃CN (700 MHz, 20 mM, 298 K).



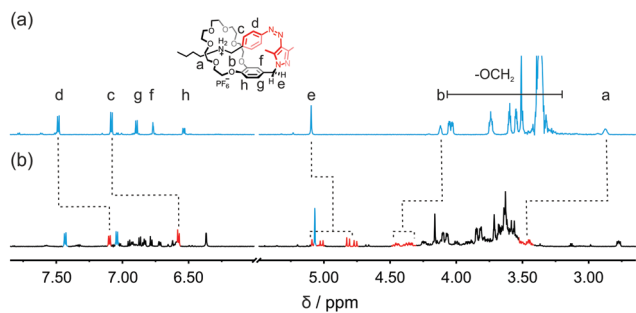


Fig. 4 Partial ^1H NMR spectra of **Z-1** in (a) $\text{DMSO}-d_6$ (700 MHz, 298 K) and (b) CD_3CN (700 MHz, 5 mM, 298 K).

reveal diastereotopic splitting as particularly nicely observed for H_e . Also consistent with a threaded structure, upfield shifting of the aromatic protons H_c and H_d and downfield shifting of the $\text{N}-\text{CH}_2$ protons H_a and H_b were observed in **Z-L**. $^1\text{H}-^1\text{H}$ COSY NMR spectrum of **Z-1** supports our assignment of **Z-L** in CD_3CN (Fig. S5, ESI †).

The light-mediated transformations between *E,E*-**DC** and **Z-L** was investigated in gas phase by tandem and ion-mobility mass spectrometry (IMS). IMS allows the separation of ions based on their size which makes it an especially powerful tool to analyse photoisomers with their typically identical elemental compositions and thus identical m/z values.^{37–39} IMS has been used to analyse the topology of intertwined molecules⁴⁰ and recently both MS and IMS utilised to identify pseudorotaxanes.²⁵ *E,E*-**DC** and **Z-L** have the same m/z , however their isotope patterns differ as *E,E*-**DC** is doubly charged (peak spacing of 0.5) while **Z-L** is singly charged (peak spacing of 1.0). Prior to UV irradiation there is one clear peak at 8.6 ms in the arrival time distribution (ATD). The corresponding mass spectrum has the peak spacing of 0.5 expected for a doubly charged ion showing *E,E*-**DC** (Fig. 5a) to be the major product. When irradiating with UV light for 5 min, the characteristic dimer peak decreases in the spectrum (Fig. 5b) whilst the ATD becomes more complex with two new major peaks at 8.4 ms and 10.9 ms. The corresponding mass spectra reveal the peak at 8.4 ms to correspond to doubly charged and that at 10.9 ms to singly charged ions, suggesting the formation of *E,Z*-**DC** and **Z-L** upon irradiation, respectively. It is noteworthy that there is also a trace amount of a doubly charged ion at 7.2 ms, which could potentially be *Z,Z*-**DC**. After 20 min of UV irradiation, the major product is **Z-L** with only trace amount of *E,E*- and *E,Z*-**DC** left as identified by the IMS and MS results (Fig. 5c).

E,E-**DC** and *E,Z*-**DC** were assigned based on energy resolved IMS measurements and further irradiation experiments utilising green light. Energy resolved IMS measurements of a sample containing all species (*i.e.* after 5 min UV irradiation) resulted in a decrease in the shoulder peak with a corresponding increase in the monomer peak whilst the initial peak is relatively unchanged (Fig. S6, ESI †). As *E,Z*-**DC** has a twisted conformation and is potentially less stable, it will more easily dissociate upon increasing collision voltage compared to *E,E*-**DC**. The same state was then also irradiated with green light (530 nm). Not only did the monomer species diminish, but the

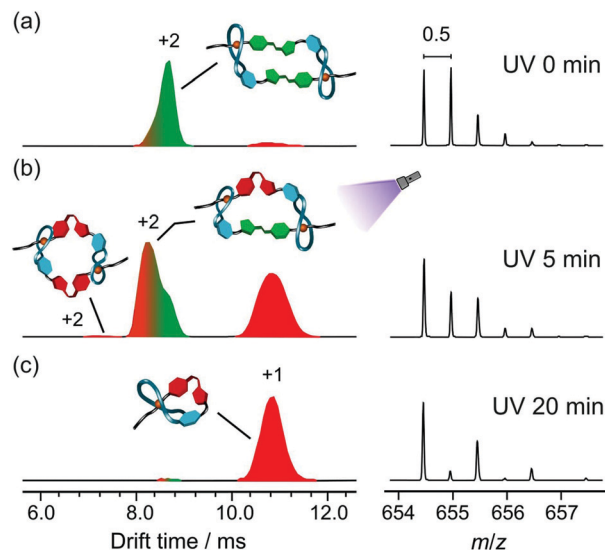


Fig. 5 Normalised arrival time distributions (ATD) in the IMS experiments and the corresponding mass spectra after (a) 0 min, (b) 5 min and (c) 20 min of UV irradiation at 365 nm.

shoulder at lower drift time (8.4 ms) also gradually decreased (Fig. S7, ESI †). After irradiating at 530 nm for 10 min, an ATD similar to Fig. 5a is obtained. *Z*-to-*E*-isomerisation of both **Z-1**, and *E,Z*-**DC** would be expected to form *E,E*-**DC**, which fits the experimental results. Notably, neither the shoulder peak nor the peak at 7 ms were increased under green light irradiation. Irradiation of the **Z-1** would result in the formation of *E-1* thus the only dimer expected to form would be the *E,E*-**DC** which was indeed observed. These findings support our hypothesis of photo-controlled transformations from *E,E*-**DC** to *E,Z*-**DC** and finally to **Z-L** under UV irradiation. The **Z**-isomer can reliably be switched back with green light to the *E*-isomer, which subsequently reassembles into the daisy chain. In addition, the **Z-L** shows a good thermal stability with a half-life in the range of several hours (Fig. S8, ESI †). Semi-empirical calculations and theoretical CCS values are in very good agreement with the experimental data and, for example, reflect the somewhat smaller size of the *E,Z*-**DC** as compared to that of the *E,E*-**DC** (ESI † , Section S5).

As observed in the NMR experiments (see above), the half-life of the thermal back isomerisation of **Z-1** significantly decreases with increasing concentration from 16 days at 38 μM to 1.5 hours at 1 mM in acetonitrile (Fig. S16, ESI †). We hypothesise that the ammonium ion can act as an acid in organic solvents and the acid-mediated thermal back relaxation of *Z*-azo compounds is known both in solution^{35,36} and in the gas phase.³⁹ This effect is potentially not only concentration dependent, but also solvent dependent. To further investigate the solvent effect for the *Z*-*E* switching, **2** and Boc-protected **2** were tested. Three UV/vis spectra of each sample were recorded in each solvent (Fig. S17, ESI †). Boc-protected **2** showed a great thermal stability in all tested solvents after irradiating at 365 nm for 10 min, whereas **2** exhibited a clear solvent dependence of the back-isomerisation rate. In polar solvents, such as CH_3CN and DMSO , a good stability of **Z-2** is observed



due to the well-solvated secondary ammonium ion. In the case of non-polar solvents like CH_2Cl_2 , CHCl_3 and DCE, a fast $Z-E$ switching is detected. The back isomerisation is more prominent because the lack of hydrogen bond acceptors in these solvent molecules makes the ammonium ion acidic enough to cause the acid-mediated $Z-E$ isomerisation.^{41,42} When looking at the dielectric constant of THF, it should fit in the category of non-polar solvent. However, **2** showed a good stability in THF. We attribute this observation to the stabilised secondary ammonium ion by the oxygen of THF, so that the protonation-assisted $Z-E$ switching is inhibited.

In the gas phase, the atom which is protonated plays an essential role in the ion's behaviour. It has been reported that a secondary amine can accommodate a proton better than azo groups, so that the E - and Z -isomers of the azobenzene can be generated and monitored by IMS.^{37,39} In our study, the ATD of **2** shifted towards shorter drift time upon UV irradiation (Fig. S9, ESI[†]). These two photoisomers can be resolved because the proton is situated at the secondary amine, thus the protonation-assisted Z - to E -isomerisation is inhibited. On the contrary, the Boc-protected **2** did not show a distinct difference in size upon UV irradiation (Fig. S10, ESI[†]). In Boc-protected **2**, the preferred protonation site is the azo nitrogen adjacent to the phenyl ring, which possesses a mesomeric stabilisation through the pyrazole ring,^{35,36} so that a fast $Z-E$ switching is occurring.

In conclusion, we demonstrated a proof of principle that the [c2]daisy chain made by **1** can be reversibly converted to the lasso-type pseudo[1]rotaxane under light irradiation. In our design, we employ an AAP to photo-control the distance between the crown ether and the secondary ammonium station in the thread, so that E -**1** forms a self-complementary E -DC, while Z -**1** self-cludes to a Z -L. These observations are not only presented in solution as demonstrated by NMR and UV/vis experiments, but also investigated in gas phase by MS and IMS.

We thank Deutsche Forschungsgemeinschaft (project number 434455294) and the European Union through the NOAH project (H2020-MSCA-ITN project ref. 765297) for funding. Support of NMR and MS experiments from the BioSupraMol core facility at FU Berlin is gratefully acknowledged.

Conflicts of interest

There are no conflicts to declare.

Notes and references

- R. Jürgen and M. Marcel, *Chem. Soc. Rev.*, 2013, **42**, 44–62.
- Examples: (a) Z. Zhang, Y. Luo, J. Chen, S. Dong, Y. Yu, Z. Ma and F. Huang, *Angew. Chem., Int. Ed.*, 2011, **50**, 1397–1401; (b) M. Zhang, S. Li, S. Dong, J. Chen, B. Zheng and F. Huang, *Macromolecules*, 2011, **44**, 9629–9634.
- C. J. Bruns and J. F. Stoddart, *Acc. Chem. Res.*, 2014, **47**, 2186–2199.
- A. Goujon, E. Moulin, G. Fuks and N. Giuseppone, *CCS Chem.*, 2019, **1**, 83–96.
- P. R. Ashton, I. Baxter, S. J. Cantrill, M. C. T. Fyfe, P. T. Glink, J. F. Stoddart, A. J. P. White and D. J. Williams, *Angew. Chem., Int. Ed.*, 1998, **37**, 1294–1297.
- B. Zheng, M. Zhang, S. Dong, J. Liu and F. Huang, *Org. Lett.*, 2012, **14**, 306–309.
- C. Romuald, A. Ardá, C. Clavel, J. Jiménez-Barbero and F. Coutrot, *Chem. Sci.*, 2012, **3**, 1851–1857.
- B. Zheng, F. Klautzsch, M. Xue, F. Huang and C. A. Schalley, *Org. Chem. Front.*, 2014, **1**, 532–540.
- K. Iwaso, Y. Takashima and A. Harada, *Nat. Chem.*, 2016, **8**, 625–632.
- S. Ikejiri, Y. Takashima, M. Osaki, H. Yamaguchi and A. Harada, *J. Am. Chem. Soc.*, 2018, **140**, 17308–17315.
- L. Gao, Z. Zhang, B. Zheng and F. Huang, *Polym. Chem.*, 2014, **5**, 5734–5739.
- K. Wang, C.-Y. Wang, Y. Zhang, S. X.-A. Zhang, B. Yang and Y.-W. Yang, *Chem. Commun.*, 2014, **50**, 9458–9461.
- L. Cao and L. Isaacs, *Org. Lett.*, 2012, **14**, 3072–3075.
- A. Goujon, T. Lang, G. Mariani, E. Moulin, G. Fuks, J. Raya, E. Buhler and N. Giuseppone, *J. Am. Chem. Soc.*, 2017, **139**, 14825–14828.
- A. Goujon, G. Mariani, T. Lang, E. Moulin, M. Rawiso, E. Buhler and N. Giuseppone, *J. Am. Chem. Soc.*, 2017, **139**, 4923–4928.
- C. J. Bruns, M. Frascioni, J. Iehl, K. J. Hartlieb, S. T. Schneebeli, C. Cheng, S. I. Stupp and J. F. Stoddart, *J. Am. Chem. Soc.*, 2014, **136**, 4714–4723.
- J. D. Hegemann, M. Zimmermann, X. Xie and M. A. Marahiel, *Acc. Chem. Res.*, 2015, **48**, 1909–1919.
- F. Saito and J. W. Bode, *Chem. Sci.*, 2017, **8**, 2878–2884.
- Q. Zhou, P. Wei, Y. Zhang, Y. Yu and X. Yan, *Org. Lett.*, 2013, **15**, 5350–5353.
- X.-S. Du, C.-Y. Wang, Q. Jia, R. Deng, H.-S. Tian, H.-Y. Zhang, K. Meguelli and Y.-W. Yang, *Chem. Commun.*, 2017, **53**, 5326–5329.
- P. Waelès, C. Clavel, K. Fournel-Marotte and F. Coutrot, *Chem. Sci.*, 2015, **6**, 4828–4836.
- C. Clavel, C. Romuald, E. Brabet and F. Coutrot, *Chem. – Eur. J.*, 2013, **19**, 2982–2989.
- A. Saura-Sanmartin, A. Martinez-Cuezva, A. Pastor, D. Bautista and J. Berna, *Org. Biomol. Chem.*, 2018, **16**, 6980–6987.
- Y. Wang, J. Sun, Z. Liu, M. S. Nassar, Y. Y. Botros and J. F. Stoddart, *Chem. Sci.*, 2017, **8**, 2562–2568.
- H. V. Schröder, J. M. Wollschläger and C. A. Schalley, *Chem. Commun.*, 2017, **53**, 9218–9221.
- G. Orlandini, L. Casimiro, M. Bazzoni, B. Cogliati, A. Credi, M. Lucarini, S. Silvi, A. Arduini and A. Secchi, *Org. Chem. Front.*, 2020, **7**, 648–659.
- S. Shinkai, M. Ishihara, K. Ueda and O. Manabe, *J. Chem. Soc., Perkin Trans. 2*, 1985, 511–518.
- G. Ragazzon, M. Baroncini, S. Silvi, M. Venturi and A. Credi, *Nat. Nanotechnol.*, 2015, **10**, 70–75.
- M. Lohse, K. Nowosinski, N. L. Traulsen, A. J. Achazi, L. K. S. von Krbek, B. Paulus, C. A. Schalley and S. Hecht, *Chem. Commun.*, 2015, **51**, 9777–9780.
- C. E. Weston, R. D. Richardson, P. R. Haycock, A. J. P. White and M. J. Fuchter, *J. Am. Chem. Soc.*, 2014, **136**, 11878–11881.
- L. Stricker, E.-C. Fritz, M. Peterlechner, N. L. Doltsinis and B. J. Ravoo, *J. Am. Chem. Soc.*, 2016, **138**, 4547–4554.
- J. Calbo, C. E. Weston, A. J. P. White, H. S. Rzepa, J. Contreras-García and M. J. Fuchter, *J. Am. Chem. Soc.*, 2017, **139**, 1261–1274.
- L. Stricker, M. Böckmann, T. M. Kirse, N. L. Doltsinis and B. J. Ravoo, *Chem. – Eur. J.*, 2018, **24**, 8639–8647.
- S. Devi, M. Saraswat, S. Grewal and S. Venkataramani, *J. Org. Chem.*, 2018, **83**, 4307–4322.
- R. S. L. Gibson, J. Calbo and M. J. Fuchter, *ChemPhotoChem*, 2019, **3**, 372–377.
- S. Ludwanowski, M. Ari, K. Parison, S. Kalthoum, P. Straub, N. Pompe, S. Weber, M. Walter and A. Walther, *Chem. – Eur. J.*, 2020, **26**, 13203–13212.
- L. H. Urner, M. Schulze, Y. B. Maier, W. Hoffmann, S. Warnke, I. Liko, K. Folmert, C. Manz, C. V. Robinson, R. Haag and K. Pagel, *Chem. Sci.*, 2020, **11**, 3538–3546.
- M. S. Scholz, J. N. Bull, N. J. A. Coughlan, E. Carrascosa, B. D. Adamson and E. J. Bieske, *J. Phys. Chem. A*, 2017, **121**, 6413–6419.
- J. M. Wollschläger and C. A. Schalley, *ChemPhotoChem*, 2019, **3**, 473–479.
- A. Krüve, K. Caprice, R. Lavendomme, J. M. Wollschläger, S. Schoder, H. V. Schröder, J. R. Nitschke, F. B. L. Cougnon and C. A. Schalley, *Angew. Chem., Int. Ed.*, 2019, **58**, 11324–11328.
- H. K. Hall, *J. Phys. Chem.*, 1956, **60**, 63–70.
- M. R. Crampton and S. D. Lord, *J. Chem. Soc., Perkin Trans. 2*, 1997, 369–376.



Electronic Supplementary Information

Light-controlled interconversion between a [c2]daisy chain and a lasso-type pseudo[1]rotaxane

Chih-Wei Chu, Daniel L. Stares and Christoph A. Schalley*

Institut für Chemie und Biochemie, Organische Chemie, Freie Universität Berlin,
Arnimallee 20, 14195 Berlin, Germany

Table of contents

1. General information	S2
2. Synthesis of thread 1 and control compound 2	S3
3. Additional NMR experiments	S10
4. IMS experiments	S13
5. UV/vis experiments	S16
6. NMR spectra	S18
7. ESI mass spectra	S27
8. References	S31

1. General information

All reagents and solvents were purchased from commercial sources and used without further purification. Dry solvents were purchased from Acros Organics in sealed containers. Precursors **S1**,^{S1, S2} **S2**,^{S3} **S5**^{S4} and **S7**^{S5} were synthesised according to reported procedures. Thin-layer chromatography was performed on silica gel-coated plates with fluorescent indicator F254 (Merck). For column chromatography, silica gel (0.04-0.063 mm; Merck) was used.

¹H and ¹³C NMR experiments were recorded on JEOL ECX 400, JEOL ECP 500, Bruker AVANCE 500 or Bruker AVANCE 700 instruments. Solvent residue signals were used as the internal standard. All shifts are reported in ppm and NMR multiplicities are abbreviated as s (singlet), d (doublet), t (triplet), q (quartet), quint (quintet), sext (sextet), m (multiplet) and br (broad). Coupling constants *J* are reported in Hertz.

UV/vis spectra were recorded on a Varian Cary 50 Bio spectrometer with a xenon lamp. Compounds were dissolved in HPLC grade solvents. Suprasil glass cuvettes with path-lengths of 1 cm or 0.1 cm were used.

Two different light sources were used in photoswitching experiments (both NMR and UV/vis). A UV hand lamp from Herolab GmbH with a 6 W tube at 365 nm was used for *E-Z*-isomerisation. A Thorlabs M530L4 LED with a LED current of 1000 mA was used for *Z-E*-isomerisation. In experiments to determine the PSS, irradiation time was 15 min in both directions.

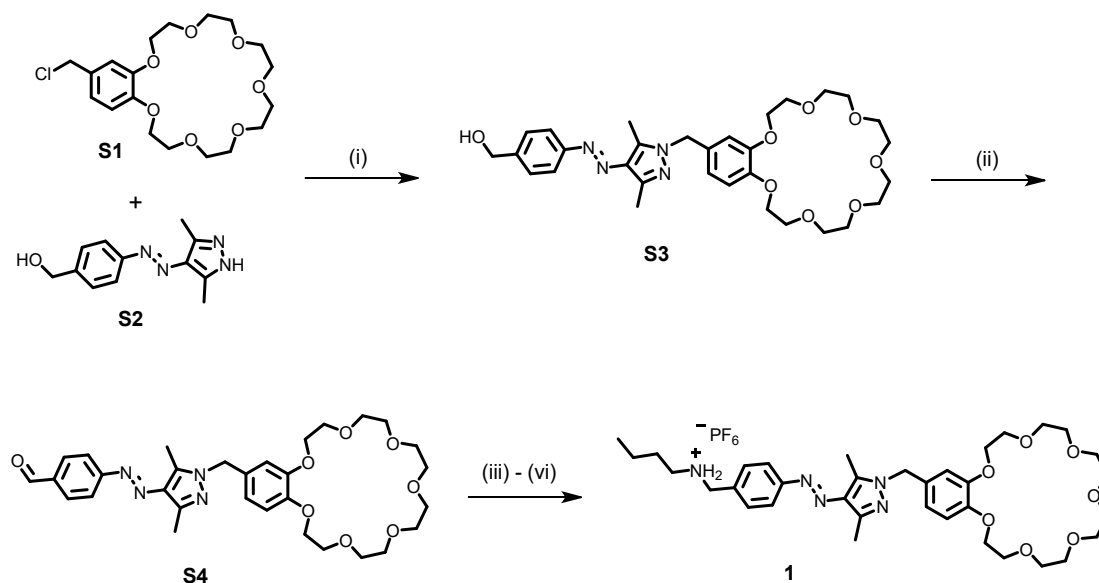
High-resolution ESI mass spectra were measured on an Agilent 6210 ESI-TOF instrument. Travelling-wave ion-mobility spectrometry mass spectrometry (IMS-MS) and collision-induced dissociation (CID) experiments were performed on a Synapt G2-S HDMS Q-TOF (Waters Co., Milford, MA, USA) instrument equipped with a Z-spray electrospray ionisation (ESI) ionisation source. A sample concentration of 10 μM in DCM was used for measurements with a flow rate of 5 μL/min. A capillary voltage of 2 kV was used with sample cone and source offset both set to 15 V. Source and desolvation temperature were set to 40 °C. IMS and CID measurements were both performed with N₂. IMS measurements used the following settings: trap gas flow 0.40 mL/min, helium cell gas flow 180 mL/min; IMS gas flow 120 mL/min; wave height 32 V; wave velocity 550 m/s. The instrument was allowed to settle for 45 minutes prior to data acquisition. IMS measurements were done for the mass-selected ion at *m/z*

654. Arrival-time distributions (ATDs) are presented in milliseconds.

Computational calculations were performed using the semi-empirical PM6 method in the program Scigress (Fujitsu, version FJ 2.9.1).

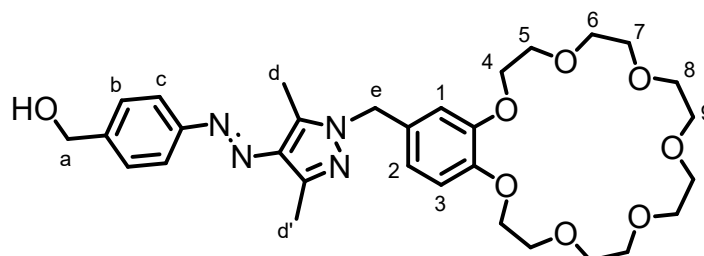
Theoretical collisional cross section calculations (CCS) in nitrogen buffer gas (${}^{\text{TM}}\text{CCS}_{\text{N}_2}$) were calculated using the trajectory method using the IMoS parallelised tool set. (<https://doi.org/10.1007/s13361-017-1661-8>)

2. Synthesis of thread 1 and control compound 2



Scheme S1. Synthesis procedures for thread 1. Reaction conditions: (i) K_2CO_3 , dry ACN, reflux; (ii) Dess-Martin periodinane, dry DCM, 0 °C; (iii) *n*-butylamine, EtOH, reflux; (iv) NaBH_4 , EtOH, 0 °C; (v) HCl, MeOH; (vi) NH_4PF_6 (aq).

Synthesis of S3



Compound **S2** (230 mg, 1.00 mmol, 1.00 eq.) and K_2CO_3 (690 mg, 5.00 mmol, 5 eq) were added to a solution of **S1** (414 mg, 1.00 mmol, 1.00 eq.) in dry ACN (30 mL) under argon atmosphere. This mixture was stirred at reflux for 4 days. After rotary evaporation, the residue was dissolved in CH_2Cl_2 (100 mL). The organic phase was washed with 1 M HCl (1×100 mL) and brine (2×100 mL), before it was dried over MgSO_4 and concentrated by rotary evaporation. Further purification was carried out by column chromatography on silica gel ($\text{CH}_2\text{Cl}_2/\text{MeOH} = 94:6$), yielding the title compound as viscous orange oil (468 mg, 78%, $R_f \sim 0.3$).

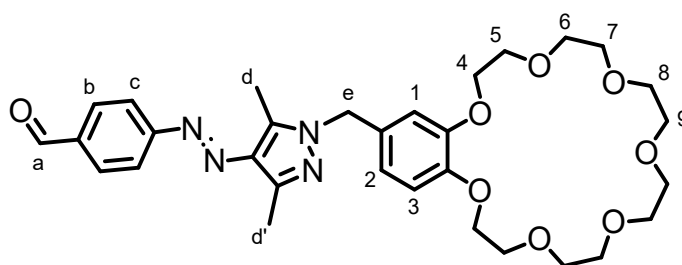
$^1\text{H NMR}$ (500 MHz, CDCl_3 , 298 K): $\delta = 7.79\text{--}7.74$ (m, H_c , 2H), $7.47\text{--}7.42$ (m, H_b , 2H),

6.84-6.79 (m, H₁ and H₃, 2H), 6.75-6.70 (m, H₂, 1H), 5.24 (s, H_e, 2H), 4.75 (s, H_a, 2H), 4.14-4.10 (m, H₄, 4H), 3.91-3.87 (m, H₅, 4H), 3.79-3.75 (m, H₆, 4H), 3.73-3.69 (m, H₇, 4H), 3.67-3.61 (m, H₈ and H₉, 8H), 2.56 (s, H_d, 3H), 2.54 (s, H_{d'}, 3H) ppm.

¹³C NMR (126 MHz, CDCl₃, 298 K): δ = 153.12, 149.37, 148.89, 142.61, 142.39, 139.31, 135.46, 129.00, 127.57, 122.19, 120.28, 114.34, 113.47, 71.22, 71.20, 71.19, 71.14, 71.12, 70.68, 69.84, 69.42, 65.08, 52.92, 13.84, 10.22 ppm.

ESI-MS (*m/z*): calculated for [C₃₁H₄₂N₄O₈Na]⁺: 621.2895, found 621.2899.

Synthesis of S4



Compound **S3** (263 mg, 0.44 mmol, 1.00 eq.) in dry CH₂Cl₂ was added dropwise to a solution of Dess-Martin periodinane (280 mg, 0.65 mmol, 1.50 eq.) in dry CH₂Cl₂ (10 mL) under argon atmosphere at 0 °C. This mixture was stirred at this temperature for 1 h and then at room temperature for additional 2 h. Afterwards, the mixture was diluted with CH₂Cl₂ (50 mL). The organic phase was washed with saturated NaHCO₃ (1×50 mL) and brine (1×100 mL), before it was dried over MgSO₄ and concentrated by rotary evaporation. Further purification was carried out by column chromatography on silica gel (CH₂Cl₂/MeOH = 97:3), yielding the title compound as viscous orange oil (200 mg, 76%, R_f ~ 0.20).

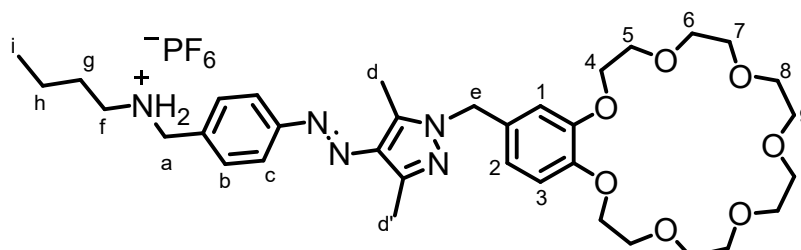
¹H NMR (700 MHz, CDCl₃, 298 K): δ = 10.06 (s, H_a, 1H), 7.98-7.96 (m, H_b, 2H), 7.90-7.87 (m, H_c, 2H), 6.83 (d, *J* = 8.2 Hz, H₃, 1H), 6.76 (d, *J* = 2.1 Hz, H₁, 1H), 6.72 (dd, *J* = 8.2, 2.1 Hz, H₂, 1H), 5.20 (s, H_e, 2H), 4.15-4.10 (m, H₄, 4H), 3.91-3.88 (m, H₅, 4H), 3.79-3.75 (m, H₆, 4H), 3.73-3.69 (m, H₇, 4H), 3.67-3.64 (m, H₈ and H₉, 8H), 2.54 (s, H_d and H_{d'}, 6H) ppm.

¹³C NMR (176 MHz, CDCl₃, 298 K): δ = 191.85, 157.38, 149.40, 148.94, 143.07, 140.43, 136.74, 133.57, 131.99, 130.83, 129.14, 122.44, 120.10, 114.39, 113.47,

71.25, 71.17, 70.70, 69.85, 69.56, 69.48, 53.17, 14.32, 10.28 ppm.

ESI-MS (m/z): calculated for $[C_{31}H_{10}N_4O_8Na]^+$: 619.2738, found 619.2743.

Synthesis of 1



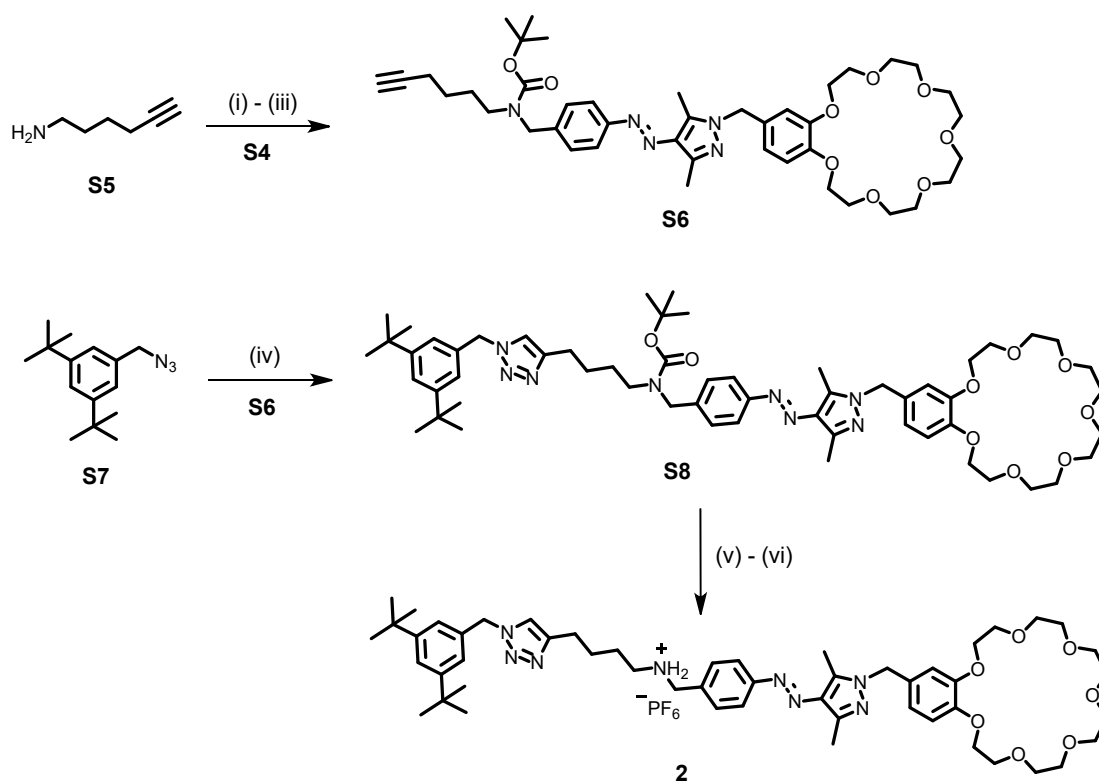
n-Butylamine (37 μ L, 0.37 mmol, 1.10 eq.) was added dropwise to a solution of **S4** (200 mg, 0.34 mmol, 1.00 eq.) in dry EtOH (10 mL) under argon atmosphere at room temperature. This mixture was heated to reflux and stirred at 95 °C overnight. Afterwards, the mixture was cooled down to 0 °C, and sodium borohydride (39 mg, 1.02 mmol, 3.00 eq.) was added slowly. The suspension was stirred at 0 °C for 1 h and then at room temperature overnight. The mixture was quenched by adding 1 mL of saturated NaHCO₃ and concentrated under reduced pressure. The residue was dissolved in CH₂Cl₂ (50 mL) and extracted with brine (3×50 mL). The organic phase was dried over MgSO₄ and concentrated by rotary evaporation. The amine was dissolved in MeOH (5 mL) and concentrated HCl (0.5 mL) was added. The mixture was stirred at room temperature for 15 minutes before 10 mL of water was added. To this solution, 1 mL of NH₄PF₆ solution (100 mg/mL) was added to precipitate the product. After stirring for 30 minutes, the precipitate was collected by vacuum filtration, washed with water and dried in a vacuum oven. The title compound was obtained as a yellow solid. (139 mg, 63% over three steps).

¹H NMR (700 MHz, DMSO-*d*₆, 298 K): δ = 8.71 (s, NH₂⁻, 2H), 7.79 (d, J = 8.3 Hz, H_b, 2H), 7.62 (d, J = 7.5 Hz, H_c, 2H), 6.92 (d, J = 8.3 Hz, H₃, 1H), 6.90 (d, J = 1.4 Hz, H₁, 1H), 6.70 (dd, H₂, J = 8.3 and 1.4 Hz, 1H), 5.24 (s, H_e, 2H), 4.21 (s, H_a, 2H), 4.08-4.03 (m, H₄, 4H), 3.76-3.71 (m, H₅, 4H), 3.61-3.57 (m, H₆, 4H), 3.56-3.52 (m, H₇, 4H), 3.52-3.47 (m, H₈ and H₉, 8H), 2.96-2.91 (t, J = 6.9 Hz, H_f, 2H), 2.56 (s, H_d, 3H), 2.41 (s, H_{d'}, 3H), 1.63-1.57 (quin, J = 7.7 Hz, H_g, 2H), 1.37-1.31 (sext, J = 7.5 Hz, H_h, 2H), 0.9 (t, J = 7.4 Hz, H_i, 1H) ppm.

¹³C NMR (176 MHz, DMSO-*d*₆, 298 K): δ = 153.19, 148.07, 147.73, 140.85, 139.94,

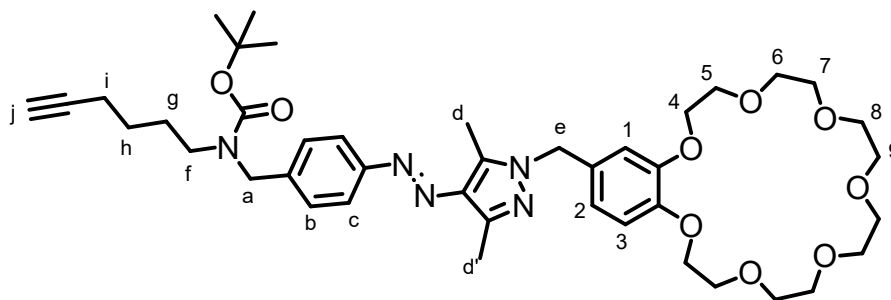
134.73, 133.04, 130.84, 129.16, 121.59, 119.82, 113.45, 113.02, 70.24, 70.22, 70.14, 69.87, 68.89, 68.41, 68.31, 51.92, 49.66, 46.42, 27.42, 19.25, 13.95, 13.47, 9.61 ppm.

ESI-MS (*m/z*): calculated for [C₃₅H₅₁N₅O₇K]⁺: 692.3420, found 692.3415.



Scheme S2. Synthesis procedures for control compound **2**. Reaction conditions: (i) **S4**, dry THF, reflux; (ii) NaBH₄, THF, 0 °C; (iii) Boc₂O, Et₃N, DCM; (iv) **S6**, Cu(ACN)₄PF₆, tris(benzyltriazolylmethyl)amine (TBTA), DCE, 45 °C; (v) HCl, MeOH; (vi) NH₄PF₆(aq).

Synthesis of S6



5-Hexynyl-1-amine (12 mg, 0.13 mmol, 1.50 eq.) was added dropwise to a solution of **S4** (50 mg, 0.084 mmol, 1.00 eq.) in dry THF (6 mL) under nitrogen atmosphere at

S7

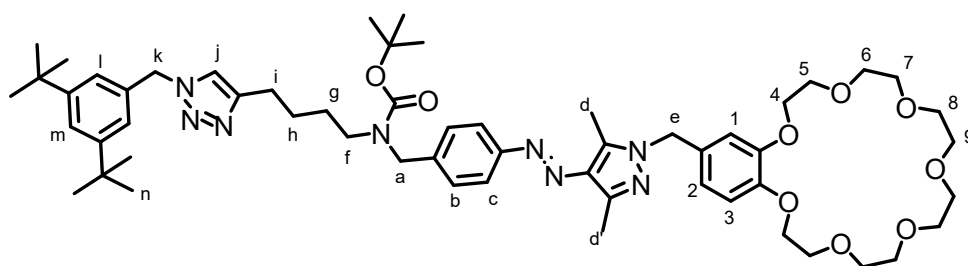
room temperature. This mixture was heated to reflux and stirred at 80 °C overnight. Afterwards, the mixture was cooled down to 0 °C, and sodium borohydride (10 mg, 0.25 mmol, 3.00 eq.) was added slowly. The suspension was stirred at 0 °C for 1 h and then at room temperature overnight. The mixture was quenched by adding 1 mL of saturated NaHCO₃ and concentrated under reduced pressure. The residue was dissolved in CH₂Cl₂ (50 mL) and extracted with 1 M NaOH (1×50 mL) and brine (1×50 mL). The organic phase was dried over MgSO₄ and concentrated by rotary evaporation. The amine was dissolved in dry DCM (10 mL) under nitrogen atmosphere, and di-*tert*-butyl dicarbonate (57 mg, 0.25 mmol, 3.00 eq.) and Et₃N (36 μL, 0.17 mmol, 2.00 eq.) were added subsequently. The mixture was stirred at room temperature overnight before extracting with 0.1 M HCl (1×30 mL), saturated NaHCO₃ (1×30 mL) and brine (1×30 mL). The organic phase was dried over MgSO₄ and concentrated by rotary evaporation. Further purification was carried out by column chromatography on silica gel (CH₂Cl₂/MeOH = 96:4), yielding the title compound as a yellow solid (33 mg, 51% over three steps, R_f ~ 0.30).

¹H NMR (700 MHz, CDCl₃, 298 K): δ = 7.73 (d, *J* = 8.0 Hz, H_b, 2H), 7.30 (m, H_c, 2H), 6.82 (d, *J* = 8.2 Hz, H₃, 1H), 6.74 (d, *J* = 2.1 Hz, H₁, 1H), 6.70 (dd, *J* = 8.2 and 2.1 Hz, H₂, 1H), 5.19 (s, H_e, 2H), 4.52-4.42 (m, H_a, 2H), 4.15-4.09 (m, H₄, 4H), 3.92-3.86 (m, H₅, 4H), 3.80-3.75 (m, H₆, 4H), 3.73-3.69 (m, H₇, 4H), 3.68-3.63 (m, H₈ and H₉, 8H), 3.29-3.12 (m, H_f, 2H), 2.52 (s, H_d, 3H), 2.51 (s, H_{d'}, 3H), 2.21-2.16 (m, H_i, 2H), 1.93 (t, *J* = 2.6 Hz, H_j, 1H), 1.52 (s, H_{Boc}, 9H), 1.51-1.40 (m, H_g and H_h, 4H) ppm.

¹³C NMR (176 MHz, CDCl₃, 298 K): δ = 152.99, 149.34, 148.78, 146.88, 142.69, 139.01, 135.63, 129.47, 128.43, 127.72, 122.04, 120.09, 114.36, 113.31, 85.31, 79.92, 71.21, 71.14, 70.68, 69.84, 69.46, 68.68, 53.02, 29.84, 28.58, 27.56, 25.81, 18.29, 14.15, 10.20 ppm.

ESI-MS (*m/z*): calculated for [C₄₂H₅₉N₅O₉Na]⁺: 800.4205, found 800.4201.

Synthesis of S8



S8

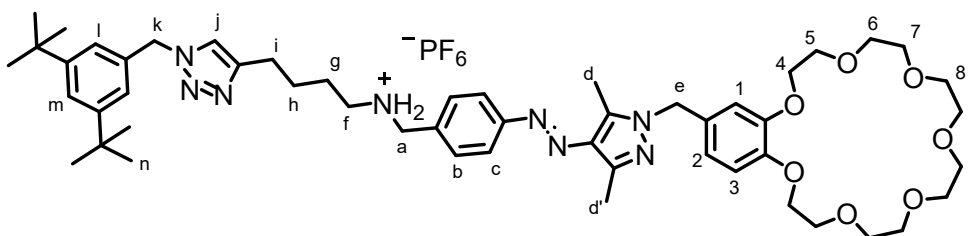
3,5-di-*tert*-butylbenzyl azide **S7** (36 mg, 0.147 mmol, 2.00 eq.) was added to a solution of **S6** (57 mg, 0.073 mmol, 1.00 eq.) in dry DCE (5 mL) under nitrogen atmosphere at room temperature. A stream of nitrogen gas was bubbled through this mixture for 15 minutes. Afterwards, tris(benzyltriazolylmethyl)amine (39 mg, 0.073 mmol, 1.00 eq.) and Cu(ACN)₄PF₆ (55 mg, 0.147 mmol, 2.00 eq.) were added subsequently before stirring at 40 °C for 3 days. The solution was extracted with saturated NaHCO₃ (2×50 mL) and brine (1×50 mL). The organic phase was dried over MgSO₄ and concentrated by rotary evaporation. Further purification was carried out by column chromatography on silica gel (CH₂Cl₂/MeOH = 95:5), yielding the title compound as a yellow solid (44 mg, 59%, R_f ~ 0.30).

¹H NMR (700 MHz, CDCl₃, 298 K): δ = 7.78 (s, H_j, 2H), 7.74-7.69 (m, H_b, 2H), 7.40 (t, J = 1.8 Hz, H_m, 1H), 7.32-7.27 (m, H_c, 2H), 7.07 (d, J = 1.7 Hz, H_l, 2H), 6.85 (d, J = 8.3 Hz, H₃, 1H), 6.77 (d, J = 2.0 Hz, H₁, 1H), 6.74 (dd, J = 8.3 and 2.0 Hz, H₂, 1H), 5.45, (s, H_k, 2H), 5.20 (s, H_e, 2H), 4.48-4.39 (m, H_a, 2H), 4.17-4.12 (m, H₄, 4H), 3.90-3.86 (m, H₅, 4H), 3.73-3.70 (m, H₆, 4H), 3.66-3.64 (m, H₇, 4H), 3.68-3.63 (m, H₈ and H₉, 8H), 3.28-3.13 (m, H_f, 2H), 2.73-2.63 (m, H_i, 2H), 2.52 (m, H_d and H_{d'}, 6H), 1.66-1.57 (m, H_h, 2H), 1.51-1.47 (s, H_g and H_{Boc}, 11H), 1.29 (s, H_n, 18H) ppm.

¹³C NMR (176 MHz, CDCl₃, 298 K): δ = 152.93, 151.84, 148.67, 148.35, 148.03, 142.78, 139.12, 135.63, 134.25, 129.27, 128.91, 128.40, 128.24, 127.74, 122.75, 122.38, 122.03, 120.71, 79.87, 70.04, 69.71, 69.36, 68.55, 54.73, 52.83, 35.02, 31.53, 28.59, 26.88, 25.55, 14.19, 10.18 ppm.

ESI-MS (*m/z*): calculated for [C₅₇H₈₂N₈O₉Na]⁺: 1045.6097, found 1045.6067.

Synthesis of 2



2 M HCl in diethyl ether (2 mL) was added dropwise to a solution of **S8** (31 mg, 0.03 mmol, 1.00 eq.) in DCM (2 mL) at 0 °C. This mixture was stirred at this temperature for one hour and at room temperature for another one hour. Afterwards, the volatiles were removed by rotary evaporation and the residue was dissolved in

DCM (50 mL) and extracted with 1 M NaOH (3×50 mL). The organic phase was dried over MgSO₄ and concentrated. The residue was purified by column chromatography on silica gel (CH₂Cl₂/MeOH/Et₃N = 95:5:0.5, R_f ~ 0.20). The amine was dissolved in MeOH (5 mL) and 1 mL of concentrated HCl was added. The solution was stirred at room temperature for 30 minutes before 10 mL of water and 1 mL of NH₄PF₆ solution (100 mg/mL) were added. After stirring for one hour, the mixture was extracted with DCM (3×50 mL). The organic phase was dried over MgSO₄ and concentrated by rotary evaporation. The title compound was obtained as a yellow solid (23 mg, 72% over two steps).

¹H NMR (700 MHz, CD₃CN, 298 K): 7.91 (s, H_j, 2H), 7.85-7.82 (m, H_b, 2H), 7.62-7.59 (m, H_c, 2H), 7.50 (t, *J* = 1.9 Hz, H_m, 1H), 7.26 (d, *J* = 1.8 Hz, H_l, 2H), 7.14-7.07 (br, NH₂, 2H), 6.95 (d, *J* = 8.3 Hz, H₃, 1H), 6.92 (d, *J* = 2.0 Hz, H₁, 1H), 6.81 (dd, *J* = 8.3 and 2.0 Hz, H₂, 1H), 5.58, (s, H_k, 2H), 5.22 (s, H_e, 2H), 4.22 (t, *J* = 6.2 Hz, H_a, 2H), 4.15-4.11 (m, H₄, 4H), 3.86-3.83 (m, H₅, 4H), 3.68-3.65 (m, H₆, 4H), 3.61-3.60 (m, H₇, 4H), 3.59-3.57 (m, H₈ and H₉, 8H), 3.12-3.08 (m, H_f, 2H), 2.82-2.78 (m, H_i, 2H), 2.61 (s, H_d, 3H), 2.45 (s, H_{d'}, 3H), 1.78-1.74 (m, H_g and H_n, 4H), 1.30 (s, H_n, 18H) ppm.

¹³C NMR (176 MHz, CD₃CN, 298 K): δ = 155.15, 152.87, 148.99, 148.59, 146.21, 142.87, 141.64, 136.14, 134.14, 132.57, 132.12, 130.55, 125.56, 124.21, 124.07, 123.04, 121.42, 113.69, 113.18, 70.68, 70.50, 70.43, 70.20, 70.14, 70.11, 68.39, 56.91, 53.11, 52.17, 48.12, 35.61, 31.55, 25.76, 25.71, 23.72, 14.25, 10.30 ppm.

ESI-MS (*m/z*): calculated for [C₅₂H₇₄N₈O₇K]⁺: 961.5312, found 961.5298.

3. Additional NMR experiments

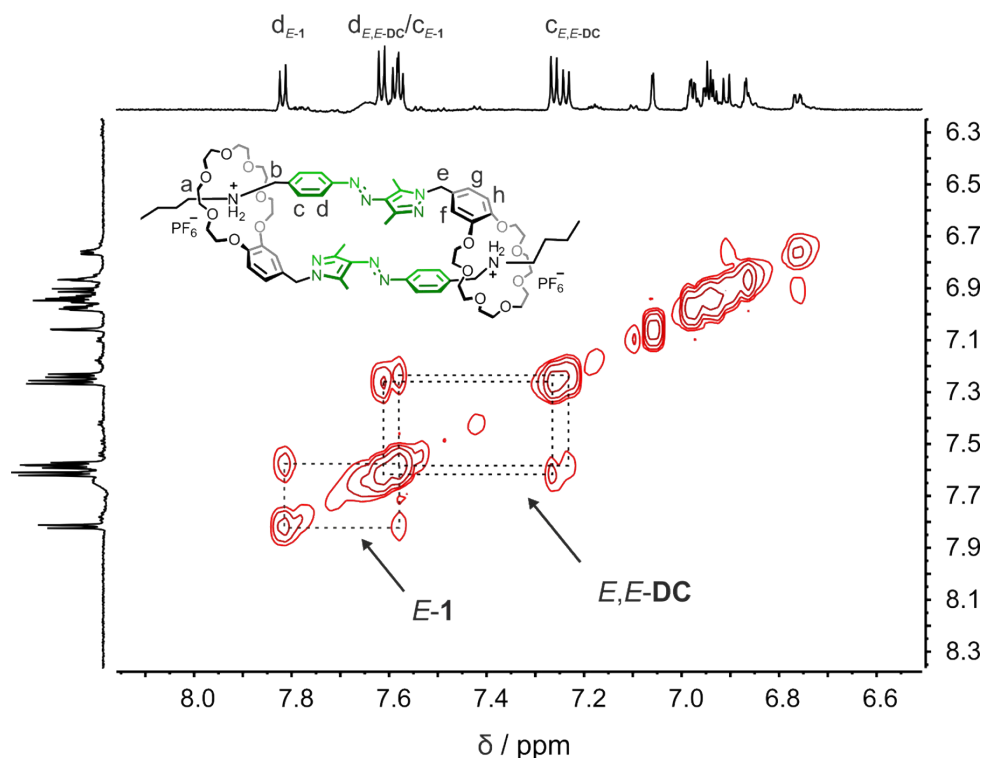


Fig. S1 Partial ^1H - ^1H COSY spectrum of *E*-1 in CD_3CN (700 MHz, 10 mM, 298 K).

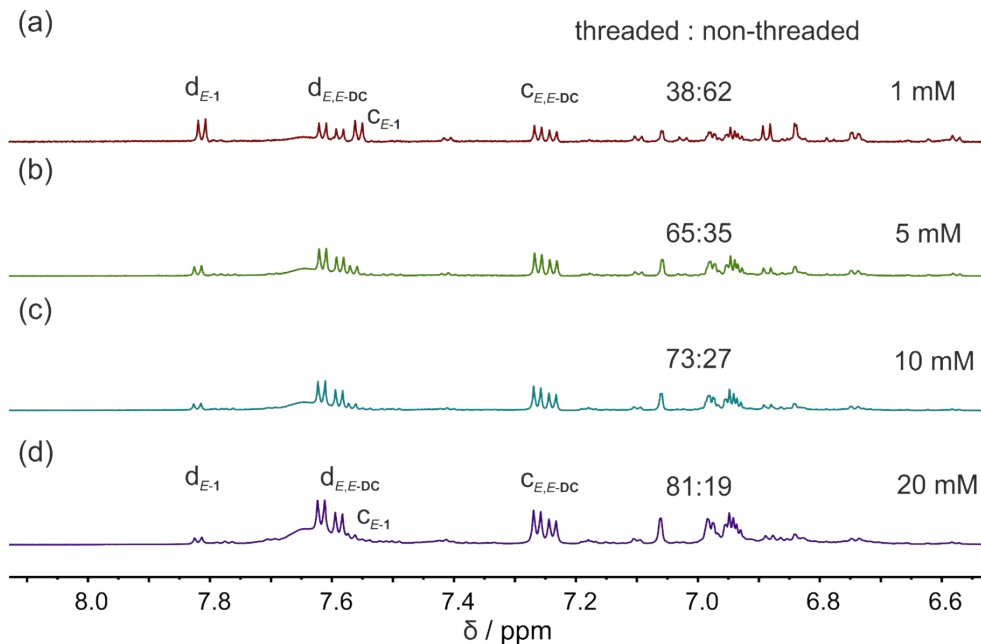


Fig. S2 Partial ^1H NMR spectra of **1** in CD_3CN at the concentrations of (a) 1 mM, (b) 5 mM, (c) 10 mM and (d) 20 mM (700 MHz, 298 K). Non-threaded *E*-monomer: *E*-1; and threaded *E*-dimer: *E,E*-DC.

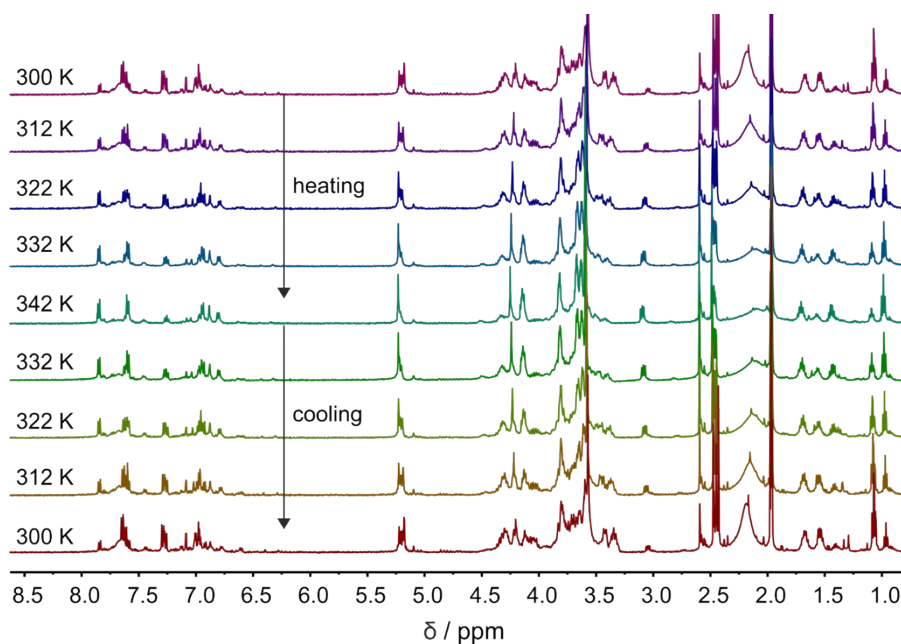


Fig. S3 VT-NMR experiment of **1** (10 mM in CD₃CN) upon heating and cooling. The characteristic signals for *E,E*-DC and diastereotopic splitting diminished at elevated temperatures and were retrieved after cooling down to 300 K.

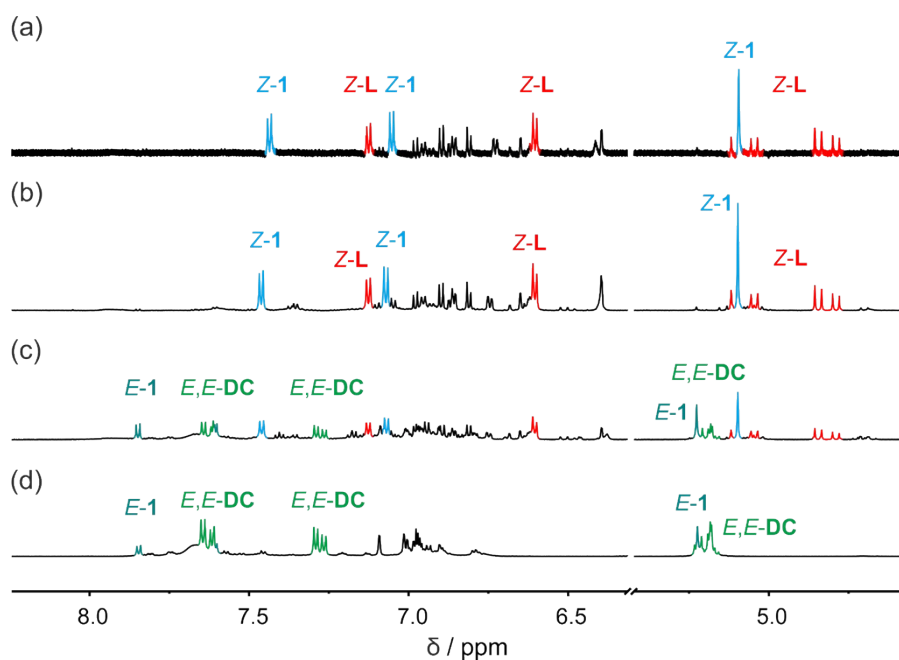


Fig. S4 Partial ¹H NMR spectra of **Z-1** in CD₃CN at the concentrations of (a) 1 mM, (b) 5 mM, (c) 10 mM and (d) 20 mM (700 MHz, 298 K). All spectra were recorded immediately after UV irradiation for 10 min. In (c) and (d), the appearance of *E-1* and *E,E*-DC is the result of increasing protonation followed by thermal backswitching. Non-threaded *E*-monomer: *E-1*; Non-threaded *Z*-monomer: *Z-1*; threaded *E*-dimer: *E,E*-DC; and threaded *Z*-monomer: *Z-L*.

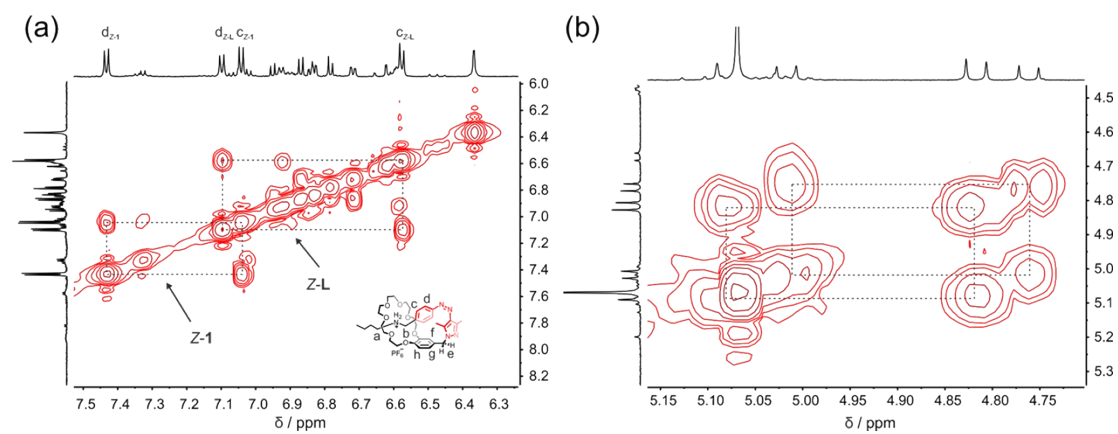


Fig. S5 Partial ^1H - ^1H COSY spectrum of Z-1 at (a) aromatic region and (b) the region of methylene protons H_e in CD_3CN (700 MHz, 5 mM, 298 K).

4. IMS experiments

In IMS experiments, the acetonitrile solutions, which were used in NMR experiments, were diluted with DCM for two reasons: On one hand, the much less competitive mixture slows down the building block exchange and thus reduces rearrangements in the MS sample solution to a minimum. On the other hand, the binding constant in the less competitive solvent mixture is higher and thus, the complexes survive even at mass spectrometric sample concentrations. These two aspects together make sure that the picture observed by mass spectrometry is as close as possible to the situation in the NMR experiments.

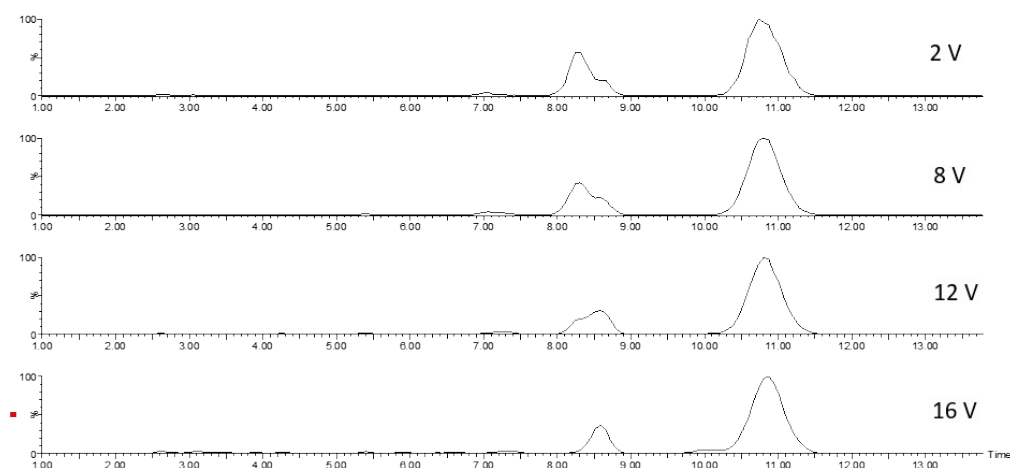


Fig. S6 Arrival-time distributions recorded in energy-resolved IMS experiments with mass-selected ions at m/z 654 after 5 min of UV irradiation. These experiments support the assignment of the peaks in the ATD to *E,Z-DC* (8.4 ms), *E,E-DC* (8.9 ms) and *Z-L* (10.9 ms): The peak for partially switched and therefore somewhat strained *E,Z-DC* vanishes at around 16 V collision voltage, while the unstrained *E,E-DC* daisy chain and the switched *Z*-isomer survive as the more stable species. ATDs are given in milliseconds.

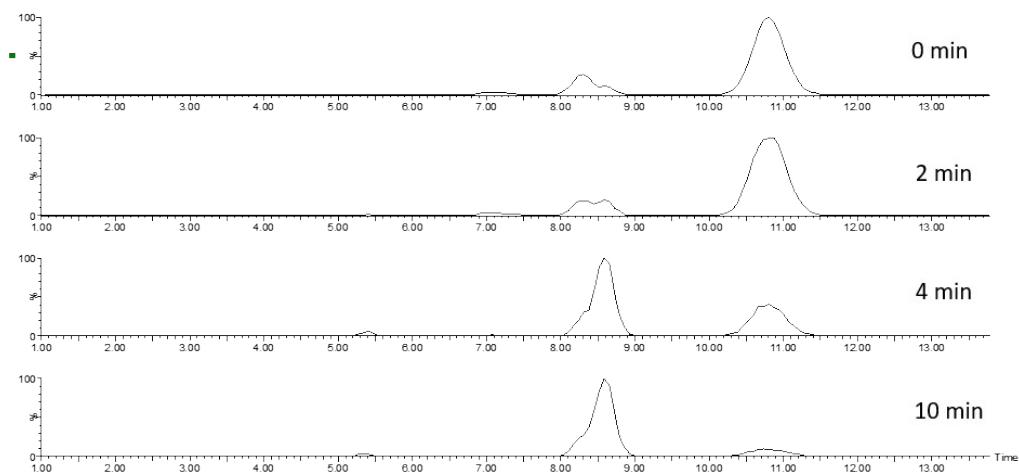


Fig. S7 ATDs of **1** under green light irradiation. At $t = 0$, the ATD was recorded with the sample after irradiating under 365 nm for 5 min. Clearly, the back-switching process occurs leading to the *E,E*-DC daisy chain. In contrast to the *E*-to-*Z* switching, the abundance of the *E,Z*-DC isomer does not change significantly indicating that the major fraction of the back-switched molecules undergo *Z*-to-*E* isomerization first and then directly assemble from two copies of *E*-1. ATDs are presented in milliseconds.

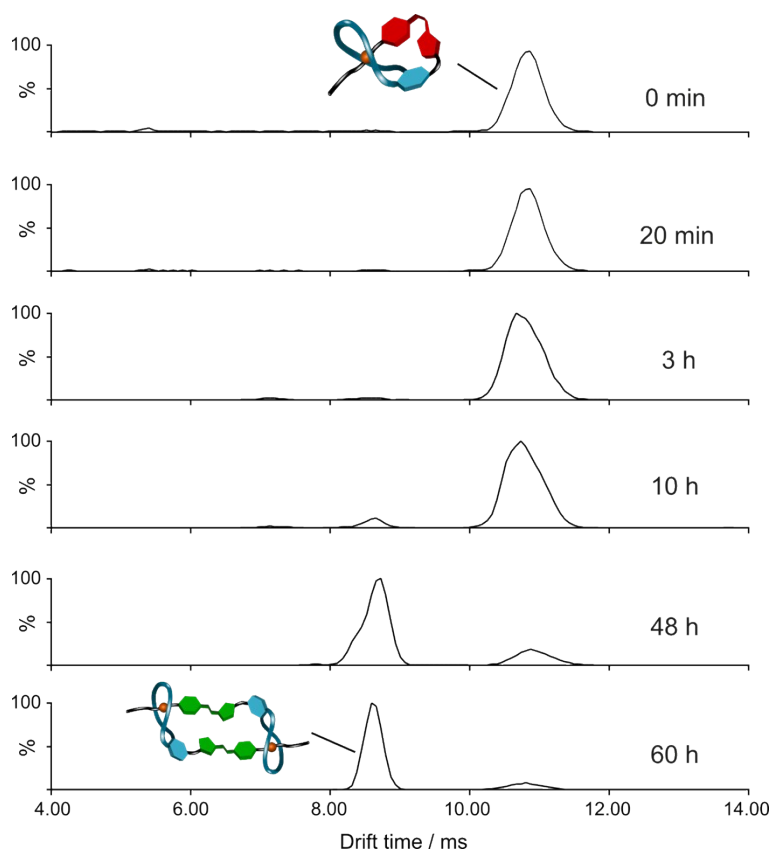


Fig. S8 Thermal stability of **Z-L** in the dark monitored by IMS. In the first 10 h, **Z-L** remains as major product. Over time, a dimer peak became visible due to **Z-to-E** back isomerisation of **1** and thus, the formation of **E,E-DC**. After 48 h, an intermediate **E,Z-DC** was clearly observed. Compared to the light-induced **Z-to-E** switching (Fig. S7), **E,Z-DC** is prominent here due to a slower process of the thermal-induced **Z-to-E** switching, so that the daisy chain assembly can compete. There is an intermediate stage, where about 50% of the compound is **E**-state and 50% is **Z**-state, so the assembly of **E,Z-DC** is expected. After 60 h in the dark, **E,E-DC** was recovered as the major product.

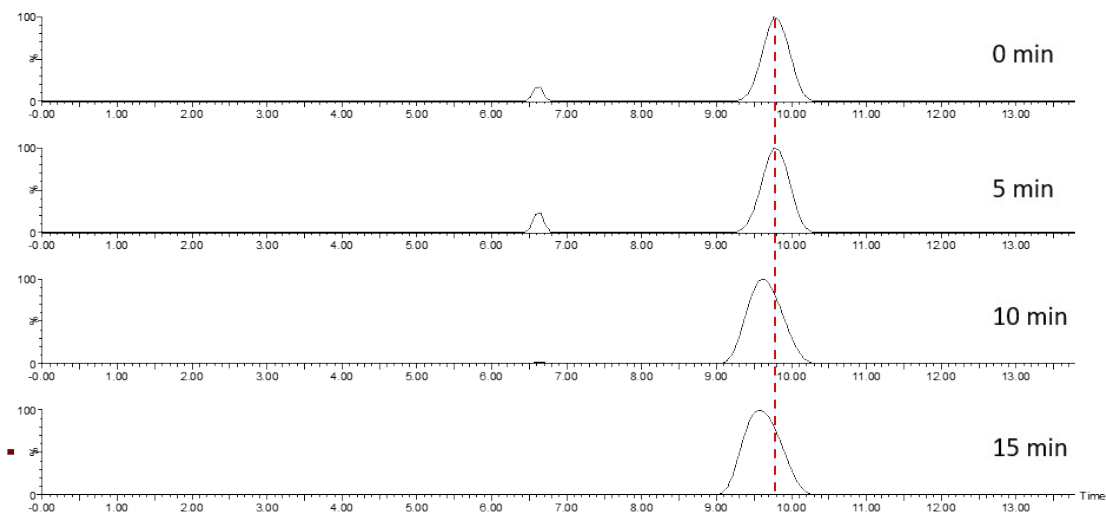


Fig. S9 ATDs of **2** under UV irradiation. The distribution shifted towards shorter drift time under UV irradiation, representing a photoswitching from *E*-**2** to *Z*-**2**. ATDs are presented in milliseconds.

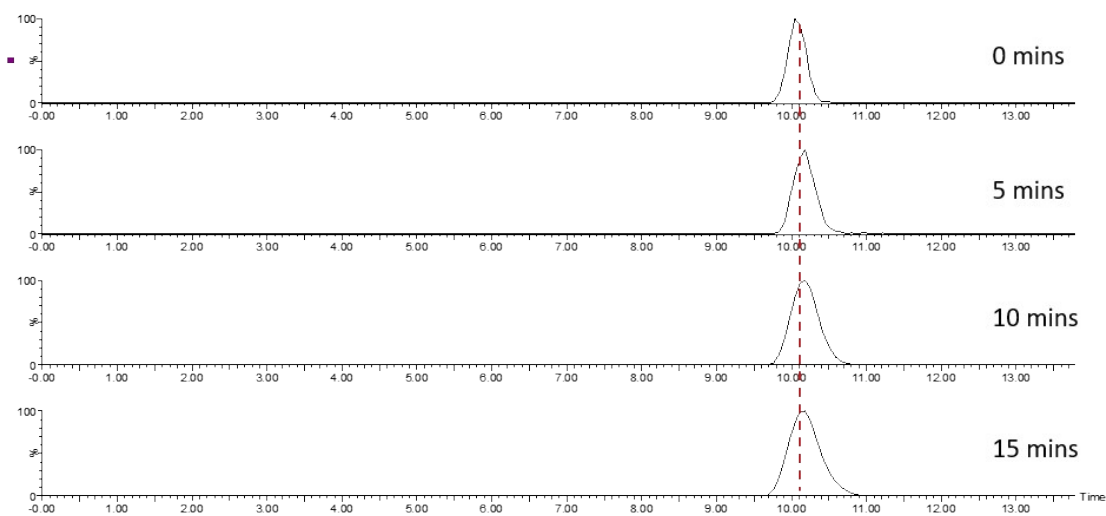


Fig. S10 ATDs of Boc-protected **2** under UV irradiation. Here, the distribution did not show a distinct difference in size due to a fast *Z*-*E* switching induced by protonation of azo nitrogen adjacent to the phenyl ring. ATDs are presented in milliseconds.

5. Computational Modelling and theoretical CCS values.

To support the assignment of the switching processes, computational modelling at the PM6 level was performed for *E,E*-DC (Fig. S11), *E,Z*-DC (Fig. S12), threaded monomer Z-L (Fig. S13), non-threaded monomer Z-1 (Fig. S14), and *E*-1 (Fig. S15). The respective structures were initially constructed to allow the maximum number of hydrogen bonds between crown ether and axle and to maximise the conjugation of the azo groups with the adjacent aromatic rings followed by optimisation at the PM6 level. These structures were then used to perform the theoretical CCS calculations (Table S1) which can be used to rationalise the proposed pathway.

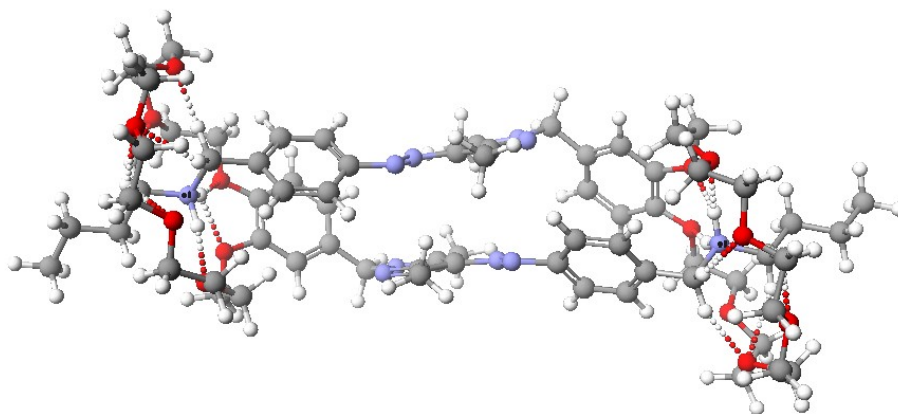


Fig. S11 PM6 optimised structure of *E,E*-DC. Hydrogen bonds are denoted by the dotted bonds.

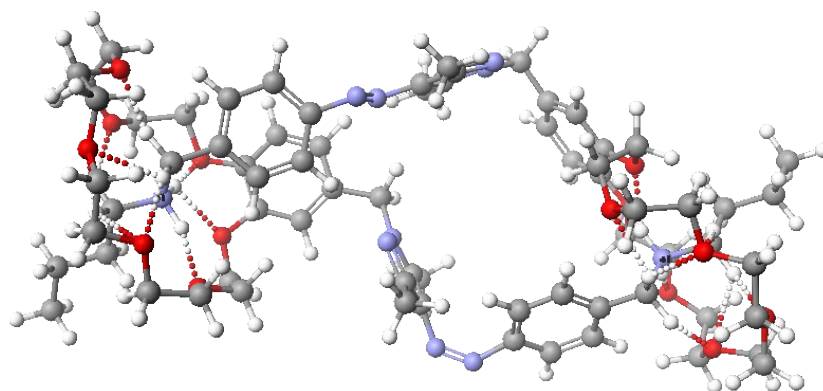


Fig. S12 PM6 optimised structure of *E,Z*-DC. Hydrogen bonds are denoted by the dotted bonds.

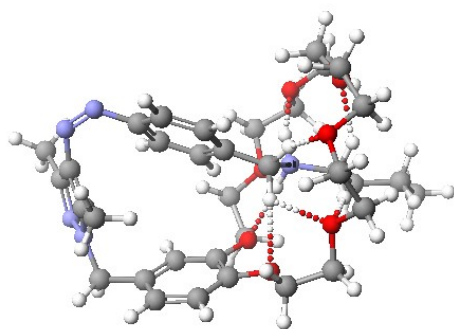


Fig. S13 PM6 optimised structure of threaded Z-L. Hydrogen bonds are denoted by the dotted bonds.

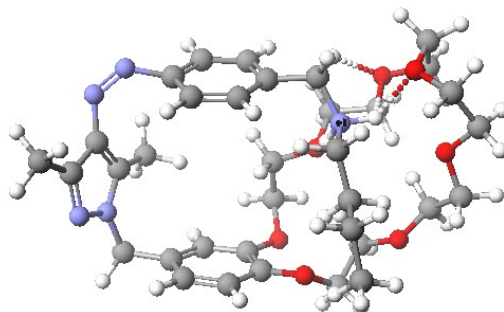


Fig. S14 PM6 optimised structure of non-threaded Z-1. Hydrogen bonds are denoted by the dotted bonds.

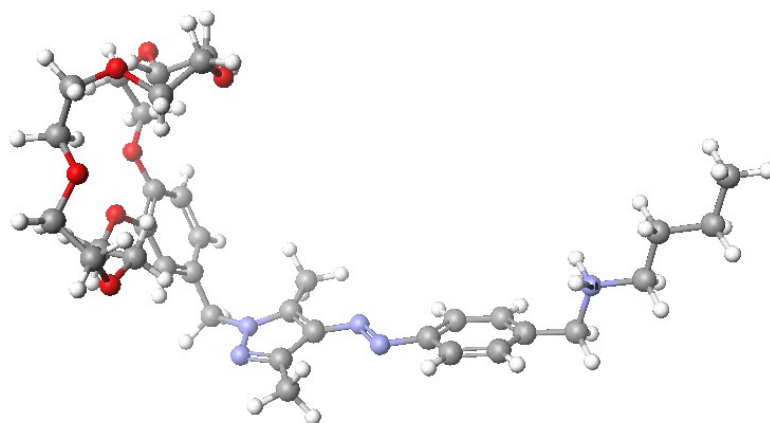


Fig. S15 PM6 optimised structure of *E*-1 (non-threaded).

Table S1: Calculated heat of formations and theoretical CCS values of the different optimised structures.

conformation	heat of formation (kJ mol ⁻¹)	TM CCS _{N₂} (Å ²)
<i>E,E-DC</i>	-600.5	467
<i>E,Z-DC</i>	-616.5	462
<i>Z-L</i> (threaded)	-327.0	278
<i>Z-1</i> (non-threaded)	-310.2	267
<i>E-1</i>	-223.3	331

E,Z-DC having a more favourable value in energy than the *E,E-DC* can explain the ready *E,E-DC* to *E,Z-DC* switching which is observed under UV irradiation. When considering the monomer which would form, the threaded *Z-L* is more stable than the non-threaded *Z-1* and will thus be expected to predominate between the two conformations. The heat of formation difference (16.8 kJ/mol) between the two though is not large enough that it would prevent the necessary dethreading seen in the back switching process. In contrast, *E-1* does not benefit from any H-bonding observed for the other conformations and hence has a much less favourable heat of formation of (-223.3 kJ/mol). Dimerization of *E-1* to *E,E-DC* would be accompanied by a binding energy of 153.9 kJ/mol. Although this is a gas-phase calculation which amplifies the benefit of non-covalent interaction as compared to solution, this clearly rationalises the driving force for dimerization which is seen by IMS. Finally, the TMCCS_{N₂} are also in alignment with the proposed pathway with the initial *E,E-DC* switching to form the smaller *E,Z-DC* before finally disassembling to form the monomer. Our calculations are gas-phase calculations in the absence of counterions and thus may be somewhat limited with respect to conclusions that can be drawn for the situation in solution. However, counterion effects as well as solvent effects on the crown ether/ammonium binding pattern likely affect the binding in a similar manner for all threaded complexes. Therefore, our calculations support our interpretation of the NMR spectroscopic and IMS data.

6. UV/vis experiments

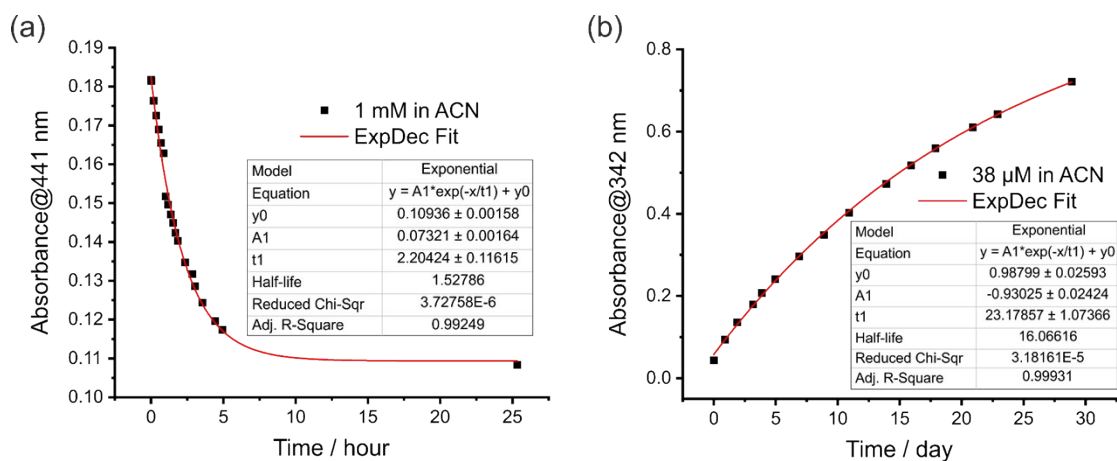


Fig. S16 Half-lives of Z-1 at concentrations of (a) 1 mM ($t_{1/2} = 1.5$ h) and (b) 38 μM ($t_{1/2} = 16$ days) in CH₃CN in the dark. At $t = 0$, the spectra were recorded with the samples right after irradiating at 365 nm for 10 min. Absorbance at 441 nm is used to follow the back isomerisation to avoid the excessively high absorbance at 342 nm at the concentration of 1 mM.

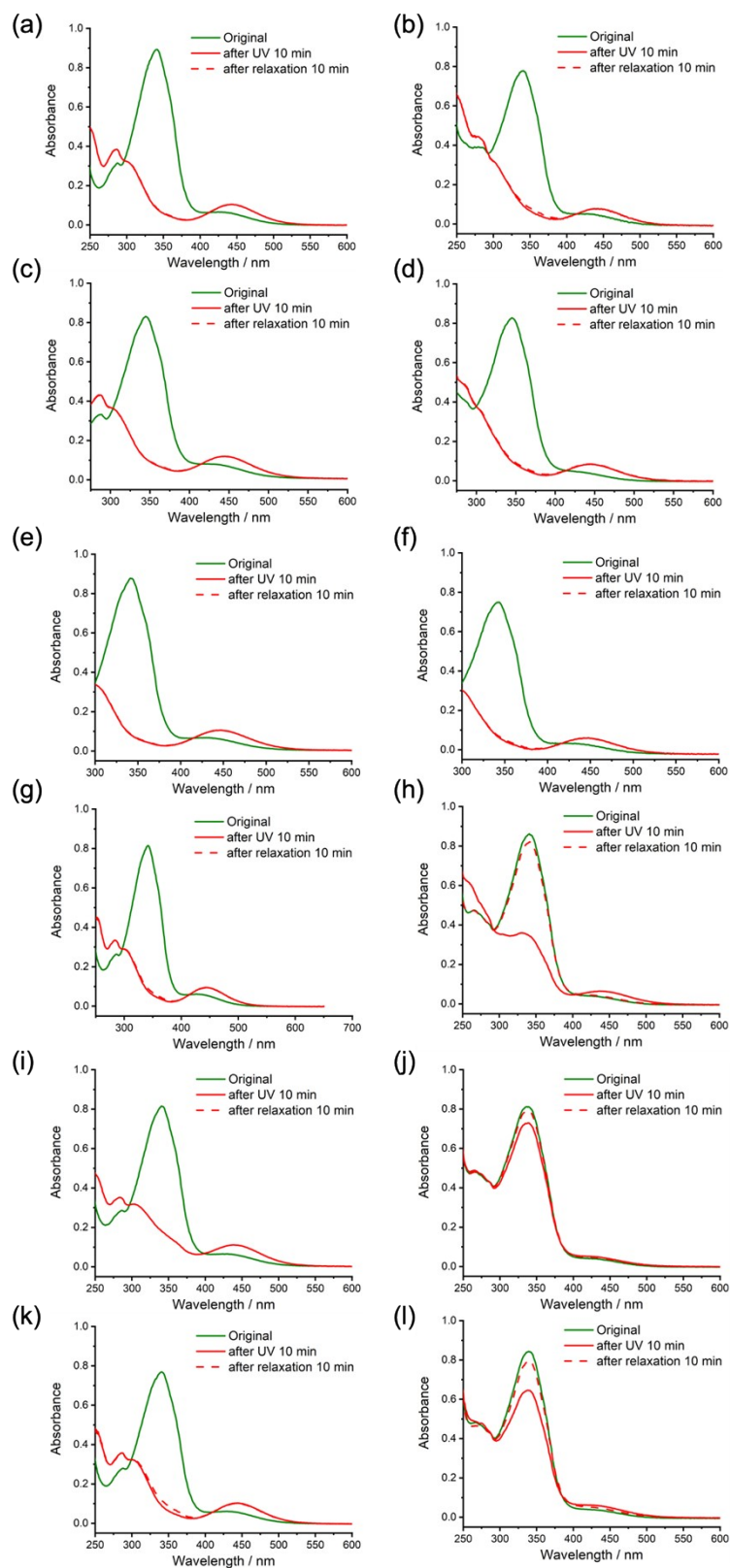


Fig. S17 UV/Vis spectra of Boc-protected **2** (left) and **2** (right) in CH₃CN (a, b), DMSO (c, d), THF (e, f), DCE (g, h), CH₂Cl₂ (i, j), CHCl₃ (k, l).

7. NMR spectra

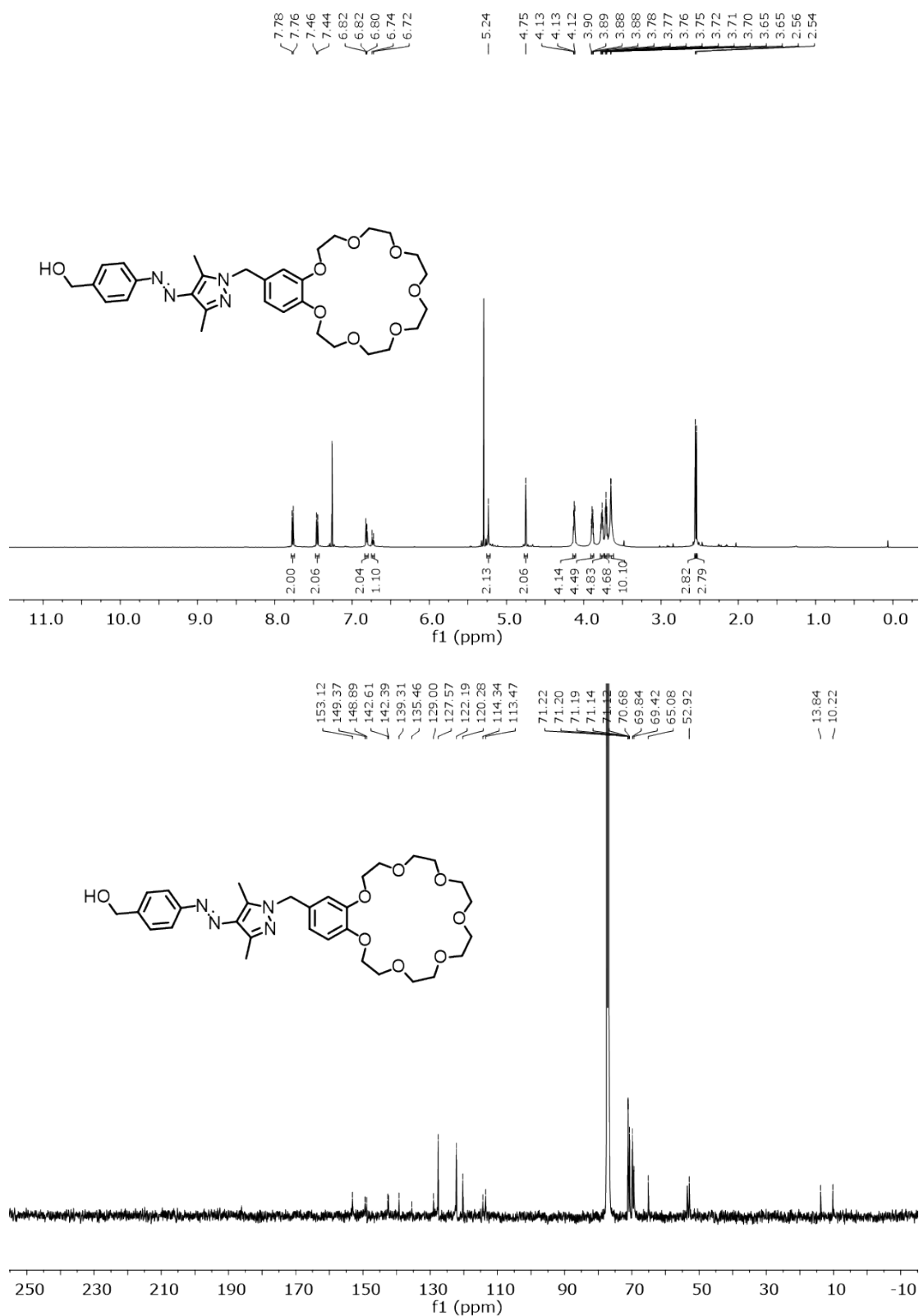


Fig. S18 ^1H (top) and ^{13}C (bottom) NMR spectrum (500/126 MHz, CDCl_3 , 298 K) of **S3**.

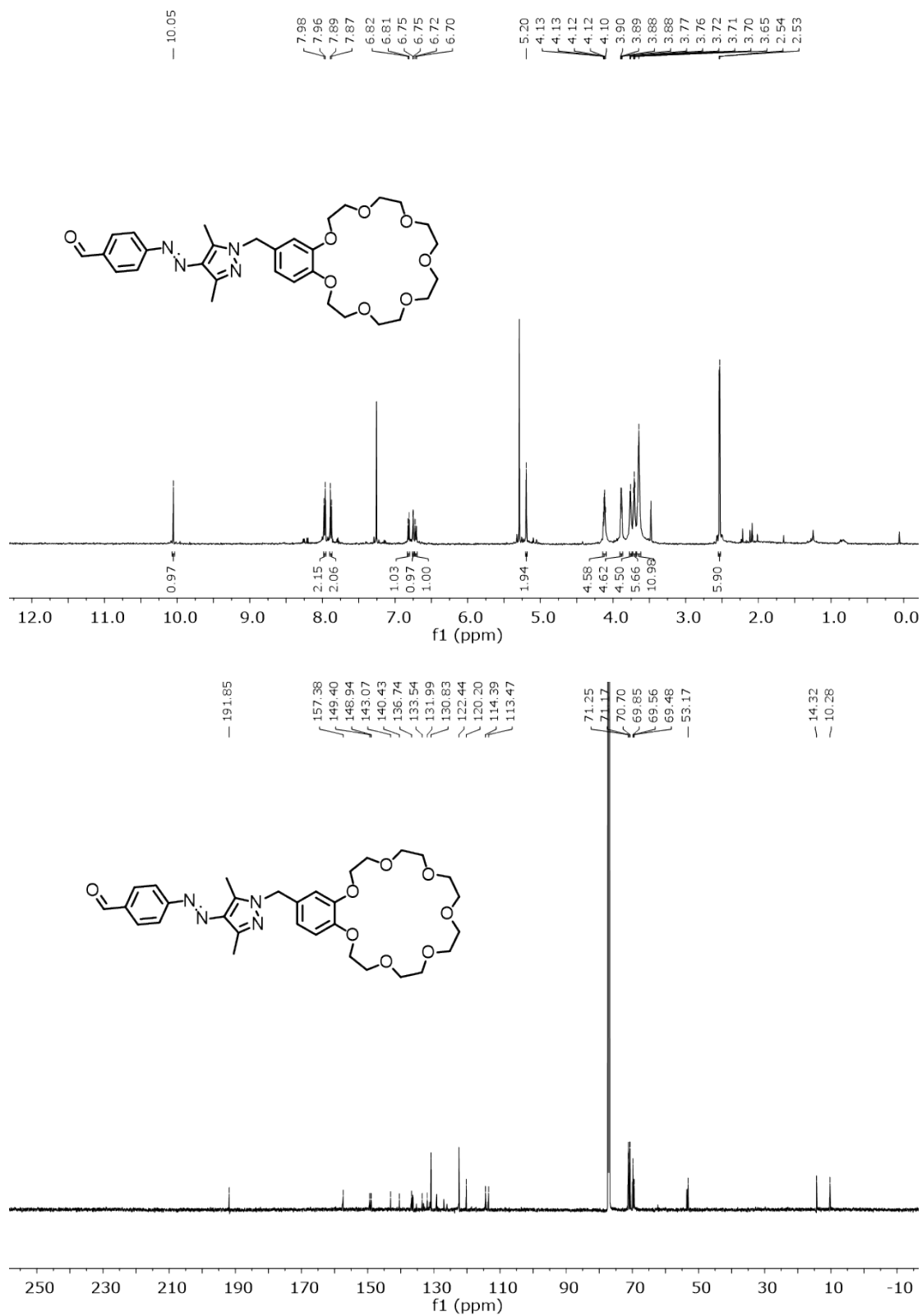


Fig. S19 ¹H (top) and ¹³C (bottom) NMR spectrum (700/176 MHz, CDCl₃, 298 K) of **S4**.

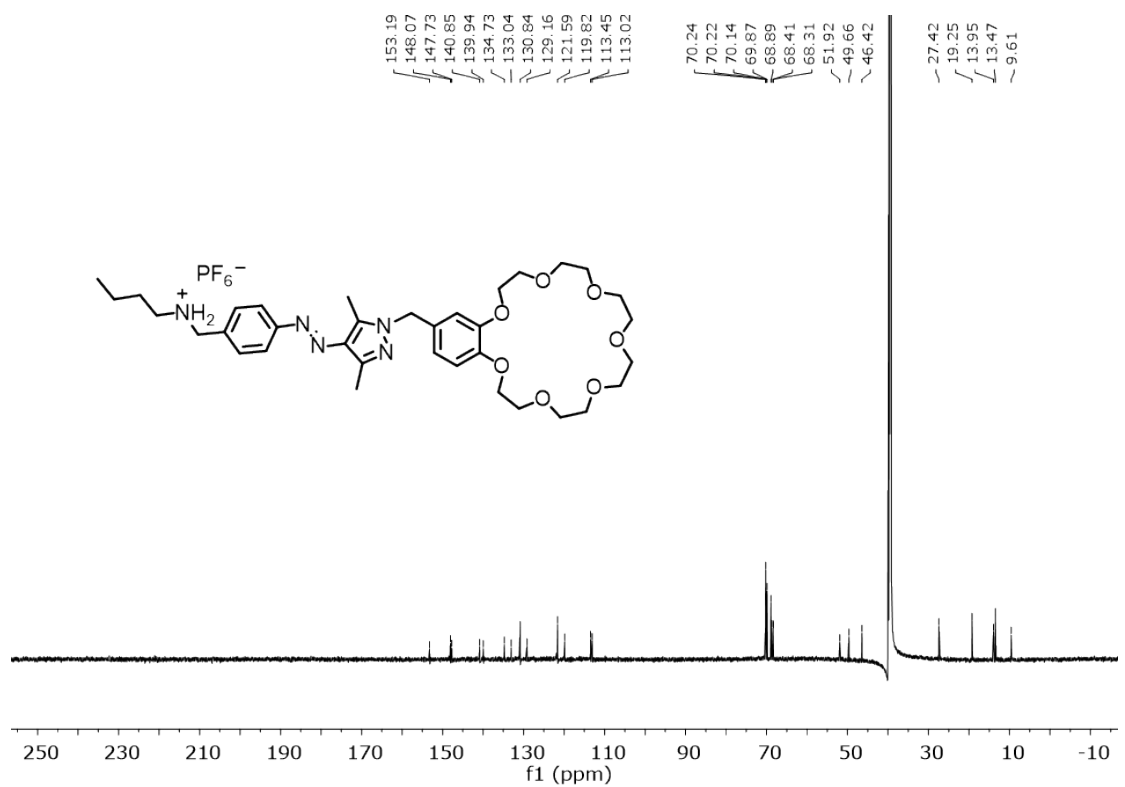
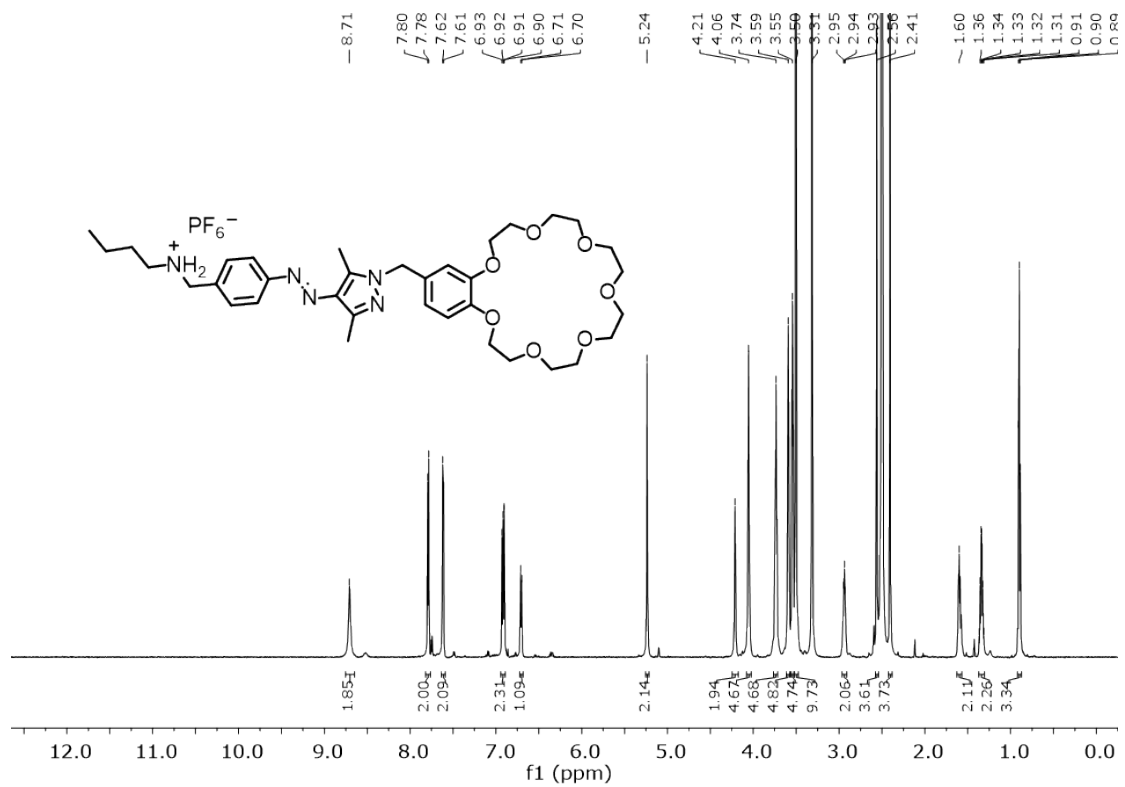


Fig. S22 ¹H (top) and ¹³C (bottom) NMR spectrum (700/176 MHz, DMSO-*d*₆, 298 K) of thread **1**.

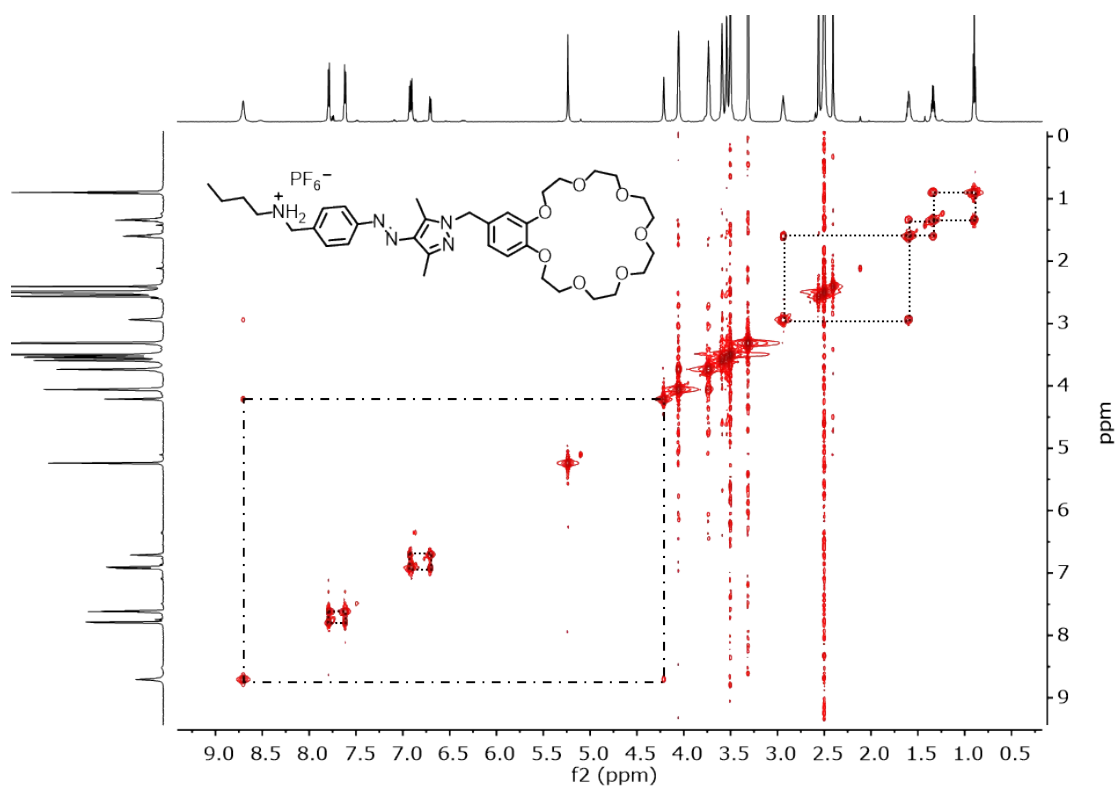


Fig. S23 COSY spectrum (700 MHz, DMSO- d_6 , 298 K) of thread 1.

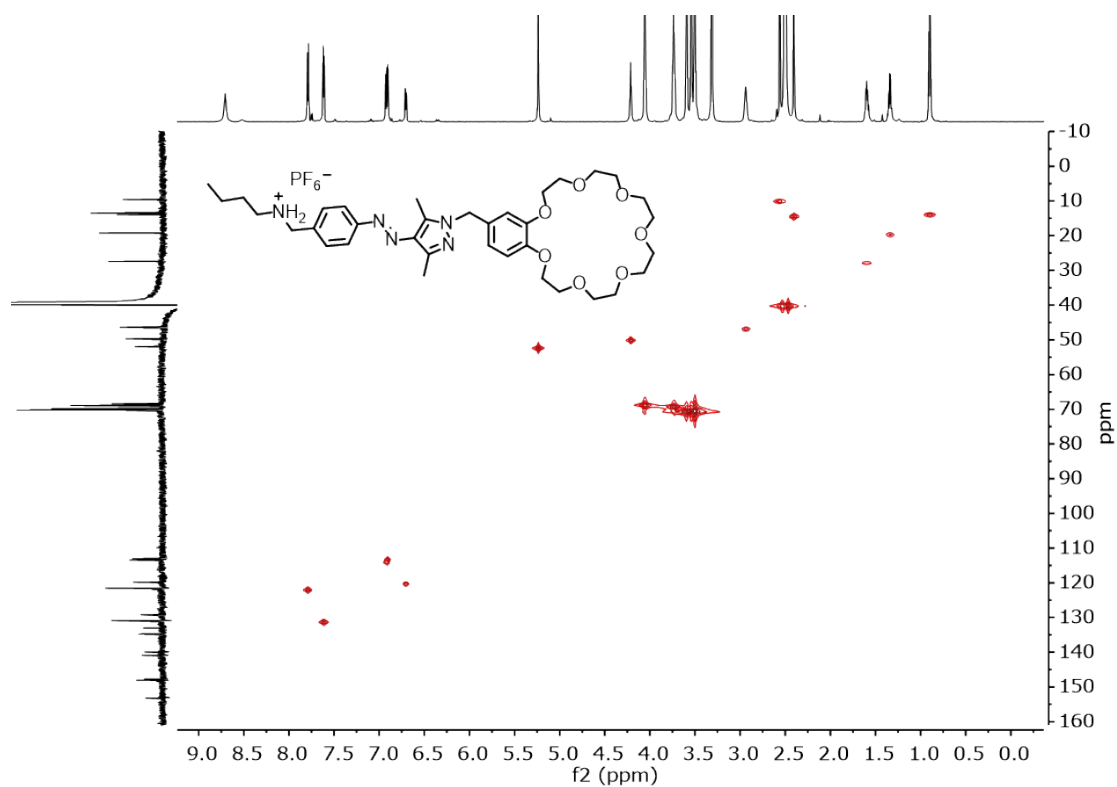


Fig. S24 HMQC spectrum (700/176 MHz, DMSO- d_6 , 298 K) of thread 1.

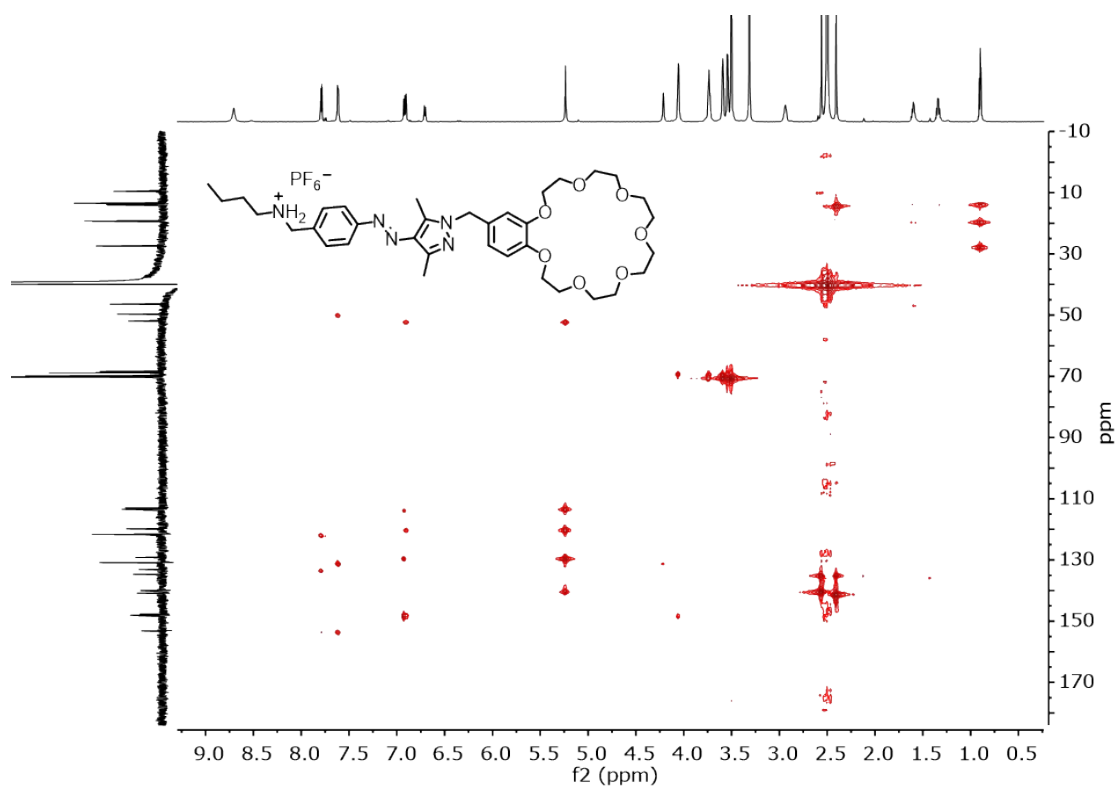


Fig. S25 HMBC spectrum (700/176 MHz, DMSO- d_6 , 298 K) of thread **1**.

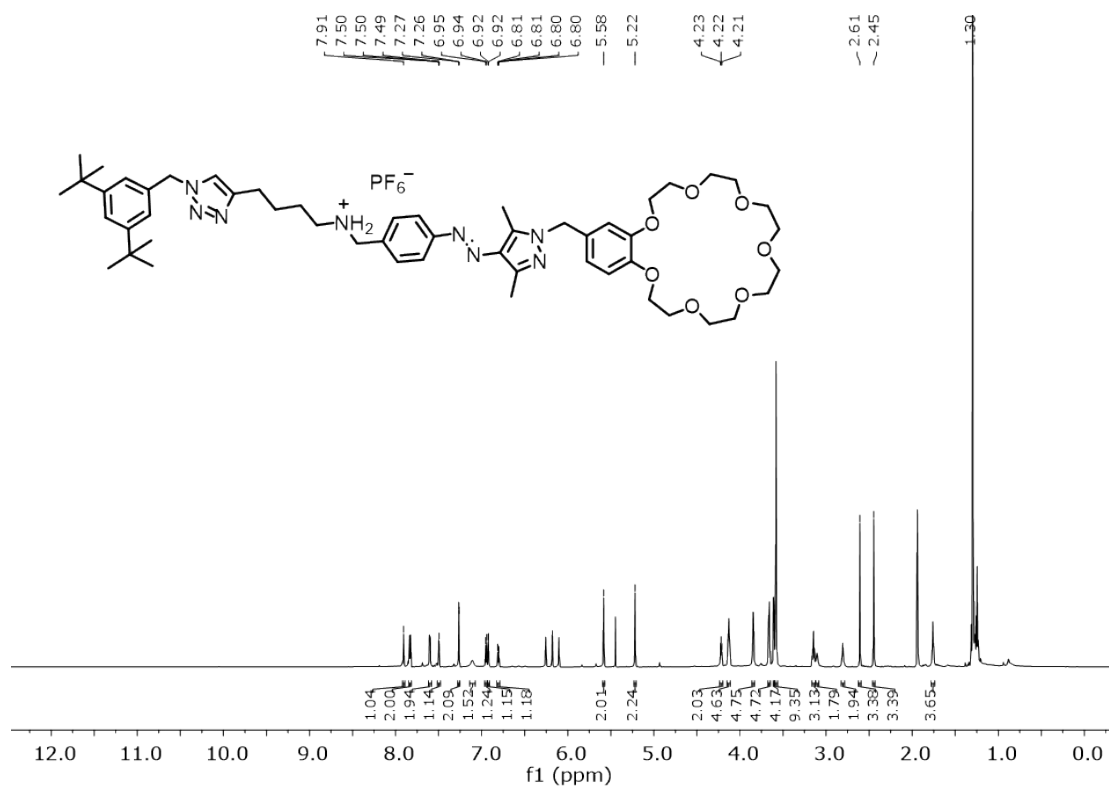


Fig. S26 ^1H NMR spectrum (700 MHz, CD_3CN , 298 K) of control compound **2**.

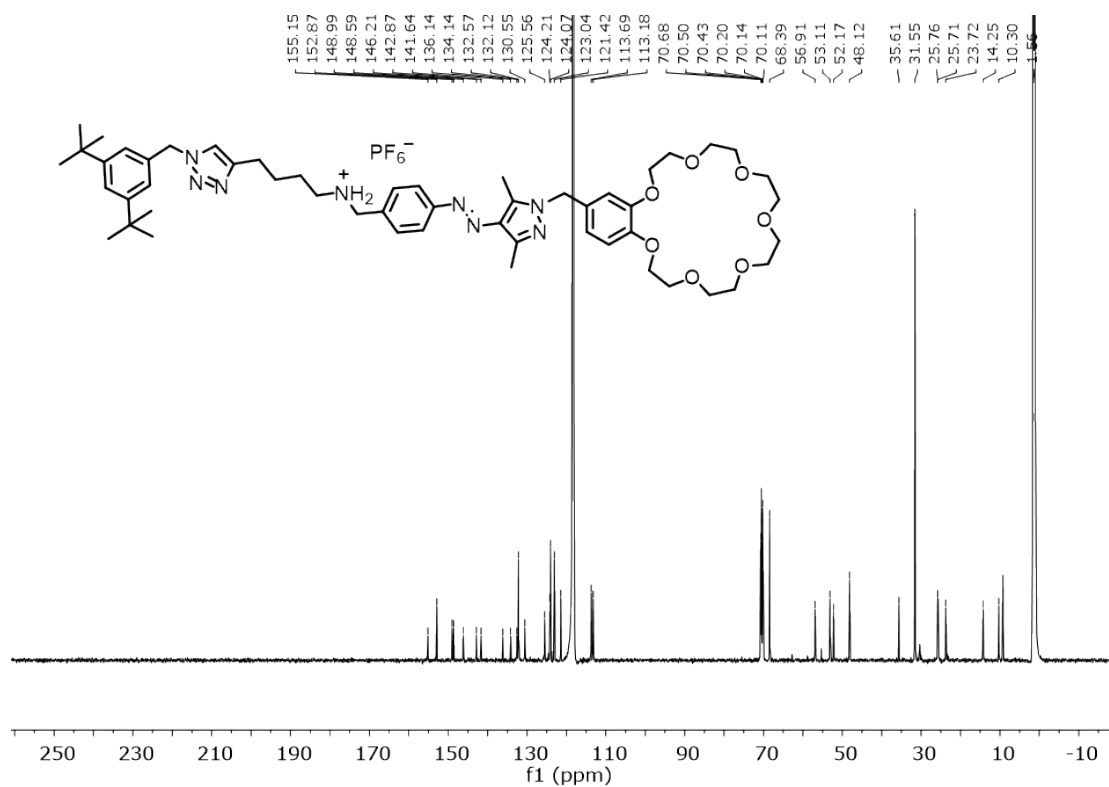


Fig. S27 ^{13}C NMR spectrum (176 MHz, CD_3CN , 298 K) of control compound **2**.

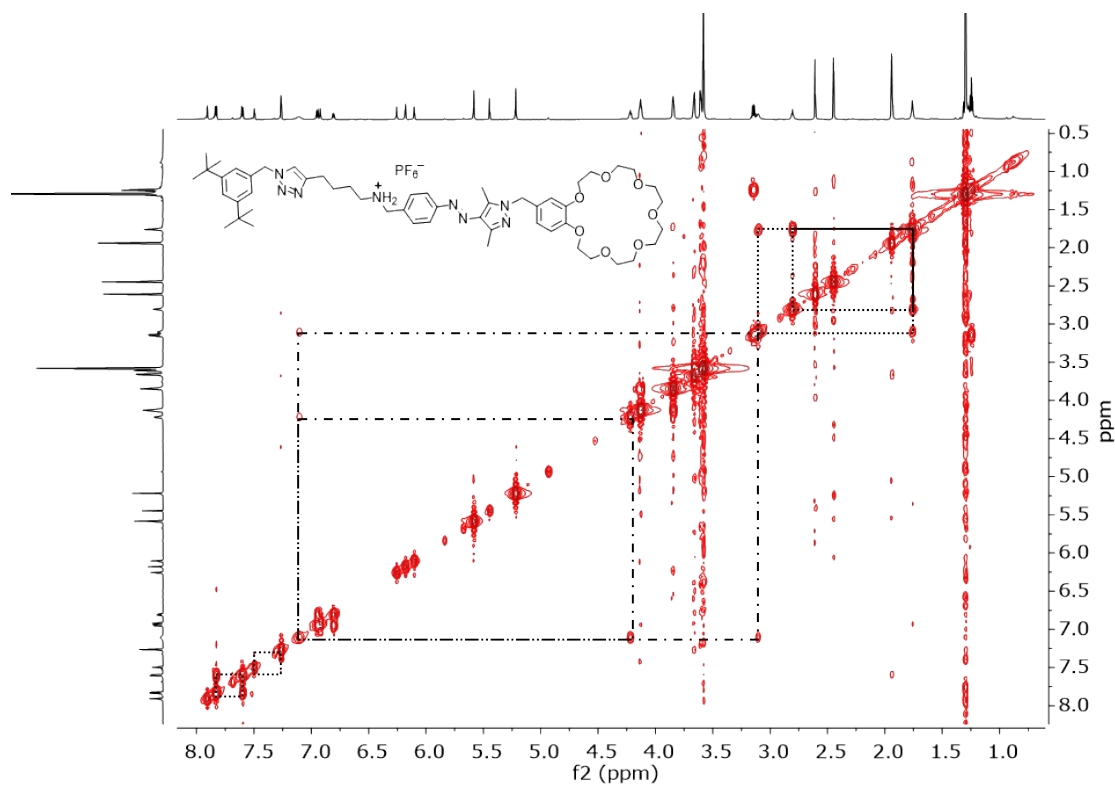


Fig. S28 COSY spectrum (700 MHz, CD_3CN , 298 K) of control compound **2**.

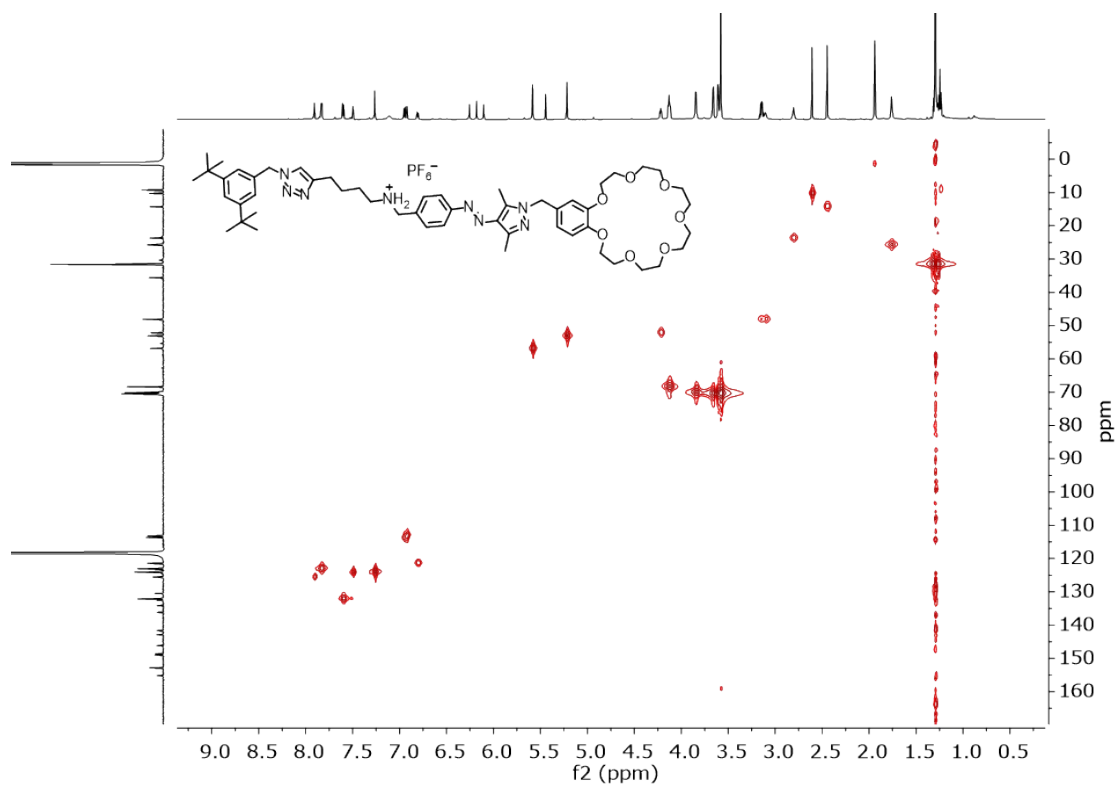


Fig. S29 HMQC spectrum (700/176 MHz, CD₃CN, 298 K) of control compound **2**.

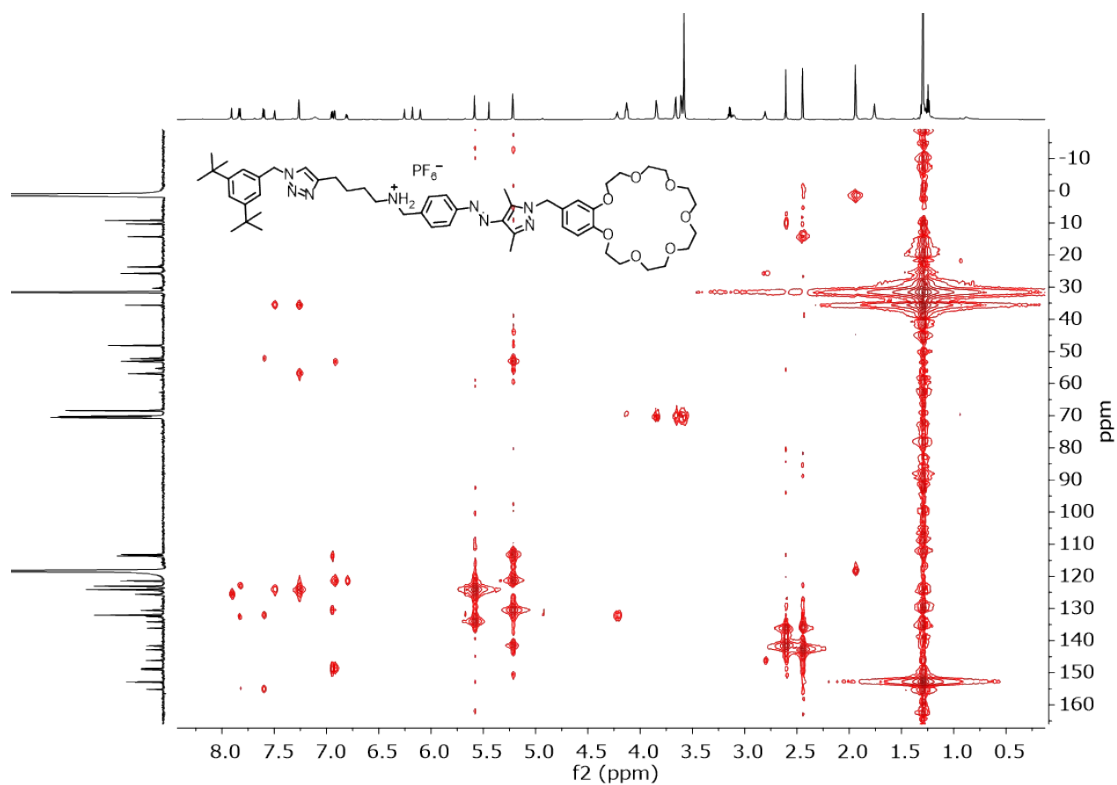


Fig. S30 HMBC spectrum (700/176 MHz, CD₃CN, 298 K) of control compound **2**.

8. ESI mass spectra

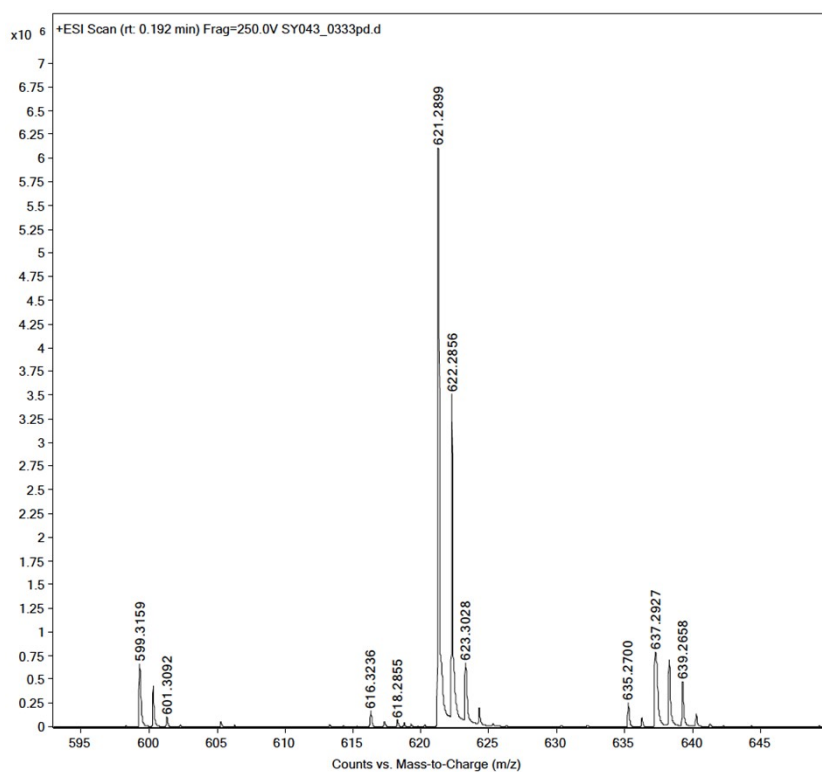


Fig. S31 ESI-MS of S3.

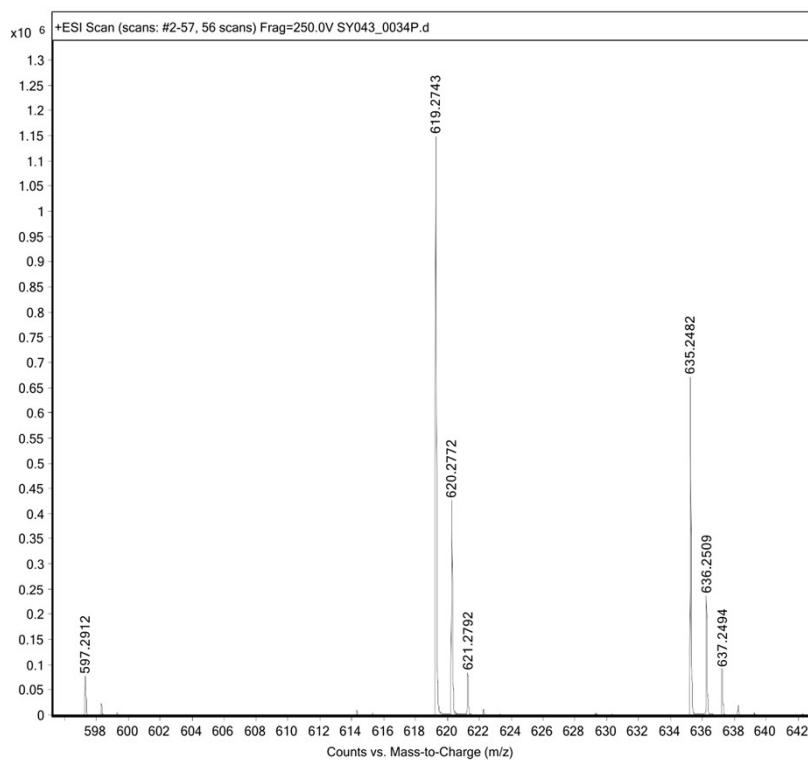


Fig. S32 ESI-MS of S4.

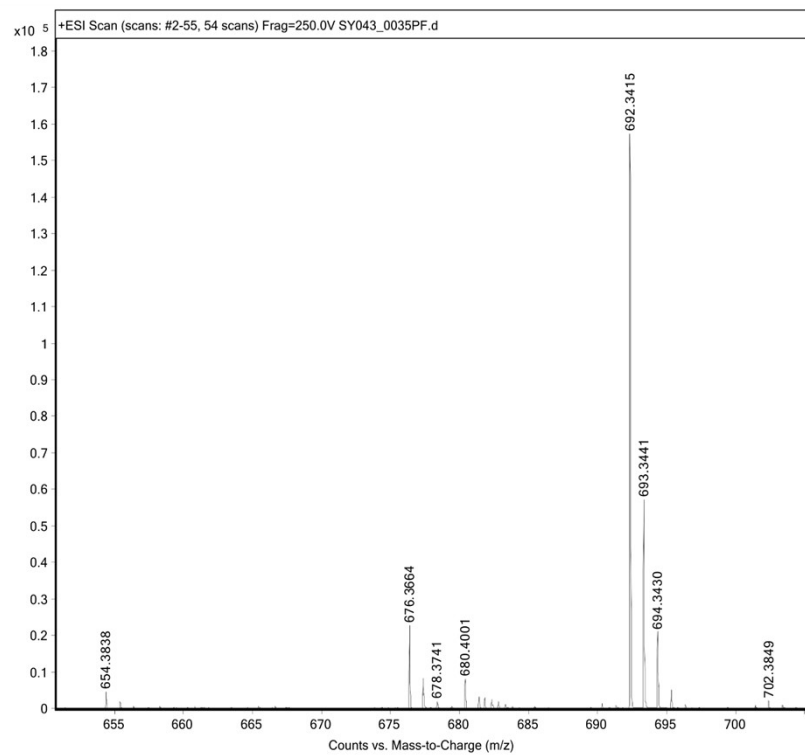
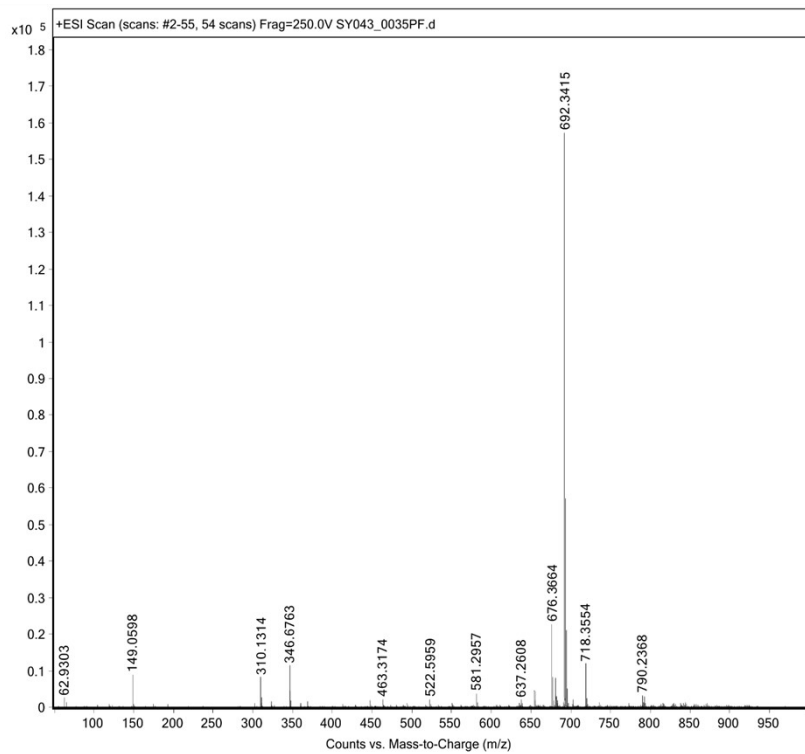


Fig. S33 ESI-MS of **1** (mostly $[1\text{-PF}_6\text{+K}]^+$). Full spectrum (top) and zoom-in (bottom).

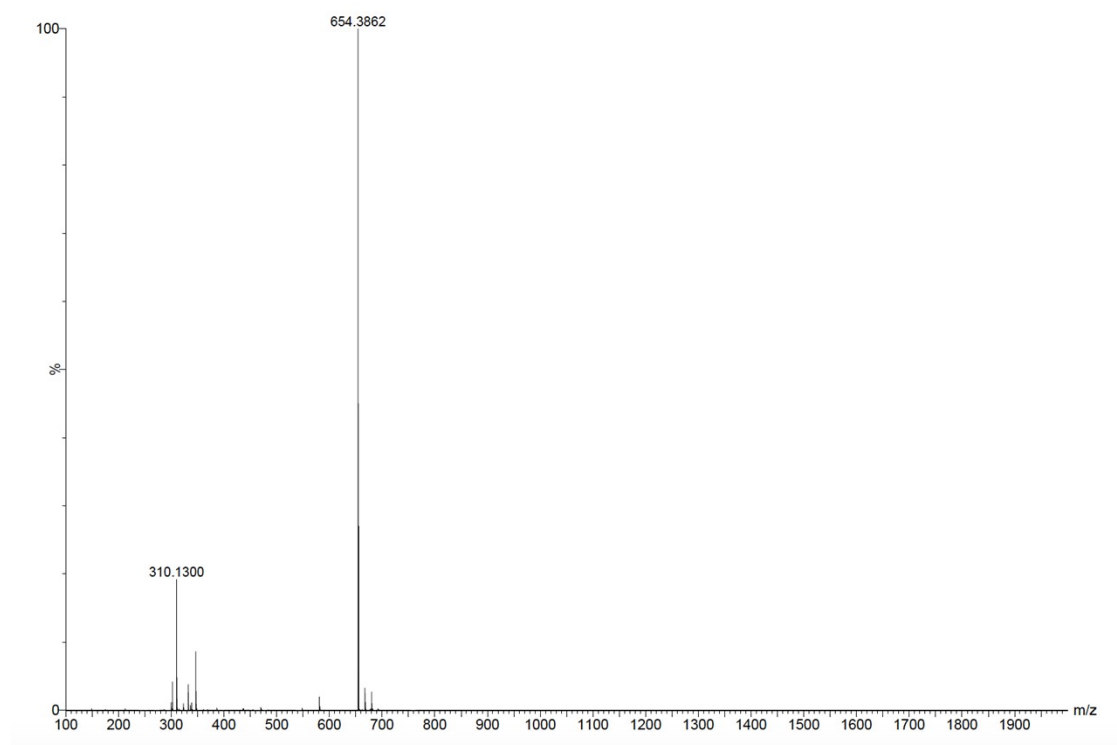


Fig. S34 Full, non-mass selected ESI-MS of **1** (mostly $[1\text{-PF}_6]^+$).

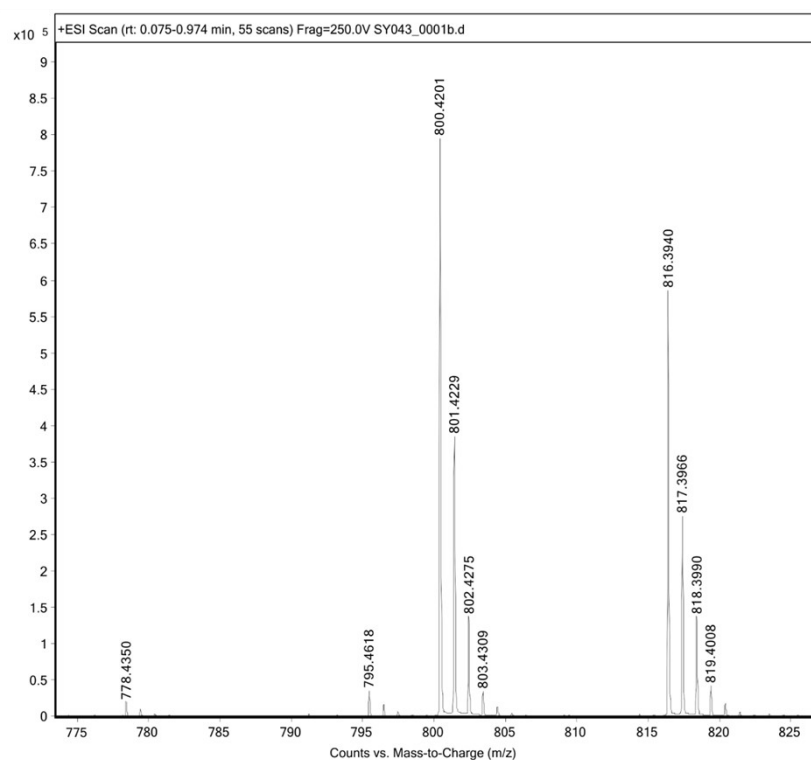


Fig. S35 ESI-MS of **S6**.

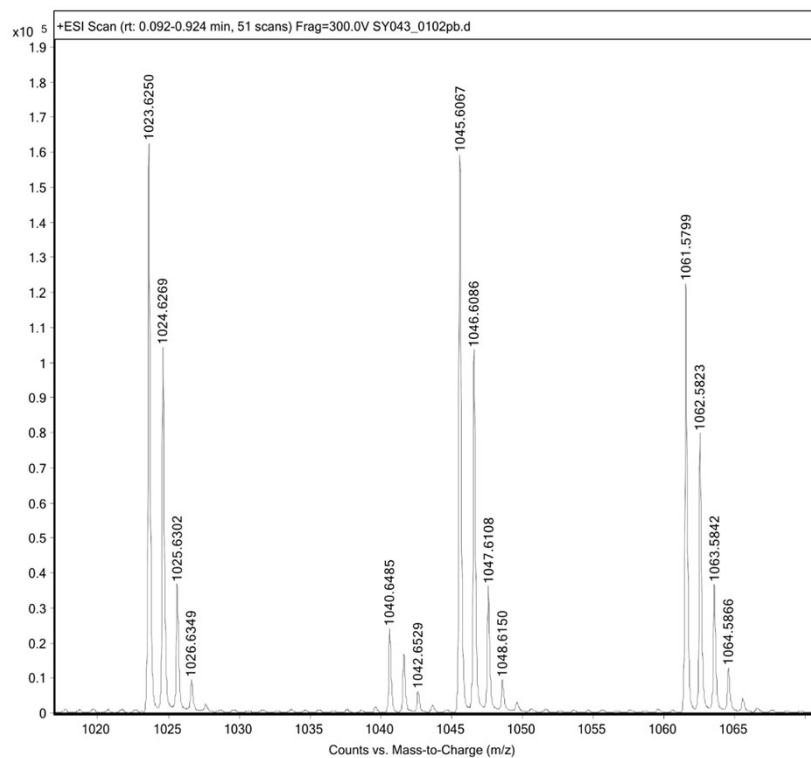


Fig. S36 ESI-MS of S8.

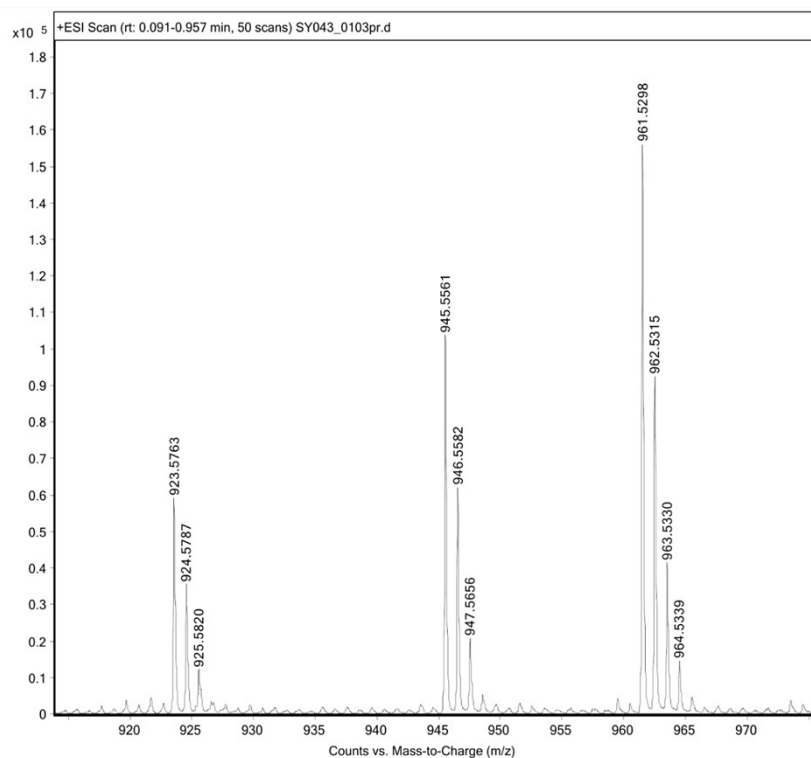


Fig. S37 ESI-MS of 2.

9. References

- S1. L. Chen, Y.-K. Tian, Y. Ding, Y.-J. Tian and F. Wang, *Macromolecules*, 2012, **45**, 8412.
- S2. W. Wang, Y. Zhang, B. Sun, L.-J. Chen, X.-D. Xu, M. Wang, X. Li, Y. Yu, W. Jiang and H.-B. Yang, *Chem. Sci.*, 2014, **5**, 4554.
- S3. C.-W. Chu, L. Stricker, T. M. Kirse, M. Hayduk and B. J. Ravoo, *Chem. Eur. J.*, 2019, **24**, 6131.
- S4. J. Budhathoki-Uprety, J. F. Reuther and B. M. Novak, *Macromolecules*, 2012, **45**, 8155.
- S5. J. J. Gassensmith, L. Barr, J. M. Baumes, A. Paek, A. Nguyen and B. D. Smith, *Org. Lett.*, 2008, **10**, 3343.



OPEN

A light-fuelled nanoratchet shifts a coupled chemical equilibrium

Michael Kathan¹✉, Stefano Crespi¹, Niklas O. Thiel¹, Daniel L. Stares², Denis Morsa³, John de Boer¹, Gianni Pacella⁴, Tobias van den Enk¹, Piermichele Kobauri¹, Giuseppe Portale⁴, Christoph A. Schalley²✉ and Ben L. Feringa¹✉

Biological molecular machines enable chemical transformations, assembly, replication and motility, but most distinctively drive chemical systems out of equilibrium to sustain life^{1,2}. In such processes, nanometre-sized machines produce molecular energy carriers by driving endergonic equilibrium reactions. However, transforming the work performed by artificial nanomachines^{3–5} into chemical energy remains highly challenging. Here, we report a light-fuelled small-molecule ratchet capable of driving a coupled chemical equilibrium energetically uphill. By bridging two imine^{6–9} macrocycles with a molecular motor^{10,11}, the machine forms crossings and consequently adopts several distinct topologies by either a thermal (temporary bond-dissociation) or photochemical (unidirectional rotation) pathway. While the former will relax the machine towards the global energetic minimum, the latter increases the number of crossings in the system above the equilibrium value. Our approach provides a blueprint for coupling continuous mechanical motion performed by a molecular machine with a chemical transformation to reach an out-of-equilibrium state.

Taking inspiration from the fundamental property of biological nanoscale machines governing transmission and directionality of motion to produce energy carriers and allowing precise mechanical functioning at the molecular level, recent years have witnessed remarkable advances towards the design of artificial molecular motors and machines (AMMs)^{2–4,12–14}. Autonomous rotary and translational movement and dynamic control of assembly, transport and catalysis have been demonstrated using molecular motors, as well as amplification, propagation and coupling of motion^{3,5,15–19}. AMMs can drive the directional movement of a secondary geared unit^{19,20}, transport and assemble molecular fragments in a specific manner^{17,21}, actively pump molecular entities^{22–25} or transduce motion from the molecular to the macroscopic scale^{26,27}. However, in order to address the fundamental question of how to shift a chemical reaction out of its equilibrium state and develop AMMs that can drive endergonic chemical processes, we need to find ways to couple a chemical (equilibrium) reaction to the continuous motion of a molecular machine^{28–30}.

Herein, we describe the design and operation of an artificial, light-fuelled molecular rotary motor that can drive a coupled chemical equilibrium energetically uphill.

Our AMM $\pm n$ (Fig. 1a; n represents the number of twists, while \pm describes the chirality of the crossing; the (S,R,R) configured

AMM $\pm n$ shown in Fig. 1a induces a positive (+) crossing per half-turn)³¹ consists of two complementary parts: two imine macrocycles bridged by a light-driven molecular rotary motor, connecting the contrarotating top and bottom halves of the central motor unit. This bridged bicyclic system can adopt several topologies by forming n crossings between the two macrocycles via two orthogonal pathways: a photochemical and a thermal one (Fig. 1a). Basically, we combine two fundamental dynamic functions of (1) a molecular rotary motor^{10,11} and (2) dynamic covalent chemical bond formation^{6–9}. The photochemical process takes advantage of a light-driven rotary motor to deliver energy to the system. Our design is based on a second-generation molecular motor¹⁰ in which the central olefinic bond, connecting the top (indane rotor part) and bottom halves (thioxanthene stator part), functions as the rotary axle. Several intrinsic features, including the combination of two stereogenic elements, that is, the helical structure and the stereogenic centre, stilbene-type *E–Z* photoisomerization and thermal helix inversion, allow for unidirectional light-driven rotary motion. Building on dynamic covalent chemistry^{6–9}, we explore reversible imine bond formation in combination with increasing strain in the system via the rotary motor.

In the thermal pathway, the imine bonds can undergo a reversible intermolecular exchange reaction with a nucleophile^{6–9}, leading to a temporary ring-opening of the bicyclic compound (Fig. 1a, brown). In this open form, the side arms can slip through or undergo an intramolecular imine exchange with the other macrocycle to generate an entangled structure. Subsequent ring-closure by intramolecular imine formation fixes the twists in the system, thus reforming the bicyclic molecule and leading to the formation of distinct topological isomers. Since the imine exchange is a dynamic and reversible process that is constrained by microscopic reversibility, the minimization of the Gibbs free energy of the system dictates the population of distinct topological states. The population of these distinct states at thermal equilibrium is shown in Fig. 1b, top, with the expected abundance indicated in brown. It should be emphasized that, in the absence of light, the motor moiety is merely serving as a rigid unit to prevent the macrocycles from unwinding in a mechanical manner.

In the photochemical pathway, the motor unit performs a unidirectional 360° rotation around its central double bond, which is solely driven by light energy and therefore not constrained by microscopic reversibility but by the Bose–Einstein relations for

¹Stratingh Institute for Chemistry, Center for Systems Chemistry and Zernike Institute for Advanced Materials, Faculty of Mathematics and Natural Sciences, University of Groningen, Groningen, the Netherlands. ²Institut für Chemie und Biochemie der Freien Universität Berlin, Berlin, Germany.

³Fritz-Haber-Institut der Max-Planck-Gesellschaft, Berlin, Germany. ⁴Macromolecular Chemistry and New Polymeric Materials and Zernike Institute for Advanced Materials, Faculty of Mathematics and Natural Sciences, University of Groningen, Groningen, the Netherlands. ✉e-mail: m.p.k.kathan@rug.nl; c.schalley@fu-berlin.de; b.l.feringa@rug.nl

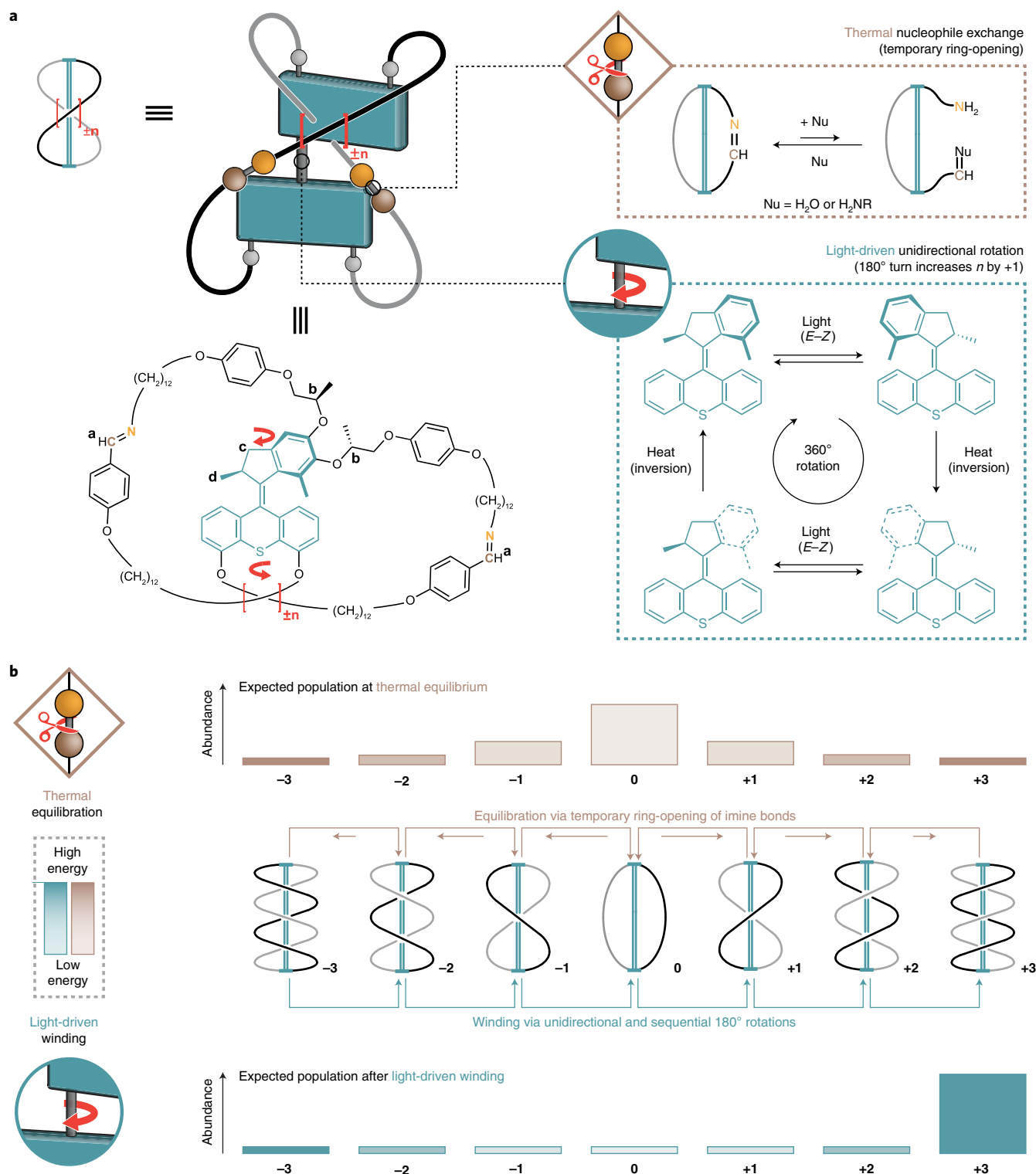


Fig. 1 | Working principle of AMM $\pm n$. **a**, A photoresponsive molecular motor is constrained by two imine macrocycles, allowing AMM $\pm n$ to adopt distinct topologies by forming twists in the strands of the bicyclic molecule. Crossings can be established by either thermal nucleophile exchange of the imines (brown), leading to temporary ring-opening of one macrocycle, or by light-driven unidirectional rotation (blue) via photochemical-induced $E-Z$ isomerization and subsequent thermal helix inversion (blue), which increases the number of chiral crossing per half-turn by +1 in the case of (S,R,R) configured $\pm n$. **b**, Thermal equilibration (brown) takes place by temporary ring-opening of the imines and will populate all accessible, distinct topological states so that the Gibbs free energy of the system is minimized. The expected population is indicated by the brown bar diagram. Light-driven winding (blue) twists the bicyclic molecule in a unidirectional and sequential manner, increasing the number of crossings in the system above its equilibrium level until mechanical resistance in the system hinders further winding. The expected population is indicated by the blue bar diagram. The maximum number of crossings that was experimentally observed is ± 3 . Lighter colour refers to lower energy, whereas darker colour refers to higher energy. Thermal nucleophile exchange (Fig. 1a, brown) leads to restoration of the initial equilibrium.

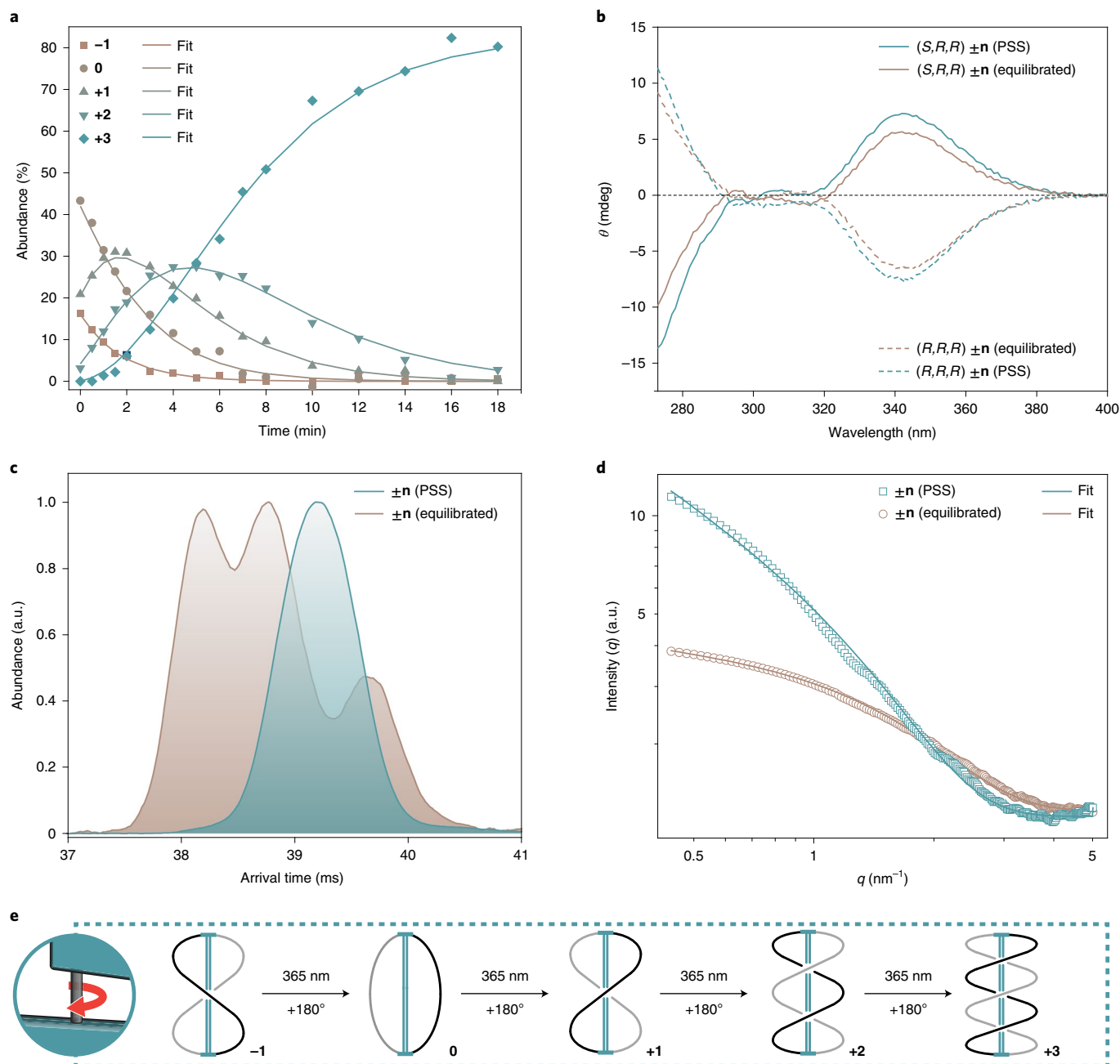


Fig. 2 | Sequence-specific, light-driven winding mechanism of AMM $\pm n$. **a**, Illumination ($\lambda_{\text{irr}} = 365 \text{ nm}$, 18 min) of an equilibrium mixture of (S,R,R) motors -1 , 0 and $+1$ yields species $+3$ via intermediate $+2$. Because of the unidirectional rotation of the motor, the process is topologically stereoconvergent and sequence specific. The representative kinetic profile was obtained by $^1\text{H-NMR}$ spectroscopy (500 MHz, 10°C , 1 mM in C_6D_6). **b**, CD spectra (0°C , $10 \mu\text{M}$ in $\text{THF}/\text{C}_6\text{D}_6$) of an equilibrated (brown) and illuminated sample (blue) at PSS of both contrarotating motor diastereomers (S,R,R) (solid lines) and $(R,R,R) \pm n$ (dashed lines). No sign inversion indicates that the motor core retains its helical chirality. **c**, IM-MS measurements: ATDs of the equilibrated (brown) and illuminated (blue) $\pm n$ sample showing a transition from three species -1 , 0 and $+1$ to one species $+3$. **d**, Scattering intensities of a $\pm n$ sample obtained by SAXS measurements (23°C , 1 mM in toluene- d_8) at equilibrium (brown, globular particles) and at PSS (blue, rod-like particles). **e**, Proposed mechanism for the photochemical formation of $+3$ in sequential and unidirectional half-turns, starting from -1 .

absorption and emission of photons. This involves a four-step rotary cycle, that is, two photochemical $E-Z$ isomerizations converting a stable to a metastable isomer each followed by a thermal helix inversion (Fig. 1a, blue). Upon illumination with ultraviolet (UV) light, its direction of rotation is governed by the methyl group at the stereogenic centre in the allylic position of the overcrowded alkene (Fig. 1a)^{10,11}. This transduction from Euclidean chirality into directed movement enables the mechanical formation

of chiral twists within the bicyclic molecule. A positive (+) crossing is induced by every 180° turn of the motor until winding is hindered by mechanical resistance in the system. The molecular motor increases the number of entanglements (strain build-up) in the bicyclic system far from its equilibrium level, performing chemical work on a coupled chemical equilibrium in a topologically stereoconvergent manner, thereby acting as a light-fuelled ratchet (see Supplementary Fig. 42 and the Supplementary Information

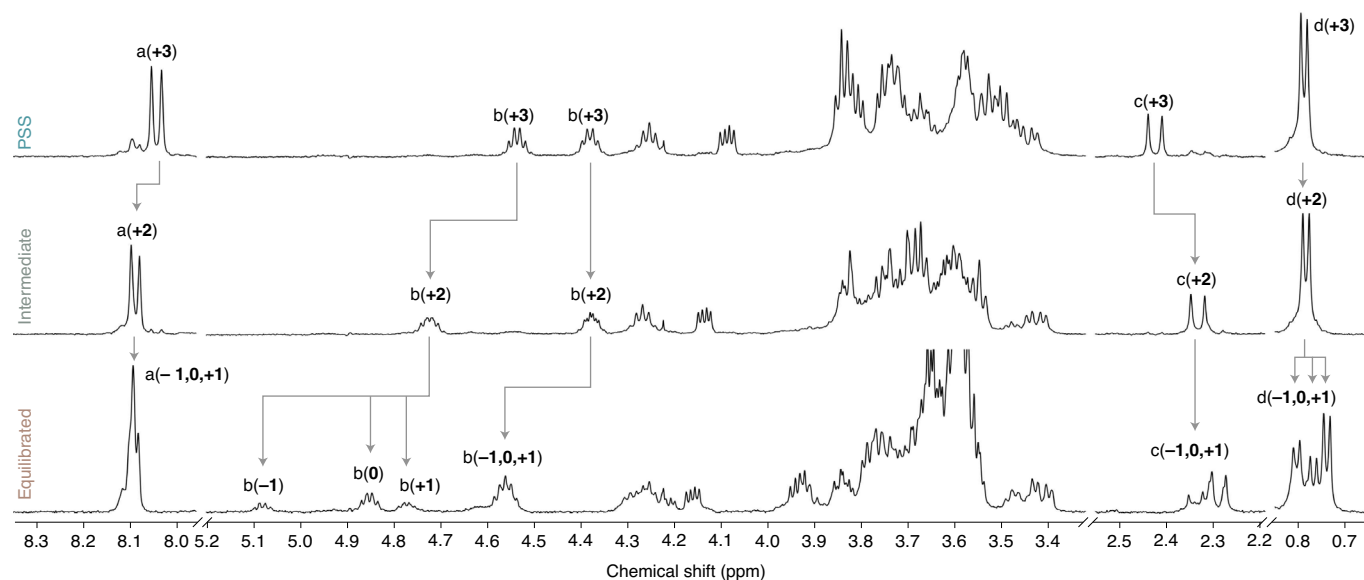


Fig. 3 | NMR spectra of $AMM_{\pm n}$ at different winding states. Partial 1H -NMR spectra (500 MHz, 10 °C, 1 mM in C_6D_6) of $(S,R,R)_{\pm n}$ at PSS ($\lambda_{irr} = 365$ nm, 18 min; top), after partial thermal relaxation (60 °C, 6 min; middle) and at equilibrium (bottom). The conversion of key signals is indicated with grey arrows (signal labels are shown in Fig. 1a; for more information see Supplementary Figs. 1–22 and Supplementary Tables 1 and 2).

for an in-depth discussion). The far-from-equilibrium distribution upon light-driven winding is shown in Fig. 1b, bottom, with the expected abundance indicated in blue. The system can return to its equilibrium state by thermal nucleophile-promoted imine exchange (Fig. 1a, brown).

To allow multiple entanglements in $AMM_{\pm n}$, the imine groups were embedded in two large rings, each featuring two flexible dodecyl hydrocarbon chains, which bridge the upper rotor and lower stator parts of the rotary motor. In order to gain access to both contrarotating diastereomers (S,R,R) and $(R,R,R)_{\pm n}$ (unless otherwise stated, $(S,R,R)_{\pm n}$ was used for all experiments) of our optically active second-generation motors, we utilized a versatile method to access the stereoisomers developed by Giuseppone et al.²⁷ After post-functionalizing the rotor part with two azide groups and the stator part with two aldehydes, in situ macrocyclization was accomplished by aza-Wittig reactions using triphenylphosphine.

By choosing this specific substitution pattern, a selective connection between the rotor and stator parts, and thus winding upon rotation, is ensured²⁷. The conversion to the imine was followed by proton nuclear magnetic resonance (1H -NMR) spectroscopy (typically 5–10% of motors are mono cyclized, Supplementary Fig. 1). The system was further characterized by one-dimensional (1D) and two-dimensional (2D) NMR (Supplementary Figs. 1–22 and Supplementary Tables 1 and 2) and circular dichroism (CD) spectroscopy (Supplementary Figs. 23–25), small angle X-ray scattering (SAXS) (Supplementary Figs. 39 and 40 and Supplementary Table 3), mass spectrometry (MS) and ion mobility (IM) (Supplementary Fig. 36). Our data show that the formation of oligomers under our experimental conditions is negligible.

To experimentally investigate the hypothesized operational routine of the nanoratchet, we initially studied the light-driven winding process of $AMM_{\pm n}$. Figure 2a shows the sequential formation of distinct topological isomers as a function of time for $(S,R,R)_{\pm n}$ (Supplementary Fig. 35 and Supplementary Data Set 1). With the help of 1H -NMR spectroscopy (Fig. 3), we could follow the compositional change of a fully equilibrated sample upon illumination with UV light (irradiation wavelength $\lambda_{irr} = 365$ nm). In thermal

equilibrium, $AMM_{\pm n}$ can adopt up to one crossing and therefore exists as a mixture of distinct topological isomers -1 , 0 and $+1$ (the ratio is $\sim 1:2:1$). The obtained kinetic profile revealed a sequence-specific and stereoconvergent reaction mechanism (Supplementary Fig. 35), only possible due to the unidirectionality of the rotary molecular motor (Supplementary Fig. 37), by which the crossings in the bicyclic molecule are increased stepwise by one, until the system selectively reaches its final state $+3$ via intermediate $+2$ (Figs. 2a and 2e). The quantum yield (Φ) decreases with more crossings (see Supplementary Figs. 35 and 41 and later Fig. 5a). Repeating the illumination experiment with a non-macrocyclized motor showed no winding (Supplementary Figs. 21 and 22). Interestingly, the helical chirality of the motor moiety of both diastereomers (S,R,R) and $(R,R,R)_{\pm n}$ at the photostationary state (PSS) is retained during the winding process as evidenced by a relative increase in the intensity of their respective CD spectra (Fig. 2b and Supplementary Figs. 23–25 and 38). The formation of topological isomer $+3$ from an equilibrium mixture of -1 , 0 and $+1$ was also observed using ion mobility interfaced with mass spectrometry (IM-MS) (Fig. 2c and Supplementary Fig. 36). The arrival time distribution (ATD) of the fully equilibrated sample shows three contributions that correspond to collision cross-sections ($^{DT}CCS_{He}$) of 351 \AA^2 , 342 \AA^2 and 338 \AA^2 . These were respectively assigned to 0 , -1 and $+1$ by matching the experimental with theoretical collision cross-sections calculated for in silico candidate structures. After illumination with UV light, the ATD becomes narrower and shows a single contribution corresponding to $^{DT}CCS_{He} = 344 \text{ \AA}^2$, which was analogously attributed to $+3$. Additional support for the change in shape of the machine came from SAXS measurements (Fig. 2d; Supplementary Figs. 39 and 40 and Supplementary Table 3). At thermal equilibrium, $AMM_{\pm n}$ adopts a globular shape with a gyration radius of $r = 0.9$ nm. After illumination with UV light, an increase in scattering intensity was observed²⁷, which can be attributed to the formation of elongated, rod-like and more compact objects with a cross-sectional radius of $r = 0.7$ nm. The combined data support a winding mechanism that is caused by the unidirectional rotation of the motor.

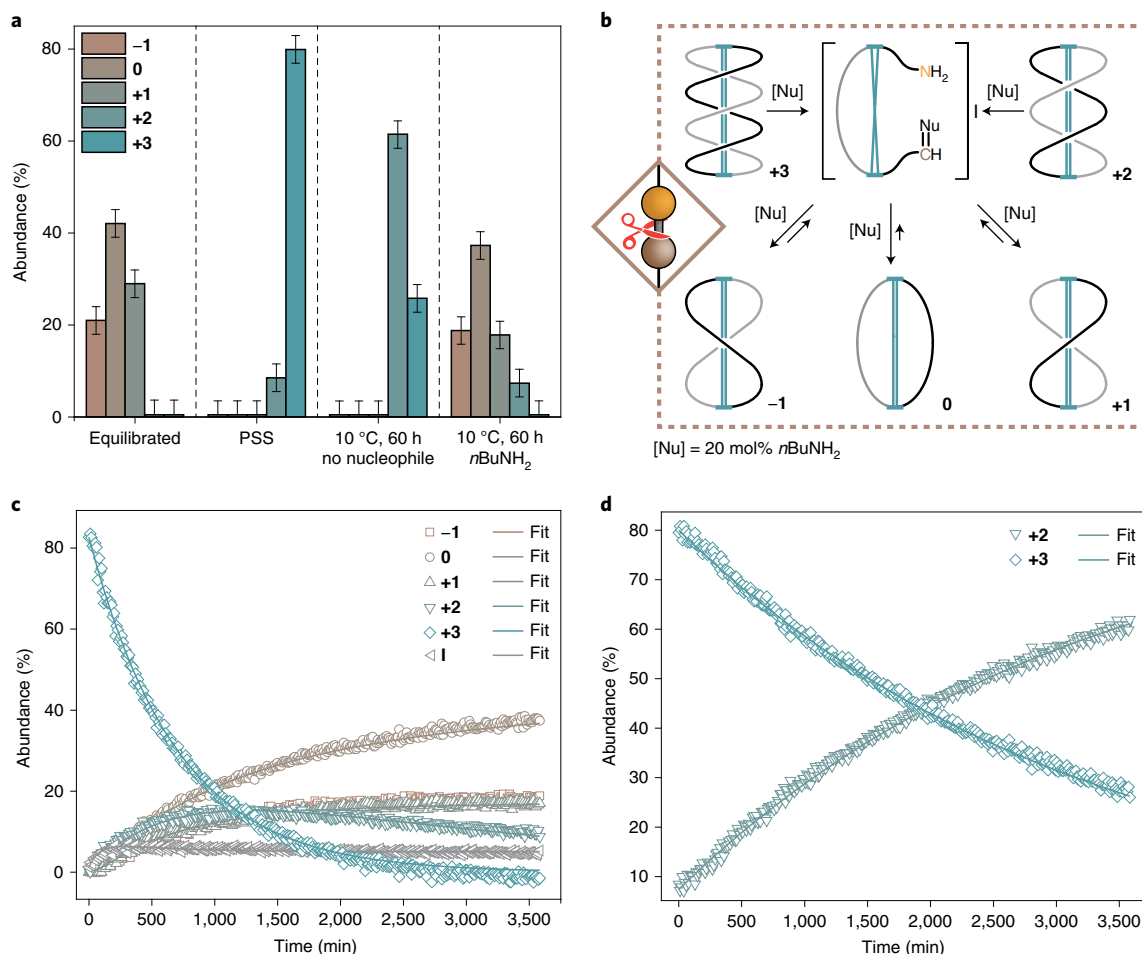


Fig. 4 | Unwinding mechanism and thermal stability of AMM $\pm n$. **a**, Chemical composition of an equilibrated $\pm n$ sample (left), a sample at PSS (middle left), without addition of external nucleophile (middle right) and after relaxation at 10 °C for 60 h with 20 mol% of $n\text{BuNH}_2$ (right). Full relaxation at 10 °C only occurs in the presence of nucleophiles. **b**, Proposed mechanism for the thermal relaxation of wound up $\pm n$ via temporary ring-opening in the presence of catalytic amounts of nucleophile. **c,d**, Representative examples for the relaxation kinetics of an irradiated $\pm n$ sample at 10 °C in the presence of 20 mol% of $n\text{BuNH}_2$ (**c**) and without nucleophiles (**d**). The chemical composition (**a**) and kinetic profiles (**c,d**) were obtained by $^1\text{H-NMR}$ spectroscopy (500 MHz, 10 °C, 1 mM in C_6D_6).

Next, we examined the unwinding of the system, both under thermal and nucleophile-assisted conditions (Fig. 4a and Supplementary Data Set 1). Full relaxation of the system at 10–40 °C can only be achieved in the presence of an external nucleophile, such as catalytic amounts of n -butyl amine ($n\text{BuNH}_2$, Figs. 4a and 4c), under purely thermodynamic control as determined by $^1\text{H-NMR}$ spectroscopy (Supplementary Fig. 27, for relaxation with water see Supplementary Figs. 33 and 34). The competing nucleophile can induce temporary ring-opening of the imine macrocycles by amine–imine exchange (forming open n -butyl imine **I** in 5%, Supplementary Fig. 27), leading to a topological reshuffling of the wound-up machine in a non-sequence-specific manner (Figs. 4b and 5a; Supplementary Figs. 27, 33 and 34), thus re-establishing the initial topological equilibrium. Interestingly, an increase in the number of crossings (and thus chemical strain) does not affect the reactivity of the imine groups towards $n\text{BuNH}_2$ and therefore the rate for amine–imine exchange, as indicated by the rate constants (k) for nucleophile-induced ring-opening of the macrocycles (Fig. 5a). A similar behaviour was already observed for thiol–disulfide exchange³² and hydrolysis of esters³³. However, the fact that ring-opening of **+3** and **+2** with $n\text{BuNH}_2$ is an irreversible process (there is no measurable rate for the ring-closure, Fig. 5a) indicates

that both topological isomers are high energy, strained species that are not populated in thermal equilibrium.

To gain further insight into the pure thermal stability of the ‘spring-loaded’ AMM, we studied the relaxation of a fully wound motor sample at different temperatures in the absence of an external nucleophile (Supplementary Figs. 26 and 28–32; trace amounts of nucleophiles, such as water, cannot be fully excluded). Under these conditions, the unwinding pathway via ring-opening is not feasible. The kinetic data associated with the various steps at 10 °C, both in the absence (grey) and presence (brown) of nucleophiles, are compiled in Fig. 5a (see also Supplementary Figs. 26–35). We found that bicyclic molecule **+3**, which is the most strained form, slowly decays at 10 °C (Fig. 5a, solid grey arrow; $k_{(+3,+2)} = 0.3 \times 10^{-3} \text{ min}^{-1}$) to selectively form less strained species **+2** after 60 h in ~60% yield (Figs. 4a and 4d, Supplementary Fig. 26). At this temperature, formation of species **-1**, **0**, or **+1** was not observed. Increasing the temperature stepwise from 10–60 °C led to an increase in the decay rate of **+3** by a factor of ~4 per 10 °C steps (Supplementary Fig. 32).

At 40 °C, complete unwinding was not observed even after one week, while full equilibration could be achieved within 42 h at 60 °C (Supplementary Figs. 29 and 30). The kinetic profiles of the relaxation processes clearly indicate a sequence-specific mechanism

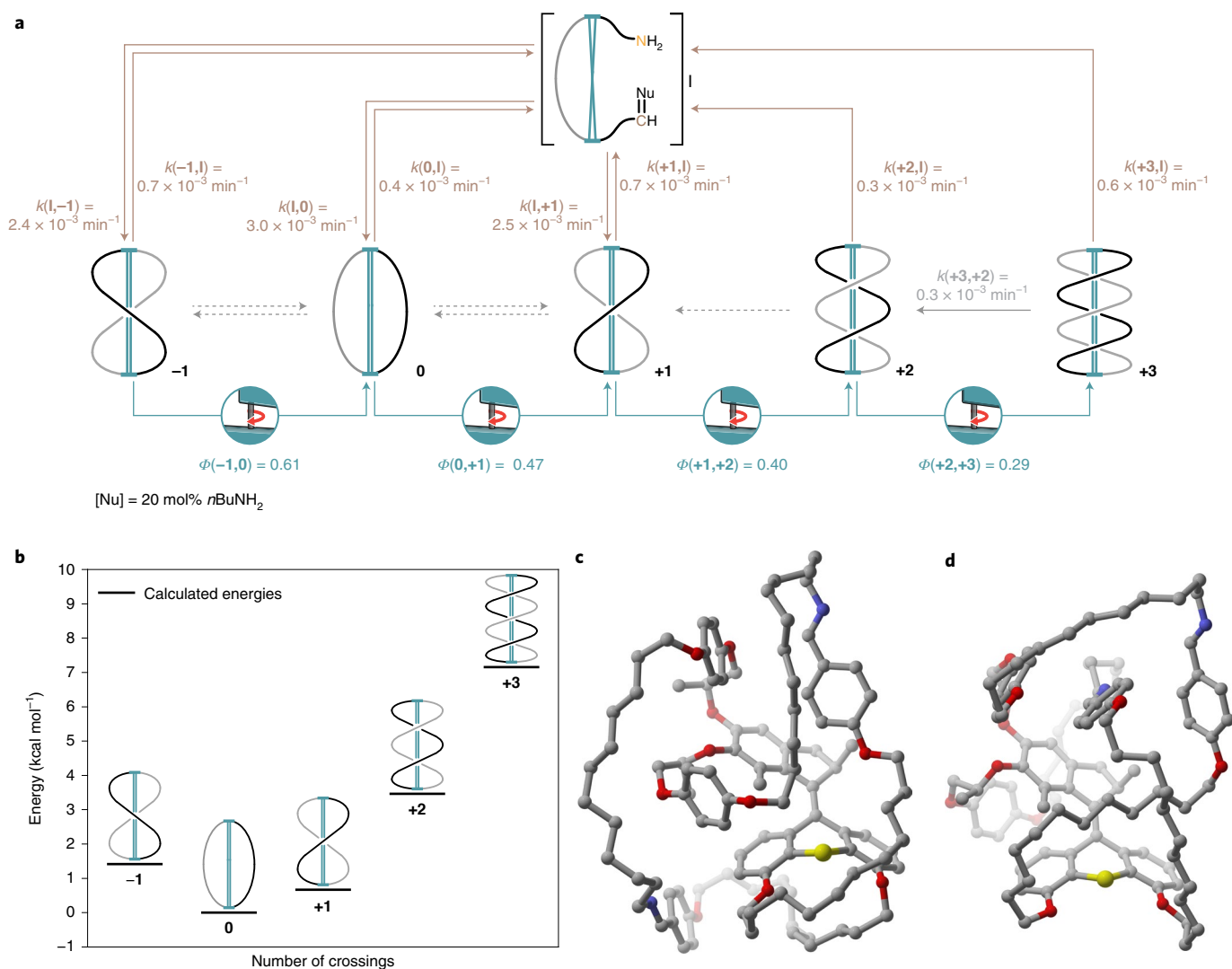


Fig. 5 | Energy, structure and detailed working mechanism of AMM $\pm n$. **a**, The full reaction scheme including all experimental rate constants/quantum yields (given as an average over at least two independent experiments) for the molecular machine operation at 10 °C shows the light-driven winding (blue; relative standard deviation ~10%), nucleophile-catalysed unwinding (brown; relative standard deviation ~35%) and sequence-specific unwinding (grey; relative standard deviation ~15%, solid arrow represents experimentally observed relaxation from $+3$ to $+2$, while dotted arrows indicate that further, sequence-specific relaxation at 10 °C is not viable). An increasing number of crossings decreases the winding and increases the unwinding process. Note that the rates for the nucleophile-catalysed unwinding are all in a narrow range irrespective of the winding-induced strain. This can be rationalized when considering that the nucleophilic attack at the imine carbon atom is likely the rate-determining step in this reaction, while the subsequent ring-opening and unwinding steps are fast and thus do not affect the kinetics of the amine-imine exchange. **b**, Calculated energies of the most stable conformer of motors -1 to $+3$ in the gas phase relative to 0 . A higher number of crossings increases the electronic energy of the system. Experimentally, the system was found to reach up to $+3$ crossings. **c, d**, Representative structures of one possible conformer of species 0 (**c**) and $+3$ (**d**). The energies and structures in Fig. 5b–d were calculated at the M06-2X/def-SVP//GFN-xTB level of theory.

that can only be caused by an intramolecular reaction (there is no direct equilibrium between -1 and $+1$ under these conditions, Supplementary Figs. 28 and 29). Most importantly, an increase in the number of crossings increases the rate of unwinding and renders the relaxations from $+3 \rightarrow +2$ and $+2 \rightarrow +1$ irreversible, suggesting that potential energy is built up during the winding process (Figs. 5a and 5b). The potential energy accumulated during the illumination process can be released in a stepwise and sequence-specific manner when enough thermal energy is provided (Supplementary Figs. 26 and 28–30).

Together with an extensive computational analysis (Supplementary Data Set 2), the experimental and calculated data give a detailed picture of the machine's working mechanism on the molecular scale

(Fig. 5a–d and Supplementary Figs. 26–35, 37 and 41). The system at thermodynamic equilibrium consists of bridged bismacrocycles -1 , 0 and $+1$, with an experimentally determined energy difference between molecule 0 (Fig. 5c) and singly twisted motors $+1$ and -1 of $\Delta G_{\text{exp}}(0, +1) = 0.24 \text{ kcal mol}^{-1}$ and $\Delta G_{\text{exp}}(0, -1) = 0.39 \text{ kcal mol}^{-1}$, respectively. Experimentally the system reaches up to three crossings, that is, $+3$ (Fig. 5b). Species $+2$ and $+3$ (Fig. 5d) were not detected in the relaxed reaction mixture (Supplementary Fig. 2), as expected from the computational studies that predicted a step increase in the potential energy per half-turn (Fig. 5b). Due to the irreversible nature of the transformation from $+3$ and $+2$ and from $+2$ and $+1$ the experimental energy difference between these species can only be estimated to be $\Delta G_{\text{exp}}(+2, +3) \geq 2 \text{ kcal mol}^{-1}$

and $\Delta G_{\text{exp}}(+1,+2) \geq 2 \text{ kcal mol}^{-1}$, respectively (under the conservative assumption that the absolute measurement error for NMR spectroscopy is $\pm 3\%$). The experimentally observed quantum yields for the light-driven winding process diminish stepwise, going from $\Phi(-1,0) = 0.61$ to $\Phi(+2,+3) = 0.29$, meaning that the winding rate decreases with increasing strain (Fig. 5a). After illumination, the sequence-specific, intramolecular unwinding irreversibly forms species +2 from +3 ($k(+3,+2) = 0.3 \times 10^{-3} \text{ min}^{-1}$) at 10°C . Full relaxation at this temperature can only be achieved in the presence of nucleophiles via dynamic and non-sequence-specific ring-opening of the imine macrocycles via intermediate I (Fig. 5a top). Under these conditions, species -1, 0 and +1 form with a comparable rate constant of $k = 2.4\text{--}3.0 \times 10^{-3} \text{ min}^{-1}$ (for the kinetics of the non-catalysed, intramolecular unwinding see Supplementary Figs. 26 and 28–30), while ring-closure to +2 and +3 was not observed. A significant dependence of the ring-opening rate on the number of crossings in the system could not be detected.

This work demonstrates how the light-driven unidirectional rotary motion in AMM $\pm n$ can decrease the overall kinetic (Fig. 5a) and thermodynamic (Fig. 5b) stability of the system during the winding process of the macrocycles. The experimental data clearly show that the small-molecule machine $\pm n$ functions as a nanoratchet able to drive a coupled chemical equilibrium energetically uphill by light. We anticipate that our study will serve as an inspiration and blueprint for the design of AMMs of ever-increasing complexity which, for instance, can store light in the form of chemical energy or perform sophisticated synthetic tasks on the molecular scale.

Online content

Any methods, additional references, Nature Research reporting summaries, source data, extended data, supplementary information, acknowledgements, peer review information; details of author contributions and competing interests; and statements of data and code availability are available at <https://doi.org/10.1038/s41565-021-01021-z>.

Received: 19 March 2021; Accepted: 29 September 2021;

Published online: 16 December 2021

References

- Goodsell, D. S. *The Machinery of Life* (Springer, 2009).
- Schliwa, M. *Molecular Motors* (Wiley-VCH, 2006).
- Balzani, V., Credi, A., Raymo, F. M. & Stoddart, J. F. Artificial molecular machines. *Angew. Chem. Int. Ed.* **39**, 3348–3391 (2000).
- Sauvage, J.-P. *Molecular Machines and Motors* (Springer, 2001).
- Balzani, V., Credi, A. & Venturi, M. *Molecular Devices and Machines: Concepts and Perspectives for the Nanoworld* (Wiley-VCH, 2008).
- Rowan, S. J., Cantrill, S. J., Cousins, G. R. L., Sanders, J. K. M. & Stoddart, J. F. Dynamic covalent chemistry. *Angew. Chem. Int. Ed.* **41**, 898–952 (2002).
- Corbett, P. T. et al. Dynamic combinatorial chemistry. *Chem. Rev.* **106**, 3652–3771 (2006).
- Lehn, J. M. From supramolecular chemistry towards constitutional dynamic chemistry and adaptive chemistry. *Chem. Soc. Rev.* **36**, 151–160 (2007).
- Belowich, M. E. & Stoddart, J. F. Dynamic imine chemistry. *Chem. Soc. Rev.* **41**, 2003–2024 (2012).
- Koumura, N., Geertsema, E. M., Van Gelder, M. B., Meetsma, A. & Feringa, B. L. Second generation light-driven molecular motors. Unidirectional rotation controlled by a single stereogenic center with near-perfect photoequilibria and acceleration of the speed of rotation by structural modification. *J. Am. Chem. Soc.* **124**, 5037–5051 (2002).

- Roke, D., Wezenberg, S. J. & Feringa, B. L. Molecular rotary motors: unidirectional motion around double bonds. *Proc. Natl Acad. Sci. USA* **115**, 9423–9431 (2018).
- Coskun, A., Banaszak, M., Astumian, R. D., Stoddart, J. F. & Grzybowski, B. A. Great expectations: can artificial molecular machines deliver on their promise? *Chem. Soc. Rev.* **41**, 19–30 (2012).
- Browne, W. R. & Feringa, B. L. Making molecular machines work. *Nat. Nanotechnol.* **1**, 25–35 (2006).
- Baroncini, M., Silvi, S. & Credi, A. Photo- and redox-driven artificial molecular motors. *Chem. Rev.* **120**, 200–268 (2020).
- Bruns, C. J. & Stoddart, J. F. *The Nature of the Mechanical Bond* (John Wiley & Sons, 2016).
- Greb, L. & Lehn, J. M. Light-driven molecular motors as four-step or two-step unidirectional rotors. *J. Am. Chem. Soc.* **136**, 13114–13117 (2014).
- Kassem, S. et al. Stereodivergent synthesis with a programmable molecular machine. *Nature* **549**, 374–378 (2017).
- García-López, V., Liu, D. & Tour, J. M. Light-activated organic molecular motors and their applications. *Chem. Rev.* **120**, 79–124 (2020).
- Uhl, E., Thumser, S., Mayer, P. & Dube, H. Transmission of unidirectional molecular motor rotation to a remote biaryl axis. *Angew. Chem. Int. Ed.* **57**, 11064–11068 (2018).
- Štacko, P. et al. Locked synchronous rotor motion in a molecular motor. *Science* **356**, 964–968 (2017).
- Lewandowski, B. et al. Sequence-specific peptide synthesis by an artificial small-molecule machine. *Science* **339**, 189–193 (2013).
- Cheng, C. et al. An artificial molecular pump. *Nat. Nanotechnol.* **10**, 547–553 (2015).
- Ragazzon, G., Baroncini, M., Silvi, S., Venturi, M. & Credi, A. Light-powered autonomous and directional molecular motion of a dissipative self-assembling system. *Nat. Nanotechnol.* **10**, 70–75 (2015).
- Ragazzon, G., Baroncini, M., Silvi, S., Venturi, M. & Credi, A. Light-powered, artificial molecular pumps: a minimalistic approach. *Beilstein J. Nanotechnol.* **6**, 2096–2104 (2015).
- Qiu, Y. et al. A molecular dual pump. *J. Am. Chem. Soc.* **141**, 17472–17476 (2019).
- Eelkema, R. et al. Molecular machines: nanomotor rotates microscale objects. *Nature* **440**, 163 (2006).
- Li, Q. et al. Macroscopic contraction of a gel induced by the integrated motion of light-driven molecular motors. *Nat. Nanotechnol.* **10**, 161–165 (2015).
- Kathan, M. & Hecht, S. Photoswitchable molecules as key ingredients to drive systems away from the global thermodynamic minimum. *Chem. Soc. Rev.* **46**, 5536–5550 (2017).
- Sell, H. et al. Towards a light driven molecular assembler. *Commun. Chem.* **2**, 62 (2019).
- Aprahamian, I. The future of molecular machines. *ACS Cent. Sci.* **6**, 347–358 (2020).
- Fielden, S. D. P., Leigh, D. A. & Woltering, S. L. Molecular knots. *Angew. Chem. Int. Ed.* **56**, 11166–11194 (2017).
- Kucharski, T. J. et al. Kinetics of thiol/disulfide exchange correlate weakly with the restoring force in the disulfide moiety. *Angew. Chem. Int. Ed.* **48**, 7040–7043 (2009).
- Akbulatov, S., Tian, Y., Kapustin, E. & Boulatov, R. Model studies of the kinetics of ester hydrolysis under stretching force. *Angew. Chem. Int. Ed.* **52**, 6992–6995 (2013).

Publisher's note Springer Nature remains neutral with regard to jurisdictional claims in published maps and institutional affiliations.



Open Access This article is licensed under a Creative Commons Attribution 4.0 International License, which permits use, sharing, adaptation, distribution and reproduction in any medium or format, as long as you give appropriate credit to the original author(s) and the source, provide a link to the Creative Commons license, and indicate if changes were made. The images or other third party material in this article are included in the article's Creative Commons license, unless indicated otherwise in a credit line to the material. If material is not included in the article's Creative Commons license and your intended use is not permitted by statutory regulation or exceeds the permitted use, you will need to obtain permission directly from the copyright holder. To view a copy of this license, visit <http://creativecommons.org/licenses/by/4.0/>.

© The Author(s) 2021

Methods

Preparation of $\pm n$ samples. A stock solution of bisaldehyde and bisazide functionalized motor **S21** (1.0 mg, 0.60 μmol , 1.0 equiv.) in C_6D_6 was lyophilized in a J. Young NMR tube. Then, PPh₃ (0.60 mg, 2.4 mmol, 4.0 equiv.) was added and the tube was put under high vacuum for 16 h. After that, the solids were dissolved in dry (distilled from CaH_2) and degassed (three freeze–pump–thaw cycles) C_6D_6 or toluene-*d*8 (0.6 ml) inside a glovebox and activated molecular sieves (3 Å) were added. The sealed NMR tube was taken out of the glovebox and heated to 60 °C for 7 d in an oil bath under exclusion of light. Subsequently, the molecular sieves were removed inside a glovebox and the sample was used for further experiments without purification. Since the system is dynamic, the formation of the bridged bis-macrocylic $\pm n$ is concentration dependent. Increasing the concentration leads to formation of an insoluble polymer. The conversion of **S21** to $\pm n$ was followed using ¹H-NMR spectroscopy by observing the decrease of the aldehyde signal (~9.7 ppm) and increase of the imine signals (~8.1 ppm). Typically, bis-macrocylic $\pm n$ forms in 90–95%.

Illumination of $\pm n$ samples for NMR spectroscopy. Typically, a J. Young NMR tube containing a 1 mM solution of equilibrated (*S,R,R*) or (*R,R,R*) $\pm n$ in 0.6 ml C_6D_6 was illuminated with a hand-held UV lamp (365 nm, 6 W) on a shaker plate for 18 min at 8 °C (in a walkable fridge) or room temperature. The distance between lamp and NMR tube was kept constant throughout the experiment. To prevent any significant relaxation, illuminated samples were cooled with a 10 °C acetone bath before the respective measurement.

CD spectroscopic measurements. CD spectra were recorded on a Jasco J-815 CD spectrometer. In a cuvette, 30 μl of a solution of (*S,R,R*) or (*R,R,R*) $\pm n$ (1 mM in C_6D_6) was diluted with degassed and dry tetrahydrofuran (THF) to a total volume of 3 ml (concentration $c = 10 \mu\text{M}$). Benzene absorbs in the deep UV region and forces a cut-off at 270 nm. Spectra of illuminated samples were either recorded after in situ illumination with a hand-held UV lamp at 365 nm for 5 min (the distance between the cuvette and the lamp was ~2 cm) or by diluting a pre-illuminated sample at PSS with THF. Partial relaxation of the irradiated sample was achieved by heating the sample to 60 °C for 10 min.

NMR spectroscopic measurements and kinetic analysis. All experiments were conducted on a Varian AVIII 500 NMR spectrometer that was precooled or prewarmed to the proper temperature. (*S,R,R*) $\pm n$ samples were typically equilibrated for 5 min inside the instrument until the lock signal reached a constant value. The experimental data were subsequently fitted using COPASI v.4.29 (ref. ³⁴). In order to obtain a fit that could give a realistic approximation of the irreversible and reversible reactions involved in each experiment, we simulated a reaction compartment of 0.6 ml (to match the volume of the solution of a typical NMR experiment) with concentration of the species involved of 1 mM. In all cases, the time unit used was minutes. The default Levenberg–Marquardt algorithm with a tolerance of 10^{-6} implemented in COPASI was used. The initial guess for the kinetic parameter estimation was to consider all species to be in equilibrium with one another. After every fitting run, visual inspection of the error associated to each kinetic constant provided indication of the relevance of a certain reaction. Kinetic constants with absolute values lower than 10^{-6} min^{-1} were approximated to 0 and the respective reaction deleted in the next iteration.

IM–MS measurements. Ion mobility measurements were performed using a custom drift-tube instrumentation hosted in the Fritz Haber Institute of the Max Planck Society (Berlin, Germany) and adapted from a previous design³⁵. The instrument is designed around a nanoelectrospray ionization source interfaced with a succession of radially confining entrance funnel, drift tube and exit funnel. This ensemble is prolonged by a quadrupole mass analyser under high vacuum and ended by an electron multiplier detector (ETP Ion Detect) for ion counting. In practice, samples were diluted to 10 μM in acetonitrile and nanoelectrospray ionization was used to generate ions using a needle voltage of 0.57 kV and a backing pressure of 0.8 bar (N_2). The ~160-cm-long drift tube was filled with helium buffer gas at a pressure of 4 mbar and subjected to a 2 kV direct current electric field for mobility separation. Ions were filtered for $m/z = 1,612 \text{ Da}$, which correspond to the singly protonated molecular ion $[\text{M} + \text{H}]^+$.

SAXS measurements. SAXS measurements were performed at the Multipurpose X-ray Instrument for Nanostructure Analysis instrument at the University of

Groningen. The instrument is built on a Cu rotating anode high brilliance X-ray source, providing X-ray photons with a wavelength of $\lambda = 0.154 \text{ nm}$. The SAXS patterns were recorded using a 2D Vantec500 detector placed 24 cm away from the sample. SAXS 1D profiles were obtained by radially averaging the scattered intensity around the origin of the image (defined by the direct beam position on the detector) using MATLAB. Standard corrections for the detector distortion and sensitivity were applied. The scattering from the buffer solution was subtracted to obtain the neat SAXS signal of the sample. The 1D SAXS profiles are plotted against the modulus of the scattering vector defined as $q = 4\pi \sin\theta/\lambda$, where θ is half of the scattering angle. The probed scattering angle range was calibrated using the known positions of the diffraction peaks from a standard Silver Behenate sample (NIST).

Data availability

All data needed to evaluate the conclusions in the paper are present in the paper and/or the Supplementary Information. Additional data related to this paper may be requested from the authors upon reasonable request.

References

- Hoops, S. et al. COPASI—a Complex Pathway Simulator. *Bioinformatics* **22**, 3067–3074 (2006).
- Warnke, S. et al. Protomers of benzocaine: solvent and permittivity dependence. *J. Am. Chem. Soc.* **137**, 4236–4242 (2015).

Acknowledgements

We thank P. van der Meulen and J. Kemink for helping with NMR measurements, R. Snee and A. Springer for mass spectrometric measurements and A. S. Lubbe and R. Costil for proof reading. We gratefully acknowledged financial support from the European Union (H2020 Excellent Science – European Research Council) under grant number 694345 (B.L.F.), (H2020 Excellent Science – Marie Skłodowska-Curie Actions) under grant number 838280 (S.C.) and NOAH project (H2020-MSCA-ITN) under grant number 765297 (D.L.S.); Ministerie van Onderwijs, Cultuur en Wetenschap (Ministry of Education, Culture and Science, Netherlands) under grant number 024.001.035 (B.L.F.) and Bonus Incentive Scheme (G. Portale); Alexander von Humboldt-Stiftung (Alexander von Humboldt Foundation) – Feodor Lynen grant (M.K.); and Deutsche Forschungsgemeinschaft (German Research Foundation) under grant number TH2510/1-1 (N.O.T.). We are grateful for the assistance of the Core Facility BioSupraMol at FU Berlin, which is supported by the Deutsche Forschungsgemeinschaft (German Research Foundation).

Author contributions

M.K. conceived the idea and designed the study. B.L.F. guided and supervised the research. M.K., N.O.T., S.C., D.L.S., D.M., G. Pacella, G. Portale and C.A.S. planned experiments. M.K., N.O.T., J.d.B. and T.v.d.E. synthesized molecules. S.C. and P.K. conducted computations. M.K., D.L.S., D.M. and C.A.S. performed mass spectrometric measurements. M.K., G. Pacella and G. Portale carried out SAXS measurements. M.K. and N.O.T. measured CD spectra. M.K. performed NMR measurements. M.K. and S.C. analysed kinetics. M.K. and B.L.F. prepared the manuscript with help from N.O.T. and S.C. All authors discussed the results and edited the manuscript.

Competing interests

The authors declare no competing interests.

Additional information

Supplementary information The online version contains supplementary material available at <https://doi.org/10.1038/s41565-021-01021-z>.

Correspondence and requests for materials should be addressed to Michael Kathan, Christoph A. Schalley or Ben L. Feringa.

Peer review information *Nature Nanotechnology* thanks Raymond Astumian and other, anonymous, reviewer(s) for their contribution to the peer review of this work.

Reprints and permissions information is available at www.nature.com/reprints.

Supplementary information

A light-fuelled nanoratchet shifts a coupled chemical equilibrium

In the format provided by the authors and unedited

Supplementary Information

A light-fueled nanoratchet shifts a coupled chemical equilibrium

Michael Kathan^{1}, Stefano Crespi¹, Niklas O. Thiel¹, Daniel L. Stares², Denis Morsa³, John de Boer¹, Gianni Pacella⁴, Tobias van den Enk¹, Piermichele Kobauri¹, Giuseppe Portale⁴, Christoph A. Schalley^{2*}, Ben L. Feringa^{1*}*

¹Stratingh Institute for Chemistry, Center for Systems Chemistry and Zernike Institute for Advanced Materials, Faculty of Mathematics and Natural Sciences, University of Groningen, Nijenborgh 4, Groningen 9747 AG, The Netherlands

²Institut für Chemie und Biochemie der Freien Universität Berlin, Arnimallee 20, 14195 Berlin, Germany

³Fritz-Haber-Institut der Max-Planck-Gesellschaft, Faradayweg 4–6, 14195 Berlin, Germany

⁴Macromolecular Chemistry and New Polymeric Materials and Zernike Institute for Advanced Materials, Faculty of Mathematics and Natural Sciences, University of Groningen, Nijenborgh 4, Groningen 9747 AG, The Netherlands

*Corresponding authors. E-mail: b.l.feringa@rug.nl, m.p.k.kathan@rug.nl, c.schalley@fu-berlin.de

General Information

Chemicals were purchased from commercial sources and used without purification. If not stated otherwise, all reactions were carried out in flame-dried glassware under a nitrogen atmosphere using standard Schlenk techniques. Solutions and reagents were added with nitrogen-flushed disposable syringes/needles. For NMR experiments, solvents were added using glass syringes and stainless steel needles (stored at 80 °C). Analytical thin layer chromatography (TLC) was performed on silica gel 60 G/UV₂₅₄ aluminium sheets from Merck (0.25 mm). Flash column chromatography was performed on silica gel Davisil LC60A (Merck type 9385, 230–400 mesh) or Reveleris X2 Flash Chromatography system (MPLC) using the indicated solvents. NMR spectra were recorded on a Varian Mercury Plus (¹H: 400 MHz, ¹³C: 100 MHz), a Varian Unity Plus (¹H: 500 MHz, ¹³C: 125 MHz) or a Bruker Innova (¹H: 600 MHz, ¹³C: 151 MHz). Chemical shifts are in parts per million (ppm) relative to TMS. For the calibration of the chemical shift, the residual solvent resonance was used as the internal standard. Data are as follows: chemical shift (δ in ppm), multiplicity (br = broad, s = singlet, d = doublet, t = triplet, p = pentet, m = multiplet), coupling constants (J in Hz), integration. High resolution mass spectra (HRMS) were recorded on an LTQ Orbitrap XL. Ion mobility (IM) measurements were performed using a custom drift-tube instrumentation hosted in the Fritz Haber Institute of the Max Planck Society (Berlin, Germany). CD spectra were measured on a Jasco J-815 CD spectrometer. SAXS measurements were performed at the Multipurpose X-ray Instrument for Nanostructure Analysis (MINA) instrument at the University of Groningen. Illuminations were carried out using a UV lamp from Vilber Lourmat (6W, $\lambda_{\text{irr}} = 365 \text{ nm}$).

The following compounds were prepared according to literature procedures: 1,12-dodecanediol mono(4-methylbenzenesulfonate) **S1**¹, 12-azidododecyl 4-methylbenzenesulfonate **S4**², 5,6-dihydroxy-2,7-dimethyl-indane-1-one **S6**³ and *N,N*-diethyl-3-methoxy-2-((2-methoxyphenyl)thio)benzamide **S9**⁴.

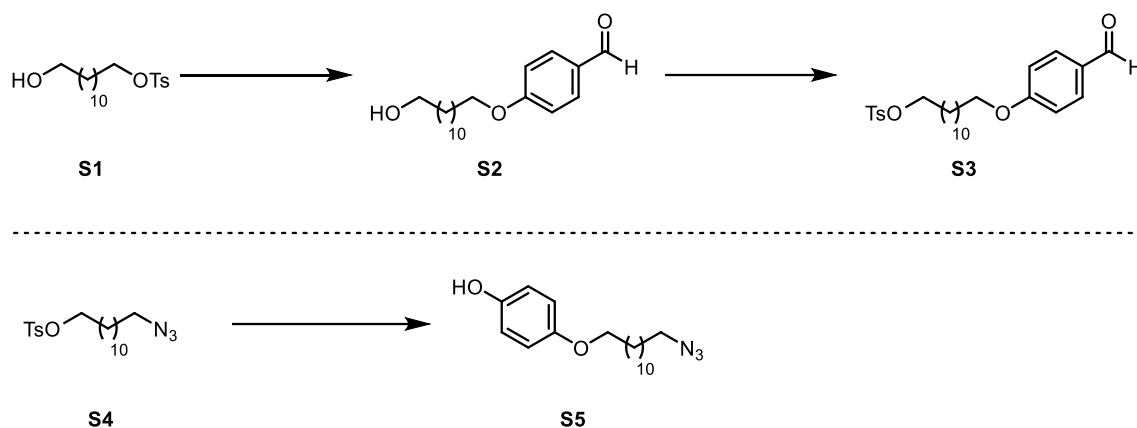
The following compounds were prepared according to modified literature procedures: **S2**⁵, **S7–S8**³, **S10–S16**^{3,4}.

Spectra of all compounds described in the synthesis section can be found in the spectra appendix at the end of the Supplementary Information.

The absolute measurement error for NMR spectroscopic measurements involving molecular machine $\pm n$ was estimated to be $\pm 3\%$. The average relative standard deviation of the fit over all individual experiments amounts to $< 0.7\%$. This confirms the proposed kinetic models and the related mechanisms for each individual experiment. The values given in the main manuscript are an average over at least two individual experiments. The relative standard deviation between these individual experiments was estimated to be $\pm 10\%$ for quantum yields; $\pm 15\%$ for intramolecular rate constants; $\pm 15\%$ for experimental Gibbs free energies at 25 °C; $\pm 35\%$ for intermolecular rate constants. For further information see also Supplementary Data Set 1.

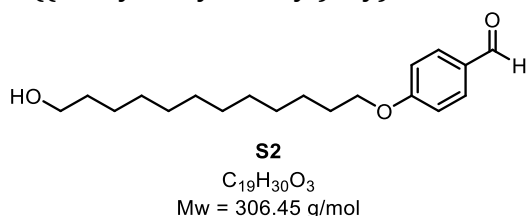
Synthesis

Synthesis of side-arms



Scheme 1 | Synthesis of side-arms. Synthesis of aldehyde linker **S3** (top) and azide linker **S5** (bottom).

4-((12-hydroxydodecyl)oxy)benzaldehyde (**S2**)⁵



In a flame-dried 3-necked flask equipped with a stirring bar and a reflux condenser, K_2CO_3 (1.74 g, 12.6 mmol, 3.00 eq.) and 4-hydroxybenzaldehyde (1.03 g, 8.42 mmol, 2.00 eq.) were suspended in dry MeCN (21 mL). Alkyl tosylate **S1** (1.50 g, 4.21 mmol, 1.00 eq.) was added and the mixture was heated to 90 °C for 6 h. Subsequently, the mixture was cooled to room temperature and all volatiles were removed under reduced pressure. To the residue, H_2O (20 mL) and ethyl acetate (20 mL) were added. The phases were separated and the aqueous layer was extracted with ethyl acetate (3x10 mL) and the combined organic layers were dried over $MgSO_4$. All volatiles were removed under reduced pressure. The title compound **S2** was obtained as an off-white solid (1.20 g, 3.92 mmol, 93%) and was used without further purification.

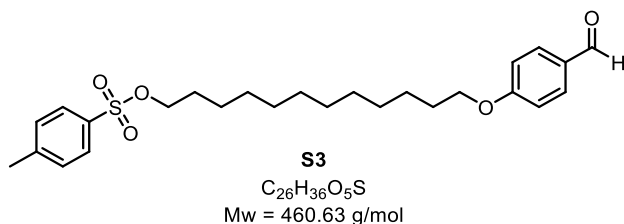
1H -NMR (400 MHz, $CDCl_3$): δ = 1.21–1.38 (m, 14H), 1.46 (p, J = 7.0, 6.3 Hz, 2H), 1.51–1.62 (m, 2H), 1.74–1.86 (m, 2H), 3.63 (t, J = 6.6 Hz, 2H), 4.03 (t, J = 6.5 Hz, 2H), 6.95–7.02 (m, 2H), 7.78–7.86 (m, 2H), 9.87 (s, 1H) ppm. The signal for *OH* could not be detected.

^{13}C -NMR (101 MHz, $CDCl_3$): δ = 25.9, 26.1, 29.2, 29.5, 29.6, 29.7, 29.7, 29.7, 32.9, 63.2, 68.3, 68.6, 114.9, 129.9, 132.1, 164.4, 191.0 ppm.

HRMS-ESI (ESI+): m/z calculated for $C_{19}H_{31}O_3^+$ ($[M+H]^+$): 307.2268, found 307.2270.

The analytical data is in accordance with the literature.

12-(4-formylphenoxy)dodecyl 4-methylbenzenesulfonate (**S3**)



In a flame-dried Schlenk-tube, 4-toluenesulfonyl chloride (560 mg, 2.94 mmol, 1.50 eq.), Et_3N (0.55 mL, 3.9 mmol, 2.0 eq.) and alcohol **S2** (600 mg, 1.96 mmol, 1.00 eq.) were dissolved in CH_2Cl_2 (9.8 mL). 4-(Dimethylamino)pyridine (24 mg, 0.20 mmol, 0.10 eq.) was added as a solid and the mixture was stirred for 14 h at room temperature. Subsequently, H_2O (10 mL) was added and the phases were separated. The aqueous layer was extracted with CH_2Cl_2 (2x8 mL) and the combined organic layers were dried over $MgSO_4$. All volatiles were removed under reduced pressure. The crude product was purified by MPLC (SiO_2 ; *n*-pentane/ CH_2Cl_2 gradient 60:40 \rightarrow 0:100). The title compound **S3** was obtained as a colorless solid (0.74 g, 1.6 mmol, 82%).

1H -NMR (400 MHz, $CDCl_3$): δ = 1.17–1.40 (m, 14H), 1.40–1.51 (m, 2H), 1.57–1.68 (m, 2H), 1.80 (p, J = 6.7 Hz, 2H), 2.44 (s, 3H), 4.02 (dt, J = 7.9, 6.5 Hz, 4H), 6.94–7.02 (m, 2H), 7.33 (d, J = 8.0 Hz, 2H), 7.75–7.86 (m, 4H), 9.87 (s, 1H) ppm.

^{13}C -NMR (101 MHz, $CDCl_3$): δ = 21.8, 25.5, 26.1, 29.0, 29.0, 29.2, 29.4, 29.5, 29.6, 29.6, 29.6, 68.5, 70.8, 114.9, 128.0, 129.9, 129.9, 132.1, 133.4, 144.7, 164.4, 190.9 ppm.

HRMS-ESI (ESI+): m/z calculated for $C_{26}H_{37}O_5S^+$ ($[M+H]^+$): 461.2356, found 461.2359.

4-((12-azidododecyl)oxy)phenol (**S5**)



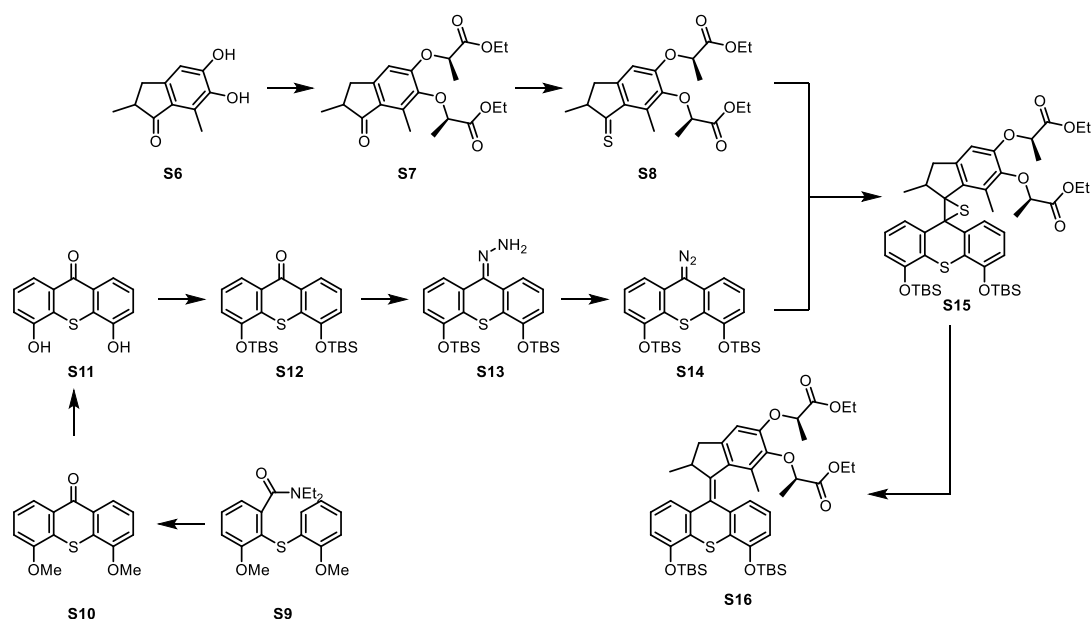
In a flame-dried 3-necked flask equipped with a stirring bar and a reflux condenser, K_2CO_3 (804 mg, 5.82 mmol, 3.00 eq.) and hydroquinone (2.14 g, 19.4 mmol, 10.0 eq.) were suspended in dry MeCN (9.7 mL). **S4** (740 mg, 1.94 mmol, 1.00 eq.) was added and the mixture was heated to 90 °C for 16 h. Subsequently, the mixture was cooled to room temperature and all volatiles were removed under reduced pressure. Then, H_2O (15 mL) and ethyl acetate (15 mL) were added to the residue. The phases were separated and the aqueous layer was extracted with ethyl acetate (3x8 mL). The combined organic layers were dried over $MgSO_4$ and all volatiles were removed under reduced pressure. The crude product was purified by MPLC (SiO_2 ; *n*-pentane/ CH_2Cl_2 gradient 70:30 \rightarrow 0:100). The title compound **S5** was obtained as an off-white solid (380 mg, 1.19 mmol, 61%).

1H -NMR (400 MHz, $CDCl_3$): δ = 1.21–1.40 (m, 14H), 1.40–1.47 (m, 2H), 1.60 (p, J = 7.0 Hz, 2H), 1.69–1.81 (m, 2H), 3.26 (t, J = 7.0 Hz, 2H), 3.89 (t, J = 6.6 Hz, 2H), 4.36 (br s, 1H), 6.70–6.82 (m, 4H) ppm.

^{13}C -NMR (101 MHz, $CDCl_3$): δ = 26.2, 26.8, 29.0, 29.3, 29.5, 29.5, 29.6, 29.6, 29.6, 29.7, 51.6, 68.9, 115.8, 116.1, 149.5, 153.4 ppm.

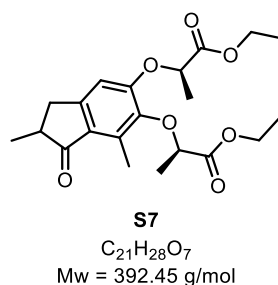
HRMS-ESI (ESI⁻): m/z for $C_{18}H_{28}N_3O_2^-$ [(M-H)⁻]: calc. 318.2187, found 318.2187.

Synthesis of the motor core



Scheme 2 | Synthesis of the motor core.

Diethyl 2,2'-((2,7-dimethyl-1-oxo-2,3-dihydro-1*H*-indene-5,6-diyl)bis(oxy))(2*R*,2'*R*)-dipropionate (**S7**)³

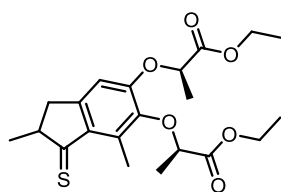


Under a nitrogen atmosphere, ketone **S6** (9.00 g, 0.05 mol, 1.00 eq.), PPh_3 (65.9 g, 0.25 mol, 5 eq.), and (*S*)-lactic ester (28.7 mL, 0.25 mol, 5.00 eq.) were dissolved in dry THF (180 mL) and DIAD (50.8 g, 0.25 mol, 5.00 eq.) in dry THF (180 mL) was slowly added at 0 °C. The reaction mixture was stirred at room temperature for 16 h. Subsequently, all volatiles were removed under reduced pressure and 400 mL *n*-pentane/ Et_2O (7:3) were added. Then, the mixture was sonicated and the precipitate removed by filtration. The filtrate was purified by MPLC (SiO_2 ; *n*-pentane/ethyl acetate gradient 95:05 → 85:15) and the title compound **S7** was obtained as a colorless oil (6.00 g, 16.0 mmol, 32%).

¹H-NMR (300 MHz, $CDCl_3$): δ = 1.18–1.28 (m, 9H), 1.55–1.71 (m, 6H), 2.45–2.70 (m, 5H), 3.18 (ddd, J = 16.7, 7.6, 2.8 Hz, 1H), 4.06–4.29 (m, 4H), 4.77–4.91 (m, 2H), 6.54 (s, 1H) ppm.

The analytical data is in accordance with the literature.

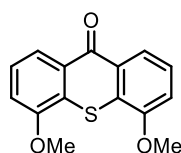
(4,5-bis((*tert*-butyldimethylsilyl)oxy)-9*H*-thioxanthen-9-ylidene)hydrazine (**S8**)³



S8
C₂₁H₂₈O₆S
Mw = 408.51 g/mol

Under a nitrogen atmosphere, indanone **S7** (350 mg, 0.892 mmol, 1.0 eq.) was dissolved in dry toluene (13 mL) and P₄S₁₀ (3.96 g, 17.8 mmol, 10.0 eq.) was added at 25 °C. After stirring at 80 °C for 2 h, the reaction mixture was quickly purified by flash column chromatography (SiO₂; first *n*-pentane, then ethyl acetate) under inert atmosphere. TLC (SiO₂; *n*-pentane/ethyl acetate 8:2) indicates full conversion of the starting material. Removal of the solvent yields product **S8** as a purple oil, which was directly used in the next reaction without further purification to avoid decomposition.

4,5-dimethoxy-9*H*-thioxanthen-9-one (**S10**)³



S10
C₁₅H₁₂O₃S
Mw = 272.32 g/mol

In a flame-dried 3-necked flask, a freshly made LDA solution (1.0 L, 0.50 M, 5.0 eq.) in dry THF was prepared at -78 °C and stirred at room temperature for 30 min. After cooling to 0 °C with an ice bath, a solution of amide **S9** (33.7 g, 98.0 mmol, 1.00 eq.) in dry THF (450 mL) was added dropwise to the LDA solution. After completion of the addition, the mixture was stirred at room temperature for 1 h. After full conversion was observed by TLC (*n*-pentane:ethyl acetate = 7:3), aq. NH₄Cl-solution (1M, 500 mL) was slowly added. The phases were separated and the aqueous layer was extracted with CH₂Cl₂ (2x500 mL). The combined organic layers were dried over MgSO₄ and all volatiles were removed under reduced pressure. The crude product was purified first by trituration in *n*-pentane/ethyl acetate and then recrystallization from ethyl acetate to afford title compound **S10** as a yellow powder (16.9 g, 62.0 mmol, 63%).

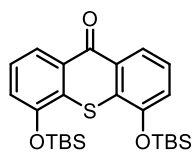
¹H-NMR (400 MHz, DMSO-*d*₆): δ = 4.03 (s, 6H), 7.44 (dd, *J* = 8.0, 1.2 Hz, 2H), 7.55 (t, *J* = 8.0 Hz, 2H), 8.06 (dd, *J* = 8.1, 1.2 Hz, 2H) ppm.

¹³C-NMR (101 MHz, DMSO-*d*₆): δ = 56.7, 113.3, 120.5, 126.2, 126.7, 129.0, 154.5, 178.9 ppm.

HRMS-ESI (ESI⁺): *m/z* calculated for C₁₅H₁₃O₃S ([M+H]⁺): 273.0580, found 273.0584.

The analytical data is in accordance with the literature.

4,5-bis((*tert*-butyldimethylsilyl)oxy)-9*H*-thioxanthen-9-one (**S12**)³



S12

$C_{25}H_{36}O_3SSi_2$
Mw = 472.79 g/mol

Cleavage of methyl ethers:

In a flame-dried 3-necked flask, thioxanthone **S10** (16.8 g, 62.0 mmol, 1.00 eq.) was dissolved in boiling CH_2Cl_2 (550 mL). The homogeneous solution was cooled to 0 °C with an ice bath and BBr_3 (29.2 mL, 308 mmol, 5.00 eq.) was added slowly. After the addition was complete, the mixture was stirred overnight and allowed to slowly warm to room temperature. Next, the mixture was cooled to 0 °C with an ice bath and MeOH (100 mL) was added slowly. After stirring for 3 h, all volatiles were removed under reduced pressure. The residue was suspended in MeOH (100 mL), which was evaporated again. Next, the crude solid was washed on a glass frit with H_2O (ca. 100 mL). Dissolving in acetone (400 mL) and drying over $MgSO_4$ delivered **S11** which was used without further purification.

TBS-protection:

In a flame-dried 3-necked-flask crude bisphenol **S11**, imidazole (12.6 g, 185 mmol, 3.00 eq.) and 4-(dimethylamino)pyridine (0.76 g, 6.2 mmol, 0.100 eq.), were dissolved in dry THF (250 mL). A solution of TBSCl (27.9 g, 185 mmol, 3.00 eq.) in dry THF (150 mL) was added and the mixture was stirred at room temperature for 16 h. Subsequently, the reaction mixture was filtered over a pad of silica gel and washed with CH_2Cl_2 (ca. 100 mL). The crude product was purified by recrystallization from EtOH and title compound **S12** was obtained as yellow needles (22 g, 47 mmol, 75% over two steps).

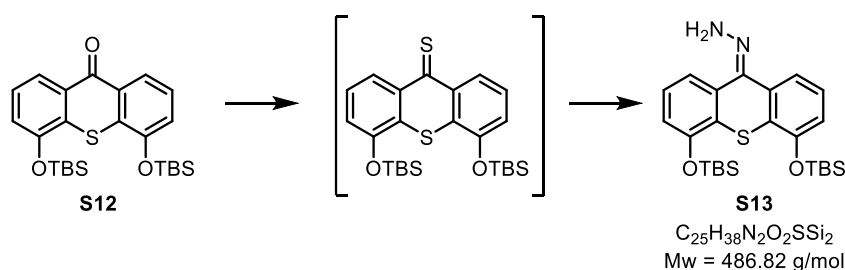
¹H-NMR (400 MHz, $CDCl_3$): δ = 0.35 (s, 12H), 1.11 (s, 18H), 7.10 (dd, J = 7.9, 1.3 Hz, 2H), 7.35 (t, J = 8.0 Hz, 2H), 8.26 (dd, J = 8.1, 1.3 Hz, 2H) ppm.

¹³C-NMR (101 MHz, $CDCl_3$): δ = -4.0, 18.6, 26.0, 102.5, 119.8, 122.2, 125.8, 130.5, 130.7, 151.5, 180.8 ppm.

HRMS-ESI (ESI+): m/z calculated for $C_{25}H_{37}O_3SSi_2^+$ ($[M+H]^+$): 473.1996, found 473.1999.

The analytical data is in accordance with the literature.

(4,5-bis((*tert*-butyldimethylsilyl)oxy)-9*H*-thioxanthen-9-ylidene)hydrazine (**S13**)³



Thioketone formation:

Under a nitrogen atmosphere in a flame-dried 3-necked flask equipped with a stirring bar and a reflux condenser, thioxanthone **S12** (2.0 g, 4.0 mmol, 1.0 eq.) was dissolved in dry toluene (20 mL). Lawesson's reagent (5.1 g, 13 mmol, 3.0 eq.) was added and the mixture was heated to 80 °C for 2 h. Subsequently, the mixture was cooled to room temperature and the crude product was purified by flash column chromatography (*n*-pentane/ethyl acetate = 4:1) and the thioketone was immediately converted further.

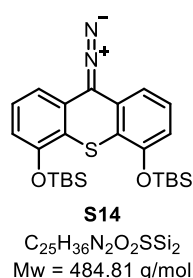
Hydrazone formation:

In a round-bottom flask, the thioketone was dissolved in THF (15 mL) and stirred at room temperature. Next, hydrazine (2.1 mL, 4.2 mmol, 10 eq.) was added and the mixture was stirred at room temperature for 2 h. During this time, the color of the reaction mixture changed from green to almost colorless. Then, all volatiles were removed under reduced pressure and the crude product was purified by MPLC (SiO₂; *n*-pentane/ethyl acetate gradient 100:0 → 80:20). The title compound **S13** (2.0 g, 4.0 mmol, 99%) was obtained as a slightly yellow oil which solidified upon standing.

¹H-NMR (400 MHz, CDCl₃): δ = 0.28 (s, 6H), 0.31 (s, 6H), 1.07 (s, 10H), 1.09 (s, 9H), 5.83 (s, 2H), 6.78 (dd, *J* = 7.9, 1.1 Hz, 1H), 6.84 (dd, *J* = 8.0, 1.1 Hz, 1H), 7.16 (t, *J* = 7.9 Hz, 1H), 7.19 (d, *J* = 8.0 Hz, 1H), 7.43 (dd, *J* = 7.8, 1.2 Hz, 1H), 7.63 (dd, *J* = 7.9, 1.1 Hz, 1H) ppm.

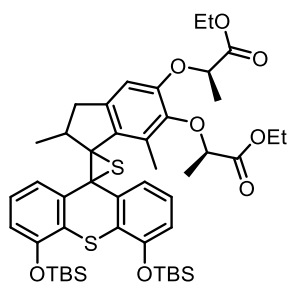
The analytical data is in accordance with the literature.

(4,5-bis((*tert*-butyldimethylsilyl)oxy)-9*H*-thioxanthen-9-ylidene)hydrazine (**S14**)³



Under an argon atmosphere and exclusion of light, hydrazone **S13** (478 mg, 0.981 mmol, 1.0 eq.) was dissolved in dry THF (13 mL). Then, MnO₂ (1.55 g, 17.8 mmol, 18 eq.; manganese(IV) oxide activated, technical grade ≥ 90%, FLUKA Cat. 63548) and Na₂SO₄ (633 mg, 4.46 mmol, 4.5 eq.) were added at 0 °C. After stirring at 0 °C for 10 min, the reaction mixture was quickly filtered with a cannula (Whatman technique) under strict exclusion of light and air and the residue was washed two more times with dry and cold THF (2 mL, 0 °C). The green filtrate was kept at 0 °C and immediately used for the next reaction.

Diethyl 2,2'-((4'',5''-bis((*tert*-butyldimethylsilyl)oxy)-2,7-dimethyl-2,3-dihydrodispiro[indene-1,2'-thiirane-3',9''-thioxanthene]-5,6-diyl)bis(oxy))(2*R*,2'*R*)-dipropionate (S15**)³**



S15

C₄₇H₆₈O₈S₂Si₂
Mw = 881.34 g/mol

Under an argon atmosphere and exclusion of light, thioketone **S8** was dissolved in dry THF (2 mL), cooled to 0 °C, and slowly added to a solution of diazo **S14** in dry THF at 0 °C. After three vacuum-argon cycles, the reaction mixture was allowed to warm up to room temperature while stirring for 16 h. Purification by MPLC (SiO₂; *n*-pentane/ethyl acetate gradient 100:0 → 90:10) affords diastereomers (*R,R,R*)-**S15** (254 mg, 0.294 mmol, 33%; elutes at 6% ethyl acetate) and (*S,R,R*)-**S15** (312 mg, 0.361 mmol, 35%; elutes at 7% ethyl acetate) with excellent separation.

(*R,R,R*)-S15

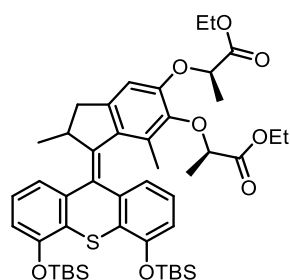
¹H-NMR (300 MHz, CDCl₃): δ = -0.08 (s, 3H), 0.08 (s, 3H), 0.23 (s, 3H), 0.25 (s, 3H), 0.91 (d, *J* = 6.9 Hz, 3H), 0.96 (s, 9H), 1.04 (s, 9H), 1.07 (s, 1H), 1.22 (t, *J* = 7.1 Hz, 3H), 1.30 (t, *J* = 7.1 Hz, 3H), 1.42 (d, *J* = 6.8 Hz, 3H), 1.52 (d, *J* = 6.7 Hz, 3H), 2.02–2.10 (m, 1H), 2.14 (s, 3H), 3.18 (dd, *J* = 14.8, 6.4 Hz, 1H), 4.10–4.29 (m, 5H), 4.60 (q, *J* = 6.7 Hz, 1H), 6.34 (s, 1H), 6.60 (d, *J* = 8.0 Hz, 1H), 6.73 (d, *J* = 7.9 Hz, 1H), 7.01 (t, *J* = 7.9 Hz, 1H), 7.10 (t, *J* = 7.9 Hz, 1H), 7.24 (d, *J* = 7.9 Hz, 1H), 7.39 (d, *J* = 8.1 Hz, 1H) ppm.

(*S,R,R*)-S15

¹H-NMR (300 MHz, CDCl₃): δ = -0.12 (s, 3H), 0.06 (s, 3H), 0.23 (s, 3H), 0.25 (s, 3H), 0.94 (s, 9H), 1.05 (s, 9H), 1.14–1.29 (m, 11H), 1.52 (d, *J* = 6.8 Hz, 3H), 2.04 (d, *J* = 15.0 Hz, 2H), 2.12 (s, 3H), 3.20 (dd, *J* = 15.0, 6.4 Hz, 1H), 4.05–4.26 (m, 5H), 4.58 (dq, *J* = 8.2, 6.8 Hz, 2H), 6.59 (dd, *J* = 8.0, 1.2 Hz, 1H), 6.73 (dd, *J* = 8.0, 1.3 Hz, 1H), 7.00 (t, *J* = 7.8 Hz, 1H), 7.10 (t, *J* = 7.9 Hz, 1H), 7.24 (dd, *J* = 7.7, 1.2 Hz, 1H), 7.38 (dd, *J* = 7.7, 1.3 Hz, 1H) ppm.

The analytical data is in accordance with the literature.

Diethyl 2,2'-((1-(4,5-bis((*tert*-butyldimethylsilyl)oxy)-9H-thioxanthen-9-ylidene)-2,7-dimethyl-2,3-dihydro-1H-indene-5,6-diyl)bis(oxy))(2*R*,2'*R*)-dipropionate³



S16
C₄₇H₆₈O₈SSi₂
Mw = 832.39 g/mol

Under an argon atmosphere, episulfide **S15** (210 mg, 0.242 mmol, 1 eq.) and PPh₃ (1.27 g, 4.82 mmol, 20 eq.) were dissolved in toluene (3 mL) and the solution was stirred at 120 °C for 3 d. Purification by MPLC (SiO₂; *n*-pentane/ethyl acetate gradient 100:0 → 90:10) afforded product **S16** as a colorless solid (190 mg, 0.227 mmol, 94%).

(*R,R,R*)-S16

¹H-NMR (600 MHz, CDCl₃): δ = 0.25 (s, 3H), 0.27 (s, 3H), 0.27 (s, 3H), 0.29 (s, 3H), 0.61 (d, *J* = 6.8 Hz, 3H), 0.98 (s, 1H), 1.09 (d, *J* = 1.9 Hz, 17H), 1.19 (s, 3H), 1.28 (dt, *J* = 9.3, 7.1 Hz, 6H), 1.52 (d, *J* = 6.8 Hz, 3H), 1.62 (d, *J* = 6.8 Hz, 3H), 2.33 (d, *J* = 14.8 Hz, 1H), 3.29–3.35 (m, 1H), 4.10 (p, *J* = 6.7 Hz, 1H), 4.18 (dd, *J* = 7.2, 2.3 Hz, 1H), 4.19–4.30 (m, 3H), 4.44 (q, *J* = 6.8 Hz, 1H), 4.77 (q, *J* = 6.7 Hz, 1H), 6.56 (s, 1H), 6.64 (dd, *J* = 7.9, 1.2 Hz, 1H), 6.66 (dd, *J* = 7.7, 1.2 Hz, 1H), 6.69 (dd, *J* = 8.0, 1.1 Hz, 1H), 6.89 (t, *J* = 7.8 Hz, 1H), 7.12 (t, *J* = 7.8 Hz, 1H), 7.29 (dd, *J* = 7.7, 1.2 Hz, 1H) ppm.

¹³C-NMR (151 MHz, CDCl₃): δ = -4.26, -4.18, -3.86, -3.81, 14.28, 14.39, 14.57, 18.53, 18.56, 18.66, 18.87, 19.11, 26.07, 38.15, 39.67, 60.83, 61.32, 73.05, 77.61, 108.31, 115.68, 116.49, 120.45, 121.14, 126.23, 126.64, 127.29, 127.73, 128.32, 131.03, 133.61, 138.48, 141.90, 142.47, 144.99, 145.58, 150.32, 152.36, 152.87, 172.32, 172.57 ppm.

(*S,R,R*)-S16

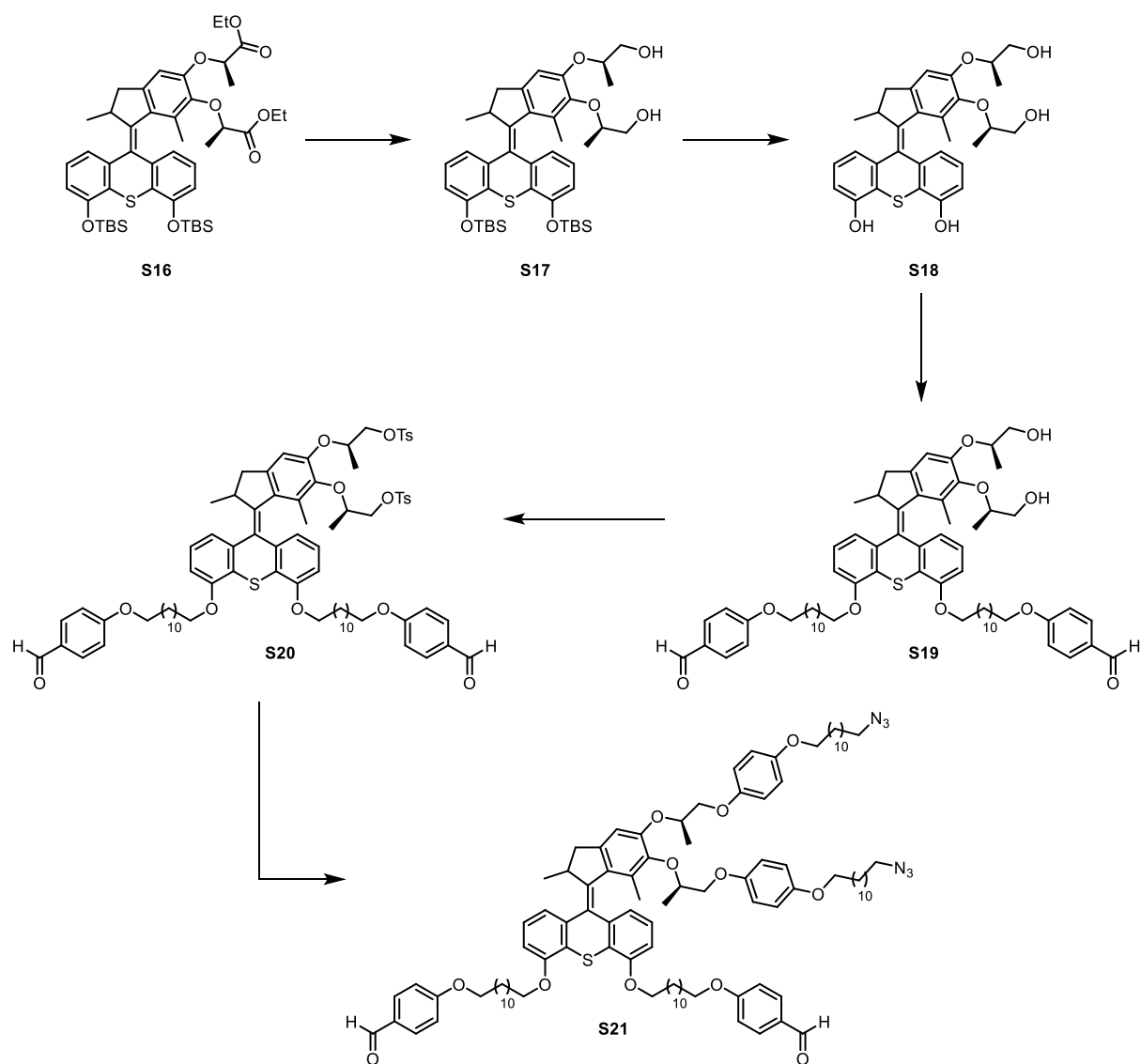
¹H-NMR (600 MHz, CDCl₃): δ = 0.25 (s, 3H), 0.27 (d, *J* = 1.5 Hz, 6H), 0.29 (s, 3H), 0.62 (d, *J* = 6.8 Hz, 3H), 1.09 (d, *J* = 4.4 Hz, 18H), 1.17–1.26 (m, 10H), 1.45 (d, *J* = 6.8 Hz, 3H), 1.61 (d, *J* = 6.8 Hz, 4H), 2.32 (d, *J* = 14.8 Hz, 1H), 3.33 (ddd, *J* = 14.9, 6.6, 1.2 Hz, 1H), 4.07–4.17 (m, 3H), 4.17–4.29 (m, 2H), 4.75 (qd, *J* = 6.7, 4.6 Hz, 2H), 6.53 (s, 1H), 6.62–6.64 (m, 2H), 6.69 (dd, *J* = 8.0, 1.1 Hz, 1H), 6.86 (t, *J* = 7.8 Hz, 1H), 7.12 (t, *J* = 7.8 Hz, 1H), 7.29 (dd, *J* = 7.7, 1.2 Hz, 1H) ppm.

¹³C-NMR (151 MHz, CDCl₃): δ = -4.23, -4.18, -3.87, -3.79, 14.22, 14.26, 14.55, 18.56, 18.68, 19.09, 26.08, 38.15, 39.61, 60.82, 61.36, 73.12, 77.08, 108.25, 115.67, 116.53, 120.40, 121.12, 126.23, 126.58, 127.32, 127.83, 128.29, 131.05, 133.59, 138.48, 141.94, 142.13, 144.60, 145.65, 149.76, 152.36, 152.89, 172.17, 172.62 ppm.

MS-ESI (ESI+): *m/z* calculated for C₄₇H₆₈O₈SSi₂H⁺ ([M+H]⁺): 832.39, found 832.39.

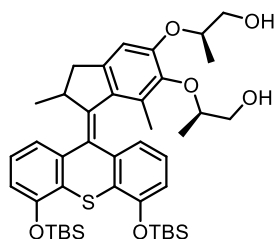
The analytical data is in accordance with the literature.

Postfunctionalization of the motor core



Scheme 3 | Postfunctionalization of the motor core.

(2*R*,2'*R*)-2,2'-((1-(4,5-bis(*tert*-butyldimethylsilyl)oxy)-9*H*-thioxanthen-9-ylidene)-2,7-dimethyl-2,3-dihydro-1*H*-indene-5,6-diyl)bis(oxy))bis(propan-1-ol) (S17)



S17

C₄₂H₆₀O₆SSi₂
Mw = 749.17 g/mol

Under a nitrogen atmosphere, fully protected motor **S16** (179 mg, 0.215 mmol, 1.00 eq.) was dissolved in dry CH₂Cl₂ (8.2 mL) and diisobutylaluminium hydride (1 M in hexanes, 2.1 mL, 10 eq.) was slowly added at 0 °C. After stirring for 1.5 h at 0 °C, additional 2 eq. of diisobutylaluminium hydride were added after 30 min and 1 h, whereby completion of the reaction was monitored by TLC (SiO₂; *n*-pentane/ethyl acetate 1:1). Then, the reaction was quenched with aq. saturated Rochelle's salt and the mixture stirred for 30 min until a clear phase separation was observed. The reaction mixture was diluted with CH₂Cl₂, washed with water, and dried over MgSO₄. Typically, the crude mixture was filtered over a pad of silica gel with CH₂Cl₂/methanol (10:1) and used for the next step without further purification. In order to fully characterize the compound, the crude reaction mixture was once purified by MPLC (SiO₂; *n*-pentane/ethyl acetate gradient 100:0 → 0:100), which provided product **S17** as a colorless solid (156 mg, 0.21 mmol, 97%).

(*R,R,R*)-S17

¹H-NMR (600 MHz, C₆D₆): δ = 0.22 (s, 3H), 0.23 (s, 3H), 0.24 (s, 3H), 0.25 (s, 3H), 0.77 (d, *J* = 6.8 Hz, 3H), 0.84 (d, *J* = 6.4 Hz, 3H), 1.15 (s, 9H), 1.17 (s, 9H), 1.20 (d, *J* = 6.3 Hz, 3H), 1.56 (s, 3H), 2.30 (d, *J* = 14.7 Hz, 1H), 3.10 (br s, 2H), 3.33–3.42 (m, 2H), 3.46 (ddd, *J* = 12.4, 8.5, 3.7 Hz, 2H), 3.64 (dd, *J* = 12.2, 2.8 Hz, 1H), 4.04–4.11 (m, 1H), 4.24 (p, *J* = 6.7 Hz, 1H), 4.35 (pd, *J* = 6.5, 3.0 Hz, 1H), 6.62 (dd, *J* = 8.0, 1.2 Hz, 1H), 6.64 (s, 1H), 6.71–6.78 (m, 2H), 6.93 (dd, *J* = 7.6, 1.2 Hz, 1H), 7.06 (t, *J* = 7.9 Hz, 1H), 7.39 (dd, *J* = 7.7, 1.1 Hz, 1H) ppm.

¹³C-NMR (151 MHz, C₆D₆): δ = -4.2, -4.1, -3.9, -3.8, 15.2, 15.7, 16.7, 18.7, 18.7, 19.2, 26.2, 26.2, 38.5, 39.8, 65.7, 66.8, 76.1, 78.4, 109.5, 116.1, 116.8, 120.9, 121.6, 126.6, 127.1, 128.6, 128.6, 128.9, 131.4, 133.3, 139.2, 142.3, 142.8, 145.0, 146.2, 151.0, 152.9, 153.4 ppm. Signals for some carbon atoms are missing due to signal overlap with C₆D₆.

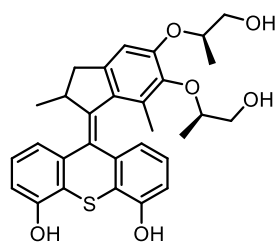
(*S,R,R*)-S17

¹H-NMR (600 MHz, C₆D₆): δ = 0.23 (dd, *J* = 11.6, 8.6 Hz, 12H), 0.76 (d, *J* = 6.8 Hz, 3H), 1.02 (d, *J* = 6.4 Hz, 3H), 1.15 (d, *J* = 9.3 Hz, 18H), 1.25 (d, *J* = 6.2 Hz, 3H), 1.47 (s, 3H), 2.30 (d, *J* = 14.7 Hz, 1H), 3.35–3.41 (m, 1H), 3.43 (dd, *J* = 12.3, 3.9 Hz, 1H), 3.48 (dd, *J* = 11.8, 6.8 Hz, 1H), 3.58 (dd, *J* = 11.8, 2.7 Hz, 1H), 3.67 (dd, *J* = 12.3, 2.6 Hz, 1H), 3.82 (s, 2H), 4.05 (tq, *J* = 9.0, 3.0 Hz, 1H), 4.12 (pd, *J* = 6.4, 2.5 Hz, 1H), 4.20 (p, *J* = 6.7 Hz, 1H), 6.61 (dd, *J* = 7.9, 1.2 Hz, 1H), 6.63 (s, 1H), 6.67–6.74 (m, 2H), 6.84 (dd, *J* = 7.6, 1.2 Hz, 1H), 7.05 (t, *J* = 7.9 Hz, 1H), 7.37 (dd, *J* = 7.8, 1.1 Hz, 1H) ppm.

¹³C-NMR (151 MHz, C₆D₆): δ = -4.2, -4.1, -4.0, -3.9, 15.3, 15.6, 16.7, 18.7, 19.1, 26.2, 38.5, 40.1, 65.4, 66.2, 76.5, 80.2, 110.5, 116.1, 116.8, 120.7, 121.8, 126.5, 126.7, 128.3, 128.7, 129.0, 131.8, 133.8, 139.0, 142.6, 142.6, 146.0, 146.1, 151.1, 152.9, 153.5 ppm. Signals for some carbon atoms are missing due to signal overlap with C₆D₆.

HRMS-ESI (ESI+): m/z calculated for $C_{42}H_{60}O_6SSi_2Na^+$ ($[M+Na]^+$): 771.3541, found 771.3523.

9-(5,6-bis(((*R*)-1-hydroxypropan-2-yl)oxy)-2,7-dimethyl-2,3-dihydro-1*H*-inden-1-ylidene)-9*H*-thioxanthene-4,5-diol (S18**)**

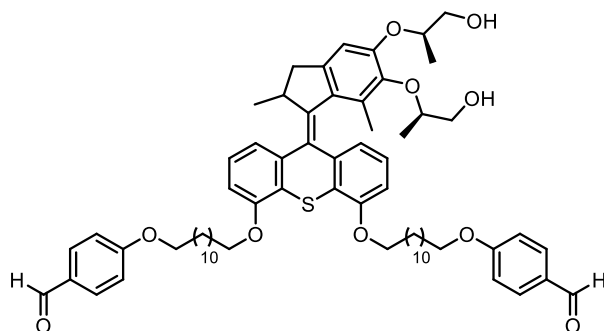


S18

$C_{30}H_{32}O_6S$
Mw = 520.64 g/mol

Under a nitrogen atmosphere, bis-TBS motor **S17** (159 mg, 0.21 mmol, 1.0 eq.) was dissolved in dry THF (14 mL) and TBAF (1M in THF, 0.67 mL, 3.1 eq.) was slowly added at 0 °C. After stirring for 5 min at 0 °C, the reaction mixture was quenched with saturated aq. NH_4Cl , diluted with CH_2Cl_2 , washed with water, and dried over $MgSO_4$. Then, the mixture was filtered over a pad of silica gel with CH_2Cl_2 /methanol (10:1) and the crude product **S18** (110 mg, 0.2 mmol, 99%) was used for the next step without further purification to avoid decomposition.

4,4'-((((9-(5,6-bis(((*R*)-1-hydroxypropan-2-yl)oxy)-2,7-dimethyl-2,3-dihydro-1*H*-inden-1-ylidene)-9*H*-thioxanthene-4,5-diyl)bis(oxy))bis(dodecane-12,1-diyl))bis(oxy))dibenzaldehyde (S19**)**



S19

$C_{68}H_{88}O_{10}S$
Mw = 1097.50 g/mol

Under a nitrogen atmosphere, deprotected motor **S18** (110 mg, 0.20 mmol, 1.0 eq.), tosylate **S3** (584 mg, 1.3 mmol, 6.0 eq.), and freshly grinded K_2CO_3 (175 mg, 1.3 mmol, 6.0 eq.) were stirred in DMF (7.5 mL) at 60 °C for 3 days. The reaction mixture was diluted with CH_2Cl_2 , washed with water, and dried over $MgSO_4$. Purification by MPLC (SiO_2 ; *n*-pentane/ethyl acetate gradient 100:0 → 30:70) afforded product **S19** as a colorless oil (0.11 g, 0.10 mmol, 47% over three steps).

(*R,R,R*)-S19

1H -NMR (600 MHz, C_6D_6): δ = 0.80 (d, J = 6.8 Hz, 3H), 0.82 (d, J = 6.4 Hz, 3H), 1.21 (d, J = 6.3 Hz, 3H), 1.23–1.38 (m, 30H), 1.41–1.52 (m, 4H), 1.52–1.60 (m, 7H), 1.66–1.78 (m, 4H), 2.32 (d, J = 14.8 Hz, 1H), 3.36–3.49 (m, 4H), 3.52 (t, J = 6.4 Hz, 4H), 3.62–3.71 (m, 2H), 3.74 (dt, J = 9.1, 6.5 Hz, 1H), 3.82 (ddt, J = 21.9, 9.0, 6.4 Hz, 2H), 4.09 (dt, J = 6.4, 3.4 Hz, 1H), 4.26–4.39 (m, 2H), 6.44–6.49

(m, 1H), 6.57 (d, $J = 7.5$ Hz, 1H), 6.64–6.69 (m, 5H), 6.84 (t, $J = 7.9$ Hz, 1H), 6.96 (dd, $J = 7.7, 1.0$ Hz, 1H), 7.45 (d, $J = 7.6$ Hz, 1H), 7.57–7.62 (m, 4H), 9.72 (s, 2H) ppm.

$^{13}\text{C-NMR}$ (151 MHz, C_6D_6): $\delta = 15.0, 15.3, 16.4, 18.9, 26.0, 26.1, 26.1, 29.0, 29.2, 29.3, 29.4, 29.5, 29.7, 29.7, 29.8, 38.3, 39.6, 65.3, 66.5, 67.9, 68.6, 75.7, 78.0, 109.0, 114.5, 120.0, 120.6, 125.4, 125.7, 126.3, 126.8, 127.5, 127.6, 127.7, 127.8, 127.8, 128.0, 130.3, 131.1, 131.6, 133.0, 138.5, 141.9, 142.1, 144.6, 145.9, 150.6, 156.1, 156.5, 163.8, 189.4$ ppm.

Signals for some carbon atoms are missing due to signal overlap with C_6D_6 .

(*S,R,R*)-**S19**

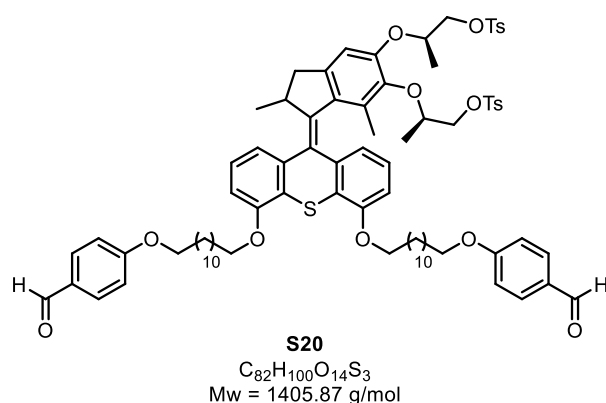
$^1\text{H-NMR}$ (600 MHz, C_6D_6): $\delta = 0.77$ (d, $J = 6.8$ Hz, 3H), 1.05 (d, $J = 6.4$ Hz, 3H), 1.23–1.37 (m, 33H), 1.39–1.52 (m, 7H), 1.57 (dq, $J = 13.7, 6.6$ Hz, 4H), 1.62–1.77 (m, 4H), 2.32 (d, $J = 14.8$ Hz, 1H), 3.38–3.46 (m, 2H), 3.49 (dd, $J = 11.8, 6.5$ Hz, 1H), 3.53 (td, $J = 6.4, 1.1$ Hz, 4H), 3.61 (dd, $J = 11.8, 2.6$ Hz, 1H), 3.64–3.70 (m, 2H), 3.74 (dt, $J = 9.0, 6.4$ Hz, 1H), 3.81 (ddt, $J = 13.0, 8.9, 6.4$ Hz, 2H), 4.07 (dq, $J = 9.8, 6.2, 4.9$ Hz, 1H), 4.17 (pd, $J = 6.3, 2.5$ Hz, 1H), 4.27 (p, $J = 6.7$ Hz, 1H), 6.45–6.50 (m, 1H), 6.57 (d, $J = 7.8$ Hz, 1H), 6.66 (s, 1H), 6.68 (d, $J = 8.6$ Hz, 4H), 6.83 (t, $J = 7.9$ Hz, 1H), 6.90 (dd, $J = 7.7, 1.0$ Hz, 1H), 7.42 (d, $J = 7.7$ Hz, 1H), 7.58–7.62 (m, 4H), 9.72 (s, 2H) ppm.

$^{13}\text{C-NMR}$ (151 MHz, C_6D_6): $\delta = 15.4, 15.7, 16.8, 19.2, 26.3, 26.4, 26.5, 29.4, 29.6, 29.6, 29.8, 29.9, 30.1, 30.1, 30.1, 38.6, 40.1, 65.4, 66.1, 68.3, 69.0, 69.1, 76.7, 80.0, 109.1, 109.2, 110.7, 114.9, 120.3, 121.1, 125.5, 126.2, 126.6, 126.7, 128.4, 128.6, 128.8, 130.6, 131.9, 132.0, 133.9, 138.6, 142.4, 142.6, 145.9, 146.2, 151.2, 156.4, 156.9, 164.2, 189.9$ ppm.

Signals for some carbon atoms are missing due to signal overlap with C_6D_6 .

HRMS-ESI (ESI⁺): m/z calculated for $\text{C}_{68}\text{H}_{88}\text{O}_{10}\text{SNa}^+$ ($[\text{M}+\text{Na}]^+$): 1119.5990, found 1119.5973.

(2*R*,2'*R*)-((1-(4,5-bis((12-(4-formylphenoxy)dodecyl)oxy)-9*H*-thioxanthen-9-ylidene)-2,7-dimethyl-2,3-dihydro-1*H*-indene-5,6-diyl)bis(oxy))bis(propane-2,1-diyl) bis(4-methylbenzenesulfonate) (S20**)**



Under a nitrogen atmosphere, bis-alcohol **S19** (110 mg, 0.10 mmol, 1.0 eq.), Et₃N (0.14 mL, 1.0 mmol, 10 eq.), 4-dimethylaminopyridine (12 mg, 0.10 mmol, 1.0 eq.), and 4-toluenesulfonyl chloride (191 mg, 1.00 mmol, 10.0 eq.) were stirred in dry CH₂Cl₂ (3.4 mL) at room temperature for 16 h. The reaction mixture was diluted with CH₂Cl₂, washed with water, and dried over MgSO₄. Purification by flash column chromatography (SiO₂; first *n*-pentane/CH₂Cl₂ 8:2, then ethyl acetate) provided product **S20** as a colorless oil (140 mg, 99%).

(*R,R,R*)-S20

¹H-NMR (600 MHz, C₆D₆): δ = 0.71 (d, *J* = 6.8 Hz, 3H), 0.91 (d, *J* = 6.3 Hz, 3H), 1.07 (d, *J* = 6.3 Hz, 3H), 1.21–1.41 (m, 37H), 1.42–1.52 (m, 7H), 1.53–1.60 (m, 4H), 1.67–1.80 (m, 4H), 1.87 (s, 3H), 1.90 (s, 3H), 2.25 (d, *J* = 14.8 Hz, 1H), 3.34 (dd, *J* = 14.8, 6.2 Hz, 1H), 3.53 (t, *J* = 6.5 Hz, 5H), 3.69–3.85 (m, 4H), 3.92–4.04 (m, 5H), 4.15 (dd, *J* = 10.1, 4.5 Hz, 1H), 4.24 (ddd, *J* = 10.2, 7.6, 5.2 Hz, 2H), 4.37 (pd, *J* = 6.2, 4.4 Hz, 1H), 6.53–6.59 (m, 2H), 6.68 (d, *J* = 8.4 Hz, 4H), 6.73–6.83 (m, 5H), 6.92 (dd, *J* = 7.7, 1.1 Hz, 1H), 7.42 (d, *J* = 7.7 Hz, 1H), 7.60 (d, *J* = 8.6 Hz, 4H), 7.80 (dd, *J* = 8.3, 3.0 Hz, 4H), 9.72 (s, 2H) ppm.

¹³C-NMR (151 MHz, C₆D₆): δ = 15.1, 16.4, 17.4, 19.1, 21.2, 21.3, 26.3, 26.3, 26.5, 26.5, 29.4, 29.6, 29.8, 29.8, 29.9, 29.9, 30.1, 30.1, 38.6, 39.9, 68.3, 69.0, 69.1, 71.7, 71.8, 72.6, 75.3, 109.1, 109.9, 110.5, 114.9, 120.3, 120.9, 125.7, 125.9, 126.7, 127.3, 129.1, 129.9, 130.0, 130.7, 131.7, 131.9, 134.0, 134.3, 134.3, 138.7, 142.0, 142.4, 144.4, 144.7, 145.3, 145.9, 150.6, 156.4, 157.0, 164.2, 189.8 ppm.

Signals for some carbon atoms are missing due to signal overlap with C₆D₆.

(*S,R,R*)-S20

¹H-NMR (600 MHz, C₆D₆): δ = 0.71 (d, *J* = 6.7 Hz, 3H), 0.98 (d, *J* = 6.4 Hz, 3H), 1.09 (d, *J* = 6.4 Hz, 3H), 1.24–1.37 (m, 30H), 1.38 (s, 3H), 1.47 (dtd, *J* = 15.4, 12.2, 9.1, 4.5 Hz, 4H), 1.53–1.61 (m, 4H), 1.70 (ddp, *J* = 19.7, 13.1, 6.1 Hz, 4H), 1.83 (s, 3H), 1.87 (s, 3H), 2.25 (d, *J* = 14.8 Hz, 1H), 3.33 (dd, *J* = 14.7, 6.1 Hz, 1H), 3.53 (td, *J* = 6.4, 1.5 Hz, 4H), 3.70 (ddt, *J* = 36.7, 9.2, 6.6 Hz, 2H), 3.76–3.86 (m, 2H), 3.99 (dd, *J* = 10.6, 4.2 Hz, 1H), 4.03 (dd, *J* = 10.2, 5.3 Hz, 1H), 4.12 (dd, *J* = 10.6, 5.8 Hz, 1H), 4.23 (dq, *J* = 10.3, 5.8, 4.8 Hz, 2H), 4.27–4.34 (m, 1H), 4.39 (h, *J* = 6.3 Hz, 1H), 6.47 (dd, *J* = 7.7, 1.5 Hz, 1H), 6.51–6.58 (m, 2H), 6.68 (d, *J* = 8.8 Hz, 4H), 6.75 (dd, *J* = 17.4, 7.9 Hz, 4H), 6.84–6.92 (m, 2H), 7.39 (d, *J* = 7.7 Hz, 1H), 7.60 (d, *J* = 8.5 Hz, 4H), 7.77–7.82 (m, 4H), 9.72 (s, 2H).

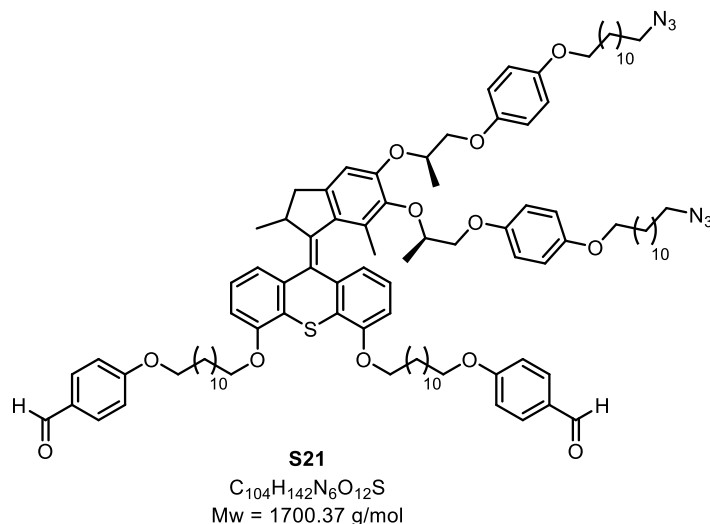
¹³C-NMR (151 MHz, C₆D₆): δ = 15.2, 16.2, 17.2, 19.1, 21.2, 21.2, 26.3, 26.4, 26.5, 29.4, 29.6, 29.7, 29.8, 29.9, 30.1, 30.1, 30.1, 30.1, 30.1, 30.1, 38.6, 39.9, 68.3, 69.0, 69.0, 71.9, 72.1, 72.7, 75.5, 109.1, 109.3,

110.4, 114.9, 120.3, 121.0, 125.6, 126.0, 126.7, 127.0, 128.3, 128.9, 129.9, 130.0, 130.7, 131.8, 131.9, 134.0, 134.1, 138.6, 142.2, 142.3, 144.4, 144.5, 145.3, 146.0, 150.2, 156.4, 156.9, 164.2, 164.2, 189.8 ppm.

Signals for some carbon atoms are missing due to signal overlap with C₆D₆.

HRMS-ESI (ESI+): *m/z* calculated for C₈₂H₁₀₀O₁₄S₃Na⁺ ([M+Na]⁺): 1427.6167, found 1427.6151.

2.3.5 4,4'-((((9-(5,6-bis(((R)-1-(4-((12-azidododecyl)oxy)phenoxy)propan-2-yl)oxy)-2,7-dimethyl-2,3-dihydro-1H-inden-1-ylidene)-9H-thioxanthene-4,5-diyl)bis(oxy))bis(dodecane-12,1-diyl))bis(oxy))dibenzaldehyde (S21)



Under a nitrogen atmosphere, bis-tosylate **S20** (30 mg, 21 μmol, 1.0 eq.), phenol **S5** (0.20 g, 0.64 mmol, 30.0 eq.), and Cs₂CO₃ (0.21 g, 0.64 mmol, 30.0 eq.) were stirred in a mixture of DMF/THF (1 mL, 7:3) at 55 °C for 9 d. The reaction mixture was diluted with CH₂Cl₂, washed with water, dried over MgSO₄, and filtered over a pad of silica gel with ethyl acetate. After purification by MPLC (SiO₂; first *n*-pentane/CH₂Cl₂ 1:1, then *n*-pentane/ethyl acetate gradient 100:0 → 80:20), product **S21** was obtained as an off-white solid (18 mg, 11 μmol, 50%).

(R,R,R)-S21

¹H-NMR (600 MHz, C₆D₆): δ = 0.78 (d, *J* = 6.7 Hz, 3H), 1.05–1.15 (m, 8H), 1.16–1.38 (m, 57H), 1.39–1.60 (m, 15H), 1.65 (s, 3H), 1.67–1.75 (m, 7H), 2.33 (d, *J* = 14.8 Hz, 1H), 2.71 (t, *J* = 6.8 Hz, 4H), 3.43 (dd, *J* = 14.9, 6.1 Hz, 1H), 3.52 (t, *J* = 6.5 Hz, 4H), 3.65–3.79 (m, 9H), 3.79–3.91 (m, 1H), 3.96 (dd, *J* = 9.7, 5.8 Hz, 1H), 4.05 (dd, *J* = 9.3, 4.0 Hz, 1H), 4.29 (p, *J* = 6.7 Hz, 1H), 4.57–4.62 (m, 1H), 4.79–4.85 (m, 1H), 6.41–6.48 (m, 1H), 6.56 (d, *J* = 8.1 Hz, 1H), 6.67 (d, *J* = 8.7 Hz, 4H), 6.79–6.92 (m, 10H), 6.95–7.01 (m, 1H), 7.39–7.46 (m, 1H), 7.56–7.63 (m, 4H), 9.72 (s, 2H) ppm.

¹³C-NMR (151 MHz, C₆D₆): δ = 15.2, 17.4, 18.5, 19.2, 26.3, 26.5, 26.5, 26.6, 27.0, 29.0, 29.4, 29.5, 29.6, 29.6, 29.8, 29.9, 29.9, 29.9, 29.9, 30.0, 30.0, 30.0, 30.1, 30.1, 30.2, 38.8, 40.1, 51.4, 68.3, 68.5, 68.5, 69.0, 69.0, 71.7, 71.7, 73.4, 76.6, 109.0, 109.4, 110.0, 114.9, 115.6, 115.7, 116.0, 116.0, 120.4, 121.0, 125.8, 126.1, 126.6, 127.1, 127.6, 128.7, 130.7, 131.8, 131.9, 133.5, 138.9, 142.2, 142.4, 146.1, 146.4, 151.7, 153.4, 153.8, 154.1, 154.3, 156.4, 156.9, 164.1, 189.8 ppm. Signals for some carbon atoms are missing due to signal overlap with C₆D₆.

(S,R,R)-S21

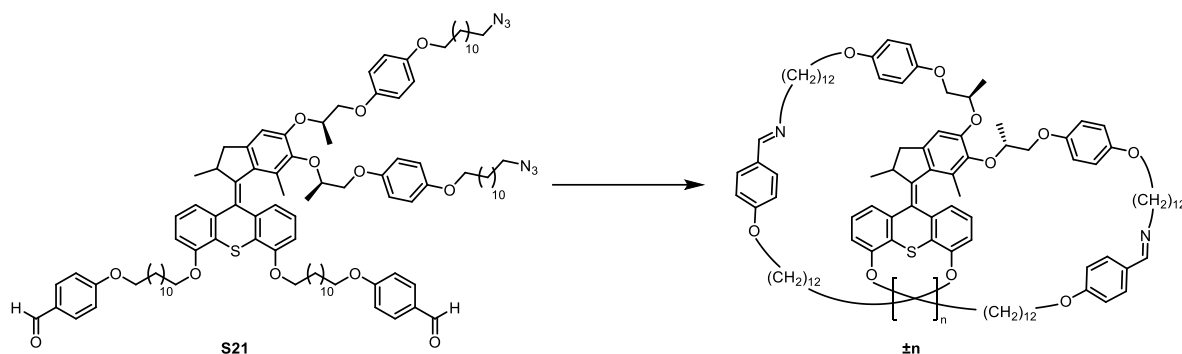
¹H-NMR (600 MHz, C₆D₆): δ = 0.80 (d, *J* = 6.8 Hz, 3H), 1.08–1.12 (m, 7H), 1.19 (m, 5H), 1.20–1.35 (m, 42H), 1.37–1.52 (m, 13H), 1.52–1.60 (m, 4H), 1.63–1.76 (m, 11H), 2.33 (d, *J* = 14.8 Hz, 1H), 2.72 (td, *J* = 6.9, 2.8 Hz, 4H), 3.43 (dd, *J* = 14.8, 6.1 Hz, 2H), 3.52 (t, *J* = 6.4 Hz, 4H), 3.63–3.77 (m, 7H), 3.77–3.83 (m, 3H), 3.93 (dd, *J* = 9.4, 6.5 Hz, 1H), 3.99 (dd, *J* = 9.6, 5.4 Hz, 1H), 4.21 (dd, *J* = 9.4, 4.6 Hz, 1H), 4.29 (p, *J* = 6.7 Hz, 2H), 4.61–4.67 (m, 2H), 4.75–4.83 (m, 2H), 6.47 (d, *J* = 7.4 Hz, 1H), 6.56 (d, *J* = 7.8 Hz, 1H), 6.67 (d, *J* = 8.1 Hz, 4H), 6.77–6.90 (m, 11H), 7.00 (dd, *J* = 7.7, 0.9 Hz, 2H), 7.14 (d, *J* = 7.9 Hz, 1H), 7.43 (d, *J* = 7.7 Hz, 1H), 7.57–7.63 (m, 4H), 9.72 (s, 2H) ppm.

¹³C-NMR (151 MHz, C₆D₆): δ = 15.1, 16.9, 18.1, 18.9, 26.0, 26.1, 26.1, 26.2, 26.6, 28.7, 29.0, 29.1, 29.2, 29.3, 29.4, 29.5, 29.5, 29.5, 29.6, 29.6, 29.7, 29.7, 29.7, 38.3, 39.6, 51.0, 67.9, 68.1, 68.1, 68.6, 71.5, 71.9, 72.8, 76.3, 108.7, 108.9, 109.9, 114.5, 115.3, 115.4, 115.5, 115.6, 120.0, 120.8, 125.4, 125.7, 126.3, 126.6, 128.3, 130.3, 131.5, 131.6, 133.3, 138.4, 141.6, 142.0, 145.9, 146.0, 150.9, 153.0, 153.3, 153.7, 153.9, 156.0, 156.5, 163.8, 189.4 ppm.

Signals for some carbon atoms are missing due to signal overlap with C₆D₆.

HRMS-ESI (ESI⁺): *m/z* calculated for C₁₀₄H₁₄₂N₆O₁₂SNa⁺ ([M+Na]⁺): 1723.0332, found 1723.0283.

General procedure for the formation of (*S,R,R*)- and (*R,R,R*)- \pm **n**



A stock solution of motor **S21** (1.0 mg, 0.60 μ mol, 1.0 eq.) in C_6D_6 was lyophilized in a J. Young NMR tube. Then, PPh_3 (0.6 mg, 2.4 mmol, 4.0 eq.) was added and the tube was put under high vacuum for 16 h. After that, the solids were dissolved in dry (distilled from CaH_2) and degassed (three freeze-pump-thaw cycles) C_6D_6 or toluene-*d*8 (0.6 mL) inside a glovebox and activated molecular sieves (3 Å) were added. The sealed NMR tube was taken out of the glovebox and heated to 60 °C for 7 d in an oil bath under exclusion of light. Subsequently, the molecular sieves were removed inside a glovebox and the sample was used for further experiments without purification. Since the system is dynamic, the formation of the bridged bis-macrocyclic \pm **n** is concentration dependent. Increasing the concentration leads to formation of an insoluble polymer. The conversion of **S21** to \pm **n** was followed using 1H -NMR spectroscopy by observing the decrease of the aldehyde signal (ca. 9.7 ppm) and increase of imine signals (ca. 8.1 ppm). Typically, bis-macrocyclic \pm **n** forms in 90-95%.

Note that PPh_3 does not engage in any kind of exchange reaction with the imines. Therefore, no influence of PPh_3 on the relaxation rate of wound \pm **n** was observed.

Diastereomer (*S,R,R*)- \pm **n** and its machine-like function was characterized and investigated by HRMS, IMS, CD and NMR spectroscopy, SAXS, and computational studies. Our data supports that the formation of oligomers under our experimental conditions is negligible.

HRMS-ESI (ESI⁺): m/z calculated for $C_{104}H_{143}N_2O_{10}S$ [M+H]⁺: 1613.0492, found: 1613.0484

Comparison of ^1H -NMR spectra of S21, equilibrated, illuminated, and partially relaxed $\pm n$ samples in C_6D_6 at 10°C

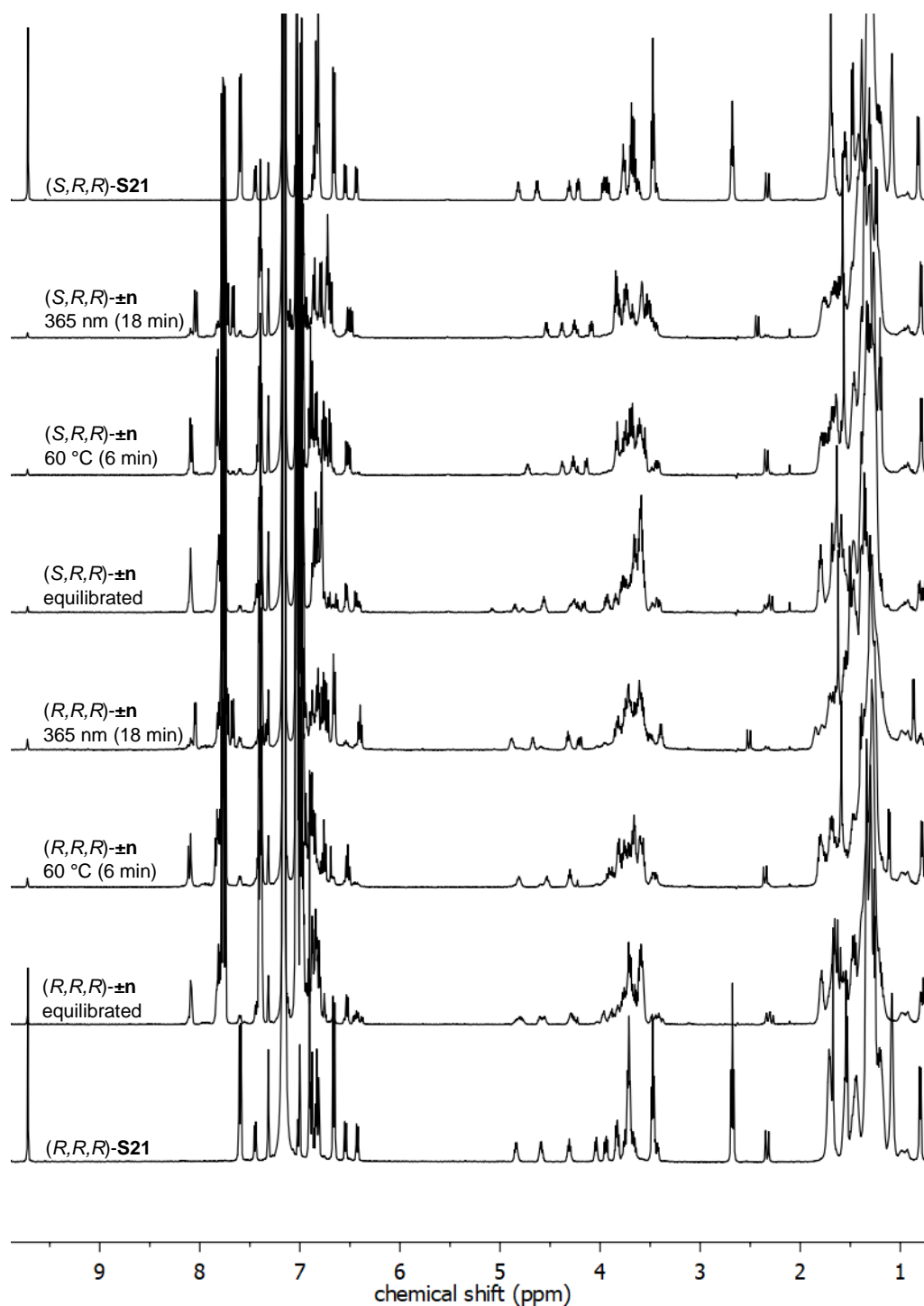
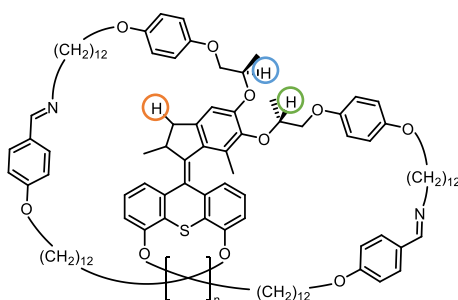
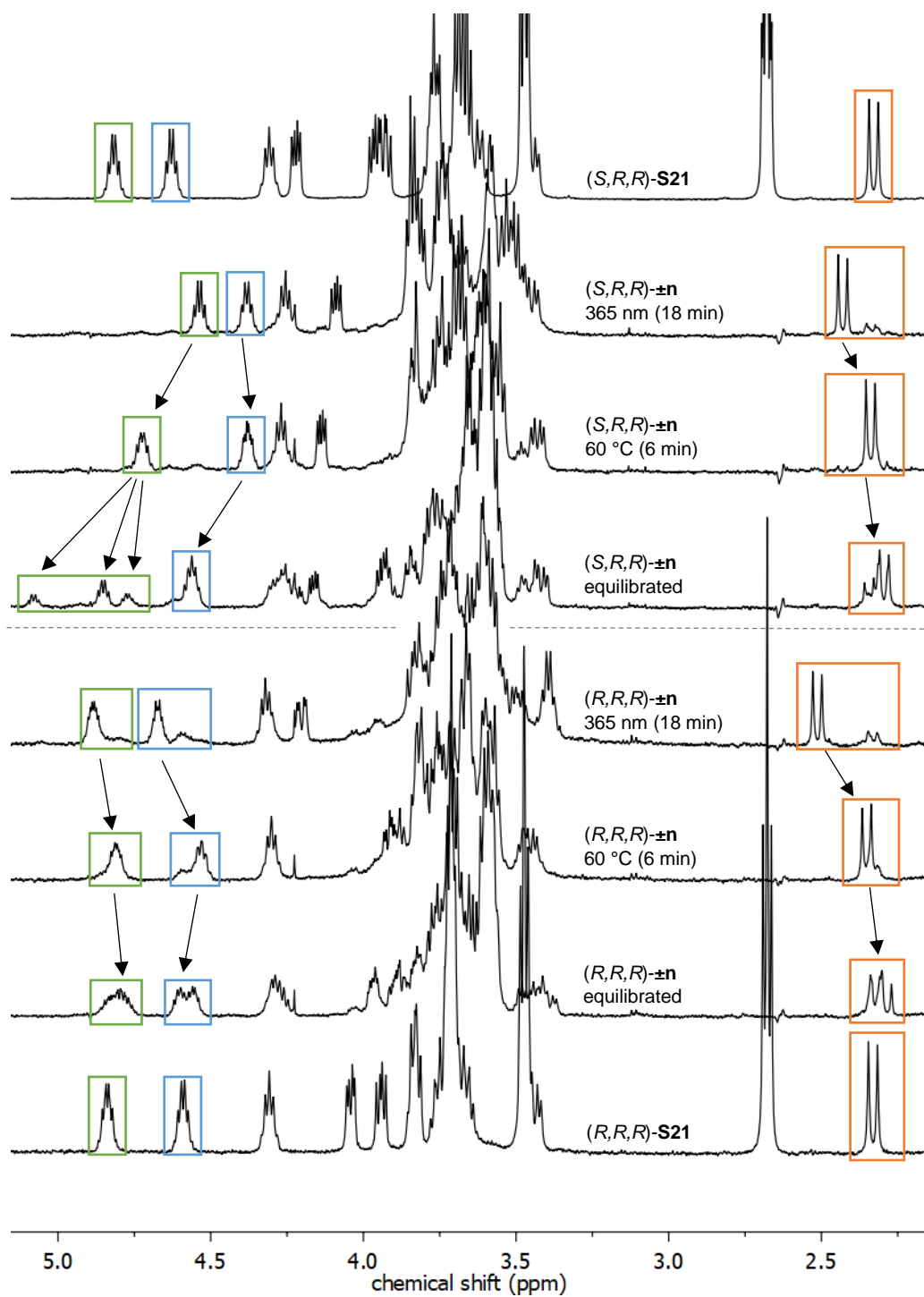
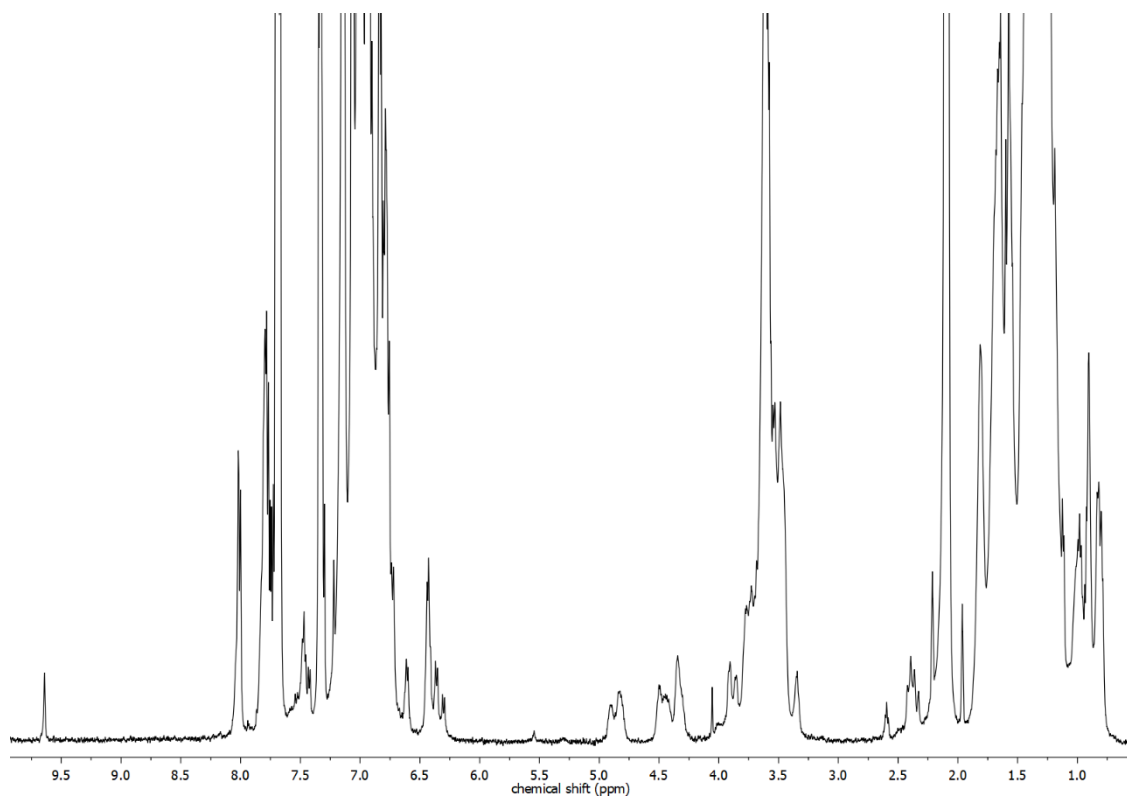


Fig. 1 | Comparison of ^1H -NMR spectra of S21 and $\pm n$ samples at different relaxation stages. C_6D_6 , $c = 1 \text{ mM}$, 10°C , 500 MHz.

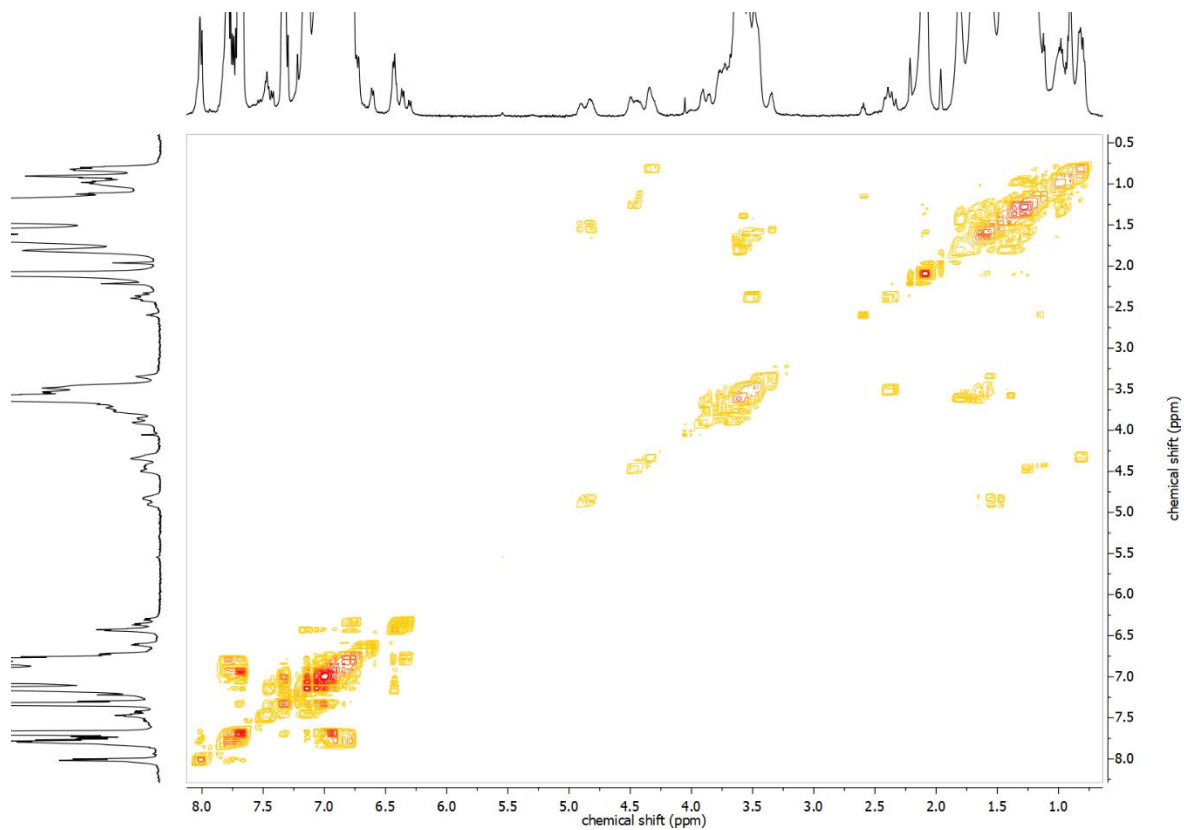


Supplementary Fig. 2 | Comparison of $^1\text{H-NMR}$ spectra of S21 and $\pm n$ samples at different relaxation stages from 5.2 to 2.2 ppm. Arrows indicate interconversion of key signals. C_6D_6 , $c = 1 \text{ mM}$, $10 \text{ }^\circ\text{C}$, 500 MHz .

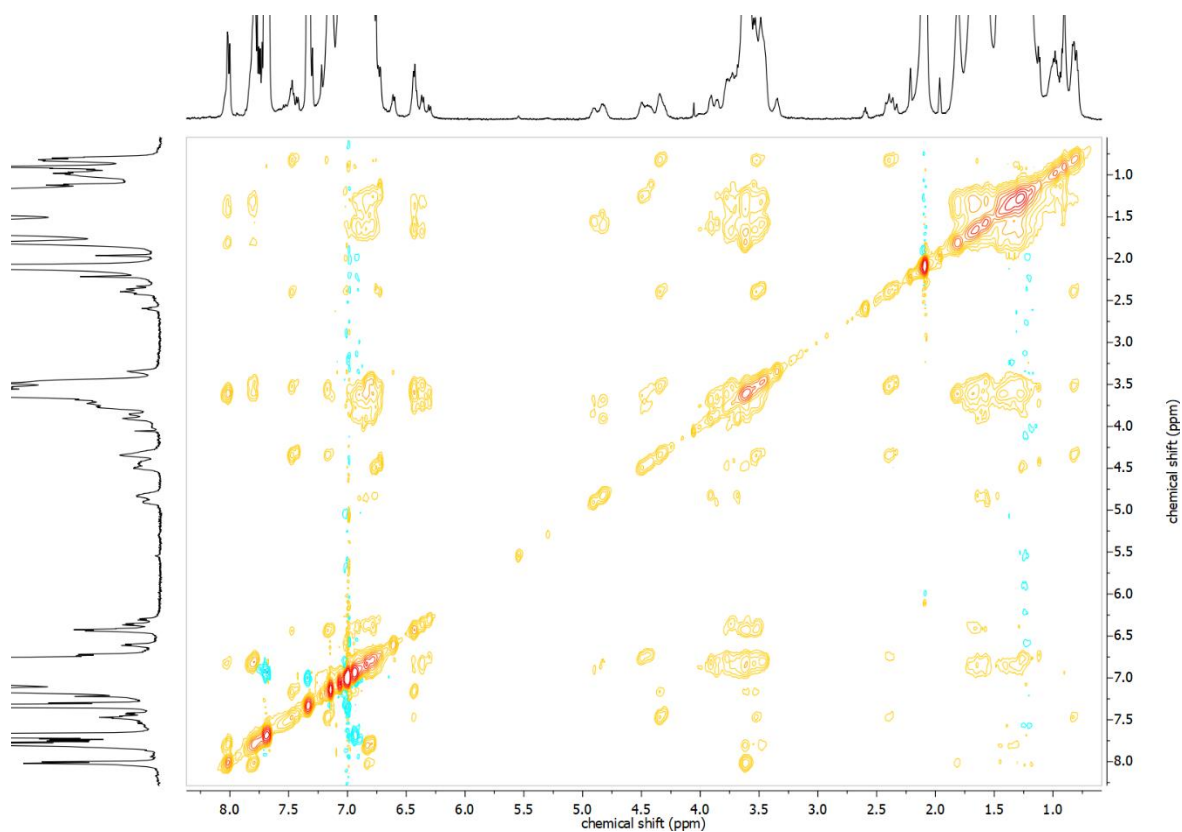
2D NMR spectra of equilibrated (*R,R,R*)-±n sample



Supplementary Fig. S3 | ¹H-NMR spectrum of an equilibrated (*R,R,R*)-±n sample. Toluene-*d*₈, *c* = 1 mM, -40 °C, 500 MHz.

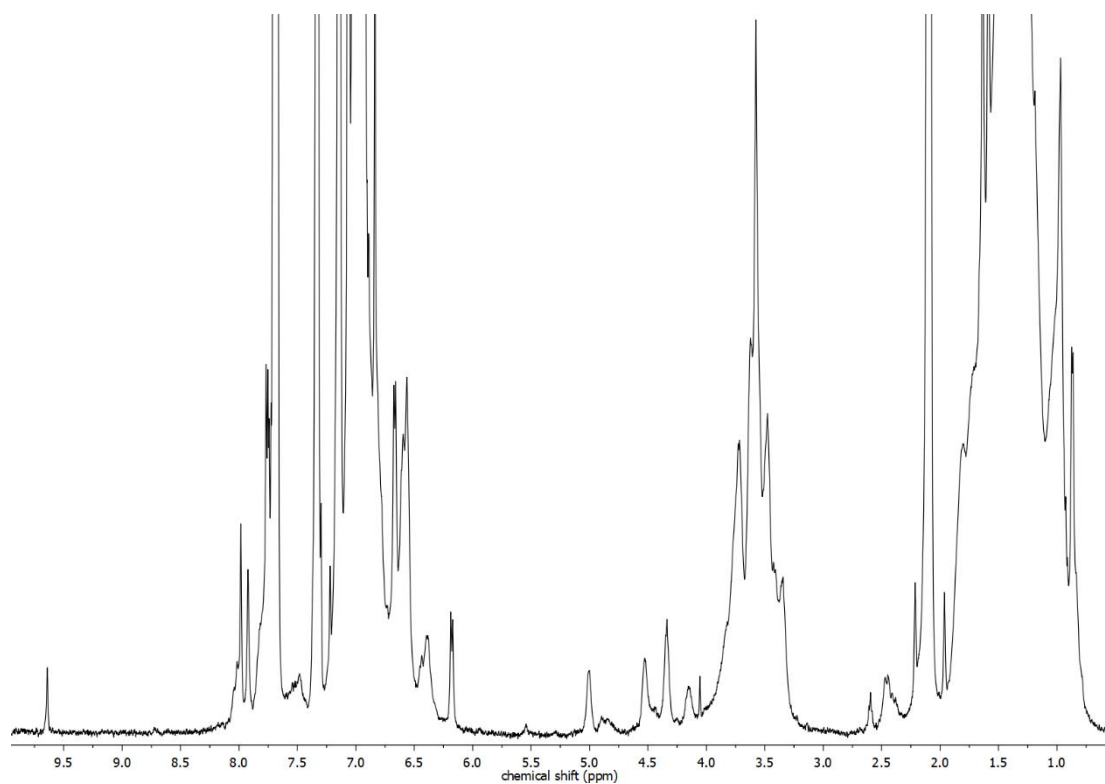


Supplementary Fig. 4 | ¹H, ¹H COSY NMR spectrum of an equilibrated (*R,R,R*)-±n sample. Toluene-*d*₈, *c* = 1 mM, -40 °C, 500 MHz.

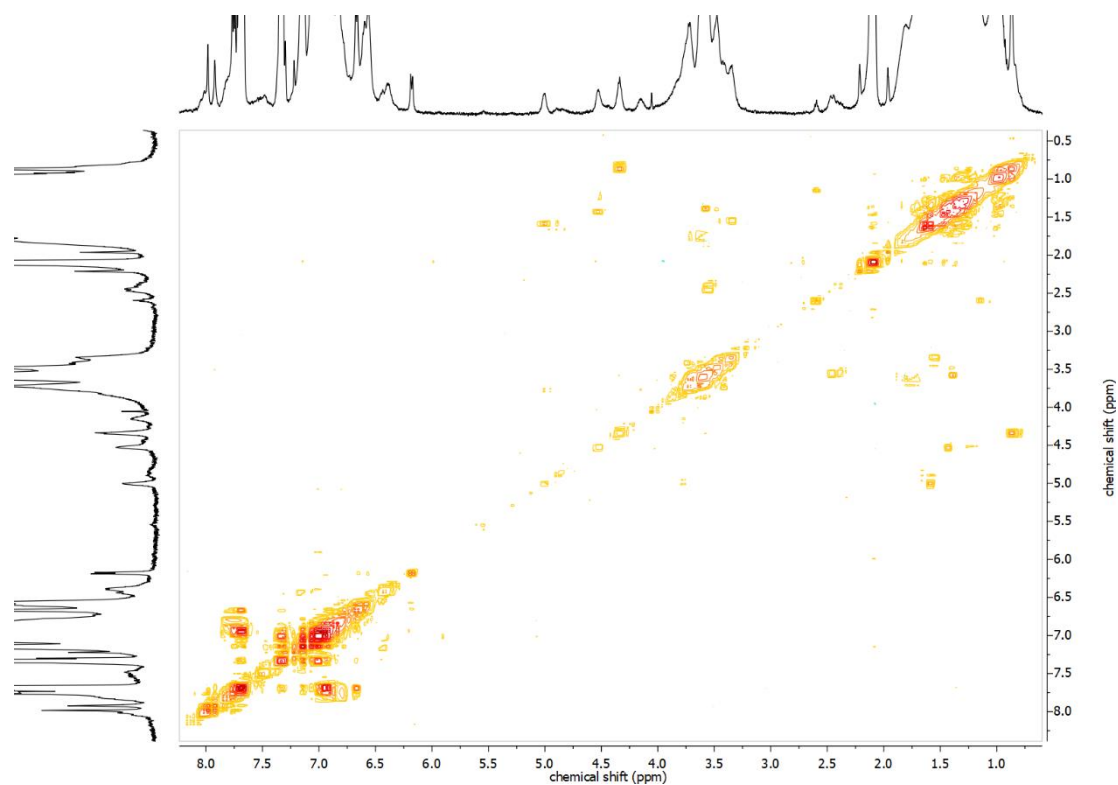


Supplementary Fig. 5 | ^1H , ^1H NOESY NMR spectrum of an equilibrated $(R,R,R)\text{-}\pm n$ sample. Toluene- d_8 , $c = 1 \text{ mM}$, $-40 \text{ }^\circ\text{C}$, 500 MHz .

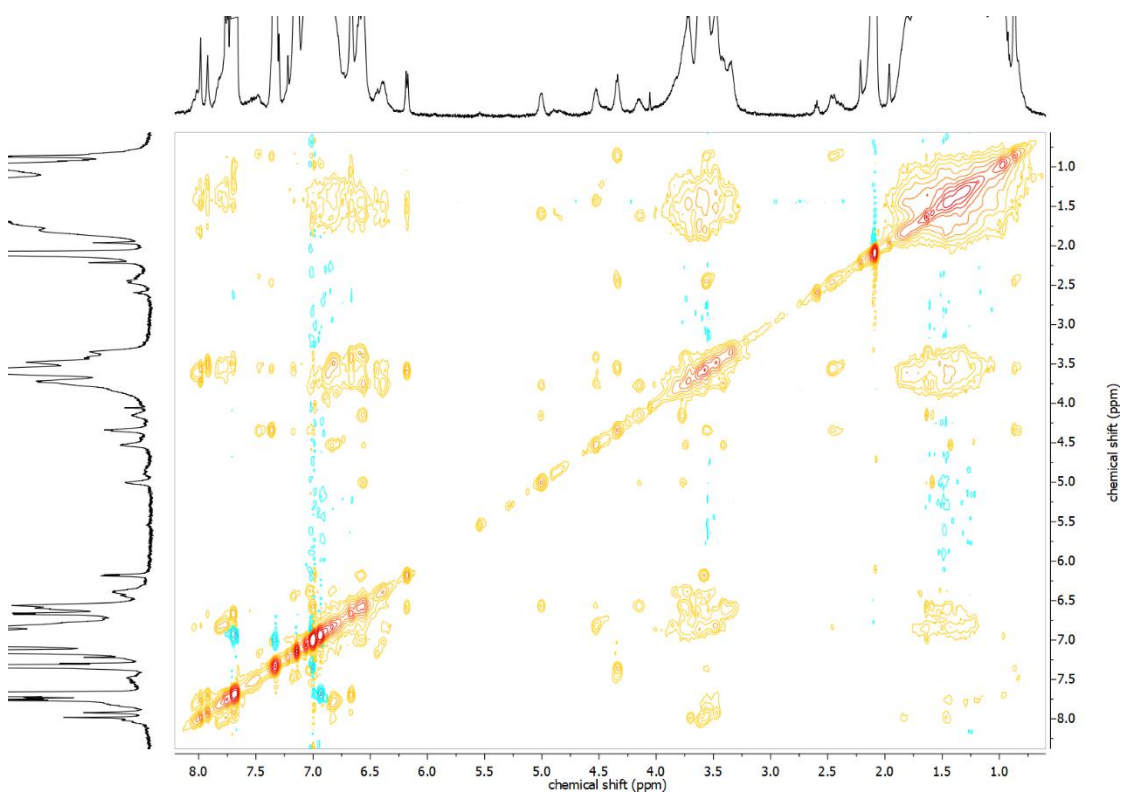
NMR spectra of illuminated $(R,R,R)\text{-}\pm n$ sample



Supplementary Fig. 6 | ^1H -NMR spectrum after illumination of $(R,R,R)\text{-}\pm n$. Toluene- d_8 , $c = 1 \text{ mM}$, $-40 \text{ }^\circ\text{C}$, 500 MHz , $\lambda_{\text{irr}} = 365 \text{ nm}$ (18 min).

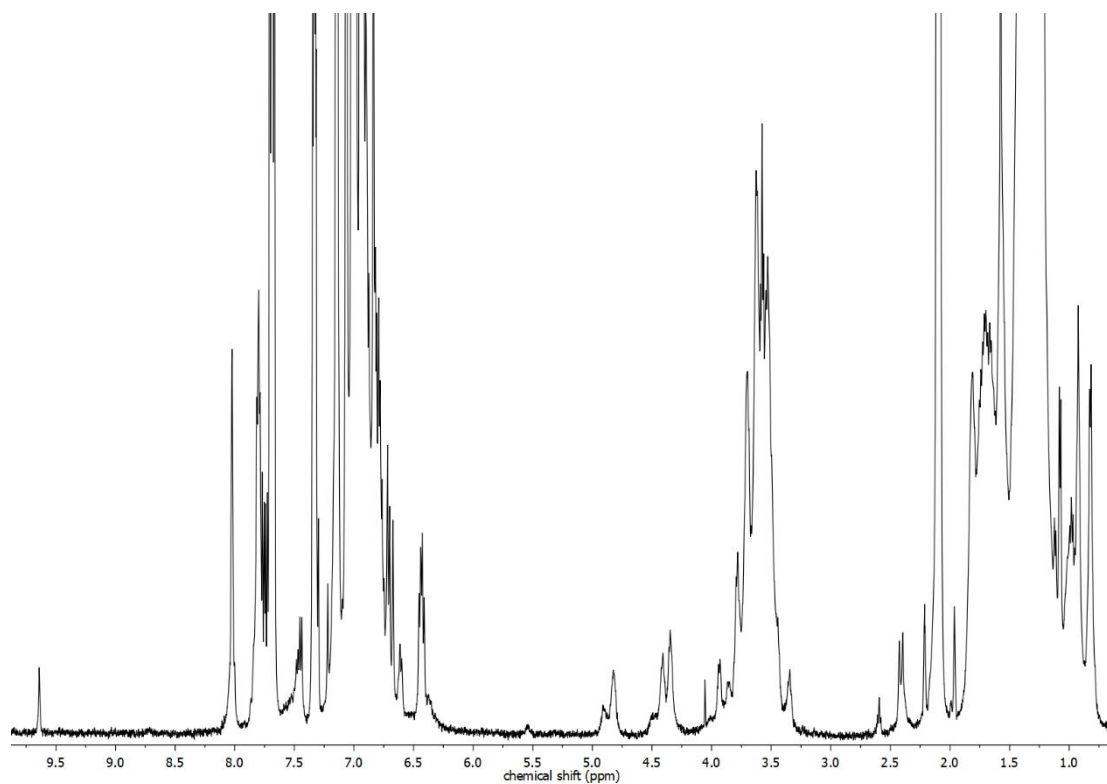


Supplementary Fig. 7 | ^1H , ^1H COSY NMR spectrum after illumination of $(R,R,R)\text{-}\pm\text{n}$. Toluene- d_8 , $c = 1 \text{ mM}$, $-40 \text{ }^\circ\text{C}$, 500 MHz , $\lambda_{\text{irr}} = 365 \text{ nm}$ (18 min).

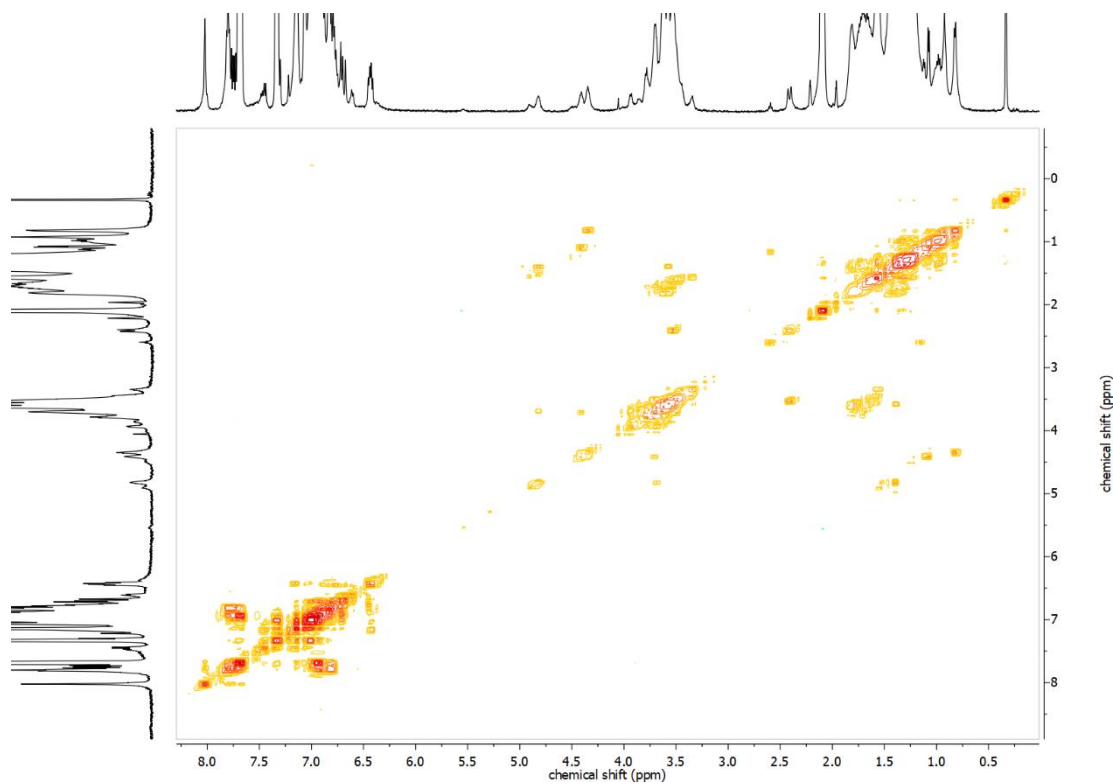


Supplementary Fig. 8 | ^1H , ^1H NOESY NMR spectrum after illumination of $(R,R,R)\text{-}\pm\text{n}$. Toluene- d_8 , $c = 1 \text{ mM}$, $-40 \text{ }^\circ\text{C}$, 500 MHz , $\lambda_{\text{irr}} = 365 \text{ nm}$ (18 min).

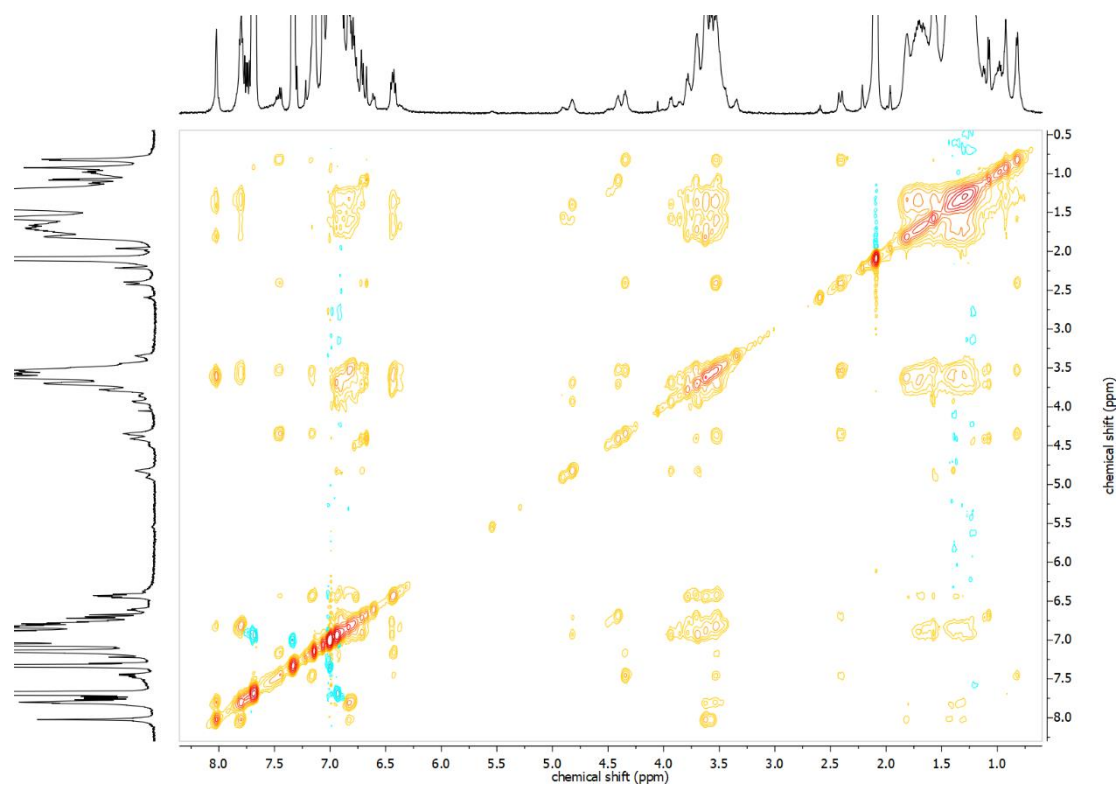
NMR spectra of partially relaxed (*R,R,R*)-±n sample



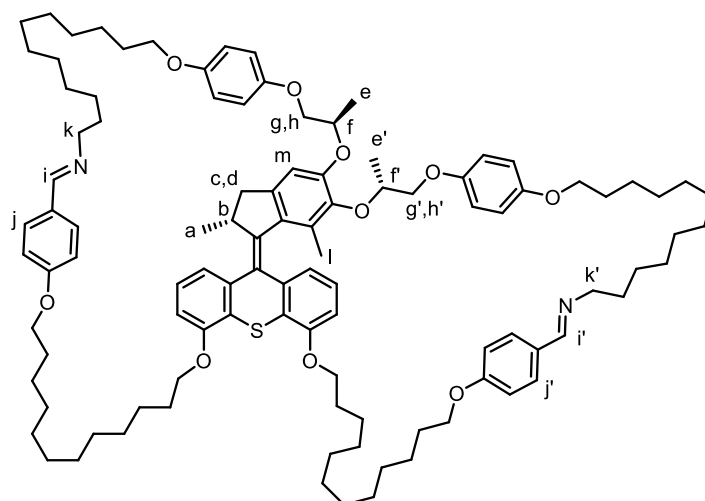
Supplementary Fig. 9 | ¹H-NMR spectrum of (*R,R,R*)-±n sample after 6 min at 60 °C. Toluene-*d*₈, *c* = 1 mM, -40 °C, 500 MHz.



Supplementary Fig. 10 | ¹H,¹H COSY NMR spectrum of (*R,R,R*)-±n sample after 6 min at 60 °C. Toluene-*d*₈, *c* = 1 mM, -40 °C, 500 MHz.



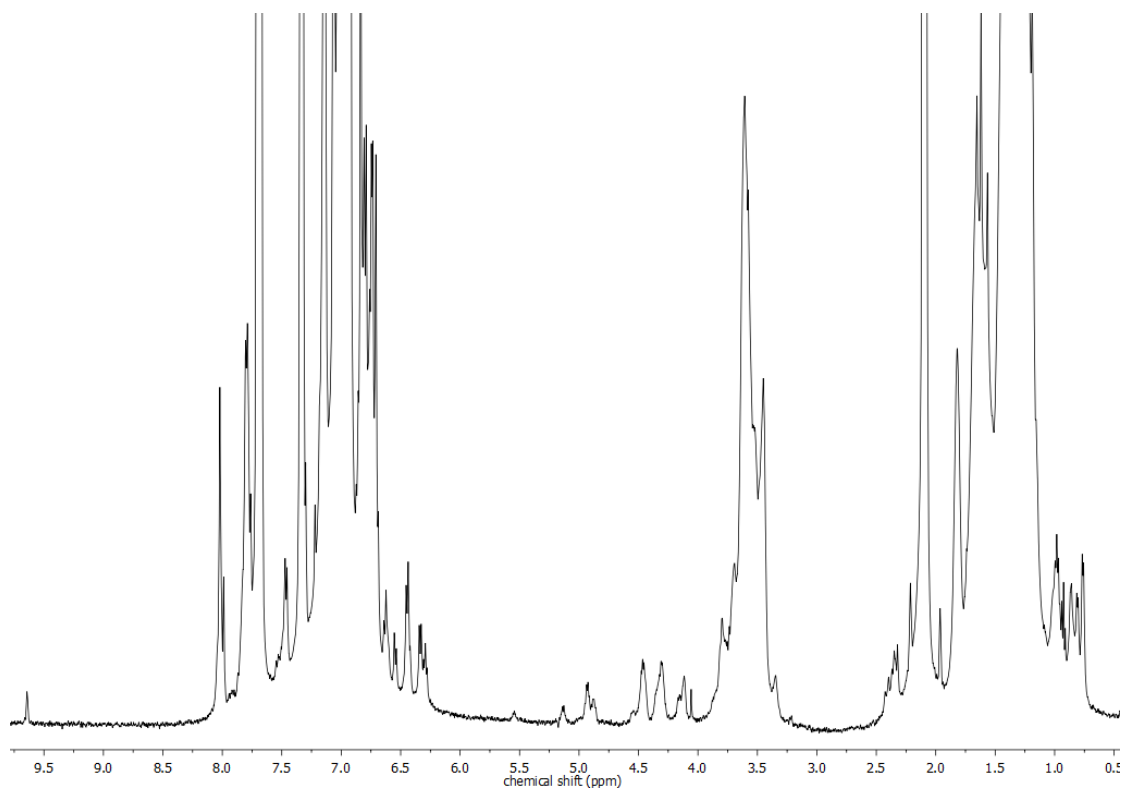
Supplementary Fig. 11 | ¹H, ¹H NOESY NMR spectrum of (*R,R,R*)-±*n* sample after 6 min at 60 °C. Toluene-*d*₈, *c* = 1 mM, -40 °C, 500 MHz.



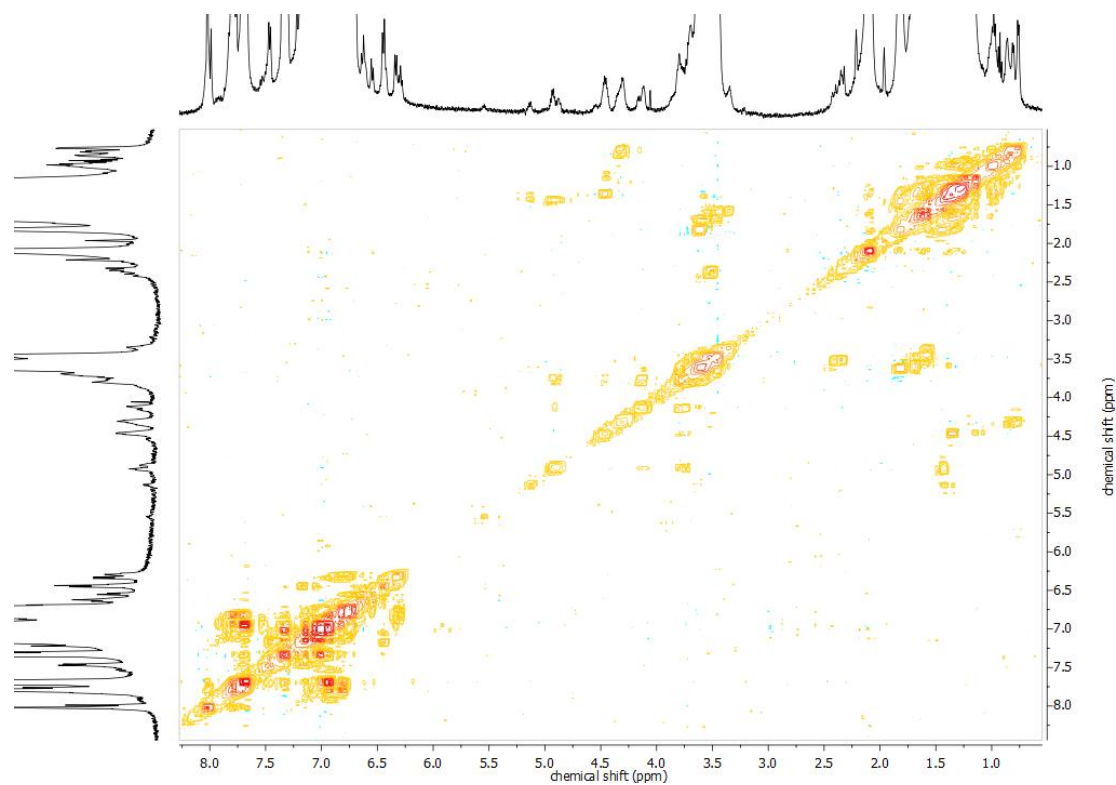
Supplementary Tab. 1 | Chemical shifts of important proton signal of (R,R,R)-±n. Toluene-d₈, c = 1 mM, -40 °C, 500 MHz.

Protons	Equilibrated	Illuminated	Partially relaxed
a	0.82	0.87	0.82
b	4.33	4.34	4.34
c,d	2.39, 3.51	2.44, 3.55	2.40, 3.53
e,e'	1.28, 1.50	1.43, 1.59	1.08, 1.40
f,f'	4.44, 4.50, 4.82, 4.91	4.53, 5.00	4.41, 4.82
g,g',h,h'	3.56, 3.60, 3.69, 3.75, 3.85, 3.90	3.41, 3.74, 3.77, 4.16	3.52, 3.69, 3.72, 3.93
i,i'	8.00, 8.02	7.92, 7.98	8.00
jj'	7.79	7.69, 7.76	7.80
k, k'	3.61	3.49, 3.59	3.60
l	1.61	1.64	-
m	6.75	6.83	6.69

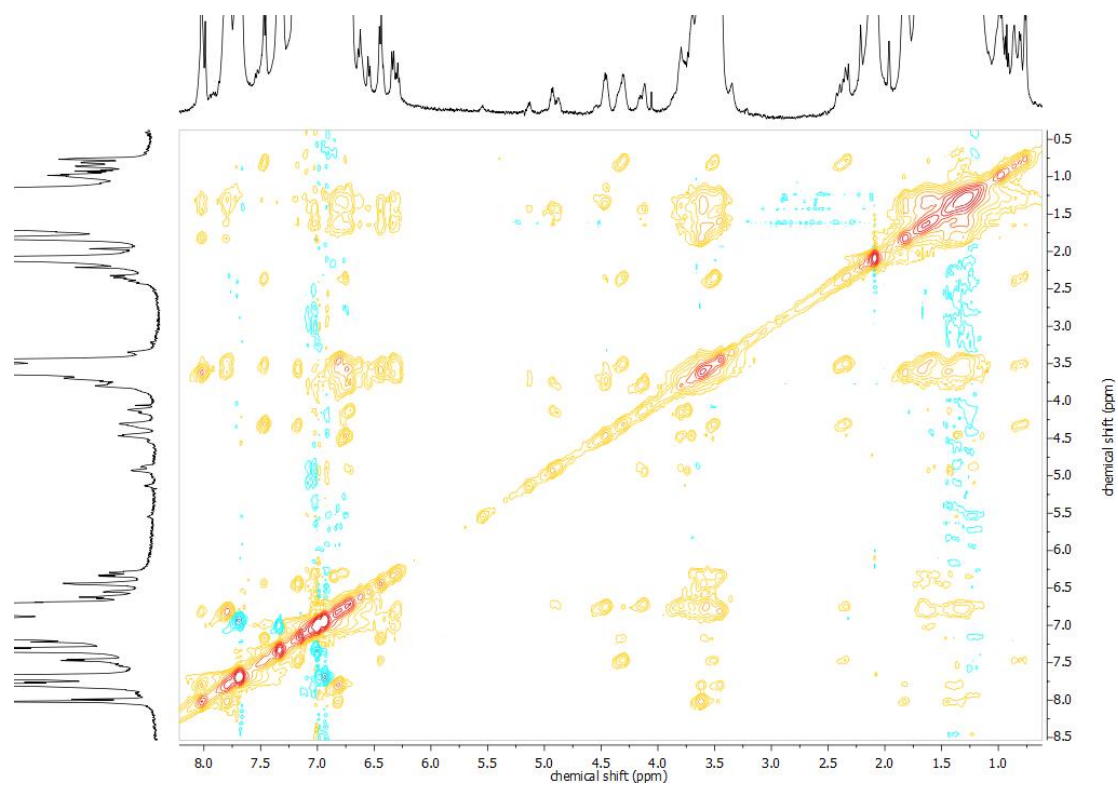
NMR spectra of equilibrated (*S,R,R*)-±n sample



Supplementary Fig. 12 | ¹H-NMR spectrum of an equilibrated (*S,R,R*)-±n sample. Toluene-*d*₈, c = 1 mM, -40 °C, 500 MHz.

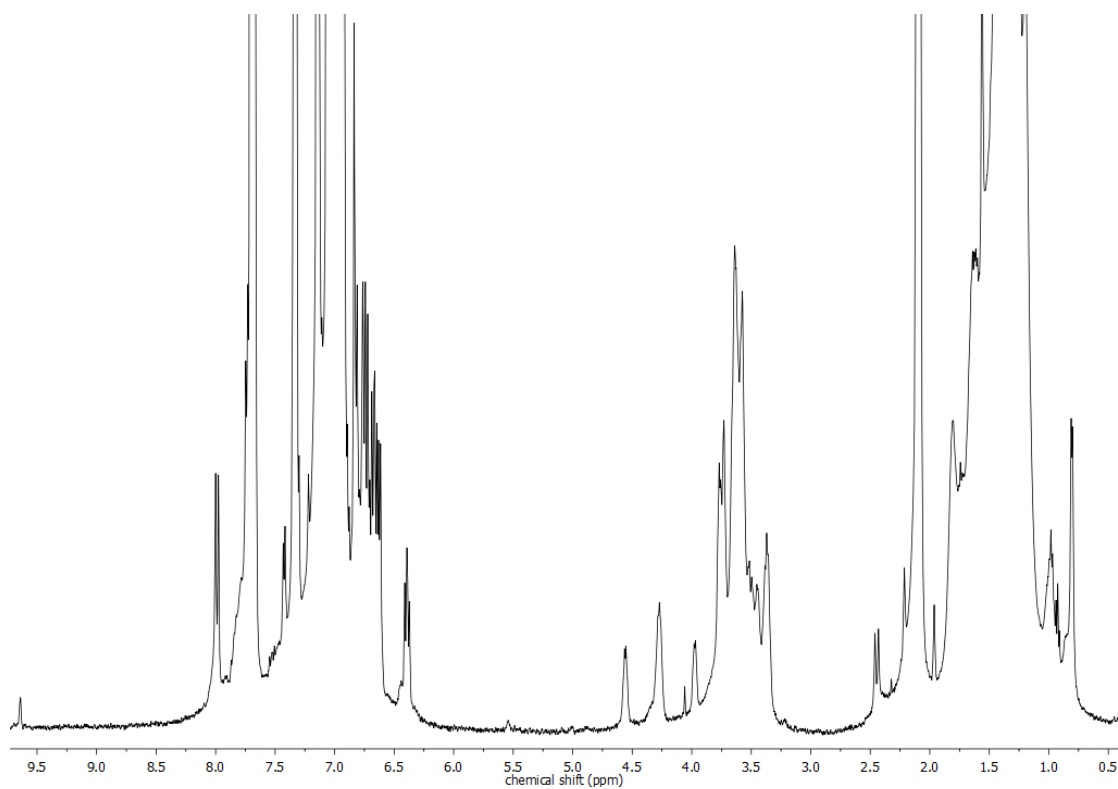


Supplementary Fig. 13 | ¹H, ¹H COSY NMR spectrum of an equilibrated (*S,R,R*)-±n sample. Toluene-*d*₈, c = 1 mM, -40 °C, 500 MHz.

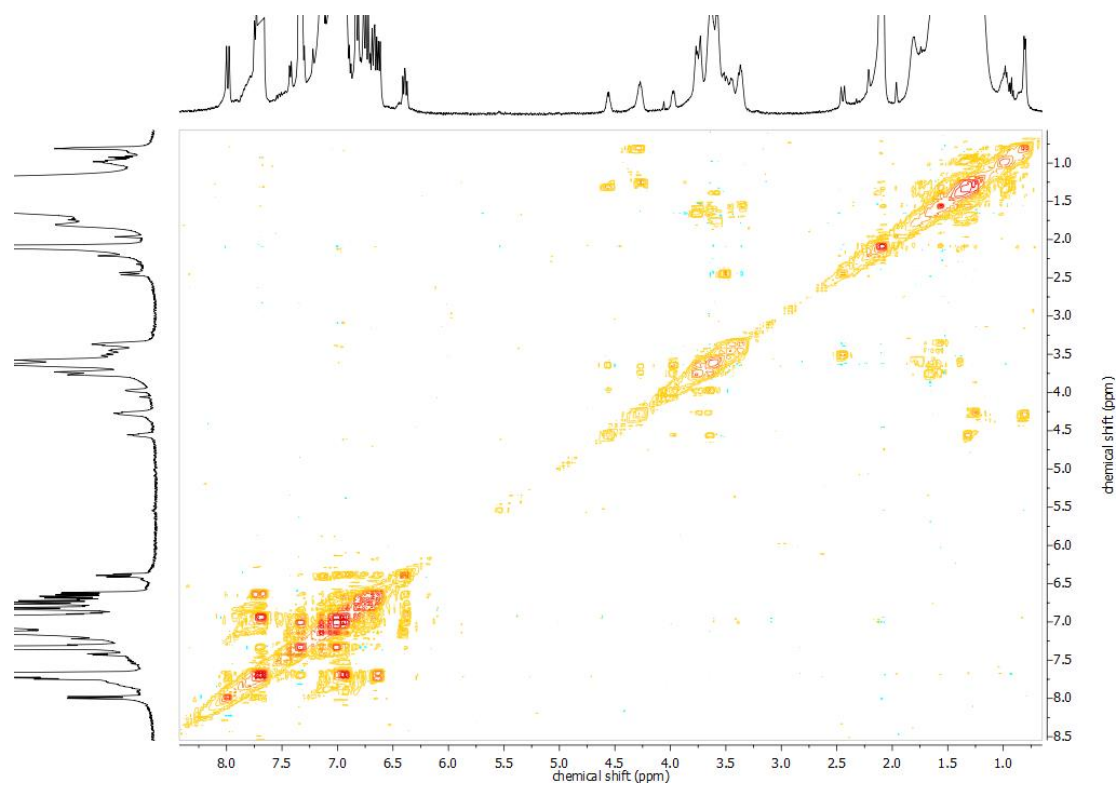


Supplementary Fig. 14 | ^1H , ^1H NOESY NMR spectrum of an equilibrated $(S,R,R)\text{-}\pm n$ sample. Toluene- d_8 , $c = 1$ mM, -40 °C, 500 MHz.

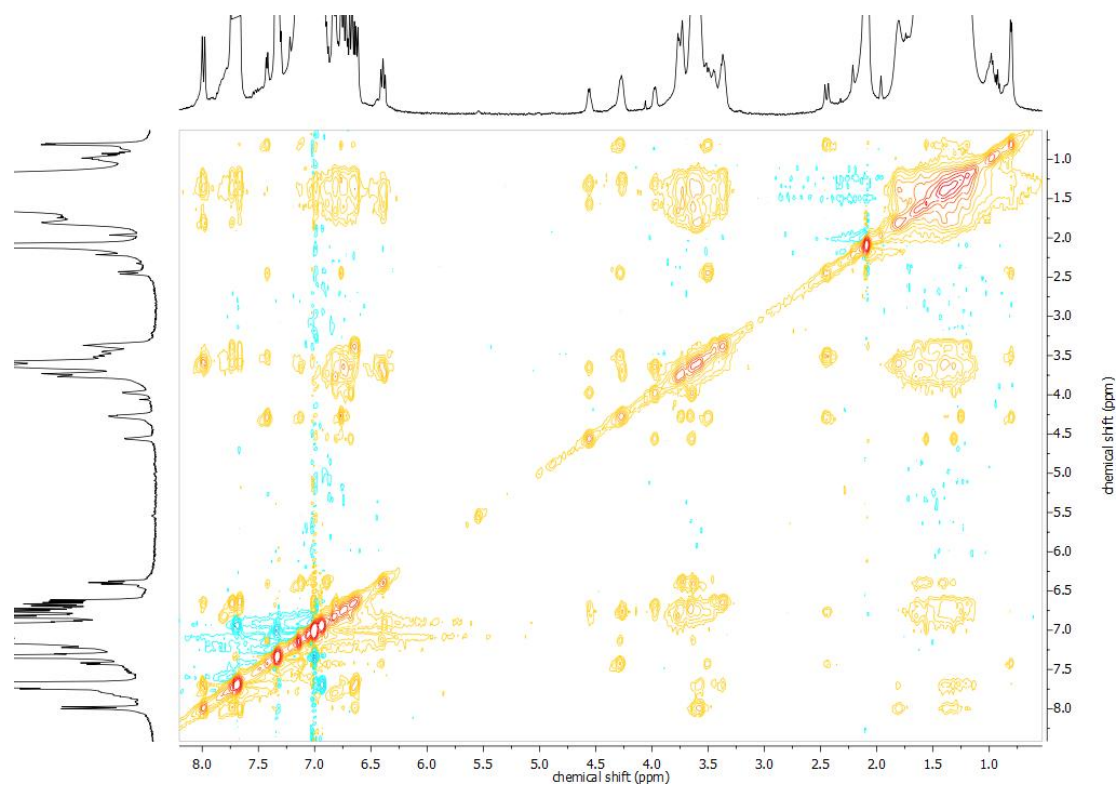
NMR spectra of illuminated $(S,R,R)\text{-}\pm n$ sample



Supplementary Fig. 15 | ^1H -NMR spectrum after illumination of $(S,R,R)\text{-}\pm n$. Toluene- d_8 , $c = 1$ mM, -40 °C, 500 MHz, $\lambda_{\text{irr}} = 365$ nm (18 min).

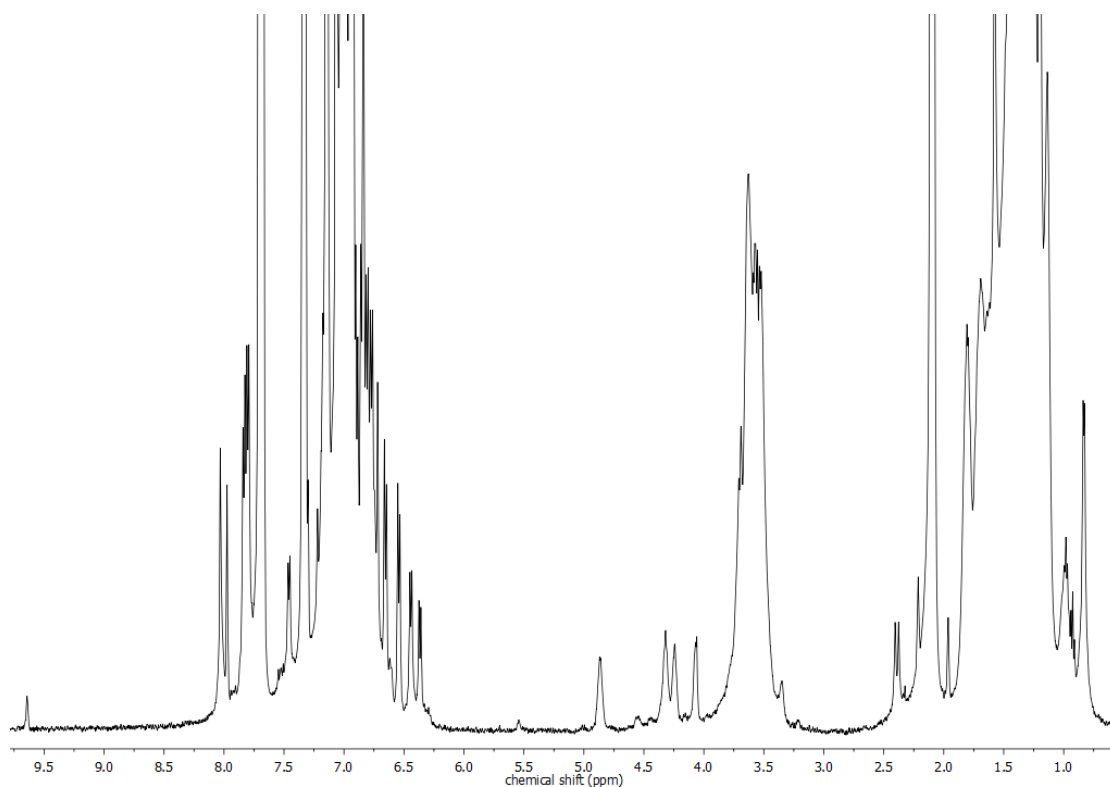


Supplementary Fig. 16 | ^1H , ^1H COSY NMR spectrum after illumination of $(S,R,R)\text{-}\pm\text{n}$. Toluene- d_8 , $c = 1$ mM, -40 $^\circ\text{C}$, 500 MHz, $\lambda_{\text{irr}} = 365$ nm (18 min).

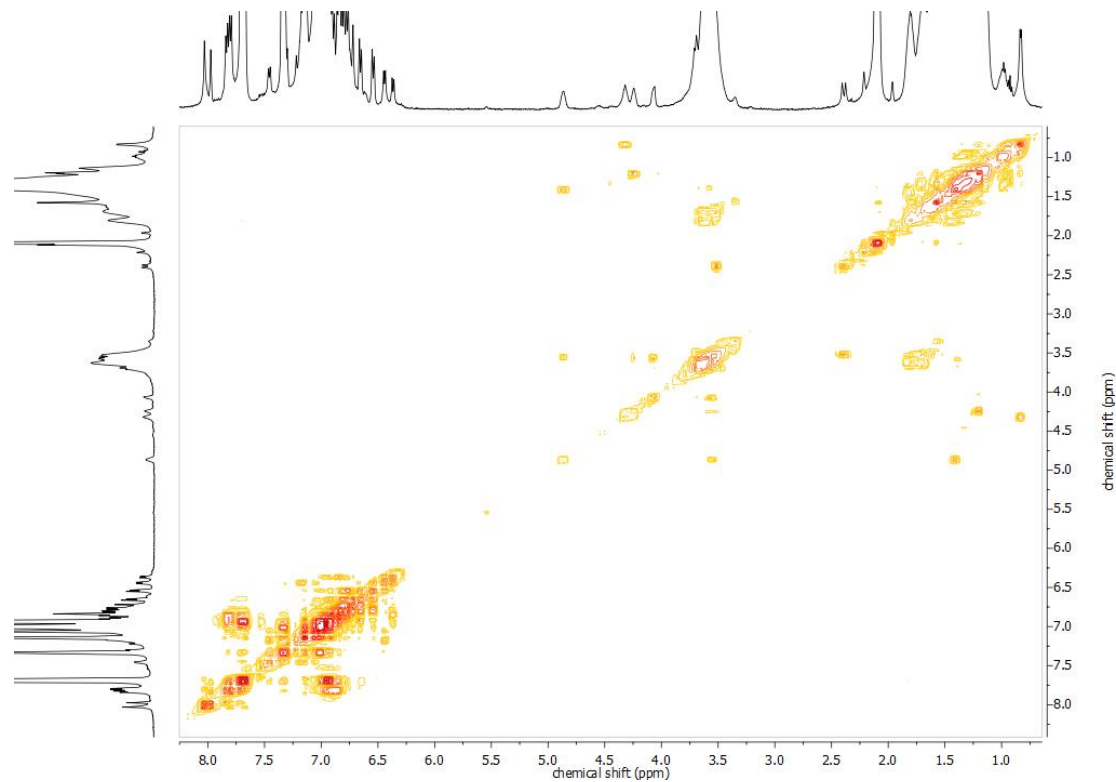


Supplementary Fig. 17 | ^1H , ^1H NOESY NMR spectrum after illumination of $(S,R,R)\text{-}\pm\text{n}$. Toluene- d_8 , $c = 1$ mM, -40 $^\circ\text{C}$, 500 MHz, $\lambda_{\text{irr}} = 365$ nm (18 min).

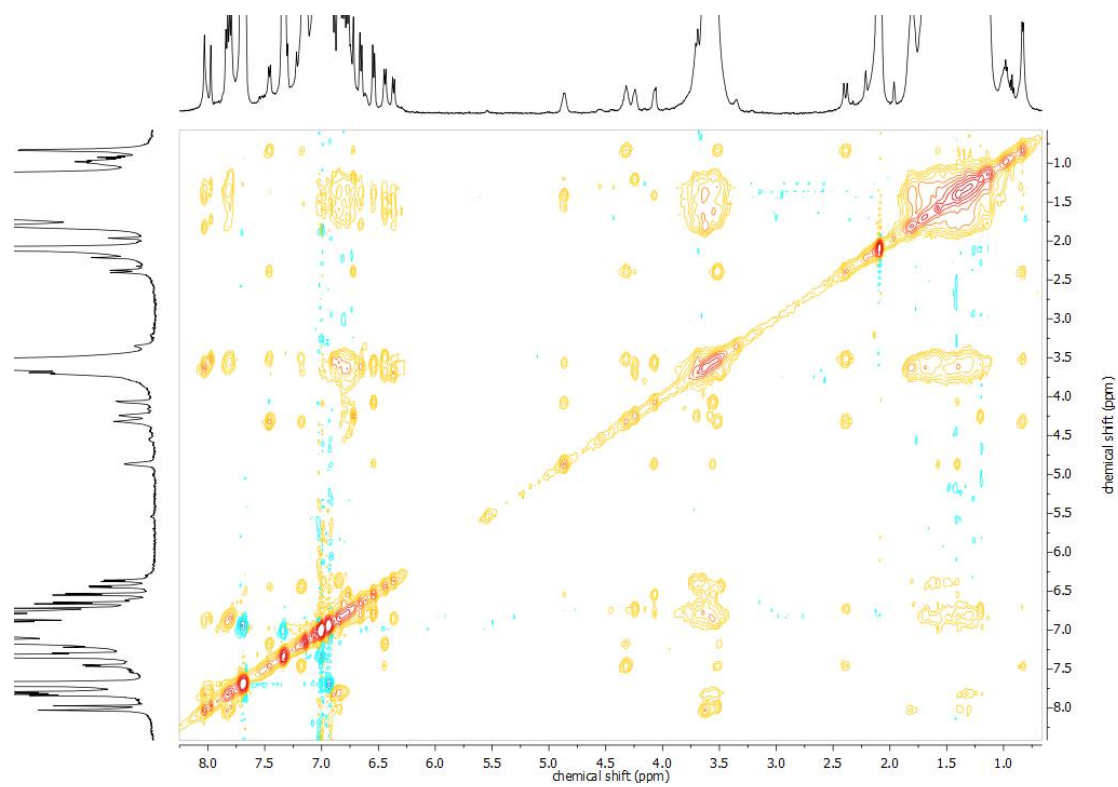
NMR spectra of partially relaxed (*S,R,R*)-±n sample



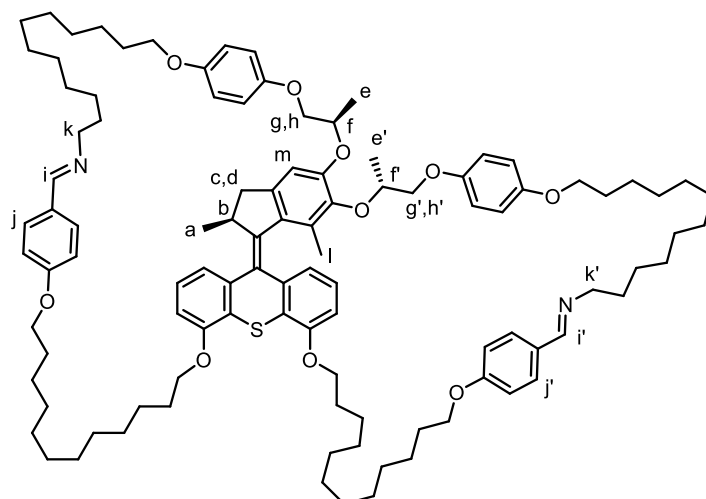
Supplementary Fig. 18 | ^1H -NMR spectrum of (*S,R,R*)-±n sample after 6 min at 60 °C. Toluene-*d*₈, *c* = 1 mM, -40 °C, 500 MHz.



Supplementary Fig. 19 | $^1\text{H},^1\text{H}$ COSY NMR spectrum of (*S,R,R*)-±n sample after 6 min at 60 °C. Toluene-*d*₈, *c* = 1 mM, -40 °C, 500 MHz.



Supplementary Fig. 20 | ^1H , ^1H NOESY NMR spectrum of $(S,R,R)\text{-}\pm n$ sample after 6 min at 60 °C. Toluene- d_8 , $c = 1$ mM, -40 °C, 500 MHz.



Supplementary Tab. 2 | Chemical shifts of important proton signal of (S,R,R)-±n. Toluene-d₈, c = 1 mM, -40 °C, 500 MHz.

Protons	Equilibrated	Illuminated	Partially relaxed
a	0.76, 0.81, 0.86	0.80	0.83
b	4.32	4.30	4.32
c,d	2.36, 3.50	2.45, 3.50	2.39, 3.52
e,e'	1.35, 1.43	1.25, 1.31	1.21, 1.41
f,f'	4.46, 4.87, 4.93, 5.13	4.26, 4.55	4.24, 4.86
g,g',h,h'	3.72, 3.78, 3.76, 4.13, 4.16	3.65, 3.74, 3.64, 3.97	3.59, 3.70, 3.56, 4.08
i,i'	8.02	7.98, 8.00	7.98, 8.03
j,j'	7.80	7.67, 7.74	7.80, 7.83
k,k'	3.47, 3.61	3.59	3.53, 3.62
l	1.56, 1.62, 1.66	1.55	1.58
m	6.71, 6.75	6.77	6.71

Light-driven winding

General illumination conditions

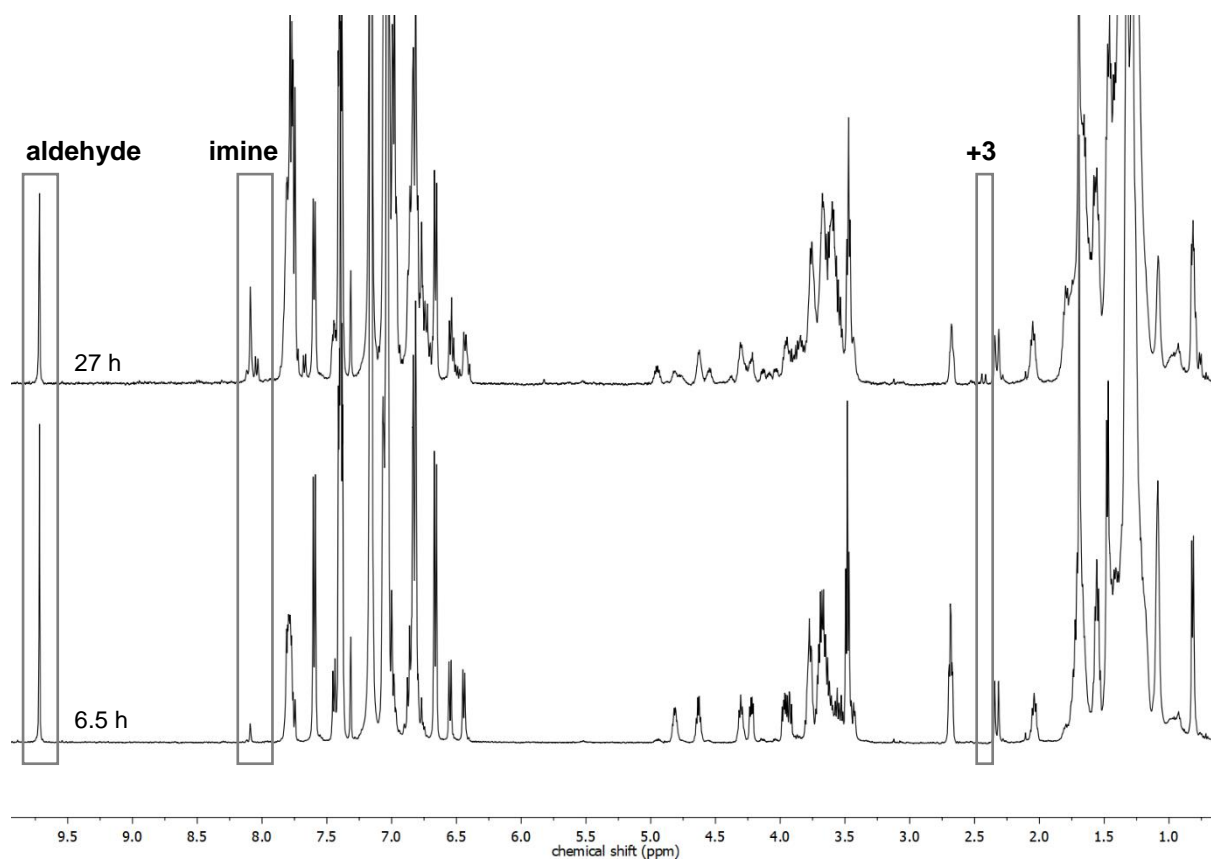
Typically, a J. Young NMR tube containing a 1 mM solution of equilibrated (*S,R,R*) or (*R,R,R*)-**±n** in 0.6 mL C₆D₆ was illuminated with a lamp for TLC control (365 nm, 6 W) on a shaker plate for 18 min at 8 °C (in a walkable fridge) or room temperature. The distance between lamp and NMR tube was kept constant throughout the experiment. To prevent any significant relaxation, illuminated samples were cooled with a 10 °C acetone bath before the respective measurement.

Stability towards oxygen

Under a nitrogen atmosphere, a sample can be irradiated and relaxed at elevated temperatures several times without noticeable fatigue. Note, that trace amounts of oxygen cannot be fully avoided, which over time has a noticeable impact on the highly dilute samples. First, residual PPh₃ acts as an oxygen scavenger and is oxidized to OPPh₃, which is then followed by photo-decomposition of (*S,R,R*) or (*R,R,R*)-**±n** upon irradiation with UV light of 365 nm. A similar behavior was observed for a comparable system by Giuseppe and co-workers ⁶.

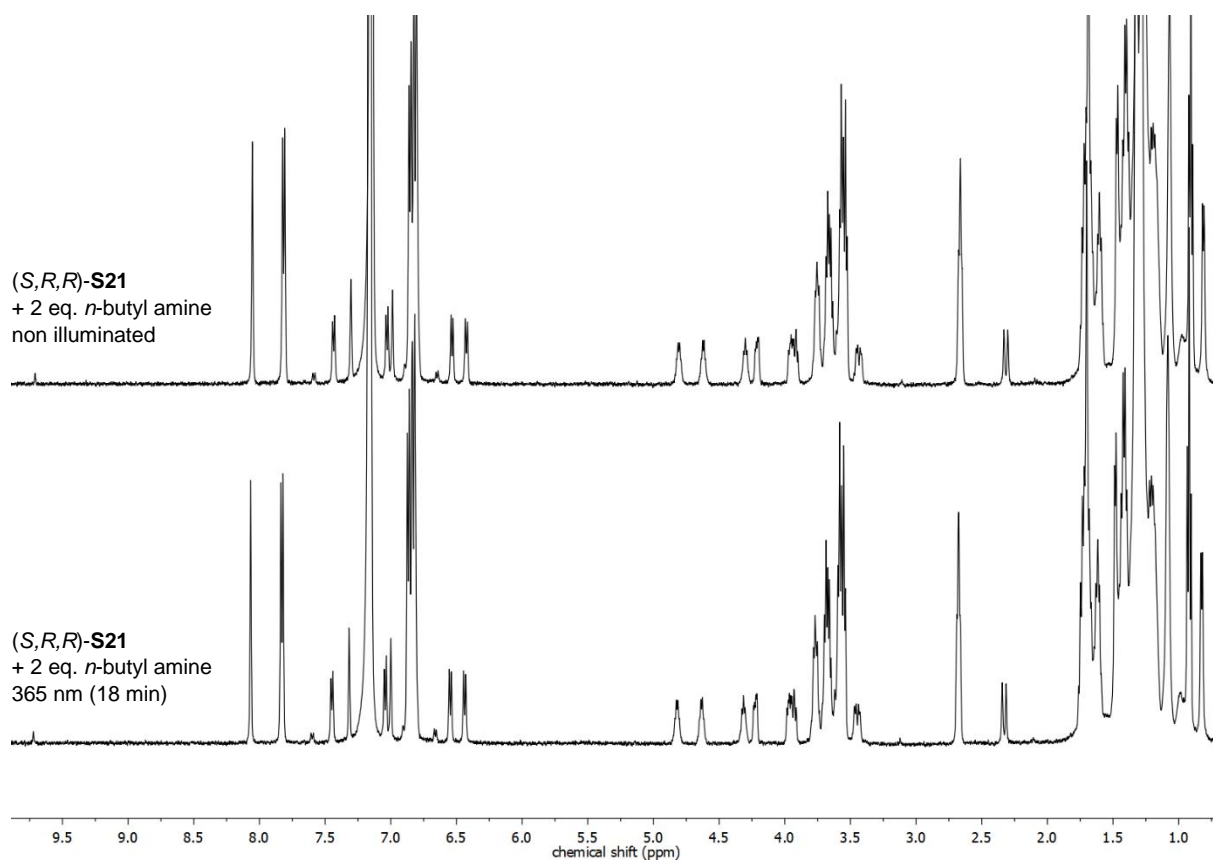
Control experiments

To check if bis-macrocyclization of the motor is necessary for the winding mechanism, a 1 mM solution of bis-azide (*S,R,R*)-**S21** in C₆D₆ was illuminated for 18 min with UV light of 365 nm. No noticeable change in the ¹H-NMR spectrum was observed. Furthermore, we investigated the influence of different macrocyclization stages of (*S,R,R*)-**S21** on the winding process. Therefore, we illuminated ($\lambda_{\text{irr}} = 365 \text{ nm}$, 18 min) a sample that was prepared according to the general procedure for imine macrocyclization after a reaction time of 6.5 h (7% aldehyde conversion) and 27 h (50% aldehyde conversion). This led to the formation of (*S,R,R*)-**+3** in 0% and 10% yield, respectively (Supplementary Fig. 21).



Supplementary Fig. 21 | $^1\text{H-NMR}$ spectra after illumination of partially macrocyclized bis-azide (S,R,R)-S21**.** After a reaction time of 6.5 h (7% aldehyde conversion, bottom) and 27 h (50% aldehyde conversion, top), (S,R,R)-**+3** forms in 0% (bottom) and 10% (top), respectively upon UV light illumination. C_6D_6 , $c = 1 \text{ mM}$, $10 \text{ }^\circ\text{C}$, 500 MHz, $\lambda_{\text{irr}} = 365 \text{ nm}$ (18 min).

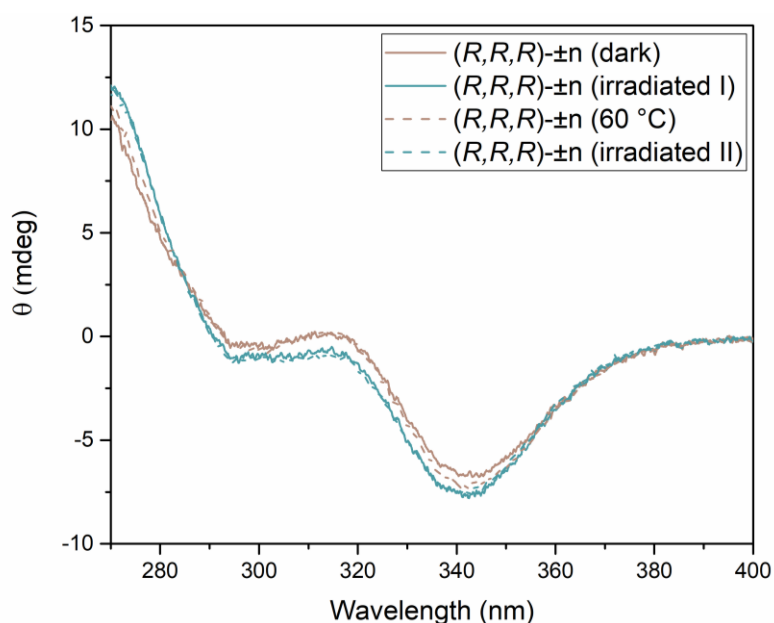
We also prepared the *n*-butyl bis-imine of compound (S,R,R)-**S21** in C_6D_6 (0.6 mL, 1 mM) by *in-situ* condensation with *n*-butyl imine (2 eq.). Almost quantitative conversion was observed after three d at $60 \text{ }^\circ\text{C}$ in presence of 3 \AA molecular sieves. Also in this case, no change was observed after illumination with UV light of 365 nm for 18 min (Supplementary Fig. 22).



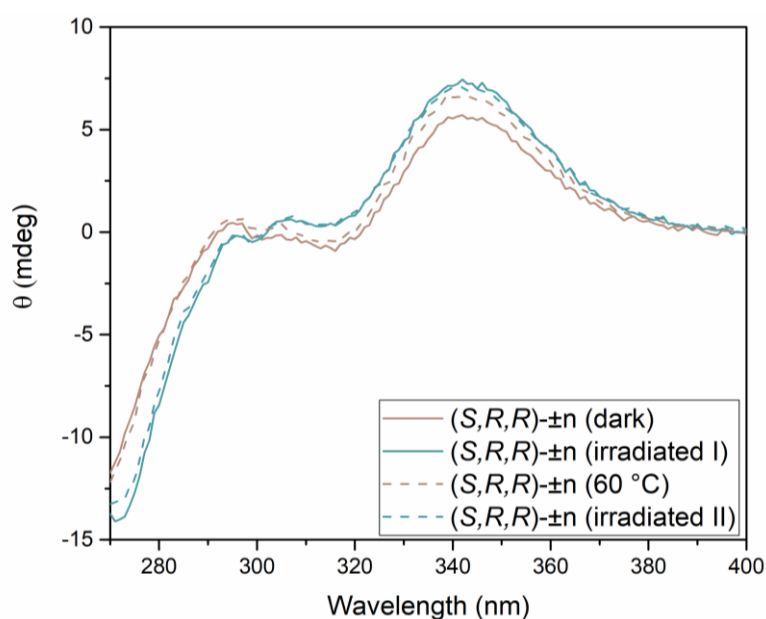
Supplementary Fig. 22 | $^1\text{H-NMR}$ spectra before and after illumination of (*S,R,R*)-**S21** bis-*n*-butyl amine. No winding of the motor was observed. C_6D_6 , $c = 1 \text{ mM}$, $10 \text{ }^\circ\text{C}$, 500 MHz , $\lambda_{\text{irr}} = 365 \text{ nm}$ (18 min).

CD Spectroscopy

In a cuvette, 30 μL of a solution of (R,R,R) - or (S,R,R) - $\pm\mathbf{n}$ (1 mM in C_6D_6) was diluted with degassed and dry THF to a total volume of 3 mL ($c = 10 \mu\text{M}$). Benzene absorbs in the deep UV region and forces a cut-off at 270 nm. Spectra of illuminated samples were either recorded after *in-situ* illumination with a TLC lamp at 365 nm for 5 min (the distance between the cuvette and the lamp was ~ 2 cm) or by diluting a pre-illuminated sample at PSS with THF. Partial relaxation of the irradiated sample was achieved by heating the sample to 60 $^\circ\text{C}$ for 10 min. Subsequent *in-situ* illumination showed that the process is reversible (Figs. 23 and 24).

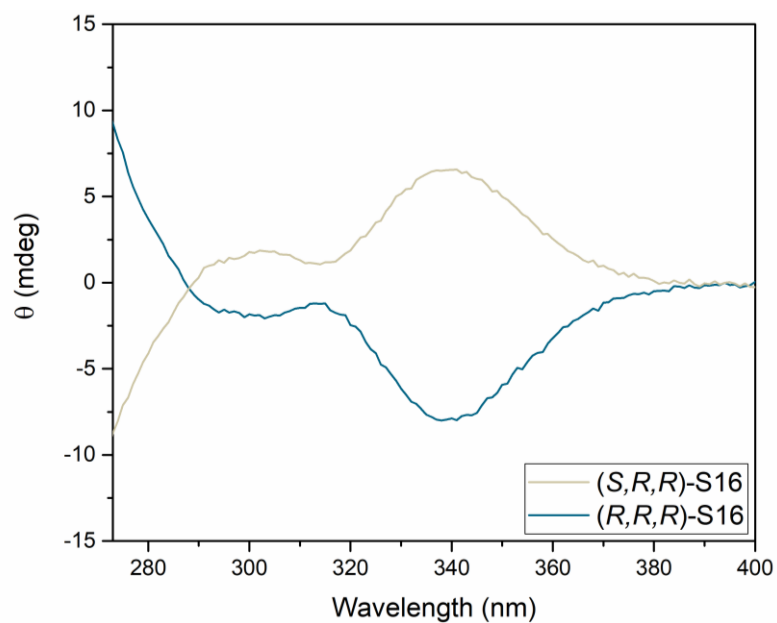


Supplementary Fig. 23 | CD spectra of (R,R,R) - $\pm\mathbf{n}$. Fully relaxed (brown, solid line), illuminated (blue, solid line), relaxed at 60 $^\circ\text{C}$ for 10 min (brown, dotted line), and illuminated (blue, dotted line). THF, $c = 1 \cdot 10^{-5}$ M, 0 $^\circ\text{C}$, $\lambda_{\text{irr}} = 365$ nm (18 min).



Supplementary Fig. 24 | CD spectra of (S,R,R) - $\pm\mathbf{n}$. Fully relaxed (brown, solid line), illuminated (blue, solid line), relaxed at 60 $^\circ\text{C}$ for 10 min (brown, dotted line), and illuminated (blue, dotted line). THF, $c = 1 \cdot 10^{-5}$ M, 0 $^\circ\text{C}$, $\lambda_{\text{irr}} = 365$ nm (18 min).

CD spectra for fully protected motors (*R,R,R*)-S16 and (*S,R,R*)-S16 were recorded as reference spectra (Supplementary Fig. 25).



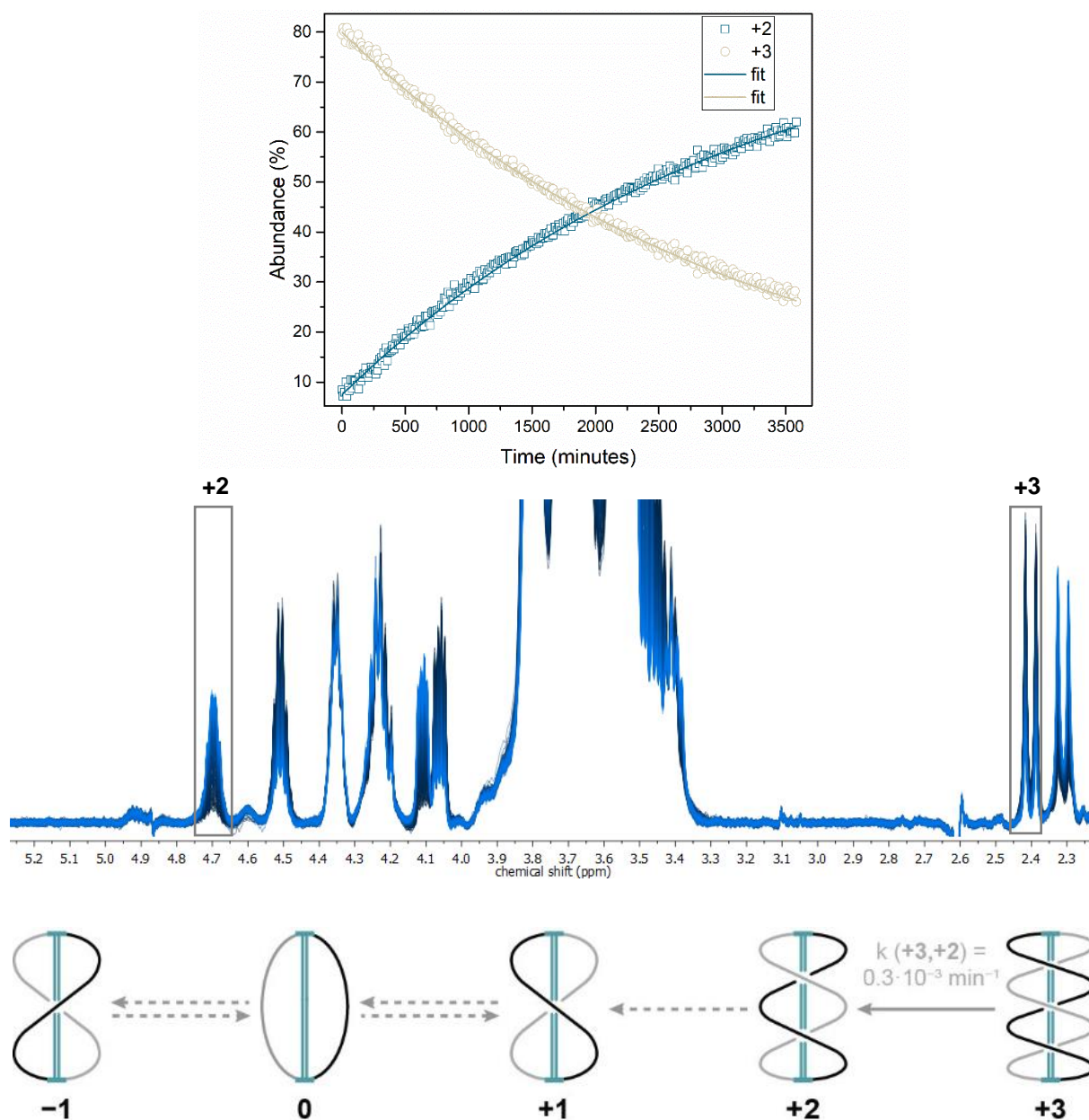
Supplementary Fig. 25 | CD spectra of (*R,R,R*)-S16 and (*S,R,R*)-S16. THF, $c = 1 \cdot 10^{-5}$ M, 0 °C.

NMR Experiments and Kinetic Analysis

General

All experiments were conducted on a Varian AVIII 500 NMR spectrometer that was pre-cooled or -warmed to the proper temperature. (S,R,R) - \pm n samples were typically equilibrated for 5 min inside the instrument until the lock signal reached a constant value. All samples were prepared according to the general procedure and were usually equilibrated at 60 °C. The experimental data were subsequently fitted using COPASI 4.29⁷. In order to obtain a fit that could give a realistic approximation of the irreversible and reversible reactions involved in each experiment, we simulated a reaction compartment of 0.6 mL (to match the volume of the solution of a typical NMR experiment) with concentration of the species involved of 1 mM. In all cases, the time unit used was minutes. The default Levenberg-Marquardt algorithm with a tolerance of $1 \cdot 10^{-6}$ implemented in COPASI was used. The initial guess for the kinetic parameter estimation was to consider all species in equilibrium with one another. After every fitting run, visual inspection of the error associated to each kinetic constant provided indication of the relevance of a certain reaction. Kinetic constants with absolute values lower than 10^{-6} min^{-1} were approximated to 0 and the respective reaction deleted in the next iteration. In the following section, the fitting of the experimental values, along with the kinetic model and the associated constants will be provided. For clarity, only a representative example of each dataset is presented. For all the output files of our kinetic simulations see Supplementary Data Set 1.

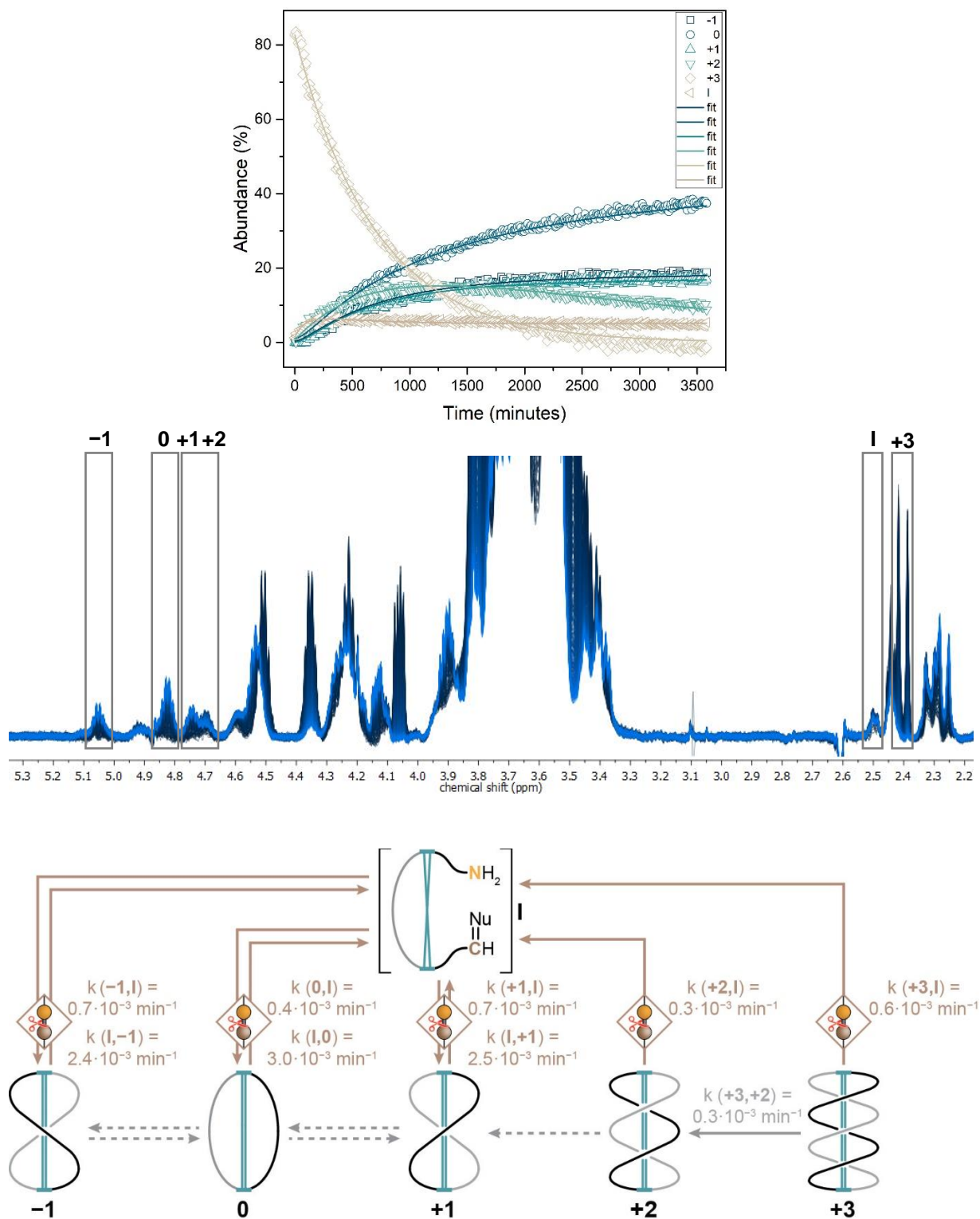
Relaxation kinetics of a (*S,R,R*)-±n sample at 10 °C without nucleophile.



Supplementary Fig. 26 | Relaxation of a (*S,R,R*)-±n sample at 10 °C without nucleophile. Kinetic trace of a representative example with fit (top), NMR stack (middle) and proposed mechanism with average rate constants (bottom). C_6D_6 , $c = 1$ mM, 500 MHz.

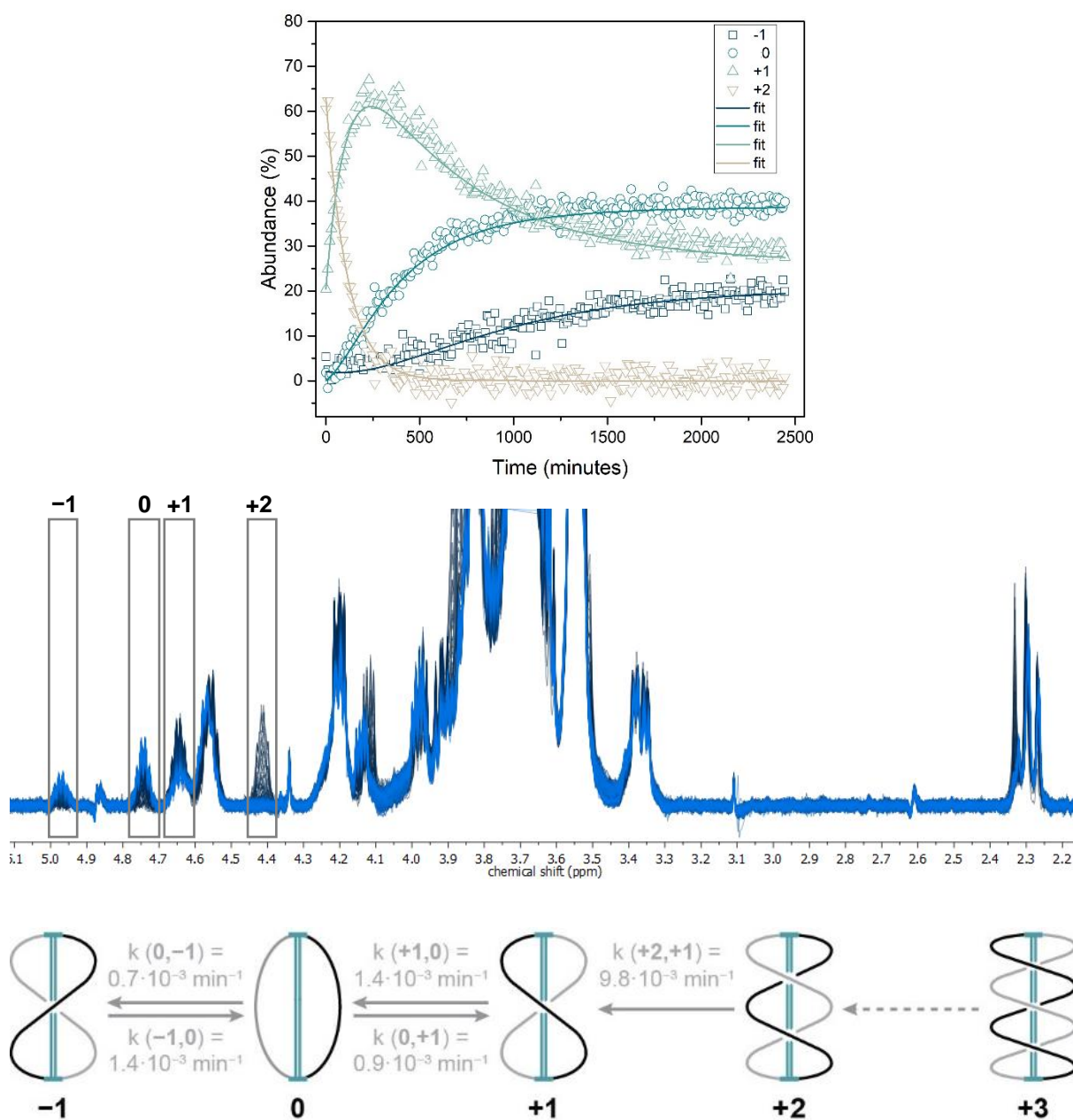
Relaxation kinetics of a (S,R,R) - $\pm n$ sample at 10 °C with 20 mol% n -butyl amine

The amine (as a stock solution in deuterated benzene) was added inside a glovebox to a pre-illuminated (S,R,R) - $\pm n$ sample (according to the general procedure). The same samples as for the relaxation experiment at 10 °C without nucleophile was used.



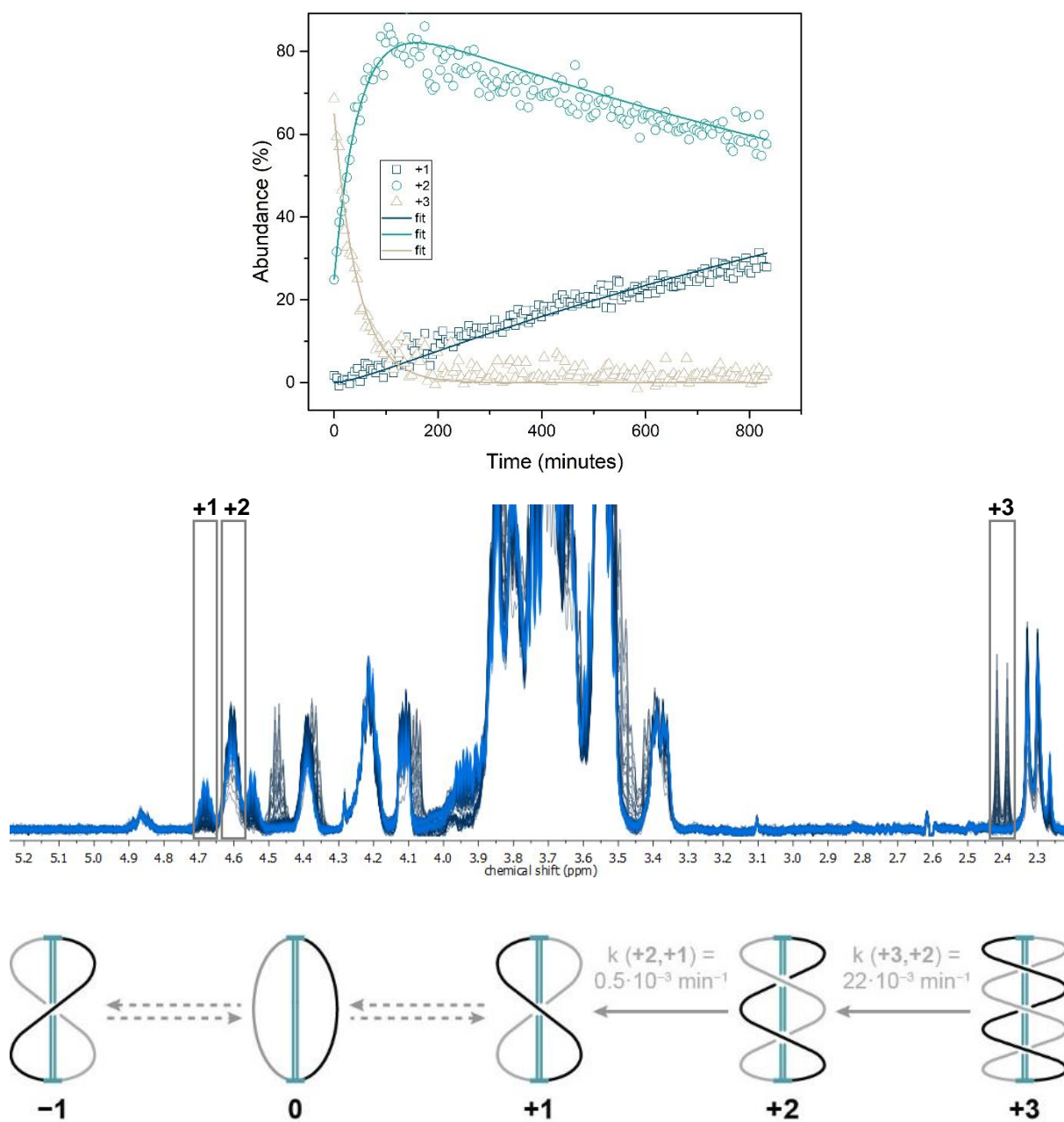
Supplementary Fig. 27 | Relaxation of a (S,R,R) - $\pm n$ sample at 10 °C with 20 mol% n -butyl amine. Kinetic trace of a representative example with fit (top), NMR stack (middle) and proposed mechanism with average rate constants (bottom). C_6D_6 , $c = 1 \text{ mM}$, 500 MHz.

Relaxation kinetics of a $(S,R,R)\text{-}\pm n$ sample at 60 °C without nucleophile

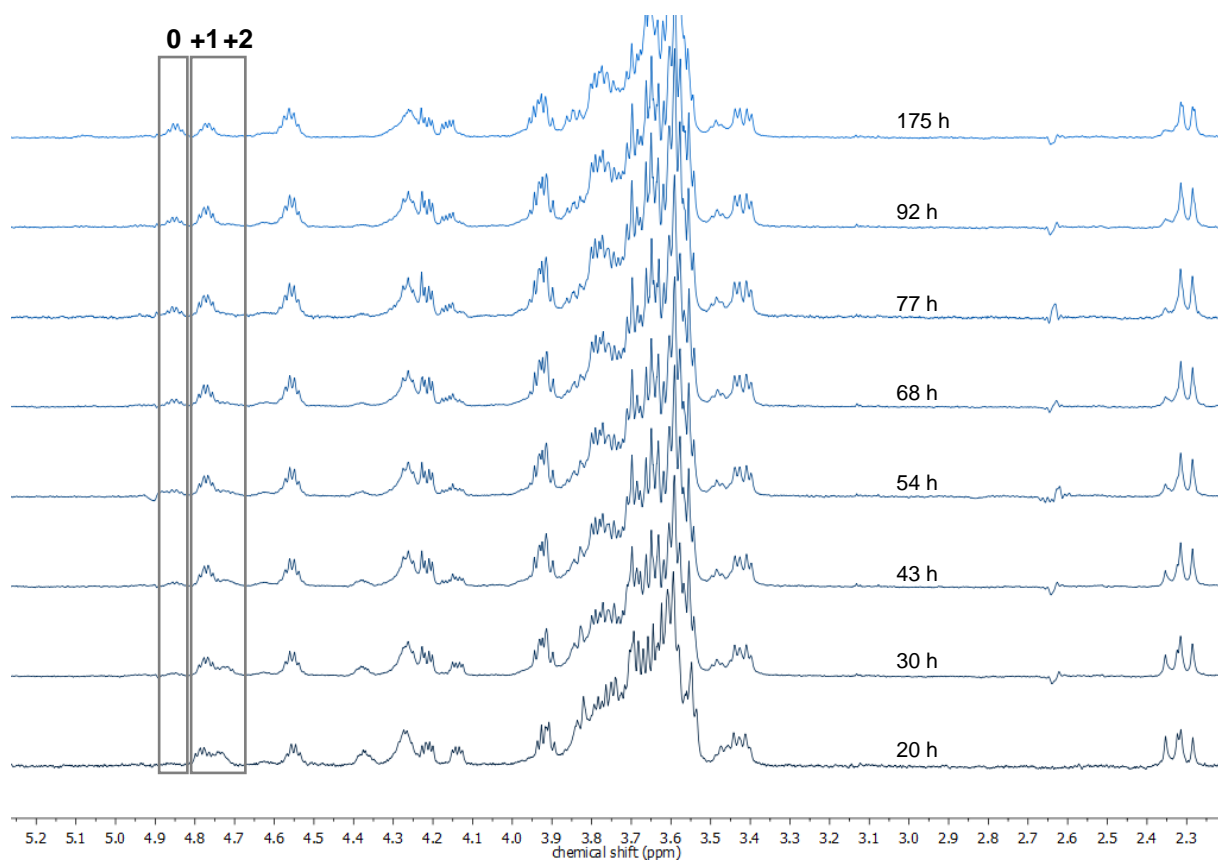


Supplementary Fig. 28 | Relaxation of a $(S,R,R)\text{-}\pm n$ sample at 60 °C without nucleophile. Kinetic trace of a representative example with fit (top), NMR stack (middle) and proposed mechanism with average rate constants (bottom). C_6D_6 , $c = 1 \text{ mM}$, 500 MHz.

Relaxation kinetics of a $(S,R,R)\text{-}\pm n$ sample at 40 °C without nucleophile

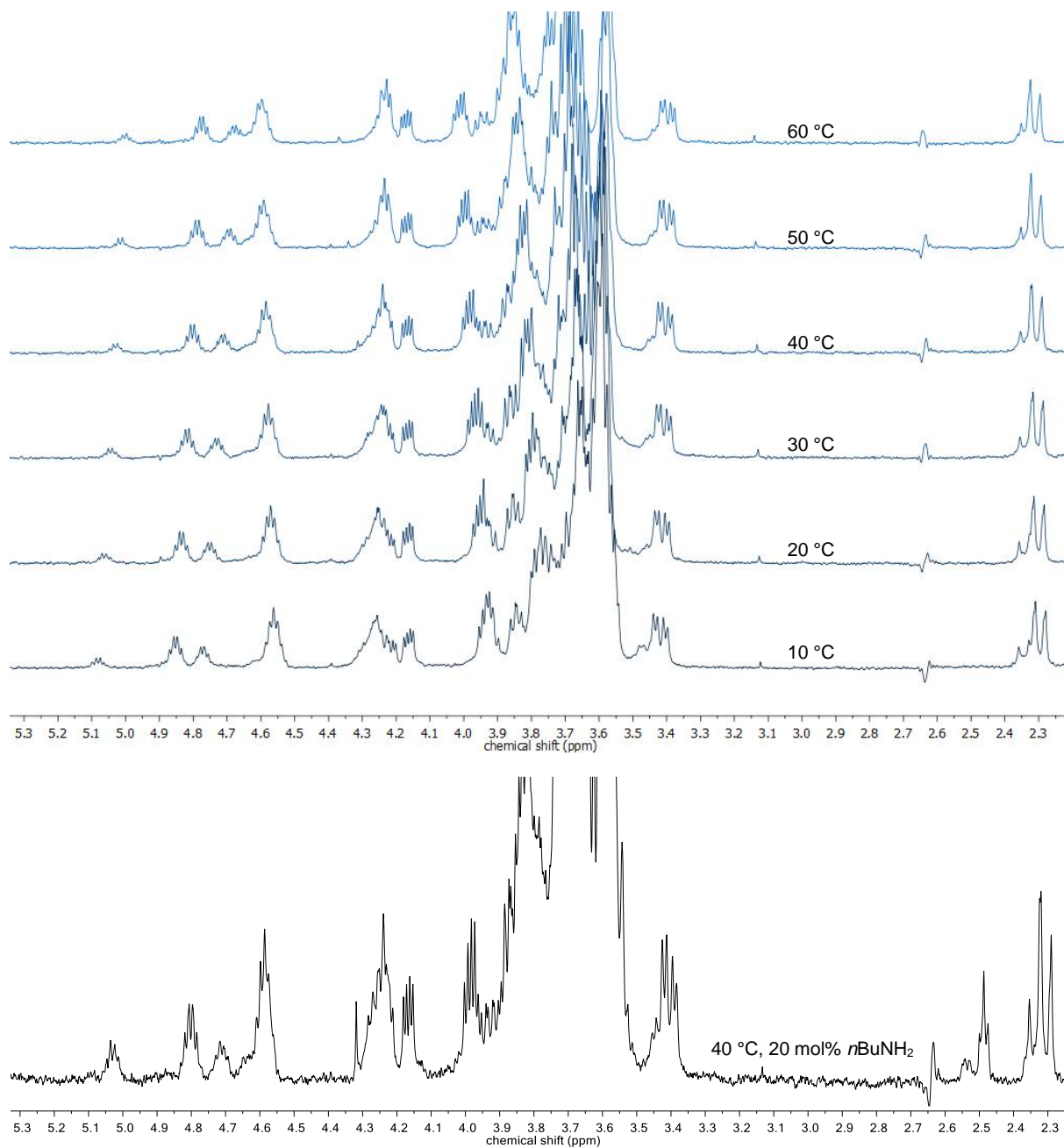


Supplementary Fig. 29 | Relaxation of a $(S,R,R)\text{-}\pm n$ sample at 40 °C without nucleophile. Kinetic trace of a representative example with fit (top), NMR stack (middle) and proposed mechanism with average rate constants (bottom). C_6D_6 , $c = 1$ mM, 500 MHz.



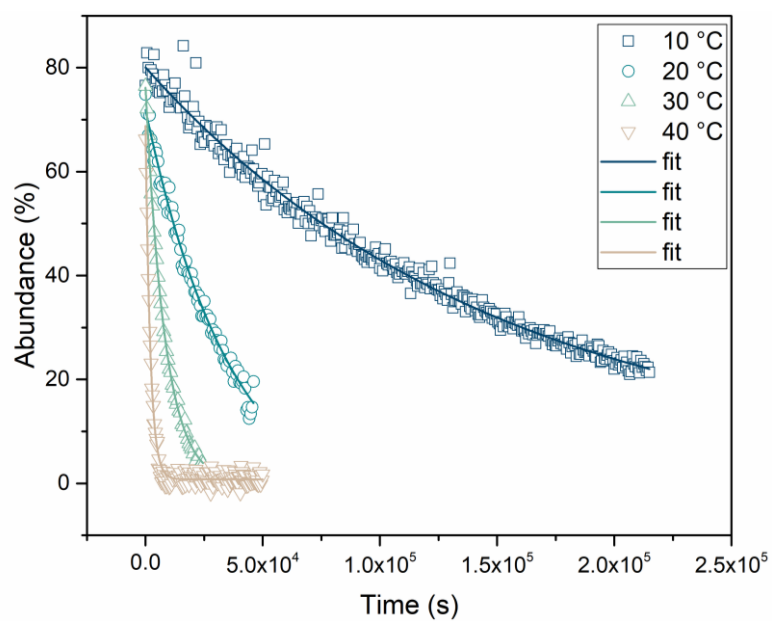
Supplementary Fig. 30 | ¹H-NMR spectra showing the relaxation of a (*S,R,R*)-±n sample at 40 °C without nucleophile over one week. C₆D₆, c = 1 mM, 500 MHz.

Relaxed (*S,R,R*)-±n sample at 10–60 °C without nucleophile and at 40 °C with 20 mol% *n*-butyl amine



Supplementary Fig. 31 | ¹H-NMR spectra of an equilibrated (*S,R,R*)-±n samples. Without nucleophile at 10–60 °C (top) and with 20 mol% *n*-butyl amine at 40 °C (bottom). C₆D₆, c = 1 mM, 500 MHz.

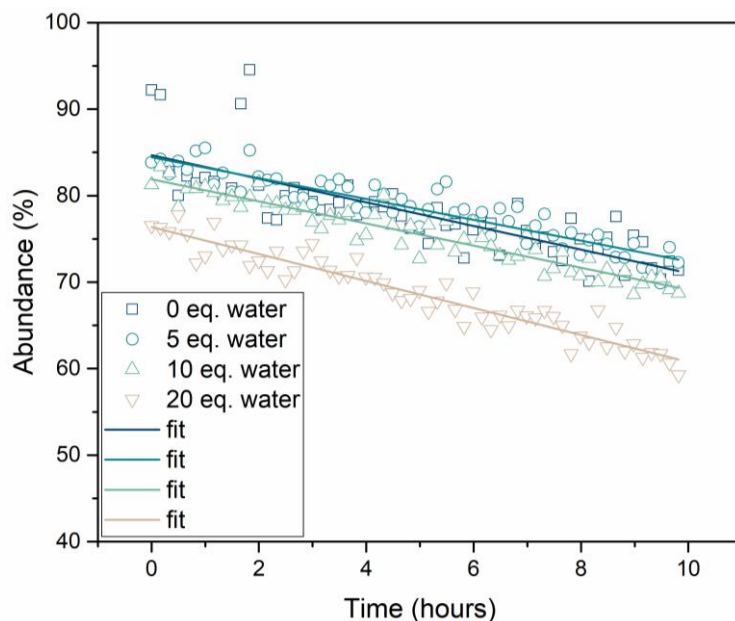
Relaxation kinetics of a (S,R,R) - $\pm n$ sample at 10–40 °C without nucleophile



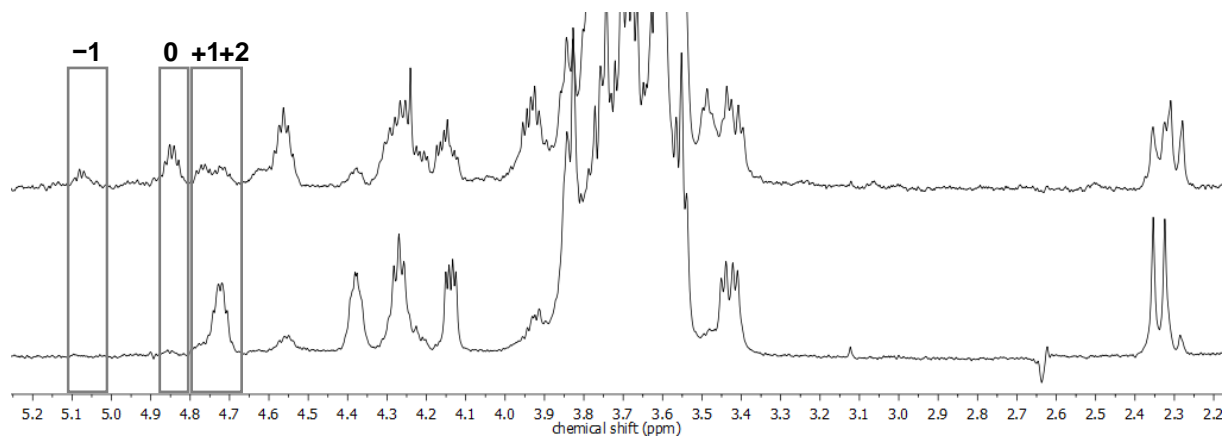
Supplementary Fig. 32 | Temperature dependent relaxation of (S,R,R) - ± 3 without nucleophile. The first order decay of (S,R,R) - ± 3 accelerates by a factor of ~ 4 per 10 °C. C_6D_6 , $c = 1$ mM, 500 MHz.

Relaxation of a $(S,R,R)\text{-}\pm n$ sample in presence of water

Water (as a stock solution in deuterated THF) was added to a relaxed $(S,R,R)\text{-}\pm n$ sample under an inert atmosphere. The same sample was used for all experiments. Water does not significantly increase the decay rate of $(S,R,R)\text{-}+3$ ($k(+3,+2) = 0.2\text{--}0.3 \cdot 10^{-3} \text{ min}^{-1}$) at 10°C . However, an illuminated sample (according to the general procedure) containing 20 eq. of water relaxed to isomers $(S,R,R)\text{-} -1$, 0 , $+1$, and $+2$ at room temperature after 3 d. A similar sample without nucleophile forms almost exclusively $(S,R,R)\text{-}+2$ under the same conditions.



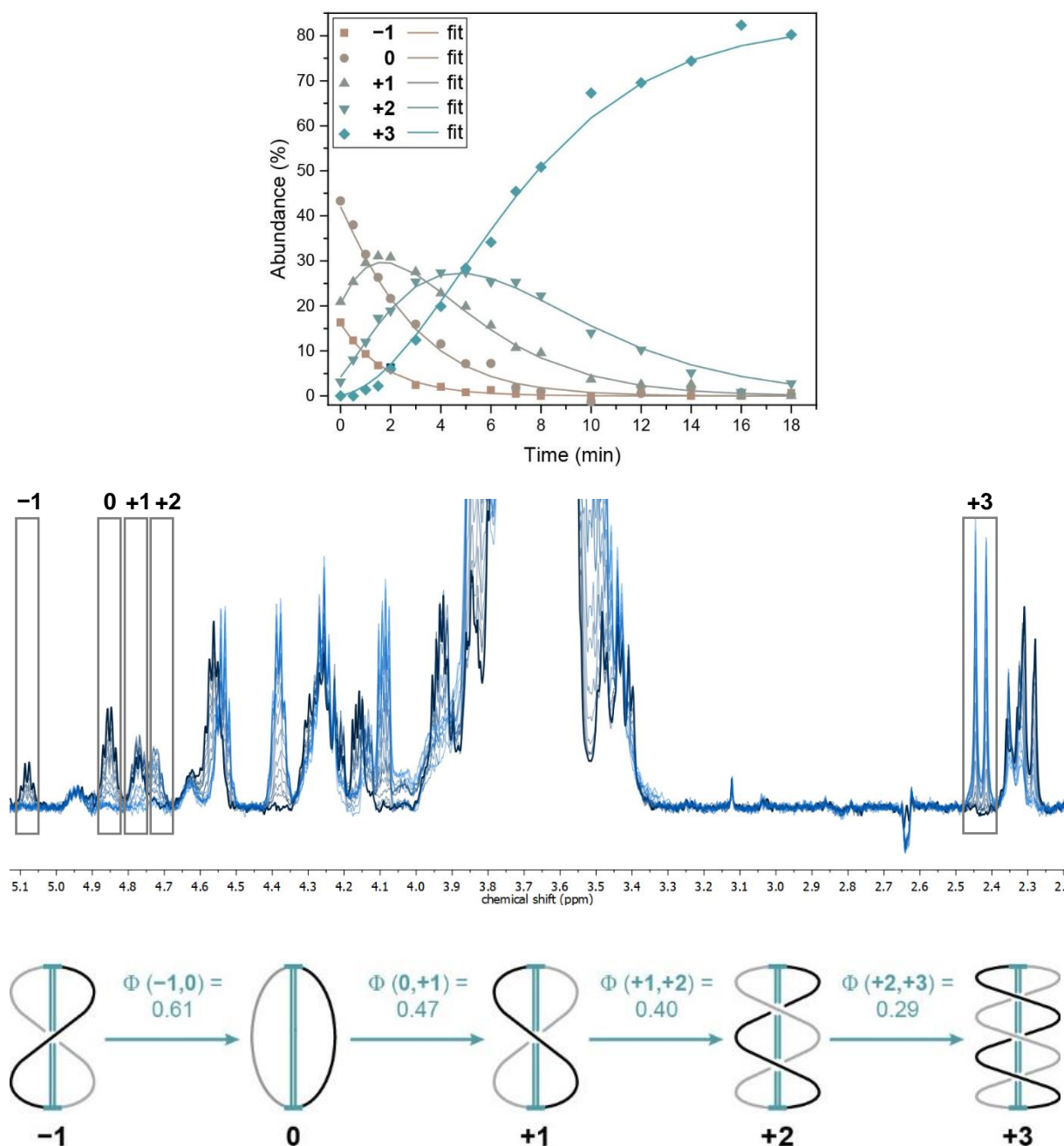
Supplementary Fig. 33 | Decay rate of $(S,R,R)\text{-}+3$ in presence of water. The amount of water has no significant effect on the decay rate of $(S,R,R)\text{-}+3$. The first order rate constant $k(+3,+2) = 0.2\text{--}0.3 \cdot 10^{-3} \text{ min}^{-1}$ was determined by initial slope approximation. C_6D_6 , $c = 1 \text{ mM}$, 10°C , 500 MHz .



Supplementary Fig. 34 | $^1\text{H-NMR}$ spectra of irradiated $(S,R,R)\text{-}\pm n$ samples at room temperature after 72 h with and without water. With 20 eq. water (top) and without external nucleophile (bottom). C_6D_6 , $c = 1 \text{ mM}$, 500 MHz .

Irradiation kinetics of a $(S,R,R)\text{-}\pm n$ sample at 10 °C without nucleophile

A relaxed $(S,R,R)\text{-}\pm n$ was illuminated at 8 °C inside a walkable fridge according to the general procedure. After each irradiation step, the sample was cooled to 10 °C with an acetone bath to prevent significant relaxation during transportation to the NMR instrument. Further experimental details for the quantum yield determination are given at page 56 of the Supplementary Information.



Supplementary Fig. 35 | Irradiation kinetics of a relaxed $(S,R,R)\text{-}\pm n$ sample. Kinetic trace of a representative example with fit (top), NMR stack (middle) and proposed mechanism with average quantum yields (bottom). C_6D_6 , $c = 1 \text{ mM}$, 10 °C, 500 MHz.

Mass Spectrometry

Ion mobility (IM) measurements were performed using a custom drift-tube instrumentation hosted in the Fritz Haber Institute of the Max Planck Society (Berlin, Germany) and adapted from a previous design⁸. The instrument is designed around a nanoelectrospray ionization (nESI) source interfaced with a succession of radially-confining entrance funnel, drift tube and exit funnel. This ensemble is prolonged by a quadrupole mass analyzer under high vacuum and ended by an electron multiplier detector (ETP Ion Detect) for ion counting. In practice, samples were diluted to 10 μM in acetonitrile and nESI was used to generate ions using a needle voltage of 0.57 kV and a backing pressure of 0.8 bar (N_2). The ~ 160 cm long drift tube was filled with helium buffer gas at a pressure of 4 mbar and subjected to a 2 kV direct current (DC) electric field for mobility separation. Ions were filtered for $m/z = 1612$ Da, which correspond to the singly-protonated molecular ion $[\text{M}+\text{H}]^+$.

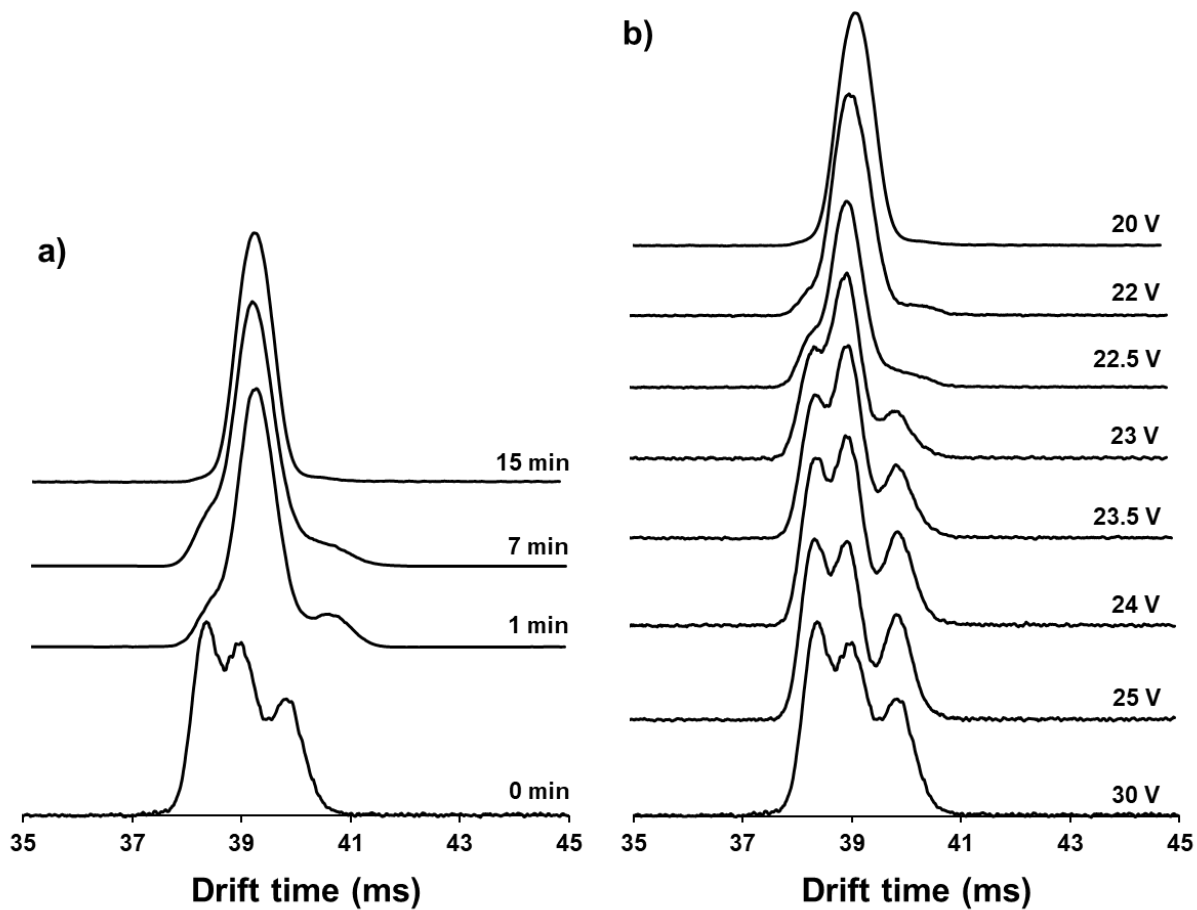
Experimental collision cross sections ($^{\text{DT}}\text{CCS}_{\text{He}}$) Ω were determined from the reduced mobility coefficient K_0 using Eq. 1⁹ after measuring the arrival time distributions (ATD) for DC voltages ranging from 1.3 kV to 2.3 kV. The contribution of each peak was extracted by fitting the ATD using multiple Gaussian functions (OriginPro 2020, OriginLab).

$$K_0 = \frac{3}{16} \frac{q}{N_0} \left(\frac{2\pi}{\mu k_B T} \right)^{1/2} \frac{1}{\Omega}$$

where q is the ion charge, N_0 is the standard gas number density, μ is the reduced mass of the ion-gas colliding partners, k_B is the Boltzmann constant and T is the temperature.

Theoretical collision cross section ($^{\text{TM}}\text{CCS}$) were calculated using the trajectory method (TM) implemented in the MobCal software suite¹⁰ as the average of 500 individual candidate structures randomly picked along the dynamics (Supplementary Data Set 2). The CCS values for all experimentally observed topological isomers of $(S,R,R)\text{-}\pm\mathbf{n}$ amount to: $^{\text{TM}}\text{CCS}_{\text{He}}(-1) = 344 \text{ \AA}^2$, $^{\text{TM}}\text{CCS}_{\text{He}}(0) = 352 \text{ \AA}^2$, $^{\text{TM}}\text{CCS}_{\text{He}}(+1) = 336 \text{ \AA}^2$, $^{\text{TM}}\text{CCS}_{\text{He}}(+2) = 328 \text{ \AA}^2$, $^{\text{TM}}\text{CCS}_{\text{He}}(+3) = 348 \text{ \AA}^2$.

Supplementary Fig. 36a shows the evolution of the ATD for increasing durations of irradiation at $\lambda_{\text{irr}} = 365$ nm. The transition is characterized by a progressive narrowing of the distribution toward the emergence of a single peak associated with **+3** after 15 min. Supplementary Fig. 36b shows the evolution of the ATD for increasing injection voltages applied on the irradiated sample. The initial single peak corresponding to **+3** at low voltage is progressively extinguished in favor of three distinct contributions corresponding to **-1**, **0** and **+1** at high voltages. This latter distribution agrees with the distribution of the non-irradiated sample, thereby validating the reversibility of the reaction pathway.



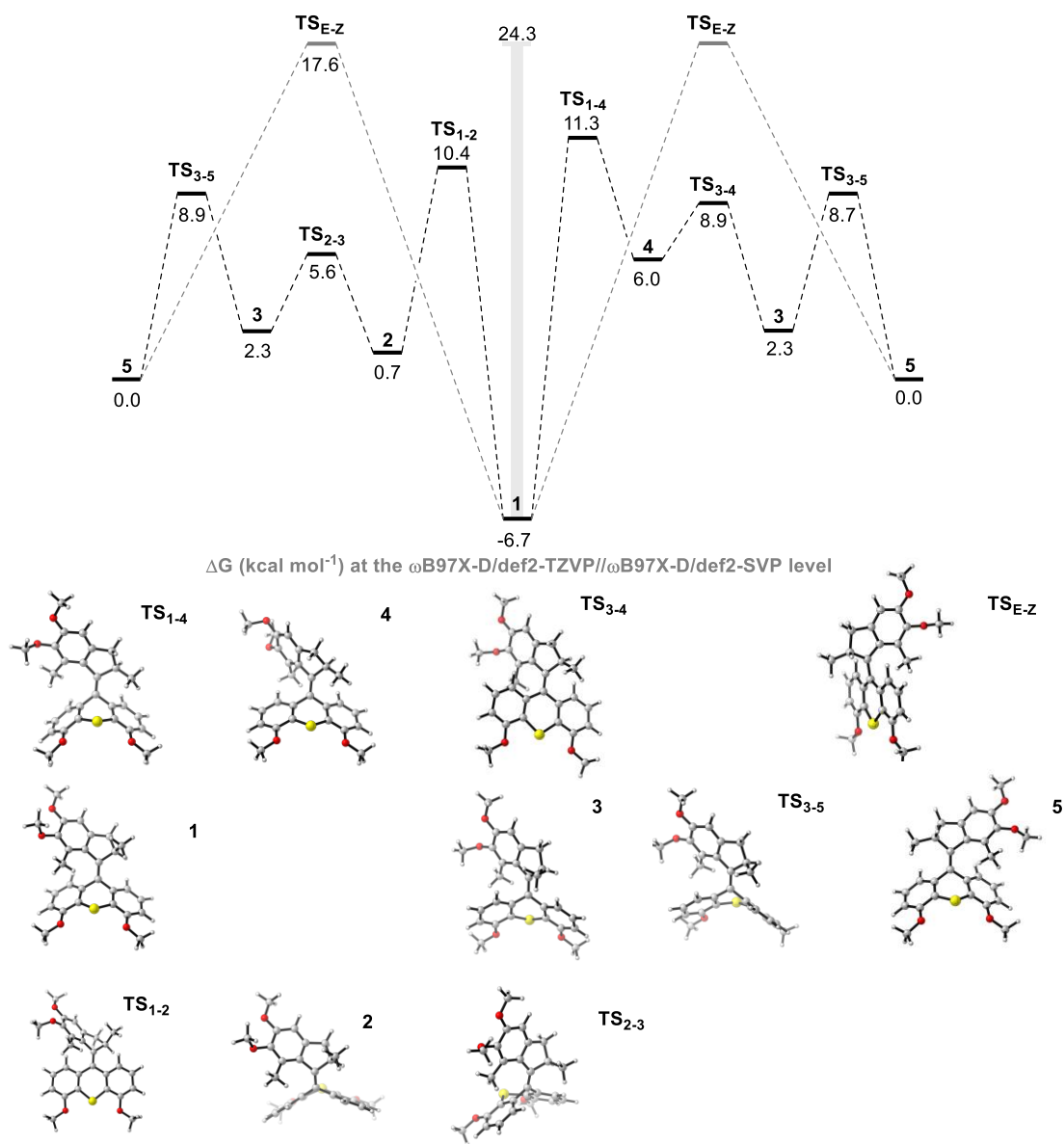
Supplementary Fig. 36 | ATDs of (S,R,R)-±n recorded on the drift tube instrumentation. a, ATDs for increasing durations of irradiation at $\lambda_{irr} = 375$ nm and **b,** increasing injection voltages from 20 V to 30 V applied on the irradiated sample.

Computational Analysis

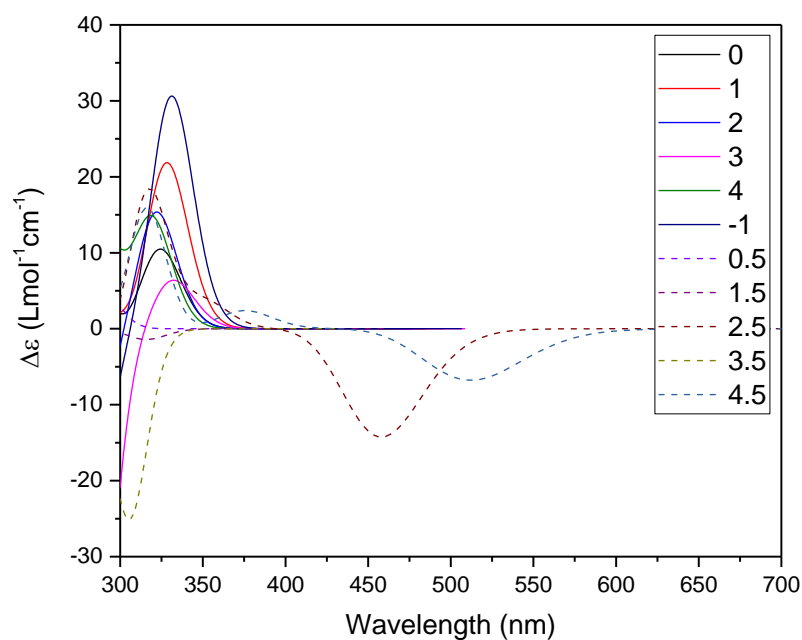
The full thermal rotational path of the motor was probed at the ω B97X-D/def2-TZVP// ω B97X-D/def2-SVP level of theory as implemented in the Gaussian 16, Version B.01 software package¹¹. The values of the Gibbs free energies (in kcal/mol) of each species are given in Supplementary Fig. 37. Two different pathways for the thermal helix inversion (THI) were considered (populating either intermediate **2** or **4**). To have a better overview of the unidirectionality of the motor, the thermal *E-Z* barrier (TEZ) was also computed using the broken-symmetry approach at the same level of theory used for calculating the thermal helix inversion step. A difference of more than 6 kcal/mol between the THI and TEZ barriers confirms the unidirectionality of the thermal step of the motor rotation.

The structures of the macrocyclic compounds in different topological isomers were modelled in the respective stable states of the motor core. All the structures were pre-screened using the CREST driver in the xTB software¹²⁻¹⁴ using the GFN force field¹⁵. In this way, the most stable conformers for each structure were picked *via* the default series of metadynamics and dynamics runs implemented in the driver. The conformers obtained following this procedure were re-optimized at the GFN2-xTB level with very tight optimization criteria. The energy was then computed with a single-point calculation at the M06-2x/def2-SVP level, as implemented in the Gaussian 16, Version B.01 software package¹¹. The energy profile of the isomerization process afforded a stepwise increase of the overall energy with a global minimum at the topological isomer **0**. The experimentally observed energy differences between the states amount to $\Delta G_{\text{exp}}(+3,+2) \geq 2.0$ kcal/mol, $\Delta G_{\text{exp}}(+2,+1) \geq 2.0$ kcal/mol, $\Delta G_{\text{exp}}(+\mathbf{1},\mathbf{0}) = 0.24$ kcal/mol and $\Delta G_{\text{exp}}(-\mathbf{1},\mathbf{0}) = 0.39$ kcal/mol by assuming that 3% of $\pm\mathbf{n}$ cannot be reliably detected by ¹H-NMR spectroscopy. These values are comparable with the computed electronic energy differences presented in Fig. 5b of the main text.

The CD spectra of (*S,R,R*)- $\pm\mathbf{n}$ with progressive number of turns was calculated at the sTDA-xTB level on the optimized structures. The results for the motor core with *S*-chirality are in Supplementary Fig. 38. The results furnish a qualitative flavor of the CD signs associated to metastable and stable states. From the computations, all the stable states show a positive Cotton effect in the most red-shifted band. The metastable states possess opposite helicity and consequently, opposite sign. Each metastable state was optimized following the same procedure previously discussed for the stable states. Every metastable state generated from a certain stable state was dubbed with an additional ".5" in the name (e.g. **+1.5** is generated by photochemical isomerization of **+1**).



Supplementary Fig. 37 | Full thermal isomerization pathways of the motor core at the ω B97X-D/def2-TZVP// ω B97X-D/def2-SVP level.



Supplementary Fig. 38 | Simulated CD spectra of the core of the different motors computed at the TDA(30 states)- ω B97X-D/def2-SVP level.

The dynamic behavior of the different topological isomer of the protonated macrocycle in vacuum were also computed, to provide a theoretical interpretation for the IM-MS results. The different stable isomers were optimized with the xTB software¹²⁻¹⁴ using the GFN force field¹⁵. A molecular dynamics simulation of 1 ns was then run using the default values recommended from the developers (298.15 K, Berendsen thermostat, SHAKE algorithm for all bonds, hydrogen mass = 4, timestep of 2 fs). 500 geometries were then sampled randomly and used to calculate the collision cross-section values. Cartesian coordinates of all structures can be found in Supplementary Data Set 2.

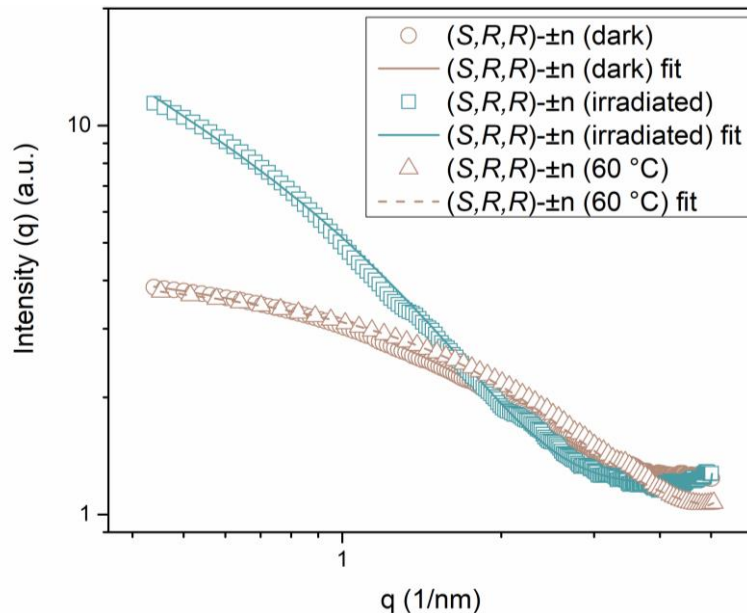
SAXS Measurements

General

SAXS measurements were performed at the Multipurpose X-ray Instrument for Nanostructure Analysis (MINA) instrument at the University of Groningen. The instrument is built on a Cu rotating anode high brilliance X-ray source, providing X-ray photons with wavelength of $\lambda = 0.154$ nm. The SAXS patterns were recorded using a 2D Vantec500 detector placed 24 cm away from the sample. SAXS 1D profiles were obtained by radially averaging the scattered intensity around the origin of the image (defined by the direct beam position on the detector) using MATLAB. Standard corrections for the detector distortion and sensitivity were applied. The scattering from the buffer solution was subtracted to obtain the neat SAXS signal of the sample. The 1D SAXS profiles are plotted against the modulus of the scattering vector defined as $q = 4\pi \sin\theta/\lambda$, where θ is half of the scattering angle. The probed scattering angle range was calibrated using known position of diffraction peaks from a standard Silver Behenate sample (NIST).

Sample preparation

A relaxed $(S,R,R)\text{-}\pm n$ sample (1 mM solution in toluene- d_8) was contained in a glass capillary of 1.5 mm diameter (wall size of 0.01 mm), flame-sealed to avoid solvent evaporation and placed in the X-ray vacuum chamber to remove air absorption and scattering. The capillary temperature was stabilized at 23 °C. After the measurement, the same solution was illuminated inside the capillary with UV light ($\lambda_{\text{irr}} = 365$ nm, 18 min) and immediately measured. To probe reversible conformation change of the molecule, the sample was allowed to relax at 60 °C for 16 h and then measured. We also measured a sample that was pre-illuminated according to the general procedure, which lead to similar results.



Supplementary Fig. 39 | Scattering intensities of a $(S,R,R)\text{-}\pm n$ sample. At equilibrium (brown circles), after illumination with 365 nm for 18 min (blue squares), and after relaxation at 60 °C for 16 h (brown triangles). 23 °C, $c = 1$ mM, toluene- d_8 .

Data analysis

As the shape of the nanoratchet in solution is not the one of a simple object (sphere, cylinder, *etc.*), SAXS profiles were further analyzed to estimate the dimensions of the nanoobject in solution using a model-independent approach. In this case, a generalized Guinier equation was used.

$$I(q) = \begin{cases} 1 & \text{for } \alpha = 0 \\ \alpha\pi q^{-\alpha} & \text{for } \alpha \neq 0 \end{cases} A \exp\left(\frac{R_\alpha^2 q^2}{3 - \alpha}\right)$$

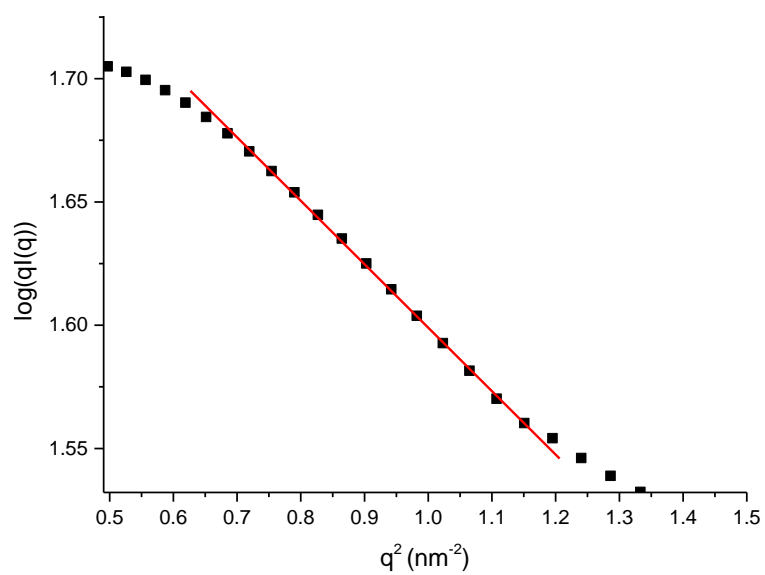
where α is the shape factor (0 for sphere, 1 for rod, and 3 for disk), R_α is the radius of gyration and A is a scaling pre-factor that depends on quantities specific of the sample (volume, contrast, and concentration) and specific of the experimental configuration (photon flux, detector sensitivity, and solid angle defined by the detector). The advantage of this approach is that no a-priori assumption is made on the shape of the nanoobject in solution, that can be inferred by the fitted value of α .

The best fitting curves obtained by this method are in Fig. 2 of the main manuscript and the fitting results are summarized in Supplementary Tab. 3. Data fitting was performed using analytical models *via* the SASFIT program¹⁶.

Supplementary Tab. 3 SAXS profile fitting results.			
	A	α	R_α (nm)
Equilibrated	3.9	0.19	0.86
Illuminated	2.1	0.85	0.88
60 °C (16 h)	3.8	0.15	0.79

Our SAXS analysis clearly suggests that the pristine molecules in solution adopt a close-to-spheroidal configuration as $\alpha = 0.19$ is close to 0 which is expected for a perfect sphere. On the contrary, winding causes a clear shape change towards an elongated-like conformation as $\alpha = 0.85$ is close to 1 which is expected for a perfect cylinder. In this case, an estimation of the cross-sectional radius of gyration for a rod-like conformation (or of the short semi-axis for an ellipsoidal conformation) can be obtained by the cross-sectional Guinier analysis¹⁷, *i.e.* fit of the linear part in the plot $\log(qI(q))$ *vs* q^2 in the range of points that satisfy the relationship $qR_c < 1$. The value of the slope is related to the cross-sectional radius as $slope = R_c^2/2$. For the irradiated sample (see Supplementary Fig. 40), we get an estimated $R_c \sim 0.7$ nm.

The larger dimension of the elongated nanoobject can be estimated assuming either an ellipsoidal shape ($R_\alpha^2 = \frac{a^2}{5} + \frac{2b^2}{5}$, with $a > b$ being the semi-axes) or a cylindrical shape ($R_\alpha^2 = \frac{R_c^2}{2} + \frac{L^2}{12}$). We thus estimate $a \sim 1.7$ nm and $L \sim 2.5$ nm. These values should be considered with care as they are based on the assumption of a well-defined geometrical shape, but can be nevertheless considered as the lower and an upper limits of the larger axis of the wound nanoobject in solution.



Supplementary Fig. 40 | Guinier plot for the irradiated sample. Red line is the linear fit that gives a slope of -0.25.

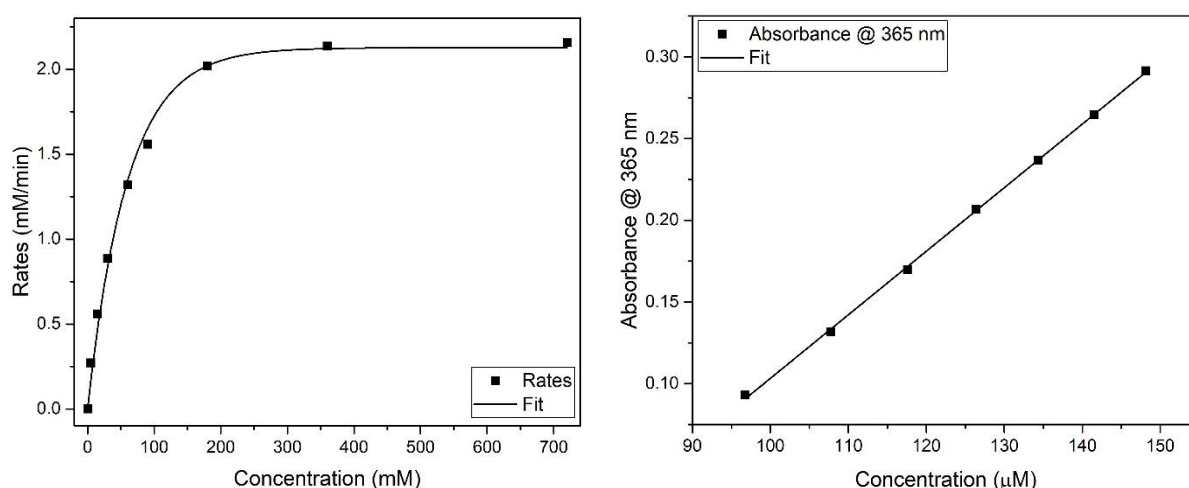
Quantum Yield Determination

The quantum yields for every single winding step of molecular machine (S,R,R)- $\pm n$ were determined by NMR spectroscopy with *ortho*-nitrobenzaldehyde (**NBA**) as an actinometer, following a literature procedure from Ji *et al.*¹⁸ The following equation was used for the fit:

$$-\frac{d[\text{NBA}]}{dt} = \Phi_{\text{NBA}} I_0 (1 - 10^{-\epsilon_{\text{NBA}} b [\text{NBA}]})$$

The molar extinction coefficient of NBA is $\epsilon_{\text{NBA}}(365\text{nm}) = 265 \text{ M}^{-1} \text{ cm}^{-1}$ and its quantum yield is $\Phi_{\text{NBA}} = 0.5$ ¹⁸. The light intensity in our irradiation setup was measured at 365 nm and corresponds to a molar photon flux $I_0(365\text{nm}) = 4.252 \text{ mM min}^{-1}$; the path length corresponds to $b = 0.027 \text{ cm}$ (Supplementary Fig. 41 left).

The molar extinction coefficient ϵ was determined for the motor core (S,R,R)-**S16** (Supplementary Fig. 41 right) and corresponds to $\epsilon(365\text{nm}) = 3891 \text{ M}^{-1} \text{ cm}^{-1}$. Based on UV/vis and CD spectroscopic experiments, we can assume that $\epsilon(365\text{nm})$ is similar for all topological isomers.



Supplementary Fig. 41 | Determination of the light intensity (I_0), path length (b) and molar extinction coefficient (ϵ) at 365 nm. The photochemical conversion rates of *ortho*-nitrobenzaldehyde to *ortho*-nitrosobenzoic acid at various concentrations give I_0 and b (left), whereas ϵ was determined by measuring the absorbance of motor core (S,R,R)-**S16** at different concentrations (right).

The quantum yield Φ was then determined by following the temporal change of a fully relaxed sample of (S,R,R)- $\pm n$ upon illumination with 365 nm by NMR spectroscopy (Supplementary Fig. 35). The kinetic profile was fitted with COPASI 4.29⁷ by applying the following equation:

$$-\frac{d[\pm n]}{dt} = \Phi I_0 (1 - 10^{-\epsilon b [\pm n]})$$

Strictly speaking, the quantum yield values provided are apparent quantum yields connecting a stable state $\pm n$ of the motor with the successive having an increased crossing number, $\pm n + 1$. The metastable form connecting these two states (and the associated ultrafast thermal reaction that populates $\pm n + 1$) is neglected because it is impossible to observe under our experimental conditions.

Energetic Considerations of the Winding Mechanism

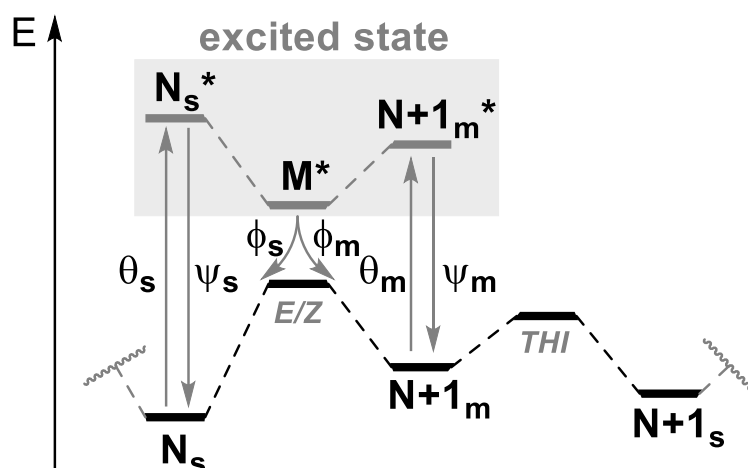
Our experiments show that AMM $\pm n$ works by an energy ratchet mechanism and the winding process is driven by light energy (only the (S,R,R) isomer is considered in this discussion).

Experimentally, the Gibbs free energy (G) of – and thus strain in – the system increases with increasing amount of crossings (N), whereas the state with zero crossings ($N = 0$) has the lowest energy. At thermal equilibrium, three states are populated, namely -1 , 0 and $+1$. States with $N > +1$ or $N < -1$ were not observed.

The system can thermally equilibrate either by intermolecular nucleophile-imine exchange or intramolecular, thermal double bond isomerization. While the rate constant (k) of the former is independent of N , the rate constant of the latter decreases with increasing N .

Light-driven winding increases N stepwise by $+1$ and occurs by a photochemical E/Z isomerization, forming a metastable isomer (experimentally not observed) that relaxes by a fast thermal helix inversion (THI). The quantum yield (Φ) of the double bond isomerization decreases with increasing N and is therefore dependent on strain in the system. Experimentally, the system reaches up to $+3$ crossings.

With these observations in mind, we can derive the conditions which limit the number of crossings in our light-driven molecular machine (assuming that no competing nucleophile is present), considering a simple model for our nanoratchet (Supplementary Fig. 42).



Supplementary Fig. 42 | Schematic representation describing the energetics of the winding mechanism. θ , ψ and ϕ are transition constants; horizontal lines represent qualitative energy levels of different winding states.

For a generic molecular motor to operate, an equilibrium between its states N_s (a stable state that was subjected to N turns), $N + 1_m$ (a metastable state that was subjected to $N+1$ turns) and $N + 1_s$ (a stable state that was subjected to $N+1$ turns) must be established, where ultimately the probabilities to find the system in a certain stable state will be regulated by the Boltzmann equation:

$$\left(\frac{p_{N+1_s}}{p_{N_s}}\right) = e^{\left(\frac{G_{N_s} - G_{N+1_s}}{k_B T}\right)}$$

p_{N+1_s} and p_{N_s} are the steady-state levels for $N + 1_s$ and N_s , G_{N_s} and G_{N+1_s} are the free energies of $N + 1_s$ and N_s , k_B is Boltzmann's constant and T is the temperature in Kelvin. This scenario can be described in more detail by considering the equilibria involving these three species on the same

potential energy surface and the possibility to populate the respective excited states of species N_s and $N + 1_m$, namely N_s^* and $N + 1_m^*$. The diabatic transition from ground to the excited state is regulated by the Bose-Einstein equations for absorption (transition constant θ), stimulated and spontaneous emission (transition constant ψ)¹⁹. It is known that for Feringa-type molecular motors the population of the productive excited state involved in the isomerization leads to the (almost barrierless) formation of a so-called dark-state M^* ^{20,21}. When an equilibrium is reached between the different species and if we consider the two surfaces separated, the ground state will have:

$$\left(\frac{p_{N+1_m}}{p_{N_s}}\right) = e^{\left(\frac{G_{N_s} - G_{N+1_m}}{k_B T}\right)} \text{ and } \left(\frac{p_{N+1_s}}{p_{N+1_m}}\right) = e^{\left(\frac{G_{N+1_m} - G_{N+1_s}}{k_B T}\right)}$$

while at the excited state:

$$\left(\frac{p_{M^*}}{p_{N_s^*}}\right) = e^{\left(\frac{G_{N_s^*} - G_{M^*}}{k_B T}\right)} \text{ and } \left(\frac{p_{M^*}}{p_{N+1_s^*}}\right) = e^{\left(\frac{G_{N+1_m^*} - G_{M^*}}{k_B T}\right)}$$

The population of M^* leads to the non-adiabatic formation^{20,21} of N_s and $N + 1_m$ with transition constants ϕ_s and ϕ_m , given the approximation that the directionality of the motion at the excited state does not depend on the state initially populated, but only by the characteristics of M^* ¹.

Given these premises, we can for example consider that at the stationary state the probability to photochemically populate the state $N + 1_m$ starting from N_s via M^* will be the product of the probabilities associated with each step involving these species¹¹:

$$P_{N_s \rightarrow N+1_m}^{h\nu} = \frac{p_{N_s} \theta_s \cdot p_{N_s^*} k_{N_s^* \rightarrow M^*} \cdot p_{M^*} \phi_m}{p_{N_s^*} \psi_s} = p_{N_s} \cdot P'_{N_s \rightarrow N+1_m}^{h\nu}$$

In this way, we can consider that at the stationary state, the sum of probabilities that lead from N_s and $N + 1_s$ should equal the sum of the ones that form $N + 1_s$ from N_s . Thus:

$$1 = \frac{P_{N_s \rightarrow N+1_m}^{h\nu} \cdot P_{N+1_m \rightarrow N+1_s} + P_{N_s \rightarrow N+1_m} \cdot P_{N+1_m \rightarrow N+1_s}}{P_{N+1_m \rightarrow N_s}^{h\nu} \cdot P_{N+1_s \rightarrow N+1_m} + P_{N+1_m \rightarrow N_s} \cdot P_{N+1_s \rightarrow N+1_m}}$$

which can be rewritten as:

$$1 = \frac{p_{N_s} \cdot P'_{N_s \rightarrow N+1_m}^{h\nu} \cdot p_{N+1_m} k_{N+1_m \rightarrow N+1_s} + p_{N_s} k_{N_s \rightarrow N+1_m} \cdot p_{N+1_m} k_{N+1_m \rightarrow N+1_s}}{p_{N+1_m} \cdot P'_{N+1_m \rightarrow N_s}^{h\nu} \cdot p_{N+1_s} k_{N+1_s \rightarrow N+1_m} + p_{N+1_m} k_{N+1_m \rightarrow N_s} \cdot p_{N+1_s} k_{N+1_s \rightarrow N+1_m}}$$

and simplified to:

$$1 = \frac{p_{N_s} k_{N+1_m \rightarrow N+1_s} \cdot (P'_{N_s \rightarrow N+1_m}^{h\nu} + k_{N_s \rightarrow N+1_m})}{p_{N+1_s} k_{N+1_s \rightarrow N+1_m} \cdot (P'_{N+1_m \rightarrow N_s}^{h\nu} + k_{N+1_m \rightarrow N_s})}$$

finally obtaining:

¹ The excited state vibrationally coherent population of conical intersections is deliberately omitted in this treatment.

¹¹ We will not consider here the possibility of an up-hill population of $N + 1_m^*$ (or N_s^*) from M^* and subsequent light emission to afford $N + 1_m$ (or N_s).

$$\left(\frac{p_{N+1_s}}{p_{N_s}}\right) = \frac{k_{N+1_m \rightarrow N+1_s} \cdot (P'^{h\nu}_{N_s \rightarrow N+1_m} + k_{N_s \rightarrow N+1_m})}{k_{N+1_s \rightarrow N+1_m} \cdot (P'^{h\nu}_{N+1_m \rightarrow N_s} + k_{N+1_m \rightarrow N_s})}$$

Thus, when $k_{N_s \rightarrow N+1_m} \ll P'^{h\nu}_{N_s \rightarrow N+1_m}$ and $k_{N+1_m \rightarrow N_s} \ll P'^{h\nu}_{N+1_m \rightarrow N_s}$ ^{III}, we have:

$$\left(\frac{p_{N+1_s}}{p_{N_s}}\right) = e^{\left(\frac{G_{N+1_m} - G_{N+1_s}}{k_B T}\right)} \cdot \frac{P'^{h\nu}_{N_s \rightarrow N+1_m}}{P'^{h\nu}_{N+1_m \rightarrow N_s}}$$

We can simplify this equation by assuming that the ratio of the photochemical probabilities is the photostationary state (PSS)²²:

$$\frac{P'^{h\nu}_{N_s \rightarrow N+1_m}}{P'^{h\nu}_{N+1_m \rightarrow N_s}} = \frac{\Phi_{N_s \rightarrow N+1_m} \varepsilon_{N_s}}{\Phi_{N+1_m \rightarrow N_s} \varepsilon_{N+1_m}}$$

thus:

$$\left(\frac{p_{N+1_s}}{p_{N_s}}\right) = e^{\left(\frac{G_{N+1_m} - G_{N+1_s}}{k_B T}\right)} \cdot \frac{\Phi_{N_s \rightarrow N+1_m} \varepsilon_{N_s}}{\Phi_{N+1_m \rightarrow N_s} \varepsilon_{N+1_m}} = \frac{k_{N+1_m \rightarrow N+1_s}}{k_{N+1_s \rightarrow N+1_m}} \cdot \frac{\Phi_{N_s \rightarrow N+1_m} \varepsilon_{N_s}}{\Phi_{N+1_m \rightarrow N_s} \varepsilon_{N+1_m}}$$

$\Phi_{N_s \rightarrow N+1_m}$ describes the quantum yield of the $N_s \rightarrow N + 1_m$ process starting from N_s upon light absorption and incorporates both the Bose-Einstein terms and the non-adiabatic terms. We can also explicitly consider the probability of the diabatic transition as proportional to the absorptivity of N_s (ε_s).

This equation can be zeroed in the following extreme cases, consequently impeding winding and thus the population of $N + 1_s$:

1. $G_{N+1_m} \ll G_{N+1_s}$, hence the metastable state ensuing from the photochemical step ($N + 1_m$) is more stable than the next "stable" state ($N + 1_s$) that is generated from the thermal helix inversion (THI) step and/or $k_{N+1_s \rightarrow N+1_m} \gg k_{N+1_m \rightarrow N+1_s}$, hence further winding is kinetically prevented;
2. $\Phi_{N_s \rightarrow N+1_m} \ll \Phi_{N+1_m \rightarrow N_s}$, given similar molar absorptivities ε_s and ε_m , hence the photochemical population of $N + 1_m$ will not be feasible;
3. $\varepsilon_s \ll \varepsilon_m$ at a given wavelength of irradiation, preventing the excitation of N_s and the formation of $N + 1_m$.

^{III} Conditions typical of a photochemically-fueled motor with an E/Z barrier that prevents the thermal population of $N + 1_m$ from N_s .

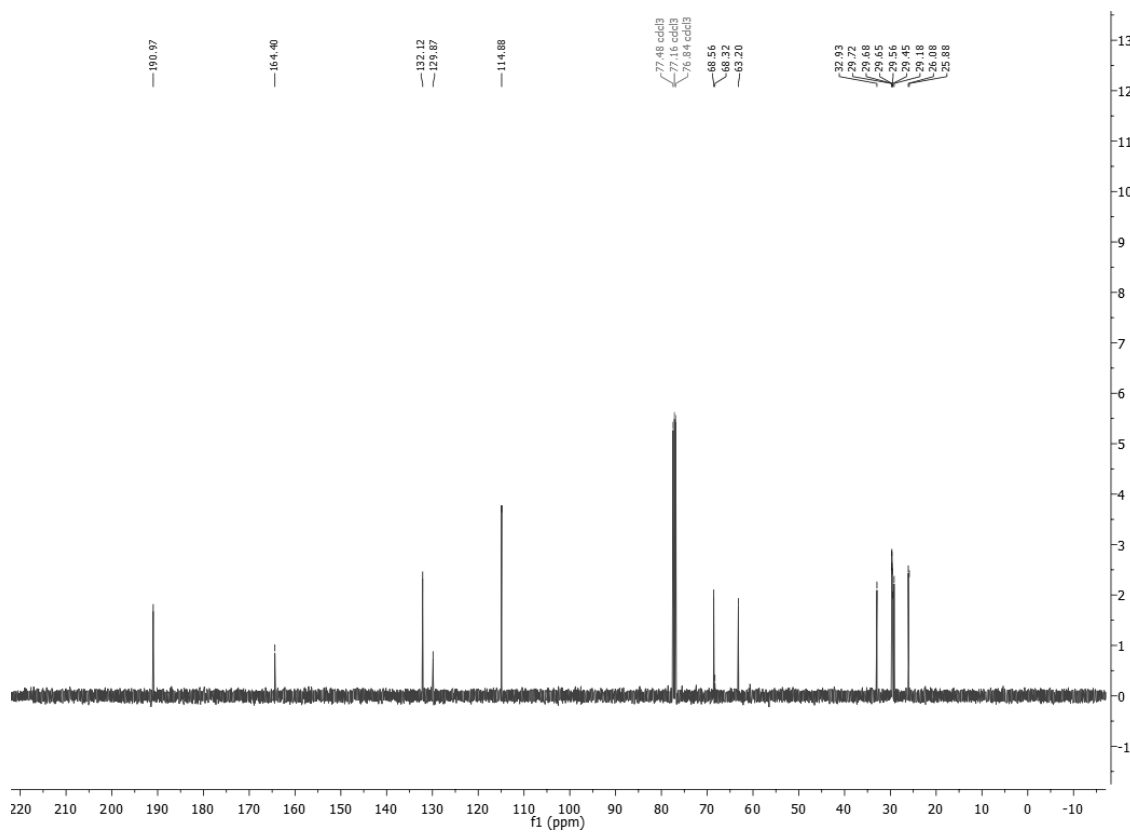
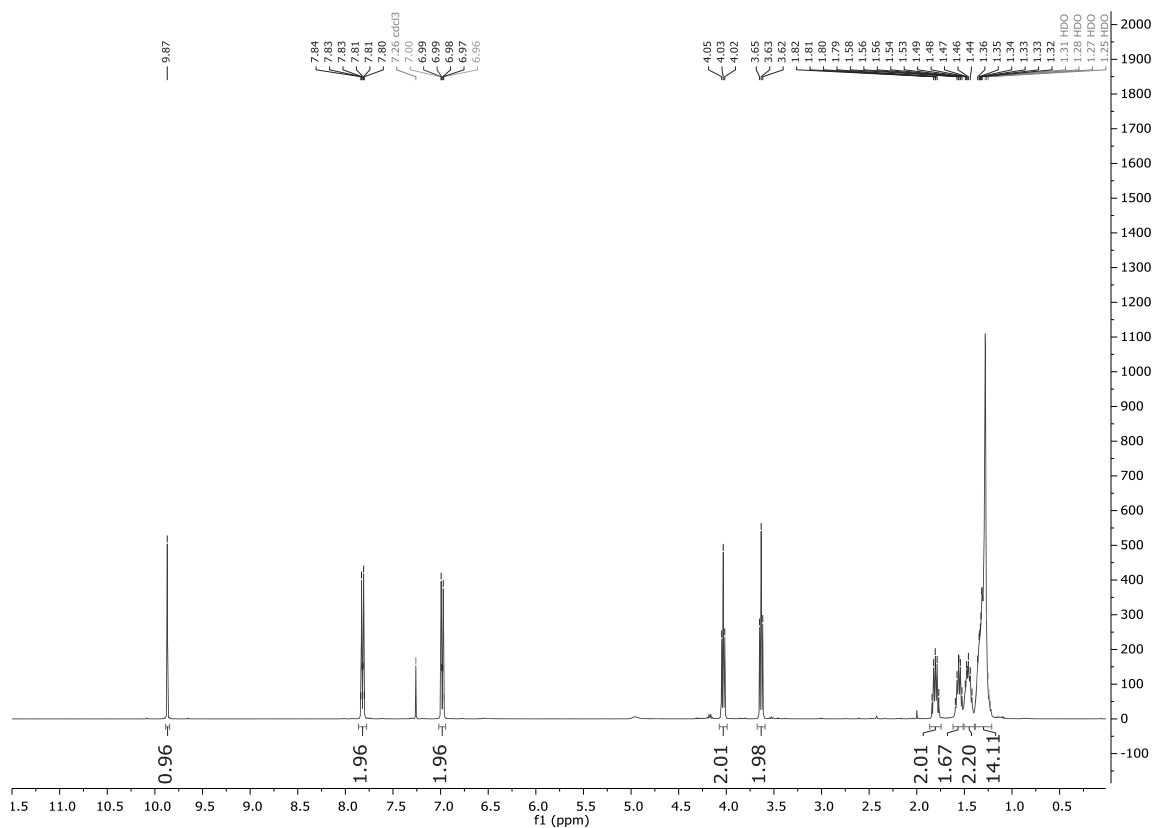
References

1. Ballot, S. & Noiret, N. Synthesis of new C60 based phosphines. *Tetrahedron Lett.* **44**, 8811–8814 (2003).
2. Konken, C. P. *et al.* Development of symmetric O-BODIPYs with different optical properties as building blocks for the synthesis of ligands for multimodal imaging. *Dye. Pigment.* **158**, 88–96 (2018).
3. Li, Q. *et al.* Gram scale synthesis of functionalized and optically pure Feringa's motors. *Tetrahedron* **73**, 4874–4882 (2017).
4. Van Dijken, D. J., Chen, J., Stuart, M. C. A., Hou, L. & Feringa, B. L. Amphiphilic Molecular Motors for Responsive Aggregation in Water. *J. Am. Chem. Soc.* **138**, 660–669 (2016).
5. Tian, Y. K., Shi, Y. G., Yang, Z. S. & Wang, F. Responsive supramolecular polymers based on the bis[alkynylplatinum(II)] terpyridine molecular tweezer/arene recognition motif. *Angew. Chemie - Int. Ed.* **53**, 6090–6094 (2014).
6. Li, Q. *et al.* Macroscopic contraction of a gel induced by the integrated motion of light-driven molecular motors. *Nat. Nanotechnol.* **10**, 161–165 (2015).
7. Hoops, S. *et al.* COPASI--a COMplex PATHway Simulator. *Bioinformatics* **22**, 3067–3074 (2006).
8. Warnke, S. *et al.* Protomers of benzocaine: Solvent and permittivity dependence. *J. Am. Chem. Soc.* **137**, 4236–4242 (2015).
9. Mason, E. A. & McDaniel, E. W. *Transport Properties of Ions in Gases. Transport Properties of Ions in Gases* (Wiley, 1988). doi:10.1002/3527602852
10. Mesleh, M. F., Hunter, J. M., Shvartsburg, A. A., Schatz, G. C. & Jarrold, M. F. Structural Information from Ion Mobility Measurements: Effects of the Long-Range Potential. *J. Phys. Chem.* **100**, 16082–16086 (1996).
11. Frisch, M. J. *et al.* Gaussian 16, Revision B.01. Gaussian, Inc., Wallingford CT 2016.
12. Grimme, S., Bannwarth, C. & Shushkov, P. A Robust and Accurate Tight-Binding Quantum Chemical Method for Structures, Vibrational Frequencies, and Noncovalent Interactions of Large Molecular Systems Parametrized for All spd-Block Elements (Z = 1-86). *J. Chem. Theory Comput.* **13**, 1989–2009 (2017).
13. Bannwarth, C., Ehlert, S. & Grimme, S. GFN2-xTB - An Accurate and Broadly Parametrized Self-Consistent Tight-Binding Quantum Chemical Method with Multipole Electrostatics and Density-Dependent Dispersion Contributions. *J. Chem. Theory Comput.* **15**, 1652–1671 (2019).
14. Pracht, P., Caldeweyher, E., Ehlert, S. & Grimme, S. A Robust Non-Self-Consistent Tight-Binding Quantum Chemistry Method for Large Molecules. *ChemRxiv* (2019). doi:10.26434/chemrxiv.8326202.v1
15. Spicher, S. & Grimme, S. Robust Atomistic Modeling of Materials, Organometallic, and Biochemical Systems. *Angew. Chemie Int. Ed.* **59**, 15665–15673 (2020).
16. Breßler, I., Kohlbrecher, J. & Thünemann, A. F. SASfit: A tool for small-angle scattering data analysis using a library of analytical expressions. *J. Appl. Crystallogr.* **48**, 1587–1598 (2015).
17. Glatter, O. & Kratky, O. *Small angle X-ray scattering*. (Academic Press, 1982).

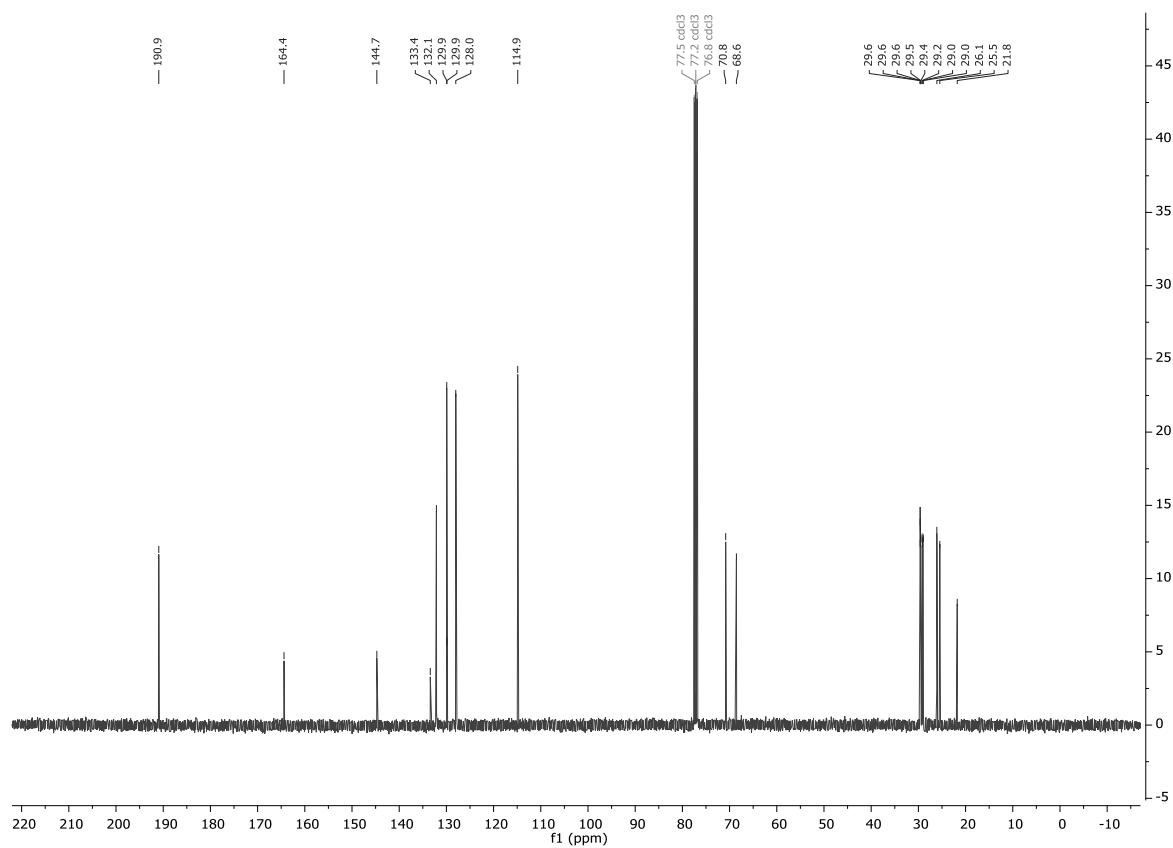
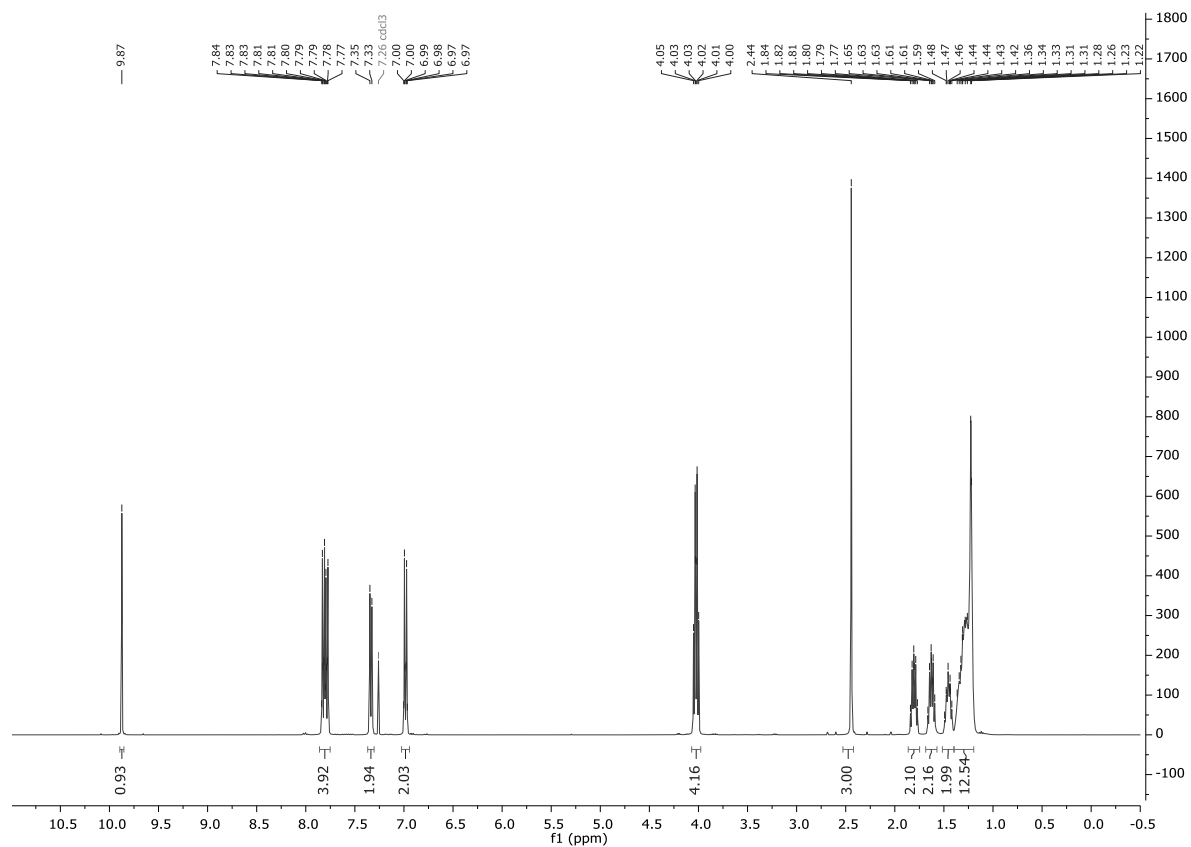
18. Ji, Y., DiRocco, D. A., Hong, C. M., Wismer, M. K. & Reibarkh, M. Facile Quantum Yield Determination via NMR Actinometry. *Org. Lett.* **20**, 2156–2159 (2018).
19. Astumian, R. D. Optical vs. chemical driving for molecular machines. *Faraday Discuss.* **195**, 583–597 (2017).
20. Conyard, J. *et al.* Ultrafast dynamics in the power stroke of a molecular rotary motor. *Nat. Chem.* **2012 47** **4**, 547–551 (2012).
21. Pooler, D. R. S. *et al.* Effect of charge-transfer enhancement on the efficiency and rotary mechanism of an oxindole-based molecular motor. *Chem. Sci.* **12**, 7486–7497 (2021).
22. Stranius, K. & Börjesson, K. Determining the Photoisomerization Quantum Yield of Photoswitchable Molecules in Solution and in the Solid State. *Sci. Rep.* **7**, 41145 (2017).

Spectra Appendix

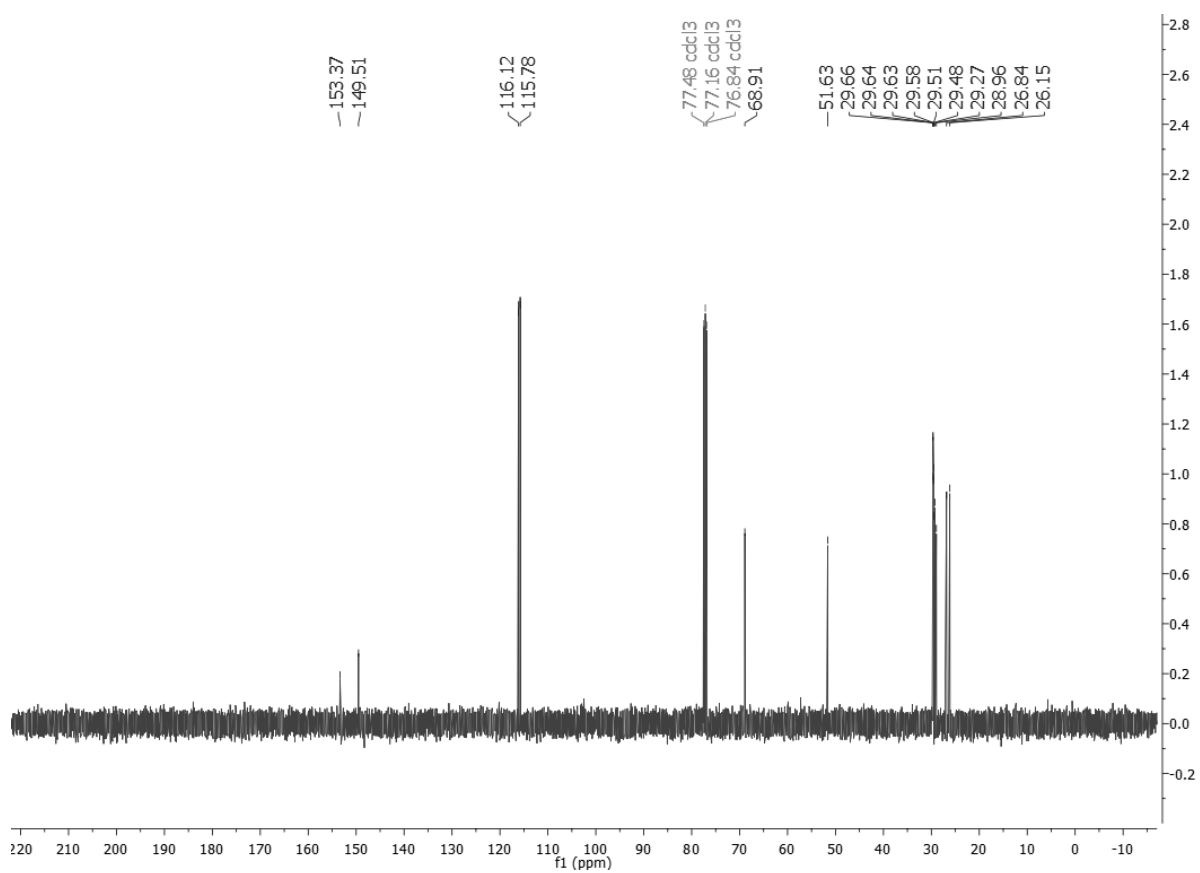
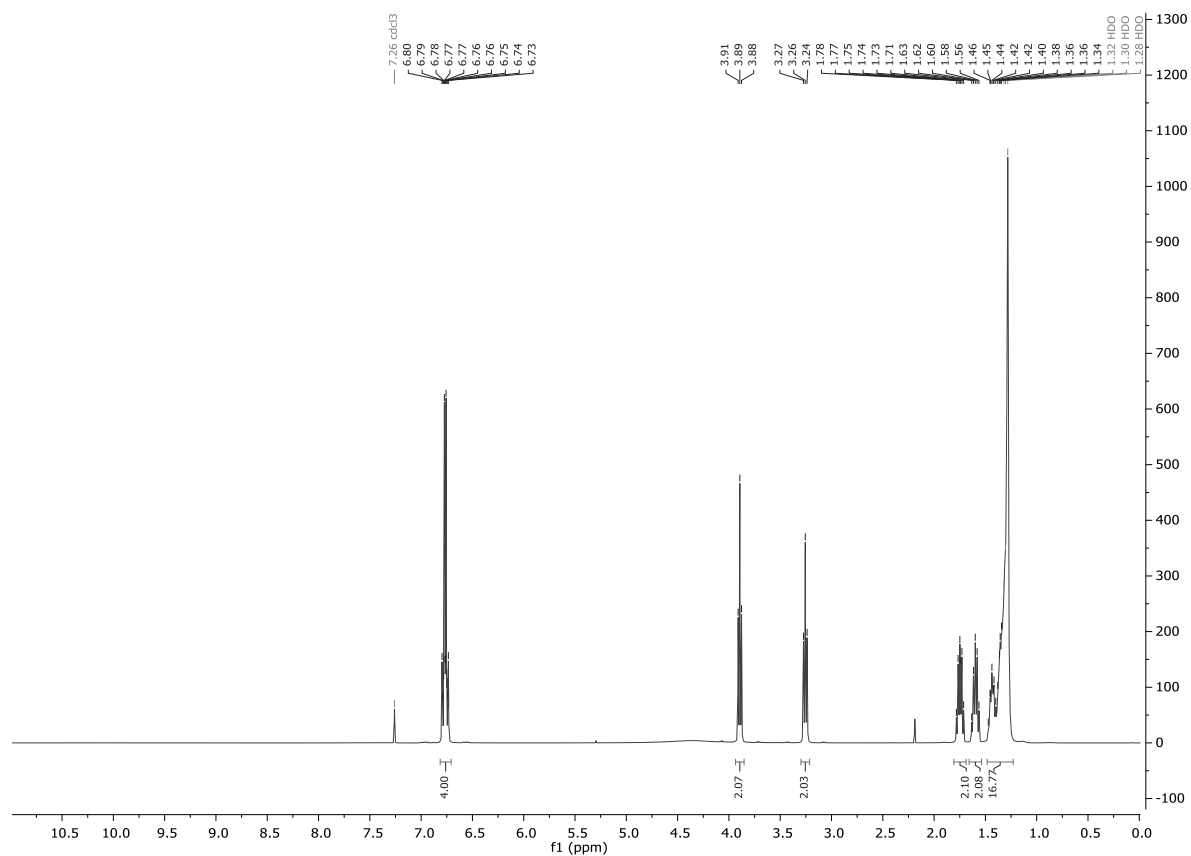
^1H and ^{13}C NMR spectra for compound S2



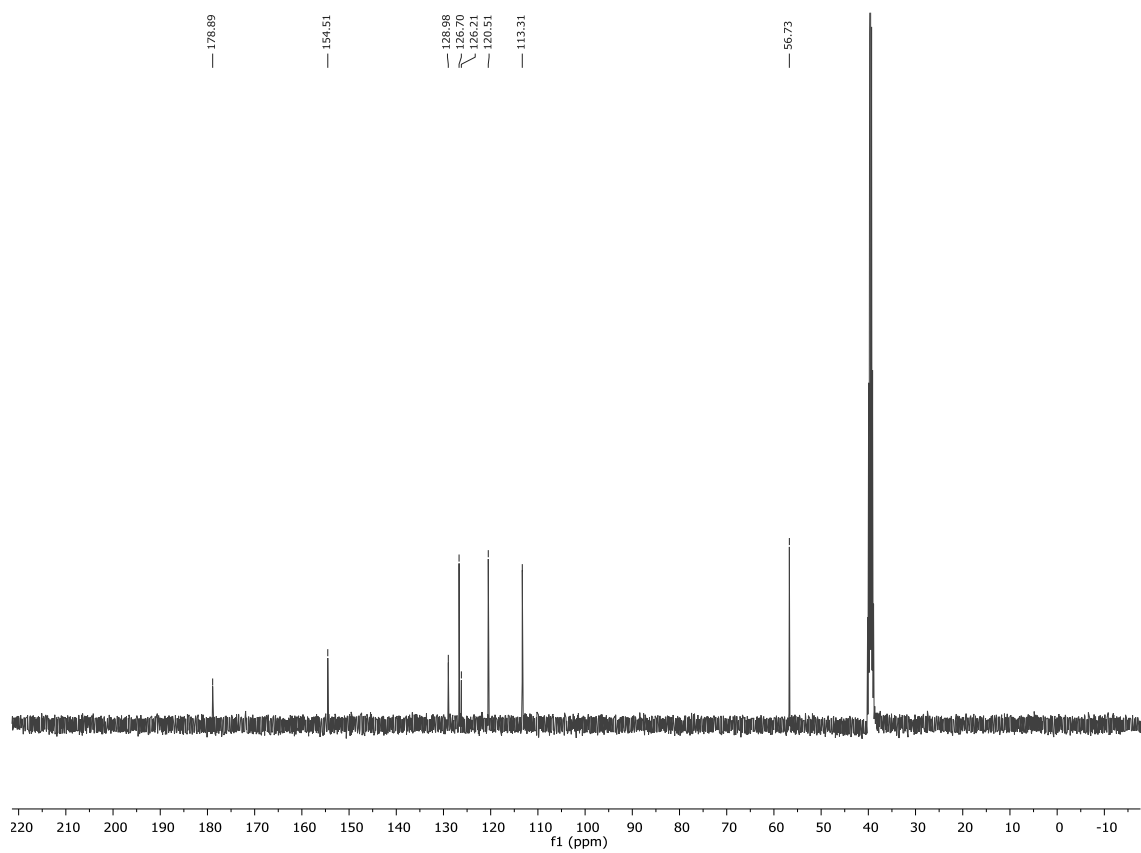
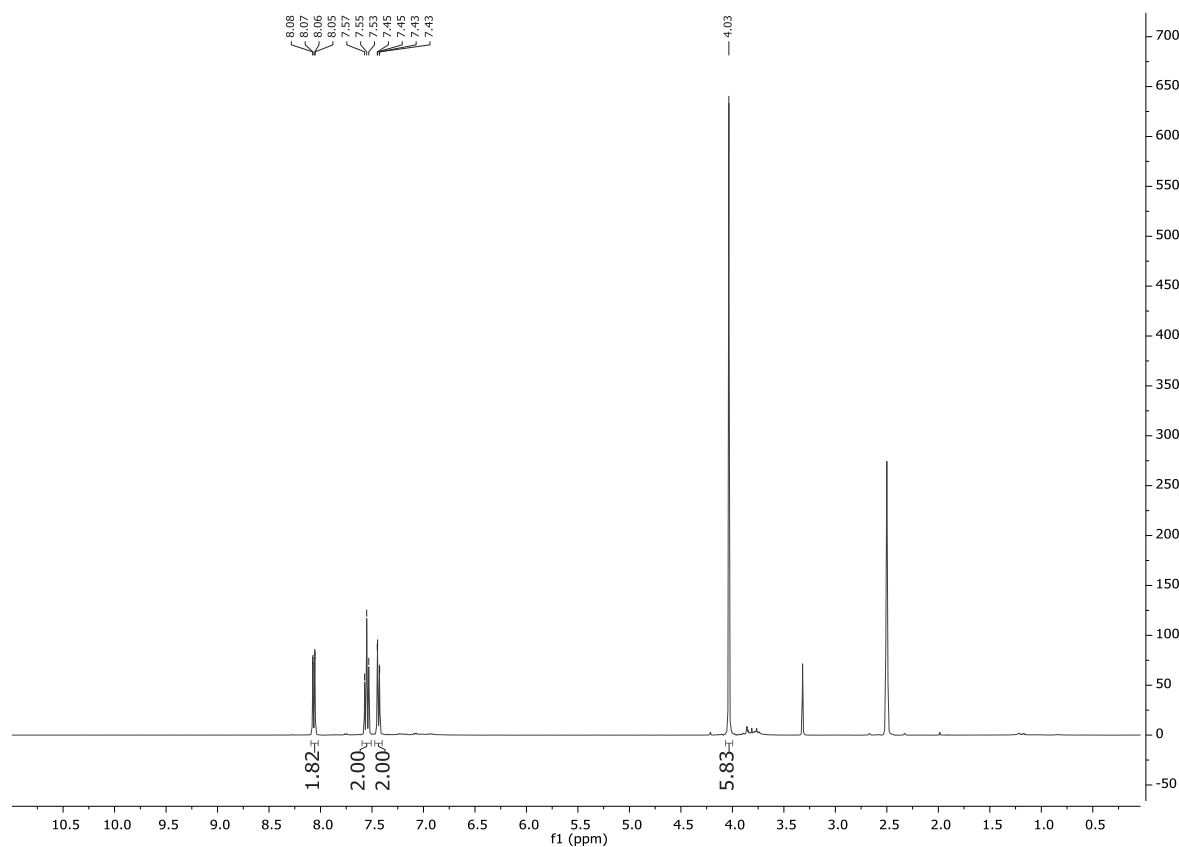
¹H and ¹³C NMR spectra for compound S3



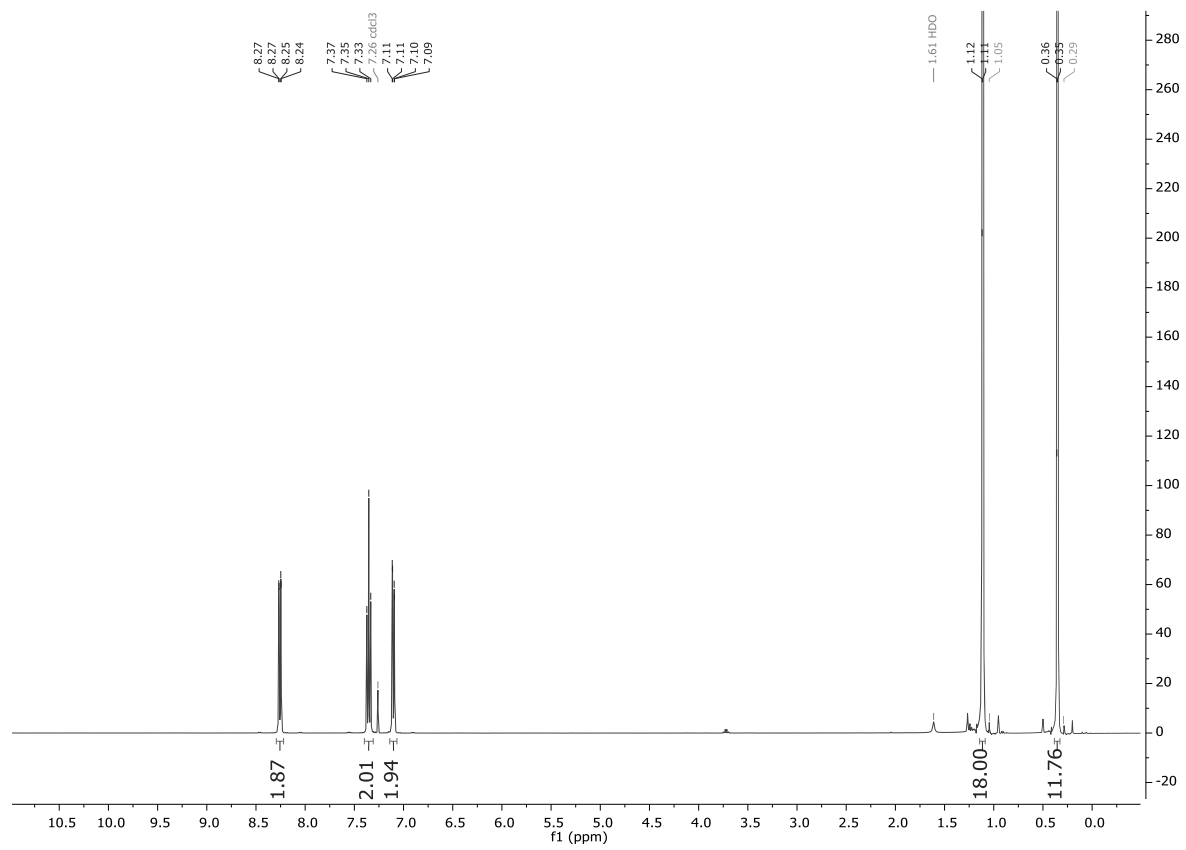
¹H and ¹³C NMR spectra for compound S5



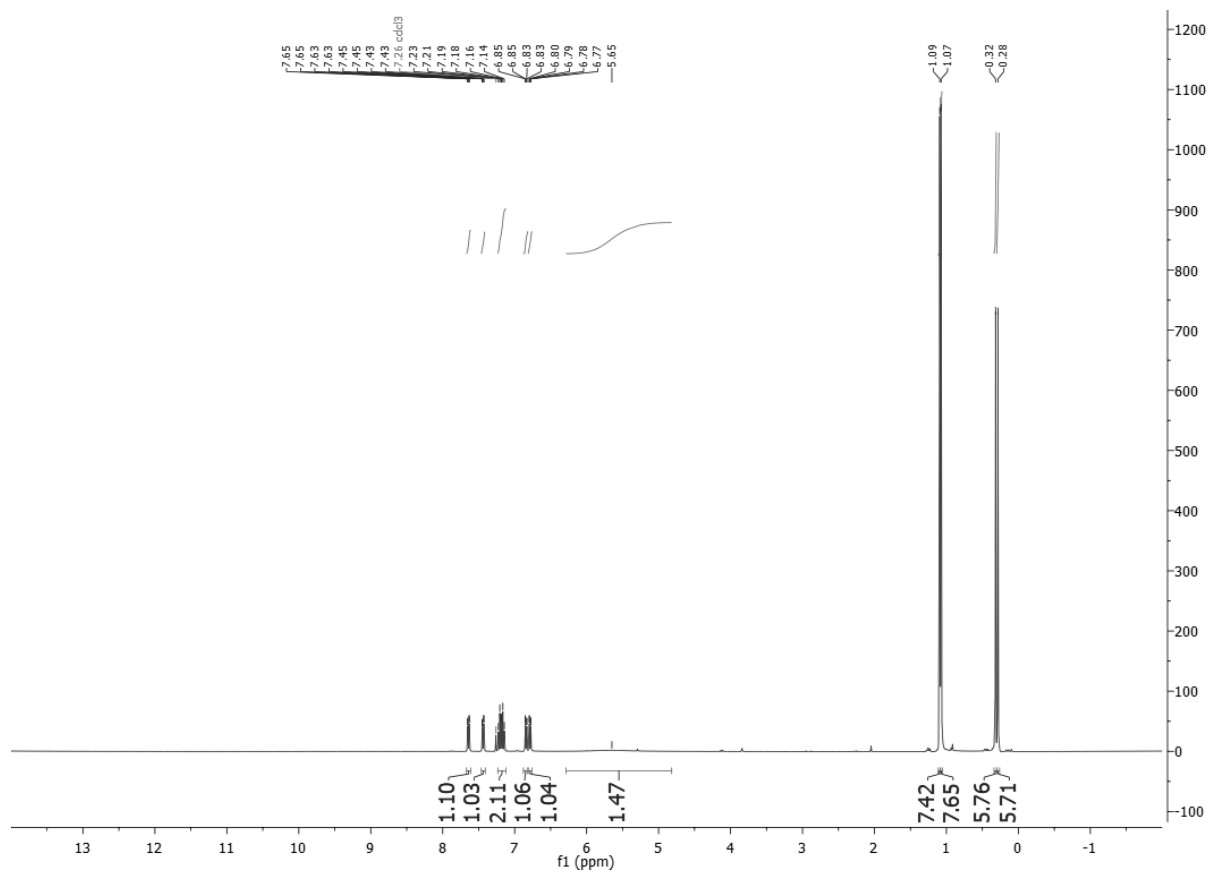
¹H and ¹³C NMR spectra for compound S10



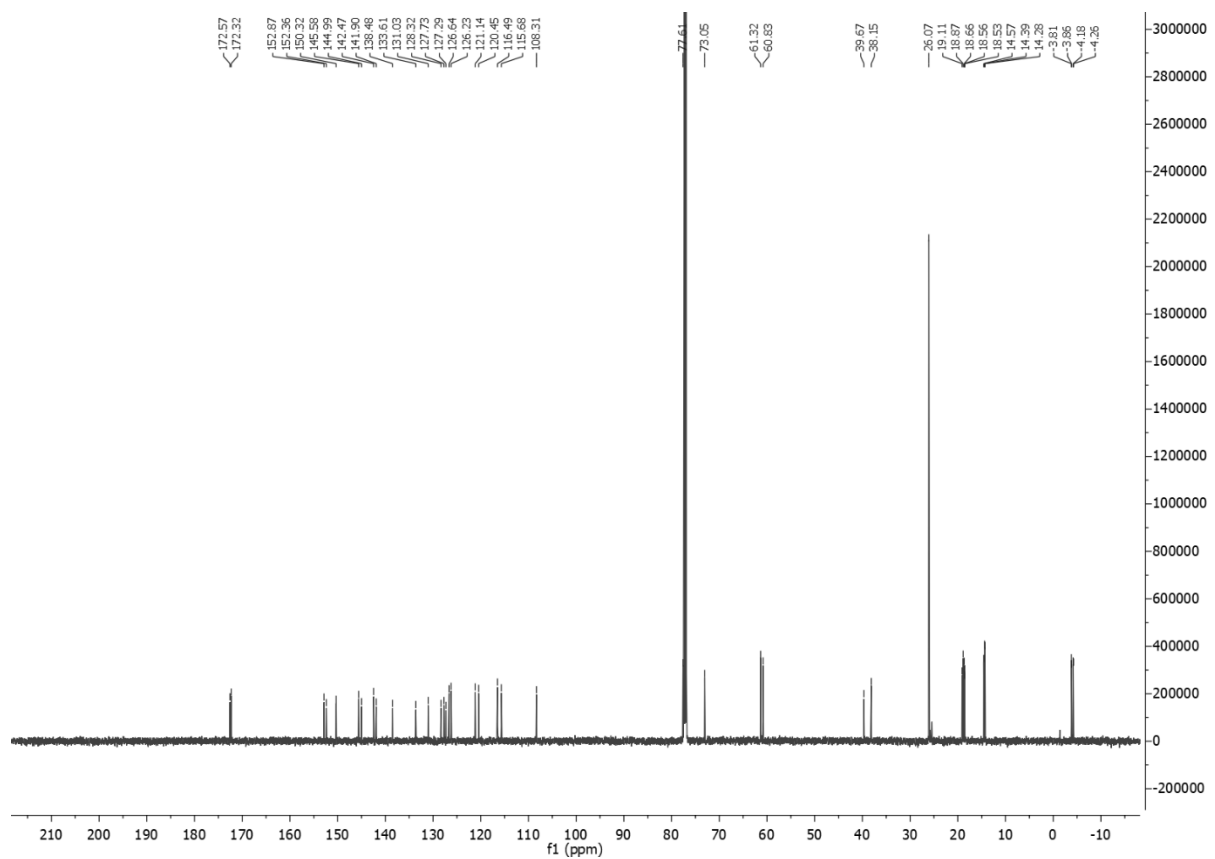
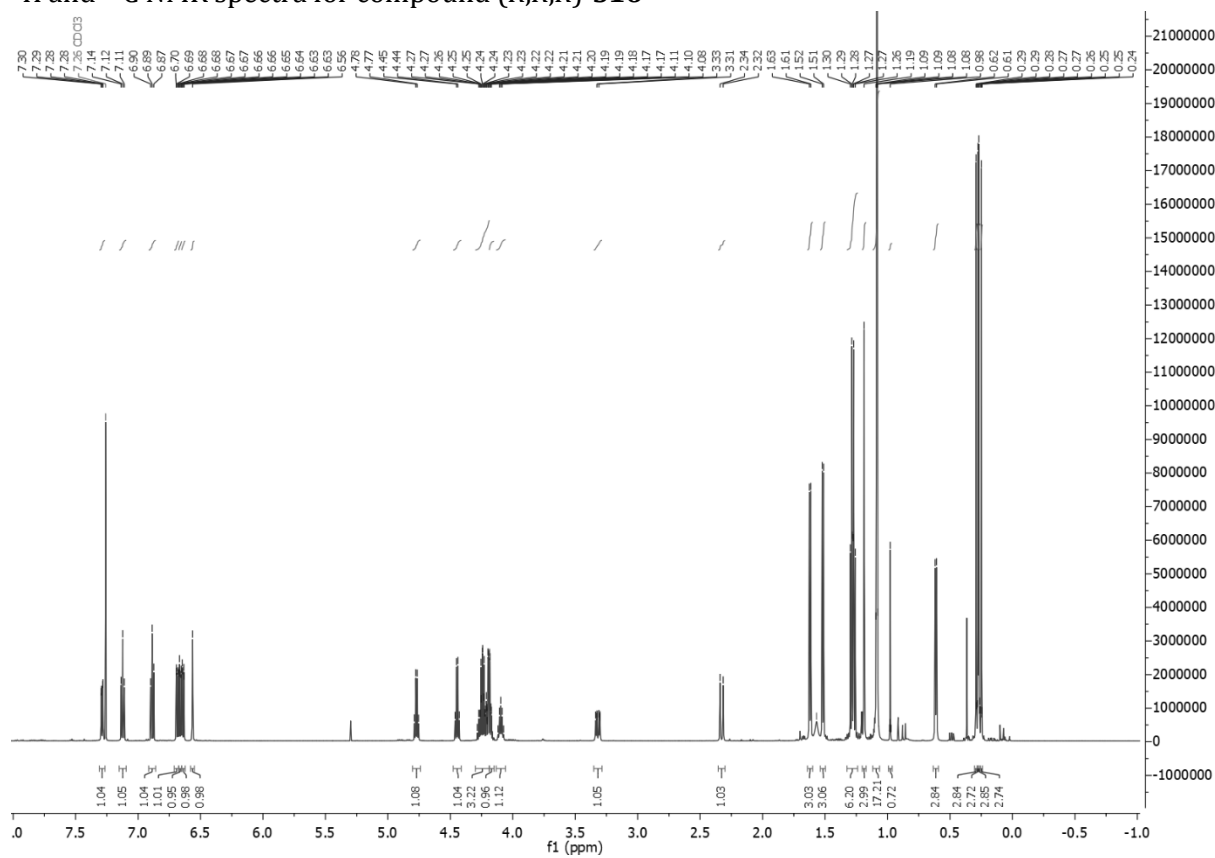
¹H NMR spectrum for compound **S12**



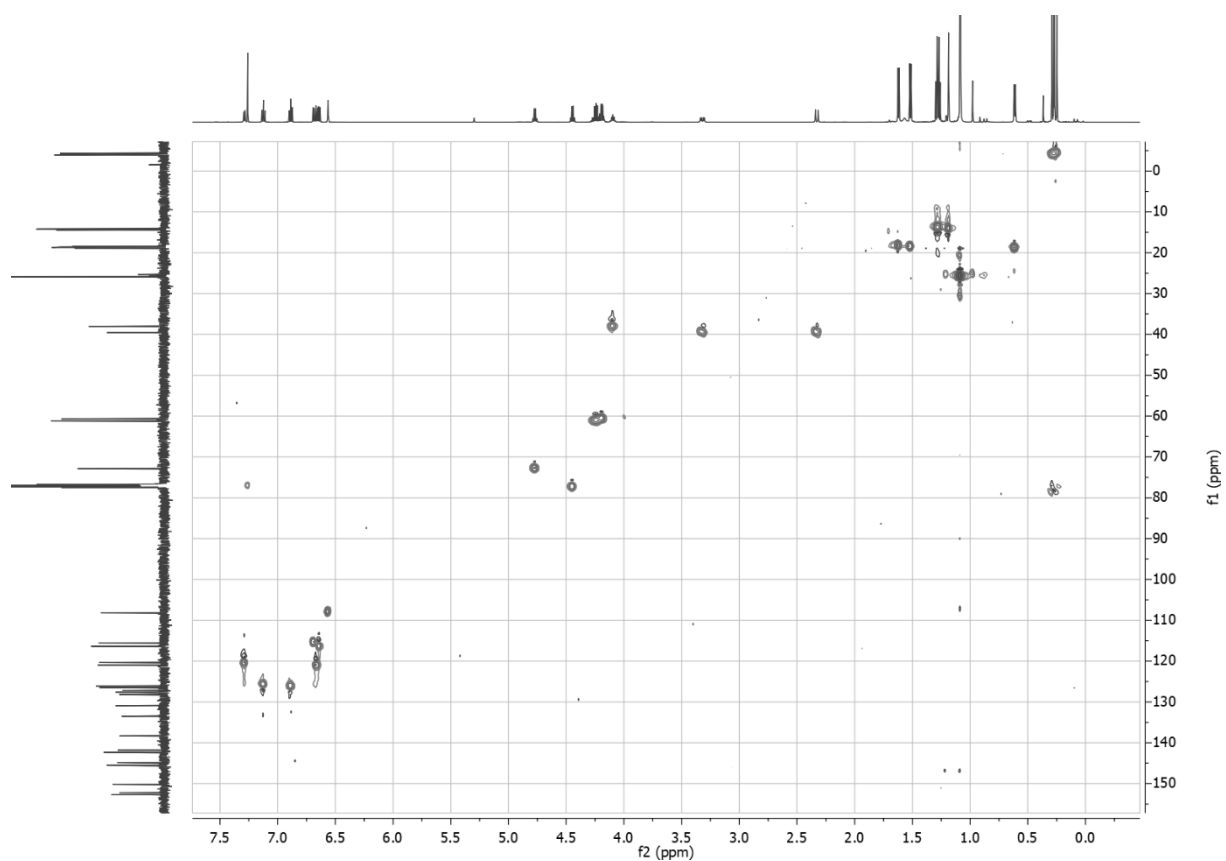
¹H NMR spectrum for compound **S13**



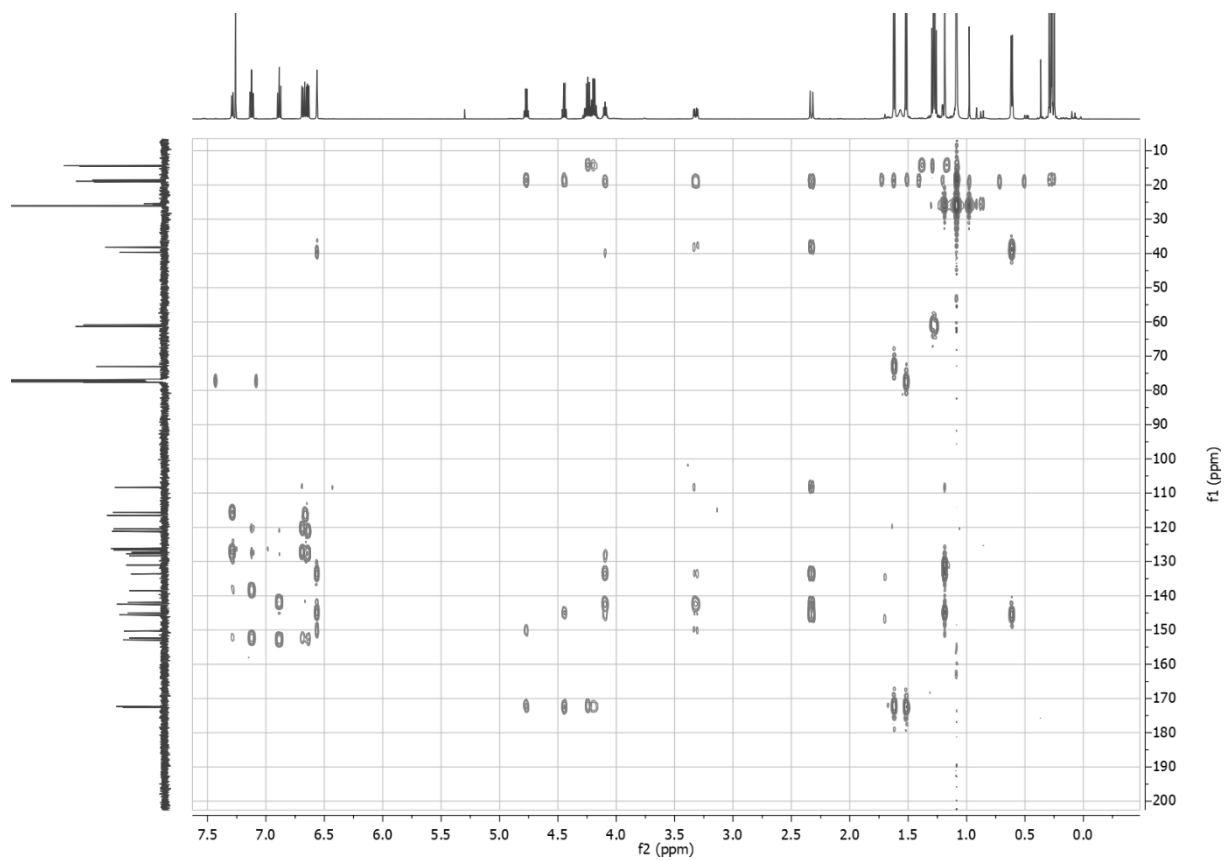
¹H and ¹³C NMR spectra for compound (*R,R*)-S16



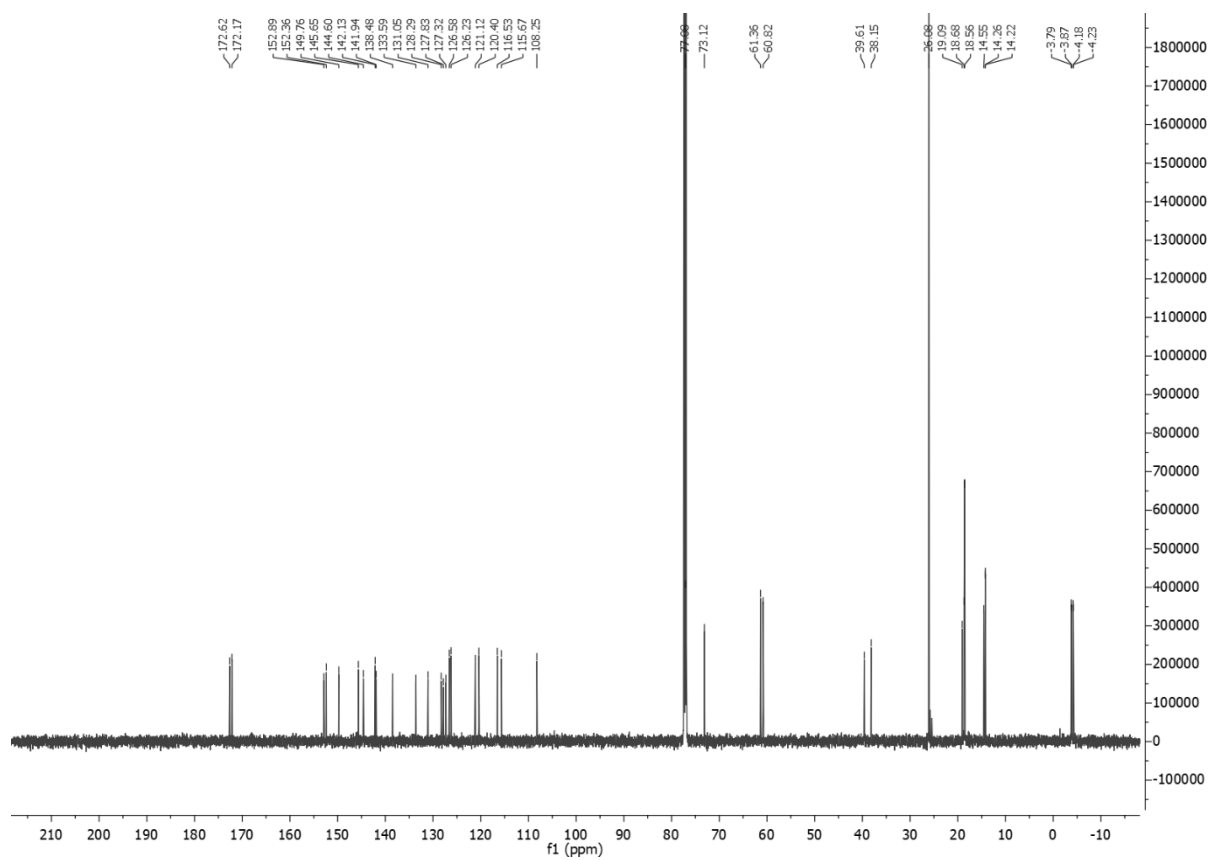
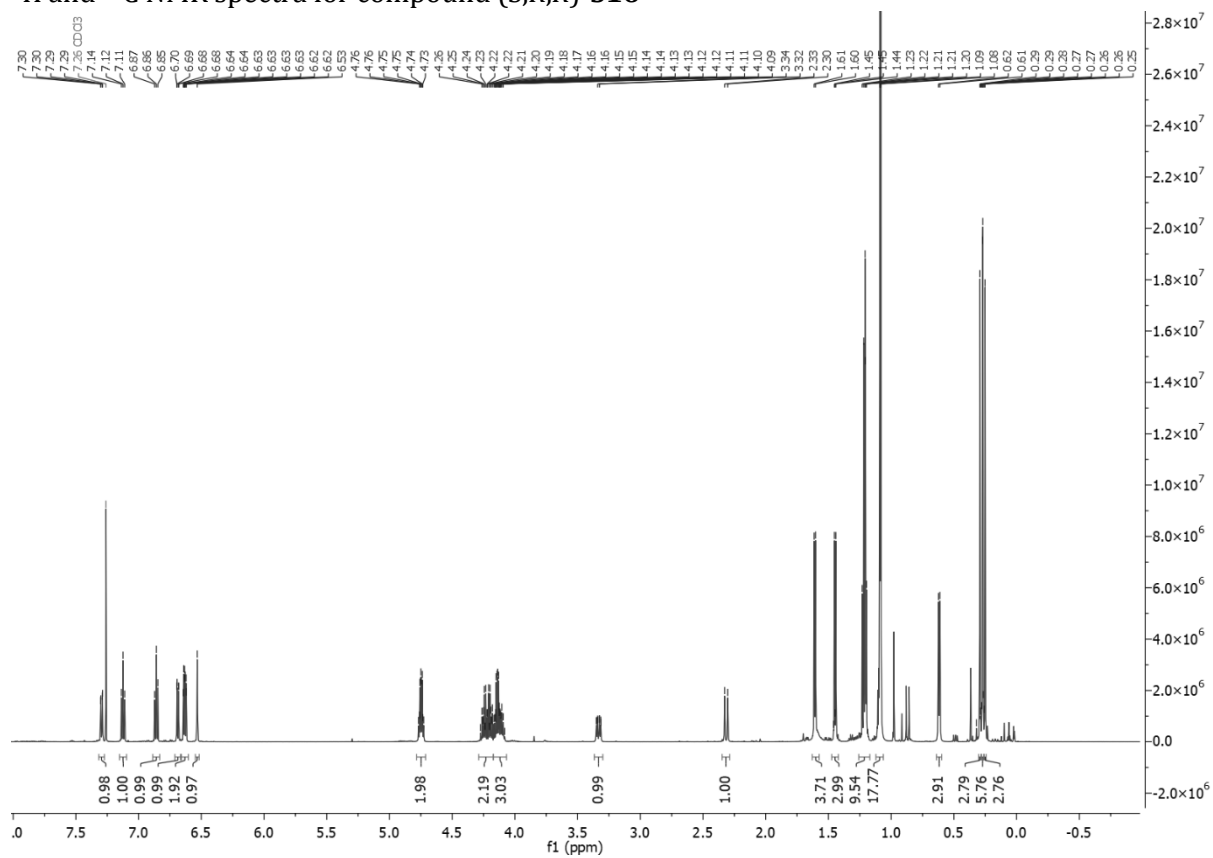
$^1\text{H}, ^{13}\text{C}$ HSQC NMR spectrum for compound (*R,R,R*)-**S16**



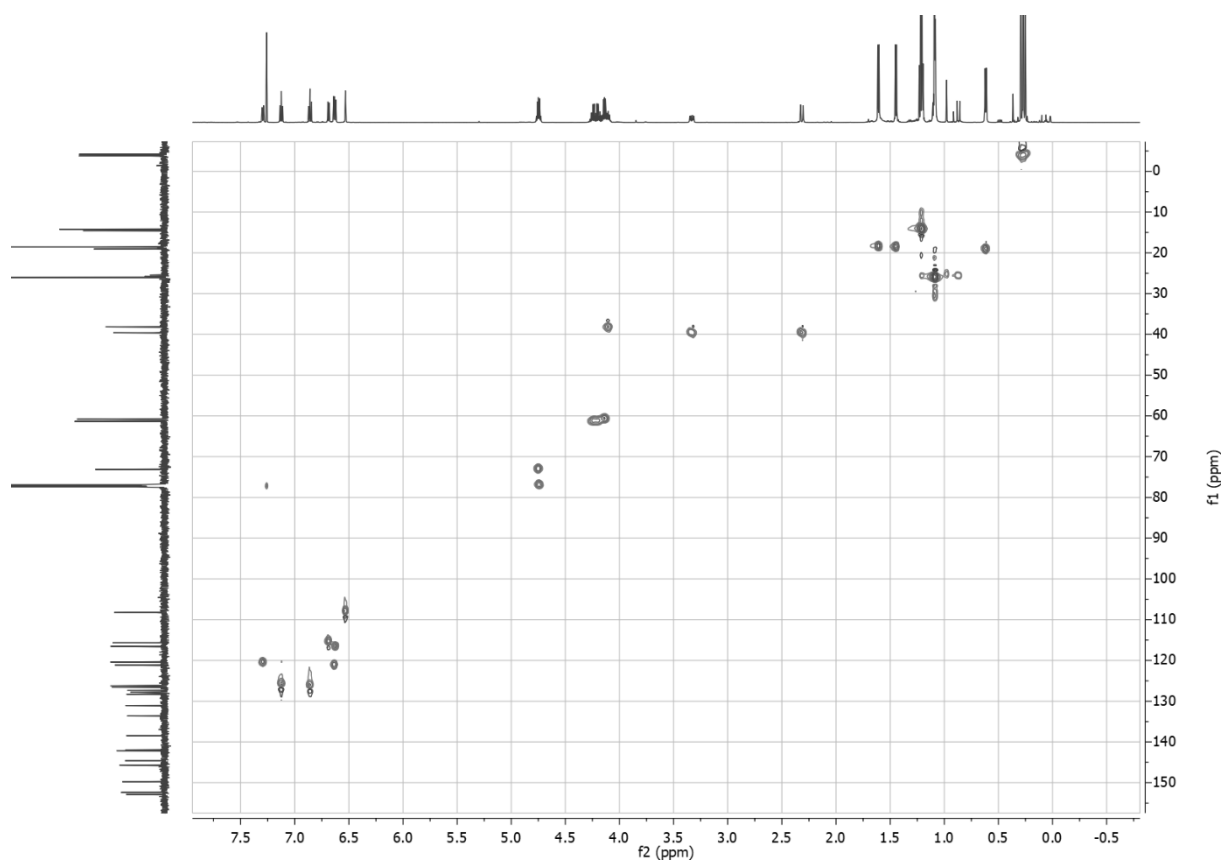
$^1\text{H}, ^{13}\text{C}$ HMBC NMR spectrum for compound (*R,R,R*)-**S16**



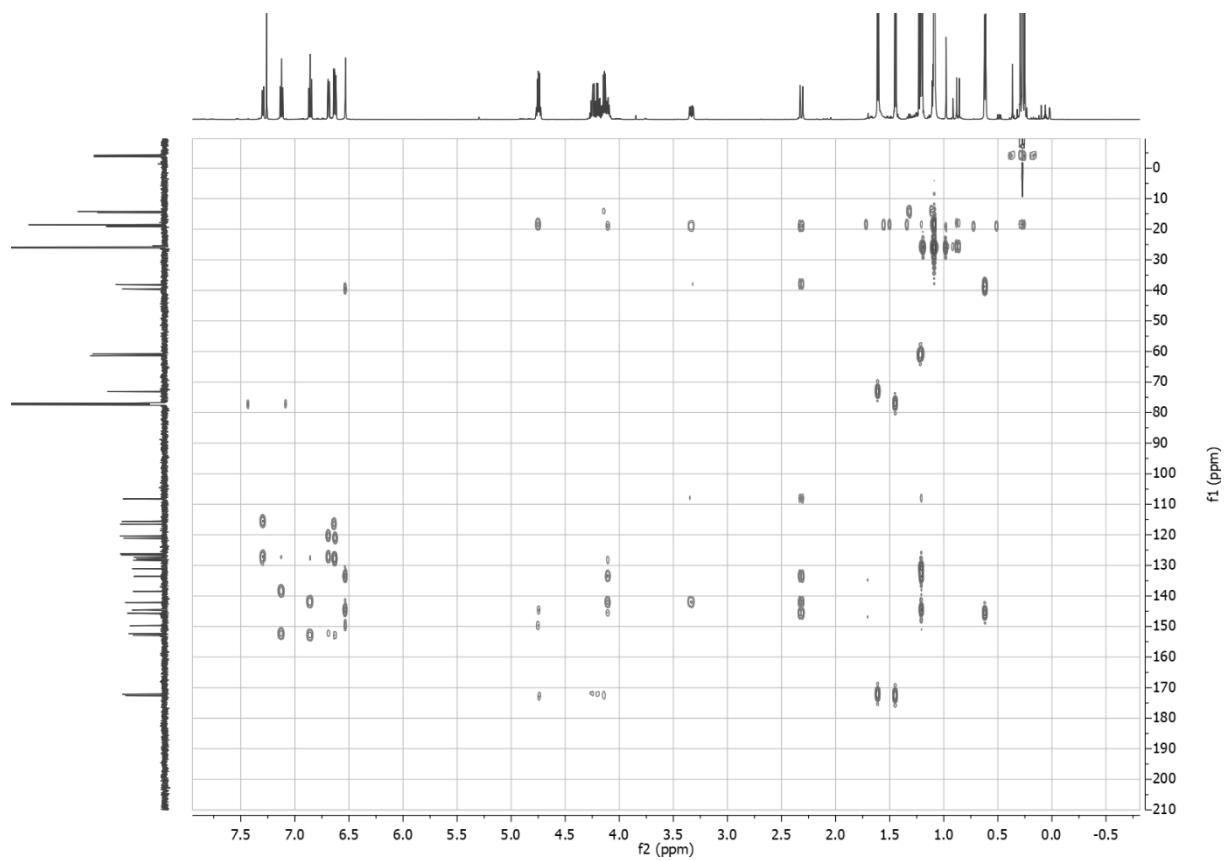
¹H and ¹³C NMR spectra for compound (S,R,R)-S16



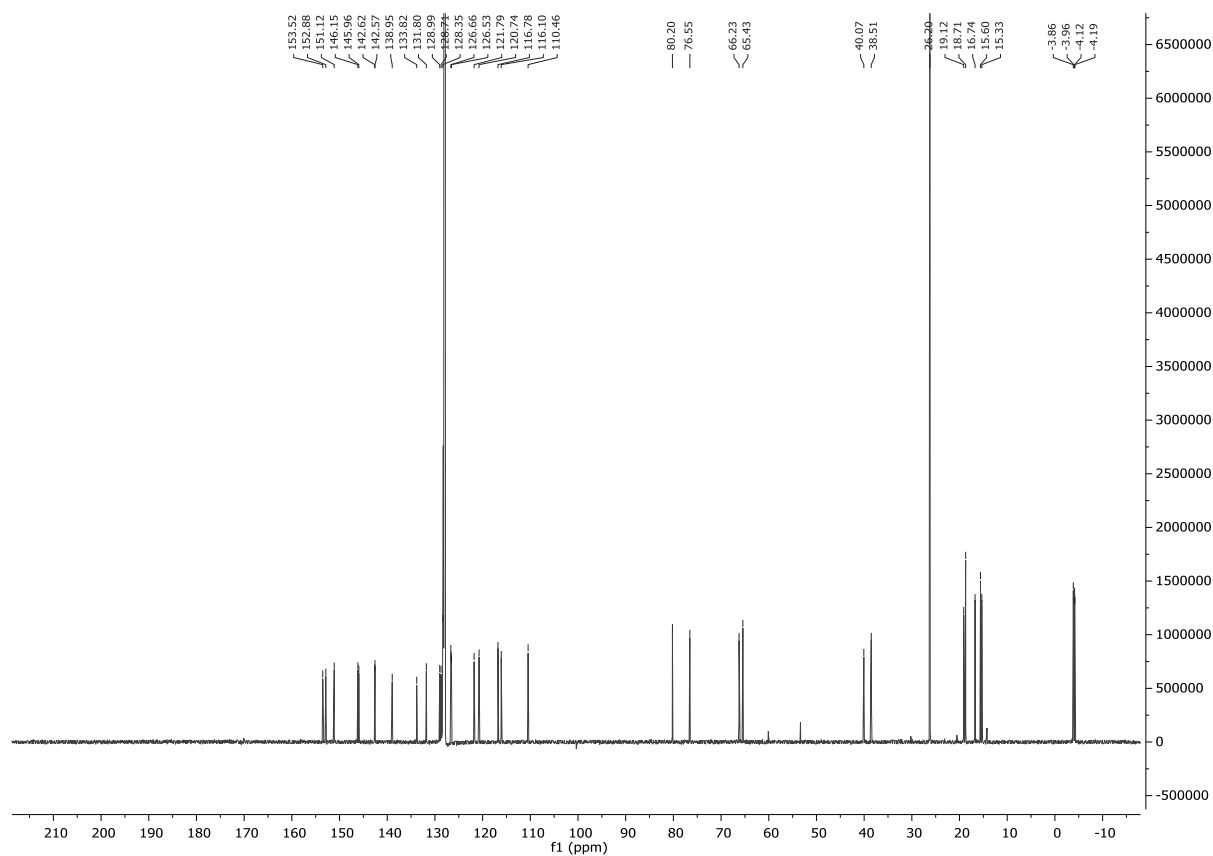
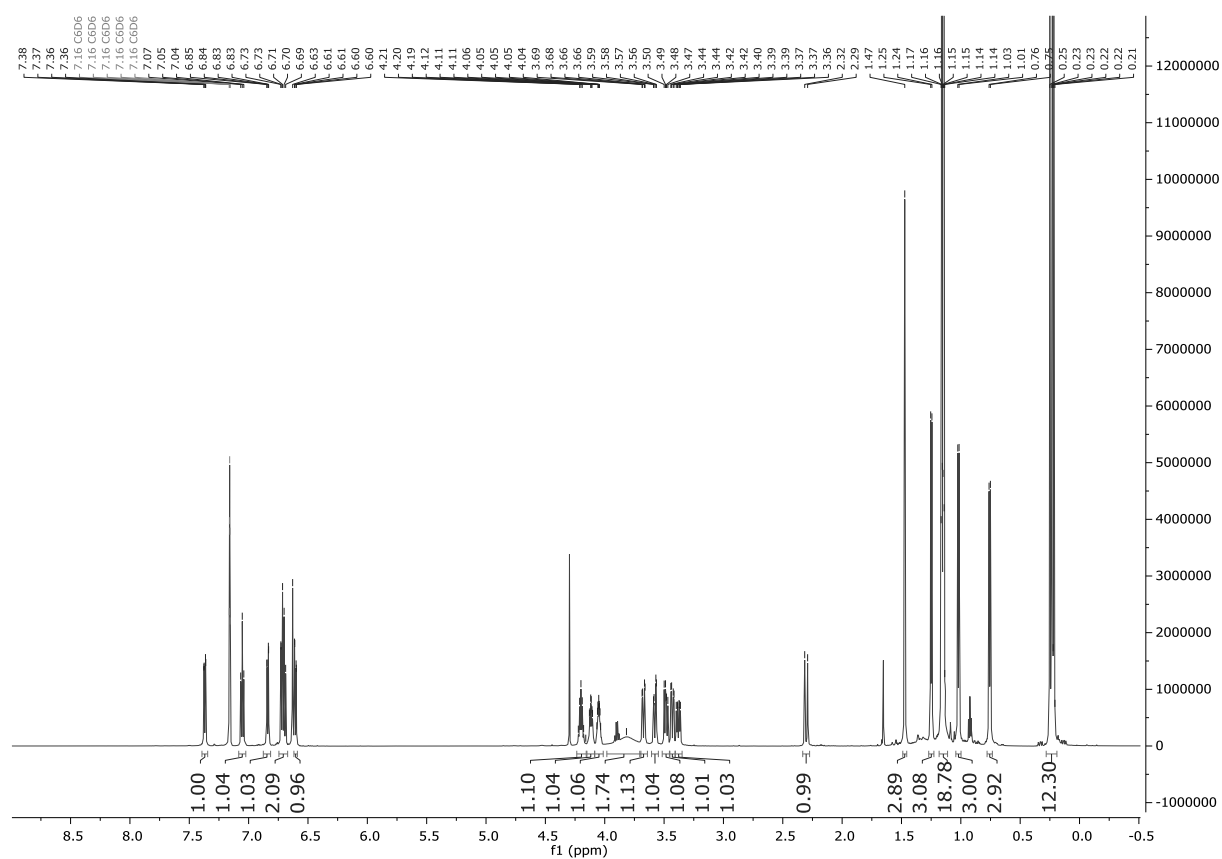
$^1\text{H}, ^{13}\text{C}$ HSQC NMR spectrum for compound (*S,R,R*)-**S16**



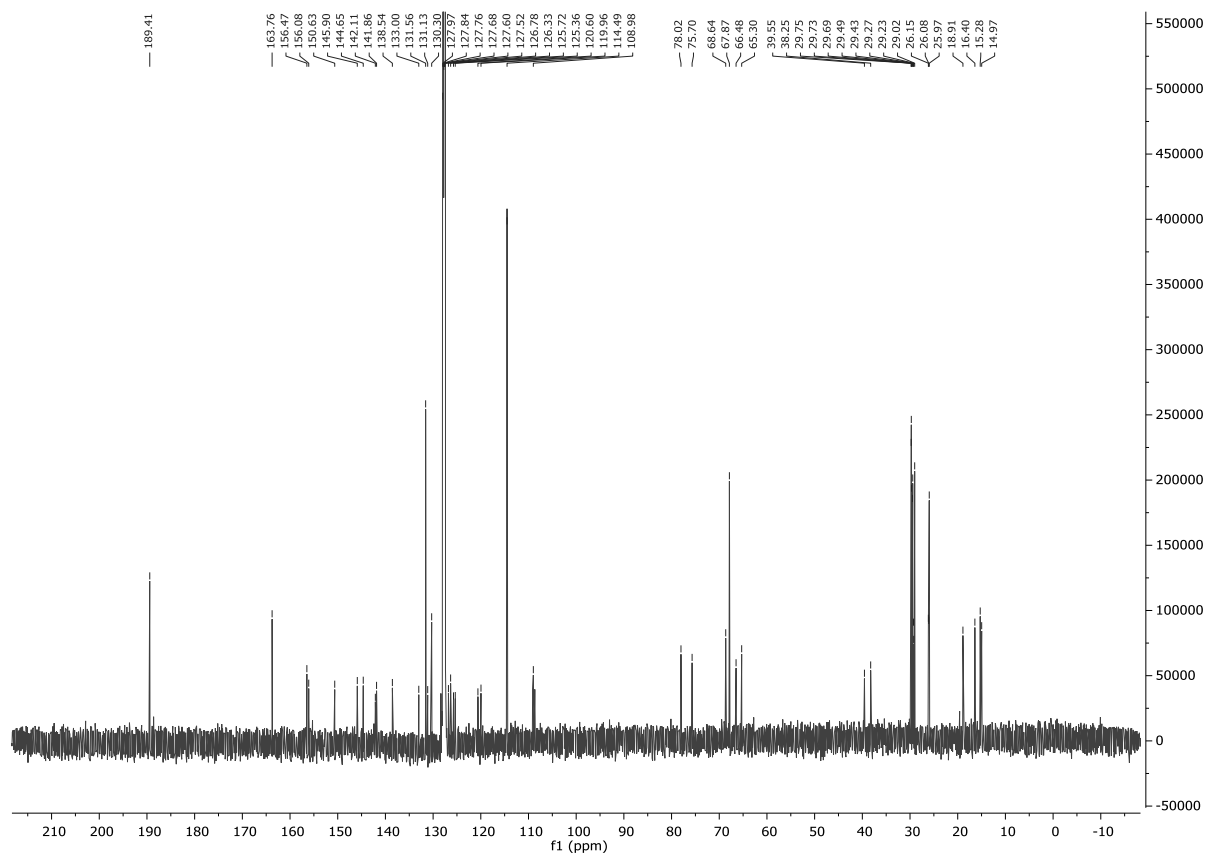
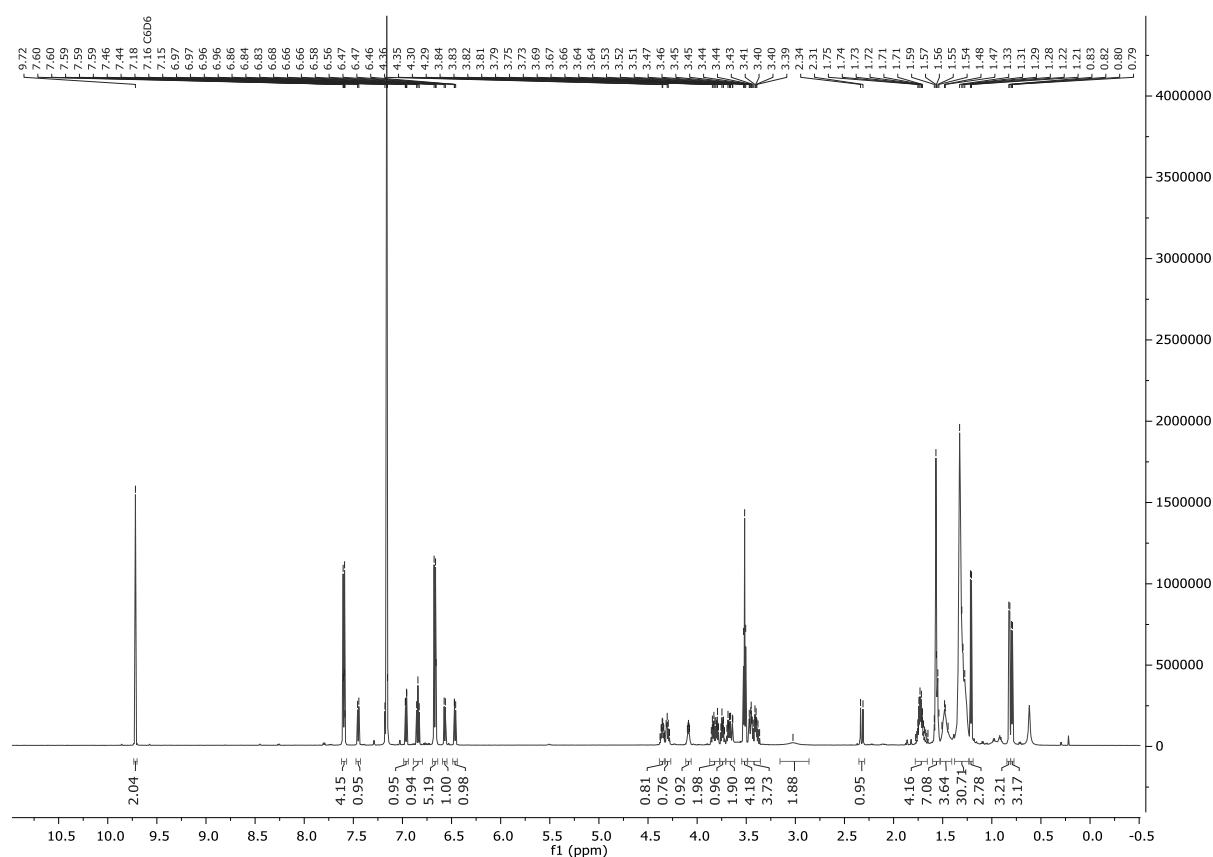
$^1\text{H}, ^{13}\text{C}$ HMBC NMR spectrum for compound (*S,R,R*)-**S16**



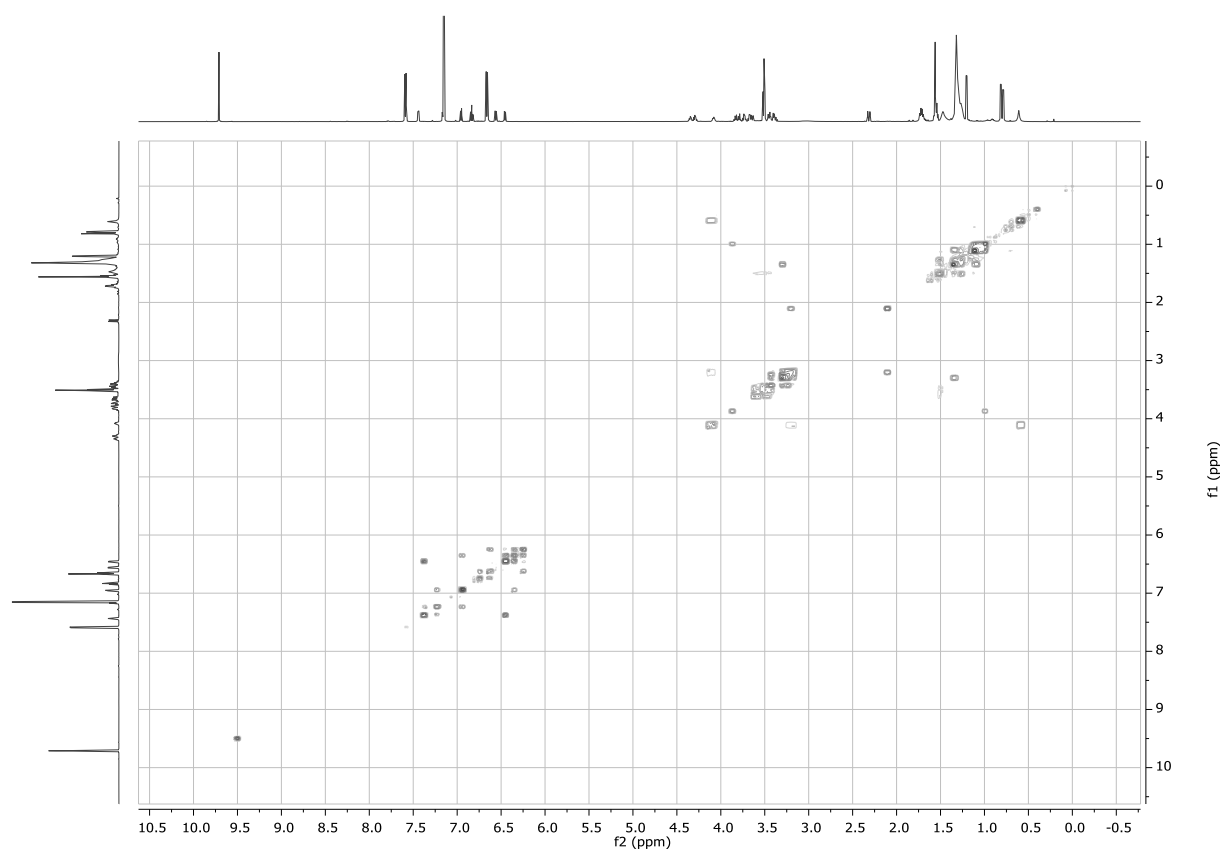
^1H and ^{13}C NMR spectrum for compound (*S,R,R*)-**S17**



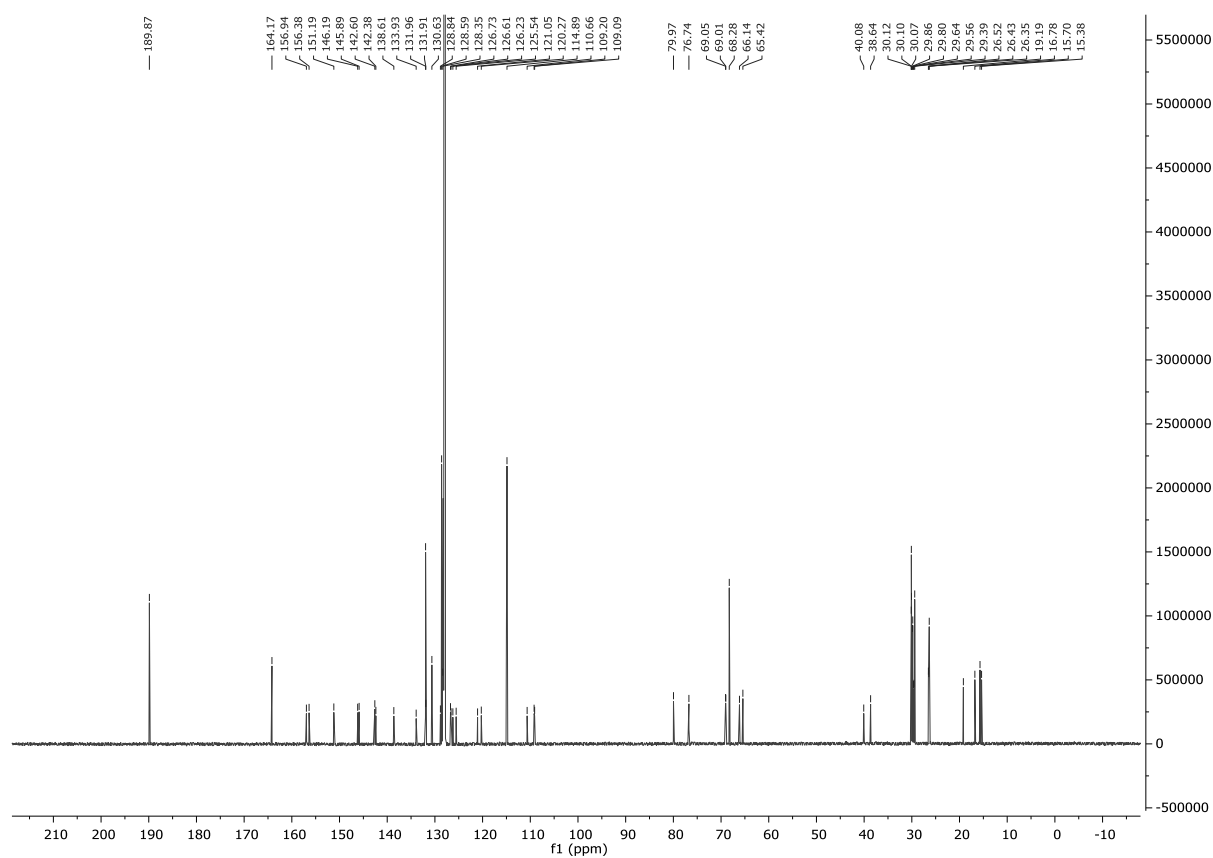
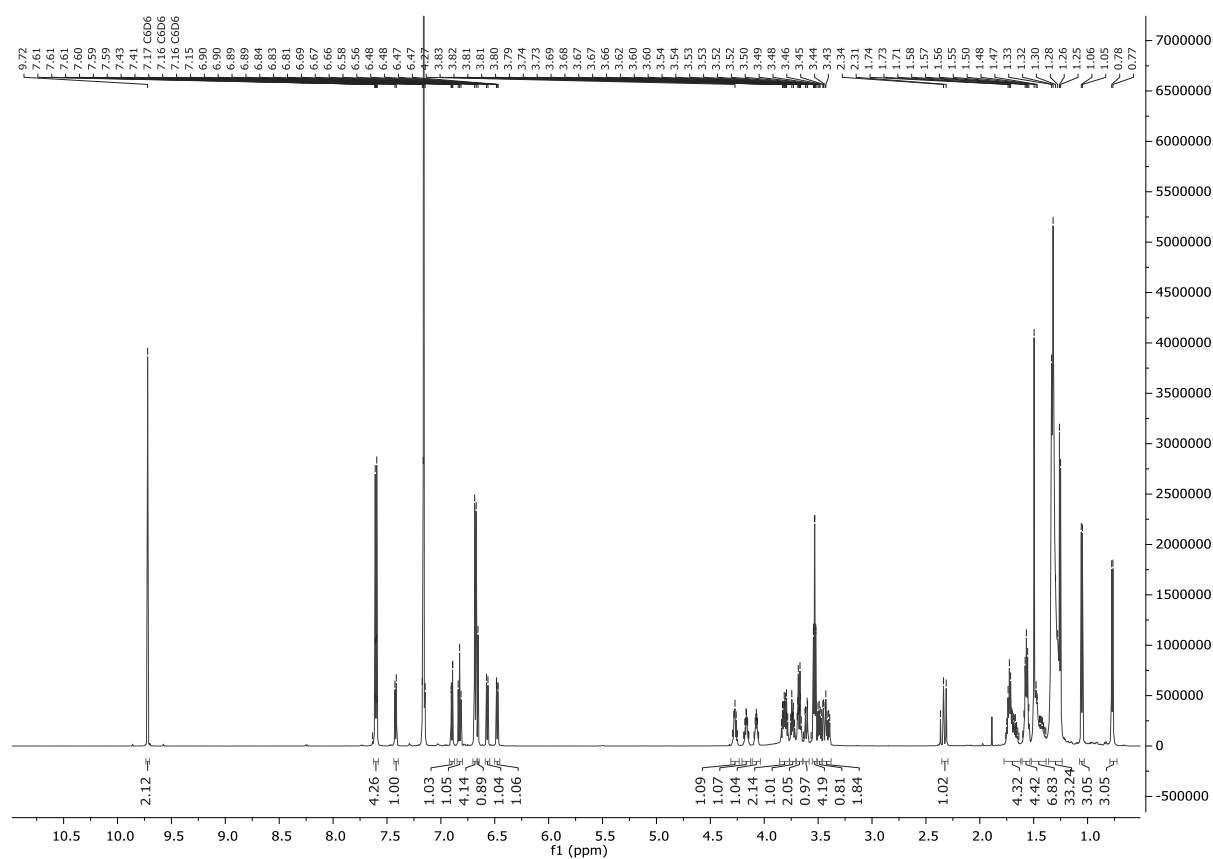
¹H and ¹³C NMR spectra for compound (*R,R,R*)-S19



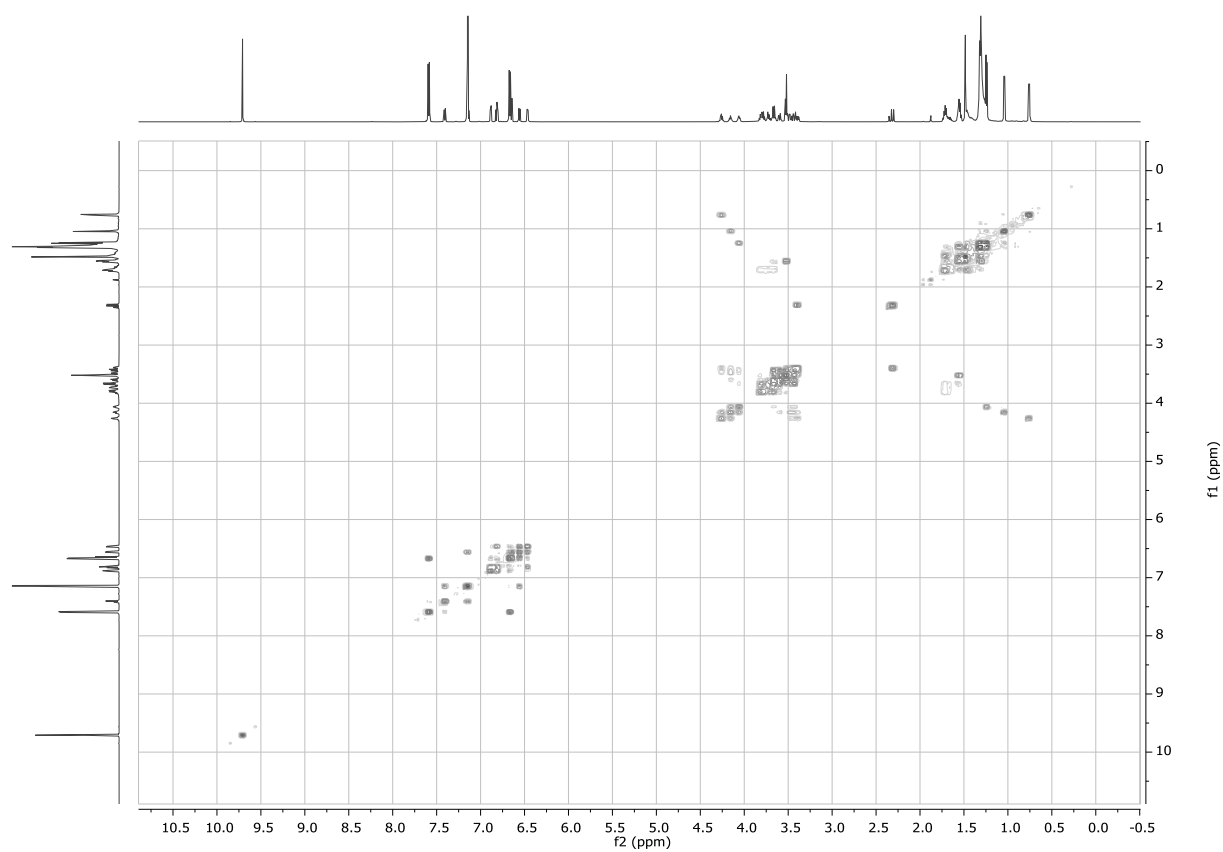
$^1\text{H}, ^1\text{H}$ COSY NMR spectrum for compound (*R,R,R*)-S19



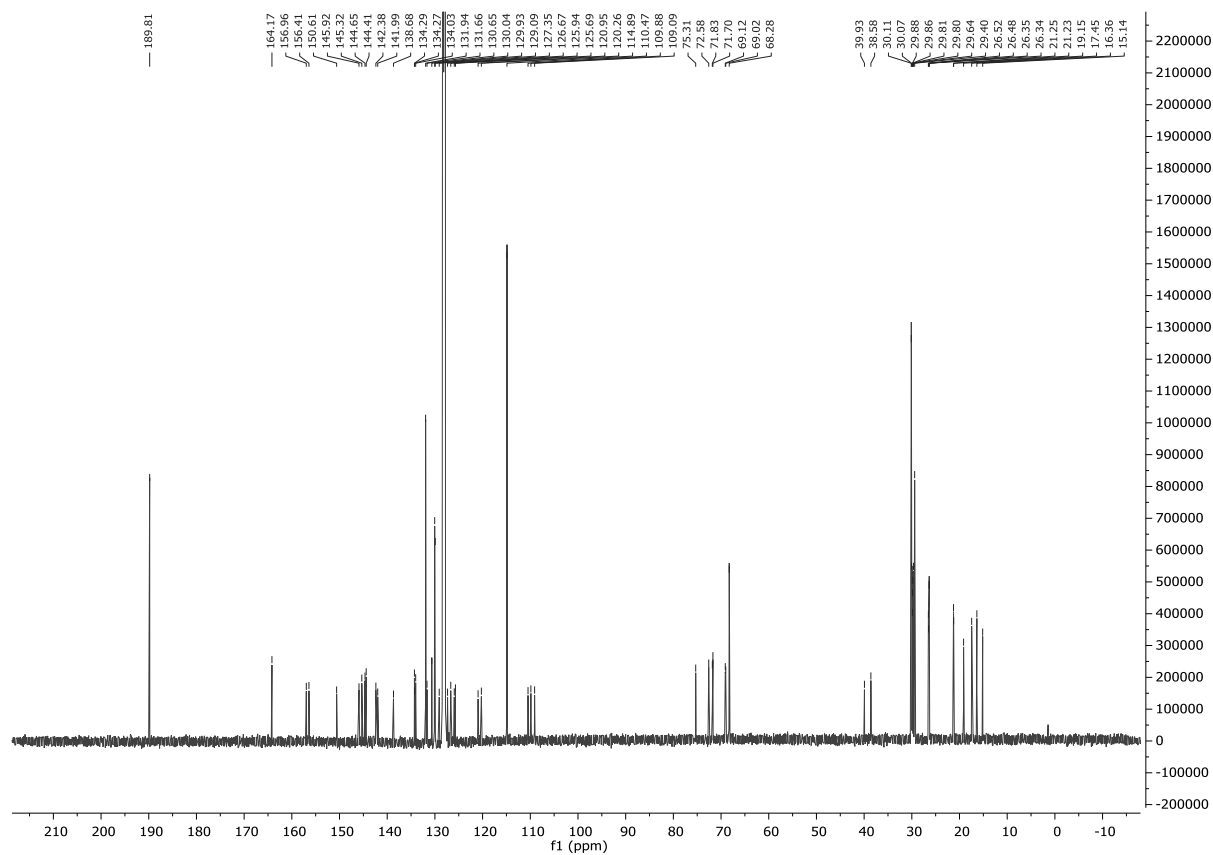
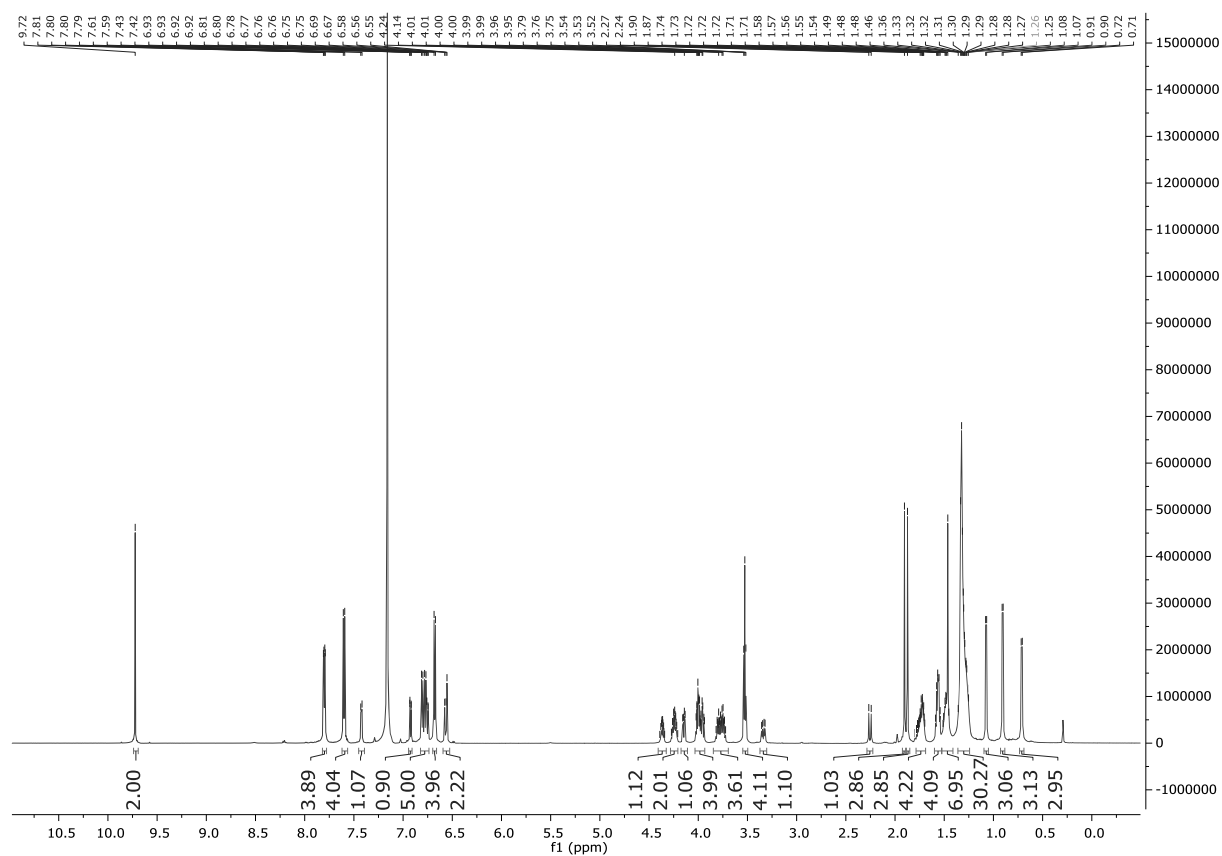
¹H and ¹³C NMR spectrum for compound (*S,R,R*)-S19



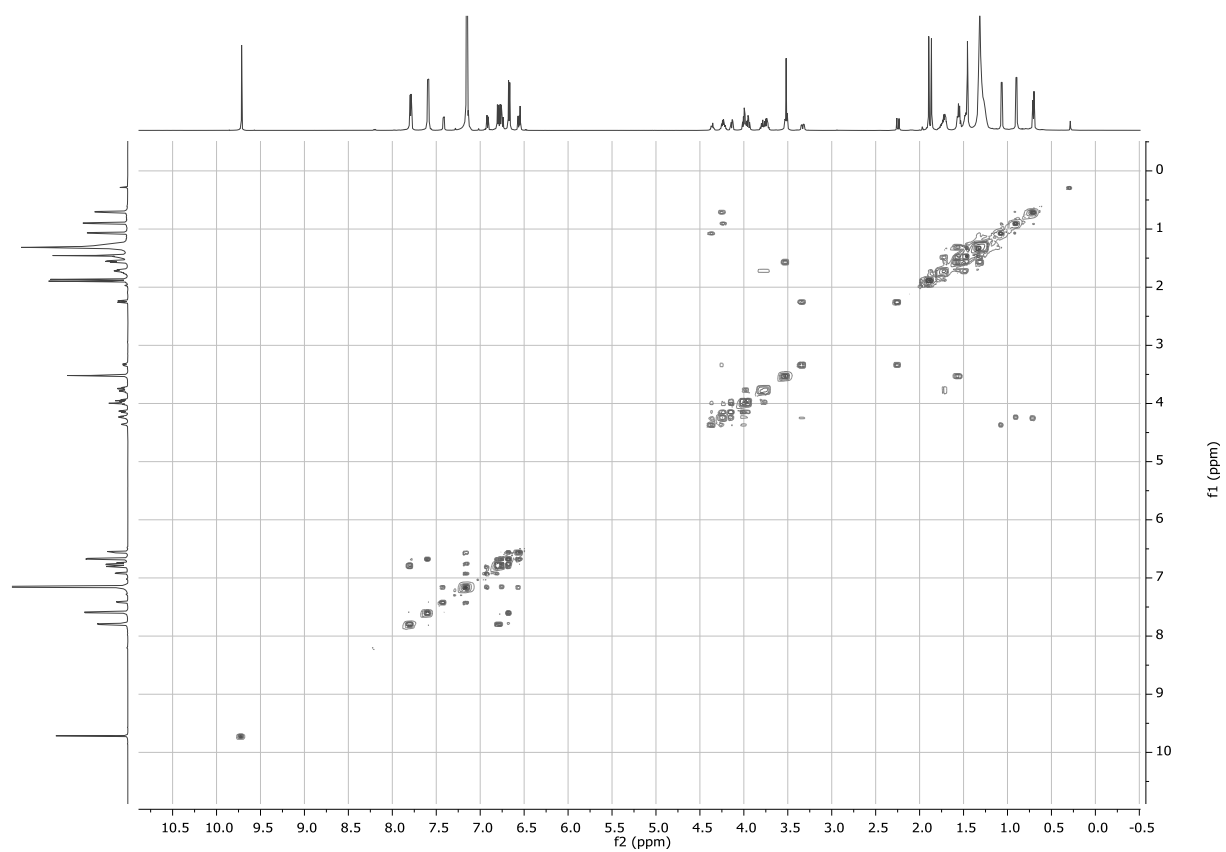
$^1\text{H}, ^1\text{H}$ COSY NMR spectrum for compound (*S,R,R*)-**S19**



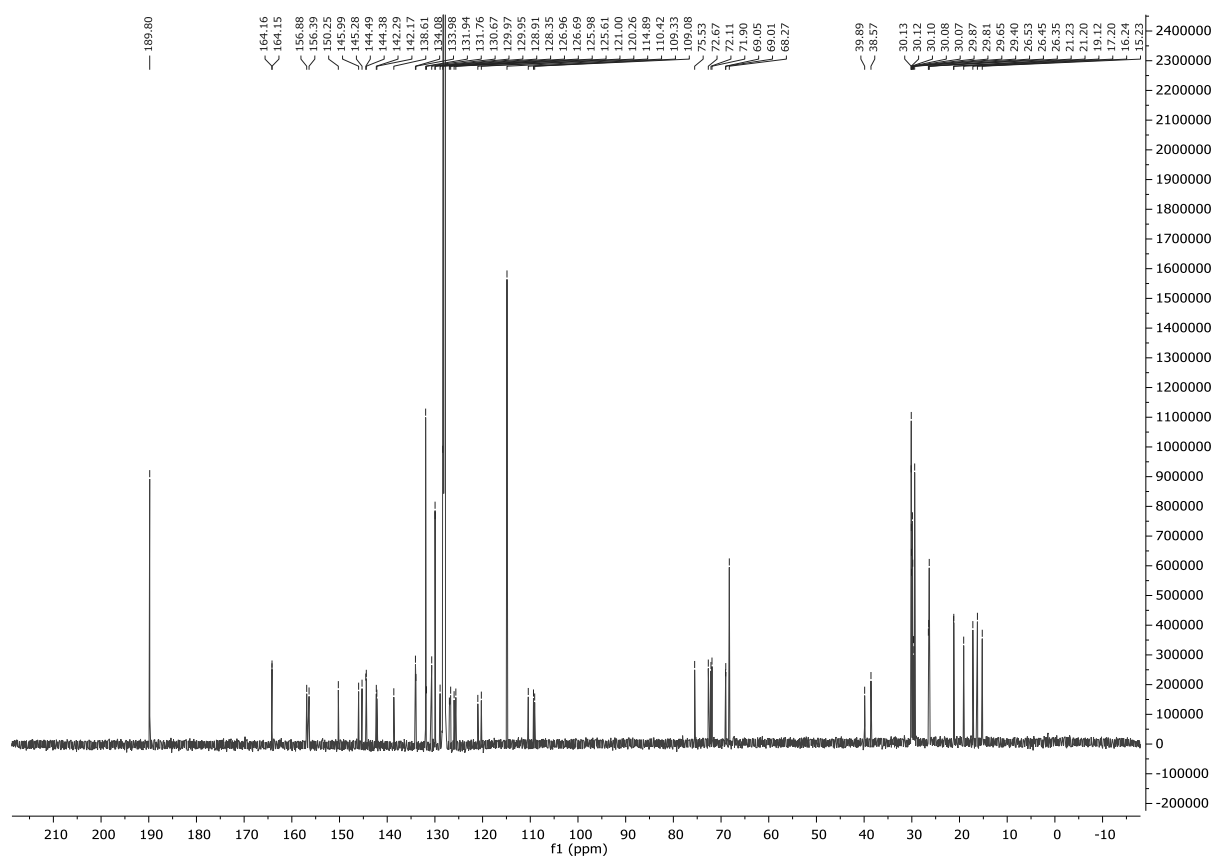
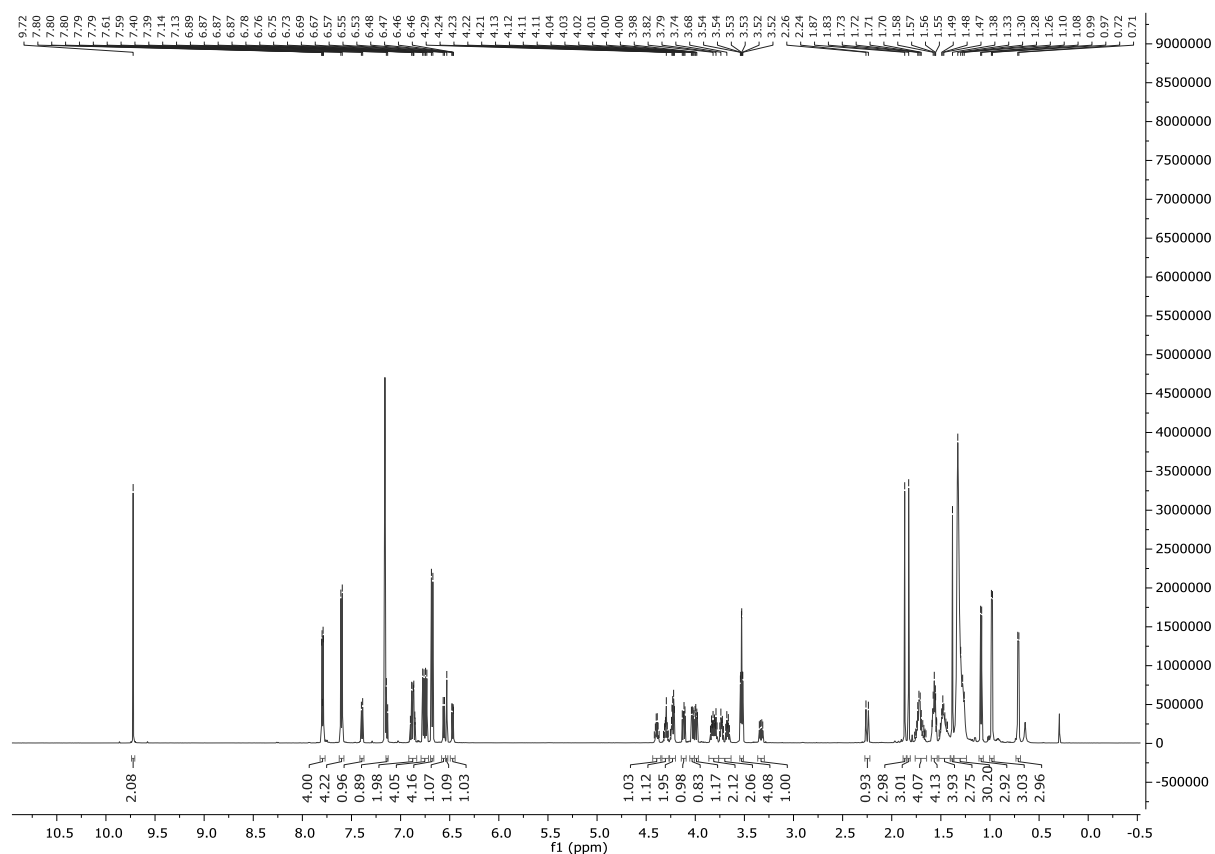
^1H and ^{13}C NMR spectra for compound (*R,R,R*)-S20



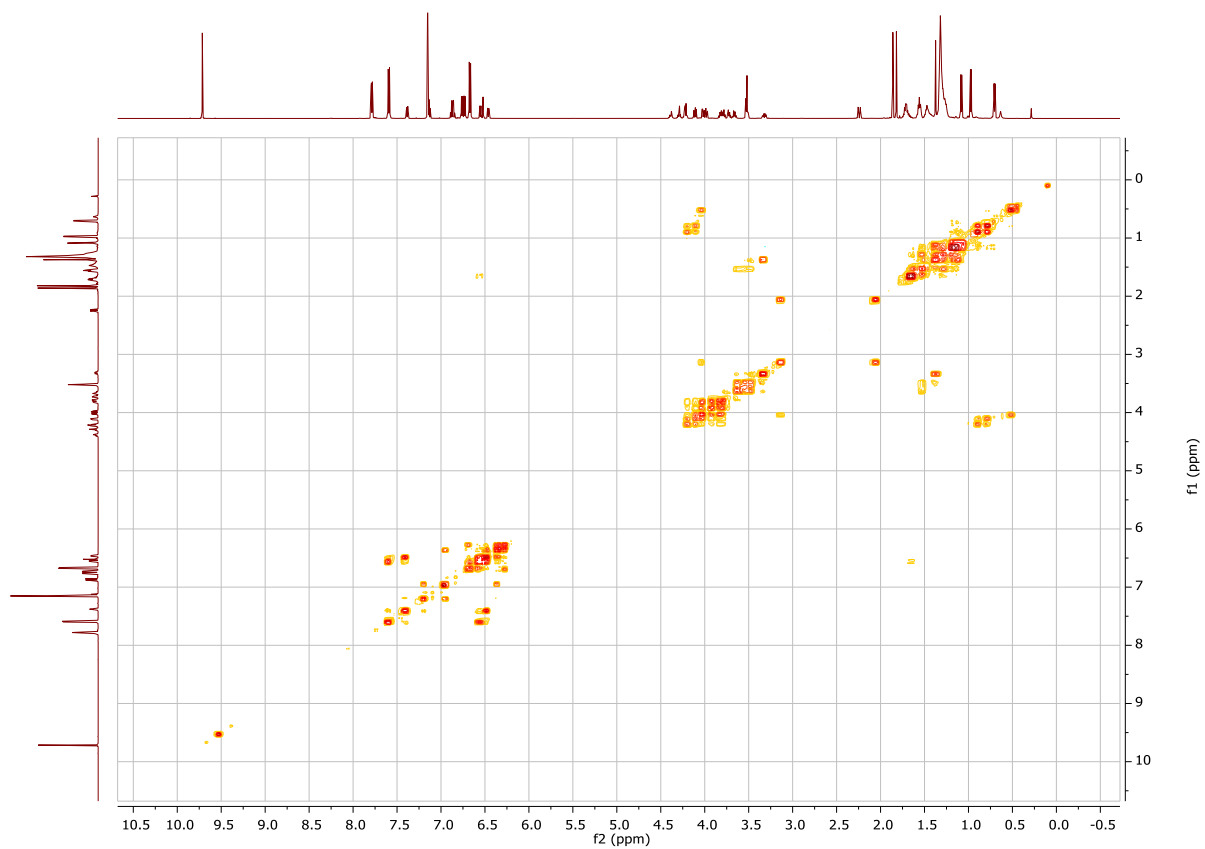
$^1\text{H}, ^1\text{H}$ COSY NMR spectrum for compound (*R,R,R*)-S20



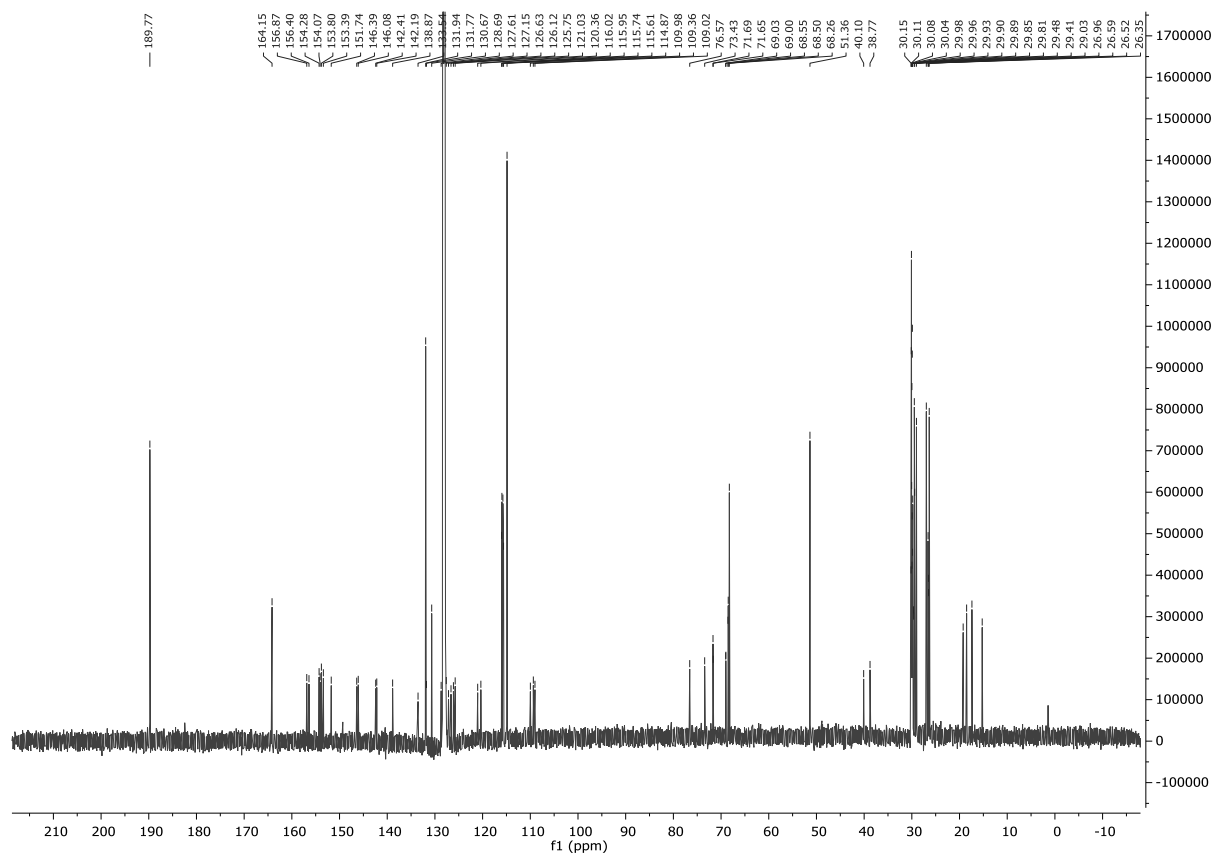
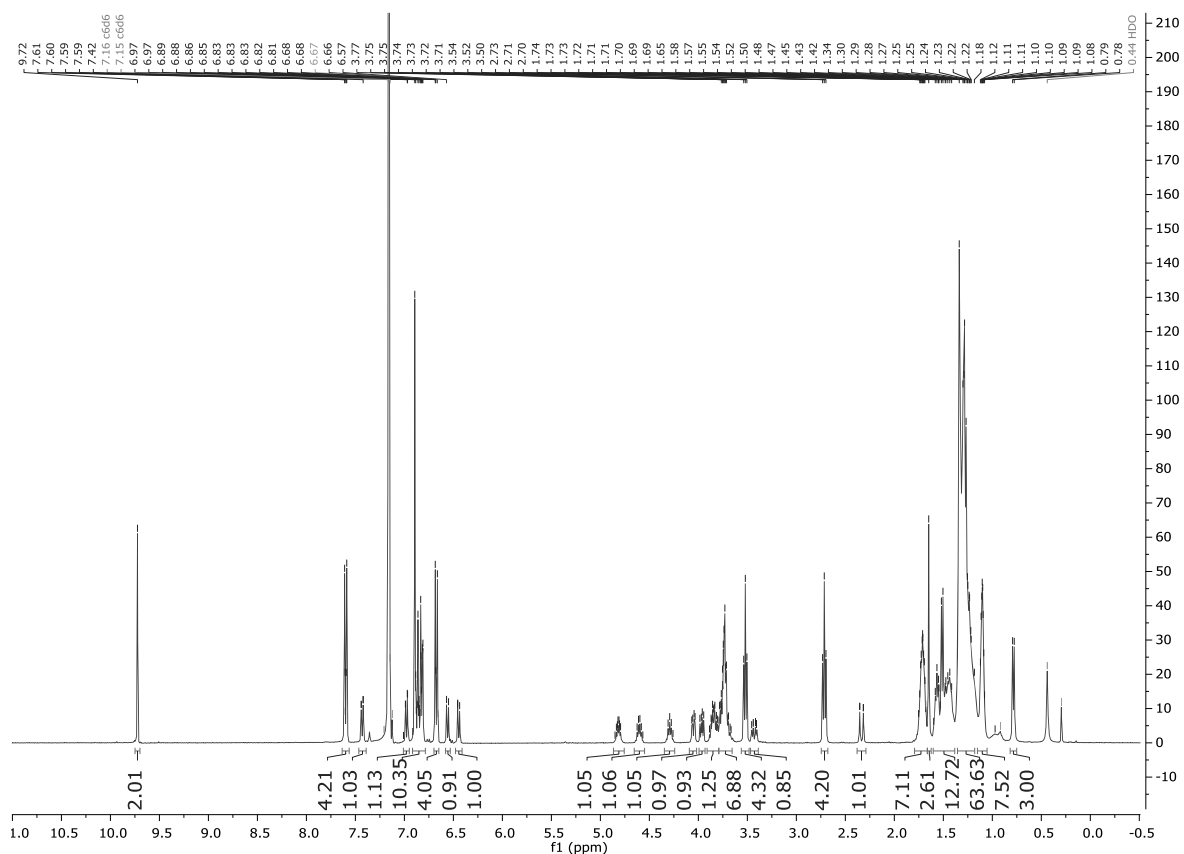
^1H and ^{13}C NMR spectra for compound (*S,R,R*)-S20



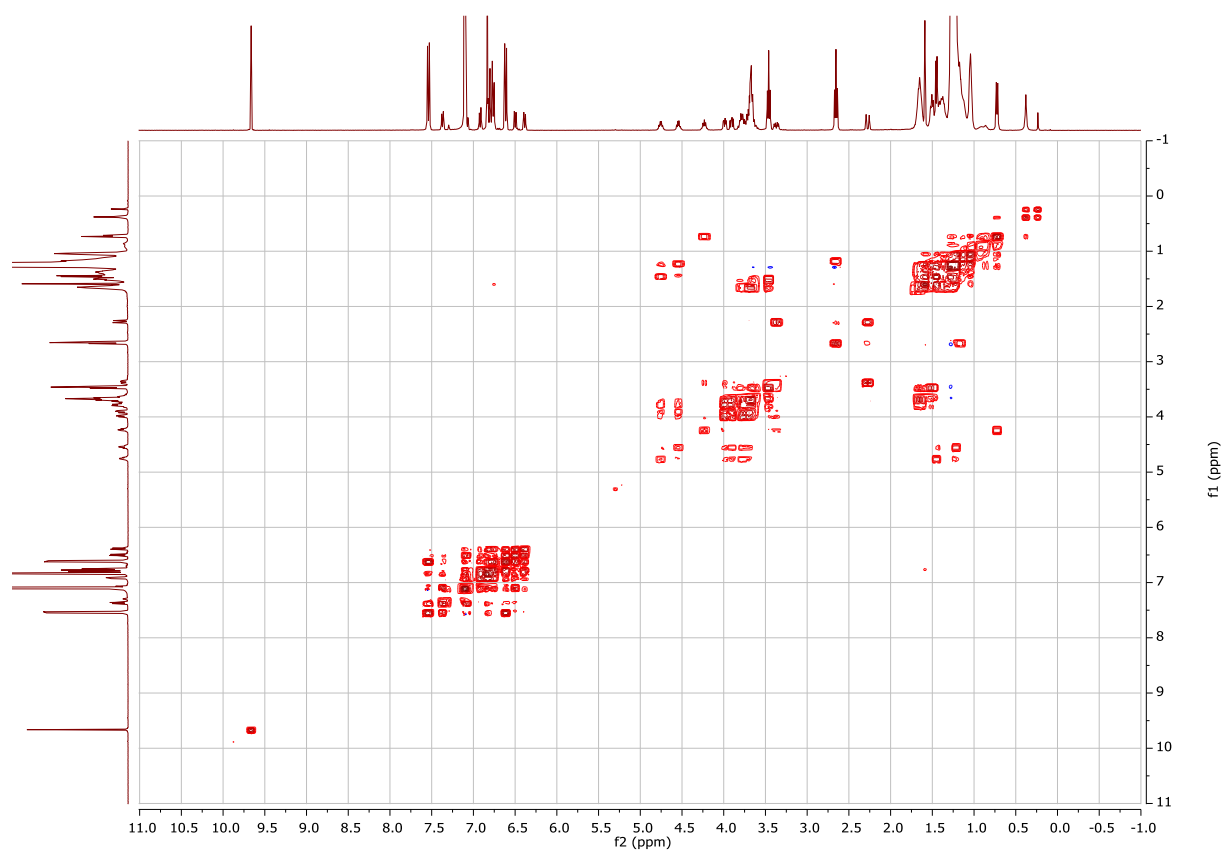
$^1\text{H}, ^1\text{H}$ COSY NMR spectrum for compound (*S,R,R*)-S20



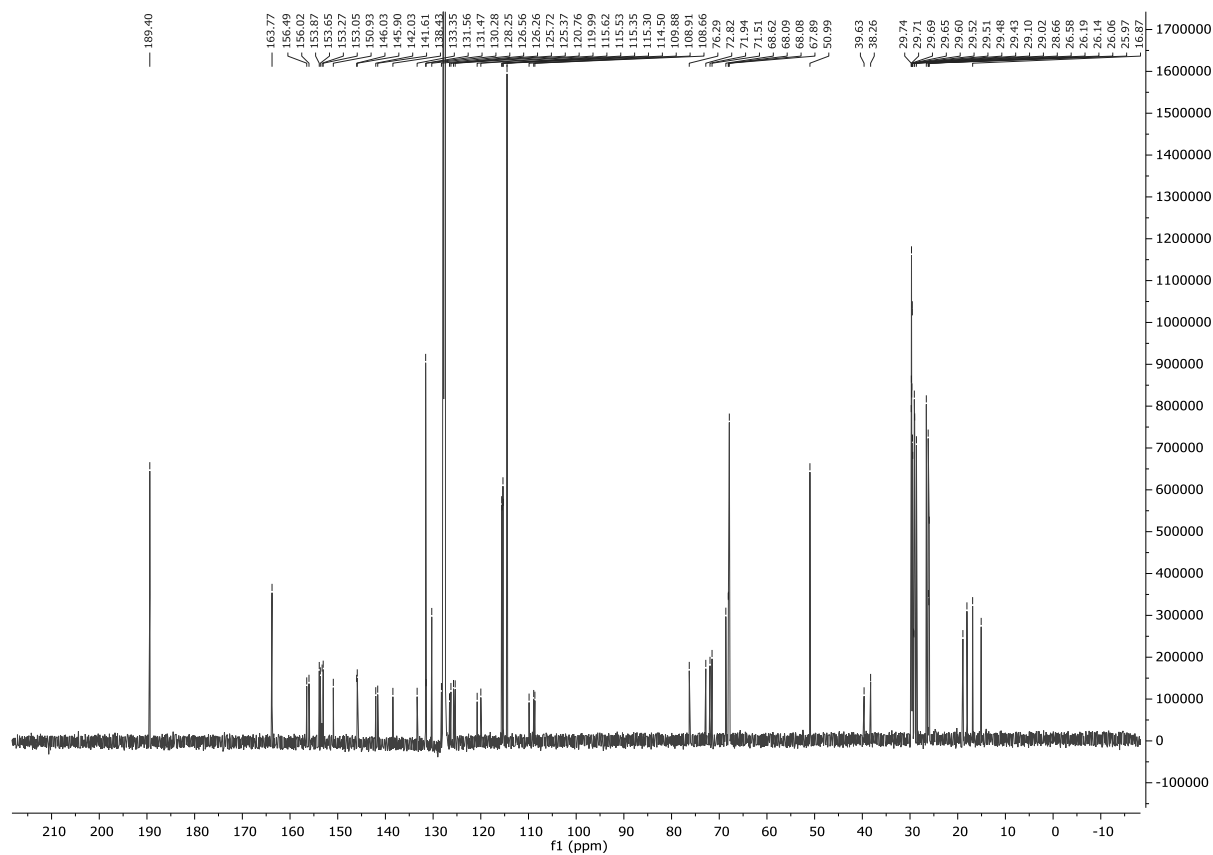
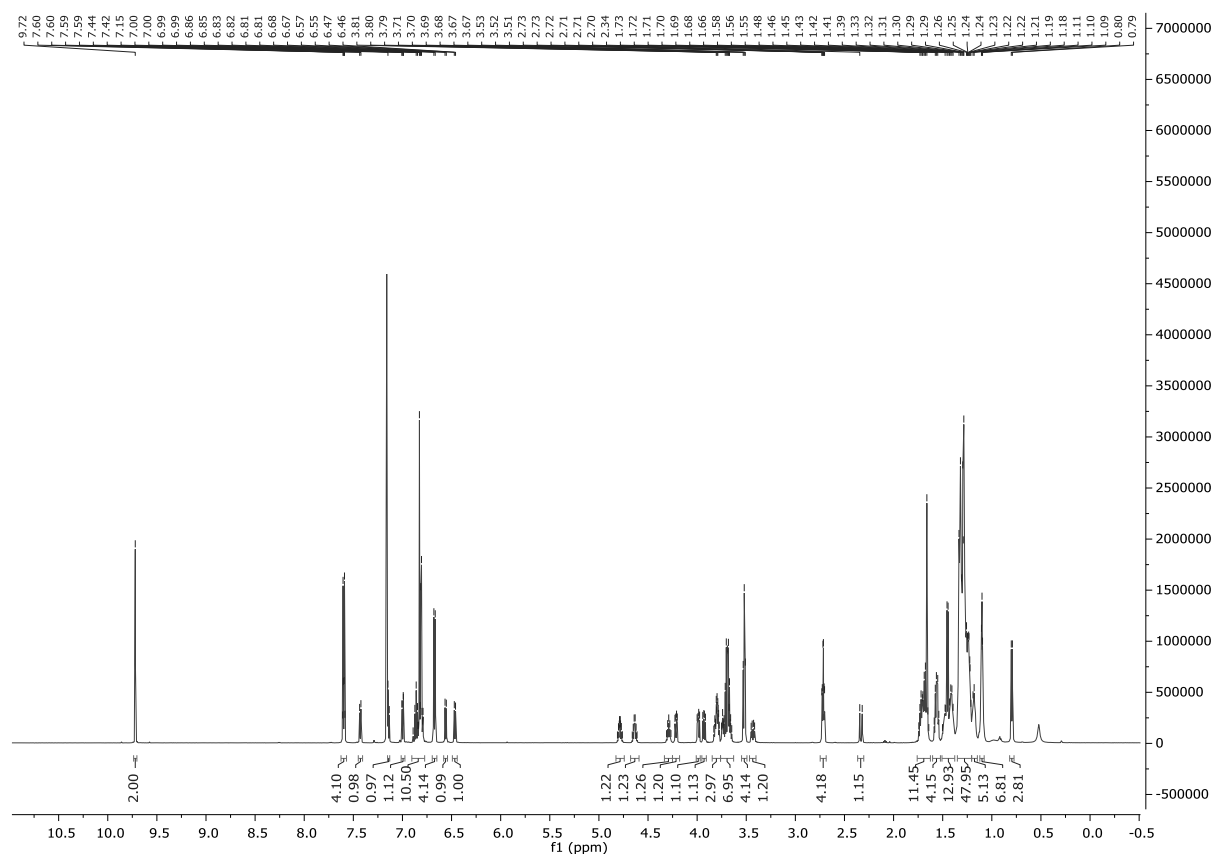
^1H and ^{13}C NMR spectra for compound (*R,R,R*)-S21



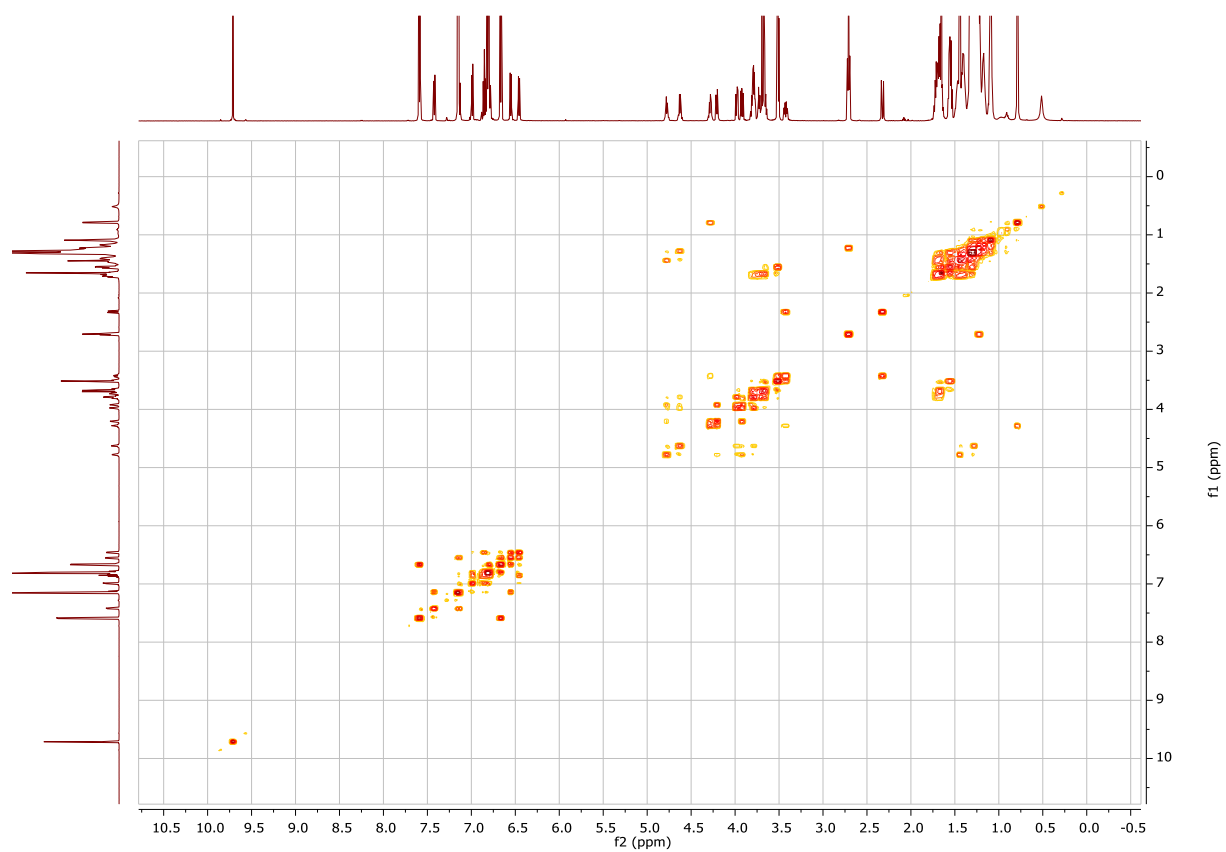
$^1\text{H}, ^1\text{H}$ COSY NMR spectrum for compound (*R,R,R*)-S21



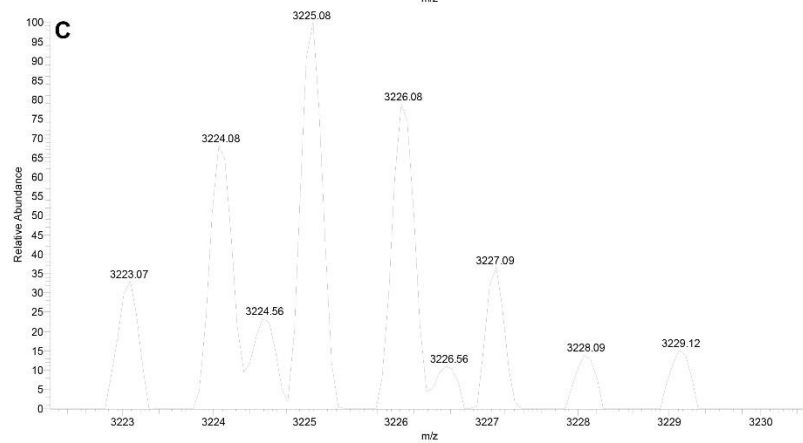
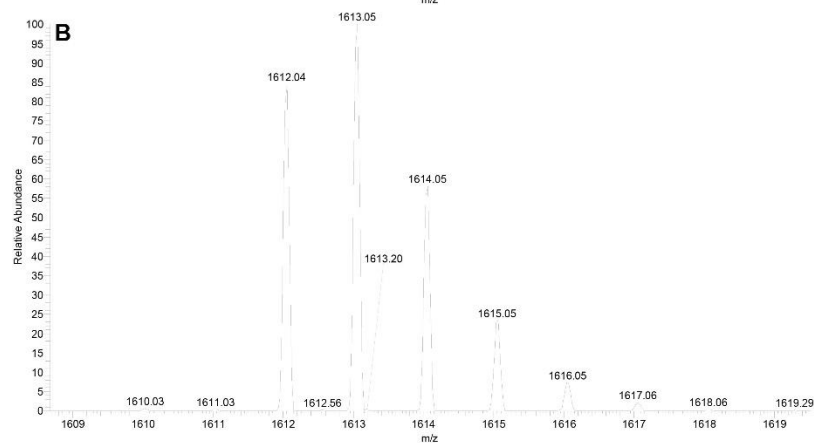
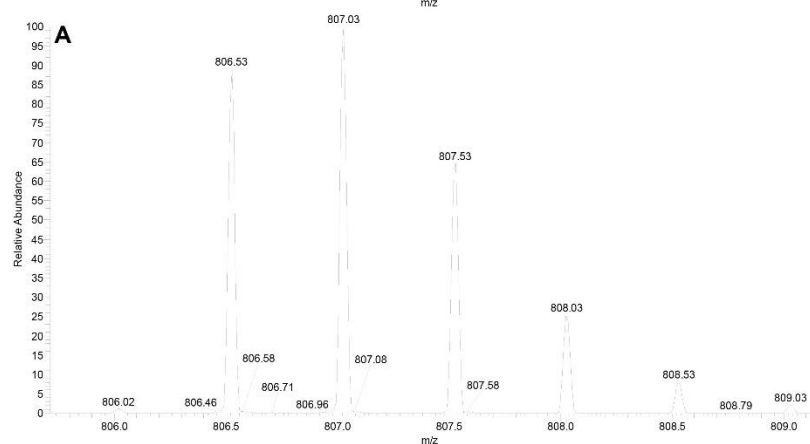
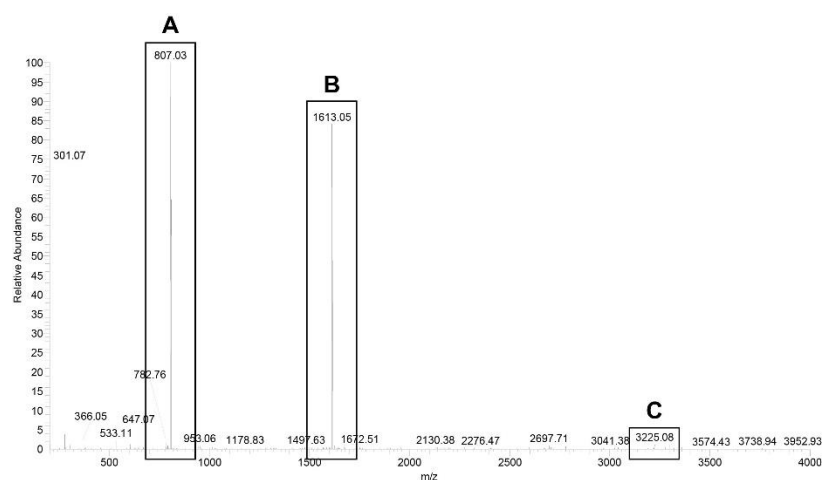
¹H and ¹³C NMR spectra for compound (S,R,R)-S21



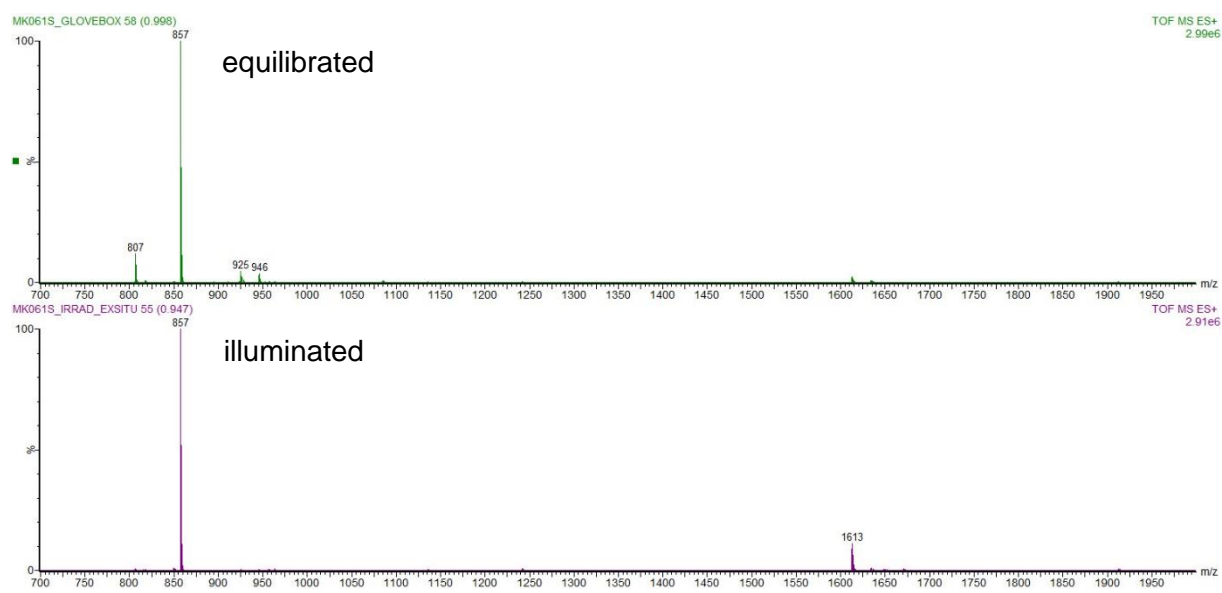
$^1\text{H}, ^1\text{H}$ COSY NMR spectrum for compound (*S,R,R*)-**S21**

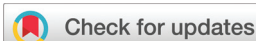


High-resolution ESI+ mass spectra of equilibrated (S,R,R)-**1n** sample



ESI+ mass spectra of equilibrated and illuminated (S,R,R)-**1n** sample



Cite this: *Inorg. Chem. Front.*, 2022, 9, 2231

Dimeric iodine(I) and silver(I) cages from tripodal N-donor ligands via the $[N-Ag-N]^+$ to $[N-I-N]^+$ cation exchange reaction†

Essi Taipale,^a Jas S. Ward,^{a*} Giorgia Fiorini,^a Daniel L. Stares,^b Christoph A. Schalley^b and Kari Rissanen^{a*}

The directionality of the $[N-I-N]^+$ halogen bond makes iodine(I) ions impeccable tools in the design and construction of $[N-I-N]^+$ halogen-bonded assemblies. The synthesis of dimeric iodine(I) cages with imidazole-derived N-donor tripodal ligands is described, as well as their corresponding silver(I) precursors. The addition of elemental iodine to the parent two-coordinate Ag(I) complexes produces iodine(I) complexes with three-center four-electron (3c-4e) $[N-I-N]^+$ bonds. Complex formation via this cation exchange was confirmed by 1H and $^1H-^{15}N$ HMBC NMR studies in solution, and additionally by electrospray ionisation and ion mobility mass spectrometry analysis (MS) in the gas phase. The structural analysis of the single crystal X-ray structures of 11 silver(I) cages and the computationally modelled iodine(I) cages, along with MS analysis, revealed structural similarities between the two different capsular assemblies. In addition to strong electrostatic interactions, C-H...F hydrogen bonds were determined to have a directing effect on the silver(I) cage formation and binding of suitably sized anions into the cavities in the solid state.

Received 10th December 2021,
Accepted 31st March 2022

DOI: 10.1039/d1qi01532j

rsc.li/frontiers-inorganic

Introduction

The term *clathrate* was first devised by H. M. Powell in 1948 when the first definition of a solid-state cage-like supramolecular structure came to life. According to Powell, a clathrate was a kind of a solid-state inclusion compound “in which two or more components are associated without an ordinary chemical union, but through the complete enclosure of one set of molecules in a suitable structure formed by another”.¹ These structures are generally further divided into two categories: the first are clathrates, *viz* lattice inclusion compounds, in which guests are trapped into a host matrix, generally speaking, a crystal lattice; the second are molecular host-guest inclusion compounds, in which the guest is trapped inside a larger, often macro- or multimacrocyclic, host molecule or a self-assembled concave entity comprising multiple components, *e.g.*, molecular capsules and cages.¹

Molecular hosts and capsular assemblies have attracted much interest since Rebek's first hydrogen-bonded supramolecular capsule in 1993.² The possibility of encapsulating various

guests in these cages has yielded a plethora of applications,³ ranging from biomedical applications and selective encapsulation,^{4,5} to stabilisation of reactive compounds using supramolecular capsular entities and catalysis in confined spaces.^{6,7} To date, various host-guest capsular assemblies have been reported using molecules such as resorcin[4]arenes,⁸⁻¹¹ calix[4]arenes,¹²⁻¹⁴ and pyridine[4]arenes.^{15,16} The self-assembled capsular assemblies comprise two or more suitable preorganised molecules spontaneously forming capsular entities with either metal coordination,¹⁷⁻²¹ or hydrogen bonding.^{22,23}

Ever since the 1990s, halogen bonding has developed into a true competitor for hydrogen bonding and other non-covalent interactions to the point that, to date, it is one of the most studied interactions in supramolecular chemistry.²⁴⁻²⁷ Halogen bonding was only recently defined by IUPAC as a net attractive interaction between the positive regions of the electrostatic potential associated with a halogen atom and a Lewis base.²⁸ Perhaps the controversial nature of the halogen bond led to its late definition, however, halogen bonding has been deftly utilised in the formation of supramolecular assemblies, amongst other non-covalent interactions, for its strength, tunability, and directionality, which provides the necessary tools for sufficient control of the self-assembly processes. Despite its utility, the use of halogen bonding in the formation of discrete molecular capsules is rare, with only a few examples previously reported using the classical halogen bond.²⁹⁻³¹

More recently, halogen bonding has also received interest in the form of halogen(I), especially iodine(I), cations.³²⁻³⁴ The

^aUniversity of Jyväskylä, Department of Chemistry, P.O. Box 35, Surfontie 9B, 40014 Jyväskylä, Finland. E-mail: kari.t.rissanen@jyu.fi

^bInstitut für Chemie und Biochemie, Organische Chemie, Freie Universität Berlin, Arnimallee 20, 14195 Berlin, Germany

† Electronic supplementary information (ESI) available. CCDC 2126429–2126441. For ESI and crystallographic data in CIF or other electronic format see DOI: <https://doi.org/10.1039/d1qi01532j>



halogen(i) cations, also known as halenium ions (X^+), can be considered as extremely polarised halogen atoms which are capable of forming symmetric three-center four-electron (3c-4e) $[L-X-L]^+$ bonds and constructing a halogen(i) complex by simultaneously interacting with two Lewis bases (L; commonly aromatic amines).³⁵⁻³⁸ The $[N-X-N]^+$ 3e-4e bonds are found to be among the strongest halogen bonds, which in addition to their high directionality and robust nature, has made them an interesting supramolecular synthon in modern-day crystal engineering.

Iodine(i) ions are commonly used in organic chemistry as halogenating agents³⁹⁻⁴² and their inherent reactivity makes them harder to isolate and structurally characterise. Recently, a number of heteroleptic or unconventional iodine(i) complexes have been prepared and characterised, mainly in the solid state.^{37,38,43-48} So far, only a few supramolecular capsular or macrocyclic⁴⁹ assemblies incorporating $[N-I-N]^+$ halogen bonds have been reported,⁵⁰⁻⁵³ which are obtained using the analogous silver(i) metallocages as the starting point for the iodine(i) cages, obtained *via* the $[N-Ag-N]^+$ to $[N-I-N]^+$ cation exchange reaction.⁵⁴

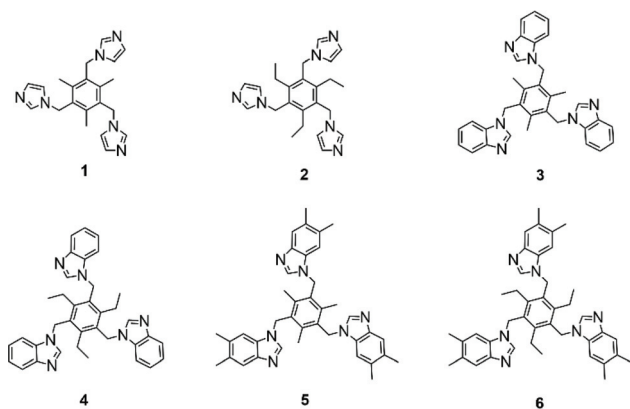
Herein, we report the solid-state structures of 11 parent silver(i) tripodal metallocages, and a comprehensive theoretical, gas, and solution-state study confirming the formation of iodine(i) $[N-I-N]^+$ cages. This report serves as further proof of the indisputable importance of halogen(i) ions as supramolecular synthons, and not just in simple monodentate ligand-complexes, but also in more sophisticated capsular assemblies.

Results and discussion

Synthesis of the silver(i) and iodine(i) cages

The imidazole- and benzoimidazole-based N-donor tripodal ligands **1-6** with a trialkylbenzene backbone were chosen for the capsular assembly (Scheme 1).

Ligands **1-6** were straightforwardly synthesised, with only **6** not being previously described in the literature. Imidazole,



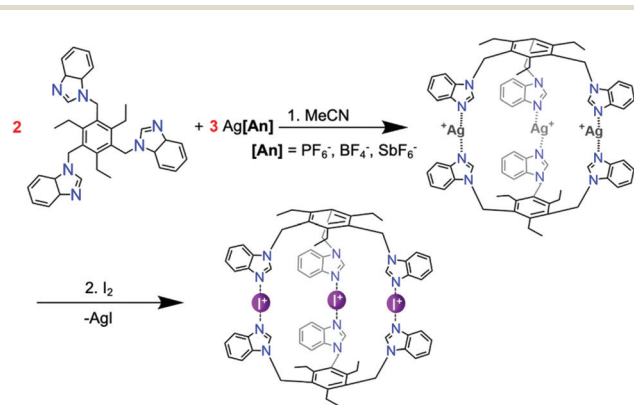
Scheme 1 The structures of N-donor tripodal ligands **1-6** used in the formation of the iodine(i) cages.

benzoimidazole, or dimethyl-benzoimidazole moieties are attached to the core benzene ring *via* methylene-linkers, making the ligands flexible and large enough to accommodate guests inside. The ligands must be able to first bind silver(i), and then iodine(i), cations leading to two distinct complexes, which in many cases prefer slightly different conformations with dissimilar bond lengths and angles. The syntheses of the ligands are straightforward and mostly follow literature procedures, with a few adaptations stated in the ESI.[†]⁵⁵

The most common route for iodine(i) complex formation is through the $[N-Ag-N]^+ \rightarrow [N-I-N]^+$ cation exchange reaction.⁵⁴ All cage reactions were performed in either acetonitrile or DMSO dictated by the lower solubility of some of the complexes. In the first step, presented in Scheme 2, two equivalents of ligand are mixed with three equivalents of a silver(i) salt (here $AgPF_6$, $AgBF_4$, or $AgSbF_6$). Many different weakly coordinating anions can be used, as it has been shown that the counteranions do not influence the linear centrosymmetric geometry of the $[N-I-N]^+$ halogen bond neither in solution nor in solid state.⁵⁶ In the second step, elemental iodine (I_2) is added to the parent silver(i) cage solution and stirred for an hour. Due to the more complex structure of the cages, the reaction requires more time for completion than for the previously reported small-ligand iodine(i) complexes.⁴⁵ Upon completion of the reaction, the silver iodide (AgI) precipitates from the solution leaving the cationic tris-iodine(i) cage with the three anions in the solution.

Crystallography of the silver(i) cages

The X-ray structures of ligands **1-5** have been previously reported,^{21,57-60} as well as the $[X-C1-Ag-1][X]_2$ cages with various counter-anions.^{17,20,61,62} For **1** and **2**, other topologies including polymeric structures have been reported,^{17,61} which is not the case for the larger ligands **3-6**. Very likely, the additional benzene rings point away from the capsule surface (Fig. 1) and thus do not hamper capsule formation, while they likely interfere with polymerization. Consequently, encountering polymeric structures was expected and one $[1-Ag]_n[OTf]_n$ structure was successfully characterized with X-ray crystallogra-



Scheme 2 The synthesis of the iodine(i) cage of tripodal ligand **4** through its analogous silver(i) metallocage.



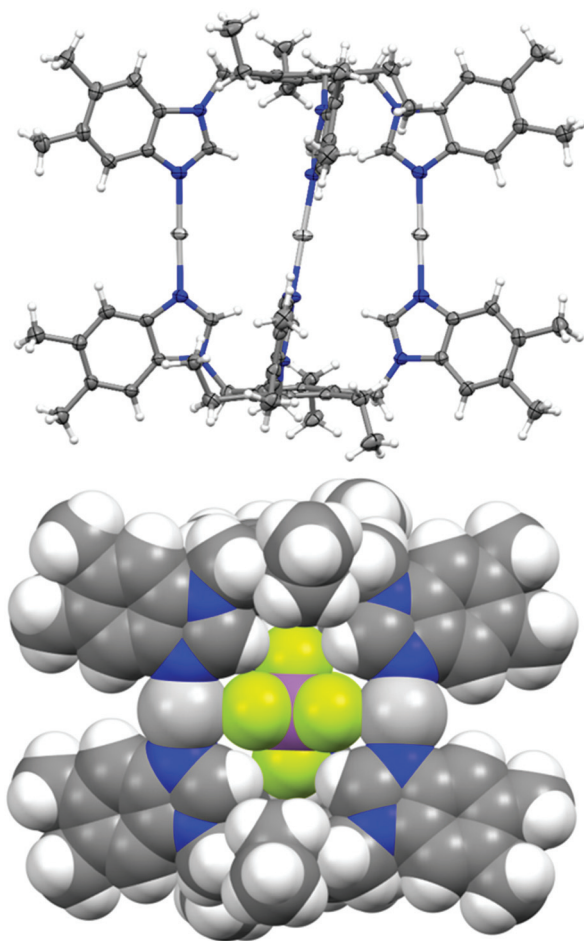


Fig. 1 The thermal ellipsoid (top) and spacefill (bottom) representations of the X-ray crystal structure of $[\text{SbF}_6\text{-C6-Ag-6}][\text{SbF}_6]_2$. Solvents and anions omitted for clarity except for the encapsulated SbPF_6^- anion in the bottom image. Thermal displacement ellipsoids are drawn at the 50% probability level. The N–Ag–N bond lengths and angles were determined to be between 2.091(4)–2.095(4) Å and 172.3(2)–173.0(2)°.

phy (Fig. S3†). In addition, cages $[\text{BF}_4\text{-C3-Ag-3}][\text{BF}_4]_2$ ¹⁸ and $[\text{BF}_4\text{-C4-Ag-4}][\text{BF}_4]_2$ ²¹ have been X-ray structurally characterised. In total, 11 single crystal X-ray structures of the analogous silver(I) cages were determined (Fig. S1–S13†), two of them polymorphs to previously reported structures.^{17,20} Unlike the halogen(I) 3c–4e bonds, the $[\text{N-Ag-N}]^+$ environment is easily distorted by the solvent or anion coordination to the silver(I) cations and angles of as small as 149° have previously been reported.⁴⁴ Further demonstrating this, the silver(I) cages were determined to have varying N–Ag bond lengths from 2.068(12) Å to 2.170(7) Å and N–Ag–N angles ranging from 163.1(2)° to 180.0(5)°. These bond lengths are similar to previously observed ones with smaller monodentate versions of these ligands.⁴⁵ However, in the silver(I) cage formation the N–Ag–N angles are more linear when compared to the simple mononuclear complexes where the anion to silver(I) cation interactions can cause distortion from linearity.⁴⁵

The cages were designed to encapsulate small guests inside the cavities of the cages. In nine out of 11 cases, the electron

density map of the X-ray crystallographic analysis indicated that one of the counterions was positioned inside the cages. However in the case of $[\text{SbF}_6\text{-C1-Ag-1}][\text{SbF}_6]_2$ and $[\text{SbF}_6\text{-C3-Ag-3}][\text{SbF}_6]_2$ the electron density inside the cavity was diffuse, indicating a heavily disordered SbF_6^- anion, and due to this they could not be modelled adequately, and were accounted for using SQUEEZE in the final model.⁶³ Fig. 1 depicts, as an example, the encapsulation of a hexafluoroantimonate(V) anion in $[\text{SbF}_6\text{-C6-Ag-6}][\text{SbF}_6]_2$ as a result of the CH...anion and cation...anion interactions between the ligand, the Ag(I) cations and the SbF_6^- anion.

Moreover, the complexes observed in the solid state generally encapsulate one anion leaving the two remaining anions outside the cage. In addition, tandem MS experiments support the anion also to be present inside the cages in solution and the gas phase. When PF_6^- is encapsulated, the collision energies, at which 50% of the cage ions are still intact is significantly higher as compared to the same cage ions carrying a triflate anion attached to the outside (Fig. S45–S47†).

The anion interactions inside the cage were estimated by determining the shortest distances between the anionic and cationic species for structures $[\text{BF}_4\text{-C3-Ag-3}][\text{BF}_4]_2$ and $[\text{PF}_6\text{-C3-Ag-3}][\text{PF}_6]_2$, $[\text{BF}_4\text{-C5-Ag-5}][\text{BF}_4]_2$ and $[\text{PF}_6\text{-C5-Ag-5}][\text{PF}_6]_2$, and also for $[\text{PF}_6\text{-C6-Ag-6}][\text{PF}_6]_2$ and $[\text{SbF}_6\text{-C6-Ag-6}][\text{SbF}_6]_2$, in which the anion resides inside the cage cavity. Many factors are to be taken into account when discussing interaction strengths, and the short distances alone do not always indicate strong interactions. Furthermore, the interaction lengths can be affected by packing in the crystal structure. However, the interaction lengths and other analyses on the crystal structures are here discussed to shed light on the type of interactions involved in the anion encapsulation.

The shortest silver(I) to fluorine (Ag...F) contact distances were found to be between 2.66(1) Å–2.802(9) Å, which is significantly shorter than the sum of the van der Waals radii for these atoms ($\text{vdW}(\text{Ag}\cdots\text{F}) = 3.19$ Å). Similarly, the C–H...F hydrogen bonds were found to be shorter than the sum of the van der Waals radii of the respective atoms ($\text{vdW}(\text{F}\cdots\text{H}) = 2.67$ Å) varying between 2.33 Å–2.66 Å. However, for cages with the shortest Ag...F contacts, the hydrogen-bond distances (C–H...F) were found to be the longest, indicating that these distances rely heavily on the orientation of the anion inside the cage cavity.

The anion-to-cage interactions were further studied with Hirshfeld surface analysis (Fig. S14–S19†) using CrystalExplorer.^{64,65} In each case, large bright red spots can be observed on the Hirshfeld surface of the anions in the regions where the fluorines are in close contact with the silver(I) cations confirming the interactions to be shorter than the van der Waals radii. Slightly smaller, though still fairly bright red spots can also be seen for the C–H...F interactions. The 2D fingerprint plots of the Hirshfeld surface analysis provide information on the unique crystal packing in each case, at the same time easily revealing similarities between the structures. The fingerprint plot depicts the relationship of the distance to the nearest atom center interior to the surface (d_i) and to the



exterior to the surface (d_e).⁶⁴ The fingerprint plots (Fig. S14–S19†) display the Ag...F and C–H...F interactions as a pair of spikes at the bottom-left part of the plot. The percentage contributions to the close intermolecular contacts can also be determined from the 2D plots. For all cages, the contribution of the Ag...F contacts was determined to be between 9–17% (largest for $[\text{BF}_4\text{-C5-Ag-5}][\text{BF}_4]_2$), whereas the C–H...F hydrogen bonds contributed 82–91% to the overall interactions. The electrostatic interactions are generally stronger than hydrogen bonding, and in here, they act in unison. Therefore, even though the Hirshfeld surface depicts Ag...F contacts to be the closest, the hydrogen bonds most certainly play a role in the stabilisation of the anion. In some cases, a small percentage (<4%) of other interactions (F...N and F...C) were observed to affect the anion binding. The results from the Hirshfeld surface analysis indicate a multitude of stabilising interactions directed toward the anion. For example, Fig. 2 depicts the X-ray crystal structure of $[\text{SbF}_6\text{-C6-Ag-6}][\text{SbF}_6]_2$ with the calculated Hirshfeld surface for the SbF_6^- anion inside the cage, where the punctures in the surface display strong cation–anion ($\text{Ag}^+\cdots\text{F}_6\text{Sb}^-$) interactions. Additionally, the strong interactions are supported by the non-disordered nature of the SbF_6^- anion with well-defined thermal movement inside the cage due to the supramolecular interactions.^{66,67}

Characterisation of the iodine(i) cages

Despite numerous silver(i) cages, to date, only the solid-state structure of dimeric $[\text{N-I-N}]^+$ halogen-bonded cage made from **1** has been reported.⁵³ The nucleophilic nature of the iodine(i)³⁸ cation renders the interactions with anions very weak, and the inability to get diffraction quality single crystals of the iodine(i) cages in this study highlights the challenge in obtaining solid-state crystal structures of larger $[\text{N-I-N}]^+$ halogen(i) assemblies with multiple 3c–4e bonds.^{50,51} Unfortunately, also in this study, the crystallisation of the $[\text{N-I-N}]^+$ cages proved to be unsuccessful. During the crystallisation, conceivably the inherent anisotropic nature of the 3c–4e $[\text{N-I-N}]^+$ bond results in conflicting anion interactions, with the repulsive nature of the $\text{I}^+\cdots\text{F}$ interactions and the attractive endohedral cavity,⁵³ making the anion encapsulation and the crystallisation process of the iodine(i) cages more problematic. Therefore, the iodine(i) cages were modelled with fixed N–I bond lengths of 2.25 Å and 180° angles for the most accurate description based on the known coordination geometry of the $[\text{N-I-N}]^+$ halogen bond (Fig. 3 and Fig. S20–S25†).^{56,68,69} The resulting calculated iodine(i) cage structures are very similar to the analogous silver(i) crystal structures (see below discussion and Fig. S12†), apart from the slight distortion of the silver(i) cages in the solid state due to packing effects.

The cage composition was further confirmed in the gas phase with electrospray ionisation mass spectrometry (ESI-MS) and ion mobility mass spectrometry (IM-MS) analysis^{51,70} (Fig. S26–S49†). For ligand **4**, the formation of the cages was verified by the detection of the ions $[\text{PF}_6\text{-C4-Ag-4}]^{2+}$ and $[\text{PF}_6\text{-C4-I-4}]^{2+}$ at m/z values of 787 and 815, respectively. Additionally, the cages were observed with other anions in the

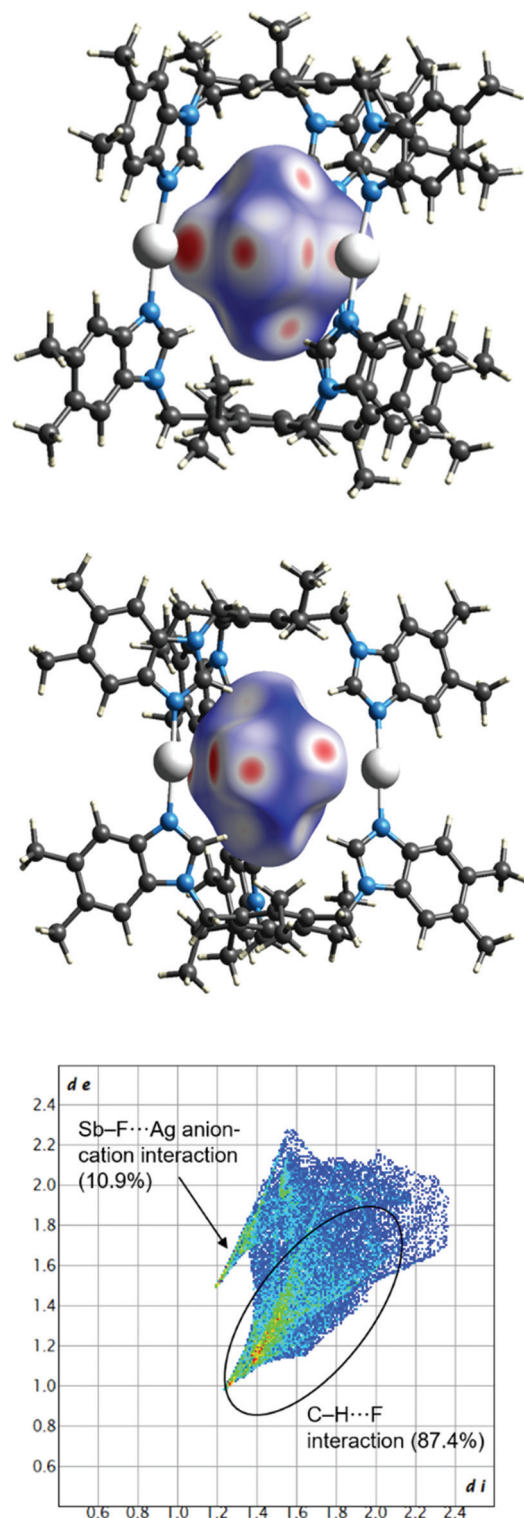


Fig. 2 Full fingerprint regions of the hexafluoroantimonate anion in the complex $[\text{SbF}_6\text{-C6-Ag-6}][\text{SbF}_6]_2$ and two views of the intermolecular contacts to the Hirshfeld surface of the anion. Other interactions contributing to the anion binding: Sb–F...C (1.7%). In the fingerprint plot, d_i represents the closest internal distance from a given point on the Hirshfeld surface, and d_e is the closest external contact (in Å).



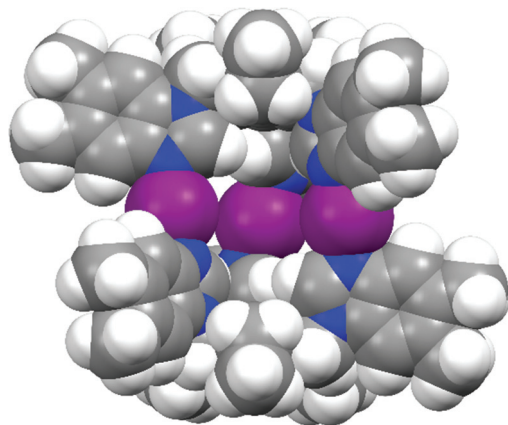


Fig. 3 The spacefill representation of the calculated structure of $[\text{PF}_6\text{-C6-I-6}][\text{PF}_6]_2$ iodine(i) cage.

gas phase, such as I^- and PF_2O_2^- . In ion mobility mass spectrometric experiments, the silver(i) and iodine(i) cages appear with very similar, narrow-width arrival time distributions confirming that the overall cage structures have not changed during the Ag(i)-to-I(i) ion exchange reactions. The IM-MS provided evidence of the cages being close in their sizes, though the iodine(i) cages are slightly bigger than the corresponding silver(i) cages. All silver(i) and iodine(i) cages depicted a narrow peak width in the arrival time distribution indicating a discrete, well-defined structure (Fig. 4). Also, the iodine(i) and silver(i) cages show closely related fragmentation patterns in collision-induced dissociation (CID) experiments (Fig. S45–S49[†]). The dissociation of the mass-selected doubly charged $[\text{PF}_6\text{-cL-Ag-L}]^{2+}$ and $[\text{PF}_6\text{-cL-I-L}]^{2+}$ ions leads to a singly charged $[\text{LAg}]^+$ and $[\text{LI}]^+$ ions, respectively. The corresponding singly charged $[\text{LAg}_2\text{PF}_6]^+$ and $[\text{LI}_2\text{PF}_6]^+$ fragments are, however, not observed, which indicates a subsequent, rapid loss of AgPF_6 or IPF_6 ion pairs leading again to a second $[\text{LAg}]^+$ and $[\text{LI}]^+$ fragment, respectively. The fact that these ion pair

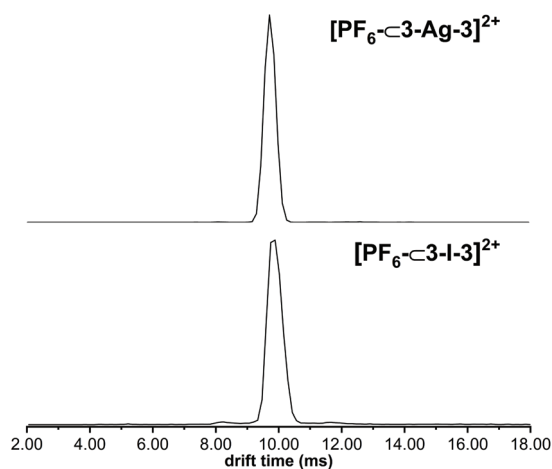


Fig. 4 ATDs of $[\text{PF}_6\text{-c3-Ag-3}]^{2+}$ (top) and $[\text{PF}_6\text{-c3-I-3}]^{2+}$ (bottom). The arrival time of both are similar and the distributions narrow.

losses do not occur similarly from the parent ions directly is in agreement with an encapsulated PF_6^- counterion, which can only escape in the form of the ion pairs when the cage has already fragmented. This assumption is also in line with the observation of 2+, but no 1+ or 3+ charge states for the intact cages. The fragmentation was studied at different collision voltages to obtain a survivor yield curve for both the silver(i) and the iodine(i) cages (Fig. S49[†]). The 50% survivor yields are obtained at collision energies of 17 V for $[\text{PF}_6\text{-cL-I-L}]^{2+}$ and of 26 V for $[\text{PF}_6\text{-cL-Ag-L}]^{2+}$. Thus, the iodine(i) cage is somewhat less stable in the gas phase than its silver(i) analogue. In conclusion, not only the sizes of the two cages are in the same range, but also the ionisation behavior (only +2 charge states) and the fragmentation patterns. This is straightforward evidence that both cages have analogous capsular structures.

The formation of the silver(i) and iodine(i) cages in solution was studied with ^1H NMR and $^1\text{H-}^{15}\text{N}$ HMBC measurements (Fig. 5 and Fig. S50–S59[†]). Ligand 1 was not included in the NMR study since similar experiments have been previously reported.⁵³ Earlier studies have shown that the formation of the silver(i) cage results in a downfield change in the ^1H NMR chemical shifts of the ligand,^{43–45,53} most prominently observed for the imidazole C(2) proton (H_a , singlet, Fig. 1, top). Changes in the ^1H NMR chemical shift range were between $\Delta\delta$ 0.16 and $\Delta\delta$ 0.48 ppm when going from the uncomplexed ligands to the silver(i) complexes. The cation exchange reaction from Ag^+ to I^+ results in a further downfield shift, which for these ligands, ranges from $\Delta\delta$ 0.16 to $\Delta\delta$ 1.21 ppm, resulting in notable shift differences between the free ligands and the iodine(i) cages of up to almost 1.7 ppm. It has been previously observed that the solubility of the complex is often lower for the I^+ complex than for the Ag^+ complex, and greatly reduced compared to the respective free ligand.⁴⁵ A complete set of measurements in CD_3CN could be performed only for two ligands (4 and 5) out of the five systems, as the solubility of some of the silver(i) and iodine(i) cages required the use of $\text{DMSO-}d_6$, and the poor solubility of the silver(i) complexes, as well as interactions with the competing DMSO , results in an incomplete conversion of the silver(i) cage to the iodine(i) cage, as confirmed by ^1H NMR spectroscopy. This is most clearly observed for ligand 2, while being much less pronounced for 3 and 6. However, the majority of the silver(i) cages fully convert to the iodine(i) cages. The conversion from the ligands to the silver(i) complexes were further studied with $^1\text{H-}^{15}\text{N}$ HMBC measurements (Fig. S51, S53, S55, S57, and S59[†]). Even though the ^1H NMR spectra could be obtained for all the silver(i) and iodine(i) cages, in most cases the decreased solubility of the iodine(i) cages would cause them to precipitate out of solution during the time required for satisfactory quality HMBC acquisitions to be collected, and therefore, a full set of ^{15}N NMR resonances were obtained for only one iodine(i) cage, $[\text{PF}_6\text{-c2-I-2}][\text{PF}_6]_2$ (Fig. S51[†]). However, as demonstrated before,⁴⁵ upon coordination to silver(i), or iodine(i), the resonance of the coordinating nitrogen (N1) is found to change markedly downfield due to the deshielding effect upon complexation. In contrast, the non-coordinating



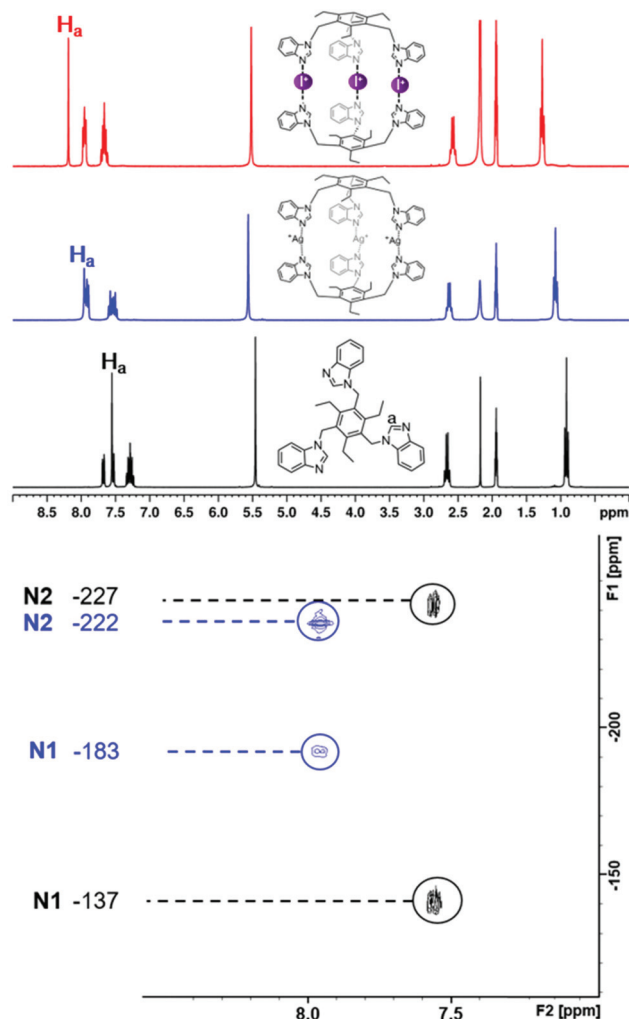


Fig. 5 The ^1H (top) and ^1H - ^{15}N HMBC* (bottom) NMR spectra of the uncomplexed ligand **4** (black), the $[\text{PF}_6\text{-C4-Ag-4}][\text{PF}_6]_2$ silver(I) complex (blue), and the $[\text{PF}_6\text{-C4-I-4}][\text{PF}_6]_2$ iodine(I) complex (red), where H_a is the proton between the coordinating (N1) and non-coordinating (N2) nitrogens. All values are in ppm and referenced to CD_3CN (^1H) and CD_3NO_2 (^{15}N) (500 MHz, 303 K). *Due to poor solubility, the ^1H - ^{15}N HMBC NMR spectra of the iodine(I) complex could not be obtained.

nitrogen (N2) is shielded and experiences only minor changes in the opposite direction. Due to low solubility, the signal of the coordinating nitrogen (N1) is in some cases undetectable, making the N2 value ever more important, and giving valuable information about the complexation. The silver(I) complexation induces a coordination shift around -50 ppm in the ^{15}N NMR resonance of N1 for all ligands, whereas the resonance of N2 only changes by around $+5$ ppm.

Conclusions

In summary, we have presented comprehensive evidence of dimeric imidazole-based iodine(I) cage formation in the solution and gas phase. The formation of the iodine(I) cages

occurs *via* the Ag^+ to I^+ cation exchange reaction from the analogous silver(I) cages. In addition to NMR and MS experiments, the silver(I) cages were also crystallised and further studied in the solid state using X-ray crystallography. The resulting endohedral cavity of the self-assembled dimeric cages yields an anion encapsulation with strong supramolecular interactions. The silver(I) crystal structure of $[\text{PF}_6\text{-C6-Ag-6}][\text{PF}_6]_2$ and the calculated structure of $[\text{PF}_6\text{-C6-I-6}][\text{PF}_6]_2$ along with the ion mobility-MS analysis, clearly display structural similarities amongst the two well-defined structures with the silver(I) cage having slightly shorter Ag-N bond lengths (2.068(12)–2.170(7) Å) and less linear N-Ag-N angles ($163.1(2)^\circ$ – $180.0(5)^\circ$) than expected for the iodine(I) cage. This is strongly reflected in the almost identical arrival time distributions determined in ion mobility mass spectrometric experiments, which reveal only a very slight size increase when the silver ions are replaced by iodine(I). The flexibility of the cages enabled them to host anions of varying sizes, forming complexes with strong supramolecular interactions in each case. In addition to anion-cation interactions, a surprisingly large contribution to the anion stabilisation was made by the C-H...F hydrogen bonds.

For all the complexes, $[\text{PF}_6\text{-CL-Ag-L}]^{2+}$ ions were observed in the mass spectra, which indicates a stronger interaction of one anion compared to the remaining two. This would suggest that the anion encapsulation occurs for each complex in the gas phase. Furthermore, this would also support the occurrence of the anion encapsulation in solution. Even though the destabilizing interactions in the $[\text{N-I-N}]^+$ cages rendered the crystallization attempts ineffective, the directionality of the $[\text{N-I-N}]^+$ halogen bond makes iodine(I) ions excellent tools in supramolecular cage design and crystal engineering. The work presented here serves as further proof of the indisputable importance of halogen(I) ions as supramolecular synthons, aiding the design of more complex supramolecular capsular assemblies.

Conflicts of interest

There are no conflicts to declare.

Acknowledgements

We gratefully acknowledge the Academy of Finland (K. R. grant no. 317259), Finnish Cultural Foundation Central Fund (J. S. W. grant number 00201148), the Magnus Ehrnrooth Foundation (J. S. W.), European Union NOAH project (D. L. S, H2020-MSCA-ITN project ref. 765297, the Core Facility BioSupraMol (supported by the Deutsche Forschungsgemeinschaft, DFG) and the University of Jyväskylä, Finland for financial support.

Notes and references

- J. W. Steed and J. L. Atwood, *Supramolecular Chemistry*, John Wiley & Sons, Ltd, Chichester, United Kingdom, 2nd edn, 2009.



- 2 R. Wyler, J. de Mendoza and J. Rebek Jr., A synthetic cavity assembles through self-complementary hydrogen bonds, *Angew. Chem., Int. Ed. Engl.*, 1993, **32**, 1699.
- 3 C. M. A. Gangemi, A. Pappalardo and G. T. Sfrazzetto, Applications of supramolecular capsules derived from resorcin[4]arenes, calix[n]arenes and metallo-ligands: From biology to catalysis, *RSC Adv.*, 2015, **5**, 51919.
- 4 T. R. Cook, V. Vajpayee, M. H. Lee, P. J. Stang and K.-W. Chi, Biomedical and biochemical applications of self-assembled metallacycles and metallacages, *Acc. Chem. Res.*, 2013, **46**, 2464.
- 5 K. Harris, D. Fujita and M. Fujita, Giant hollow MnL2n spherical complexes: Structure, functionalisation and applications, *Chem. Commun.*, 2013, **49**, 6703.
- 6 A. Galan and P. Ballester, Stabilization of reactive species by supramolecular encapsulation, *Chem. Soc. Rev.*, 2016, **45**, 1720.
- 7 M. Yoshizawa, M. Tamura and M. Fujita, Diels-Alder in aqueous molecular hosts: Unusual regioselectivity and efficient catalysis, *Science*, 2006, **312**, 251.
- 8 K. Twum, K. Rissanen and N. K. Beyeh, Recent advances in halogen bonded assemblies with resorcin[4]arenes, *Chem. Rec.*, 2021, **21**, 386.
- 9 N. K. Beyeh and K. Rissanen, Dimeric resorcin[4]arene capsules in the solid state, *Isr. J. Chem.*, 2011, **51**, 769.
- 10 H. Mansikkamäki, M. Nissinen and K. Rissanen, C-Methyl resorcin[4]arene packing motifs with alkyl ammonium salts: From molecular capsules to channels and tubes, *CrystEngComm*, 2005, **7**, 519.
- 11 R. Puttreddy, N. K. Beyeh, E. Kalenius, R. H. A. Ras and K. Rissanen, 2-Methylresorcinarene: A very high packing coefficient in a mono-anion based dimeric capsule and the X-ray crystal structure of the tetra-anion, *Chem. Commun.*, 2016, **52**, 8115.
- 12 I. Thondorf, F. Broda, K. Rissanen, M. Vysotsky and V. Böhmer, Dimeric capsules of tetraurea calix[4]arenes. MD simulations and X-ray structure, a comparison, *J. Chem. Soc.*, 2002, **2**, 1796.
- 13 M. Chas, G. Gil-Ramírez and P. Ballester, Exclusive self-assembly of a polar dimeric capsule between tetraurea calix[4]pyrrole and tetraurea calix[4]arene, *Org. Lett.*, 2011, **13**, 3402.
- 14 D. Ken and J. Rebek, Synthesis and assembly of self-complementary calix[4]arenes, *Proc. Natl. Acad. Sci. U. S. A.*, 1995, **92**, 12403.
- 15 A. Kiesilä, N. K. Beyeh, J. O. Moilanen, R. Puttreddy, S. Götz, K. Rissanen, P. Barran, A. Lützen and E. Kalenius, Thermodynamically driven self-assembly of pyridinearene to hexameric capsules, *Org. Biomol. Chem.*, 2019, **17**, 6980.
- 16 A. Kiesilä, L. Kivijärvi, N. K. Beyeh, J. O. Moilanen, M. Groessl, T. Rothe, S. Götz, F. Topić, K. Rissanen, A. Lützen and E. Kalenius, Simultaneous endo and exo complex formation of pyridine[4]arene dimers with neutral and anionic guests, *Angew. Chem., Int. Ed.*, 2017, **56**, 10942.
- 17 W.-Y. Sun, J. Fan, T.-A. Okamura, J. Xie, K.-B. Yu and N. Ueyama, Self-assembly of frameworks with specific topologies: Construction and anion exchange properties of M3L2 architectures by tripodal ligands and silver(I) salts, *Chem. – Eur. J.*, 2001, **7**, 2557.
- 18 C.-Y. Su, Y.-P. Cai, C.-L. Chen, F. Lissner, B.-S. Kang and W. Kaim, Self-assembly of trigonal-prismatic metallocages encapsulating BF₄⁻ or CuI₃²⁻ as anionic guests: Structures and mechanism of formation, *Angew. Chem., Int. Ed.*, 2002, **41**, 3371.
- 19 V. Amendola, M. Boiocchi, B. Colasson, L. Fabbri, M.-J. Rodriguez Douton and F. Ugozzoli, A metal-based trisimidazolium cage that provides six C-H hydrogen-bond-donor fragments and includes anions, *Angew. Chem., Int. Ed.*, 2006, **45**, 6920.
- 20 H.-K. Liu, X. Huang, T. Lu, X. Wang, W.-Y. Sun and B.-S. Kang, Discrete and infinite 1D, 2D/3D cage frameworks with inclusion of anionic species and anion-exchange reactions of Ag₃L₂ type receptor with tetrahedral and octahedral anions, *Dalton Trans.*, 2008, 3178.
- 21 S. Bhattacharya and B. K. Saha, Conformation driven complexation of two analogous benzimidazole based tripodal ligands with Ag(I) resulting in a trigonal prism and a coordination polymer, *J. Chem. Sci.*, 2016, **128**, 207.
- 22 H. Mansikkamäki, M. Nissinen and K. Rissanen, *Chem. Commun.*, 2002, 1902.
- 23 H. Mansikkamäki, M. Nissinen, C. A. Schalley and K. Rissanen, Self-assembling resorcinarene capsules: Solid and gas phase studies on encapsulation of small alkyl ammonium cations, *New J. Chem.*, 2003, **27**, 88.
- 24 G. Cavallo, P. Metrangolo, R. Milani, T. Pilati, A. Priimagi, G. Resnati and G. Terraneo, The halogen bond, *Chem. Rev.*, 2016, **116**, 2478.
- 25 L. C. Gilday, S. W. Robinson, T. A. Barendt, M. J. Langton, B. R. Mullaney and P. D. Beer, Halogen bonding in supramolecular chemistry, *Chem. Rev.*, 2015, **115**, 7118.
- 26 M. H. Kolář and P. Hobza, Computer modeling of halogen bonds and other σ -hole interactions, *Chem. Rev.*, 2016, **116**, 5155.
- 27 H. Wang, W. Wang and W. J. Jin, σ -Hole bond vs π -hole bond: A comparison based on halogen bond, *Chem. Rev.*, 2016, **116**, 5072.
- 28 G. R. Desiraju, P. Shing Ho, L. Kloo, A. C. Legon, R. Marquardt, P. Metrangolo, P. Politzer, G. Resnati and K. Rissanen, Definition of the halogen bond (IUPAC recommendations 2013), *Pure Appl. Chem.*, 2013, **85**, 1711.
- 29 C. B. Aakeröy, A. Rajbanshi, P. Metrangolo, G. Resnati, M. F. Parisi, J. Desper and T. Pilati, The quest for a molecular capsule assembled via halogen bonds, *CrystEngComm*, 2012, **14**, 6366.
- 30 Y.-J. Zhu, Y. Gao, M.-M. Tang, J. Rebek Jr. and Y. Yu, Dimeric capsules self-assembled through halogen and chalcogen bonding, *Chem. Commun.*, 2021, **57**, 1543.
- 31 N. K. Beyeh, F. Pan and K. Rissanen, A halogen-bonded dimeric resorcinarene capsule, *Angew. Chem., Int. Ed.*, 2015, **54**, 7303.
- 32 J. A. Creighton, I. Haque and J. L. Wood, The iododipyridinium ion, *Chem. Commun.*, 1966, 229.



- 33 J. A. Creighton, I. Haque and J. L. Wood, The iododipyridinium ion, *Chem. Commun.*, 1966, 892.
- 34 I. Haque and J. L. Wood, The vibrational spectra and structure of the bis(pyridine)iodine(i), bis(pyridine)bromine(i), bis(γ -picoline)iodine(i) and bis(γ -picollne)bromine(i) cations, *J. Mol. Struct.*, 1968, 2, 217.
- 35 A.-C. C. Carlsson, M. Uhrbom, A. Karim, U. Brath, J. Gräfenstein and M. Erdélyi, Solvent effects on halogen bond symmetry, *CrystEngComm*, 2013, 15, 3087.
- 36 L. Turunen and M. Erdélyi, Halogen bonds of halonium ions, *Chem. Soc. Rev.*, 2020, 49, 2688.
- 37 A. C. Reiersølmoen, S. Battaglia, S. Oien-Odegaard, A. K. Gupta, A. Fiksdahl, R. Lindh and M. Erdélyi, Symmetry of three-center, four-electron bonds, *Chem. Sci.*, 2020, 11, 7979.
- 38 S. Yu, P. Kumar, J. S. Ward, A. Frontera and K. Rissanen, A “nucleophilic” iodine in a halogen-bonded iodonium complex manifests an unprecedented $I^+ \cdots Ag^+$ interaction, *Chem*, 2021, 7, 948.
- 39 J. Barluenga, J. M. González, M. A. García-Martín, P. J. Campos and G. Asensio, An expeditious and general aromatic iodination procedure, *J. Chem. Soc., Chem. Commun.*, 1992, 1016.
- 40 J. Ezquerra, C. Pedregal, C. Lamas, J. Barluenga, M. Pérez, M. A. García-Martín and J. M. González, Efficient reagents for the synthesis of 5-, 7-, and 5,7-substituted indoles starting from aromatic amines: Scope and limitations, *J. Org. Chem.*, 1996, 61, 5804.
- 41 G. Espuña, G. Arsequell, G. Valencia, J. Barluenga, M. Pérez and J. M. González, Control of the iodination reaction on activated aromatic residues in peptides, *Chem. Commun.*, 2000, 1307.
- 42 J. Barluenga, F. González-Bobes, M. C. Murguía, S. R. Ananthoju and J. M. González, Bis(pyridine)iodonium tetrafluoroborate (IPy2BF4): A versatile oxidizing reagent, *Chem. – Eur. J.*, 2004, 10, 4206.
- 43 J. S. Ward, G. Fiorini, A. Frontera and K. Rissanen, Asymmetric $[N-I-N]^+$ halonium complexes, *Chem. Commun.*, 2020, 56, 8428.
- 44 J. S. Ward, A. Frontera and K. Rissanen, Iodonium complexes of the tertiary amines quinuclidine and 1-ethylpiperidine, *Dalton Trans.*, 2021, 50, 8297.
- 45 E. Taipale, M. Siepmann, K.-N. Truong and K. Rissanen, Iodine(i) and silver(i) complexes of benzoimidazole and pyridylcarbazole derivatives, *Chem. – Eur. J.*, 2021, 27(69), 17412–17419.
- 46 J. S. Ward, A. Frontera and K. Rissanen, Nucleophilic iodonium interactions (NIIs) in 2-coordinate iodine(i) and silver(i) complexes, *Chem. Commun.*, 2021, 57, 5094.
- 47 A. Vanderkooy, A. K. Gupta, T. Földes, S. Lindblad, A. Orthaber, I. Pápai and M. Erdélyi, Halogen bonding helicates encompassing iodonium cations, *Angew. Chem., Int. Ed.*, 2019, 58, 9012.
- 48 J. S. Ward, A. Frontera and K. Rissanen, Utility of three-coordinate silver complexes toward the formation of iodonium ions, *Inorg. Chem.*, 2021, 60, 5383.
- 49 S. Yu, E. Kalenius, A. Frontera and K. Rissanen, Macrocyclic complexes based on $[N \cdots I \cdots N]^+$ halogen bonds, *Chem. Commun.*, 2021, 57, 12464–12467.
- 50 L. Turunen, U. Warzok, R. Puttreddy, N. K. Beyeh, C. A. Schalley and K. Rissanen, $[N \cdots I^+ \cdots N]$ Halogen-bonded dimeric capsules from tetrakis(3-pyridyl)ethylene cavitands, *Angew. Chem., Int. Ed.*, 2016, 55, 14033.
- 51 U. Warzok, M. Marianski, W. Hoffmann, L. Turunen, K. Rissanen, K. Pagel and C. A. Schalley, Surprising solvent-induced structural rearrangements in large $[N \cdots I^+ \cdots N]$ halogen-bonded supramolecular capsules: An ion mobility-mass spectrometry study, *Chem. Sci.*, 2018, 9, 8343.
- 52 L. Turunen, U. Warzok, C. A. Schalley and K. Rissanen, Nano-sized $I_{12}L_6$ molecular capsules based on the $[N \cdots I^+ \cdots N]$ halogen bond, *Chem*, 2017, 3, 861.
- 53 L. Turunen, A. Peuronen, S. Forsblom, E. Kalenius, M. Lahtinen and K. Rissanen, Tetrameric and dimeric $[N \cdots I^+ \cdots N]$ halogen-bonded supramolecular cages, *Chem. – Eur. J.*, 2017, 23, 11714.
- 54 A.-C. C. Carlsson, J. Gräfenstein, J. L. Laurila, J. Bergquist and M. Erdélyi, Symmetry of $[N-X-N]^+$ halogen bonds in solution, *Chem. Commun.*, 2012, 48, 1458.
- 55 Y. Yuan, Z.-L. Jiang, J.-M. Yan, G. Gao, A. S. C. Chan and R.-G. Xie, A convenient and effective synthesis of tris-bridged tricationic azolophanes, *Synth. Commun.*, 2000, 30, 4555.
- 56 M. Bedin, A. Karim, M. Reitti, A.-C. C. Carlsson, F. Topic, M. Cetina, F. Pan, V. Havel, F. Al-Ameri, V. Sindelar, K. Rissanen, J. Gräfenstein and M. Erdélyi, Counterion influence on the N-I-N halogen bond, *Chem. Sci.*, 2015, 6, 3746.
- 57 W.-Y. Sun, J. Fan, J. Hu, K.-B. Yu and W.-X. Tang, Molecular structure and 1H , ^{13}C NMR assignments of 1,3,5-tris(imidazol-1-ylmethyl)-2,4,6-trimethylbenzene, *J. Chem. Crystallogr.*, 2000, 30, 115.
- 58 S. N. L. Andree, A. S. Sinha and C. B. Aakeröy, Structural examination of halogen-bonded co-crystals of tritopic acceptors, *Molecules*, 2018, 23, 163.
- 59 C. E. Willans, S. French, K. M. Anderson, L. J. Barbour, J.-A. Gertenbach, G. O. Lloyd, R. J. Dyer, P. C. Junk and J. W. Steed, Tripodal imidazole frameworks: Reversible vapour sorption both with and without significant structural changes, *Dalton Trans.*, 2011, 40, 573.
- 60 C. B. Aakeröy, M. Smith and J. Desper, Finding a single-molecule receptor for citramalic acid through supramolecular chelation, *Can. J. Chem.*, 2015, 93, 822–825.
- 61 J. Fan, W.-Y. Sun, T. Okamura, J. Xie, W.-X. Tang and N. Ueyama, First example of a dumbbell-like architecture containing M_3L_2 cages and terephthalate anions, *New J. Chem.*, 2002, 26, 199.
- 62 J. Fan, H.-F. Zhu, T. Okamura, W.-Y. Sun, W.-X. Tang and N. Ueyama, Discrete and infinite cage-like frameworks with inclusion of anionic and neutral species and with interpenetration phenomena, *Chem. – Eur. J.*, 2003, 9, 4724.
- 63 A. L. Spek, PLATON SQUEEZE: A tool for the calculation of the disordered solvent contribution to the calculated struc-



- ture factors, *Acta Crystallogr., Sect. C: Struct. Chem.*, 2015, **71**, 9.
- 64 A.-C. C. Carlsson, K. Mehmeti, M. Uhrbom, A. Karim, M. Bedin, R. Puttreddy, R. Kleinmaier, A. A. Neverov, B. Nekoueishahraki, J. Gräfenstein, K. Rissanen and M. Erdélyi, Substituent effects on the [N-I-N]⁺ halogen bond, *J. Am. Chem. Soc.*, 2016, **138**, 9853.
- 65 A.-C. C. Carlsson, J. Gräfenstein, A. Budnjo, J. L. Laurila, J. Bergquist, A. Karim, R. Kleinmaier, U. Brath and M. Erdélyi, Symmetric halogen bonding is preferred in solution, *J. Am. Chem. Soc.*, 2012, **134**, 5706.
- 66 M. A. Spackman and D. Jayatilaka, Hirshfeld surface analysis, *CrystEngComm*, 2009, **11**, 19.
- 67 P. R. Spackman, M. J. Turner, J. J. McKinnon, S. K. Wolff, D. J. Grimwood, D. Jayatilaka and M. A. Spackman, CrystalExplorer: A program for Hirshfeld surface analysis, visualization and quantitative analysis of molecular crystals, *J. Appl. Crystallogr.*, 2021, **54**, 1006.
- 68 S. Mecozzi and J. Rebek Jr., The 55% solution: A formula for molecular recognition in the liquid state, *Chem. – Eur. J.*, 1998, **4**, 1016.
- 69 K. Rissanen, Crystallography of encapsulated molecules, *Chem. Soc. Rev.*, 2017, **46**, 2638.
- 70 E. Kalenius, M. Groessel and K. Rissanen, Ion mobility-mass spectrometry of supramolecular complexes and assemblies, *Nat. Rev. Chem.*, 2019, **3**, 4.



Electronic Supplementary Information

**Dimeric iodine(I) and silver(I) cages from tripodal
N-donor ligands via the $[N-Ag-N]^+$ to $[N-I-N]^+$
cation exchange reaction**

Essi Taipale,^a Jas S. Ward,^{*a} Giorgia Fiorini,^a Daniel L. Stares,^b Christoph A. Schalley,^b
and Kari Rissanen^{*a}

a. University of Jyväskylä, Department of Chemistry, P. O. BOX 35, Survontie 9B,
40014 Jyväskylä, Finland. E-mail: kari.t.rissanen@jyu.fi

b. Institut für Chemie und Biochemie, Organische Chemie, Freie Universität Berlin,
Arnimallee 20, 14195 Berlin, Germany.

Contents

Experimental	3
General Details	3
Synthesis and Characterisation: Ligands	4
Synthesis and Characterisation: Silver(I) Cages	10
Synthesis and Characterisation: Iodine(I) Cages	15
X-Ray Crystallography	18
X-Ray Experimental Details	19
Hirshfeld Surface Analysis	32
Computational Methods	37
General.....	37
The Cartesian Coordinates	40
HRMS, IM-MS, and CID	60
^1H NMR and ^1H-^{15}N HMBC Spectra of Synthesised Compounds.....	85
^{19}F NMR Spectra of Selected Compounds.....	95
References	99

Experimental

General Details

All reagents and solvents obtained from commercial suppliers were used without further purification. The syntheses of all prepared compounds are described below. Compound **1** was prepared according to literature procedures and compounds **2** - **6** were prepared with slight modifications of the first synthesis.¹ All used solvents were acquired dry from commercial suppliers. For NMR assignments, ¹H and ¹⁵N NMR spectra were recorded using Bruker Avance III 500 MHz spectrometer, whereas ¹⁹F NMR was recorded using Bruker 300 Avance instrument, all at 303 K. Chemical shifts are reported on the δ scale in ppm using the residual solvent signal as internal standard (CD₃CN; δ H 1.94, DMSO-*d*₆; δ H 2.50). For ¹H NMR spectroscopy, each resonance was assigned according to the following conventions: chemical shift (δ) measured in ppm, observed multiplicity, number of hydrogens, and observed coupling constant (J Hz). Multiplicities are denoted as s (singlet), d (doublet), t (triplet), q (quartet) m (multiplet), and br (broad). Spectral windows of 4 ppm (¹H) and 600 ppm (¹⁵N) were used in the ¹H-¹⁵N HMBC spectroscopy, with 2048 points in the direct dimension and 512 increments used in the indirect dimension, and subsequent peak shape analysis was performed.

Abbreviations:

CID = collision-induced dissociation

DMF = dimethylformamide

DMSO = dimethylsulfoxide

HMBC = heteronuclear multiple bond correlation

HRMS = high resolution mass spectrometry

IM-MS = ion mobility mass spectrometry

MeCN = acetonitrile

MeOH = methanol

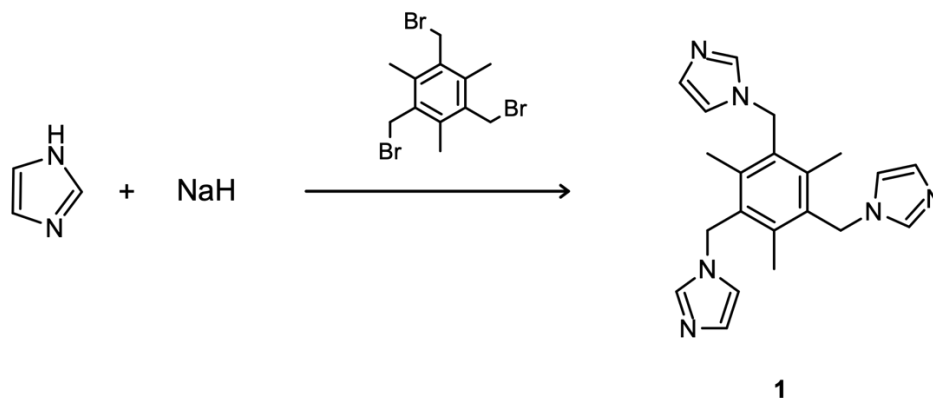
NMR = nuclear magnetic resonance

SY = survivor yield

TBME = methyl tert-butyl ether

THF = tetrahydrofuran

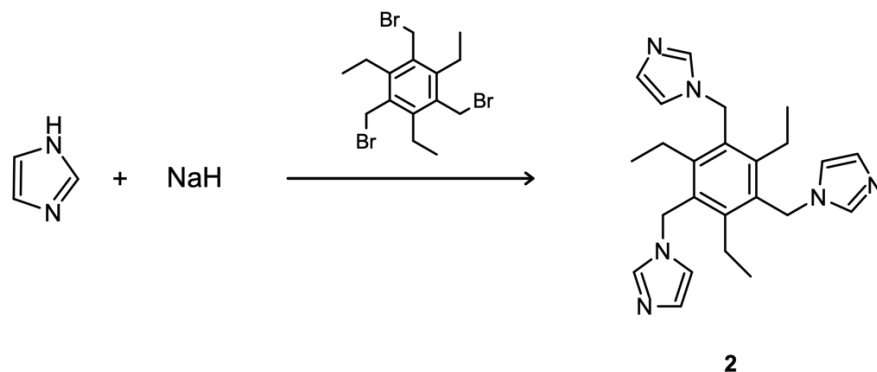
Synthesis and Characterisation: Ligands



Scheme S1. Synthesis of compound 1.

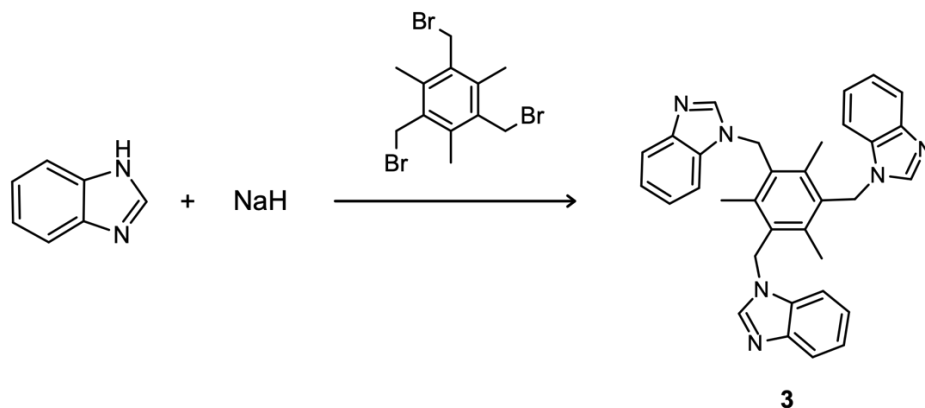
Synthesis of compound 1 (1,1',1''-((2,4,6-trimethylbenzene-1,3,5-triyl)tris(methylene))tris(1H-imidazole)).¹ To a solution of imidazole (5.926 mmol, 403.4 mg) in dry DMF (6 mL) under argon, 6.121 mmol NaH (146.9 mg) was added. After stirring for 30 minutes at ambient temperature, 1,3,5-tris(bromomethyl)-2,4,6-trimethylbenzene (1.975 mmol, 788.0 mg) in dry DMF (6 mL) was added dropwise over 2 hours. The mixture was stirred for 20 hours, the solvent was removed under reduced pressure and the residue was washed with water after which a white solid was obtained (334.9 mg, 47%). ¹H NMR (500 MHz, CD₃CN) δ 7.32 (s, 3H), 6.90 (s, 3H), 6.82 (s, 3H), 5.27 (s, 6H), 2.28 (s, 9H).

5



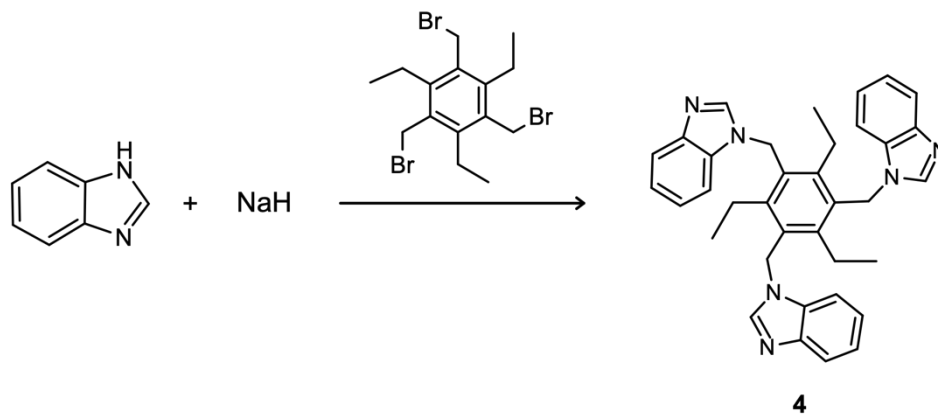
Scheme S2. Synthesis of compound 2.

Synthesis of compound 2 (1,1',1''-((2,4,6-triethylbenzene-1,3,5-triyl)tris(methylene))tris(1H-imidazole)).¹ All the glassware was oven-dried overnight to remove any moisture. Imidazole (7.453 mmol, 507.4 mg) and 1,3,5-tris(bromomethyl)-2,4,6-triethylbenzene (2.4841 mmol, 1095.6 mg) were weighed in air. A flask with imidazole was evacuated, flushed with argon three times, and left under vacuum. The flask was introduced into a glove box where 7.700 mmol NaH (184.8 mg) was weighed and added to the flask. The flask was connected to a Schlenk line, put under argon, and dry DMF (6 mL) was added. After stirring at ambient temperature for 30 minutes, 1,3,5-tris(bromomethyl)-2,4,6-triethylbenzene in DMF (6 mL) and THF (6 mL) was added dropwise over 1 hour. The mixture was stirred for 20 hours, the solvent was removed under reduced pressure and the residue was washed with water after which a white solid was obtained (859.6 mg, 86%). ¹H NMR (500 MHz, CD₃CN) δ 7.30 (s, 3H), 6.90 (s, 3H), 6.81 (s, 3H), 5.26 (s, 6H), 2.66 (q, *J* = 7.54 Hz, 6H), 0.91 (t, *J* = 7.54 Hz, 9H).



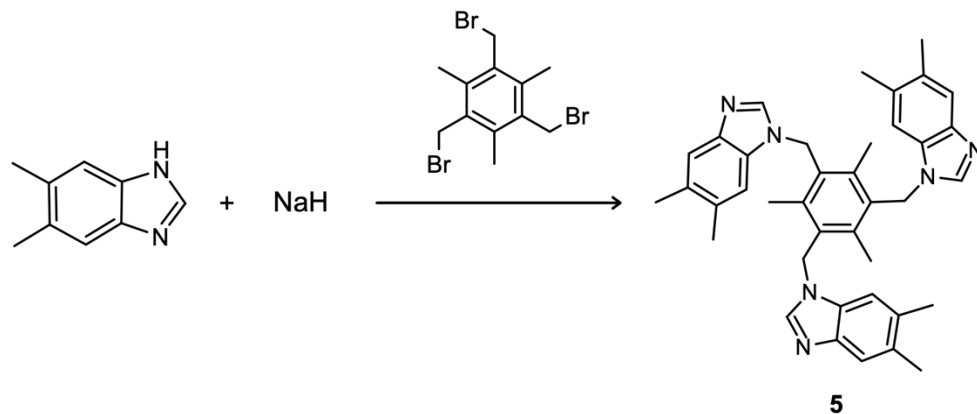
Scheme S3. Synthesis of compound **3**.

Synthesis of compound 3 (1,1',1''-((2,4,6-trimethylbenzene-1,3,5-triyl)tris(methylene))tris(1H-benzo[d]imidazole)).¹ All the glassware was oven-dried overnight to remove any moisture. 1H-benzo[d]imidazole (5.880 mmol, 694.7 mg) and 1,3,5-tris(bromomethyl)-2,4,6-trimethylbenzene (1.959 mmol, 781.4 mg) were weighed in air. A flask with 1H-benzo[d]imidazole was evacuated, flushed with argon three times, and left under vacuum. The flask was introduced into a glove box where 6.071 mmol NaH (145.7 mg) was weighed and added to the flask. The flask was connected to a Schlenk line, put under argon and dry DMF (6 mL) was added. After stirring at ambient temperature for 30 minutes, 1,3,5-tris(bromomethyl)-2,4,6-trimethylbenzene in DMF (6 mL) was added dropwise over 2 hours. The mixture was stirred for 20 hours, the solvent was removed under reduced pressure and the residue was washed with water after which a white solid was obtained (630.6 mg, 63%). ¹H NMR (500 MHz, CD₃CN) δ 7.88 (s, 3H), 7.66 (br, 3H), 7.54 (br, 3H) 7.22 (t, 6H), 5.52 (s, 6H) 2.24 (s, 9H).



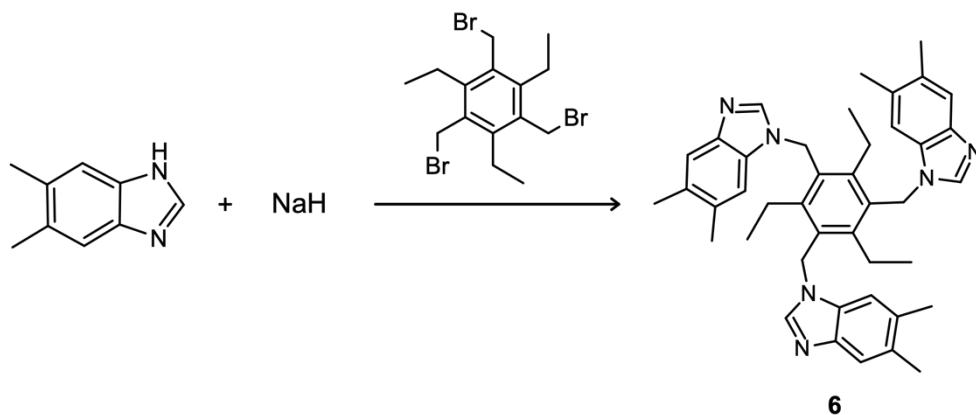
Scheme S4. Synthesis of compound **4**.

Synthesis of compound 4 (1,1',1''-((2,4,6-triethylbenzene-1,3,5-triyl)tris(methylene))tris(1H-benzo[d]imidazole)).¹ All the glassware was oven-dried overnight to remove any moisture. 1H-benzo[d]imidazole (5.427 mmol, 641.2 mg) and 1,3,5-tris(bromomethyl)-2,4,6-triethylbenzene (1.809 mmol, 797.9 mg) were weighed in air. A flask with 1H-benzo[d]imidazole was evacuated, flushed with argon three times, and left under vacuum. The flask was introduced into a glove box where 5.609 mmol NaH (134.6 mg) was weighted and added to the flask. The flask was connected to a Schlenk line, put under argon and dry DMF (6 mL) was added. After stirring at ambient temperature for 30 minutes, 1,3,5-tris(bromomethyl)-2,4,6-triethylbenzene in DMF (6 mL) and THF (6 mL) was added dropwise over 2 hours. The mixture was stirred for 20 hours, the solvent was removed under reduced pressure and the residue was washed with water after which a white solid was obtained (859.0 mg, 86%). ¹H NMR (500 MHz, CD₃CN) δ 7.68 (d, *J* = 7.90 Hz, 3H), 7.55 (s, 3H), 7.54 (d, *J* = 8.07 Hz, 3H), 7.31 (dt, *J* = 0.88, 7.94 Hz, 3H), 7.26 (dt, *J* = 0.94, 7.58 Hz, 3H), 5.45 (s, 6H), 2.65 (q, *J* = 7.52 Hz, 6H), 0.91 (t, *J* = 7.52 Hz, 9H).



Scheme S5. Synthesis of compound 5.

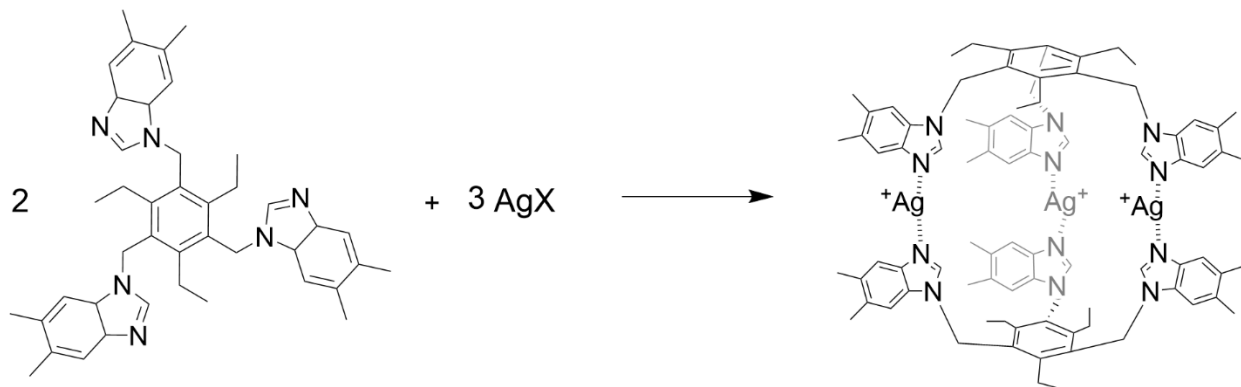
Synthesis of compound 5 (1,1',1''-((2,4,6-trimethylbenzene-1,3,5-triyl)tris(methylene))tris(5,6-dimethyl-1H-benzo[d]imidazole)).¹ All the glassware was oven-dried overnight to remove any moisture. 5,6-dimethyl-1H-benzo[d]imidazole (5.043 mmol, 737.3 mg) and 1,3,5-Tris(bromomethyl)-2,4,6-trimethylbenzene (1.681 mmol, 670.7 mg) were weighed in air. A flask with 5,6-dimethyl-1H-benzo[d]imidazole was evacuated, flushed with argon three times, and left under vacuum. The flask was introduced into a glove box where 5.213 mmol NaH (125.1 mg) was weighed and added to the flask. The flask was connected to a Schlenk line and put under argon and dry DMF (6 mL) was added. After stirring at ambient temperature for 30 minutes, 1,3,5-Tris(bromomethyl)-2,4,6-trimethylbenzene in 12 mL DMF was added dropwise over 2 hours. The mixture was stirred for 20 hours, the solvent was removed under reduced pressure and the residue was washed with water (2 × 50 mL) after which a light brown solid was obtained (718.2 mg, 72%). ¹H NMR (500 MHz, CD₃CN) δ 7.42 (s, 6H), 7.24 (s, 3H), 5.37 (s, 6H), 2.35 (d, *J* = 9.90 Hz, 18H), 2.23 (s, 9H).



Scheme S6. Synthesis of compound 6.

Synthesis of compound 6 (1,1',1''-((2,4,6-triethylbenzene-1,3,5-triyl)tris(methylene))tris(5,6-dimethyl-1H-benzo[d]imidazole)). All the glassware was oven-dried overnight to remove any moisture. 5,6-dimethyl-1H-benzo[d]imidazole (4.710 mmol, 688.6 mg) and 1,3,5-Tris(bromomethyl)-2,4,6-triethylbenzene (1.570 mmol, 692.5 mg) were weighted in air. A flask with 5,6-dimethyl-1H-benzo[d]imidazole was evacuated, flushed with argon three times, and left under vacuum. The flask was introduced into a glove box where 4.867 mmol NaH (116.8 mg) was weighted and added to the flask. The flask was connected to a Schlenk line and put under argon and dry DMF (6 mL) was added. After stirring at ambient temperature for 30 minutes, 1,3,5-Tris(bromomethyl)-2,4,6-triethylbenzene in DMF (6 mL) and THF (6 mL) was added dropwise over 2 hours. The mixture was stirred for 20 hours, the solvent was removed under reduced pressure and the residue was washed with water (2 × 50 mL) after which a brown solid was obtained (736.6 mg, 74%). ¹H NMR (500 MHz, CD₃CN) δ 7.43 (s, 3H), δ 7.40 (s, 3H), 7.27 (s, 3H), 5.39 (s, 6H), 2.64 (q, *J* = 7.47 Hz, 6H), 2.35 (d, *J* = 14.63 Hz, 18H), 0.91 (t, *J* = 7.48 Hz, 9H). ¹³C NMR (126 MHz, DMSO-*d*₆) δ 145.49, 142.19, 141.64, 132.75, 131.00, 130.12, 129.90, 119.53, 110.37, 42.70, 22.93, 20.13, 19.86, 15.15. Elemental analysis found: C 78.07%; H 6.98%; N 13.57%. Calculated for (C₄₂H₄₈N₆ · 0.5 H₂O): C 78.10%; H 7.49 %; N 13.01%.

Synthesis and Characterisation: Silver(I) Cages



Scheme S7. The general synthesis of silver(I) cages described using ligand **6**. Reactions for all ligands were performed in either CH₃CN or DMSO. AgPF₆ was used for NMR analysis, other salts (AgBF₄ and AgSbF₆) were also used in the crystallization of compounds.

This section describes the synthesis of silver(I) cages. Various silver(I) salts were used in the attempts of obtaining good quality single crystals for the X-ray diffraction studies. Crystallization conditions for each crystal are described below. Furthermore, NMR experiments (¹H and ¹H-¹⁵N HMBC) and HRMS experiments were conducted with samples of cages constructed using silver(I) hexafluorophosphate.

Synthesis of [BF₄-C1-Ag-1][BF₄]₂

The silver complexation of ligand **1** with AgBF₄ was performed in small glass vials. Both the ligand **1** (10.0 mg, 0.0277 mmol) and the silver(I) salt (8.1 mg, 0.042 mol) were weighed in their own vials. The ligand and the silver(I) salt were dissolved in MeCN separately (200 μl + 200 μl), and to aid solubility, few drops of DMSO were added to the ligand solution. Once completely dissolved, the ligand was added to the silver(I) salt. The mixture was stirred for 1 hour. The single crystals for the X-ray diffraction experiments (see Figure S1) were grown from diffusion of methanol to the MeCN/DMSO mixture in room temperature.

Synthesis of [PF₆-C1-Ag-1][PF₆]₂

The silver complexation of ligand **1** with AgPF₆ was performed in small glass vials. Both the ligand **1** (10.0 mg, 0.0277 mmol) and the silver(I) salt (10.5 mg, 0.0415 mol) were weighed in their own vials. The ligand and the silver(I) salt were dissolved in MeCN separately (200 μl + 200 μl). Once completely dissolved, the

ligand was added to the silver(I) salt. The mixture was stirred for 1 hour. The cages for all ligands with AgPF₆ were characterized with mass spectrometry ([PF₆-c1-Ag-1]²⁺ *m/z* 594.0453, see Figure S26). This is a known complex, and therefore, other characterization was not performed.

Synthesis of [SbF₆-c1-Ag-1][SbF₆]₂

The silver complexation of ligand **1** with AgSbF₆ was performed in small glass vials. Both the ligand **1** (10.0 mg, 0.0277 mmol) and the silver(I) salt (14.3 mg, 0.0416 mol) were weighed in their own vials. The ligand and the silver(I) salt were dissolved in MeCN separately (200 μl + 200 μl). Once completely dissolved, the ligand was added to the silver(I) salt. The mixture was stirred for 1 hour. The single crystals for the X-ray diffraction experiments (see Figure S2) were grown from diffusion of methanol to the MeCN in fridge (+4 °C).

Synthesis of [1-Ag-1]_n[OTf]_n

The silver complexation of ligand **1** with AgOTf was performed in small glass vials. Both the ligand **1** (10.0 mg, 0.0277 mmol) and the silver(I) salt (10.7 mg, 0.0416 mol) were weighed in their own vials. The ligand and the silver(I) salt were dissolved in MeCN separately (200 μl + 200 μl). Once completely dissolved, the ligand was added to the silver(I) salt. The mixture was stirred for 1 hour. The single crystals for the X-ray diffraction experiments (see Figure S3) were grown from evaporation of MeCN in room temperature.

Synthesis of [PF₆-c2-Ag-2][PF₆]₂

The silver complexation of ligand **2** with AgPF₆ was performed in small glass vials. Both the ligand **2** (10.0 mg, 0.0248 mmol) and the silver(I) salt (9.4 mg, 0.037 mol) were weighed in their own vials. The ligand and the silver(I) salt were dissolved in DMSO separately (200 μl + 200 μl). Once completely dissolved, the ligand was added to the silver(I) salt. The mixture was stirred for 1 hour and characterized. For NMR experiments, the solvents were switched to deuterated ones. The NMR experiments (Figure S50 and Figure S51) revealed effectively a 100% conversion from the ligand to the silver(I) complex. The single crystals for the X-ray diffraction experiments were not obtained due to poor solubility preventing any valid crystallization attempts. However, the cages for all ligands with AgPF₆ were characterized with mass spectrometry ([PF₆-c2-Ag-2]²⁺ *m/z* 636.0905, see Figure S29). ¹H NMR (500 MHz, DMSO-*d*₆) δ 7.76 (s, 6H), 7.44 (s, 6H), 7.23 (s, 6H), 5.33 (s, 12H), 2.65 (q, unresolved, 12H), 0.79 (t, *J* = 7.05 Hz, 18H).

Synthesis of [PF₆-c3-Ag-3][PF₆]₂

The silver complexation of ligand **3** with AgPF₆ was performed in small glass vials. Both the ligand **3** (10.0 mg, 0.0196 mmol) and the silver(I) salt (7.4 mg, 0.029 mol) were weighed in their own vials. The ligand and

the silver(I) salt were dissolved in MeCN separately (200 μ l + 200 μ l). Once completely dissolved, the ligand was added to the silver(I) salt. The mixture was stirred for 1 hour and characterized. For NMR experiments, the solvents were switched to deuterated ones. The NMR experiments (Figure S52 and Figure S53) revealed effectively a 100% conversion from the ligand to the silver(I) complex. The single crystals for the X-ray diffraction experiments (see Figure S4) were grown from diffusion of TMBE to the MeCN in room temperature. In addition, the cages for all ligands with AgPF₆ were characterized with mass spectrometry ([PF₆-C3-Ag-3]²⁺ *m/z* 743.0927, see Figure S32). ¹H NMR (500 MHz, DMSO-*d*₆) δ 8.09 (d, *J* = 8.11 Hz, 6H), 8.05 (s, 6H), 7.91 (d, *J* = 7.93 Hz, 6H), 7.53 (t, *J* = 7.56 Hz, 6H), 7.46 (t, *J* = 7.54 Hz, 6H), 5.70 (s, 6H), 2.37 (s, 18H).

Synthesis of [SbF₆-C3-Ag-3][SbF₆]₂

The silver complexation of ligand **3** with AgSbF₆ was performed in small glass vials. Both the ligand **3** (10.0 mg, 0.0196 mmol) and the silver(I) salt (10.1 mg, 0.0294 mol) were weighed in their own vials. The ligand and the silver(I) salt were dissolved in MeCN separately (200 μ l + 200 μ l). Once completely dissolved, the ligand was added to the silver(I) salt. The mixture was stirred for 1 hour. The single crystals for the X-ray diffraction experiments (Figure S5) were grown from diffusion of methanol to the MeCN in fridge (+4 °C).

Synthesis of [4-Ag-4][PF₆]₃

The silver complexation of ligand **4** with AgPF₆ was performed in small glass vials. Both the ligand **4** (10.0 mg, 0.0181 mmol) and the silver(I) salt (6.9 mg, 0.027 mol) were weighed in their own vials. The ligand and the silver(I) salt were dissolved in MeCN separately (200 μ l + 200 μ l). Once completely dissolved, the ligand was added to the silver(I) salt. The mixture was stirred for 1 hour and characterized. For NMR experiments, the solvents were switched to deuterated ones. The NMR experiments (Figure S54 and Figure S55) revealed effectively a 100% conversion from the ligand to the silver(I) complex. The single crystals for the X-ray diffraction experiments (Figure S6) were grown from evaporation of the MeCN in fridge (+4 °C). In addition, the cages for all ligands with AgPF₆ were characterized with mass spectrometry ([PF₆-C4-Ag-4]²⁺ *m/z* 787.1420, see Figure S36). ¹H NMR (500 MHz, CD₃CN) δ 7.95 (s, 6H), 7.93 (*overlapping doublets*, 6H), 7.91 (*overlapping doublets*, 6H), 7.58 (t, *J* = 7.62 Hz, 6H), 7.51 (t, *J* = 7.55 Hz, 6H) 5.56 (s, 12H), 2.62 (q, *J* = 7.23 Hz, 12H), 1.08 (t, *J* = 7.32 Hz, 18H).

Synthesis of [4-Ag-4][SbF₆]₃

The silver complexation of ligand **4** with AgSbF₆ was performed in small glass vials. Both the ligand **4** (10.0 mg, 0.0181 mmol) and the silver(I) salt (9.3 mg, 0.027 mol) were weighed in their own vials. The ligand and the silver(I) salt were dissolved in MeCN separately (200 μ l + 200 μ l). Once completely dissolved, the ligand was added to the silver(I) salt. The mixture was stirred for 10 minutes and characterized. The single crystals

for the X-ray diffraction experiments (Figure S7) were grown from evaporation of the MeCN in fridge (+4 °C).

Synthesis of [BF₄-c5-Ag-5][BF₄]₂

The silver complexation of ligand **5** with AgBF₄ was performed in small glass vials. Both the ligand **5** (10.0 mg, 0.0168 mmol) and the silver(I) salt (4.9 mg, 0.025 mol) were weighed in their own vials. The ligand and the silver(I) salt were dissolved in DMSO separately (200 μl + 200 μl). Once completely dissolved, the ligand was added to the silver(I) salt. The mixture was stirred for 1 hour. The single crystals for the X-ray diffraction experiments (Figure S8) were grown from diffusion of CHCl₃ to the DMSO in room temperature.

Synthesis of [PF₆-c5-Ag-5][PF₆]₂

The silver complexation of ligand **5** with AgPF₆ was performed in small glass vials. Both the ligand **5** (10.0 mg, 0.0168 mmol) and the silver(I) salt (6.4 mg, 0.025 mol) were weighed in their own vials. The ligand and the silver(I) salt were dissolved in DMSO separately (200 μl + 200 μl). Once completely dissolved, the ligand was added to the silver(I) salt. The mixture was stirred for 1 hour and characterized. For NMR experiments, the solvents were switched to deuterated ones. The NMR experiments (Figure S56 and Figure S57) revealed effectively a 100% conversion from the ligand to the silver(I) complex. The single crystals for the X-ray diffraction experiments (Figure S9) were grown from diffusion of CHCl₃ to the DMSO in room temperature. In addition, the cages for all ligands with AgPF₆ were characterized with mass spectrometry ([PF₆-c5-Ag-5]²⁺ *m/z* 827.1843, see Figure S39). ¹H NMR (500 MHz, CD₃CN) δ 7.82 (s, 6H), 7.68 (d, *J* = 3.47 Hz, 12H), 5.49 (s, 12H), 2.48 (s, 18H), 2.45 (s, 18H), 2.27 (s, 18H).

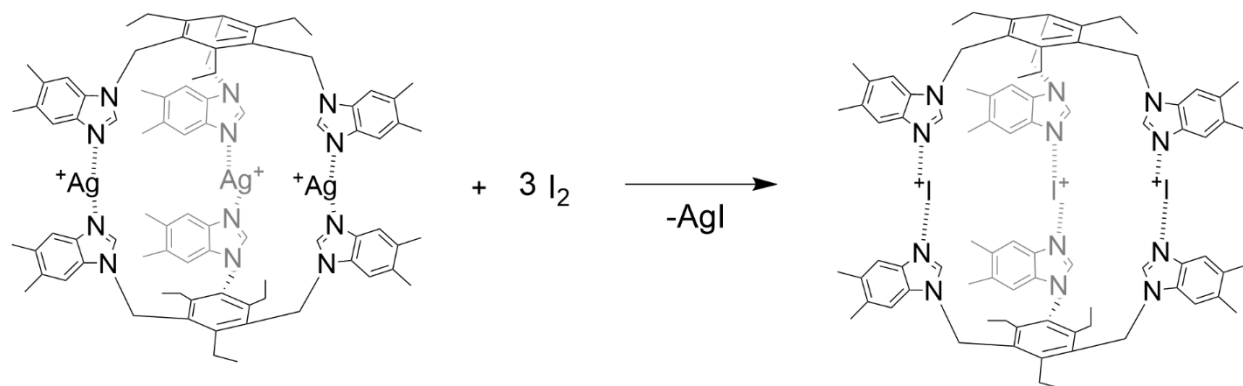
Synthesis of [PF₆-c6-Ag-6][PF₆]₂

The silver complexation of ligand **6** with AgPF₆ was performed in small glass vials. Both the ligand **6** (10.0 mg, 0.0157 mmol) and the silver(I) salt (6.0 mg, 0.024 mol) were weighed in their own vials. The ligand and the silver(I) salt were dissolved in DMSO separately (200 μl + 200 μl). Once completely dissolved, the ligand was added to the silver(I) salt. The mixture was stirred for 1 hour and characterized. For NMR experiments, the solvents were switched to deuterated ones. The NMR experiments (Figure S58 and Figure S59) revealed effectively a 100% conversion from the ligand to the silver(I) complex. The single crystals for the X-ray diffraction experiments (Figure S10) were grown from diffusion of CHCl₃ to the DMSO in room temperature. In addition, the cages for all ligands with AgPF₆ were characterized with mass spectrometry ([PF₆-c6-Ag-6]²⁺ *m/z* 871.2361, see Figure S42). ¹H NMR (500 MHz, DMSO-*d*₆) δ 7.88 (s, 12H), 7.66 (s, 6H), 5.57 (s, 12H), 2.61 (s, 12H), 2.42 (s, 18H), 2.35 (s, 18H), 0.91 (s, 18H).

Synthesis of [SbF₆-c6-Ag-6][SbF₆]₂

The silver complexation of ligand **6** with AgSbF₆ was performed in small glass vials. Both the ligand **6** (10.0 mg, 0.0157 mmol) and the silver(I) salt (8.1 mg, 0.023 mol) were weighed in their own vials. The ligand and the silver(I) salt were dissolved in MeCN separately (200 μl + 200 μl). Once completely dissolved, the ligand was added to the silver(I) salt. The mixture was stirred for 1 hour. The single crystals for the X-ray diffraction experiments (Figure S11) were grown from evaporation of the MeCN in fridge (+4 °C).

Synthesis and Characterisation: Iodine(I) Cages



Scheme S8. The general synthesis of iodine(I) cages described using ligand **6**. Reactions for all ligands were performed in either CH_3CN or DMSO.

This section describes the synthesis of iodine(I) cages. The NMR experiments (^1H and ^1H - ^{15}N HMBC) and HRMS experiments were conducted with samples of cages constructed using silver(I) hexafluorophosphate. Unfortunately, all crystal structures for the iodine(I) cages remained elusive.

Synthesis of $[\text{PF}_6\text{-c1-I-1}][\text{PF}_6]_2$

The cation exchange reaction from $[\text{PF}_6\text{-c1-Ag-1}][\text{PF}_6]_2$ to $[\text{PF}_6\text{-c1-I-1}][\text{PF}_6]_2$ was performed in small glass vials. Both the silver(I) cage (10.0 mg, 0.00676 mmol) and the elemental iodine (7.82 mg, 0.0308 mol) were weighed in their own vials. The silver(I) cage and the elemental iodine were dissolved in MeCN separately (200 μl + 200 μl). Once completely dissolved, the elemental iodine was added to the silver(I) cage. The mixture was stirred for 1 hour and the formed silver iodide was filtered from the solution. The cages for all ligands with AgPF_6 were characterized with mass spectrometry ($[\text{L}_2\text{I}_3 + \text{PF}_6]^{2+}$ m/z 632.0462, see Figure S27). This is a known complex, and therefore, other characterization was not performed.

Synthesis of $[\text{PF}_6\text{-c2-I-2}][\text{PF}_6]_2$

The cation exchange reaction from $[\text{PF}_6\text{-c2-Ag-2}][\text{PF}_6]_2$ to $[\text{PF}_6\text{-c2-I-2}][\text{PF}_6]_2$ was performed in small glass vials. Both the silver(I) cage (10.0 mg, 0.00640 mmol) and the elemental iodine (7.20 mg, 0.0284 mol) were weighed in their own vials. The silver(I) cage and the elemental iodine were dissolved in DMSO separately (200 μl + 200 μl). Once completely dissolved, the elemental iodine was added to the silver(I) cage. The mixture was stirred for 1 hour, centrifuged for 5 minutes and the formed silver iodide was filtered

from the solution. For NMR experiments (Figure S50 and Figure S51), the solvents were switched to deuterated ones. A conversion from the silver(I) to the iodine(I) complex was revealed by the NMR experiments, however, multiple species were observed due to the highly competitive nature of DMSO and perhaps an incomplete conversion resulting from the low solubility of the ligand and the silver(I) cage. The single crystals for the X-ray diffraction experiments were not obtained due to poor solubility preventing any valid crystallization attempts. However, the cages for all ligands with AgPF₆ were characterized with mass spectrometry ([PF₆-c1-I-1]²⁺ *m/z* 665.0902, see Figure S30). ¹H NMR (500 MHz, DMSO-*d*₆) δ 8.99 (s, 6H), 7.74 (s, 6H), 7.61 (s, 6H), 5.50 (s, 12H), 2.66 (q, unresolved, 12H), 0.79 (t, unresolved, 18H).

Synthesis of [PF₆-c3-I-3][PF₆]₂

The cation exchange reaction from [PF₆-c3-Ag-3][PF₆]₂ to [PF₆-c3-I-3][PF₆]₂ was performed in small glass vials. Both the silver(I) cage (10.0 mg, 0.00562 mmol) and the elemental iodine (5.98 mg, 0.0236 mol) were weighed in their own vials. The silver(I) cage and the elemental iodine were dissolved in DMSO separately (200 μl + 200 μl). Once completely dissolved, the elemental iodine was added to the silver(I) cage. The mixture was stirred for 1 hour, centrifuged for 5 minutes and the formed silver iodide was filtered from the solution. For NMR experiments (Figure S52 and Figure S53), the solvents were switched to deuterated ones. A conversion from the silver(I) to the iodine(I) complex was revealed by the NMR experiments, however, multiple species were observed due to the highly competitive nature of DMSO and perhaps an incomplete conversion resulting from the low solubility of the ligand and the silver(I) cage. The single crystals for the X-ray diffraction experiments were not obtained due to poor solubility preventing any valid crystallization attempts. However, the cages for all ligands with AgPF₆ were characterized with mass spectrometry ([PF₆-c3-I-3]²⁺ *m/z* 773.0915, see Figure S34). ¹H NMR (500 MHz, DMSO-*d*₆) δ 8.70 (s, 6H), 8.20 (d, unresolved, 6H), 7.96 (d, unresolved, 6H), 7.64 (t, unresolved, 12H), 5.70 (s, 6H), 2.32 (s, 18H).

Synthesis of [PF₆-c4-I-4][PF₆]₂

The cation exchange reaction from [PF₆-c4-Ag-4][PF₆]₂ to [PF₆-c4-I-4][PF₆]₂ was performed in small glass vials. Both the silver(I) cage (10.0 mg, 0.00536 mmol) and the elemental iodine (5.61 mg, 0.0221 mol) were weighed in their own vials. The silver(I) cage and the elemental iodine were dissolved in MeCN separately (200 μl + 200 μl). Once completely dissolved, the elemental iodine was added to the silver(I) cage. The mixture was stirred for 1 hour and the formed silver iodide was filtered from the solution. For NMR experiments, the solvents were switched to deuterated ones. The NMR experiments (Figure S54 and Figure S55) revealed effectively a 100% conversion from the ligand to the silver(I) complex. The single crystals for the X-ray diffraction experiments were not obtained due to poor solubility preventing any valid crystallization attempts. However, the cages for all ligands with AgPF₆ were characterized with mass

spectrometry ($[\text{PF}_6\text{-c4-I-4}]^{2+}$ m/z 815.1360, see Figure S37). ^1H NMR (500 MHz, CD_3CN) δ 8.17 (s, 6H), 7.94 (m, 12H), 7.65 (m, 12H), 5.50 (s, 12H), 2.56 (q, $J = 7.45$ Hz, 12H), 1.25 (t, $J = 7.45$ Hz, 18H).

Synthesis of $[\text{PF}_6\text{-c5-I-5}][\text{PF}_6]_2$

The cation exchange reaction from $[\text{PF}_6\text{-c5-Ag-5}][\text{PF}_6]_2$ to $[\text{PF}_6\text{-c5-I-5}][\text{PF}_6]_2$ was performed in small glass vials. Both the silver(I) cage (10.0 mg, 0.00513 mmol) and the elemental iodine (6.2 mg, 0.024 mol) were weighed in their own vials. The silver(I) cage and the elemental iodine were dissolved in MeCN separately (200 μl + 200 μl). Once completely dissolved, the elemental iodine was added to the silver(I) cage. The mixture was stirred for 1 hour and the formed silver iodide was filtered from the solution. For NMR experiments, the solvents were switched to deuterated ones. The NMR experiments (Figure S56 and Figure S57) revealed effectively a 100% conversion from the ligand to the silver(I) complex. The single crystals for the X-ray diffraction experiments were not obtained due to poor solubility preventing any valid crystallization attempts. However, the cages for all ligands with AgPF_6 were characterized with mass spectrometry ($[\text{PF}_6\text{-c5-I-5}]^{2+}$ m/z 857.1865, see Figure S40). ^1H NMR (500 MHz, CD_3CN) δ 8.03 (s, 6H), 7.73 (s, 6H), 7.70 (s, 6H), 5.49 (s, 12H), 2.50 (s, 18H), 2.49 (s, 18H), 2.29 (s, 18H).

Synthesis of $[\text{PF}_6\text{-c6-I-6}][\text{PF}_6]_2$

The cation exchange reaction from $[\text{PF}_6\text{-c6-Ag-6}][\text{PF}_6]_2$ to $[\text{PF}_6\text{-c6-I-6}][\text{PF}_6]_2$ was performed in small glass vials. Both the silver(I) cage (10.0 mg, 0.00492 mmol) and the elemental iodine (5.0 mg, 0.020 mol) were weighed in their own vials. The silver(I) cage and the elemental iodine were dissolved in DMSO separately (200 μl + 200 μl). Once completely dissolved, the elemental iodine was added to the silver(I) cage. The mixture was stirred for 1 hour, centrifuged for 5 minutes and the formed silver iodide was filtered from the solution. For NMR experiments (Figure S58 and Figure S59), the solvents were switched to deuterated ones. A conversion from the silver(I) to the iodine(I) complex was revealed by the NMR experiments, however, multiple species were observed due to the highly competitive nature of DMSO and perhaps an incomplete conversion resulting from the low solubility of the ligand and the silver(I) cage. The single crystals for the X-ray diffraction experiments were not obtained due to poor solubility preventing any valid crystallization attempts. However, the cages for all ligands with AgPF_6 were characterized with mass spectrometry ($[\text{PF}_6\text{-c6-Ag-6}]^{2+}$ m/z 899.2325, see Figure S43). ^1H NMR (500 MHz, $\text{DMSO-}d_6$) δ 8.61 (s, 6H), 7.93 (s, 6H), 7.64 (s, 6H), 5.54 (s, 12H), 2.59 (q, unresolved, 12H), 2.43 (s, 18H), 2.34 (s, 18H), 0.80 (t, $J = 7.31$ Hz, 18H).

X-Ray Crystallography

The single crystal X-ray data for **[BF₄-c3-Ag-3][BF₄]₂** and **[PF₆-c3-I-3][PF₆]₂** were collected at 120 K using an Agilent Super-Nova diffractometer with an Eos detector using mirror monochromated Mo-K α ($\lambda = 0.71073$ Å) radiation. The single crystal X-ray data for all the other compounds were collected at 120 K using an Agilent Super-Nova dual-wavelength diffractometer with an Atlas detector using mirror-monochromated Cu-K α ($\lambda = 1.54184$ Å) radiation. The program CrysAlisPro⁴ was used for the data collection and reduction on both Super-Nova diffractometers. The intensities were corrected for absorption using a gaussian face index absorption correction method.⁴ The structures were solved with intrinsic phasing (*SHELXT*)⁵ and refined by full-matrix least-squares on F^2 using the *OLEX2* software,⁶ which utilizes the *SHELXL-2015* module.⁷ Non-hydrogen atoms were assigned anisotropic displacement parameters unless stated otherwise. Isotropic displacement parameters for all H atoms were constrained to multiples of the equivalent displacement parameters of their parent atoms with $U_{iso}(H) = 1.2 U_{eq}(\text{parent atom})$.

X-Ray Experimental Details

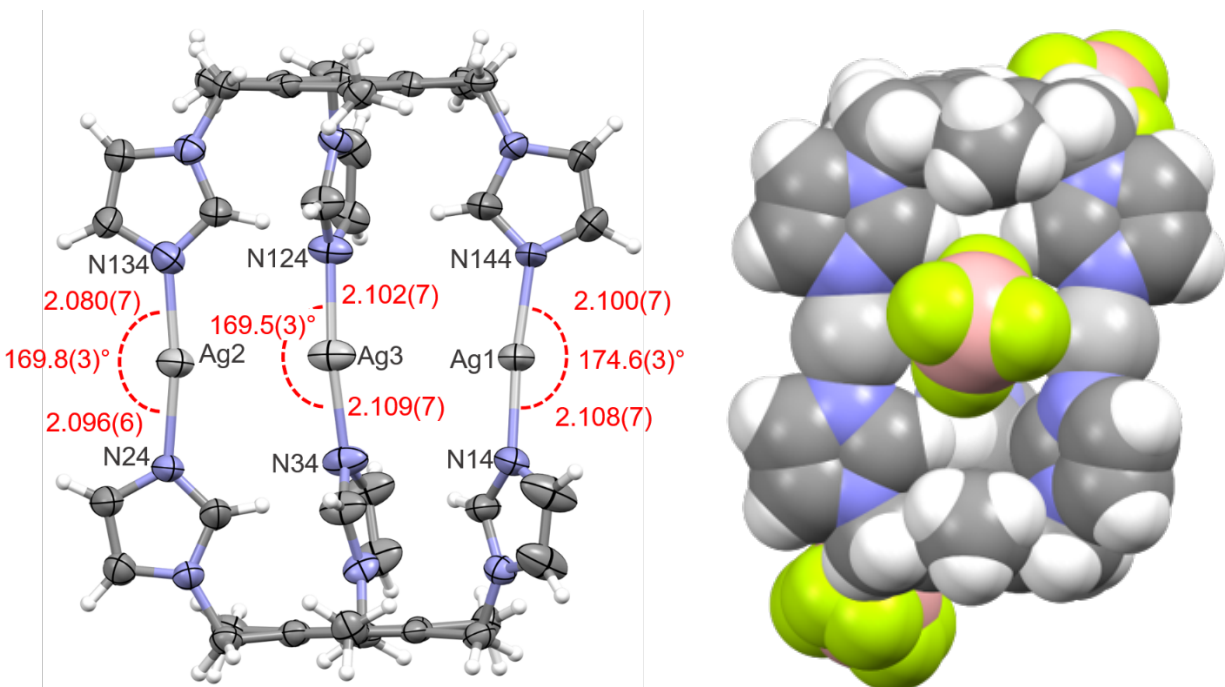


Figure S1. The ellipsoid (left) and spacefill (right) representations of the $[\text{BF}_4\text{-c1-Ag-1}][\text{BF}_4]_2$ Ag-coordination cage (thermal displacement ellipsoids are drawn at a 50% probability level; anions (left) and solvent molecules are omitted for clarity; all lengths are in Å). A polymorph to ConQuest Refcode: UBOGOH.²

Crystal data for $[\text{BF}_4\text{-c1-Ag-1}][\text{BF}_4]_2$ (obtained from MeCN/DMSO/MeOH mixture): CCDC-2126429, $[\text{C}_{42}\text{H}_{48}\text{Ag}_3\text{N}_{12}](\text{BF}_4)_3$, $M = 1304.96 \text{ g mol}^{-1}$, colourless yellow, $0.07 \times 0.06 \times 0.03 \text{ mm}^3$, monoclinic, space group $C2/c$, $a = 33.594(2) \text{ \AA}$, $b = 10.9898(7) \text{ \AA}$, $c = 34.777(3) \text{ \AA}$, $\beta = 117.075(10)^\circ$, $V = 11432.6 \text{ \AA}^3$, $Z = 8$, $D_{\text{calc}} = 1.516 \text{ g cm}^{-3}$, $F(000) = 5184$, $\mu = 8.86 \text{ mm}^{-1}$, $T = 120.00(10) \text{ K}$, $\theta_{\text{max}} = 77.1^\circ$, 25435 total reflections, 6167 with $I_o > 2\sigma(I_o)$, $R_{\text{int}} = 0.074$, 11643 data, 692 parameters, 60 restraints, GooF = 1.01, $R = 0.072$ and $wR = 0.207 [I_o > 2\sigma(I_o)]$, $0.81 < d\Delta\rho < -0.92 \text{ e\AA}^{-3}$.

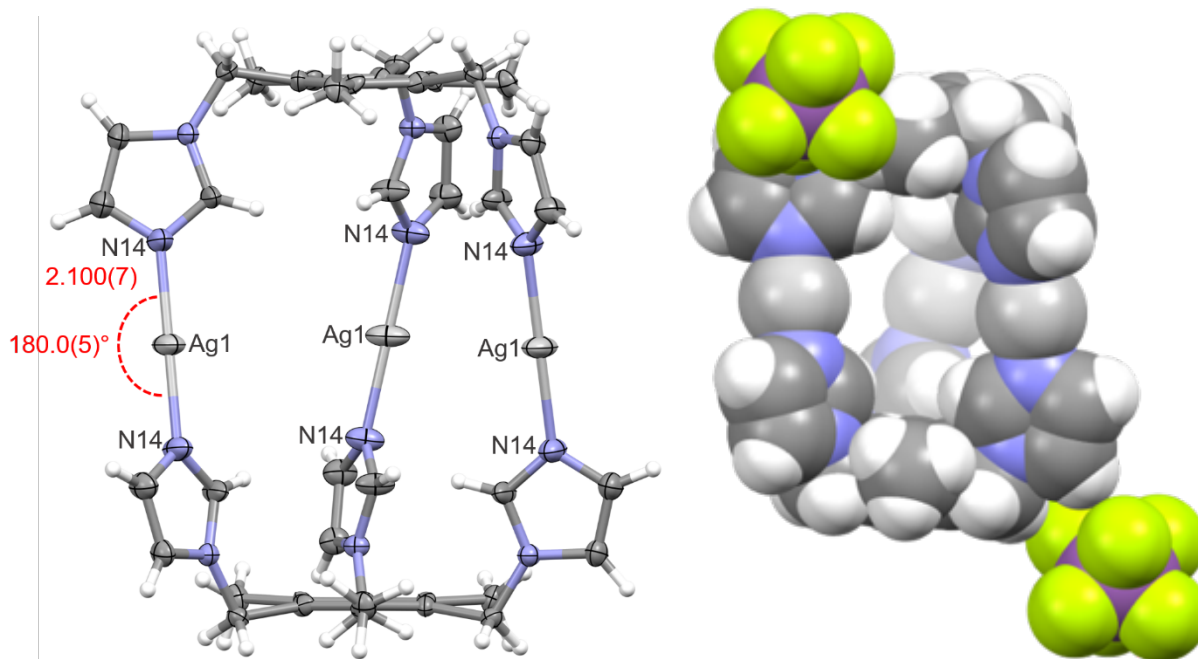


Figure S2. The ellipsoid (left) and spacefill (right) representations of the $[\text{SbF}_6\text{-c1-Ag-1}][\text{SbF}_6]_2$ helical Ag-coordination cage. Disordered SbF_6^- was found inside the cage yet could not be adequately modeled and was squeezed (thermal displacement ellipsoids are drawn at a 50% probability level; anions (left) and solvent molecules are omitted for clarity; all lengths are in Å). A polymorph to ConQuest Refcode: BOCQIU.³

Crystal data for $[\text{SbF}_6\text{-c1-Ag-1}][\text{SbF}_6]_2$ (obtained from MeCN/MeOH): CCDC-2126430, $[\text{C}_{42}\text{H}_{48}\text{Ag}_3\text{N}_{12}](\text{F}_6\text{Sb})_2^+$, $M = 1516.00 \text{ g mol}^{-1}$, colourless block, $0.10 \times 0.08 \times 0.04 \text{ mm}^3$, trigonal, space group $P321$, $a = 11.2651(1) \text{ Å}$, $c = 14.4922(2) \text{ Å}$, $V = 1592.71 \text{ Å}^3$, $Z = 1$, $D_{\text{calc}} = 1.581 \text{ g cm}^{-3}$, $F(000) = 735$, $\mu = 14.53 \text{ mm}^{-1}$, $T = 120.00(10) \text{ K}$, $\theta_{\text{max}} = 76.9^\circ$, 22336 total reflections, 2244 with $I_o > 2\sigma(I_o)$, $R_{\text{int}} = 0.032$, 2246 data, 110 parameters, no restraints, $\text{Goof} = 1.17$, $R = 0.036$ and $wR = 0.095 [I_o > 2\sigma(I_o)]$, $1.95 < d\Delta\rho < -1.25 \text{ eÅ}^{-3}$.

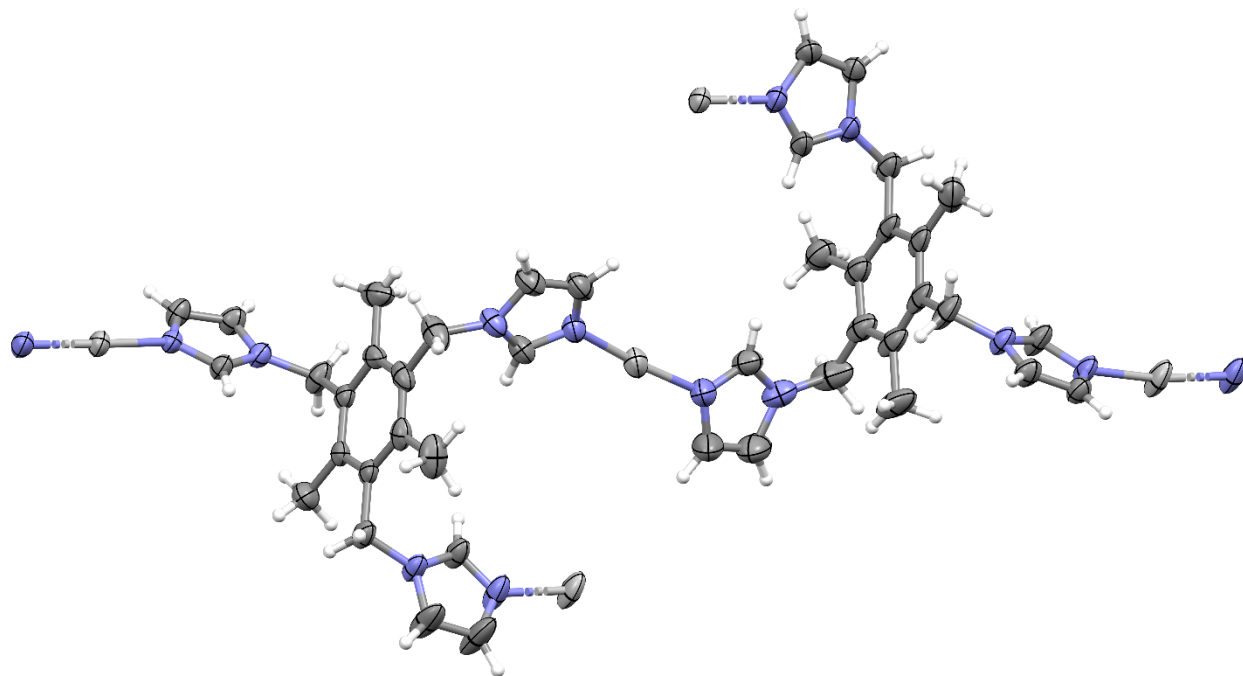


Figure S3. The ellipsoid representation of a polymeric $[1\text{-Ag-}]_n[\text{OTf}]_n$ structure with N–Ag bond lengths between 2.085 Å - 2.118 Å (thermal displacement ellipsoids are drawn at a 50% probability level; anions and solvent molecules are omitted for clarity; all lengths are in Å).

Crystal data for $[1\text{-Ag-}]_n[\text{OTf}]_n$ (obtained from MeCN): CCDC- CCDC-2126431, $([\text{C}_{42}\text{H}_{48}\text{Ag}_3\text{N}_{12}](\text{CF}_3\text{O}_3\text{S})_3)_n \cdot (\text{CH}_3\text{CN})_2$, $M = 1573.85 \text{ gmol}^{-1}$, colourless block, $0.17 \times 0.11 \times 0.06 \text{ mm}^3$, triclinic, space group $P-1$, $a = 10.0952(3) \text{ \AA}$, $b = 13.0031(4) \text{ \AA}$, $c = 23.6956(8) \text{ \AA}$, $\alpha = 98.866(3)^\circ$, $\beta = 94.235(3)^\circ$, $\gamma = 98.103(3)^\circ$, $V = 3028.09(17) \text{ \AA}^3$, $Z = 2$, $D_{\text{calc}} = 1.726 \text{ gcm}^{-3}$, $F(000) = 1576$, $\mu = 9.48 \text{ mm}^{-1}$, $T = 120.00(10) \text{ K}$, $\theta_{\text{max}} = 76.6^\circ$, 21209 total reflections, 10176 with $I_o > 2\sigma(I_o)$, $R_{\text{int}} = 0.031$, 12306 data, 829 parameters, 114 restraints, $\text{GooF} = 1.04$, $R = 0.062$ and $wR = 0.163 [I_o > 2\sigma(I_o)]$, $2.46 < d\Delta\rho < -1.57 \text{ e\AA}^{-3}$.

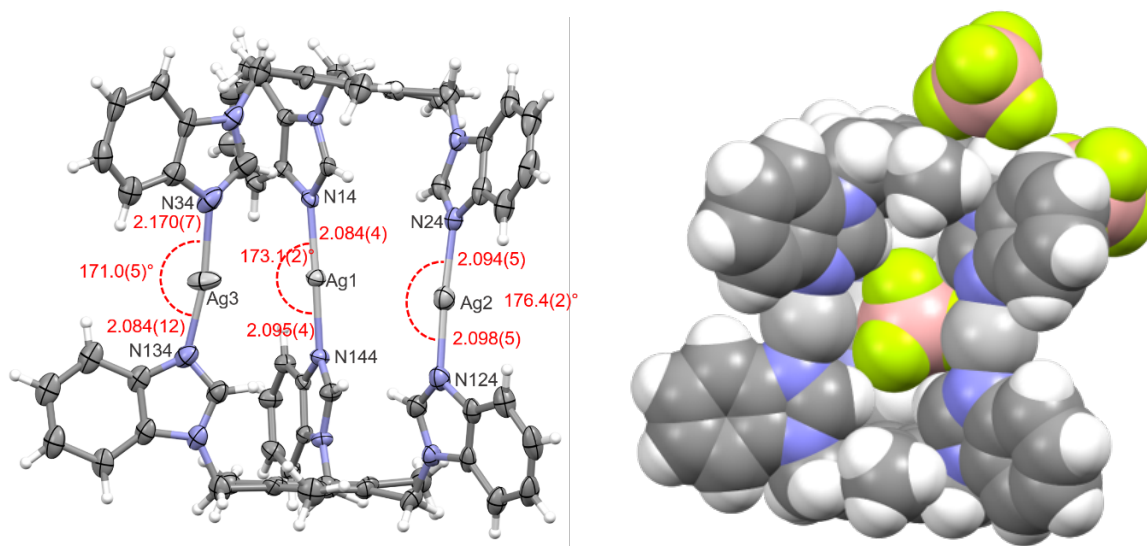


Figure S4 The ellipsoid (left) and spacefill (right) representations of the $[\text{BF}_4\text{-c3-Ag-3}][\text{BF}_4]_2$ Ag-coordination cage (thermal displacement ellipsoids are drawn at a 50% probability level; anions (left) and solvent molecules are omitted for clarity; all lengths are in Å).

Crystal data for $[\text{BF}_4\text{-c3-Ag-3}][\text{BF}_4]_2$ (obtained from MeCN/MeOH): CCDC- CCDC-2126432, $[\text{C}_{66}\text{H}_{60}\text{Ag}_3\text{N}_{12}][\text{BF}_4]_3 \cdot \text{CH}_3\text{CN}$, $M = 1646.35 \text{ g mol}^{-1}$, colourless needle, $0.58 \times 0.23 \times 0.13 \text{ mm}^3$, tetragonal, space group $P4_2/n$, $a = 27.6361(8) \text{ \AA}$, $c = 18.0738(7) \text{ \AA}$, $V = 13803.9(10) \text{ \AA}^3$, $Z = 8$, $D_{\text{calc}} = 1.584 \text{ g cm}^{-3}$, $F(000) = 6608$, $\mu = 0.93 \text{ mm}^{-1}$, $T = 120.00(10) \text{ K}$, $\theta_{\text{max}} = 26.6^\circ$, 14129 total reflections, 8755 with $I_o > 2\sigma(I_o)$, $R_{\text{int}} = 0.053$, 14129 data, 976 parameters, 217 restraints, $\text{GoF} = 1.02$, $R = 0.067$ and $wR = 0.139 [I_o > 2\sigma(I_o)]$, $0.91 < d\Delta\rho < -0.65 \text{ e \AA}^{-3}$.

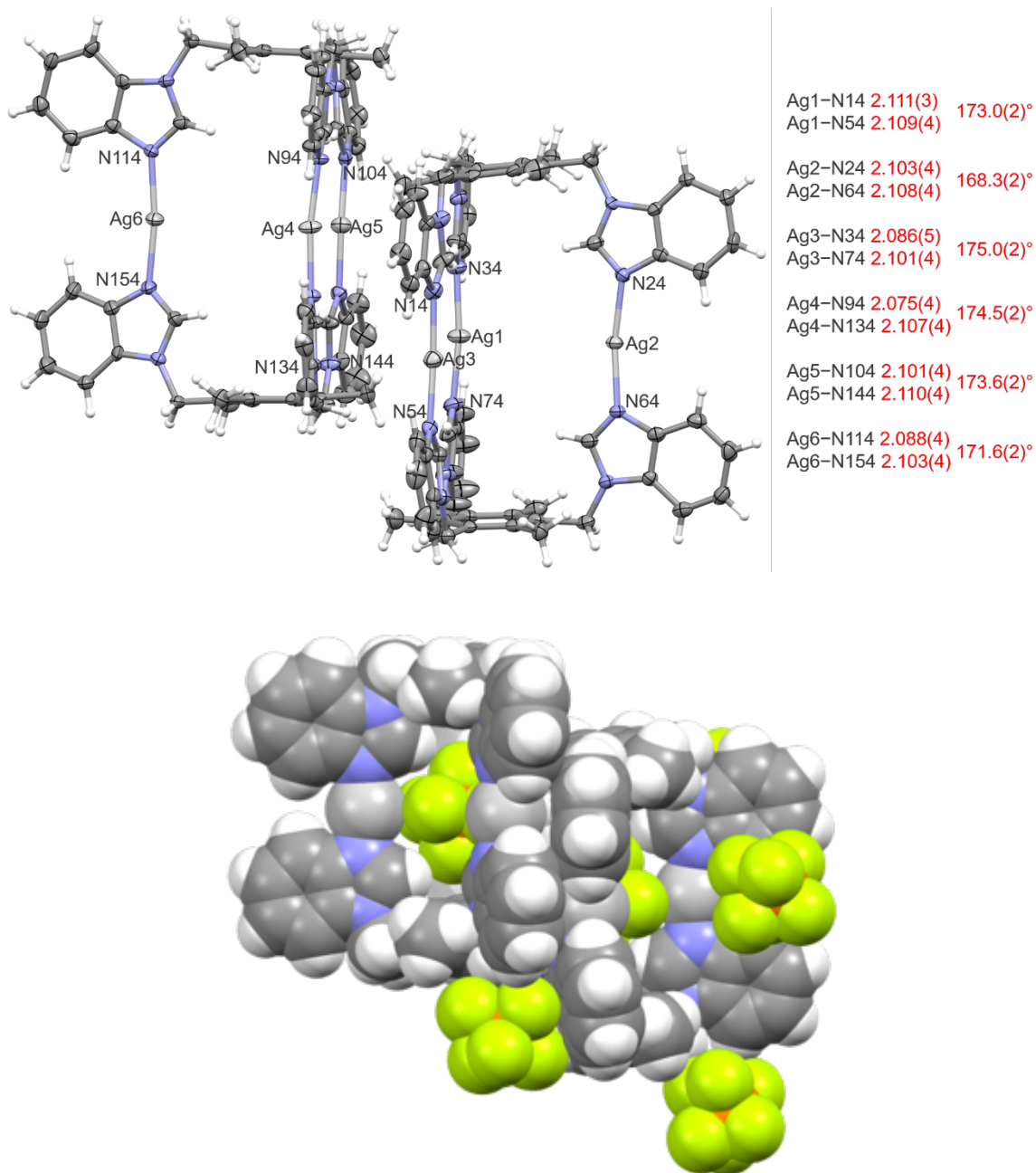


Figure S5. The ellipsoid (top) and spacefill (bottom) in the crystal structure (bottom) of $[\text{PF}_6\text{-c3-Ag-3}][\text{PF}_6]_2$ with face-to-face π -stacking between cages and slipped π - π interactions between dimers (thermal displacement ellipsoids are drawn at a 50% probability level; anions (top) and solvents omitted for clarity; all lengths are in Å).

Crystal data for $[\text{PF}_6\text{-c3-Ag-3}][\text{PF}_6]_2$ (obtained from MeCN/TBME): CCDC-2126433, $[\text{C}_{66}\text{H}_{60}\text{Ag}_3\text{N}_{12}][\text{PF}_6]_3 \cdot \text{CH}_3\text{CN}$, $M = 1861.88 \text{ g mol}^{-1}$, colourless plate, $0.40 \times 0.33 \times 0.09 \text{ mm}^3$, triclinic, space group $P-1$, $a = 15.7817(3) \text{ \AA}$, $b = 17.6300(6) \text{ \AA}$, $c = 31.5534(8) \text{ \AA}$, $\alpha = 99.766(2)^\circ$, $\beta = 99.078(2)^\circ$, $\gamma = 109.096(2)^\circ$, $V = 7958.5(4) \text{ \AA}^3$, $Z = 4$, $D_{\text{calc}} = 1.554 \text{ g cm}^{-3}$, $F(000) = 3728$, $\mu = 0.88 \text{ mm}^{-1}$, $T = 120.00(10) \text{ K}$, $\theta_{\text{max}} = 29.0^\circ$, 67347 total reflections, 21779 with $I_o > 2\sigma(I_o)$, $R_{\text{int}} = 0.044$, 36389 data, 2027 parameters, 542 restraints, $\text{Goof} = 1.03$, $R = 0.063$ and $wR = 0.183 [I_o > 2\sigma(I_o)]$, $1.88 < d\Delta\rho < -1.02 \text{ e \AA}^{-3}$.

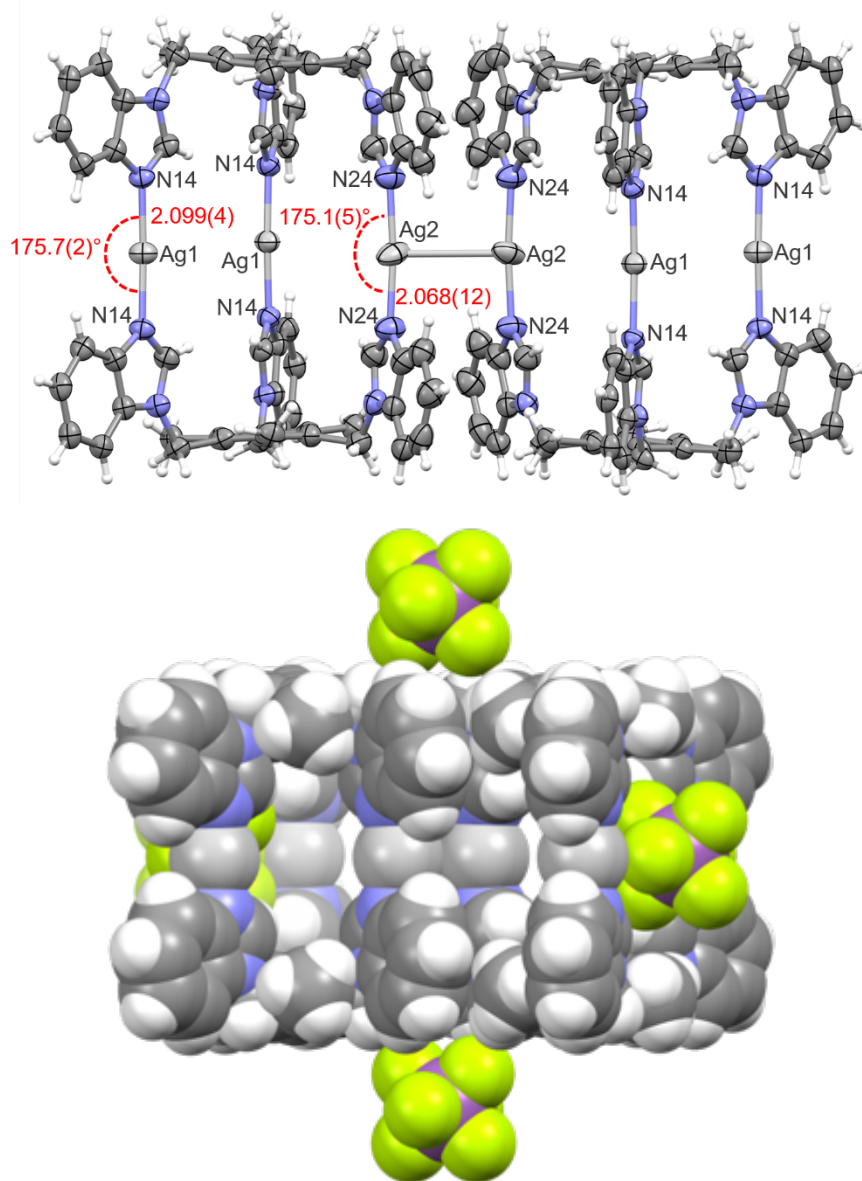


Figure S6. The ellipsoid (top) and spacefill (bottom) representations of the $[\text{SbF}_6\text{-c3-Ag-3}][\text{SbF}_6]_2$ Ag-coordination cage (thermal displacement ellipsoids are drawn at a 50% probability level; anions (top) and solvent molecules are omitted for clarity; all lengths are in Å).

Crystal data for $[\text{SbF}_6\text{-c3-Ag-3}][\text{SbF}_6]_2$ (obtained from MeCN/MeOH): CCDC-2126434, $[\text{C}_{66}\text{H}_{60}\text{Ag}_3\text{N}_{12}][\text{SbF}_6]_3$, $M = 1580.62 \text{ g mol}^{-1}$, colourless needle, $0.37 \times 0.07 \times 0.05 \text{ mm}^3$, tetragonal, space group $I4/mcm$, $a = 27.1562(1) \text{ Å}$, $c = 19.7887(3) \text{ Å}$, $V = 14593.4(2) \text{ Å}^3$, $Z = 8$, $D_{\text{calc}} = 1.439 \text{ g cm}^{-3}$, $F(000) = 6288$, $\mu = 9.77 \text{ mm}^{-1}$, $T = 120.00(10) \text{ K}$, $\theta_{\text{max}} = 74.5^\circ$, 69353 total reflections, 3480 with $I_o > 2\sigma(I_o)$, $R_{\text{int}} = 0.051$, 3961 data, 261 parameters, no restraints, $\text{GooF} = 1.04$, $R = 0.050$ and $wR = 0.151 [I_o > 2\sigma(I_o)]$, $1.82 < d\Delta\rho < -0.89 \text{ e Å}^{-3}$.

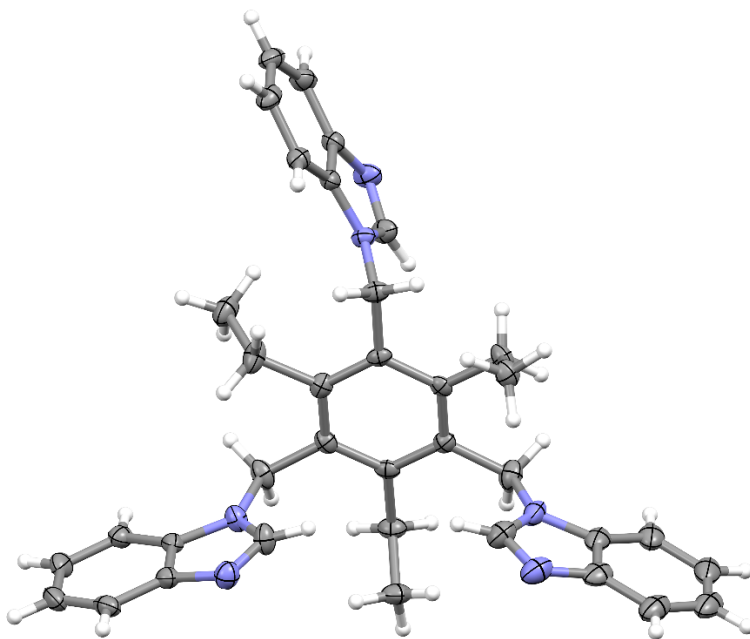


Figure S7. The ellipsoid representation of ligand **4** (thermal displacement ellipsoids are drawn at a 50% probability level; anions (left) and solvent molecules are omitted for clarity; all lengths are in Å).

Crystal data for **4** (obtained from MeCN): CCDC-2126435, $C_{36}H_{36}N_6 \cdot H_2O$, $M = 570.72 \text{ g mol}^{-1}$, colourless plate, $0.39 \times 0.12 \times 0.03 \text{ mm}^3$, monoclinic, space group $P2_1/c$, $a = 19.3863(2) \text{ \AA}$, $b = 11.2138(1) \text{ \AA}$, $c = 13.9566(1) \text{ \AA}$, $\beta = 103.799(1)^\circ$, $V = 2946.51(5) \text{ \AA}^3$, $Z = 4$, $D_{\text{calc}} = 1.287 \text{ g cm}^{-3}$, $F(000) = 1216$, $\mu = 0.63 \text{ mm}^{-1}$, $T = 120.00(10) \text{ K}$, $\theta_{\text{max}} = 76.5^\circ$, 6110 total reflections, 5245 with $I_o > 2\sigma(I_o)$, $R_{\text{int}} = 0.022$, 6110 data, 407 parameters, 60 restraints, $\text{Goof} = 1.03$, $R = 0.047$ and $wR = 0.126 [I_o > 2\sigma(I_o)]$, $0.55 < d\Delta\rho < -0.32 \text{ e \AA}^{-3}$.

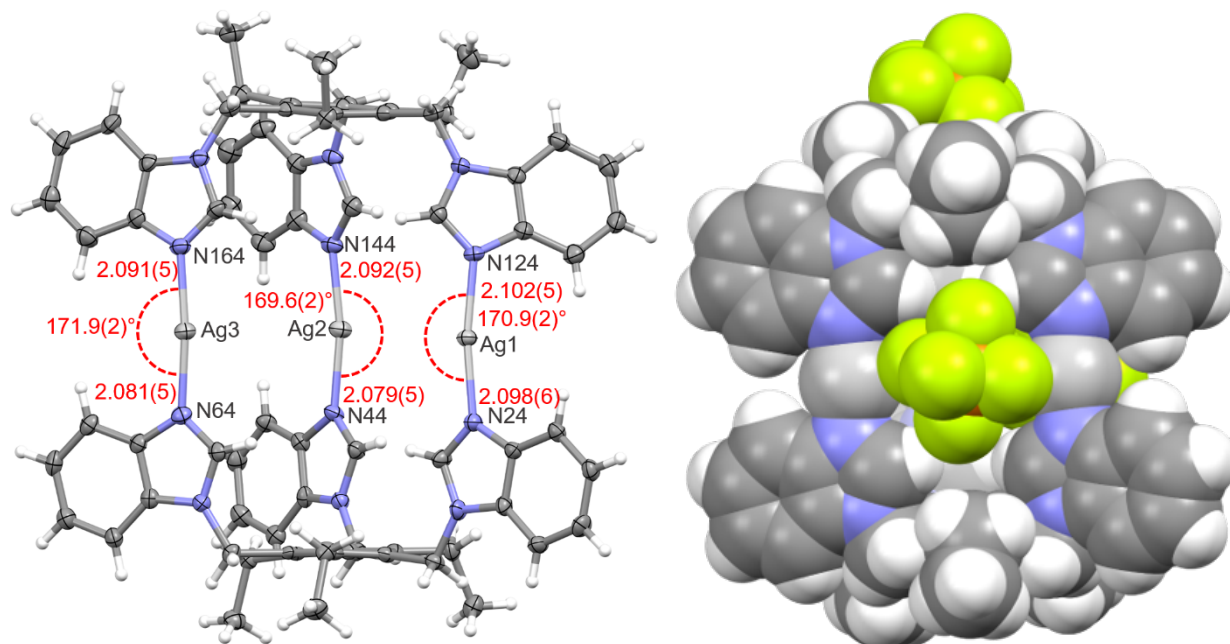


Figure S8. The ellipsoid (left) and spacefill (right) representations of the **[4-Ag-4][PF₆]₃** Ag-coordination cage (thermal displacement ellipsoids are drawn at a 50% probability level; anions (left) and solvent molecules are omitted for clarity; all lengths are in Å).

Crystal data for **[4-Ag-4][PF₆]₃** (obtained from MeCN): CCDC-2126436, [C₇₂H₇₂Ag₃N₁₂][PF₆]₃·(CH₃CN)₄, $M = 2028.15 \text{ g mol}^{-1}$, colourless block, $0.09 \times 0.05 \times 0.04 \text{ mm}^3$, orthorhombic, space group *Pbca*, $a = 24.2463(5) \text{ \AA}$, $b = 18.9896(4) \text{ \AA}$, $c = 36.0946(7) \text{ \AA}$, $V = 16619.9(6) \text{ \AA}^3$, $Z = 8$, $D_{\text{calc}} = 1.621 \text{ g cm}^{-3}$, $F(000) = 8192$, $\mu = 6.99 \text{ mm}^{-1}$, $T = 120.00(10) \text{ K}$, $\theta_{\text{max}} = 72.1^\circ$, 38547 total reflections, 11290 with $I_o > 2\sigma(I_o)$, $R_{\text{int}} = 0.050$, 11328 data, 1201 parameters, 213 restraints, GooF = 1.06, $R = 0.063$ and $wR = 0.212 [I_o > 2\sigma(I_o)]$, $1.92 < d\Delta\rho < -0.98 \text{ e \AA}^{-3}$.

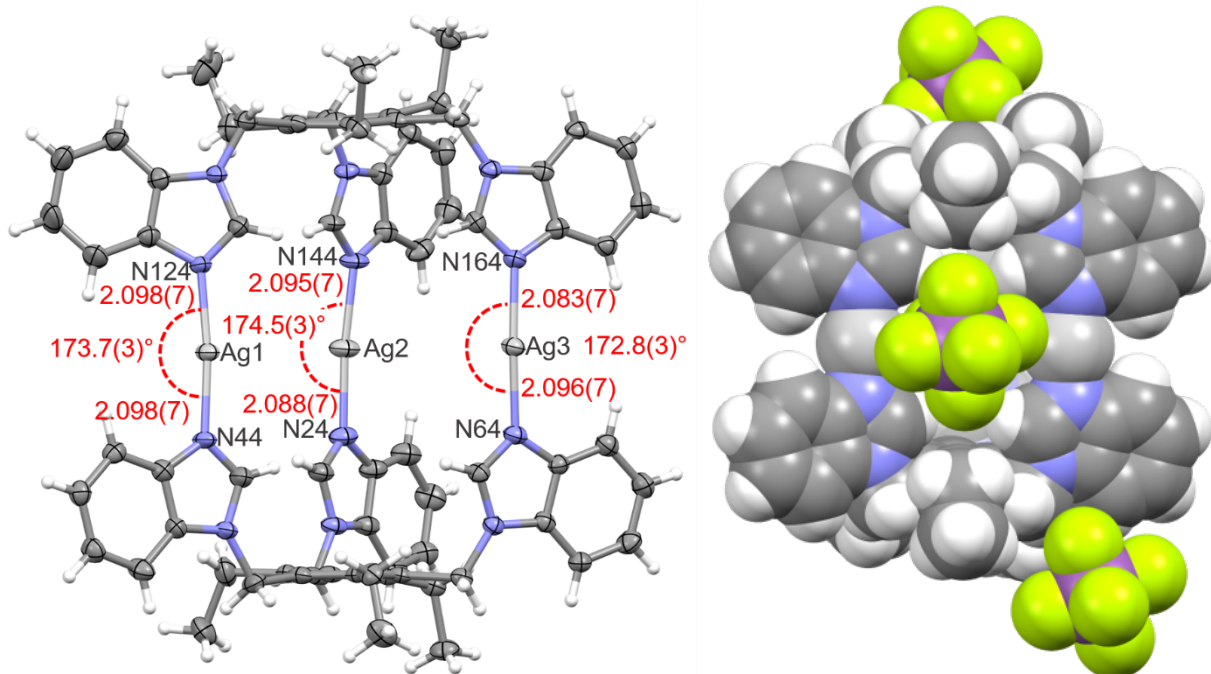


Figure S9. The ellipsoid (left) and spacefill (right) representations of the **[4-Ag-4][SbF₆]₃** Ag-coordination cage (thermal displacement ellipsoids are drawn at a 50% probability level; anions (left) and solvent molecules are omitted for clarity; all lengths are in Å).

Crystal data for **[4-Ag-4][SbF₆]₃** (obtained from MeCN): CCDC-2126437, **[C₇₂H₇₂Ag₃N₁₂][SbF₆]₃·4(CH₃CN)**, $M = 2300.49 \text{ g mol}^{-1}$, colourless block, $0.11 \times 0.07 \times 0.04 \text{ mm}^3$, triclinic, space group $P-1$ (No. 2), $a = 13.8575(3) \text{ \AA}$, $b = 18.1569(4) \text{ \AA}$, $c = 19.1122(3) \text{ \AA}$, $\alpha = 88.904(2)^\circ$, $\beta = 86.763(2)^\circ$, $\gamma = 68.015(2)^\circ$, $V = 4452.00(17) \text{ \AA}^3$, $Z = 2$, $D_{\text{calc}} = 1.716 \text{ g cm}^{-3}$, $F(000) = 2264$, $\mu = 13.08 \text{ mm}^{-1}$, $T = 120.00(10) \text{ K}$, $\theta_{\text{max}} = 72.1^\circ$, 81954 total reflections, 15020 with $I_o > 2\sigma(I_o)$, $R_{\text{int}} = 0.059$, 17476 data, 1149 parameters, 198 restraints, $\text{Goof} = 1.09$, $R = 0.080$ and $wR = 0.226 [I_o > 2\sigma(I_o)]$, $4.68 < d\Delta\rho < -1.32 \text{ e \AA}^{-3}$.

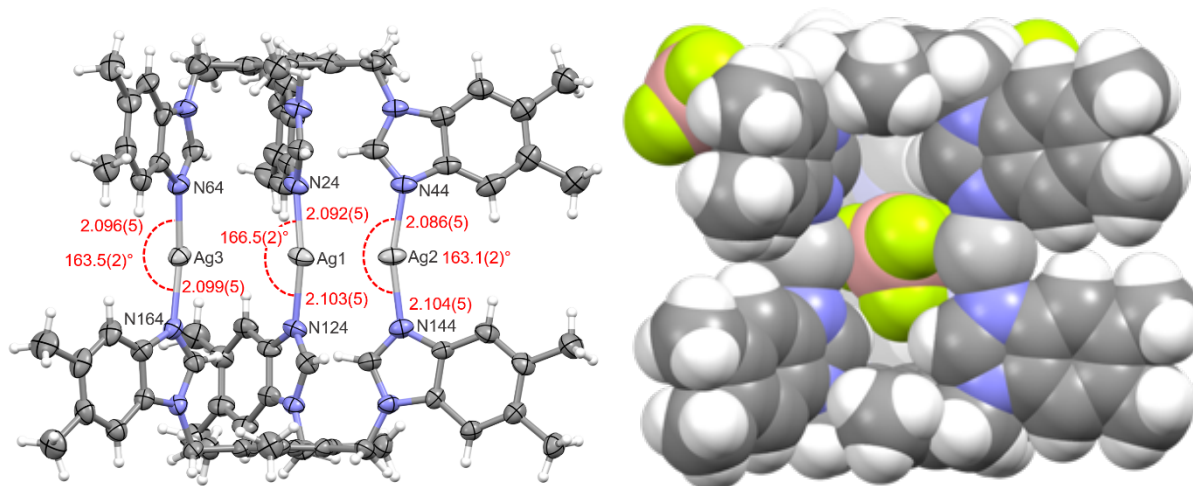


Figure S10. The ellipsoid (left) and spacefill (right) representations of the **[BF₄-c5-Ag-5][BF₄]₂** Ag-coordination cage (thermal displacement ellipsoids are drawn at a 50% probability level; anions (left) and solvent molecules are omitted for clarity; all lengths are in Å).

Crystal data for **[BF₄-c5-Ag-5][BF₄]₂** (obtained from DMSO/CHCl₃): CCDC-2126438, ([C₇₈H₈₄Ag₃N₁₂]₂[BF₄]₅)⁺, $M = 3460.40 \text{ g mol}^{-1}$, colourless needle, $0.09 \times 0.04 \times 0.03 \text{ mm}^3$, triclinic, space group $P-1$, $a = 17.8788(12) \text{ \AA}$, $b = 17.8878(13) \text{ \AA}$, $c = 19.5219(12) \text{ \AA}$, $\alpha = 65.003(7)^\circ$, $\beta = 76.579(5)^\circ$, $\gamma = 68.523(7)^\circ$, $V = 5243.4(7) \text{ \AA}^3$, $Z = 1$, $D_{\text{calc}} = 1.096 \text{ g cm}^{-3}$, $F(000) = 1759$, $\mu = 4.91 \text{ mm}^{-1}$, $T = 120.00(10) \text{ K}$, $\theta_{\text{max}} = 72.1^\circ$, 33231 total reflections, 12333 with $I_o > 2\sigma(I_o)$, $R_{\text{int}} = 0.060$, 20213 data, 1019 parameters, 124 restraints, GooF = 0.95, $R = 0.062$ and $wR = 0.179 [I_o > 2\sigma(I_o)]$, $1.43 < d\Delta\rho < -1.13 \text{ e\AA}^{-3}$.

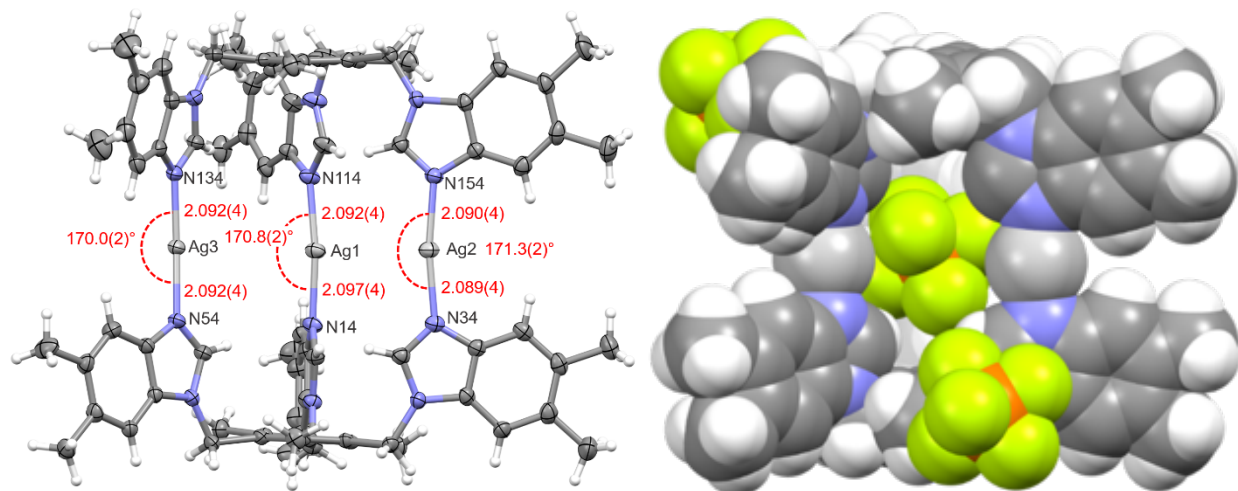


Figure S11. The ellipsoid (left) and spacefill (right) representations of the $[\text{PF}_6\text{-c5-Ag-5}][\text{PF}_6]_2$ Ag-coordination cage (thermal displacement ellipsoids are drawn at a 50% probability level, anions (left) and solvent molecules are omitted for clarity; all lengths are in Å).

Crystal data for $[\text{PF}_6\text{-c5-Ag-5}][\text{PF}_6]_2$ (obtained from DMSO/ CHCl_3): CCDC-2126439, $[\text{C}_{78}\text{H}_{84}\text{Ag}_3\text{N}_{12}][\text{PF}_6]_3 \cdot 6((\text{CH}_3)_2\text{SO}) \cdot 2(\text{H}_2\text{O})$, $M = 2470.90 \text{ gmol}^{-1}$, colourless block, $0.13 \times 0.09 \times 0.08 \text{ mm}^3$, triclinic, space group $P-1$, $a = 18.0250(4) \text{ \AA}$, $b = 18.7080(4) \text{ \AA}$, $c = 19.9407(4) \text{ \AA}$, $\alpha = 62.663(2)^\circ$, $\beta = 79.563(2)^\circ$, $\gamma = 69.602(2)^\circ$, $V = 5596.9(2) \text{ \AA}^3$, $Z = 2$, $D_{\text{calc}} = 1.466 \text{ gcm}^{-3}$, $F(000) = 2532$, $\mu = 6.36 \text{ mm}^{-1}$, $T = 120.00(10) \text{ K}$, $\theta_{\text{max}} = 76.7^\circ$, 44929 total reflections, 20051 with $I_o > 2\sigma(I_o)$, $R_{\text{int}} = 0.030$, 22995 data, 1505 parameters, 348 restraints, $\text{Goof} = 1.04$, $R = 0.063$ and $wR = 0.188 [I_o > 2\sigma(I_o)]$, $1.92 < d\Delta\rho < -1.94 \text{ e\AA}^{-3}$.

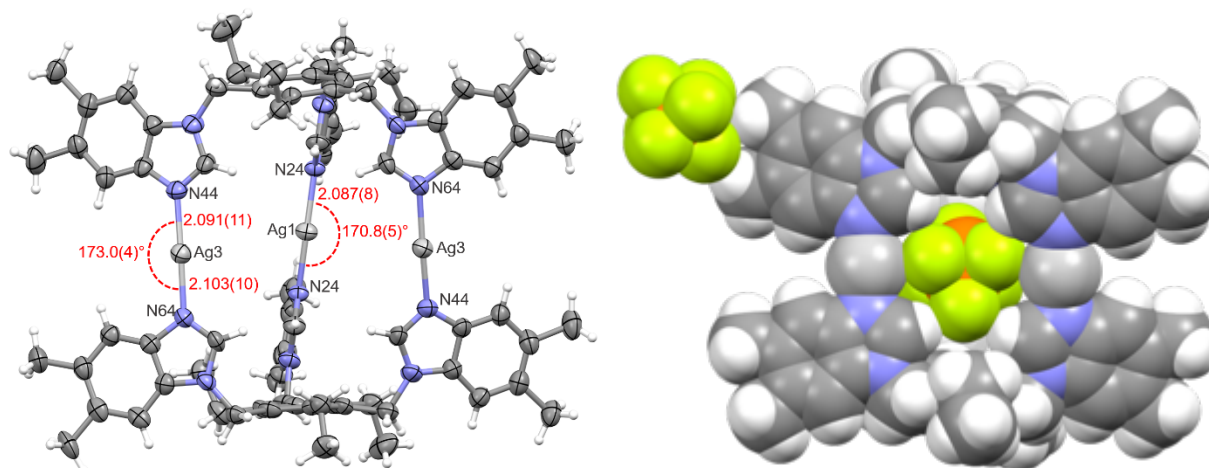


Figure S12. The ellipsoid (left) and spacefill (right) representations of the $[\text{PF}_6\text{-c6-Ag-6}][\text{PF}_6]_2$ Ag-coordination cage (thermal displacement ellipsoids are drawn at a 50% probability level; anions (left) and solvent molecules are omitted for clarity; all lengths are in Å).

Crystal data for $[\text{PF}_6\text{-c6-Ag-6}][\text{PF}_6]_2$ (obtained from DMSO/ CHCl_3): CCDC-2126440, $[\text{C}_{84}\text{H}_{96}\text{Ag}_3\text{N}_{12}][\text{PF}_6]_3$, $M = 2032.24 \text{ g mol}^{-1}$, yellow block, $0.12 \times 0.07 \times 0.04 \text{ mm}^3$, tetragonal, space group $I-42d$, $a = 31.1905(4) \text{ \AA}$, $c = 18.7751(4) \text{ \AA}$, $V = 18265.3(6) \text{ \AA}^3$, $Z = 8$, $D_{\text{calc}} = 1.478 \text{ g cm}^{-3}$, $F(000) = 8256$, $\mu = 6.35 \text{ mm}^{-1}$, $T = 120.00(10) \text{ K}$, $\theta_{\text{max}} = 76.9^\circ$, 19296 total reflections, 6509 with $I_o > 2\sigma(I_o)$, $R_{\text{int}} = 0.061$, 8786 data, 567 parameters, 63 restraints, $\text{Goof} = 1.00$, $R = 0.062$ and $wR = 0.186 [I_o > 2\sigma(I_o)]$, $1.80 < d\rho < -0.90 \text{ e\AA}^{-3}$.

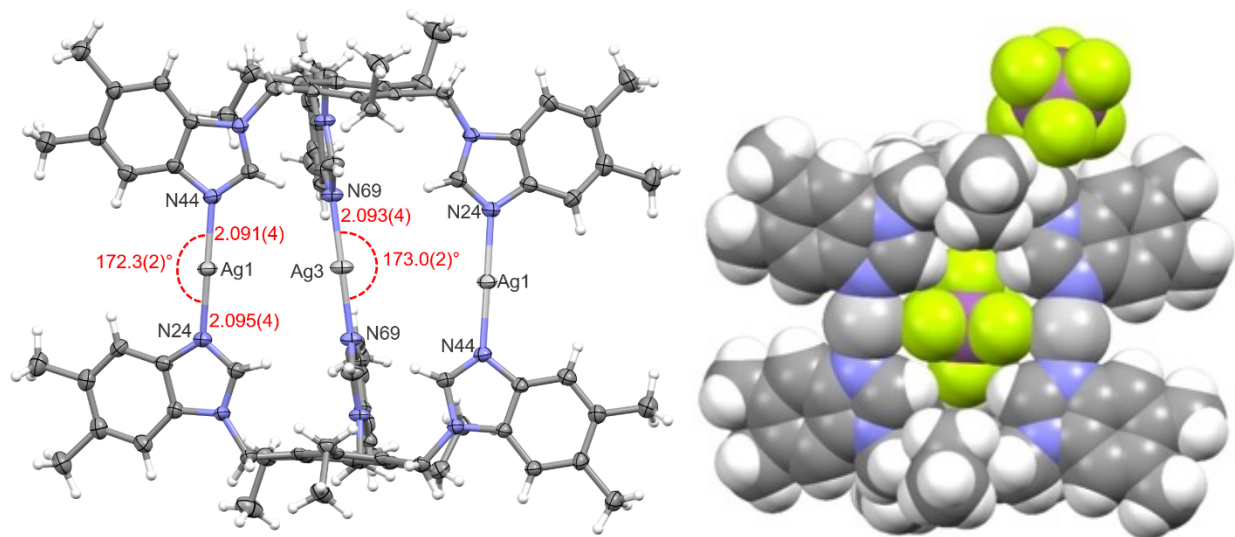


Figure S13. The ellipsoid (left) and spacefill (right) representations of the **[SbF₆-c6-Ag-6][SbF₆]₂** Ag-coordination cage (thermal displacement ellipsoids are drawn at a 50% probability level; anions (left) and solvent molecules are omitted for clarity; all lengths are in Å).

Crystal data for **[SbF₆-c6-Ag-6][SbF₆]₂** (obtained from MeCN): CCDC-2126441, [C₈₄H₉₆Ag₃N₁₂][SbF₆]₃, $M = 2304.58 \text{ gmol}^{-1}$, colourless block, $0.15 \times 0.09 \times 0.08 \text{ mm}^3$, tetragonal, space group $I-42d$, $a = 31.6145(1) \text{ \AA}$, $c = 19.0400(1) \text{ \AA}$, $V = 19030.04(16) \text{ \AA}^3$, $Z = 8$, $D_{\text{calc}} = 1.609 \text{ gcm}^{-3}$, $F(000) = 9120$, $\mu = 12.22 \text{ mm}^{-1}$, $T = 120.00(10) \text{ K}$, $\theta_{\text{max}} = 76.9^\circ$, 64325 total reflections, 9900 with $I_o > 2\sigma(I_o)$, $R_{\text{int}} = 0.028$, 9982 data, 551 parameters, 6 restraints, $\text{Goof} = 1.03$, $R = 0.028$ and $wR = 0.073 [I_o > 2\sigma(I_o)]$, $1.02 < d\Delta\rho < -1.11 \text{ e\AA}^{-3}$.

Hirshfeld Surface Analysis

Hirshfeld surface⁸ plots and 2-D fingerprint calculations were made using *CrystalExplorer*⁹ package version 21.5. X-ray crystal structure files (“cifs”) were imported, and Hirshfeld surfaces were generated for all host-guest complexes using very high resolution available in Crystal Explorer package version 21.5 and mapped with the d_{norm} . The corresponding contact distances to the Hirshfeld surfaces and fingerprint plots can be found in the following figures.

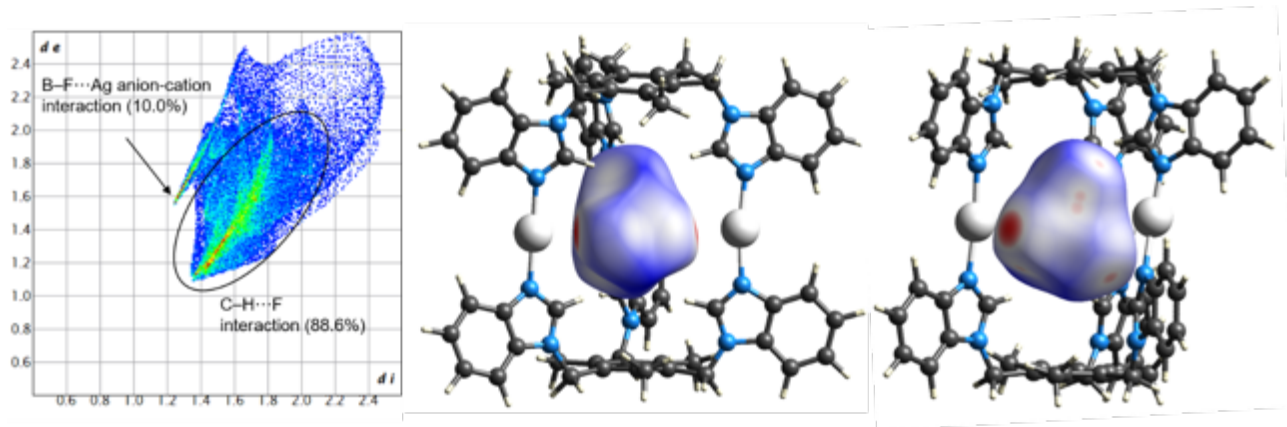


Figure S14. Full fingerprint regions of the tetrafluoroborate anion in the complex $[\text{BF}_4-\text{c}3-\text{Ag}-3][\text{BF}_4]_2$ and two views of the intermolecular contacts to the Hirshfeld surface of the anion. Other interactions contributing to the anion binding: $\text{B-F}\cdots\text{N}$ (0.5%) and $\text{B-F}\cdots\text{C}$ (0.9%). In the fingerprint plot, d_i represents the closest internal distance from a given point on the Hirshfeld surface, and d_e is the closest external contact (in Å).

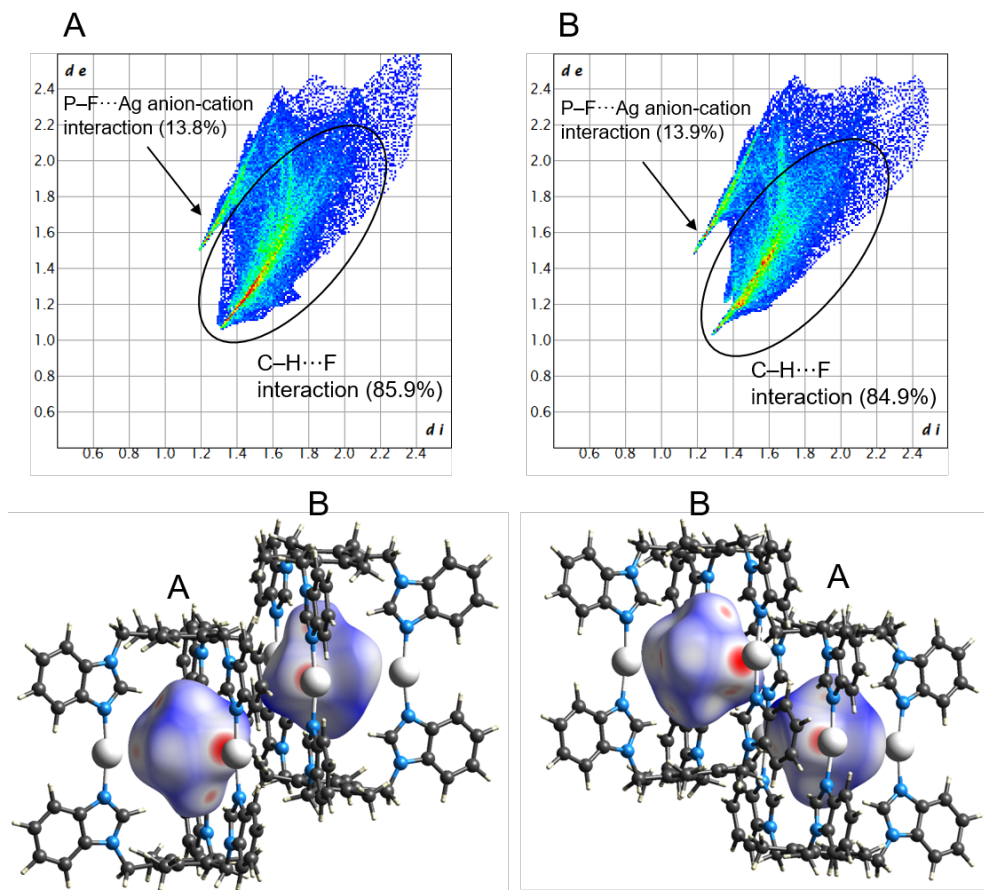


Figure S15. Full fingerprint regions of the hexafluorophosphate anion in the complex $[\text{PF}_6\text{-c3-Ag-3}][\text{PF}_6]_2$ and two views of the intermolecular contacts to the Hirshfeld surface of the anion. Other interactions contributing to the anion binding: P-F...N (A: 0.1%, B: 0.9%) and P-F...C (A: 0.2%, B: 0.3%). In the fingerprint plot, d_i represents the closest internal distance from a given point on the Hirshfeld surface, and d_e is the closest external contact (in Å).

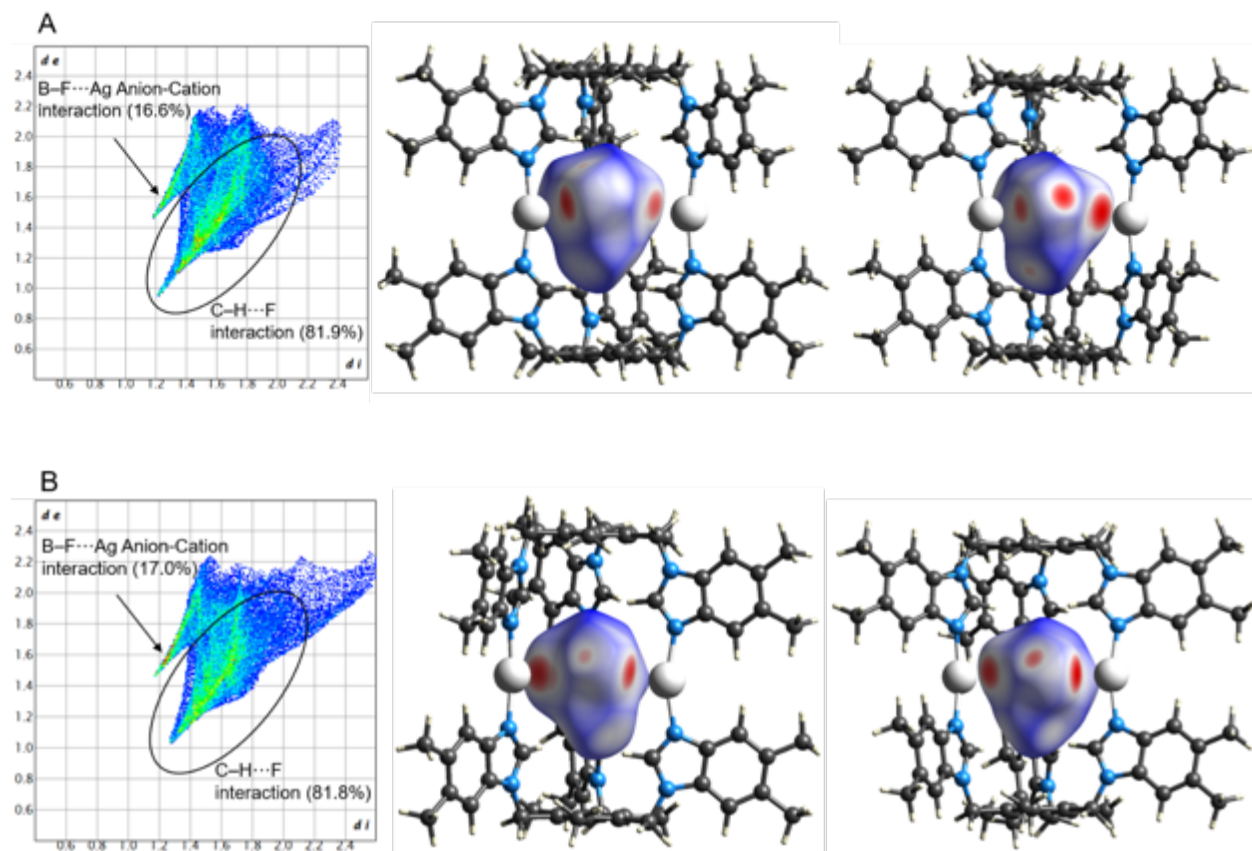


Figure S16. Full fingerprint regions of the tetrafluoroborate anion in the complex $[\text{BF}_4\text{-c5-Ag-5}][\text{BF}_4]_2$ and two views of the intermolecular contacts to the Hirshfeld surface of the anion (disordered over two positions with occupancies A: 35% B: 65%). Other interactions contributing to the anion binding: B-F \cdots C (A: 1.5%, B: 1.2%). In the fingerprint plot, d_i represents the closest internal distance from a given point on the Hirshfeld surface, and d_e is the closest external contact (in Å).

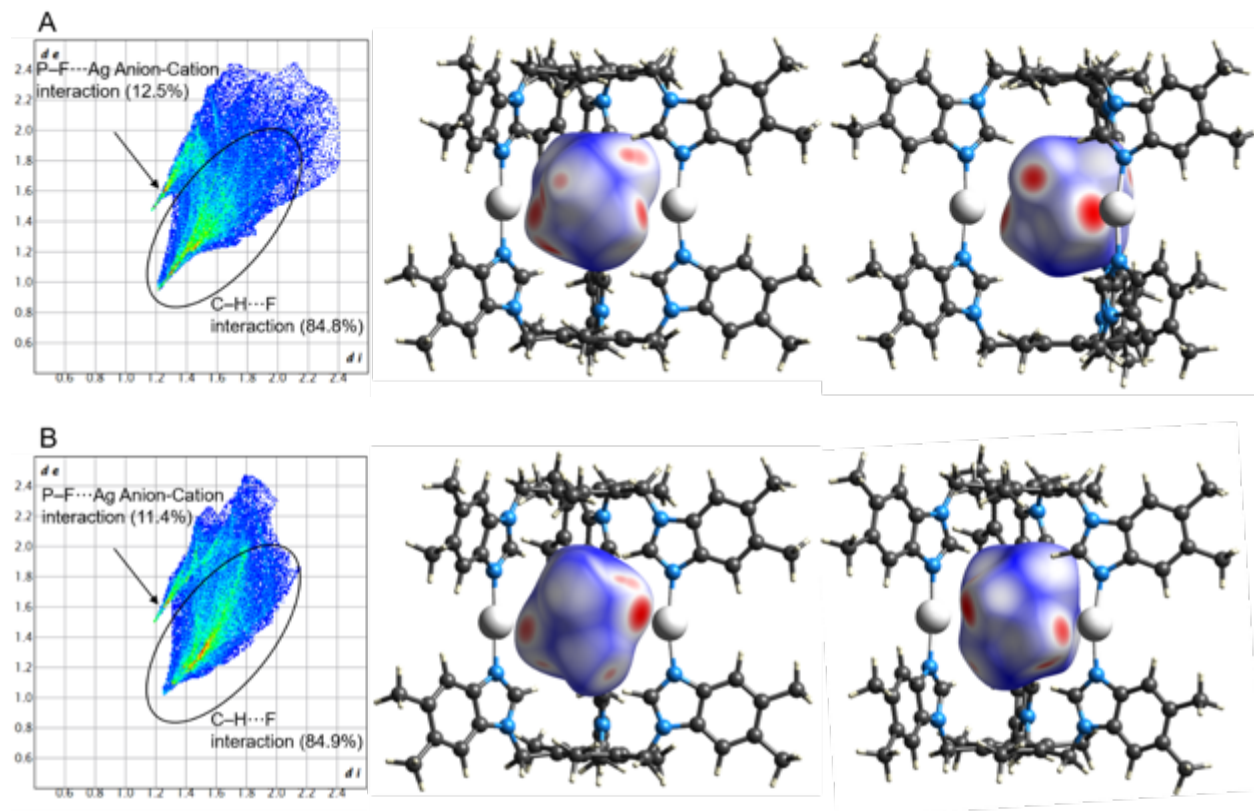


Figure S17. Full fingerprint regions of the hexafluorophosphate anion in the complex $[\text{PF}_6\text{-c5-Ag-5}][\text{PF}_6]_2$ and two views of the intermolecular contacts to the Hirshfeld surface of the anion (disordered over two positions with occupancies A: 48% B: 52%). Other interactions contributing to the anion binding: B-F...N (A: 0.3%, B: 0.2%) and B-F...C (A: 2.4%, B: 3.5%). In the fingerprint plot, d_i represents the closest internal distance from a given point on the Hirshfeld surface, and d_e is the closest external contact (in Å).

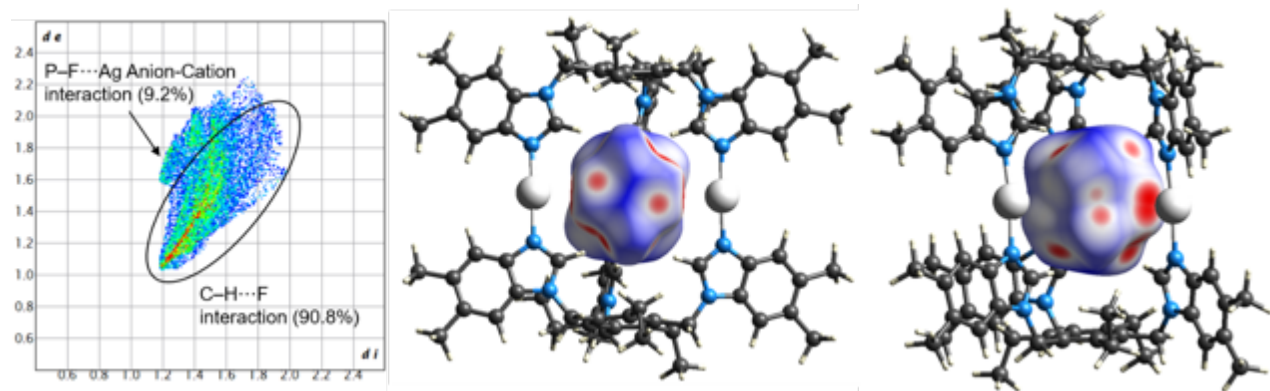


Figure S18. Full fingerprint regions of the hexafluorophosphate anion in the complex $[\text{PF}_6\text{-c6-Ag-6}][\text{PF}_6]_2$ and two views of the intermolecular contacts to the Hirshfeld surface of the anion. In the fingerprint plot d_i represents closest internal distance from a given point on the Hirshfeld surface, and d_e is the closest external contact (in Å). The anion was found in a special position inside the cage due to high symmetry and the two different disordered positions (50:50) could not be modelled separately in the Hirshfeld analysis, and thus, are displayed here together.

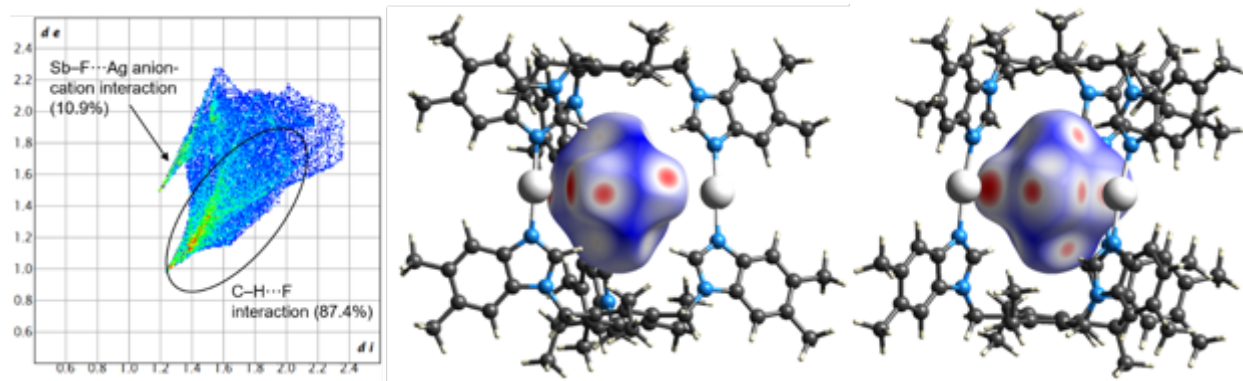


Figure S19. Full fingerprint regions of the hexafluoroantimonate anion in the complex $[\text{SbF}_6\text{-c6-Ag-6}][\text{SbF}_6]_2$ and two views of the intermolecular contacts to the Hirshfeld surface of the anion. Other interactions contributing to the anion binding: $\text{Sb-F}\cdots\text{C}$ (1.7%). In the fingerprint plot, d_i represents the closest internal distance from a given point on the Hirshfeld surface, and d_e is the closest external contact (in Å).

Computational Methods

General

The cage geometries were modelled at MM-level (MMFF) so that only the N-I distances were fixed to the previously observed bond distances value of 2.25 Å (from single crystal X-ray crystallographic studies of several [N-I-N]⁺ complexes), all other bond distances and angles were free, using SPARTAN18 software.¹⁰

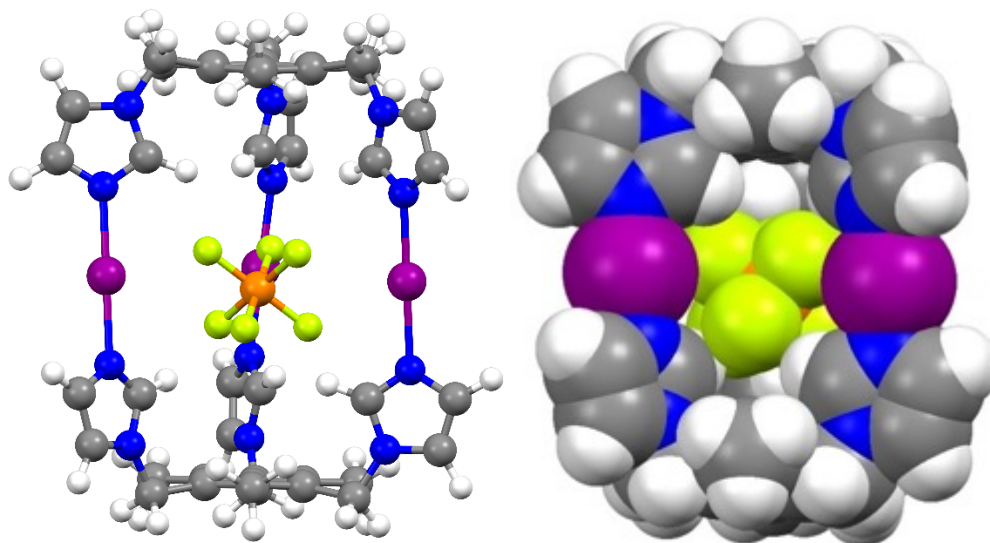


Figure S20. The ball-and-stick (left) and spacefill (right) representations of the modeled structure of $[\text{PF}_6\text{-c1-I-1}][\text{PF}_6]_2$ iodine(I) cage.

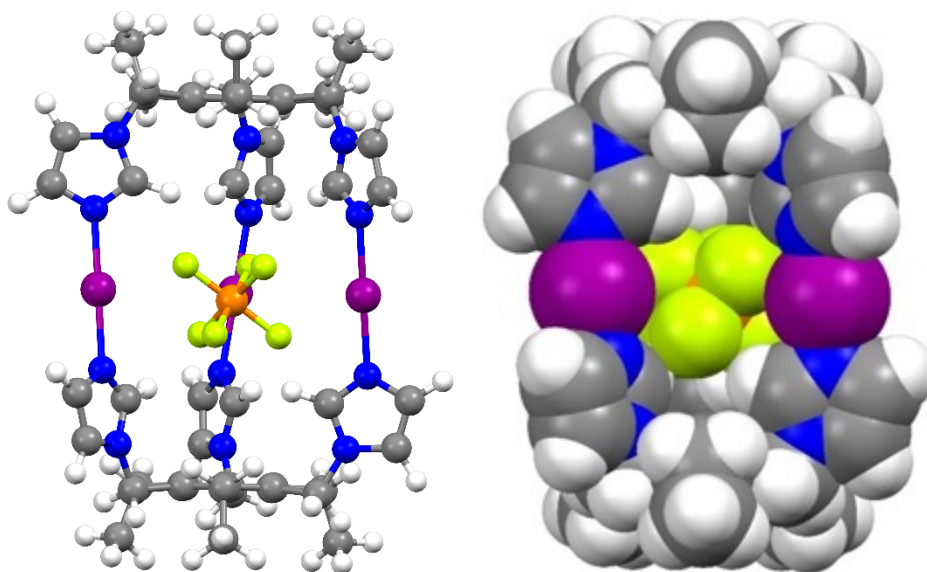


Figure S21. The ball-and-stick (left) and spacefill (right) representations of the modeled structure of $[\text{PF}_6\text{-c2-I-2}][\text{PF}_6]_2$ iodine(I) cage.

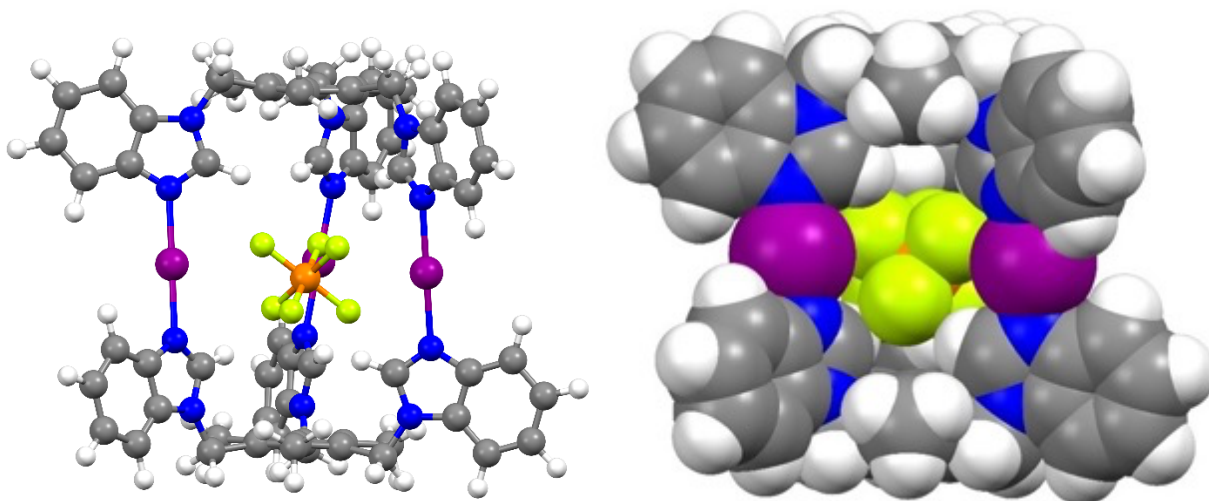


Figure S22. The ball-and-stick (left) and spacefill (right) representations of the modeled structure of $[\text{PF}_6\text{-c3-I-3}][\text{PF}_6]_2$ iodine(I) cage.

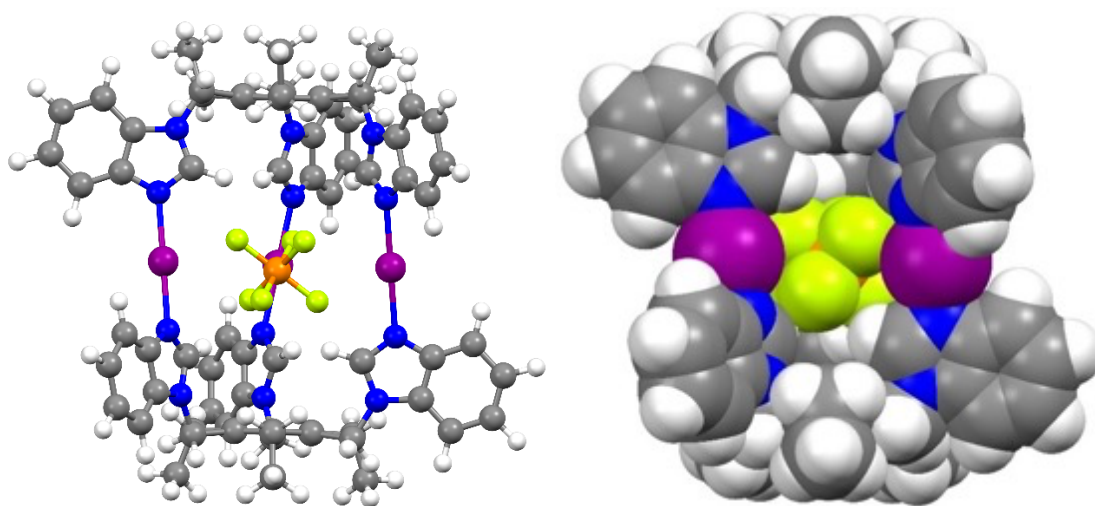


Figure S23.. The ball-and-stick (left) and spacefill (right) representations of the modeled structure of $[\text{PF}_6\text{-c4-I-4}][\text{PF}_6]_2$ iodine(I) cage.

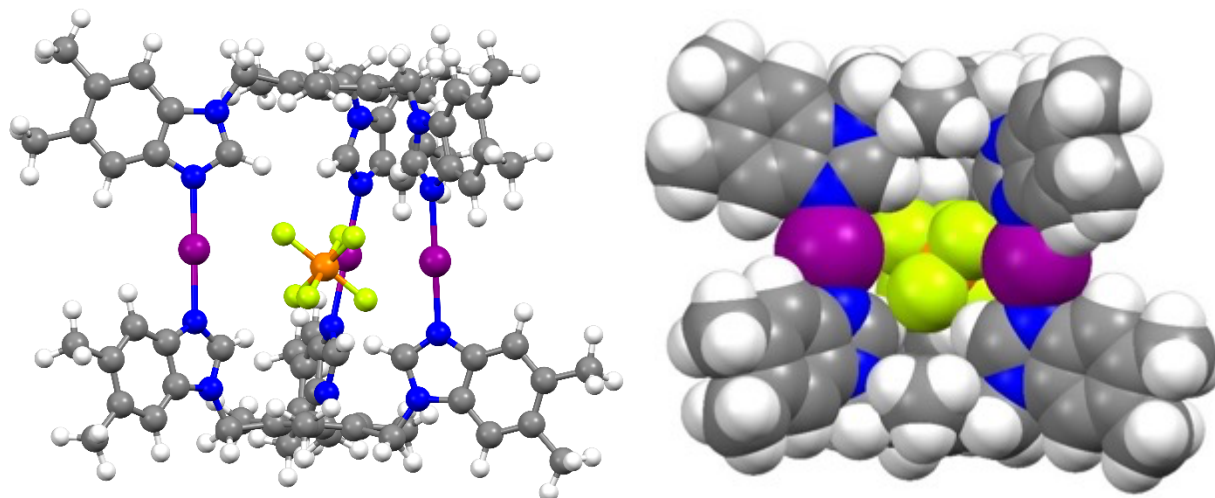


Figure S24. The ball-and-stick (left) and spacefill (right) representations of the modeled structure of $[\text{PF}_6\text{-c5-I-5}][\text{PF}_6]_2$ iodine(I) cage.

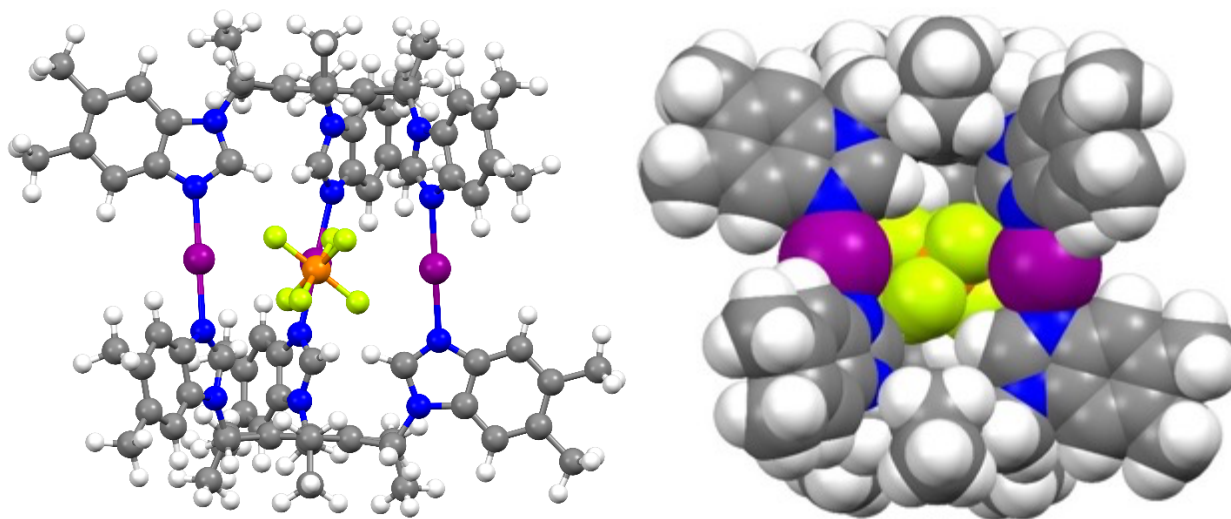


Figure S25. The ball-and-stick (left) and spacefill (right) representations of the modeled structure of $[\text{PF}_6\text{-c6-I-6}][\text{PF}_6]_2$ iodine(I) cage.

The Cartesian Coordinates

[PF₆-C₁-I-1][PF₆]₂

C	0.827000	1.155000	5.236000
C	-0.830000	-1.164000	5.278000
C	-0.591000	1.295000	5.280000
C	1.419000	-0.142000	5.279000
C	0.589000	-1.300000	5.235000
C	-1.417000	0.134000	5.235000
C	1.712000	2.388000	5.271000
H	1.234000	3.250000	4.800000
H	2.631000	2.232000	4.699000
C	-2.928000	0.283000	5.270000
H	-3.435000	-0.561000	4.797000
C	1.215000	-2.682000	5.268000
H	0.620000	-3.400000	4.695000
H	2.200000	-2.699000	4.796000
C	-1.214000	2.674000	5.521000
H	-0.605000	3.234000	6.240000
H	-2.205000	2.607000	5.981000
C	2.925000	-0.291000	5.519000
H	3.106000	-1.100000	6.237000
H	3.363000	0.600000	5.980000
C	-1.712000	-2.394000	5.517000
H	-1.159000	-3.219000	5.977000
H	-2.503000	-2.147000	6.236000
N	-1.340000	3.461000	4.289000
N	3.669000	-0.575000	4.286000
N	-2.330000	-2.895000	4.284000
C	-1.435000	3.003000	3.022000
H	-1.406000	1.978000	2.679000
C	3.320000	-0.262000	3.021000
H	2.417000	0.225000	2.678000
C	-1.885000	-2.747000	3.018000
H	-1.012000	-2.209000	2.676000
N	-2.748000	-3.411000	2.255000
N	-1.579000	4.083000	2.260000
N	4.327000	-0.677000	2.257000
C	5.357000	-1.224000	2.953000
C	4.952000	-1.163000	4.259000
C	-1.621000	5.249000	2.957000
C	-1.472000	4.866000	4.262000
C	-3.737000	-4.031000	2.950000
C	-3.481000	-3.712000	4.256000
H	-3.252000	1.158000	4.698000
C	0.831000	1.159000	-5.200000
C	-0.832000	-1.154000	-5.246000

C	1.419000	-0.138000	-5.245000
C	-0.586000	1.303000	-5.244000
C	-1.415000	0.145000	-5.201000
C	0.586000	-1.294000	-5.202000
C	1.715000	2.392000	-5.226000
H	2.684000	2.214000	-4.752000
H	1.270000	3.210000	-4.650000
C	1.212000	-2.676000	-5.229000
H	0.574000	-3.426000	-4.756000
C	-2.926000	0.294000	-5.227000
H	-3.256000	1.222000	-4.753000
H	-3.412000	-0.501000	-4.653000
C	2.923000	-0.286000	-5.480000
H	3.263000	0.473000	-6.195000
H	3.179000	-1.244000	-5.944000
C	-1.210000	2.680000	-5.478000
H	-2.037000	2.595000	-6.194000
H	-0.507000	3.380000	-5.941000
C	-1.712000	-2.382000	-5.482000
H	-2.670000	-2.124000	-5.945000
H	-1.224000	-3.055000	-6.197000
N	3.705000	-0.159000	-4.245000
N	-1.712000	3.292000	-4.243000
N	-1.992000	-3.124000	-4.248000
C	3.290000	-0.373000	-2.978000
H	2.302000	-0.650000	-2.636000
C	-1.320000	3.038000	-2.976000
H	-0.586000	2.321000	-2.634000
C	-1.969000	-2.659000	-2.980000
H	-1.715000	-1.665000	-2.637000
N	-2.339000	-3.685000	-2.218000
N	4.363000	-0.181000	-2.215000
N	-2.023000	3.871000	-2.213000
C	-2.850000	4.693000	-2.909000
C	-2.661000	4.335000	-4.215000
C	5.488000	0.125000	-2.912000
C	5.083000	0.142000	-4.218000
C	-2.637000	-4.812000	-2.916000
C	-2.421000	-4.468000	-4.222000
H	2.143000	-2.700000	-4.654000
I	-2.544000	-3.549000	0.018000
I	-1.801000	3.977000	0.024000
I	4.345000	-0.429000	0.021000
H	-3.448000	5.416000	-2.386000
H	-3.074000	4.691000	-5.147000
H	-1.448000	5.411000	5.194000
H	-1.755000	6.177000	2.436000
H	6.413000	0.280000	-2.389000
H	5.597000	0.322000	-5.149000

H	5.412000	-1.457000	5.190000
H	6.228000	-1.572000	2.431000
H	-2.965000	-5.691000	-2.394000
H	-2.522000	-5.002000	-5.154000
H	-3.966000	-3.964000	5.187000
H	-4.474000	-4.611000	2.428000
H	-3.273000	0.373000	6.304000
H	1.963000	2.641000	6.306000
H	1.309000	-3.027000	6.302000
H	1.411000	-2.978000	-6.262000
H	1.878000	2.717000	-6.258000
H	-3.287000	0.274000	-6.260000
P	0.000000	0.000000	-0.328000
F	0.993000	0.891000	-1.279000
F	0.275000	-1.304000	-1.280000
F	-1.267000	0.415000	-1.279000
F	-0.994000	-0.889000	0.622000
F	-0.273000	1.304000	0.624000
F	1.266000	-0.417000	0.623000

[PF₆-C₂-I-2][PF₆]₂

C	0.808000	1.175000	5.383000
C	-0.812000	-1.187000	5.397000
C	-0.619000	1.291000	5.399000
C	1.430000	-0.115000	5.398000
C	0.616000	-1.293000	5.381000
C	-1.425000	0.107000	5.382000
C	1.671000	2.437000	5.439000
H	1.176000	3.268000	4.931000
H	2.582000	2.293000	4.846000
C	-2.950000	0.224000	5.437000
H	-3.422000	-0.621000	4.927000
C	1.277000	-2.672000	5.435000
H	0.697000	-3.388000	4.842000
H	2.245000	-2.658000	4.927000
C	-1.274000	2.671000	5.547000
H	-0.751000	3.254000	6.310000
H	-2.307000	2.627000	5.896000
C	2.953000	-0.238000	5.545000
H	3.196000	-0.984000	6.308000
H	3.432000	0.678000	5.895000
C	-1.680000	-2.444000	5.543000
H	-1.126000	-3.317000	5.892000
H	-2.447000	-2.283000	6.306000
N	-1.286000	3.428000	4.289000
N	3.614000	-0.606000	4.287000
N	-2.329000	-2.832000	4.285000

C	-1.427000	2.939000	3.039000
H	-1.505000	1.905000	2.732000
C	3.261000	-0.237000	3.037000
H	2.403000	0.348000	2.732000
C	-1.834000	-2.709000	3.035000
H	-0.899000	-2.258000	2.730000
N	-2.737000	-3.272000	2.237000
N	-1.464000	4.004000	2.242000
N	4.200000	-0.737000	2.240000
C	5.194000	-1.389000	2.897000
C	4.834000	-1.311000	4.215000
C	-1.397000	5.190000	2.901000
C	-1.284000	4.838000	4.218000
C	-3.798000	-3.807000	2.895000
C	-3.551000	-3.535000	4.212000
H	-3.281000	1.085000	4.845000
C	0.858000	1.147000	-5.359000
C	-0.860000	-1.143000	-5.377000
C	1.424000	-0.168000	-5.377000
C	-0.562000	1.322000	-5.376000
C	-1.418000	0.175000	-5.360000
C	0.562000	-1.310000	-5.361000
C	1.777000	2.369000	-5.409000
H	2.722000	2.164000	-4.899000
H	1.348000	3.184000	-4.815000
C	1.160000	-2.717000	-5.412000
H	0.511000	-3.434000	-4.903000
C	-2.936000	0.360000	-5.411000
H	-3.232000	1.280000	-4.900000
H	-3.428000	-0.420000	-4.817000
C	2.940000	-0.346000	-5.520000
H	3.326000	0.336000	-6.282000
H	3.231000	-1.338000	-5.868000
C	-1.166000	2.725000	-5.518000
H	-1.950000	2.719000	-6.281000
H	-0.452000	3.473000	-5.865000
C	-1.772000	-2.367000	-5.522000
H	-2.777000	-2.122000	-5.869000
H	-1.375000	-3.042000	-6.285000
N	3.658000	-0.114000	-4.261000
N	-1.727000	3.229000	-4.259000
N	-1.930000	-3.106000	-4.264000
C	3.230000	-0.386000	-3.010000
H	2.268000	-0.775000	-2.703000
C	-1.279000	2.993000	-3.008000
H	-0.461000	2.354000	-2.701000
C	-1.950000	-2.601000	-3.012000
H	-1.806000	-1.574000	-2.703000
N	-2.204000	-3.637000	-2.216000

N	4.253000	-0.088000	-2.213000
N	-2.049000	3.730000	-2.211000
C	-2.971000	4.479000	-2.870000
C	-2.777000	4.169000	-4.188000
C	5.363000	0.336000	-2.873000
C	4.997000	0.325000	-4.190000
C	-2.391000	-4.809000	-2.877000
C	-2.219000	-4.485000	-4.194000
H	2.081000	-2.754000	-4.819000
I	-2.468000	-3.451000	0.011000
I	-1.755000	3.863000	0.016000
I	4.223000	-0.411000	0.013000
C	1.428000	-3.201000	-6.834000
H	2.118000	-2.542000	-7.369000
H	0.510000	-3.254000	-7.425000
H	1.870000	-4.202000	-6.810000
C	2.063000	2.844000	-6.829000
H	2.568000	2.076000	-7.421000
H	2.709000	3.727000	-6.805000
H	1.148000	3.112000	-7.366000
C	-3.490000	0.371000	-6.832000
H	-3.076000	1.193000	-7.423000
H	-4.578000	0.489000	-6.808000
H	-3.264000	-0.555000	-7.369000
C	-3.491000	0.321000	6.859000
H	-3.087000	1.185000	7.395000
H	-3.246000	-0.567000	7.450000
H	-4.582000	0.418000	6.838000
C	1.463000	-3.191000	6.857000
H	2.108000	-2.535000	7.449000
H	1.924000	-4.183000	6.836000
H	0.512000	-3.273000	7.393000
C	2.027000	2.856000	6.862000
H	2.656000	3.751000	6.841000
H	2.573000	2.073000	7.396000
H	1.135000	3.086000	7.453000
H	-3.622000	5.129000	-2.319000
H	-3.242000	4.504000	-5.103000
H	-1.213000	5.408000	5.132000
H	-1.448000	6.110000	2.350000
H	6.252000	0.575000	-2.321000
H	5.519000	0.561000	-5.105000
H	5.292000	-1.659000	5.128000
H	6.016000	-1.803000	2.345000
H	-2.630000	-5.699000	-2.326000
H	-2.276000	-5.055000	-5.109000
H	-4.080000	-3.760000	5.126000
H	-4.569000	-4.311000	2.343000
P	0.000000	0.000000	-0.215000

F	1.086000	0.773000	-1.167000
F	0.126000	-1.326000	-1.169000
F	-1.212000	0.555000	-1.167000
F	-1.087000	-0.769000	0.738000
F	-0.122000	1.325000	0.740000
F	1.209000	-0.557000	0.738000

[PF₆]⁻3-I-3][PF₆]₂

C	0.854000	1.139000	5.220000
C	-0.855000	-1.142000	5.264000
C	-0.561000	1.311000	5.264000
C	1.416000	-0.170000	5.264000
C	0.560000	-1.309000	5.220000
C	-1.413000	0.169000	5.220000
C	1.765000	2.353000	5.256000
H	1.308000	3.224000	4.780000
H	2.683000	2.175000	4.687000
C	-2.921000	0.351000	5.256000
H	-3.446000	-0.480000	4.780000
C	1.156000	-2.706000	5.255000
H	0.543000	-3.412000	4.686000
H	2.139000	-2.745000	4.780000
C	-1.152000	2.703000	5.511000
H	-0.528000	3.233000	6.239000
H	-2.146000	2.658000	5.967000
C	2.917000	-0.354000	5.510000
H	3.064000	-1.160000	6.239000
H	3.375000	0.529000	5.967000
C	-1.765000	-2.350000	5.510000
H	-1.229000	-3.188000	5.966000
H	-2.536000	-2.075000	6.239000
N	-1.253000	3.499000	4.285000
N	3.657000	-0.665000	4.285000
N	-2.404000	-2.835000	4.285000
C	-1.388000	3.042000	3.023000
H	-1.413000	2.013000	2.692000
C	3.329000	-0.319000	3.023000
H	2.450000	0.217000	2.692000
C	-1.941000	-2.724000	3.022000
H	-1.037000	-2.231000	2.692000
N	-2.813000	-3.349000	2.239000
N	-1.494000	4.110000	2.240000
N	4.307000	-0.762000	2.240000
C	5.323000	-1.367000	2.912000
C	4.920000	-1.310000	4.254000
C	-1.477000	5.293000	2.913000
C	-1.326000	4.916000	4.255000

C	-3.845000	-3.926000	2.912000
C	-3.594000	-3.607000	4.254000
H	-3.226000	1.235000	4.687000
C	0.797000	1.179000	-5.194000
C	-0.798000	-1.180000	-5.239000
C	1.421000	-0.100000	-5.239000
C	-0.623000	1.282000	-5.239000
C	-1.419000	0.101000	-5.194000
C	0.623000	-1.279000	-5.194000
C	1.645000	2.438000	-5.221000
H	2.616000	2.289000	-4.743000
H	1.175000	3.245000	-4.650000
C	1.288000	-2.643000	-5.221000
H	0.674000	-3.410000	-4.743000
C	-2.934000	0.207000	-5.221000
H	-3.290000	1.122000	-4.743000
H	-3.397000	-0.604000	-4.650000
C	2.929000	-0.203000	-5.480000
H	3.230000	0.564000	-6.203000
H	3.210000	-1.154000	-5.943000
C	-1.288000	2.639000	-5.480000
H	-2.103000	2.516000	-6.203000
H	-0.605000	3.358000	-5.943000
C	-1.641000	-2.434000	-5.480000
H	-2.605000	-2.202000	-5.943000
H	-1.127000	-3.078000	-6.203000
N	3.712000	-0.047000	-4.253000
N	-1.815000	3.238000	-4.253000
N	-1.897000	-3.190000	-4.253000
C	3.309000	-0.296000	-2.988000
H	2.334000	-0.624000	-2.657000
C	-1.398000	3.014000	-2.988000
H	-0.627000	2.333000	-2.656000
C	-1.911000	-2.718000	-2.989000
H	-1.707000	-1.709000	-2.657000
N	-2.243000	-3.741000	-2.207000
N	4.361000	-0.072000	-2.207000
N	-2.118000	3.813000	-2.207000
C	-2.997000	4.603000	-2.881000
C	-2.812000	4.246000	-4.223000
C	5.485000	0.294000	-2.882000
C	5.082000	0.313000	-4.224000
C	-2.488000	-4.897000	-2.882000
C	-2.271000	-4.557000	-4.224000
H	2.222000	-2.639000	-4.651000
I	-2.526000	-3.543000	0.016000
I	-1.805000	3.959000	0.017000
I	4.331000	-0.416000	0.016000
C	-1.279000	5.865000	5.275000

H	-1.172000	5.600000	6.321000
C	-1.385000	7.205000	4.872000
H	-1.357000	7.994000	5.629000
C	-1.533000	7.572000	3.518000
H	-1.614000	8.631000	3.266000
C	-1.584000	6.613000	2.498000
H	-1.702000	6.884000	1.456000
C	-3.901000	5.571000	-2.467000
H	-4.028000	5.835000	-1.424000
C	-4.636000	6.187000	-3.489000
H	-5.365000	6.961000	-3.237000
C	-4.457000	5.838000	-4.843000
H	-5.052000	6.354000	-5.601000
C	-3.537000	4.857000	-5.246000
H	-3.406000	4.604000	-6.292000
C	6.775000	0.593000	-2.467000
H	7.067000	0.571000	-1.425000
C	7.676000	0.922000	-3.489000
H	8.710000	1.166000	-3.237000
C	7.284000	0.941000	-4.844000
H	8.028000	1.199000	-5.602000
C	5.974000	0.635000	-5.246000
H	5.690000	0.648000	-6.292000
C	6.519000	-1.935000	2.497000
H	6.812000	-1.968000	1.455000
C	7.324000	-2.459000	3.517000
H	8.282000	-2.918000	3.265000
C	6.933000	-2.404000	4.871000
H	7.602000	-2.822000	5.628000
C	5.719000	-1.825000	5.275000
H	5.436000	-1.786000	6.321000
C	-4.935000	-4.678000	2.497000
H	-5.111000	-4.916000	1.455000
C	-5.791000	-5.114000	3.517000
H	-6.668000	-5.714000	3.265000
C	-5.548000	-4.803000	4.871000
H	-6.245000	-5.173000	5.628000
C	-4.440000	-4.040000	5.275000
H	-4.264000	-3.815000	6.320000
C	-2.438000	-5.491000	-5.247000
H	-2.284000	-5.251000	-6.293000
C	-2.828000	-6.778000	-4.844000
H	-2.976000	-7.552000	-5.602000
C	-3.040000	-7.108000	-3.490000
H	-3.345000	-8.126000	-3.238000
C	-2.874000	-6.164000	-2.468000
H	-3.039000	-6.406000	-1.425000
H	1.492000	-2.941000	-6.254000
H	-3.294000	0.179000	-6.254000

H	1.802000	2.763000	-6.254000
H	2.018000	2.602000	6.290000
H	-3.263000	0.446000	6.290000
H	1.245000	-3.050000	6.290000
P	-0.000000	0.000000	-0.338000
F	0.980000	0.904000	-1.290000
F	0.293000	-1.301000	-1.290000
F	-1.273000	0.397000	-1.290000
F	-0.981000	-0.902000	0.613000
F	-0.291000	1.300000	0.614000
F	1.272000	-0.398000	0.613000

[PF₆-C₄-I-4][PF₆]₂

C	0.836000	1.160000	5.368000
C	-0.838000	-1.164000	5.385000
C	-0.589000	1.307000	5.385000
C	1.427000	-0.144000	5.385000
C	0.587000	-1.304000	5.368000
C	-1.422000	0.143000	5.368000
C	1.728000	2.401000	5.422000
H	1.253000	3.243000	4.912000
H	2.635000	2.235000	4.829000
C	-2.944000	0.295000	5.422000
H	-3.435000	-0.537000	4.912000
C	1.216000	-2.698000	5.421000
H	0.619000	-3.400000	4.829000
H	2.182000	-2.707000	4.911000
C	-1.211000	2.702000	5.536000
H	-0.677000	3.254000	6.314000
H	-2.247000	2.683000	5.876000
C	2.947000	-0.303000	5.536000
H	3.157000	-1.042000	6.313000
H	3.448000	0.604000	5.876000
C	-1.735000	-2.401000	5.536000
H	-1.200000	-3.289000	5.876000
H	-2.480000	-2.214000	6.313000
N	-1.193000	3.466000	4.285000
N	3.598000	-0.700000	4.285000
N	-2.405000	-2.767000	4.285000
C	-1.375000	2.979000	3.040000
H	-1.509000	1.946000	2.748000
C	3.267000	-0.299000	3.039000
H	2.440000	0.334000	2.748000
C	-1.892000	-2.681000	3.039000
H	-0.931000	-2.280000	2.748000
N	-2.799000	-3.201000	2.220000
N	-1.372000	4.024000	2.220000

N	4.171000	-0.824000	2.219000
C	5.144000	-1.537000	2.851000
C	4.791000	-1.465000	4.205000
C	-1.241000	5.223000	2.851000
C	-1.127000	4.881000	4.206000
C	-3.902000	-3.687000	2.851000
C	-3.663000	-3.417000	4.205000
H	-3.253000	1.164000	4.829000
C	0.829000	1.164000	-5.354000
C	-0.832000	-1.167000	-5.371000
C	1.426000	-0.136000	-5.371000
C	-0.595000	1.304000	-5.371000
C	-1.423000	0.137000	-5.354000
C	0.593000	-1.300000	-5.354000
C	1.717000	2.409000	-5.403000
H	2.666000	2.229000	-4.892000
H	1.267000	3.213000	-4.809000
C	1.227000	-2.691000	-5.404000
H	0.596000	-3.423000	-4.893000
C	-2.945000	0.284000	-5.403000
H	-3.264000	1.195000	-4.892000
H	-3.416000	-0.508000	-4.809000
C	2.947000	-0.277000	-5.519000
H	3.298000	0.407000	-6.296000
H	3.263000	-1.264000	-5.858000
C	-1.234000	2.691000	-5.519000
H	-2.001000	2.654000	-6.296000
H	-0.537000	3.459000	-5.858000
C	-1.714000	-2.413000	-5.519000
H	-2.727000	-2.193000	-5.858000
H	-1.298000	-3.059000	-6.296000
N	3.662000	-0.013000	-4.268000
N	-1.820000	3.178000	-4.267000
N	-1.843000	-3.165000	-4.268000
C	3.250000	-0.322000	-3.020000
H	2.308000	-0.765000	-2.727000
C	-1.346000	2.976000	-3.020000
H	-0.491000	2.381000	-2.726000
C	-1.904000	-2.653000	-3.020000
H	-1.817000	-1.616000	-2.726000
N	-2.114000	-3.679000	-2.202000
N	4.243000	0.009000	-2.202000
N	-2.129000	3.671000	-2.202000
C	-3.104000	4.379000	-2.835000
C	-2.917000	4.073000	-4.190000
C	5.344000	0.499000	-2.836000
C	4.985000	0.490000	-4.190000
C	-2.240000	-4.877000	-2.836000
C	-2.069000	-4.562000	-4.191000

H	2.148000	-2.704000	-4.810000
I	-2.453000	-3.435000	0.009000
I	-1.749000	3.842000	0.009000
I	4.201000	-0.407000	0.009000
C	-3.502000	0.281000	-6.823000
H	-3.112000	1.114000	-7.415000
H	-4.592000	0.371000	-6.796000
H	-3.253000	-0.639000	-7.360000
C	1.508000	-3.172000	-6.823000
H	2.180000	-2.497000	-7.361000
H	0.591000	-3.251000	-7.415000
H	1.975000	-4.161000	-6.797000
C	1.993000	2.893000	-6.823000
H	2.520000	2.139000	-7.415000
H	2.616000	3.792000	-6.796000
H	1.072000	3.137000	-7.360000
C	2.095000	2.815000	6.843000
H	2.746000	3.695000	6.819000
H	2.623000	2.021000	7.379000
H	1.211000	3.069000	7.434000
C	-3.486000	0.406000	6.843000
H	-4.573000	0.530000	6.819000
H	-3.062000	1.260000	7.380000
H	-3.264000	-0.487000	7.434000
C	1.391000	-3.223000	6.843000
H	1.828000	-4.226000	6.819000
H	0.440000	-3.283000	7.379000
H	2.054000	-2.584000	7.434000
C	-0.990000	5.857000	5.192000
H	-0.910000	5.622000	6.248000
C	-0.968000	7.187000	4.742000
H	-0.867000	7.995000	5.470000
C	-1.081000	7.517000	3.375000
H	-1.062000	8.570000	3.085000
C	-1.223000	6.531000	2.389000
H	-1.317000	6.775000	1.338000
C	-4.091000	5.238000	-2.375000
H	-4.216000	5.465000	-1.323000
C	-4.913000	5.797000	-3.362000
H	-5.710000	6.486000	-3.073000
C	-4.735000	5.500000	-4.729000
H	-5.400000	5.968000	-5.459000
C	-3.729000	4.629000	-5.178000
H	-3.601000	4.418000	-6.234000
C	6.582000	0.924000	-2.375000
H	6.840000	0.919000	-1.324000
C	7.476000	1.357000	-3.363000
H	8.472000	1.703000	-3.074000
C	7.130000	1.351000	-4.730000

H	7.868000	1.693000	-5.460000
C	5.873000	0.915000	-5.179000
H	5.626000	0.910000	-6.235000
C	6.268000	-2.206000	2.388000
H	6.525000	-2.247000	1.337000
C	7.051000	-2.823000	3.374000
H	7.953000	-3.365000	3.084000
C	6.709000	-2.755000	4.740000
H	7.358000	-3.248000	5.469000
C	5.568000	-2.071000	5.192000
H	5.324000	-2.023000	6.247000
C	-5.044000	-4.325000	2.389000
H	-5.209000	-4.528000	1.338000
C	-5.969000	-4.695000	3.374000
H	-6.890000	-5.205000	3.084000
C	-5.740000	-4.433000	4.741000
H	-6.491000	-4.749000	5.469000
C	-4.577000	-3.787000	5.192000
H	-4.414000	-3.600000	6.247000
C	-2.145000	-5.543000	-5.179000
H	-2.025000	-5.327000	-6.235000
C	-2.395000	-6.850000	-4.730000
H	-2.469000	-7.660000	-5.460000
C	-2.564000	-7.153000	-3.363000
H	-2.762000	-8.188000	-3.075000
C	-2.491000	-6.162000	-2.376000
H	-2.624000	-6.383000	-1.324000
P	-0.000000	0.000000	-0.186000
F	1.105000	0.744000	-1.140000
F	0.092000	-1.329000	-1.140000
F	-1.197000	0.585000	-1.140000
F	-1.106000	-0.741000	0.768000
F	-0.088000	1.328000	0.768000
F	1.195000	-0.588000	0.768000

[PF₆-C₅-I-5][PF₆]₂

C	0.850000	1.138000	5.222000
C	-0.852000	-1.147000	5.264000
C	-0.564000	1.306000	5.266000
C	1.416000	-0.170000	5.265000
C	0.563000	-1.311000	5.220000
C	-1.414000	0.162000	5.221000
C	1.759000	2.354000	5.257000
H	1.299000	3.224000	4.783000
H	2.677000	2.179000	4.688000
C	-2.922000	0.341000	5.256000
H	-3.445000	-0.492000	4.780000

C	1.162000	-2.706000	5.254000
H	0.551000	-3.413000	4.684000
H	2.145000	-2.743000	4.779000
C	-1.159000	2.697000	5.512000
H	-0.537000	3.228000	6.241000
H	-2.153000	2.649000	5.968000
C	2.918000	-0.350000	5.510000
H	3.067000	-1.156000	6.238000
H	3.374000	0.533000	5.967000
C	-1.759000	-2.358000	5.508000
H	-1.222000	-3.195000	5.964000
H	-2.531000	-2.085000	6.237000
N	-1.261000	3.493000	4.287000
N	3.657000	-0.659000	4.284000
N	-2.397000	-2.843000	4.282000
C	-1.392000	3.035000	3.024000
H	-1.413000	2.007000	2.693000
C	3.326000	-0.316000	3.022000
H	2.446000	0.217000	2.692000
C	-1.935000	-2.726000	3.020000
H	-1.033000	-2.229000	2.690000
N	-2.806000	-3.352000	2.238000
N	-1.499000	4.104000	2.243000
N	4.305000	-0.757000	2.240000
C	5.323000	-1.357000	2.913000
C	4.924000	-1.299000	4.252000
C	-1.488000	5.286000	2.918000
C	-1.340000	4.909000	4.256000
C	-3.836000	-3.935000	2.911000
C	-3.585000	-3.619000	4.250000
H	-3.229000	1.224000	4.687000
C	0.799000	1.181000	-5.194000
C	-0.800000	-1.175000	-5.240000
C	1.421000	-0.100000	-5.240000
C	-0.621000	1.286000	-5.239000
C	-1.419000	0.107000	-5.195000
C	0.620000	-1.277000	-5.196000
C	1.650000	2.438000	-5.219000
H	2.621000	2.287000	-4.742000
H	1.182000	3.245000	-4.648000
C	1.283000	-2.642000	-5.223000
H	0.667000	-3.408000	-4.746000
C	-2.933000	0.216000	-5.221000
H	-3.288000	1.132000	-4.743000
H	-3.398000	-0.594000	-4.651000
C	2.928000	-0.206000	-5.480000
H	3.231000	0.561000	-6.203000
H	3.209000	-1.157000	-5.943000
C	-1.282000	2.645000	-5.478000

H	-2.097000	2.524000	-6.201000
H	-0.598000	3.363000	-5.940000
C	-1.646000	-2.427000	-5.482000
H	-2.610000	-2.194000	-5.944000
H	-1.133000	-3.072000	-6.205000
N	3.711000	-0.051000	-4.253000
N	-1.808000	3.244000	-4.251000
N	-1.902000	-3.183000	-4.255000
C	3.306000	-0.297000	-2.988000
H	2.330000	-0.622000	-2.657000
C	-1.394000	3.015000	-2.986000
H	-0.624000	2.332000	-2.655000
C	-1.912000	-2.711000	-2.990000
H	-1.705000	-1.704000	-2.658000
N	-2.245000	-3.735000	-2.211000
N	4.358000	-0.074000	-2.208000
N	-2.113000	3.814000	-2.205000
C	-2.988000	4.608000	-2.880000
C	-2.802000	4.255000	-4.219000
C	5.484000	0.287000	-2.883000
C	5.083000	0.304000	-4.222000
C	-2.495000	-4.889000	-2.887000
C	-2.281000	-4.550000	-4.226000
H	2.217000	-2.641000	-4.652000
I	-2.523000	-3.541000	0.014000
I	-1.805000	3.956000	0.019000
I	4.328000	-0.415000	0.016000
C	-1.299000	5.855000	5.278000
H	-1.194000	5.570000	6.319000
C	-1.409000	7.207000	4.887000
C	-1.556000	7.578000	3.516000
C	-1.599000	6.602000	2.500000
H	-1.714000	6.854000	1.453000
C	-3.887000	5.576000	-2.462000
H	-4.002000	5.823000	-1.414000
C	-4.630000	6.210000	-3.478000
C	-4.447000	5.860000	-4.851000
C	-3.521000	4.869000	-5.242000
H	-3.375000	4.606000	-6.283000
C	6.771000	0.581000	-2.465000
H	7.043000	0.556000	-1.417000
C	7.691000	0.909000	-3.481000
C	7.296000	0.927000	-4.854000
C	5.974000	0.620000	-5.244000
H	5.673000	0.627000	-6.286000
C	6.518000	-1.919000	2.494000
H	6.793000	-1.944000	1.447000
C	7.342000	-2.445000	3.509000
C	6.949000	-2.389000	4.881000

C	5.723000	-1.808000	5.273000
H	5.424000	-1.758000	6.314000
C	-4.920000	-4.688000	2.492000
H	-5.080000	-4.912000	1.444000
C	-5.787000	-5.140000	3.506000
C	-5.541000	-4.829000	4.879000
C	-4.424000	-4.058000	5.271000
H	-4.232000	-3.825000	6.312000
C	-2.453000	-5.478000	-5.249000
H	-2.297000	-5.219000	-6.290000
C	-2.848000	-6.777000	-4.860000
C	-3.060000	-7.111000	-3.487000
C	-2.884000	-6.152000	-2.470000
H	-3.041000	-6.376000	-1.422000
H	1.487000	-2.941000	-6.256000
H	-3.293000	0.189000	-6.254000
H	1.807000	2.764000	-6.252000
H	2.012000	2.603000	6.292000
H	-3.265000	0.434000	6.290000
H	1.252000	-3.051000	6.288000
C	-3.050000	-7.817000	-5.940000
H	-2.371000	-8.661000	-5.785000
H	-2.844000	-7.406000	-6.934000
H	-4.086000	-8.170000	-5.937000
C	-3.487000	-8.507000	-3.094000
H	-2.735000	-9.237000	-3.409000
H	-4.452000	-8.751000	-3.550000
H	-3.602000	-8.599000	-2.009000
C	-6.987000	-5.971000	3.111000
H	-6.929000	-6.962000	3.571000
H	-7.034000	-6.112000	2.026000
H	-7.911000	-5.473000	3.419000
C	-6.478000	-5.330000	5.956000
H	-6.154000	-5.005000	6.951000
H	-6.502000	-6.424000	5.958000
H	-7.487000	-4.938000	5.793000
C	8.299000	1.273000	-5.933000
H	9.123000	0.553000	-5.930000
H	8.690000	2.283000	-5.777000
H	7.841000	1.247000	-6.928000
C	9.113000	1.237000	-3.087000
H	9.807000	0.524000	-3.542000
H	9.249000	1.182000	-2.001000
H	9.369000	2.253000	-3.400000
C	8.662000	-3.068000	3.114000
H	9.492000	-2.523000	3.575000
H	8.809000	-3.038000	2.029000
H	8.693000	-4.118000	3.421000
C	7.851000	-2.951000	5.958000

H	8.810000	-2.425000	5.962000
H	8.016000	-4.021000	5.795000
H	7.407000	-2.835000	6.953000
C	-5.248000	6.556000	-5.930000
H	-4.996000	6.174000	-6.925000
H	-5.036000	7.630000	-5.926000
H	-6.318000	6.390000	-5.775000
C	-5.625000	7.277000	-3.083000
H	-5.354000	8.235000	-3.538000
H	-5.647000	7.421000	-1.998000
H	-6.634000	6.991000	-3.398000
C	-1.676000	9.033000	3.122000
H	-0.783000	9.584000	3.430000
H	-2.563000	9.478000	3.583000
H	-1.775000	9.146000	2.037000
C	-1.374000	8.268000	5.966000
H	-0.530000	8.946000	5.804000
H	-1.253000	7.825000	6.960000
H	-2.309000	8.836000	5.969000
P	0.000000	0.000000	-0.337000
F	0.981000	0.904000	-1.288000
F	0.292000	-1.300000	-1.290000
F	-1.273000	0.399000	-1.288000
F	-0.982000	-0.902000	0.614000
F	-0.290000	1.300000	0.616000
F	1.271000	-0.400000	0.615000

[PF₆-C₆-I-6][PF₆]₂

C	0.831000	1.159000	5.371000
C	-0.835000	-1.170000	5.386000
C	-0.593000	1.302000	5.388000
C	1.427000	-0.143000	5.387000
C	0.590000	-1.305000	5.370000
C	-1.423000	0.136000	5.371000
C	1.721000	2.403000	5.425000
H	1.243000	3.243000	4.916000
H	2.628000	2.240000	4.832000
C	-2.945000	0.283000	5.423000
H	-3.434000	-0.550000	4.913000
C	1.223000	-2.698000	5.422000
H	0.628000	-3.401000	4.828000
H	2.190000	-2.704000	4.912000
C	-1.219000	2.695000	5.539000
H	-0.688000	3.247000	6.318000
H	-2.256000	2.673000	5.877000
C	2.947000	-0.298000	5.538000
H	3.159000	-1.035000	6.316000

H	3.446000	0.611000	5.876000
C	-1.729000	-2.409000	5.536000
H	-1.191000	-3.297000	5.873000
H	-2.473000	-2.225000	6.314000
N	-1.201000	3.459000	4.289000
N	3.598000	-0.695000	4.286000
N	-2.399000	-2.774000	4.284000
C	-1.379000	2.973000	3.043000
H	-1.511000	1.940000	2.751000
C	3.265000	-0.296000	3.042000
H	2.437000	0.335000	2.750000
C	-1.887000	-2.683000	3.039000
H	-0.927000	-2.281000	2.748000
N	-2.795000	-3.202000	2.221000
N	-1.374000	4.019000	2.226000
N	4.169000	-0.822000	2.223000
C	5.143000	-1.532000	2.855000
C	4.792000	-1.458000	4.206000
C	-1.247000	5.217000	2.859000
C	-1.136000	4.875000	4.210000
C	-3.897000	-3.691000	2.853000
C	-3.657000	-3.426000	4.204000
H	-3.257000	1.151000	4.831000
C	0.834000	1.164000	-5.351000
C	-0.836000	-1.160000	-5.369000
C	1.427000	-0.139000	-5.368000
C	-0.589000	1.310000	-5.368000
C	-1.422000	0.146000	-5.352000
C	0.589000	-1.299000	-5.352000
C	1.728000	2.406000	-5.399000
H	2.676000	2.222000	-4.888000
H	1.281000	3.211000	-4.804000
C	1.217000	-2.693000	-5.402000
H	0.584000	-3.423000	-4.892000
C	-2.943000	0.299000	-5.401000
H	-3.258000	1.211000	-4.889000
H	-3.417000	-0.491000	-4.807000
C	2.946000	-0.285000	-5.516000
H	3.300000	0.396000	-6.294000
H	3.259000	-1.274000	-5.854000
C	-1.222000	2.699000	-5.514000
H	-1.988000	2.665000	-6.293000
H	-0.522000	3.465000	-5.851000
C	-1.722000	-2.403000	-5.518000
H	-2.735000	-2.179000	-5.855000
H	-1.310000	-3.049000	-6.297000
N	3.661000	-0.022000	-4.265000
N	-1.809000	3.186000	-4.263000
N	-1.852000	-3.155000	-4.267000

C	3.247000	-0.329000	-3.017000
H	2.304000	-0.769000	-2.724000
C	-1.337000	2.979000	-3.016000
H	-0.484000	2.383000	-2.722000
C	-1.910000	-2.644000	-3.020000
H	-1.820000	-1.608000	-2.725000
N	-2.120000	-3.672000	-2.204000
N	4.241000	0.002000	-2.201000
N	-2.121000	3.674000	-2.198000
C	-3.093000	4.385000	-2.833000
C	-2.905000	4.083000	-4.185000
C	5.343000	0.489000	-2.835000
C	4.987000	0.479000	-4.186000
C	-2.249000	-4.868000	-2.840000
C	-2.081000	-4.553000	-4.191000
H	2.138000	-2.709000	-4.808000
I	-2.453000	-3.432000	0.009000
I	-1.746000	3.841000	0.014000
I	4.199000	-0.409000	0.011000
C	-1.004000	5.848000	5.198000
H	-0.928000	5.593000	6.249000
C	-0.980000	7.190000	4.760000
C	-1.091000	7.524000	3.376000
C	-1.229000	6.522000	2.395000
H	-1.321000	6.747000	1.339000
C	-4.076000	5.244000	-2.370000
H	-4.187000	5.455000	-1.313000
C	-4.908000	5.818000	-3.351000
C	-4.726000	5.520000	-4.736000
C	-3.710000	4.642000	-5.174000
H	-3.566000	4.421000	-6.225000
C	6.578000	0.911000	-2.372000
H	6.818000	0.900000	-1.315000
C	7.491000	1.345000	-3.353000
C	7.142000	1.338000	-4.738000
C	5.873000	0.898000	-5.175000
H	5.609000	0.884000	-6.227000
C	6.264000	-2.199000	2.390000
H	6.504000	-2.231000	1.334000
C	7.063000	-2.822000	3.369000
C	6.719000	-2.752000	4.754000
C	5.569000	-2.061000	5.193000
H	5.310000	-2.000000	6.244000
C	-5.036000	-4.328000	2.387000
H	-5.183000	-4.519000	1.331000
C	-5.974000	-4.710000	3.367000
C	-5.740000	-4.448000	4.751000
C	-4.566000	-3.798000	5.191000
H	-4.384000	-3.606000	6.242000

C	-2.161000	-5.529000	-5.181000
H	-2.042000	-5.292000	-6.232000
C	-2.414000	-6.848000	-4.744000
C	-2.582000	-7.156000	-3.360000
C	-2.501000	-6.150000	-2.377000
H	-2.630000	-6.353000	-1.321000
C	-2.514000	-7.940000	-5.788000
H	-1.752000	-8.705000	-5.610000
H	-2.354000	-7.545000	-6.797000
H	-3.509000	-8.396000	-5.765000
C	-2.859000	-8.575000	-2.917000
H	-2.038000	-9.233000	-3.215000
H	-3.797000	-8.932000	-3.354000
H	-2.956000	-8.641000	-1.828000
C	-7.235000	-5.414000	2.920000
H	-7.287000	-6.415000	3.361000
H	-7.263000	-5.531000	1.832000
H	-8.116000	-4.835000	3.212000
C	-6.754000	-4.875000	5.791000
H	-6.432000	-4.597000	6.801000
H	-6.880000	-5.962000	5.773000
H	-7.716000	-4.387000	5.606000
C	8.137000	1.798000	-5.780000
H	9.030000	1.165000	-5.757000
H	8.419000	2.841000	-5.601000
H	7.716000	1.740000	-6.790000
C	8.858000	1.814000	-2.909000
H	9.636000	1.181000	-3.346000
H	8.963000	1.762000	-1.820000
H	9.017000	2.855000	-3.206000
C	8.304000	-3.561000	2.923000
H	9.196000	-3.107000	3.365000
H	8.420000	-3.526000	1.834000
H	8.243000	-4.615000	3.213000
C	7.594000	-3.417000	5.794000
H	8.599000	-2.983000	5.776000
H	7.653000	-4.494000	5.607000
H	7.192000	-3.279000	6.803000
C	-5.622000	6.154000	-5.778000
H	-5.360000	5.819000	-6.788000
H	-5.519000	7.243000	-5.755000
H	-6.666000	5.876000	-5.600000
C	-5.998000	6.767000	-2.906000
H	-5.839000	7.758000	-3.343000
H	-6.006000	6.883000	-1.817000
H	-6.979000	6.385000	-3.205000
C	-1.070000	8.969000	2.931000
H	-0.128000	9.443000	3.222000
H	-1.910000	9.514000	3.373000

H	-1.158000	9.053000	1.842000
C	-0.842000	8.280000	5.801000
H	0.061000	8.869000	5.616000
H	-0.761000	7.861000	6.810000
H	-1.720000	8.933000	5.784000
C	1.496000	-3.174000	-6.822000
H	2.172000	-2.501000	-7.359000
H	0.580000	-3.249000	-7.415000
H	1.960000	-4.165000	-6.796000
C	2.005000	2.889000	-6.818000
H	2.529000	2.134000	-7.411000
H	2.632000	3.787000	-6.791000
H	1.085000	3.138000	-7.355000
C	-3.500000	0.299000	-6.820000
H	-3.107000	1.130000	-7.412000
H	-4.590000	0.393000	-6.794000
H	-3.255000	-0.622000	-7.358000
C	-3.488000	0.392000	6.844000
H	-3.067000	1.247000	7.381000
H	-3.264000	-0.501000	7.435000
H	-4.576000	0.513000	6.820000
C	1.400000	-3.223000	6.842000
H	2.060000	-2.583000	7.434000
H	1.839000	-4.226000	6.818000
H	0.448000	-3.286000	7.379000
C	2.087000	2.817000	6.847000
H	2.735000	3.699000	6.823000
H	2.617000	2.024000	7.383000
H	1.202000	3.069000	7.438000
P	0.000000	0.000000	-0.179000
F	1.109000	0.740000	-1.132000
F	0.086000	-1.329000	-1.134000
F	-1.194000	0.591000	-1.133000
F	-1.110000	-0.736000	0.774000
F	-0.082000	1.328000	0.775000
F	1.192000	-0.594000	0.774000

HRMS, IM-MS, and CID

Measurements were performed with a Waters Synapt G2-S Q-TOF traveling wave ion mobility mass spectrometer (Manchester, UK) equipped with a Z-spray electrospray ionization source. Solutions of the different ligands, AgPF₆, and I₂ with 5 mM concentration in DMSO were prepared. Silver(I) complexes were formed via the addition of AgPF₆ solution to the respective ligand solution and stirred for 10 minutes. The cation exchange was completed by the addition of I₂ solution to the previously prepared silver(I) complexes followed by centrifugation for 20 minutes and filtering. The final sample concentration of 100 μM was achieved via dilution with acetonitrile and the injection flow rate was 2 μL/min. A capillary voltage of 1.20 kV was used with the sample cone and source offset both set to 15 eV. The source and desolvation temperatures were 100 °C and 250 °C, respectively. The drift cell was operated with N₂ as the drift gas and was turned on 45 minutes prior to measuring to allow the pressures to settle. A wave velocity of 550 m/s and a wave height of 25 V was used for the measurements. Collision-induced dissociation (CID) was completed in the transfer cell with N₂ as the collision gas. IMS and CID were performed with mass selected ions as indicated in the spectra. Data for the survival yield (SY) analysis was obtained by taking measurements with increasing CID voltage until the parent ion was fragmented completely. Data was exported and processed in Origin pro 2020 (OriginLab corporation). The relative parent ion intensity was plotted against collision voltage and the curves were fit with a sigmoidal gaussian with the equation $y = a/(1+\exp(-k*(x-xc)))$ to obtain the 50% SY voltage (SY50%).

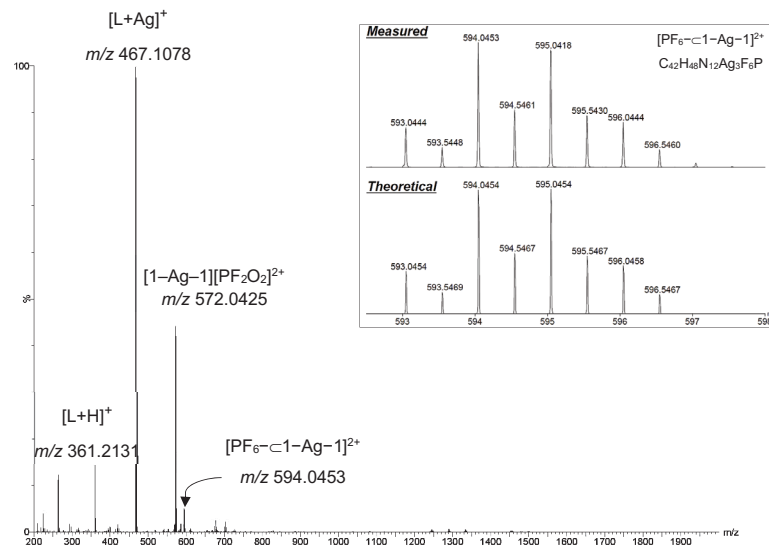


Figure S26. ESI-TOF mass spectrum of $[\text{PF}_6\text{-c1-Ag-1}][\text{PF}_6]_2$. Inset: Isotope pattern of the $[\text{PF}_6\text{-c1-Ag-1}]^{2+}$ ion. Hydrolysis of the anion results in $[\text{1-Ag-1}][\text{PF}_2\text{O}_2]^{2+}$ seen for all complexes.

S61

62

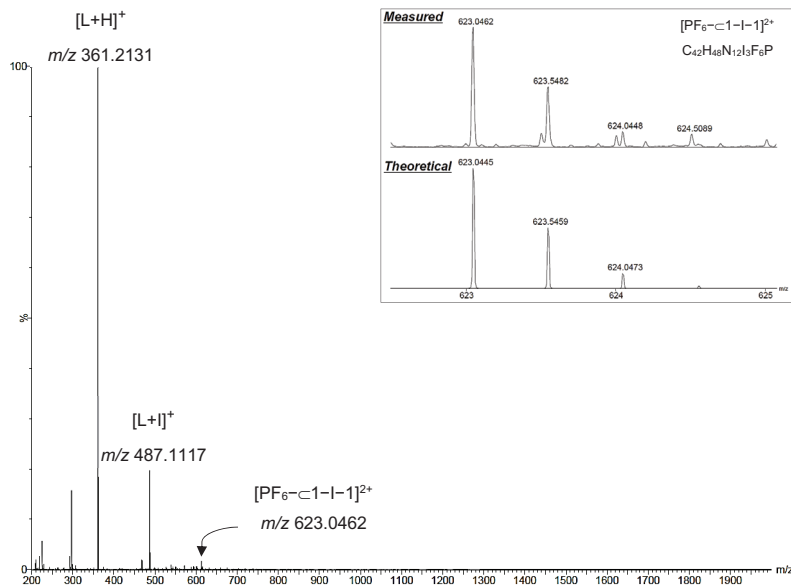


Figure S27. ESI-TOF mass spectrum of $[\text{PF}_6\text{-c1-l-1}][\text{PF}_6]_2$. Inset: Isotope pattern of the $[\text{PF}_6\text{-c1-l-1}]^{2+}$ ion.

S62

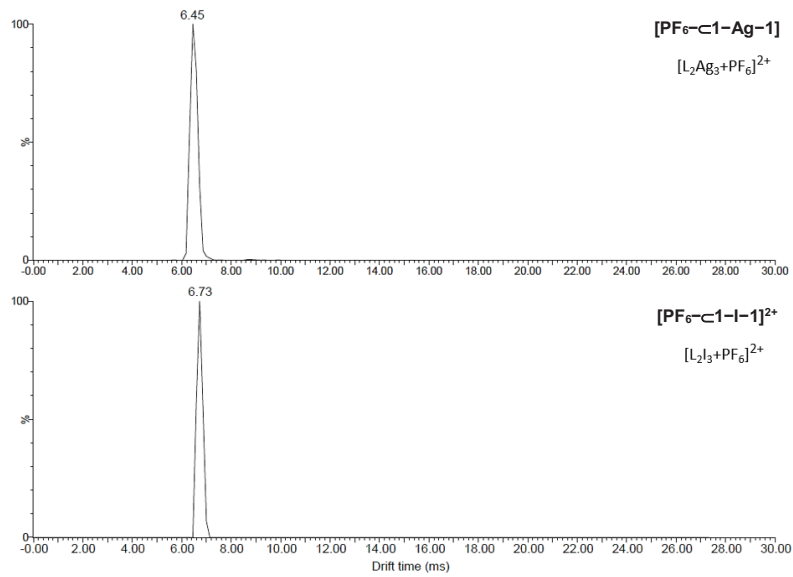


Figure S28. Comparison of arrival time distributions of $[\text{PF}_6\text{-c1-Ag-1}]^{2+}$ (top) and $[\text{PF}_6\text{-c1-l-1}]^{2+}$ (bottom). Both arrival time distributions are narrow peaks consistent with a single species and appear at very similar times indicating two closely analogous structures.

S63

64

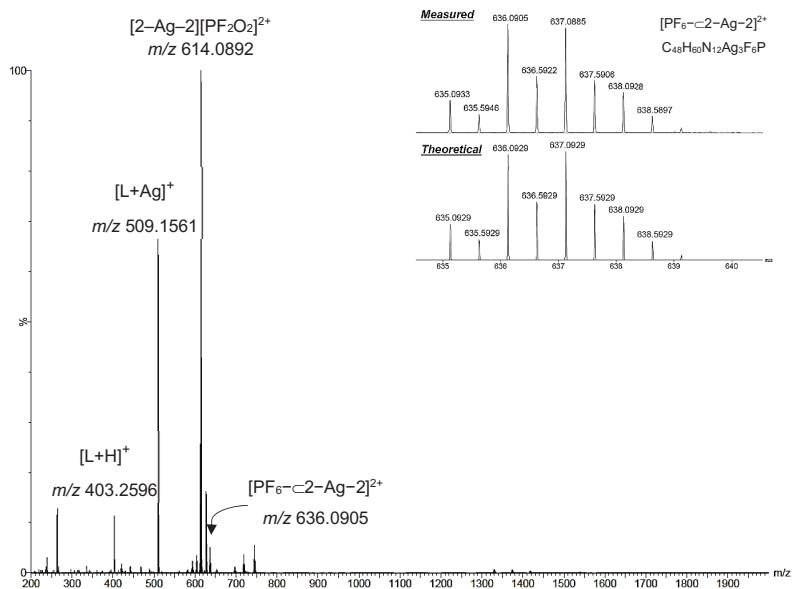


Figure S29. ESI-TOF mass spectrum of $[\text{PF}_6\text{-c2-Ag-2}][\text{PF}_6]_2$. Inset: Isotope pattern of the $[\text{PF}_6\text{-c2-Ag-2}]^{2+}$ ion.

S64

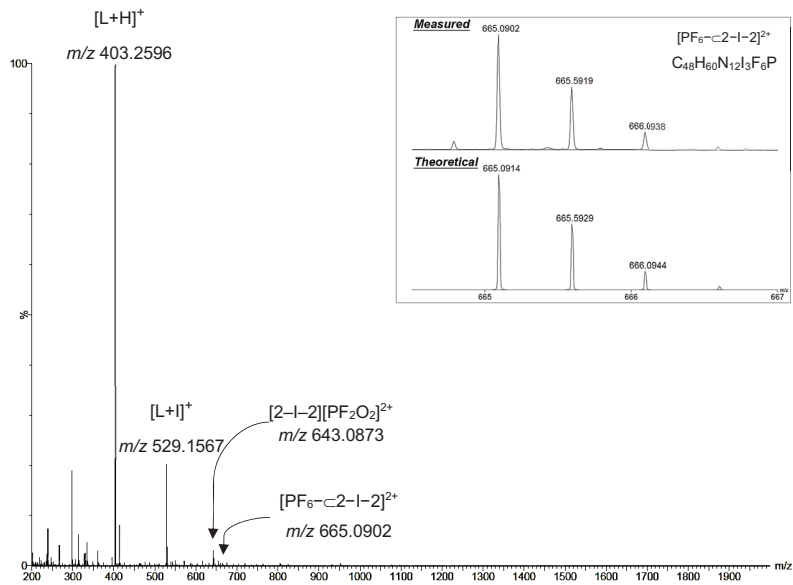


Figure S30. ESI-TOF mass spectrum of $[\text{PF}_6\text{-c2-l-2}][\text{PF}_6]_2$. Inset: Isotope pattern of the $[\text{PF}_6\text{-c2-l-2}]^{2+}$ ion.

S65

66

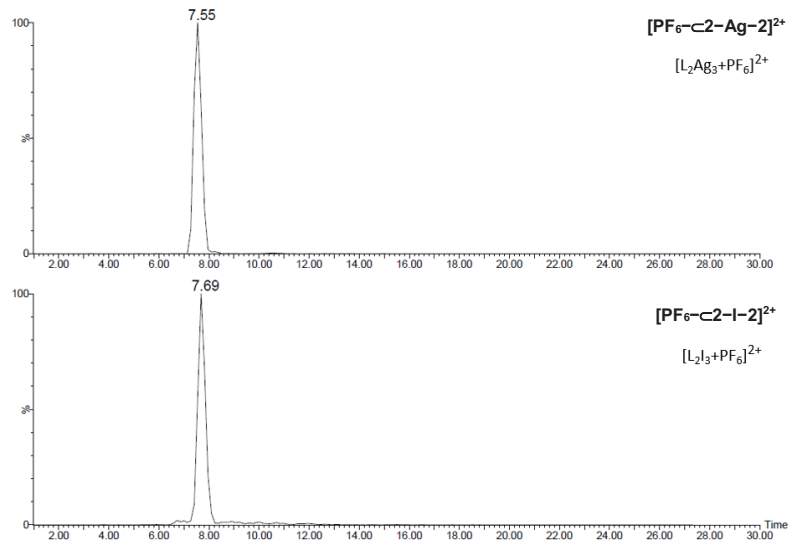


Figure S31. Comparison of arrival time distributions of $[\text{PF}_6\text{-c2-Ag-2}]^{2+}$ (top) and $[\text{PF}_6\text{-c2-l-2}]^{2+}$ (bottom).

S66

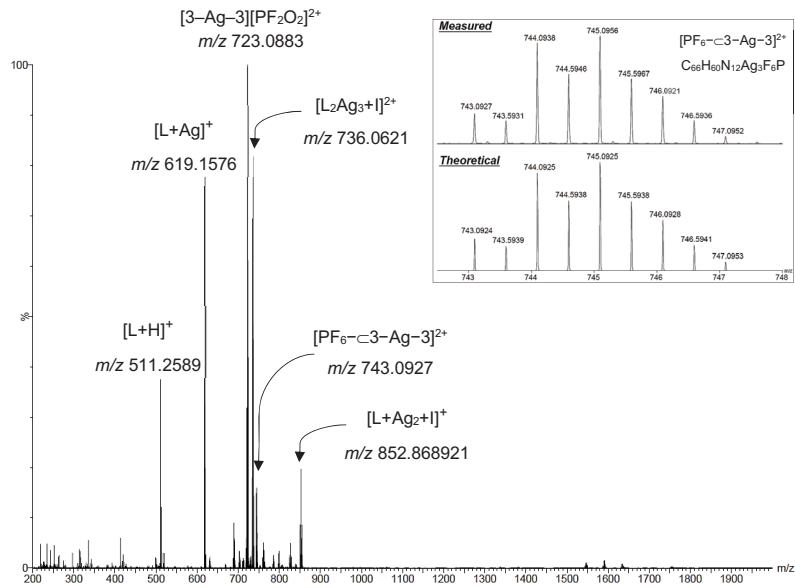


Figure S32. ESI-TOF mass spectrum of $[\text{PF}_6\text{-c3-Ag-3}][\text{PF}_6]_2$. Inset: Isotope pattern of the $[\text{PF}_6\text{-c3-Ag-3}]^{2+}$ ion.

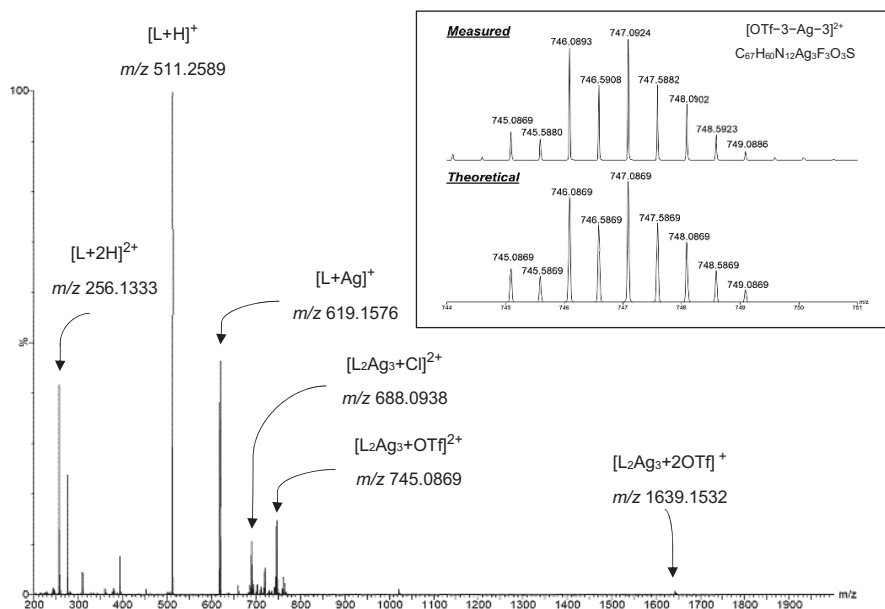


Figure S33. ESI-TOF mass spectrum of $[\text{3-Ag-3}][\text{OTf}]_3$. Inset: Isotope pattern of the $[\text{OTf-3-Ag-3}]^{2+}$ ion.

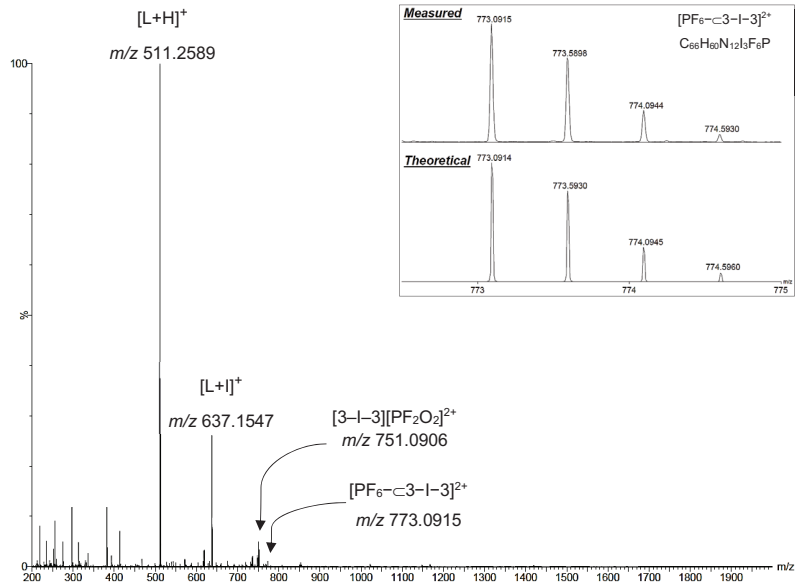


Figure S34. ESI-TOF mass spectrum of $[\text{PF}_6\text{-c3-l-3}][\text{PF}_6]_2$. Inset: Isotope pattern of the $[\text{PF}_6\text{-c3-l-3}]^{2+}$ ion.

S69

70

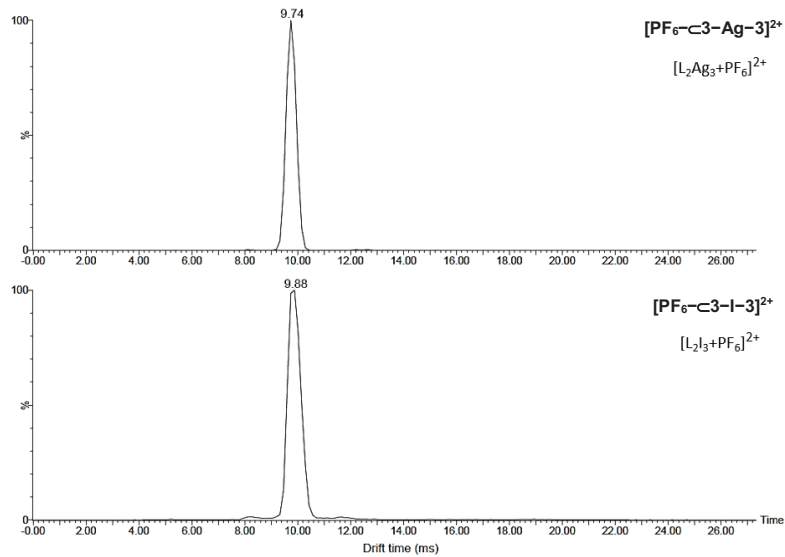


Figure S35. Comparison of arrival time distributions of $[\text{PF}_6\text{-c3-Ag-3}]^{2+}$ (top) and $[\text{PF}_6\text{-c3-l-3}]^{2+}$ (bottom).

S70

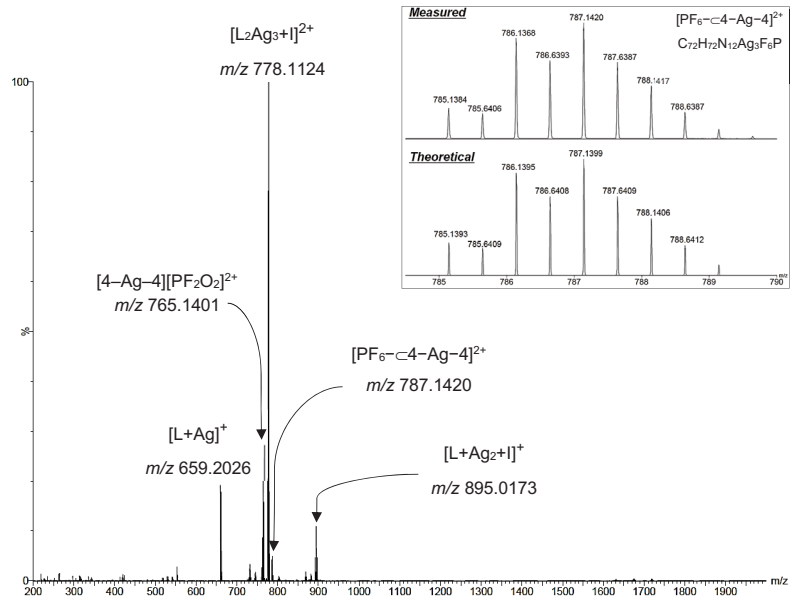


Figure S36. ESI-TOF mass spectrum of $[\text{PF}_6\text{-c4-Ag-4}][\text{PF}_6]_2$. Inset: Isotope pattern of the $[\text{PF}_6\text{-c4-Ag-4}]^{2+}$ ion.

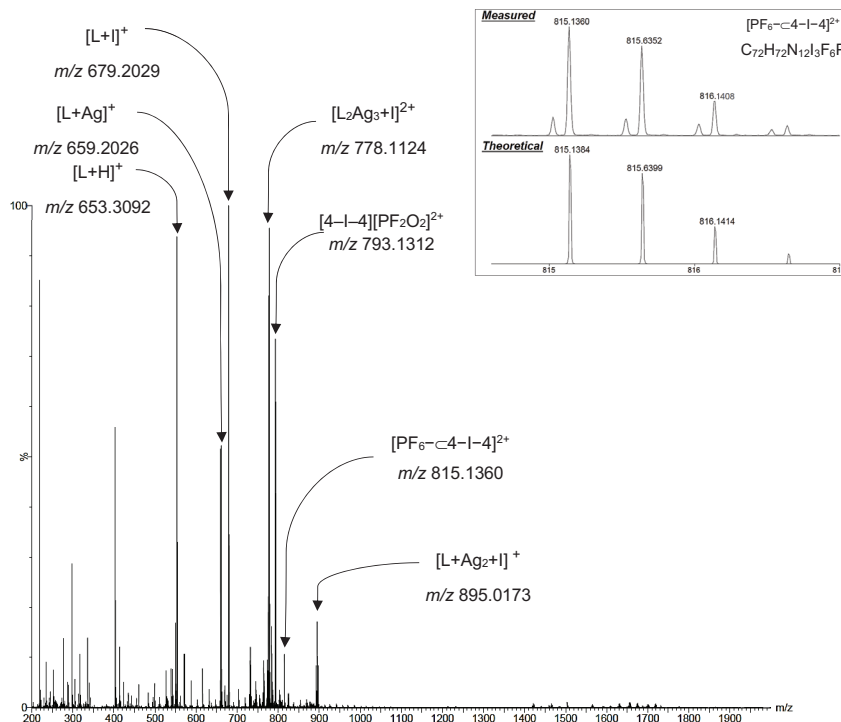


Figure S37. ESI-TOF mass spectrum of $[\text{PF}_6\text{-c4-I-4}][\text{PF}_6]_2$. Inset: Isotope pattern of the $[\text{PF}_6\text{-c4-I-4}]^{2+}$ ion.

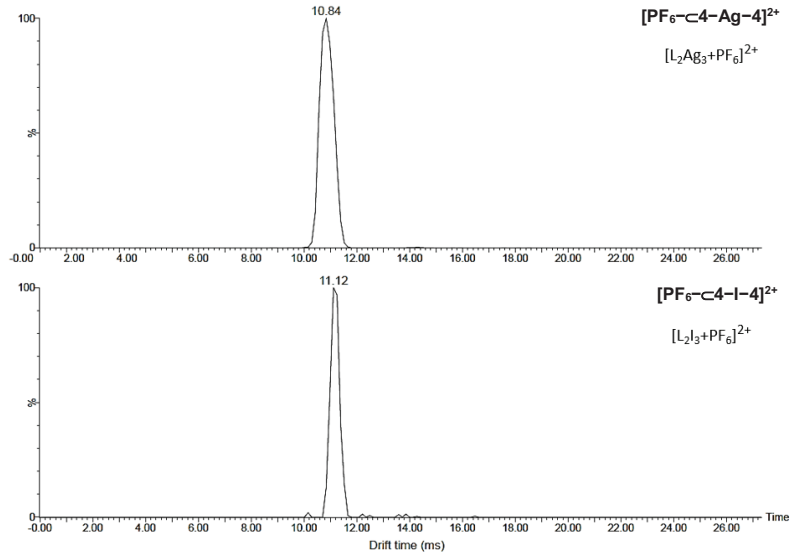


Figure S38. Comparison of arrival time distributions of $[\text{PF}_6\text{-c4-Ag-4}]^{2+}$ (top) and $[\text{PF}_6\text{-c4-l-4}]^{2+}$ (bottom).

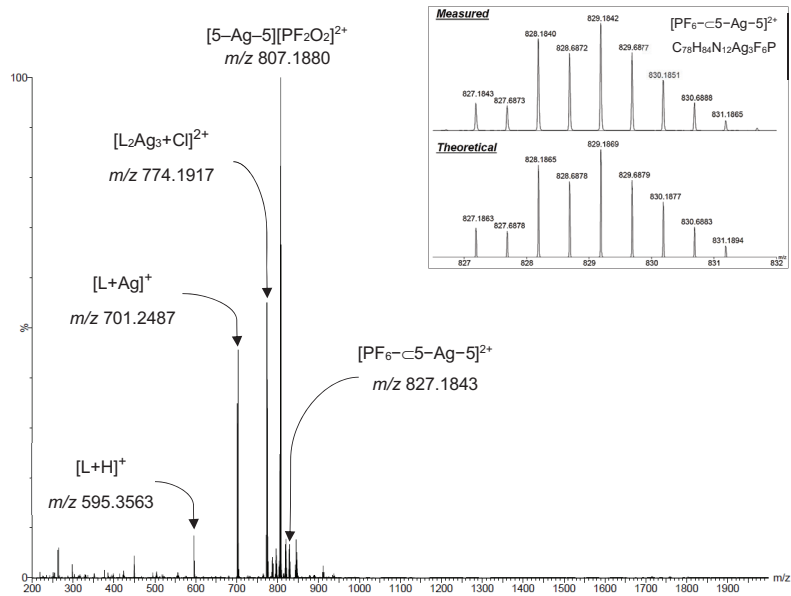


Figure S39. ESI-TOF mass spectrum of $[\text{PF}_6\text{-c5-Ag-5}][\text{PF}_6]_2$. Inset: Isotope pattern of the $[\text{PF}_6\text{-c5-Ag-5}]^{2+}$ ion.

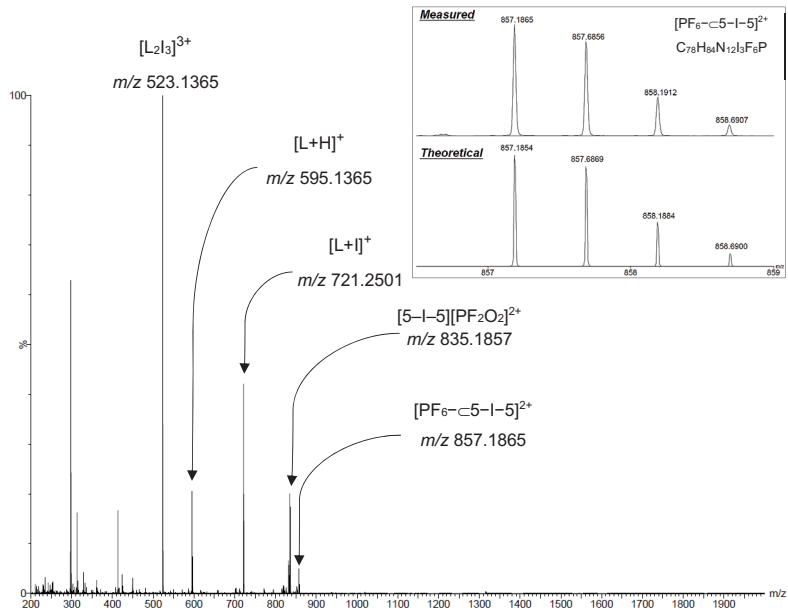


Figure S40. ESI-TOF mass spectrum of $[\text{PF}_6\text{-c5-l-5}][\text{PF}_6]_2$. Inset: Isotope pattern of the $[\text{PF}_6\text{-c5-l-5}]^{2+}$ ion.

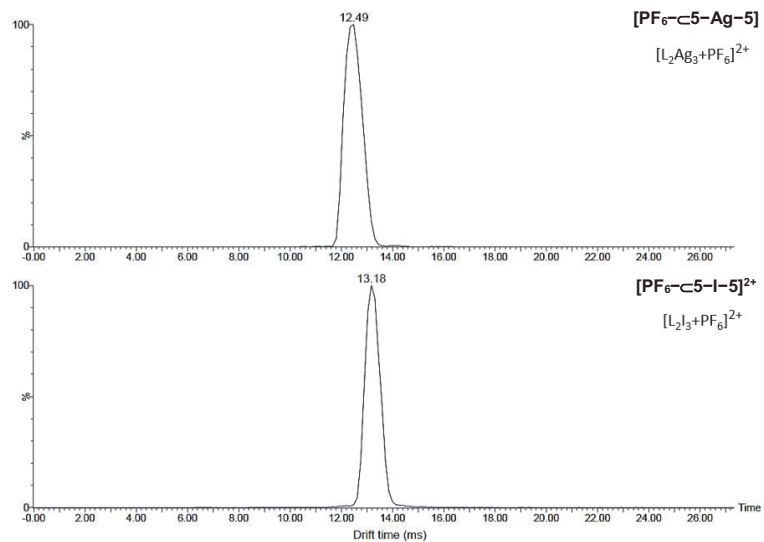


Figure S41. Comparison of arrival time distributions of $[\text{PF}_6\text{-c5-Ag-5}]^{2+}$ (top) and $[\text{PF}_6\text{-c5-l-5}]^{2+}$ (bottom).

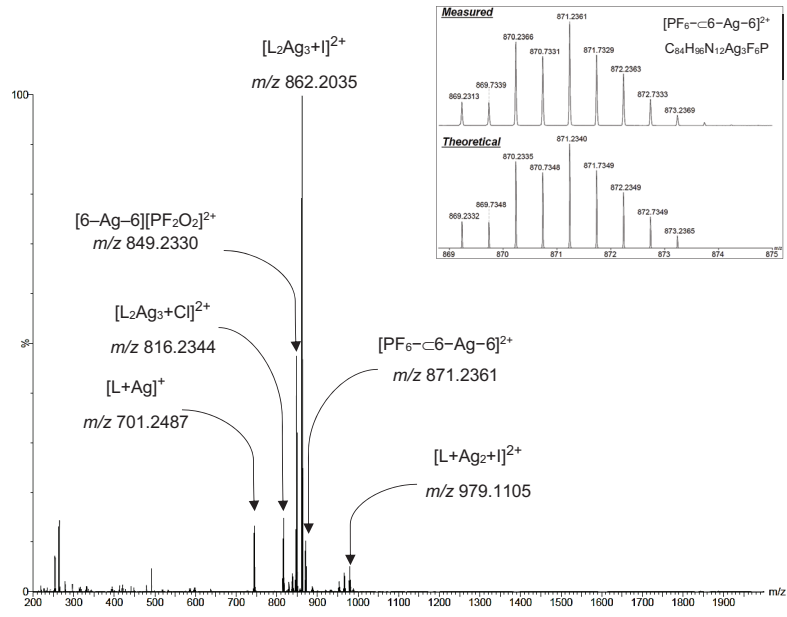


Figure S42. ESI-TOF mass spectrum of $[\text{PF}_6\text{-c6-Ag-6}][\text{PF}_6]_2$. Inset: Isotope pattern of the $[\text{PF}_6\text{-c6-Ag-6}]^{2+}$ ion.

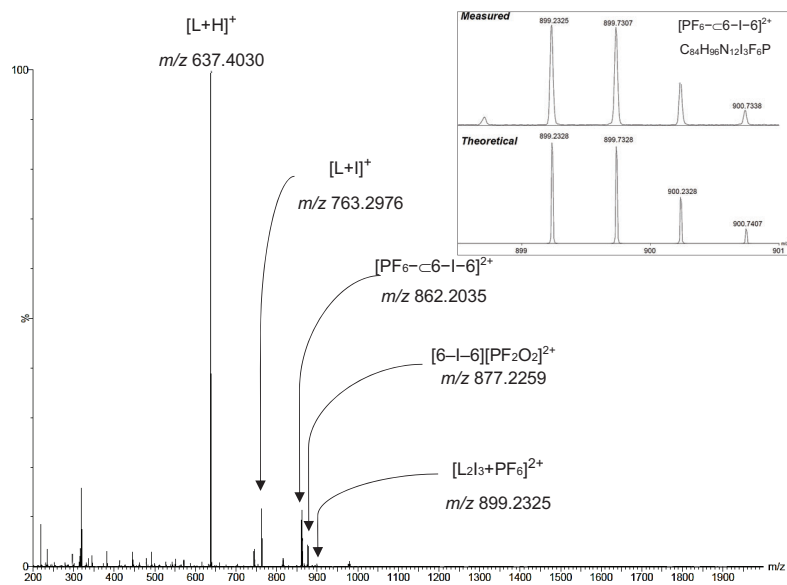


Figure S43. ESI-TOF mass spectrum of $[\text{PF}_6\text{-c6-I-6}][\text{PF}_6]_2$. Inset: Isotope pattern of the $[\text{PF}_6\text{-c6-I-6}]^{2+}$ ion.

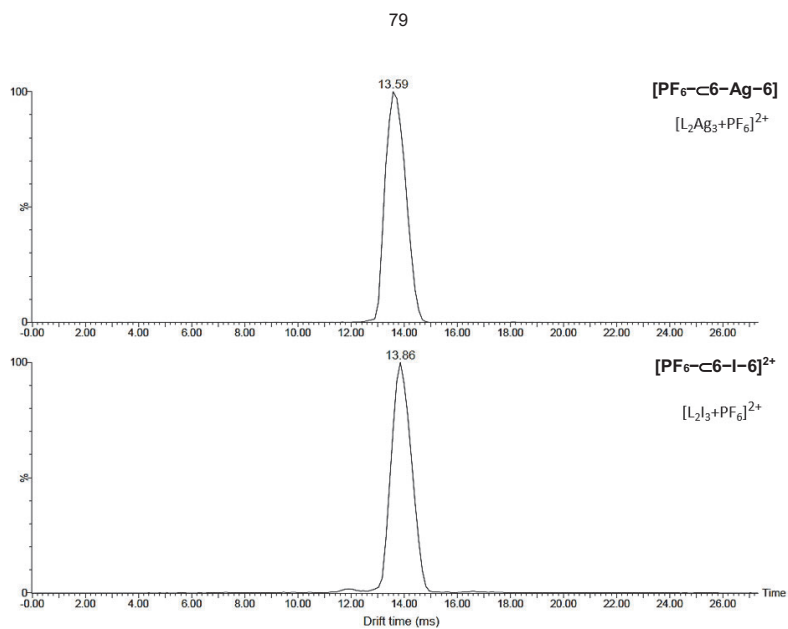


Figure S44. Comparison of arrival time distributions of [PF₆-c6-Ag-6]²⁺ (top) and [PF₆-c6-l-6]²⁺ (bottom).

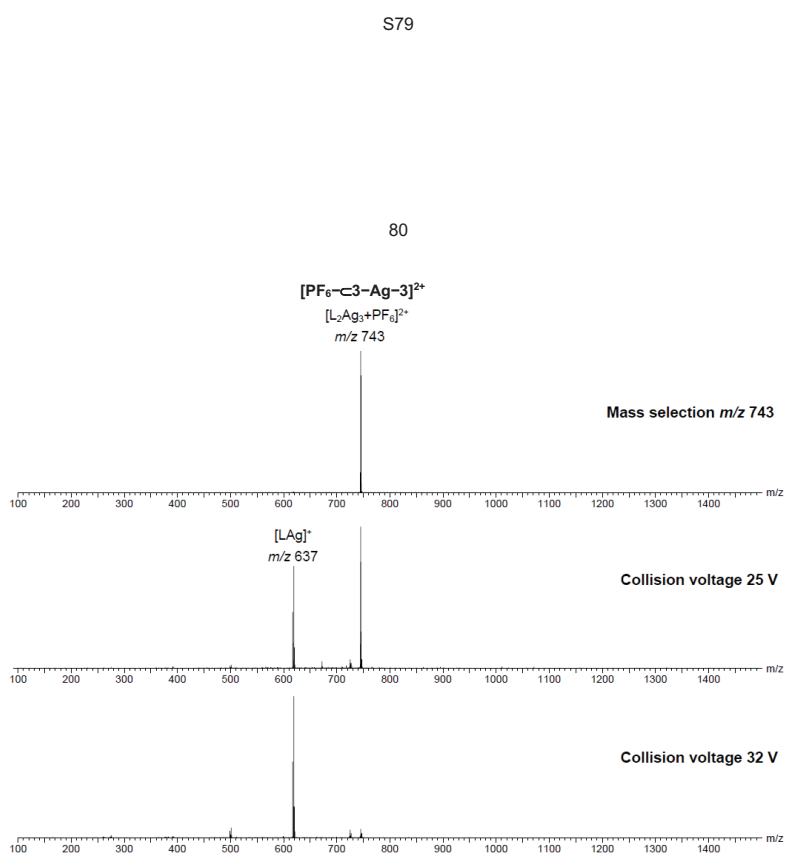


Figure S45. Collision-induced dissociation (CID) spectra of [PF₆-c3-Ag-3]²⁺ with increasing collision energies (from top to bottom). The second expected singly charged fragment, [LAg₂PF₆]⁺, undergoes a rapid subsequent loss of an AgPF₆ ion pair and forms a second [LAg]⁺ ion.

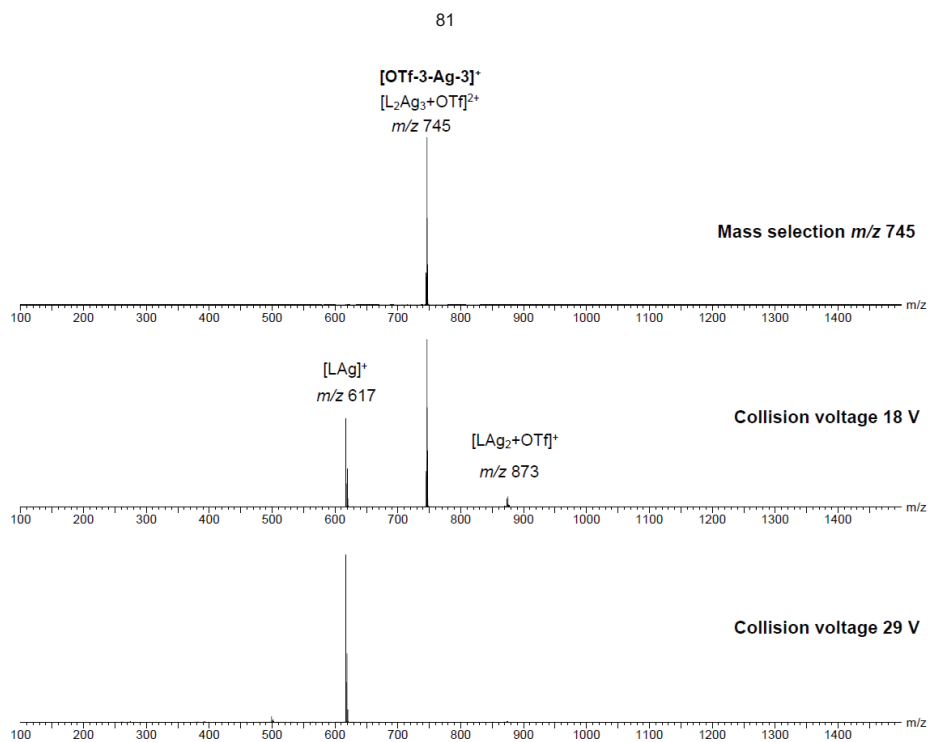


Figure S46. CID spectra of [OTf-3-Ag-3]²⁺ with increasing collision energies (from top to bottom).

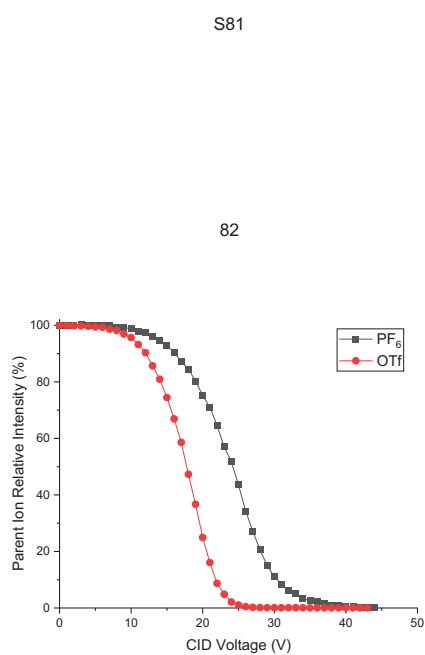


Figure S47. Survivor yield (SY) curve of [Y-3-Ag-3]²⁺ where Y is the respective counterion. The SY shows a greater relative gas-phase stability of [PF₆-3-Ag-3]²⁺ (SY50 = 26 V) compared to [OTf-3-Ag-3]²⁺ (SY50 = 18 V). This is due to the encapsulation of the PF₆ which does not occur for the OTf.

83

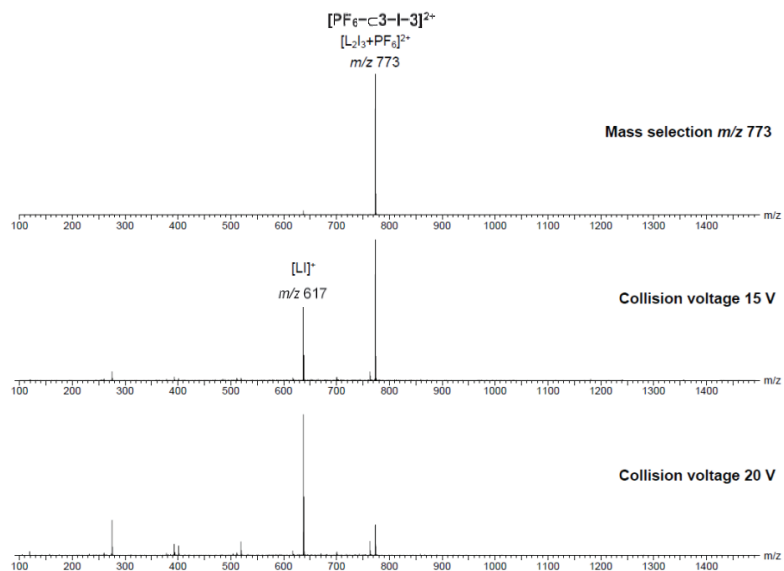


Figure S48. CID spectra of $[\text{PF}_6\text{-c3-I-3}]^{2+}$ with increasing collision energies (from top to bottom). The second expected singly charged fragment, $[\text{L}_2\text{PF}_6]^+$, undergoes a rapid subsequent loss of an IPF_6 ion pair and forms a second $[\text{L}]^+$ ion.

S83

84

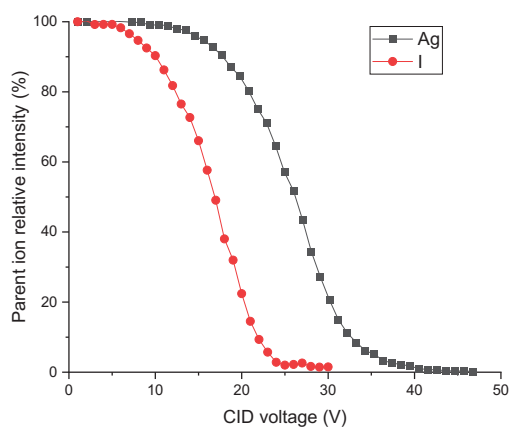


Figure S49. Survivor yield (SY) curve of $[\text{PF}_6\text{-c3-X-3}]^{2+}$ where X is the respective metal. The SY shows a greater relative gas-phase stability of $[\text{PF}_6\text{-c3-Ag-3}]^{2+}$ (SY50 = 26 V) compared to $[\text{PF}_6\text{-c3-I-3}]^{2+}$ (SY50 = 17 V).

S84

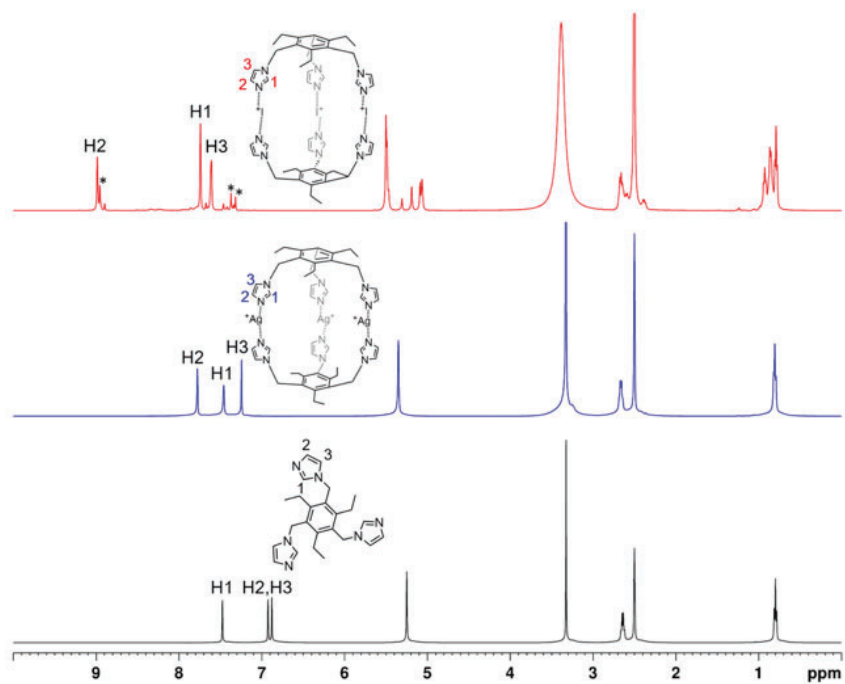
^1H NMR and ^1H - ^{15}N HMBC Spectra of Synthesised Compounds

Figure S50. ^1H NMR spectra of 2, $[\text{PF}_6\text{-c2-Ag-2}][\text{PF}_6]_2$ and $[\text{PF}_6\text{-c2-I-2}][\text{PF}_6]_2$ in $\text{DMSO-}d_6$ (303 K, 500 MHz) with minor incompletely exchanged intermediates or cage dissociation due to interactions with DMSO (*) in the iodine(I) complex.

S85

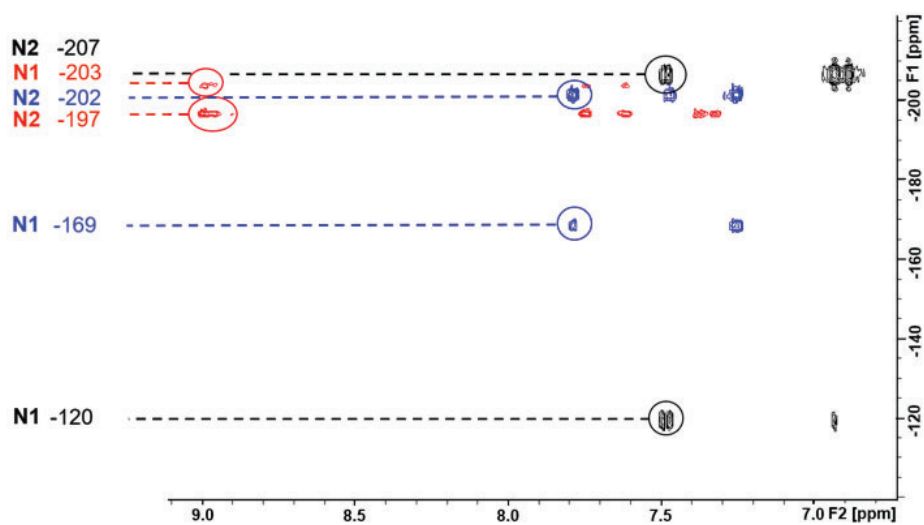


Figure S51. ^1H - ^{15}N HMBC correlation spectra of the uncomplexed 2 (black), the silver complex $[\text{PF}_6\text{-c2-Ag-2}][\text{PF}_6]_2$ (blue) and the iodine(I) complex $[\text{PF}_6\text{-c2-I-2}][\text{PF}_6]_2$ (red) in $\text{DMSO-}d_6$ (303 K, 500 MHz).

S86

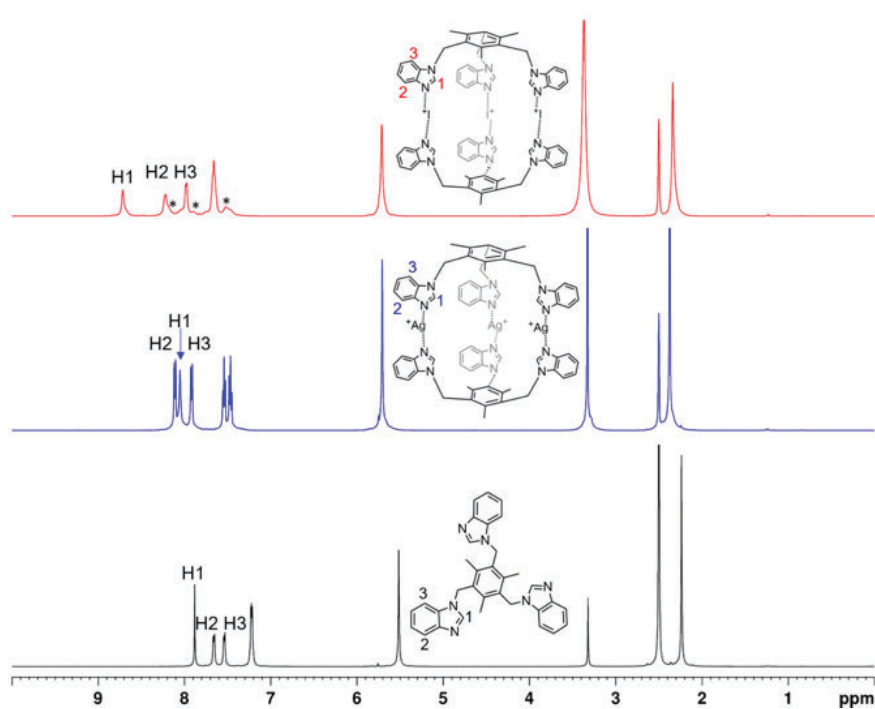


Figure S52. ^1H NMR spectra of 3, $[\text{PF}_6\text{-c3-Ag-3}][\text{PF}_6]_2$ and $[\text{PF}_6\text{-c3-I-3}][\text{PF}_6]_2$ in $\text{DMSO-}d_6$ (303 K, 500 MHz) with minor incompletely exchanged intermediates or cage dissociation due to interactions with DMSO (*) in the iodine(I) complex.

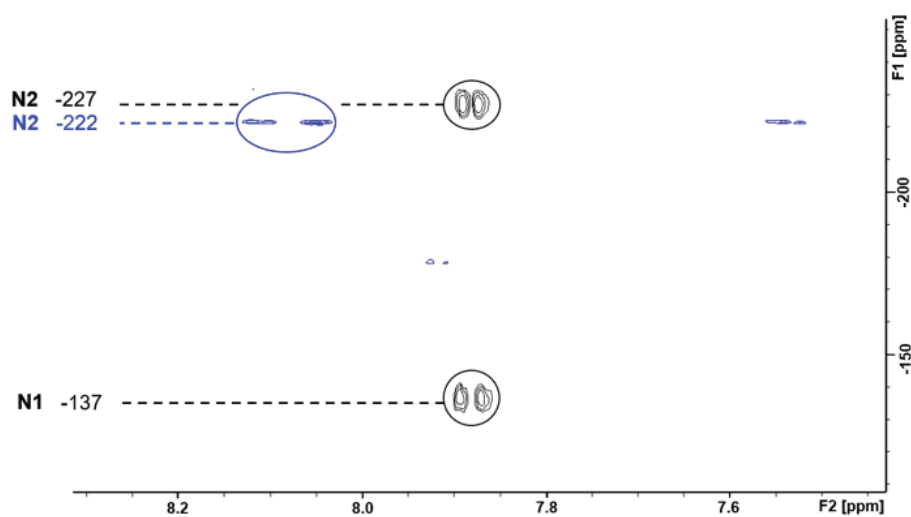


Figure S53. ^1H - ^{15}N HMBC correlation spectra of the uncomplexed 3 (black) and the silver complex $[\text{PF}_6\text{-c3-Ag-3}][\text{PF}_6]_2$ (blue) in $\text{DMSO-}d_6$ (303 K, 500 MHz).

89

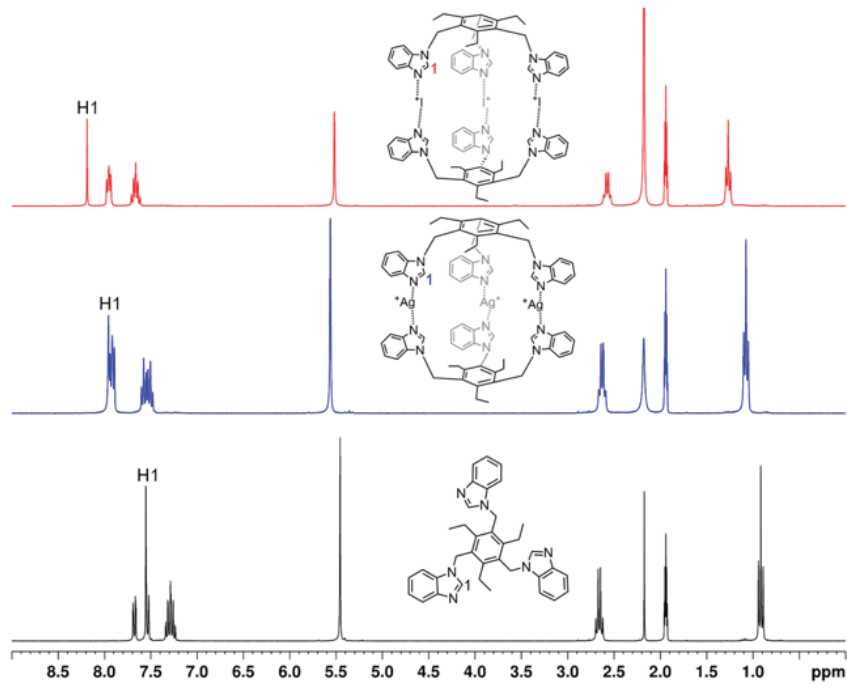


Figure S54. ^1H NMR spectra of **4**, $[\text{PF}_6\text{-c4-Ag-4}][\text{PF}_6]_2$ and $[\text{PF}_6\text{-c4-I-4}][\text{PF}_6]_2$ in CD_3CN (303 K, 500 MHz).

S89

90

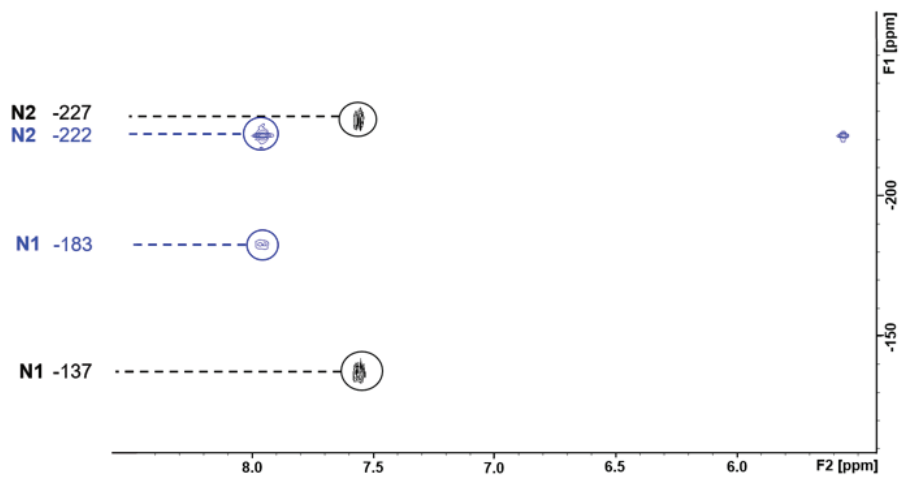


Figure S55. ^1H - ^{15}N HMBC correlation spectra of the uncomplexed **4** (black) and the silver complex $[\text{PF}_6\text{-c4-Ag-4}][\text{PF}_6]_2$ (blue) in CD_3CN (303 K, 500 MHz).

S90

91

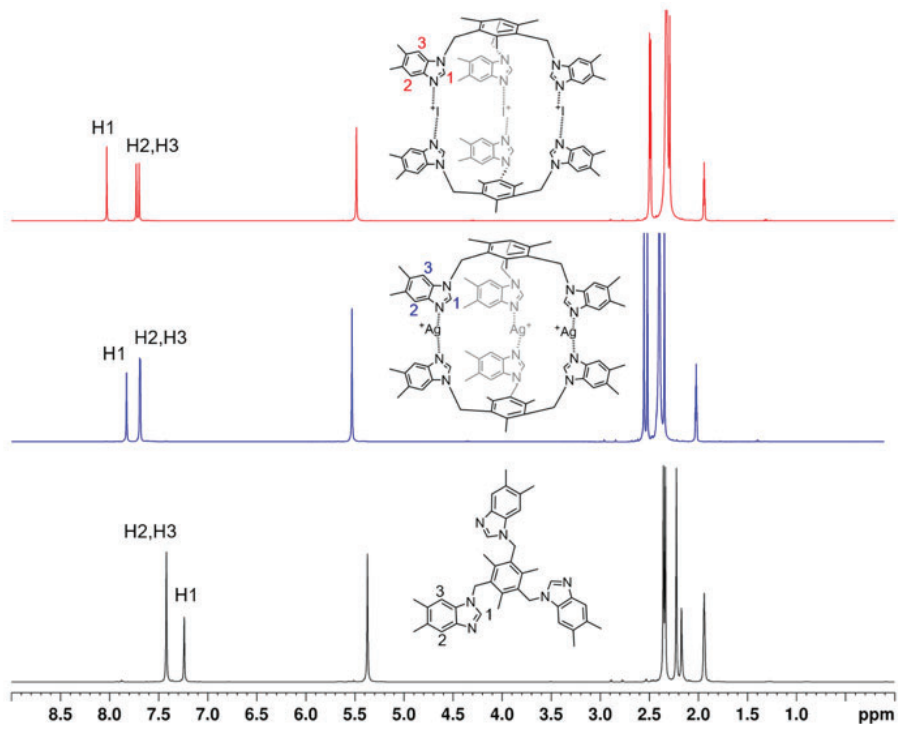


Figure S56. ¹H NMR spectra of 5, [PF₆-c5-Ag-5][PF₆]₂ and [PF₆-c5-I-5][PF₆]₂ in CD₃CN (303 K, 500 MHz).

S91

92

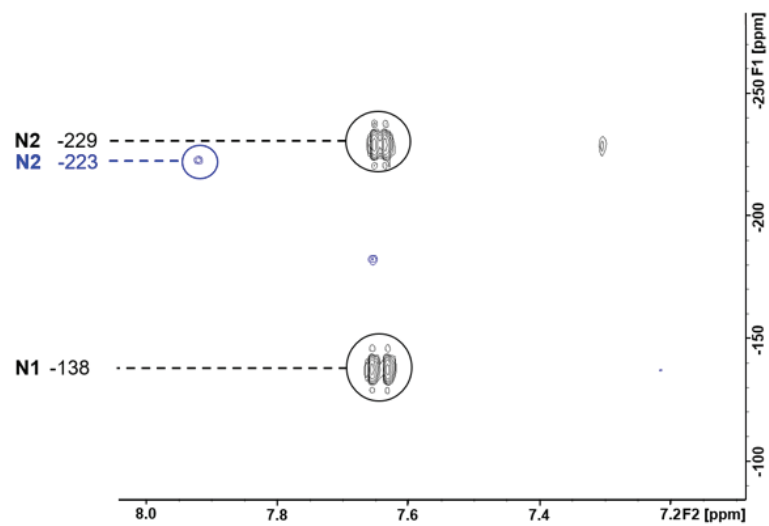


Figure S57. ¹H-¹⁵N HMBC correlation spectra of the uncomplexed 5 (black) and the silver complex [PF₆-c5-Ag-5][PF₆]₂ (blue) in CD₃CN (303 K, 500 MHz).

S92

93

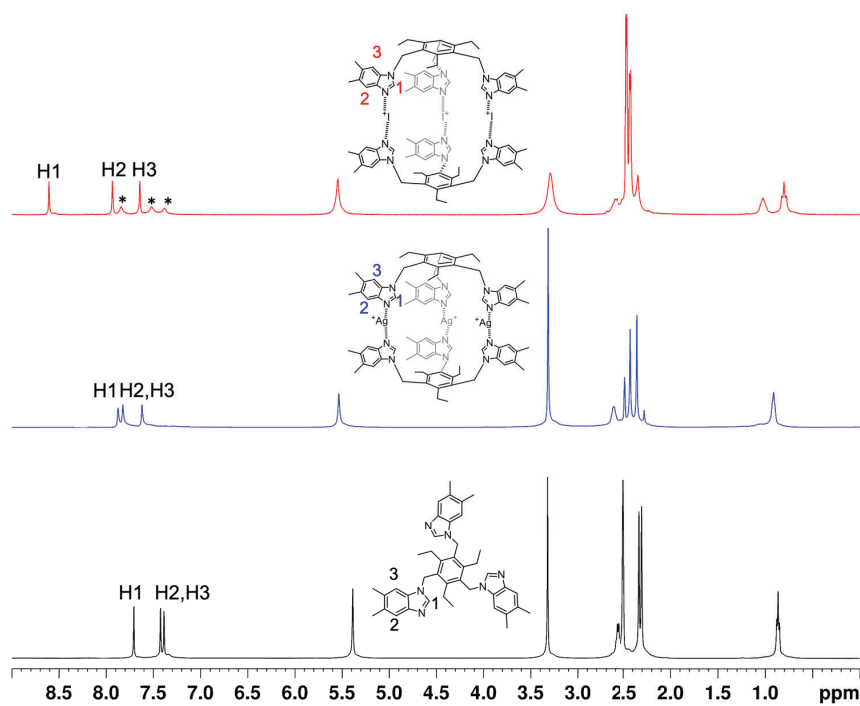


Figure S58. ^1H NMR spectra of **6**, $[\text{PF}_6\text{-c6-Ag-6}][\text{PF}_6]_2$ and $[\text{PF}_6\text{-c6-I-6}][\text{PF}_6]_2$ in $\text{DMSO-}d_6$ (303 K, 500 MHz) with minor incompletely exchanged intermediates or cage dissociation due to interactions with DMSO (*) in the iodine(I) complex.

S93

94

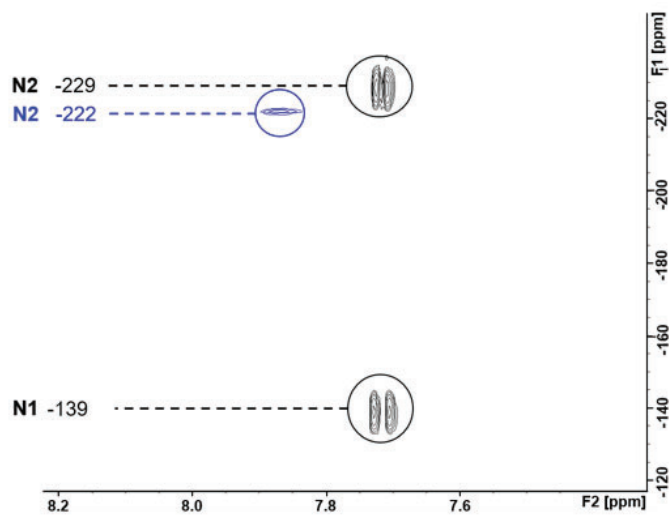


Figure S59. ^1H - ^{15}N HMBC correlation spectra of the uncomplexed **6** (black) and the silver complex $[\text{PF}_6\text{-c6-Ag-6}][\text{PF}_6]_2$ (blue) in $\text{DMSO-}d_6$ (303 K, 500 MHz).

S94

^{19}F NMR Spectra of Selected Compounds

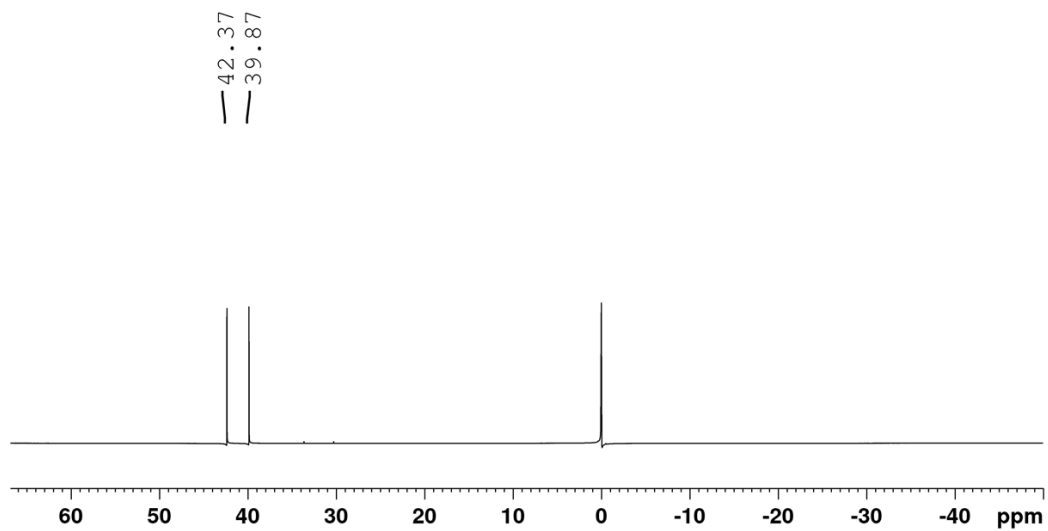


Figure S60. The ^{19}F NMR spectrum of AgPF_6 in CD_3CN . All values are in ppm and referenced to an internal standard of $\text{C}_6\text{H}_5\text{F}$ (303K, 282.39 MHz).

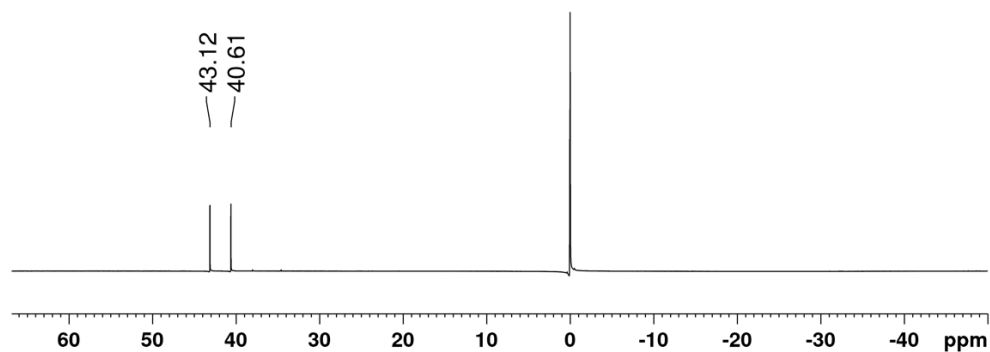


Figure S61. The ^{19}F NMR spectrum of $[\text{PF}_6\text{-c5-Ag-5}[\text{PF}_6]_2]$ in CD_3CN . All values are in ppm and referenced to an internal standard of $\text{C}_6\text{H}_5\text{F}$ (303 K, 282.39 MHz).

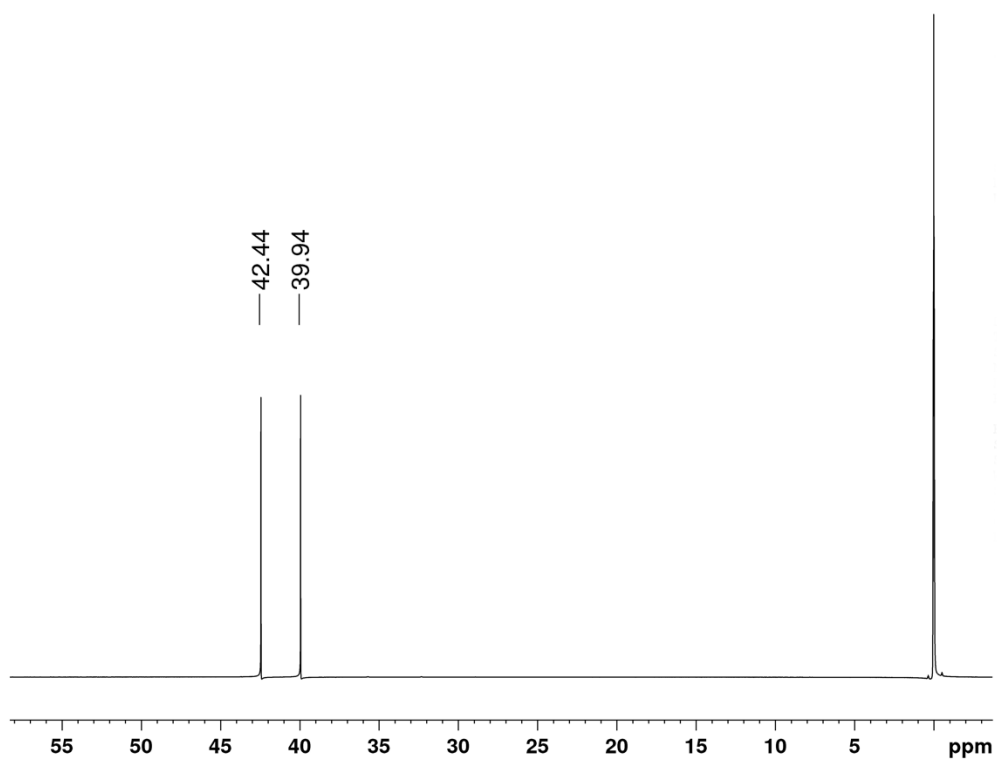


Figure S62. The ^{19}F NMR spectrum of $[\text{PF}_6\text{-C5-I-5}][\text{PF}_6]_2$ in CD_3CN . All values are in ppm and referenced to an internal standard of $\text{C}_6\text{H}_5\text{F}$ (303 K, 282.39 MHz).

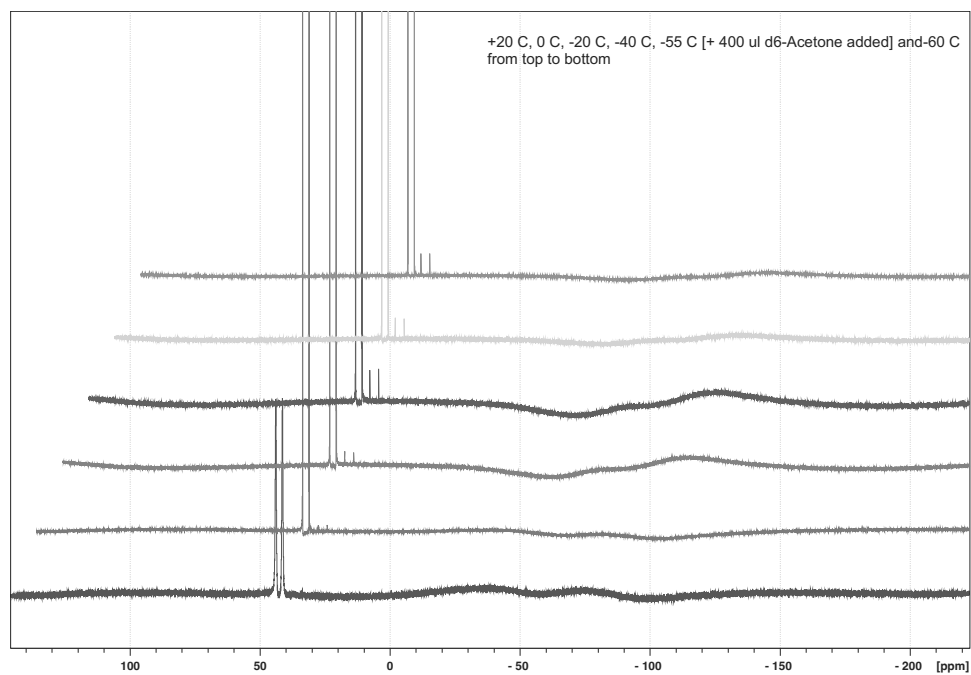


Figure S63. The ^{19}F NMR spectra of $[\text{PF}_6\text{-c5-I-5}][\text{PF}_6]_2$ in CD_3CN with variable temperature. All values are in ppm and referenced to an internal standard of $\text{C}_6\text{H}_5\text{F}$ (282.39 MHz).

S97

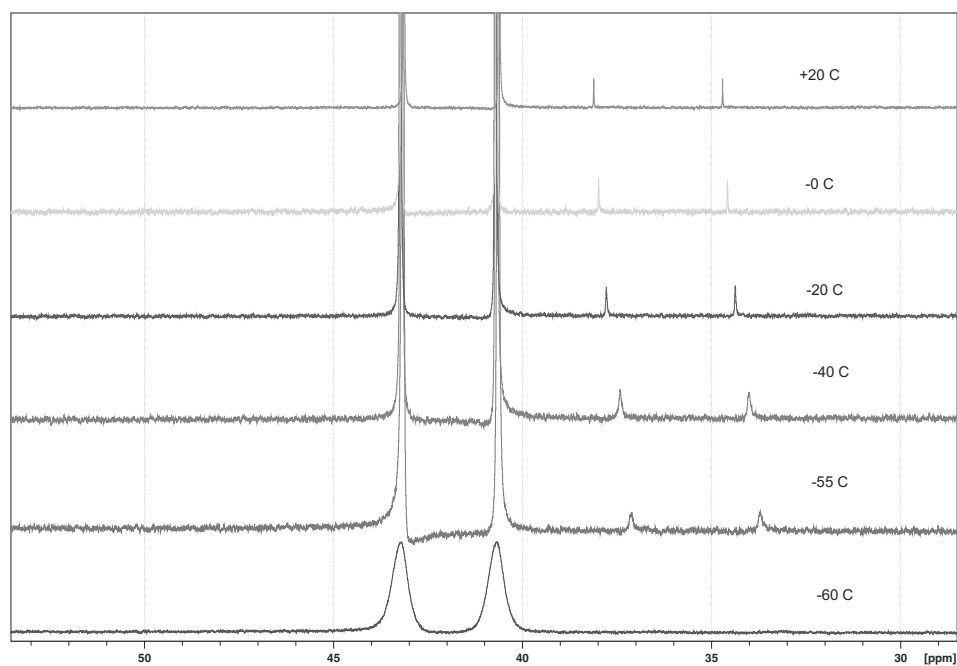


Figure S64. The ^{19}F NMR spectra of $[\text{PF}_6\text{-c5-I-5}][\text{PF}_6]_2$ in CD_3CN with variable temperature (and added acetone- d_6). All values are in ppm and referenced to an internal standard of $\text{C}_6\text{H}_5\text{F}$ (282.39 MHz). The larger peaks are overlaid to show the change of the relative position of the smRealler peaks.

S98

References

- ¹ Y. Yuan, Z.-L. Jiang, J.-M. Yan, G. Gao, A. S. C. Chan, R.-G. Xie, *Synth. Commun.* 2000, **30**(24), 4555.
- ² W.-Y. Sun, J. Fan, T.-A. Okamura, J. Xie, K.-B. Yu, N. Ueyama, *Chem. Eur. J.*, 2001, **7**, 2557.
- ³ H.-K. Liu, X. Huang, T. Lu, X. Wang, W.-Y. Sun, B.-S. Kang, *Dalton Trans.*, 2008, 3178.
- ⁴ *CrysAlisPro*, 2014, v 1.171.36.35; Agilent Technologies, Ltd, Yarton, UK.
- ⁵ G. M. Sheldrick, *Acta Crystallogr. Sect. A*, 2015, **71**, 3.
- ⁶ O. V Dolomanov, L. J. Bourhis, R. J. Gildea, J. A. K. Howard and H. Puschmann, *J. Appl. Crystallogr.*, 2009, **42**, 339.
- ⁷ G. M. Sheldrick, *Acta Crystallogr. Sect. C*, 2015, **71**, 3.
- ⁸ M. A. Spackman, D. Jayatilaka, *CrystEngComm*, 2009, **11**, 19.
- ⁹ P. R. Spackman, M. J. Turner, J. J. McKinnon, S. K. Wolff, D. J. Grimwood, D. Jayatilaka, M. A. Spackman, *J. Appl. Cryst.*, 2021, **54**, 1006.
- ¹⁰ SPARTAN'18, Wavefunction Inc, Irvine, Ca 92612, USA, 2018.


 Cite this: *Chem. Commun.*, 2023, 59, 11811

 Received 31st August 2023,
 Accepted 12th September 2023

DOI: 10.1039/d3cc04291j

rsc.li/chemcomm

Binding modes of high stoichiometry guest complexes with a Co_8L_{12} cage uncovered by mass spectrometry†

 Daniel L. Stares,^{‡a} Cristina Mozaceanu,^{‡b} Michael D. Ward^{*,b} and Christoph A. Schalley^{*,a}

We demonstrate how different modes of guest binding with a Co_8L_{12} cubic cage can be determined using ESI-MS. High stoichiometry guest binding was observed, with the guests preferentially binding externally, but internal guest inclusion was also seen at higher guest loading.

Self-assembled metal–organic cages are some of the most sophisticated and complex synthetic host structures.^{1,2} Characterisation of these hosts typically relies on either NMR or X-ray crystallography with it being less common to utilise mass spectrometry (MS) for structural analysis. MS has the general benefits that an ion of interest can be mass-selected, so it does not require completely pure samples; it is highly sensitive and data can be obtained relatively quickly.³ For self-assembled systems more specifically, MS has the added advantage that it deals with isolated ions, free from any competitive solvent, and as such, any dynamic exchange processes which can complicate characterisation in solution are absent.⁴ Because of this, the mass-to-charge ratio (m/z) of an ion easily furnishes a system's stoichiometry which can be especially useful when studying host–guest systems capable of binding multiple guest molecules.^{5,6} Beyond stoichiometry, structural information such as guest binding mode can be gained through tandem MS techniques such as ion-mobility mass spectrometry (IMS) and collision-induced dissociation (CID).^{7–10} IMS separates ions based on their size and can thus distinguish isomers that vary due to different isomeric ligands, guest binding position and even diastereomeric composition of the cage.^{11–15} CID is a dissociation technique, where ions are collided with a neutral buffer gas to induce fragmentation and can be used to probe

structural features of the cage as well as guest binding modes.^{16–18}

The Co_8L_{12} cubic cage ($\text{H}^{\text{W}}\text{Co}$) (Fig. 1), based on hydroxymethyl-substituted bis-bidentate ligands (L^{W}) which span the edges of an approximately cubic array of $\text{Co}(\text{II})$ ions, can bind guests internally and externally and is also capable of binding multiple guests.^{19–22} However, multiple guest binding has only been demonstrated using X-ray crystallography and NMR spectroscopy under forcing conditions with a large excess of guest.^{19–21} Detailed MS studies, which are well suited to studying higher stoichiometry guest binding, have currently not been performed. Herein, a combination of IMS and CID experiments were used to investigate the host–guest properties of $\text{H}^{\text{W}}\text{Co}$, particularly to uncover its multiple guest binding capabilities. The results serve as a further case study of the benefit of MS in the study of host–guest chemistry of metal–organic cages especially by allowing observation of different binding modes.

$\text{H}^{\text{W}}\text{Co}$ ionises through loss of BF_4^- counterions generating charge states from 5+ to 10+ (Fig. 2). Additionally, some

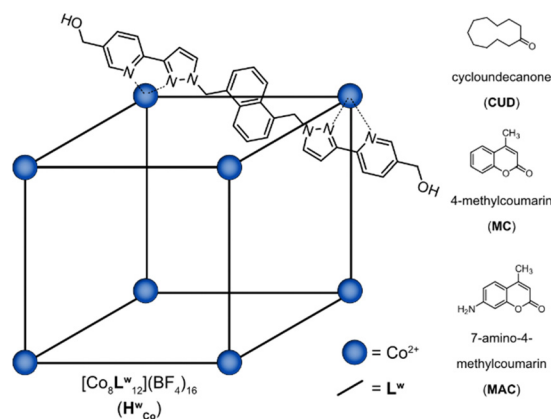


Fig. 1 Structure of the $\text{H}^{\text{W}}\text{Co}$ cage and the guests used in the current study.

^a Institut für Chemie und Biochemie, Freie Universität Berlin, Arnimallee 20, Berlin, 14195, Germany. E-mail: c.schalley@fu-berlin.de

^b Department of Chemistry, University of Warwick, Coventry CV4 7AL, UK. E-mail: m.d.ward@warwick.ac.uk

† Electronic supplementary information (ESI) available: Sample preparation, instrumental parameters, computational details and additional figures. See DOI: <https://doi.org/10.1039/d3cc04291j>

‡ Authors contributed equally.



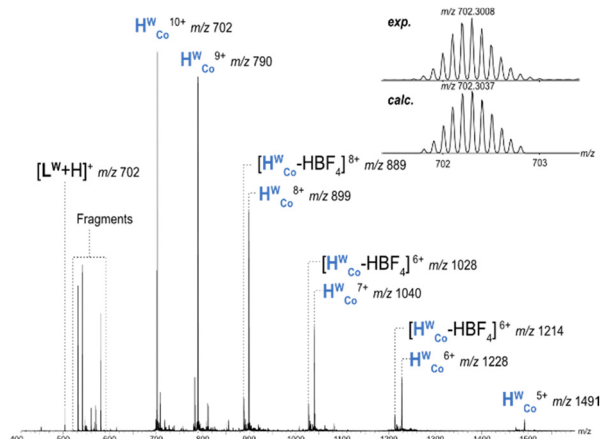


Fig. 2 ESI-MS spectrum of 10 μM $\text{H}^{\text{W}}_{\text{Co}}$ in H_2O , the 10+ to 5+ cage charge states are marked. Fragmentation products and cage species resulting from the loss of HBF_4 are also observed. The experimental vs. calculated m/z values for $\text{H}^{\text{W}}_{\text{Co}}^{10+}$ are shown in the inset.

fragment ions were present and a loss of neutral HBF_4 (likely as HF and BF_3) was also observed for charge states 5+ to 9+. The charge state distribution could be shifted towards higher charges by increasing the capillary voltage, but cage fragmentation became more pronounced and charge states over 10+ were still not observed (Fig. S1, ESI †). This indicates that charge states over 10+ are not stable enough to survive in the instrument with the six counterions necessary to counterbalance the charge repulsion within the cage. X-ray crystal structures of $\text{H}^{\text{W}}_{\text{Co}}$ show discrete binding of six counterions in the portals of the faces which will significantly reduce charge repulsion of the cage as these counterions are surrounded by four metal centres and their respective charges.^{23,24} The removal of these six counterions during ionisation would thus be more difficult

than peripherally bound ones requiring higher capillary voltages to do so, and, if successfully removed, would lead to significant destabilisation.²⁵ The interplay of these two factors can explain why charge states greater than 10+ are not observed. CID of the cage showed fragmentation into face, corner and edge fragments, (Fig. S2 and S3, ESI †) but overall, the cage is relatively stable, considering the charge state, with $\text{H}^{\text{W}}_{\text{Co}}^{10+}$ surviving until a collision voltage of 8 V (Fig. S4, ESI †).

The host-guest chemistry of $\text{H}^{\text{W}}_{\text{Co}}$ was then explored with guests whose binding has been studied in solution and the solid state: cycloundecanone (CUD); 4-methylcoumarin (MC); and 7-amino-4-methylcoumarin (MAC) (Fig. 1). CUD has been shown to bind strongly inside the cavity of $\text{H}^{\text{W}}_{\text{Co}}$ in water driven by the hydrophobic effect with a 1:1 $\text{H}^{\text{W}}_{\text{Co}}/\text{CUD}$ stoichiometry.²⁶ In contrast, it has been shown that multiple guest binding is possible when MC and MAC are used as guests.¹⁹ Accordingly, a 1:1 $\text{H}^{\text{W}}_{\text{Co}}/\text{CUD}$ complex was observed in the mass spectrum with no evidence of multiple guests binding (Fig. S5, ESI †) whilst for MC, small signals for the 1:2 complex were seen in addition to the 1:1 $\text{H}^{\text{W}}_{\text{Co}}/\text{MC}$ complex (Fig. S6, ESI †). With MAC, strong signals were observed for $\text{H}^{\text{W}}_{\text{Co}}/(1-4)\text{MAC}$ complexes with even higher host:guest stoichiometries also seen albeit at lower signal intensities (Fig. 3a and Fig. S7, ESI †). The results for CUD and MC are consistent with what has previously been observed in solution and the solid state but the higher stoichiometries associated with MAC binding are observed for the first time.

For all three guests, CID of the 1:1 $\text{H}^{\text{W}}_{\text{Co}}/\text{Guest}(\text{G})^{8+}$ species resulted in complete guest loss to the free $\text{H}^{\text{W}}_{\text{Co}}^{8+}$ at low collision voltages before further fragmentation of $\text{H}^{\text{W}}_{\text{Co}}^{8+}$ as seen for the free cage (Fig. S3, S4 and S8-S10, ESI †). Although a lower charge state was mass-selected to reduce Coulomb repulsion and instrument conditions were softened as much as

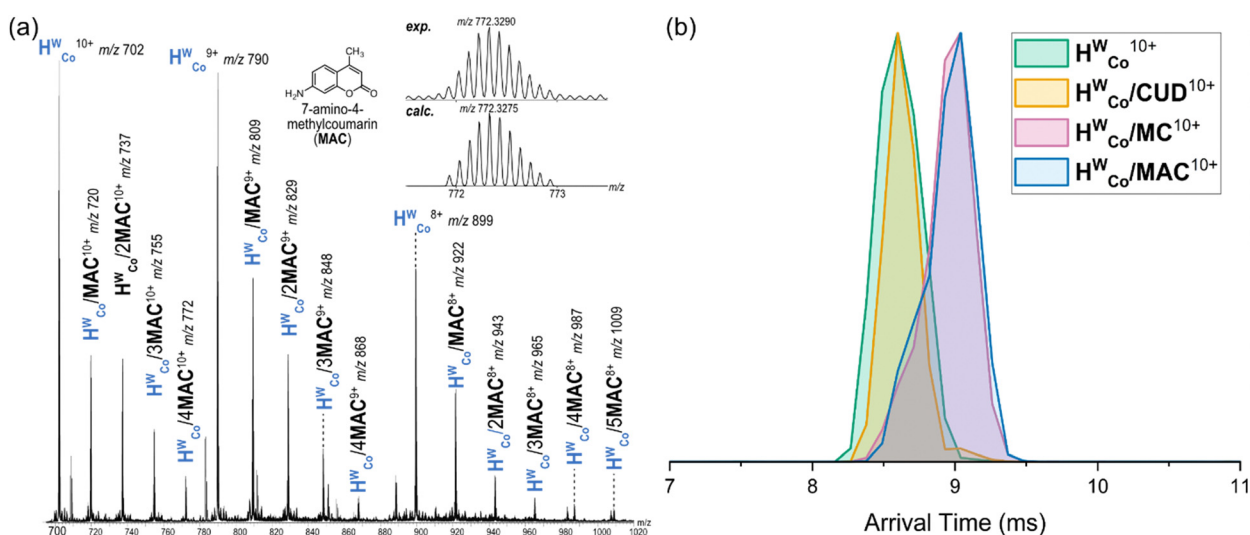


Fig. 3 (a) ESI-HRMS spectrum of $\text{H}^{\text{W}}_{\text{Co}}$ with MAC (10 $\mu\text{M}/50 \mu\text{M}$) in 5% $\text{CH}_3\text{OH}/\text{H}_2\text{O}$. Multiple guest binding stoichiometries with up to 5 MACs bound are observed. The experimental vs. calculated m/z values for the $\text{H}^{\text{W}}_{\text{Co}}/4\text{MAC}^{10+}$ are shown in the inset (b) ATDs of $\text{H}^{\text{W}}_{\text{Co}}^{10+}$, $\text{H}^{\text{W}}_{\text{Co}}/\text{CUD}^{10+}$, $\text{H}^{\text{W}}_{\text{Co}}/\text{MC}^{10+}$, $\text{H}^{\text{W}}_{\text{Co}}/\text{MAC}^{10+}$. The ATDs of $\text{H}^{\text{W}}_{\text{Co}}^{10+}$ and $\text{H}^{\text{W}}_{\text{Co}}/\text{CUD}^{10+}$ overlap indicating encapsulation whilst $\text{H}^{\text{W}}_{\text{Co}}/\text{MC}^{10+}$ and $\text{H}^{\text{W}}_{\text{Co}}/\text{MAC}^{10+}$ have longer arrival times consistent with external binding.



possible, a portion of empty cage was still observed after mass selection of $\text{H}^{\text{W}}_{\text{Co}}/\text{G}^{8+}$ ions without additional collision voltages applied. This means that some guest dissociation can occur just from transmission through the instrument. The relative intensities of $\text{H}^{\text{W}}_{\text{Co}}/\text{CUD}^{8+}$ and $\text{H}^{\text{W}}_{\text{Co}}/\text{MAC}^{8+}$ (71 and 77%, respectively) after mass selection are considerably higher than that for $\text{H}^{\text{W}}_{\text{Co}}/\text{MC}^{8+}$ (47%) meaning that higher proportions of the CUD and MAC complexes survive transmission through the instrument (Fig. S11, ESI[†]). Complete guest loss was observed at low collision voltages with all guests but as the $\text{H}^{\text{W}}_{\text{Co}}/\text{G}$ complexes do not represent 100% of the total intensity after mass selection, it is not possible to complete a full survival yield analysis to determine relative stabilities of the guests. Thus, no reasonable conclusion about the stabilities of the host:guest complexes can be drawn other than that all three guests are lost at similar collision voltages.

IMS of the different 1 : 1 $\text{H}^{\text{W}}_{\text{Co}}/\text{G}$ complexes showed comparable arrival times for $\text{H}^{\text{W}}_{\text{Co}}^{10+}$ and $\text{H}^{\text{W}}_{\text{Co}}/\text{CUD}^{10+}$ with longer arrival times for $\text{H}^{\text{W}}_{\text{Co}}/\text{MC}^{10+}$ and $\text{H}^{\text{W}}_{\text{Co}}/\text{MAC}^{10+}$ (Fig. 3b). A straightforward explanation of these results is that CUD is encapsulated in the central cavity of $\text{H}^{\text{W}}_{\text{Co}}$ as seen in crystal structures,²⁶ and hence does not contribute significantly to the collisional cross section (CCS) of the cage ion, whereas both MC and MAC are bound to the external cage surface increasing the CCS and hence arrival times. Although a comparison of absolute CCS values is difficult due to a lack of suitable calibrants and issues with the theoretical calculations for metal-organic complexes,²⁷ relative comparisons of theoretical CCS values are still insightful as any errors cancel each other out. Here, theoretical CCS values using the trajectory method ($^{\text{TM}}\text{CCS}_{\text{N}_2}$) were calculated for universal force field (UFF) optimised structures of $\text{H}^{\text{W}}_{\text{Co}}^{10+}$ and $\text{H}^{\text{W}}_{\text{Co}}/\text{G}^{10+}$ with the different guests.^{28,29} They supported the above assessment by showing the same general results as the IMS with very similar $^{\text{TM}}\text{CCS}_{\text{N}_2}$ values for $\text{H}^{\text{W}}_{\text{Co}}^{10+}$ and $\text{H}^{\text{W}}_{\text{Co}}/\text{CUD}^{10+}$ when the CUD was encapsulated; with increases in the $^{\text{TM}}\text{CCS}_{\text{N}_2}$ values of $\text{H}^{\text{W}}_{\text{Co}}/\text{MC}^{10+}$ and $\text{H}^{\text{W}}_{\text{Co}}/\text{MAC}^{10+}$ with MAC and MC binding externally *via* hydrogen bonding with L^{W} (Fig. S12, ESI[†]). Thus, the IMS experiments strongly support encapsulation of CUD in the host cavity, with external binding of MAC and MC for the 1 : 1 stoichiometries.

Encapsulation of CUD in solution is driven by the hydrophobic effect which is not present in the gas-phase and thus CUD complexes may be expected to not be observed *via* MS. However, CUD is capable of $=\text{O} \cdots \text{H}-\text{C}$ hydrogen bonds in the *fac* tris-chelate pocket of the cavity and guest loss would also be partially prevented by the counterions in the face-portals increasing the dissociation barrier and enabling a significant amount of the CUD complex to survive after ionisation.²⁶ External binding of MC likely involves $=\text{O} \cdots \text{H}-\text{O}$ hydrogen bonds with the hydroxy groups of L^{W} . Compared to MC, the presence of the aniline in MAC would enable it to form an additional $\text{O}-\text{H} \cdots \text{NH}_2$ hydrogen bond with the corner of the cage. Computational models at the B97-3c level of theory implemented in the Orca program shows that both *mer* and *fac* corner units of $\text{H}^{\text{W}}_{\text{Co}}$ are ideally suited to accommodate two

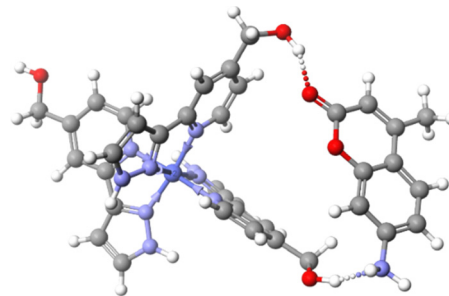


Fig. 4 Binding mode of MAC with two L^{W} in a *mer* tris-chelate corner of $\text{H}^{\text{W}}_{\text{Co}}$. Structure was optimised at the B97-3c level of theory.

hydrogen bonds with MAC (Fig. 4 and Fig. S13, ESI[†]).^{30–32} The aniline might also enable ion pairing by deprotonating the OH to give $\text{R}-\text{NH}_3^+ \cdots \text{O}-\text{R}'^-$ interactions. These additional interactions available to MAC could potentially explain the higher stoichiometry complexes not observed for the other guests. Furthermore, the binding modes of MC and MAC *via* hydrogen bonding with the cage exterior also justify the difficulty in observing the complexes in solution as those measurements are performed in competitive solvents such as H_2O where cavity binding dominates due to the hydrophobic effect.¹⁹

The arrival time distributions (ATD) of the $\text{H}^{\text{W}}_{\text{Co}}/n\text{MAC}^{10+}$ complexes show increasing arrival times with increasing n but also show shoulder regions at earlier arrival times which increase in magnitude with additional MACs until clear double peaks are seen in the ATDs of $\text{H}^{\text{W}}_{\text{Co}}/3\text{MAC}^{10+}$ and $\text{H}^{\text{W}}_{\text{Co}}/4\text{MAC}^{10+}$ (Fig. 5a). This can be explained by two concurrent binding modes: one where all MAC are bound externally and the other where one MAC has been encapsulated. The increasing proportion of encapsulated MAC at higher guest loading indicates that it preferentially binds externally but at high enough guest loading, probability will dictate that one will be encapsulated. The ATDs show that the contribution coming from the binding mode with one MAC encapsulated is slightly larger than the lower stoichiometry with all guests bound externally (*e.g.* $\text{H}^{\text{W}}_{\text{Co}}/3\text{MAC}^{10+}$ with one MAC encapsulated is slightly larger than the $\text{H}^{\text{W}}_{\text{Co}}/2\text{MAC}^{10+}$ with all MAC bound externally), whereas $\text{H}^{\text{W}}_{\text{Co}}^{10+}$ and $\text{H}^{\text{W}}_{\text{Co}}/\text{CUD}^{10+}$ overlap (Fig. 3b). This could reflect the better fit of the conformationally flexible CUD, whereas encapsulation of the more rigid MAC and MC likely leads to some expansion of the cage which is reflected in the longer arrival times.

It should be noted that due to the facile guest loss, the observed ions could well be derived from higher guest stoichiometry complexes which have subsequently undergone guest loss in the instrument. Energy-resolved IMS can study this by performing CID in the trap cell prior to IMS and monitoring the changes in the ATDs allowing an assessment of the stability of different binding modes.³³ Measurements with mass selected $\text{H}^{\text{W}}_{\text{Co}}/4\text{MAC}^{10+}$ led to dissociation of MAC to form $\text{H}^{\text{W}}_{\text{Co}}/3\text{MAC}^{10+}$. When comparing the ATD of the 'free' $\text{H}^{\text{W}}_{\text{Co}}/3\text{MAC}^{10+}$ (mass selected from full spectrum) it showed that the $\text{H}^{\text{W}}_{\text{Co}}/3\text{MAC}^{10+}$ formed purely from dissociation of the $\text{H}^{\text{W}}_{\text{Co}}/4\text{MAC}^{10+}$ only had one major contribution in the ATD which



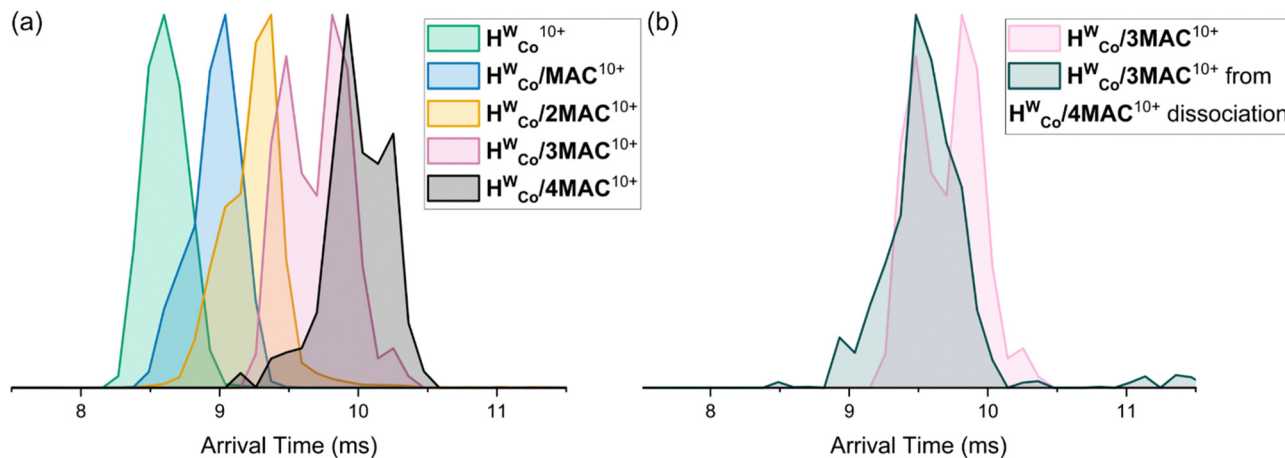


Fig. 5 (a) ATDs of $\text{H}^{\text{W}}_{\text{Co}}/n\text{MAC}^{10+}$ with $n = 1-4$. (b) ATDs of 'free' $\text{H}^{\text{W}}_{\text{Co}}/3\text{MAC}^{10+}$ and $\text{H}^{\text{W}}_{\text{Co}}/3\text{MAC}^{10+}$ formed purely from dissociation of $\text{H}^{\text{W}}_{\text{Co}}/4\text{MAC}^{10+}$.

correlated to the earlier contribution of that of the 'free' $\text{H}^{\text{W}}_{\text{Co}}/3\text{MAC}^{10+}$ (Fig. 5b). This means that externally bound guests dissociate more easily than internally bound ones even though encapsulation occurs less readily.

In conclusion, the MS techniques of IMS and CID were used to study a Co_8L_{12} cubic cage and its host-guest properties with three different guests. The studies demonstrated a major stabilising effect of the counterions binding in the faces of the portals. The host-guest properties of the cage showed that guests had different preferences for external or internal binding. Higher stoichiometries of guest binding, which have not been seen with other techniques, were observed and investigated. These showed that MAC preferentially binds externally but could also be driven inside the cavity at high guest loading. These results demonstrate the ability of MS to investigate metal-organic hosts and probe guest binding modes.

We thank the European Union through the NOAH project (H2020-MSCA-ITN project Ref. 765297) and FU Berlin for funding. Support for measurements by the BioSupraMol core facility at FU Berlin is gratefully acknowledged. Thank you to those at Warwick for help with cage synthesis.

Conflicts of interest

There are no conflicts to declare.

Notes and references

- 1 F. J. Rizzuto, L. K. S. von Krbeke and J. R. Nitschke, *Nat. Rev. Chem.*, 2019, **3**, 204–222.
- 2 D. Fujita, Y. Ueda, S. Sato, N. Mizuno, T. Kumasaka and M. Fujita, *Nature*, 2016, **540**, 563–566.
- 3 C. A. Schalley, *Mass Spectrom. Rev.*, 2001, **20**, 253–309.
- 4 Z. Qi, T. Heinrich, S. Moorthy and C. A. Schalley, *Chem. Soc. Rev.*, 2015, **44**, 515–531.
- 5 A. J. McConnell, *Chem. Soc. Rev.*, 2022, **51**, 2957–2971.
- 6 W. Meng, B. Breiner, K. Rissanen, J. D. Thoburn, J. K. Clegg and J. R. Nitschke, *Angew. Chem., Int. Ed.*, 2011, **50**, 3479–3483.
- 7 H. Wang, C. Guo and X. Li, *CCS Chem.*, 2021, **4**, 785–808.
- 8 E. Kalenius, M. Groessel and K. Rissanen, *Nat. Rev. Chem.*, 2019, **3**, 4–14.

- 9 C. Vicent, V. Martinez-Agramunt, V. Gandhi, C. Larriba-Andaluz, D. G. Gusev and E. Peris, *Angew. Chem., Int. Ed.*, 2021, **60**, 15412–15417.
- 10 K. J. Endres, K. Barthelmes, A. Winter, R. Antolovich, U. S. Schubert and C. Wesdemiotis, *Rapid Commun. Mass Spectrom.*, 2020, **34**, e8717.
- 11 K. E. Ebbert, L. Schneider, A. Platzek, C. Drechsler, B. Chen, R. Rudolf and G. H. Clever, *Dalton Trans.*, 2019, **48**, 11070–11075.
- 12 G. Carroy, V. Lemaury, C. Henoumont, S. Laurent, J. De Winter, E. De Pauw, J. Cornil and P. Gerbault, *J. Am. Soc. Mass Spectrom.*, 2018, **29**, 121–132.
- 13 H. Lee, J. Tessarolo, D. Langbehn, A. Baksi, R. Herges and G. H. Clever, *J. Am. Chem. Soc.*, 2022, **144**, 3099–3105.
- 14 T. R. Schulte, J. J. Holstein and G. H. Clever, *Angew. Chem., Int. Ed.*, 2019, **58**, 5562–5566.
- 15 M. C. Pfrunder, D. L. Marshall, B. L. J. Poad, E. G. Stovell, B. I. Loomans, J. P. Blinco, S. J. Blanksby, J. C. McMurtrie and K. M. Mullen, *Angew. Chem., Int. Ed.*, 2022, **61**, e202212710.
- 16 E. Taipale, J. S. Ward, G. Fiorini, D. L. Stares, C. A. Schalley and K. Rissanen, *Inorg. Chem. Front.*, 2022, **9**, 2231–2239.
- 17 L. Sleno and D. A. Volmer, *J. Mass Spectrom.*, 2004, **39**, 1091–1112.
- 18 S. Ibáñez, C. Vicent and E. Peris, *Angew. Chem., Int. Ed.*, 2022, **61**, e202112513.
- 19 C. G. P. Taylor, S. P. Argent, M. D. Ludden, J. R. Piper, C. Mozaceanu, S. A. Barnett and M. D. Ward, *Chem. – Eur. J.*, 2020, **26**, 3054–3064.
- 20 C. Mozaceanu, C. G. Taylor, J. R. Piper, S. P. Argent and M. D. Ward, *Chemistry*, 2020, **2**, 22–32.
- 21 C. G. Taylor, J. S. Train and M. D. Ward, *Chemistry*, 2020, **2**, 510–524.
- 22 C. Mozaceanu, A. B. Solea, C. G. P. Taylor, B. Sudittapong and M. D. Ward, *Dalton Trans.*, 2022, **51**, 15263–15272.
- 23 W. Cullen, M. C. Misuraca, C. A. Hunter, N. H. Williams and M. D. Ward, *Nat. Chem.*, 2016, **8**, 231–236.
- 24 M. D. Ward, C. A. Hunter and N. H. Williams, *Acc. Chem. Res.*, 2018, **51**, 2073–2082.
- 25 B. Hasenknopf, J.-M. Lehn, B. O. Kneisel, G. Baum and D. Fenske, *Angew. Chem., Int. Ed. Engl.*, 1996, **35**, 1838–1840.
- 26 S. Turega, W. Cullen, M. Whitehead, C. A. Hunter and M. D. Ward, *J. Am. Chem. Soc.*, 2014, **136**, 8475–8483.
- 27 N. Geue, T. S. Bennett, A.-A.-M. Arama, L. A. I. Ramakers, G. F. S. Whitehead, G. A. Timco, P. B. Armentrout, E. J. L. McInnes, N. A. Burton, R. E. P. Winpenny and P. E. Barran, *J. Am. Chem. Soc.*, 2022, **144**, 22528–22539.
- 28 V. Shrivastav, M. Nahin, C. J. Hogan and C. Larriba-Andaluz, *J. Am. Soc. Mass Spectrom.*, 2017, **28**, 1540–1551.
- 29 A. K. Rappé, C. J. Casewit, K. Colwell, W. A. Goddard and W. M. Skiff, *J. Am. Chem. Soc.*, 1992, **114**, 10024–10035.
- 30 J. G. Brandenburg, C. Bannwarth, A. Hansen and S. Grimme, *J. Chem. Phys.*, 2018, **148**, 064104.
- 31 F. Neese, *Wiley Interdiscip. Rev.: Comput. Mol. Sci.*, 2012, **2**, 73–78.
- 32 F. Neese, *Wiley Interdiscip. Rev.: Comput. Mol. Sci.*, 2022, **12**, e1606.
- 33 X. Li, Y.-T. Chan, G. R. Newkome and C. Wesdemiotis, *Anal. Chem.*, 2011, **83**, 1284–1290.



Binding Modes of High Stoichiometry Guest Complexes with a Co₈L₁₂ Cage Uncovered by Mass Spectrometry

Daniel L. Stares^{†a}, Cristina Mozaceanu ^{†b}, Michael D. Ward^{*b} and Christoph A. Schalley^{*a}

a - Institut für Chemie und Biochemie Freie Universität Berlin, Arnimallee 20, 14195 Berlin, Germany

b - Department of Chemistry, University of Warwick, Coventry CV4 7AL, United Kingdom

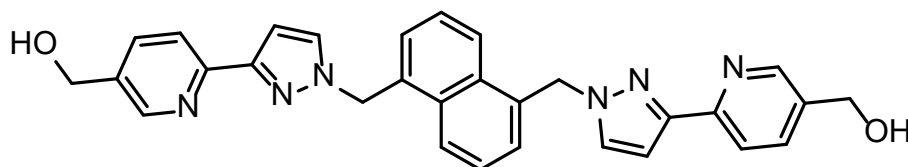
Table of Contents

Experimental section	2
Sample Preparation	3
Mass spectrometer instrumental parameters.....	3
Computational and TM CCS _{N2} calculations.....	4
References	11

Experimental section

The solvents and guests were purchased from commercial sources. The H^W cage was synthesised according to published procedures.¹

L^W ligand



Chemical formula: $C_{30}H_{26}N_6O_2$

H^WCo : $[Co_8L^W_{12}](BF_4)_{16}$

Chemical formula: $Co_8C_{360}H_{312}N_{72}O_{24}B_{16}F_{64}$

Sample Preparation

A 100 μM stock solution of H^WCo in H_2O was prepared by heating and vigorously stirring the solution for 2 h at 80 $^{\circ}C$. The resulting solution was used to prepare a 1:10 diluted host solution in H_2O (10 μM), which was used in the experiments.

A 100 μM stock solution of **MAC** in 10% CH_3OH / H_2O was prepared. This solution together with the 100 μM H^WCo were used to prepare the solution of 10 μM H^WCo / 50 μM **MAC** in 5% CH_3OH / H_2O , by mixing the following: 100 μL of 100 μM H^WCo + 500 μL of 100 μM **MAC** + 400 μL H_2O .

A 100 μM stock solution of **MC** in 10% CH_3OH / H_2O was prepared. This solution together with the 100 μM H^WCo were used to prepare the solution of 10 μM H^WCo / 50 μM **MC** in 5% CH_3OH / H_2O , by mixing the following: 100 μL of 100 μM H^WCo + 500 μL of 100 μM **MC** + 400 μL H_2O .

A 100 μM stock solution of **CUD** in 10% $DMSO / H_2O$ was prepared. This solution together with the 100 μM H^WCo were used to prepare the solution of 10 μM H^WCo / 50 μM **CUD** in 5% $DMSO / H_2O$, by mixing the following: 100 μL of 100 μM H^WCo + 500 μL of 100 μM **CUD** + 400 μL H_2O .

Prior to their injection in the MS equipment, all solutions were centrifuged. All used solvents were of LC-MS grade.

Mass spectrometer instrumental parameters

Electrospray ionisation quadrupole-time-of-flight mass spectrometric (ESI-Q-TOF-MS) experiments were performed using a Synapt G2-S HDMS (Waters Co., Milford, MA, USA) instrument. ESI-HRMS and CID experiments were done using the following instrumental parameters: flow rate 5 $\mu\text{L}/\text{min}$, capillary voltage 1.63 kV, sample cone voltage 25 V, source offset 30 V, source temperature 85 $^{\circ}\text{C}$, desolvation temperature 200 $^{\circ}\text{C}$, nebulizer gas 4 bar, desolvation gas flow 180 Lh^{-1} . CID experiments employed N_2 as buffer gas and were performed in the transfer cell of the MS instrument, at collision voltages of 2–15 V with a 1 V increment. IMS measurements were done using an IMS wave velocity of 600 ms^{-1} and IMS wave height of 18 V. MassLynxTM (version 4.1) software was used for data acquisition and processing. Origin pro 2023 (OriginLab corporation) was used to plot graphs.

Computational and TMCCS_{N2} calculations

Energy minimised structures were calculated using the universal force field (UFF) level of theory implemented in Avogadro.² Structures were initially generated from crystal structures by deleting solvent molecules and performing a minimisation for gas-phase structures. For the $\text{H}^{\text{W}}\text{Co}^{10+}$ the counterions in the portal were retained and the others deleted. The respective guests were added and structures minimised again at UFF level. Theoretical TMCCS_{N2} values were calculated using the trajectory method implemented in IMoS software (Larriba Lab).³ Figures were generated using Scigress (Fujitsu software). Corner structure with MAC bound was optimised at the B97-3c level of theory implemented in the ORCA software.⁴⁻⁶

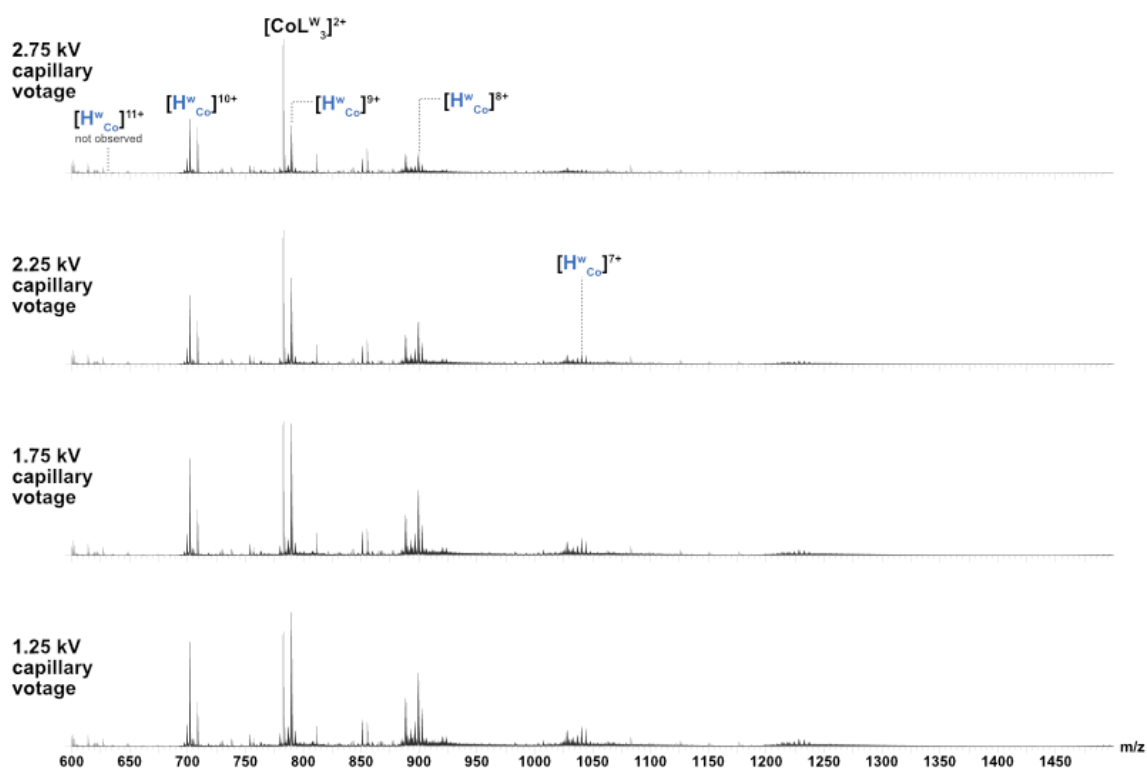


Fig. S1: ESI-MS of 10 μM $\text{H}^{\text{W}}_{\text{Co}}$ in H_2O at different capillary voltages. The ratio between the different charge states changes and cage fragmentation dominates at higher capillary voltages likely as a result of the increased charged repulsion at higher charge states. $\text{H}^{\text{W}}_{\text{Co}}{}^{11+}$ was never observed.

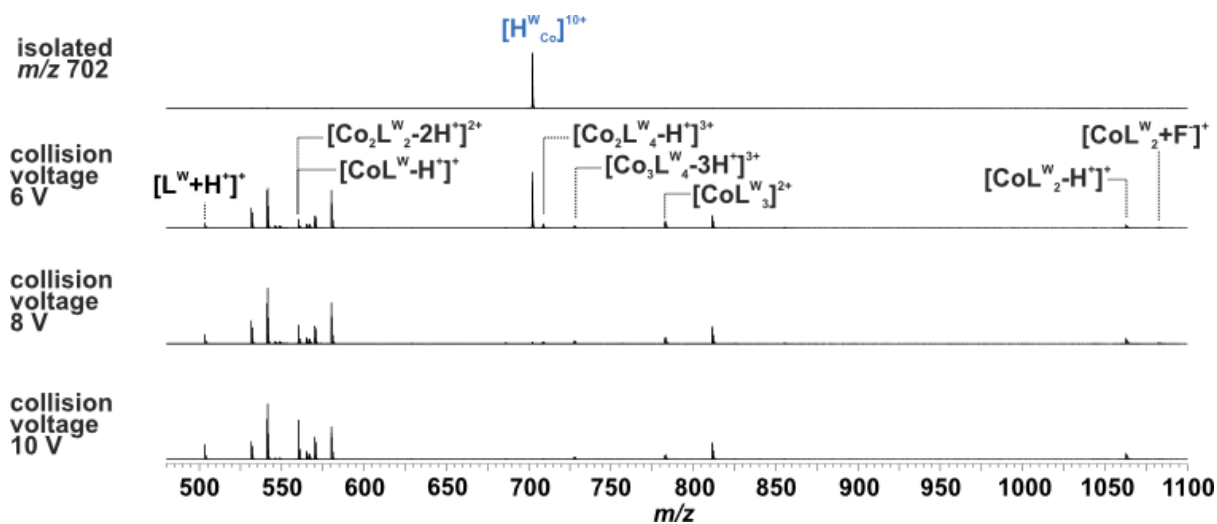


Fig. S2: Stacked MS/MS spectra of $\text{H}^{\text{W}}_{\text{Co}}{}^{10+}$ ion (blue) at collision voltages 2–12 V. The $\text{H}^{\text{W}}_{\text{Co}}{}^{10+}$ ion was fragmented completely at 8 V.

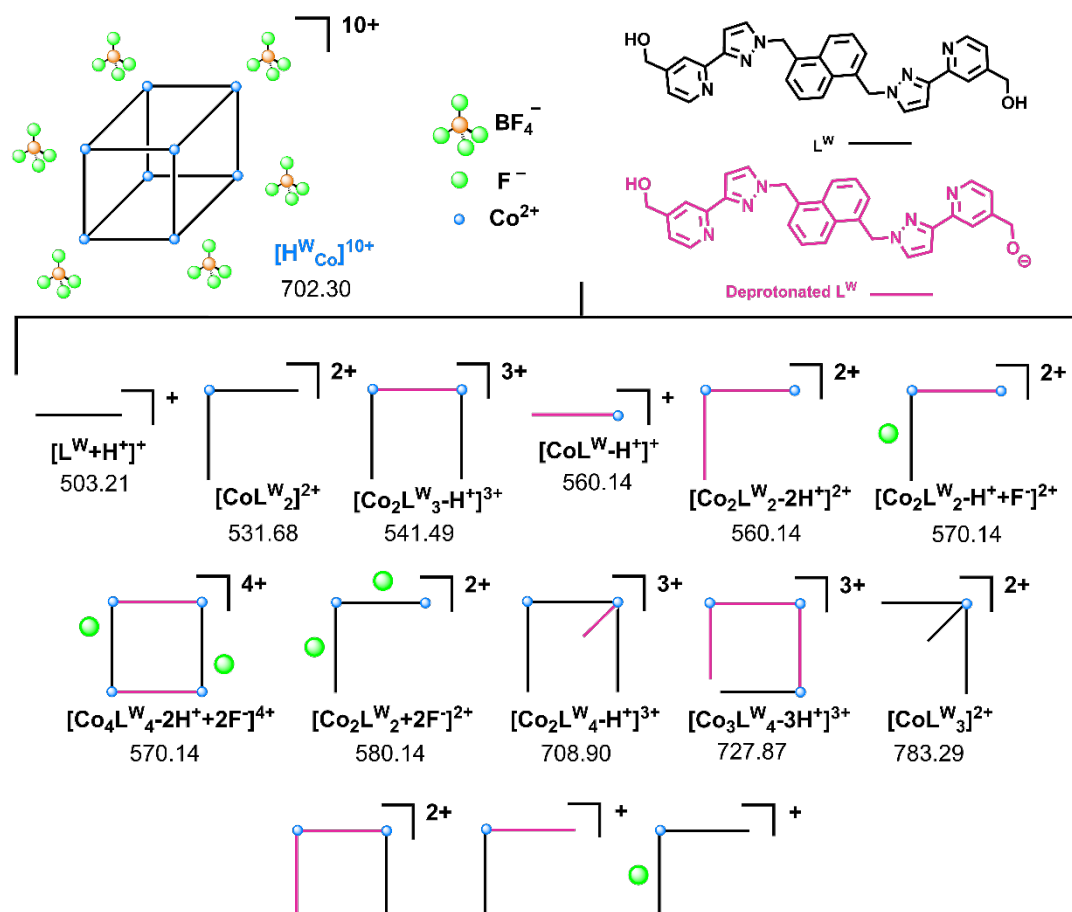


Fig. S3: Representation of the fragments of $[H^W Co]^{10+}$, their labels and m/z values. The deprotonated ligand L^W (pink) was chosen arbitrarily. The BF_4^- and F^- anions were also placed arbitrarily.

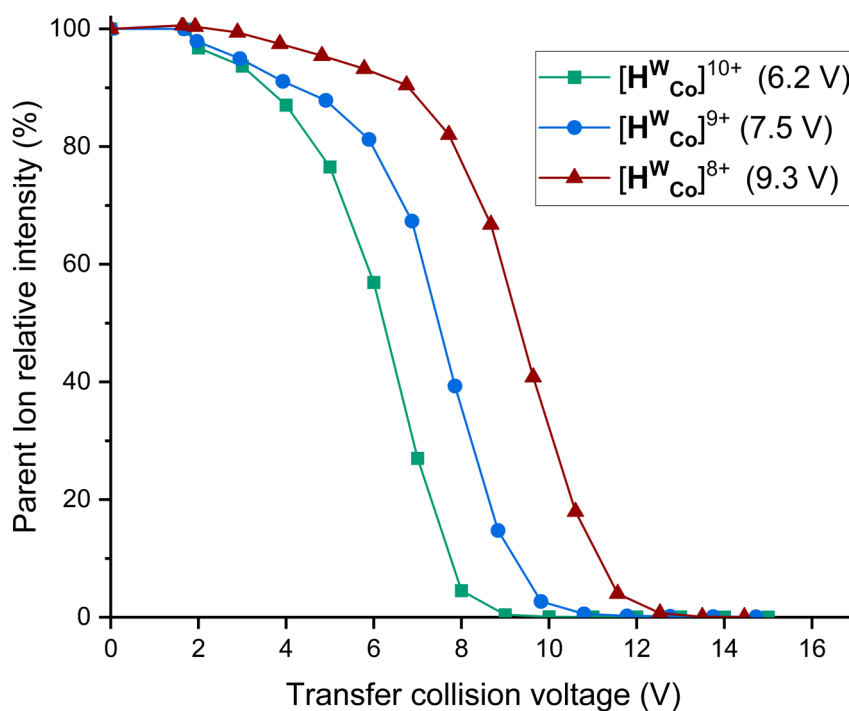


Fig. S4: Parent ion relative intensity versus transfer collision voltage for $H^W Co^{10+}$, $H^W Co^{9+}$; $H^W Co^{8+}$. The inflection point of the curves, which can be used to compare relative stabilities, is shown in parentheses

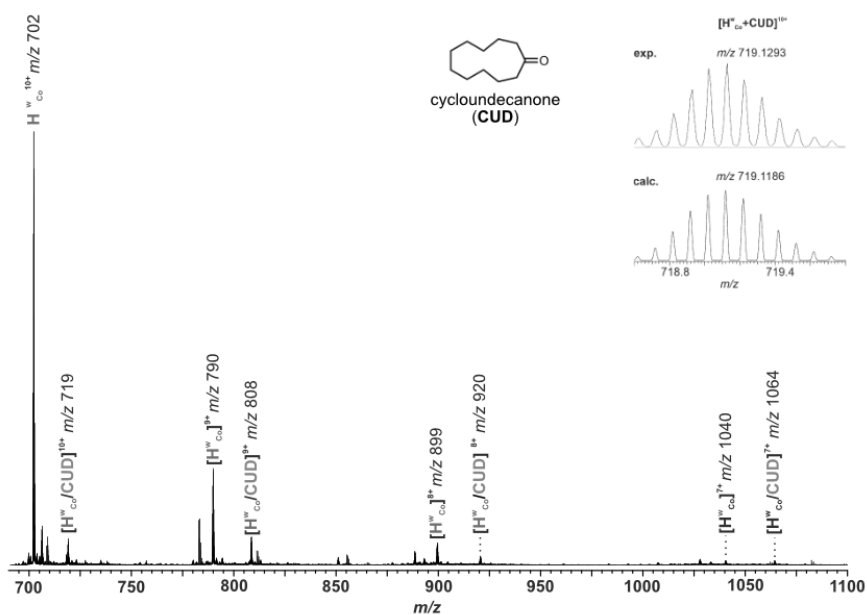


Fig. S5: ESI-HRMS spectrum of $H^{w, co}/CUD$ (10 μ M / 50 μ M) in 5% DMSO/H₂O. The inset Fig. represents the calculated vs experimental isotopic patterns and m/z values for the $H^{w, co}/CUD^{10+}$ ion.

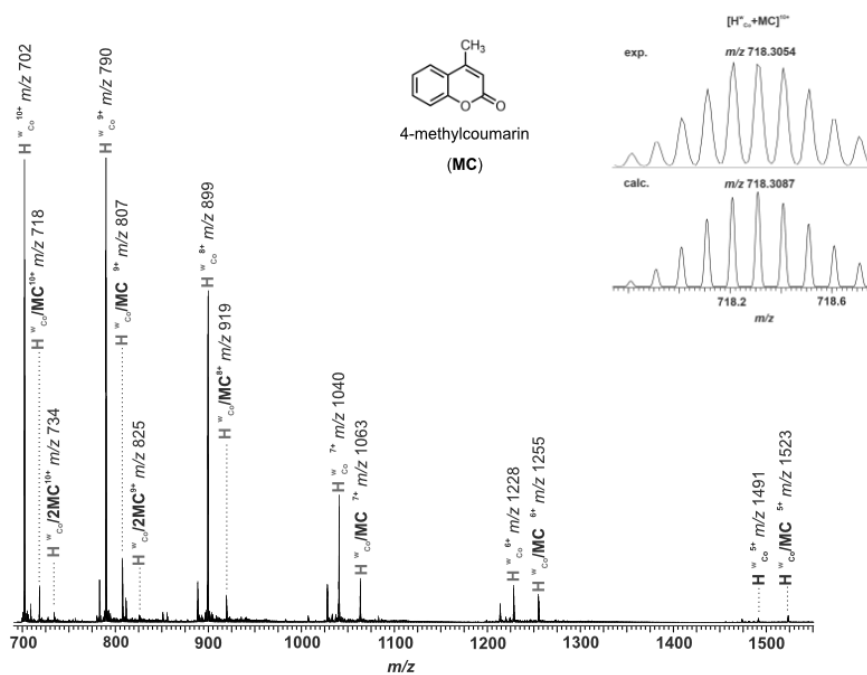


Fig. S6: ESI-HRMS spectrum of $H^{w, co}/MC$ (10 μ M / 50 μ M) in 5% CH₃OH/H₂O.

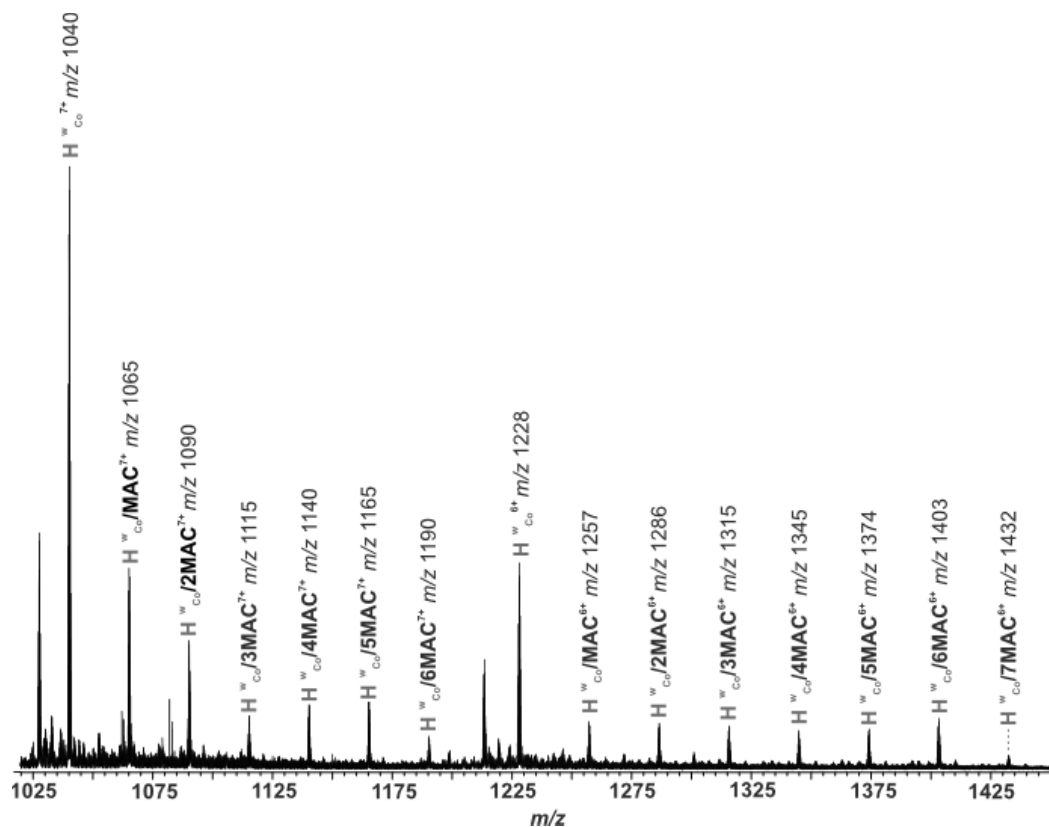


Fig. S7: 1025-1425 m/z region of ESI-HRMS spectrum of H^{W}_{Co} with **MAC** (10 μ M / 50 μ M) in 5% CH_3OH/H_2O . Stoichiometry with 7 **MAC** are observed albeit at low signal intensity.

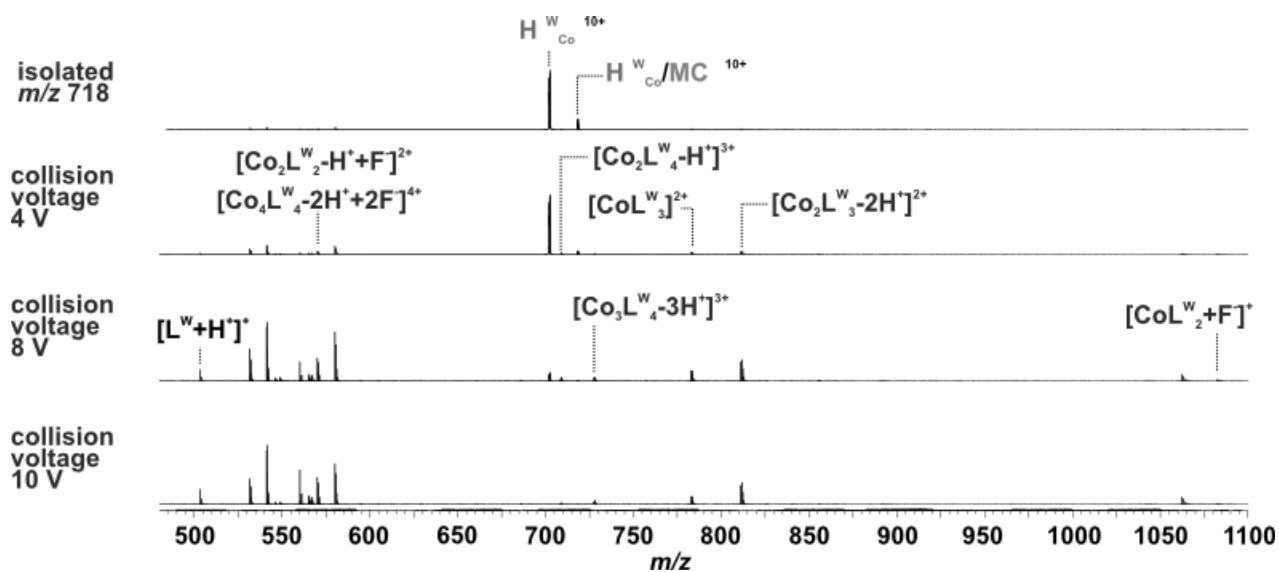


Fig. S8: Stacked CID spectra of mass selected H^{W}_{Co}/CUD^{3+} (10 μ M / 50 μ M) in 5% $DMSO/H_2O$.

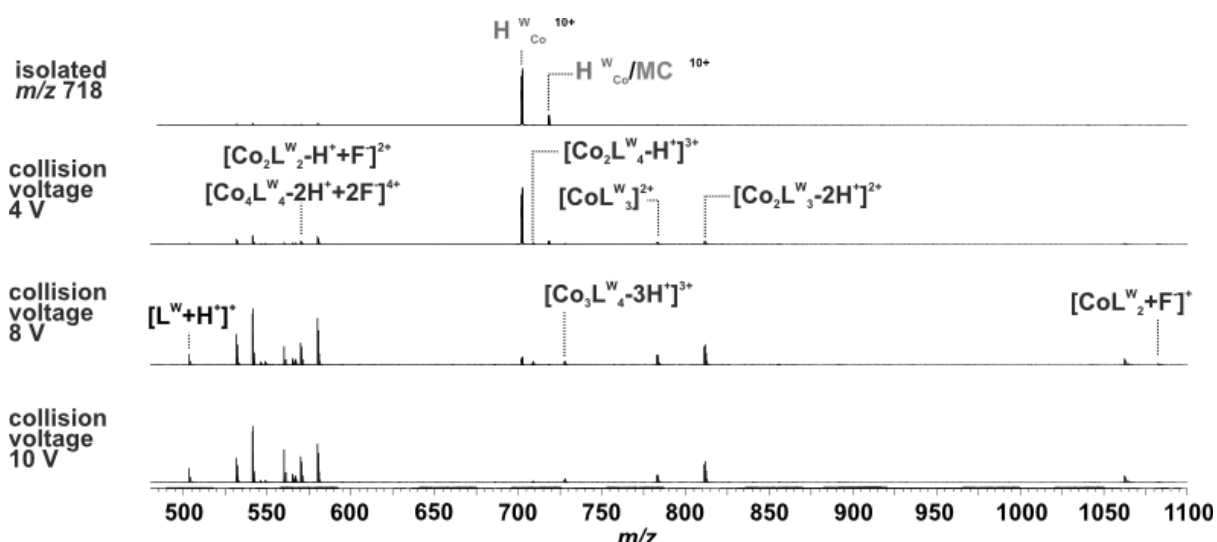


Fig. S9: Stacked CID spectra of mass-selected H^W_{Co}/MC^{10+} ($10 \mu M / 50 \mu M$) in 5% CH_3OH/H_2O .

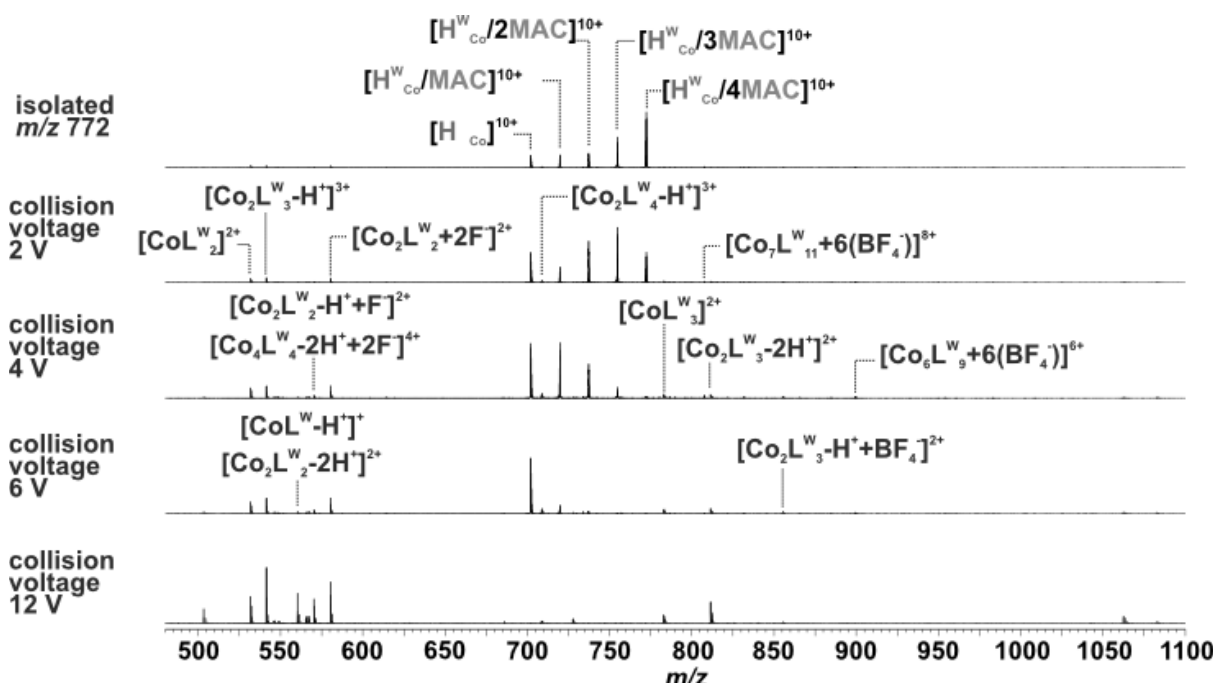


Fig. S10: Stacked CID MS/MS spectra of mass-selected ions $H^W_{Co}/4MAC^{10+}$. A gradual loss of the **MAC** is observed when increasing the CID voltage.

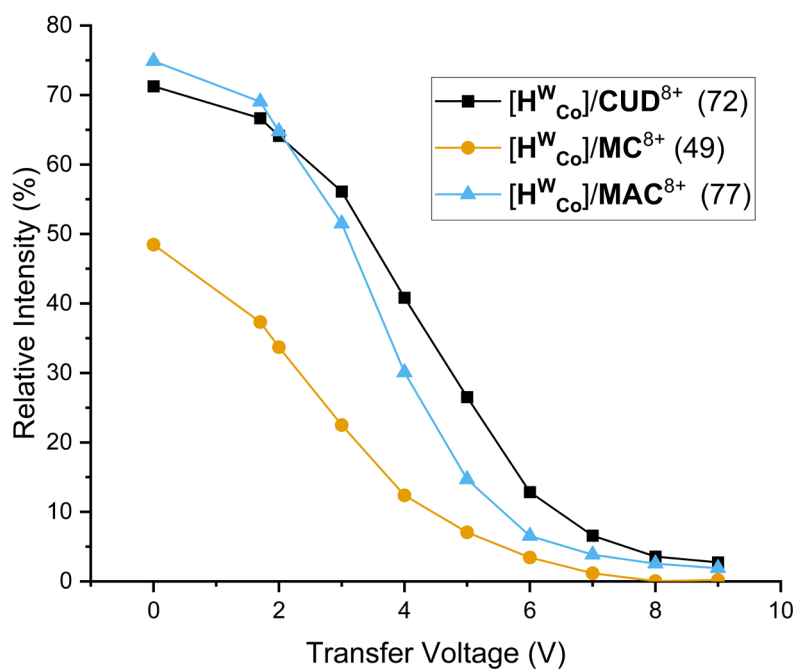


Fig. S11: Relative ion intensity versus transfer collision voltage for the H^W_{Co}/G^{8+} with the different guests.

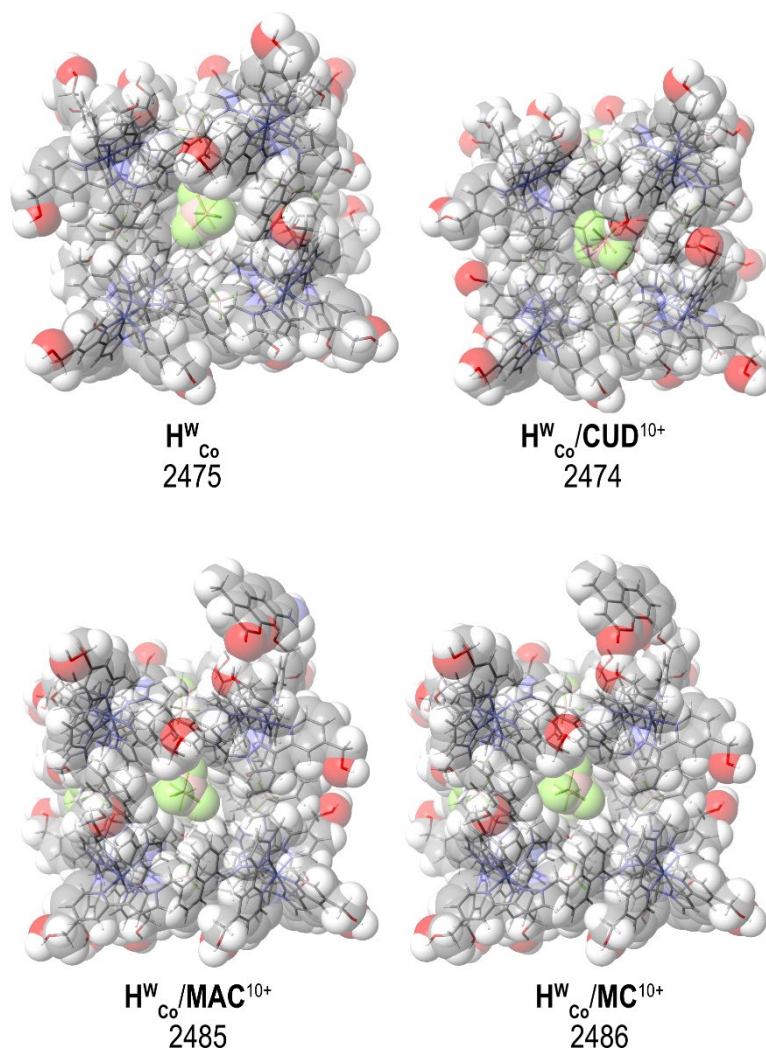


Fig. S12: UFF structures of $H^W_{Co}^{10+}$ (top left) H^W_{Co}/CUD^{10+} (top right) H^W_{Co}/MAC^{10+} (bottom left) H^W_{Co}/MC^{10+} (bottom right) used for $^{TM}CCS_{N_2}$ calculations. The $^{TM}CCS_{N_2}$ (\AA^2) is shown underneath the structures.

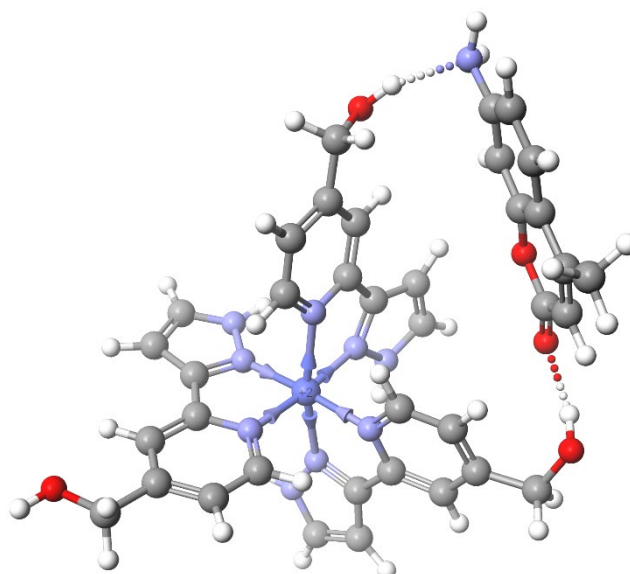


Fig. S13: Binding mode of MAC with two L^w in a *fac* corner of H^{W}_{Co} . Structure was optimised at the B97-3c level of theory.

References

1. M. Whitehead, S. Turega, A. Stephenson, C. A. Hunter and M. D. Ward, *Chem. Sci.*, 2013, **4**, 2744-2751.
2. A. K. Rappé, C. J. Casewit, K. Colwell, W. A. Goddard III and W. M. Skiff, *J. Am. Chem. Soc.*, 1992, **114**, 10024-10035.
3. V. Shrivastav, M. Nahin, C. J. Hogan and C. Larriba-Andaluz, *J. Am. Soc. Mass Spectrom.*, 2017, **28**, 1540-1551.
4. J. G. Brandenburg, C. Bannwarth, A. Hansen and S. Grimme, *J. Chem. Phys.*, 2018, **148**.
5. F. Neese, *WIREs: Comput. Mol. Sci.*, 2012, **2**, 73-78.
6. F. Neese, *WIREs: Comput. Mol. Sci.*, 2022, **12**, e1606.

Hot Paper

Encapsulation in Charged Droplets Generates Distorted Host-Guest Complexes**

Daniel L. Stares,^[a] Agnieszka Szumna,^{*,[b]} and Christoph A. Schalley^{*,[a]}*Dedicated to Wei Jiang. May he rest in peace.*

The ability of various hydrogen-bonded resorcinarene-based capsules to bind α,ω -alkylbisDABCONium (**DnD**) guests of different lengths was investigated in solution and in the gas-phase. While no host-guest interactions were detected in solution, encapsulation could be achieved in the charged droplets formed during electrospray ionisation (ESI). This included guests, which are far too long in their most stable conformation to fit inside the cavity of the capsules. A combination of three mass spectrometric techniques, namely, collision-induced dissociation, hydrogen/deuterium exchange, and ion-mobility mass spectrometry, together with computational modelling allow us to determine the binding mode of the **DnD** guests

inside the cavity of the capsules. Significant distortions of the guest into horseshoe-like arrangements are required to optimise cation- π interactions with the host, which also adopt distorted geometries with partially open hydrogen-bonding seams when binding longer guests. Such quasi “spring-loaded” capsules can form in the charged droplets during the ESI process as there is no competition between guest encapsulation and ion pair formation with the counterions that preclude encapsulation in solution. The encapsulation complexes are sufficiently stable in the gas-phase – even when strained – because non-covalent interactions significantly strengthen in the absence of solvent.

Introduction

Electrospray ionisation (ESI) is the most common method of generating gaseous ions as it is soft and proceeds directly from solution.^[1] ESI is also capable of accelerating reaction rates,^[2] facilitating the self-assembly of supramolecular systems^[3] and is even able to form complexes which cannot be observed in solution,^[4] a prominent example of this being the serine octamer clusters.^[5] An interesting aspect of ESI is that the charged droplets which form offer an environment where charge neutrality is violated enabling novel chemistry to occur. This can potentially be useful for hosts binding charged guests as the counterion(s) will be stripped away obviating any ion

pairing issues that may be present in solution, enhancing binding by enabling direct interaction of the naked ion with the host. In addition, as the droplets undergo desolvation, there is a concentration increase which further facilitates binding.^[6] Because of these factors, it is possible to generate unusual host-guest complexes and binding modes not observed in solution. These complexes then survive transfer into the gas-phase due to the strengthening of most non-covalent interactions in the absence of solvent.^[7]

To study the unique complexes which form in charged droplets, it is necessary to utilise mass spectrometry (MS). As mass-to-charge ratio (m/z) alone does not provide details on an ion's structure, the investigation requires more advanced MS techniques such as collision-induced dissociation (CID), gas-phase hydrogen deuterium exchange (HDX), and ion-mobility mass spectrometry (IMS). With these techniques, it is possible to elucidate structural and energetic information of an ion and thus gain insight into the chemistry occurring in the charged droplets.

Resorcinarenes are widely used hosts which can bind cations thanks to an electron-rich bowl-shaped cavity.^[8] Resorcinarenes can self-assemble into dimeric^[9] and hexameric capsules^[10] and offer great versatility owing to potential modifications of both their upper and lower rims, forming diverse hydrogen-bonded,^[11] metallo-supramolecular,^[12] anion-based,^[13] and halogen-bonded capsules.^[14] Such modular design allows for the modification of cavity size and function potentially encapsulating a range of guests both in terms of size^[15] and class of guest, with anion binding even possible with the appropriate modifications.^[16]

Herein, we report the encapsulation of different length dicationic α,ω -alkylbisDABCONium (**DnD**) guests into hydrogen-

[a] D. L. Stares, Prof. Dr. C. A. Schalley
Institut für Chemie und Biochemie
Freie Universität Berlin
Arnimallee 20, 14195 Berlin (Germany)
E-mail: c.schalley@fu-berlin.de

[b] Prof. A. Szumna
Institute of Organic Chemistry
Polish Academy of Sciences
Kasprzaka 44/52, Warsaw (Poland)
E-mail: agnieszka.szumna@icho.edu.pl

[**] A previous version of this manuscript has been deposited on a preprint server (<https://chemrxiv.org/engage/chemrxiv/article-details/648c70714f8b1884b7638f6f>).

Supporting information for this article is available on the WWW under <https://doi.org/10.1002/chem.202302112>

© 2023 The Authors. Chemistry - A European Journal published by Wiley-VCH GmbH. This is an open access article under the terms of the Creative Commons Attribution Non-Commercial License, which permits use, distribution and reproduction in any medium, provided the original work is properly cited and is not used for commercial purposes.

bonded resorcinarene-based capsules. No interaction was seen in solution by nuclear magnetic resonance (NMR), but encapsulation could be promoted via ESI, including guests which should be too long to fit inside the cavity. In these cases, encapsulation requires large distortions of the host-guest complexes which could be uncovered by a combination of MS and computational modelling. The encapsulation of these guests is a prototypical example of chemistry occurring under conditions violating electroneutrality, forming complexes not observed in solution. This offers qualitative insight into the enhanced non-covalent interactions in the absence of solvent and highlights the three very different environments the complexes encounter: solution, charged droplets and the gas-phase.

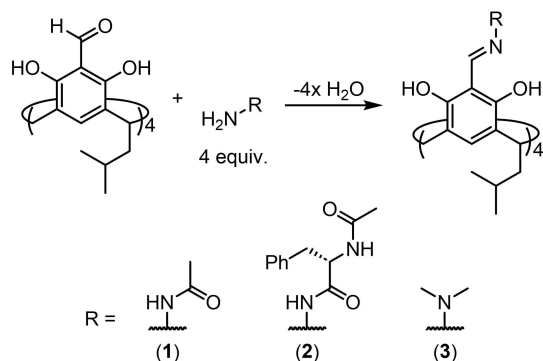
Results and Discussion

The cavitands are synthesised by acylhydrazone formation between a hydrazide containing strand to a tetraformylated resorcinarene precursor (Scheme 1) (full synthetic details and characterisation can be found in the Supporting Information). Previously, cavitands capable of dimerising via N–H...O hydrogen bonds were prepared by attaching mono-, di-, tri- and tetrapeptide strands to the upper rim of resorcinarenes.^[17] It was expected that the longer strands would result in larger cavities when dimerising. However, cavity size did not change as the capsules were only engaging the first amino acid for

intermolecular hydrogen bonding leaving the terminal ends of the strands unbound.

In the current study, the strand was shortened to an acetyl moiety which resulted in the formation of a new hydrogen-bonded dimer of this type (**1**) (Figure 1a). Dimer formation of **1** was supported by both Diffusion-Ordered Spectroscopy (DOSY) and Rotating Frame Overhauser Enhancement Spectroscopy (ROESY) (Figures S3 & S4) and suggests a binding motif involving a continuous seam of eight hydrogen bonds propagating around the capsule (Figure 1a). Comparing HF-3c optimised models of **1**₂ (Figure 1a) and the previously reported phenylalanine peptide capsule **2**₂ (Figure 1b)^[17a] shows that shortening the chain to an acetyl moiety reduces the dimensions of the capsule and thus **1**₂ and **2**₂ can be used to monitor the effect of cavity size on guest binding.^[18] DABCO heads connected by alkyl chains of different lengths (**DnD**, *n* = 2–12, Figure 1c) were used as guests which should bind with the electron-rich resorcinarene cores via cation- π interactions.^[19] The guest's double charge allows interaction with both hemispheres of **1**₂ and **2**₂ whilst Coulomb repulsion between the two charges should favour full extension of the **DnD** enabling an assessment of guest size on binding.

Because of the ring current within the four aromatic rings of the resorcinarene core, encapsulation of the guest into the capsule's cavity would produce clear upfield shifts of the guest's ¹H NMR signals. NMR measurements for these compounds were hampered by solubility issues as **1**₂ and the **DnD**·(PF₆)₂ salts were not soluble in the same solvent at the concentrations required for NMR. Solvent mixtures can be used, but this was complicated by the competitive nature of most polar solvents for hydrogen bonding meaning they can only be used in small amounts.^[17] A 4:1 chloroform:acetonitrile mixture dissolved **1**₂ and **D5D**·(PF₆)₂ however, no shifts that indicate encapsulation were observed (Figure S11).^[20] The same result was obtained when guest salts with tetrakis[3,5-bis(trifluoromethyl)phenyl]borate (**BArF**) counterions were used.^[21] **BArF** is less coordinating than PF₆[−] and increases solubility in non-polar solvents such that **D9D**·(**BArF**)₂ and **1**₂ were both soluble in pure dichloromethane (DCM). Still, no interaction between host and guest was observed (Figure S12). No changes were seen when samples were re-measured after several days (Figure S13), nor was interaction seen when measuring with different **DnD**



Scheme 1. Formation of the cavitands via acylhydrazone chemistry.^[17]

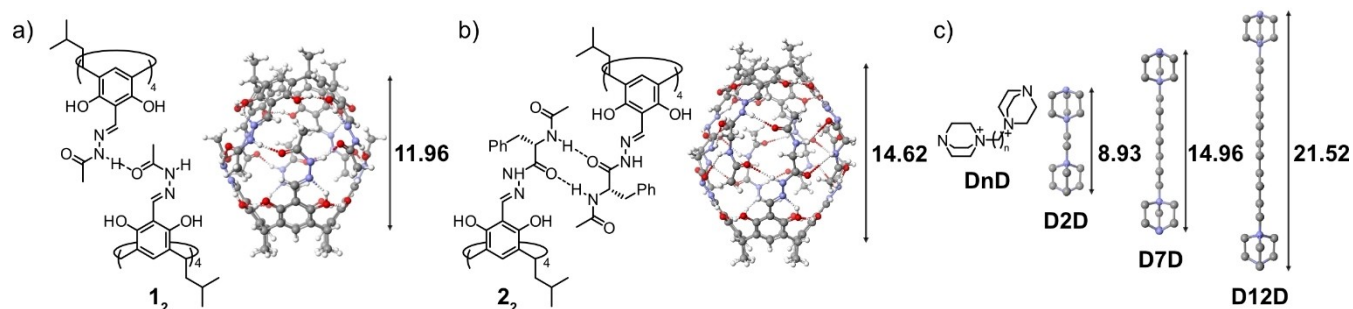


Figure 1. a) Acetylhydrazoneresorcinarene capsule (**1**₂). b) Phenylalanineresorcinarene capsule (**2**₂). The distances from lower rim to lower rim are marked in Å. c) **DnD**²⁺ guests which should be fully extended due to charge repulsion. The (CH₂)₃N–N(CH₂)₃ distance is marked in Å. All models were optimised at the HF-3c level of theory.

guests (Figure S14). Thus, from the NMR analysis, it is clear that guest encapsulation does not occur in solution, even in non-competitive solvents such as DCM.

In marked contrast, strong signals for ions corresponding to the dimer/guest complex ($[M_2 + DnD]^{2+}$) were observed via ESI-MS for all guests with both 1_2 and 2_2 (Figures S16–21), even when measuring samples in competitive solvents such as acetonitrile (Figure S22–24). As the complexes do not exist in solution before ionisation and we can safely rule out their formation in the gas-phase after the ESI process, the only conclusion is that the encapsulation has occurred in the positively charged droplets *during* ESI. In ESI, ions are formed via the desolvation of analyte ions in charged droplets (Figure S15).^[22] These droplets contain an excess of positive charges from guests without counterions and thus, the effect of ion pair formation is waived. This allows interactions between the naked cation and the capsule and when coupled with the concurrent increase in concentration during desolvation, enables encapsulation that cannot be seen by NMR. Consequently, such encapsulation represents supramolecular chemistry occurring under conditions violating electroneutrality.

Although this clear-cut difference between NMR and MS results can be understood, some DnD should be too long to bind so it is still surprising to see interactions between 1_2 or 2_2 and *all* guests. A straightforward explanation would be that this is due to a non-specific interaction between host and guest occurring during ESI, i.e., the DnD guests are binding externally rather than truly being encapsulated. To investigate this, the disassembly of the ions was studied via collision-induced dissociation (CID) where ions are accelerated by an electric field and collided with a neutral buffer gas. This converts some of the ions' kinetic energy into internal energy eventually leading to fragmentation, if this energy is sufficiently high (Figure 2a).^[23] CID of the mass-selected $[M_2 + DnD]^{2+}$ ions resulted in loss of one cavitand unit to the $[M + DnD]^{2+}$ ion before further dissociation of the guest (Figures 2b and c). The intact free guest was not observed for the shorter chain length guests ($n \leq 3$) due to the strong repulsion of the two charges in the gas-phase over such a short range (Figure S26),^[24] but the initial cavitand loss was seen for all guests and hosts. This dissociation pathway already supports the hypothesis of guest encapsulation over non-specific binding as guest loss would certainly dominate, if the guest was non-specifically bound to the outer surface of the capsule. The relatively high collision voltage required to induce dissociation also speaks against non-specific binding as such an interaction would only be weak and the non-specific complexes would thus dissociate at much lower collision voltages.^[25] A relative ranking of gas-phase stabilities can be determined by survival yield (SY) plots which can be constructed by calculating parent ion relative intensity at increasing collision voltages and plotting the two against each other.^[26] This produces a sigmoidal curve where the inflection point represents the voltage at which the parent ion intensity is half of the total intensity ($SY_{50\%}$), with higher $SY_{50\%}$ values indicating greater stability (Figure S27). For $[1_2 + DnD]^{2+}$, a similar stability is observed for $n=2-5$ followed by a gradual and consistent decrease in $SY_{50\%}$ values at longer chain lengths

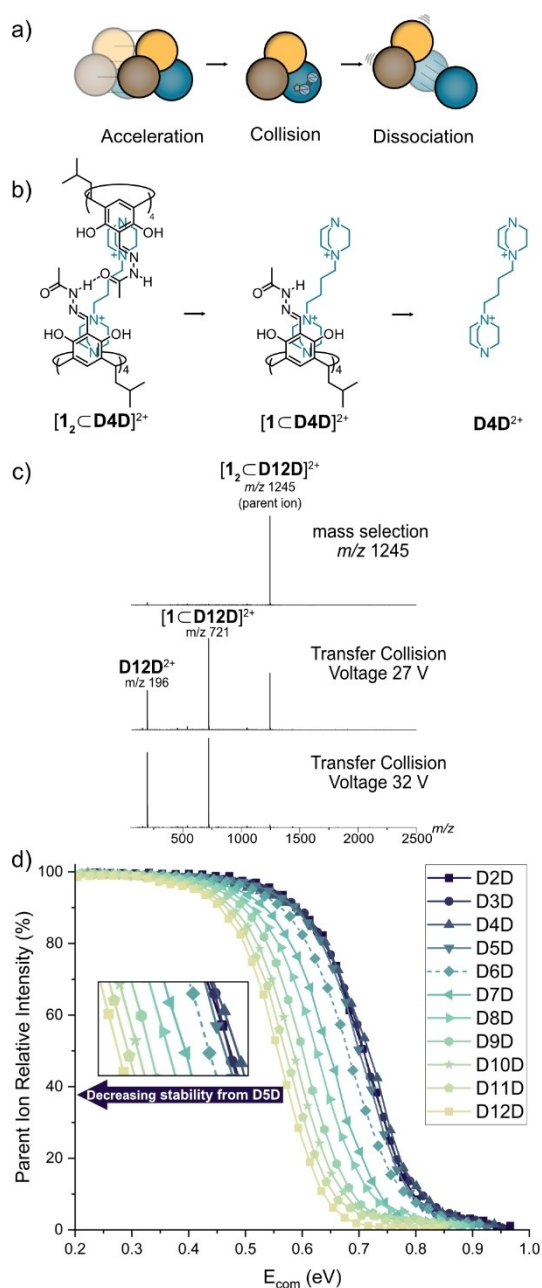


Figure 2. a) Principles of CID where the ions are accelerated into an inert collision gas converting kinetic energy into internal energy of the ion. Dissociation of the ion will follow if the internal energy is sufficiently high. b) Representative fragmentation pathway of $[1_2 + D4D]^{2+}$ ion, which was also seen for the other hosts and guests with $n \leq 3$. c) CID spectra for $[1_2 + D12D]^{2+}$, measurements performed on a Synapt G2-S in the transfer cell with N_2 as collision gas. d) SY curves of $[1_2 + DnD]^{2+}$ with a zoom of the $SY_{50\%}$ region shown in the inset. Note that the collision voltage was converted to the centre of mass energy (E_{com}) as described in the Supporting Information.

(Figure 2d). The same trend was also observed for 2_2 , but the stability decreases from $n=7$ (Figure S28), reflecting the larger cavity of 2_2 compared to 1_2 .

The CID results indicate guest encapsulation even for those DnD longer than the cavity. A possible explanation for the encapsulation of these guests is a rupturing of the intermolecular hydrogen bonding between the cavitands with the guest

bridging the two partially or completely separated monomers (Figure 3a). To investigate this, measurements were performed with an *N,N*-dimethylhydrazone derivative (**3**) (Figure 3b) which cannot form intermolecular hydrogen bonds so can only dimerise via a bridging guest. In contrast to **1**₂ and **2**₂, [**3**₂ + DnD]²⁺ ions were only observed for $n \geq 5$ indicating that dimeric complexes with shorter guests are not very stable. SY analysis of [**3**₂ + DnD]²⁺ showed *increasing* stability with guest length until **D10D** where a plateau was reached (Figure 3c). This stability trend is expected for a complex in which no additional interactions between host cavitands exist where very short guests can only bridge the two monomers with destabilizing steric clashes between them. The steric clashes reduce with medium-sized guests permitting dimer formation. This becomes energetically more favourable with guest length until a threshold distance is reached where the two monomers are fully

separated so that stability does not change anymore with longer guests. The fact that the inverse trend is observed for **3**₂ suggests **1**₂ and **2**₂ are maintaining hydrogen bonding between the cavitands in some manner (Figure 3d).

An explanation for encapsulation, while maintaining hydrogen bonding between the cavitands, would involve distortion of the guests from their fully extended form to fit inside the cavity. It has been demonstrated in solution that alkane guests can bind inside resorcinarene capsules by coiling into a helical arrangement.^[27] If a similar coiling is occurring here, the SY trends where longer guests destabilize the capsule can be rationalised by the strain associated with deviation from the ideal guest geometry in addition to the increased charge repulsion at the reduced distance. Guest coiling can be monitored via gas-phase hydrogen/deuterium exchange (HDX) experiments which can be conducted with a Fourier-Transform Ion-Cyclotron-Resonance (FTICR) mass spectrometer. FTICRs allow precise control of reaction intervals with both the number and rate of exchange(s) being structurally informative.^[28] HDX will shift from a fast concerted, Grothuss-like mechanism, to a slower non-concerted process that involves unfavourable charge separation species when a continuous hydrogen-bonding seam that runs around the capsule is disrupted (Figure S29).^[29] The hydrogen bonding pattern of **1**₂ would be expected to remain intact if the guests are coiling inside the cavity, and thus should produce similar HDX results with all guests. In the series of [**1**₂ + DnD]²⁺ ions, irrespective of the encapsulated guest, up to 24 exchanges were observed corresponding to the 8 N–H and 16 O–H hydrogens (Figures 4a and S30). However, the rate of exchange continually decreased from $n=5$ onwards, correlating closely to the CID results, and suggests guest binding modes which impact the N–H...O bonds between the strands. The HDX indicates that smaller guests allow the capsule to form a fully closed, non-disrupted seam which results in fast exchange whilst for the intermediate-sized guests, the seam is opened occasionally due to steric clash with the guests reducing the exchange rate. The rate further slows with the longer guests as they have a constantly partially open seam preventing efficient exchange.

These situations can be distinguished from each other with the orthogonal technique of IMS which provides structural information by separating ions based on their size and shape.^[30] Simply speaking, IMS acts as a wind tunnel for ions by transmitting them through a drift cell filled with an inert drift gas where low-energy collisions with the drift gas decelerates the ions resulting in different arrival times at the detector. The collision cross section (CCS) of an ion is its effective area that will undergo collisions with the drift gas and is thus a molecular property related to size and shape. CCS will influence the arrival time of an ion as a smaller ion will undergo fewer collisions and will have a shorter arrival time than a larger ion experiencing more collisions.^[31] Arrival time will also be dependent on an ion's charge as well as instrumental conditions, but, for ions of the of the same charge measured under the same conditions, arrival times can be directly compared to assess relative size differences. For host-guest systems, IMS can be used to infer conformational differences as well as guest binding modes.^[32]

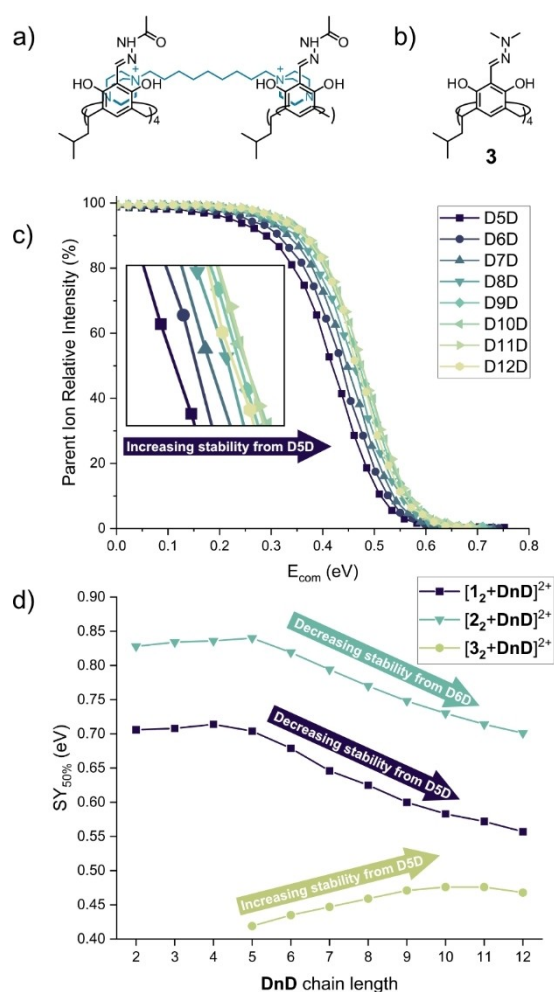


Figure 3. a) Potential non-hydrogen-bonded dimer where a DnD bridges across the two cavitands. b) *N,N*-dimethylhydrazoneresorcinarene (**3**). c) SY curves of [**3**₂ + DnD]²⁺ with $n = 5$ –12. A zoom of the SY_{50%} region of the curves is shown in the inset. CID measurements performed on a Synapt G2-S in the transfer cell with N₂ as collision gas. Note that the collision voltage was converted to the centre of mass energy (E_{com}) as described in the Supporting Information. d) Plot of collected SY_{50%} of [**M**₂ + DnD] for **1**₂, **2**₂, **3**₂. This is done to visualise the stability trends of the hosts but the kinetic shift differences are too large to make a reliable direct comparison between them.

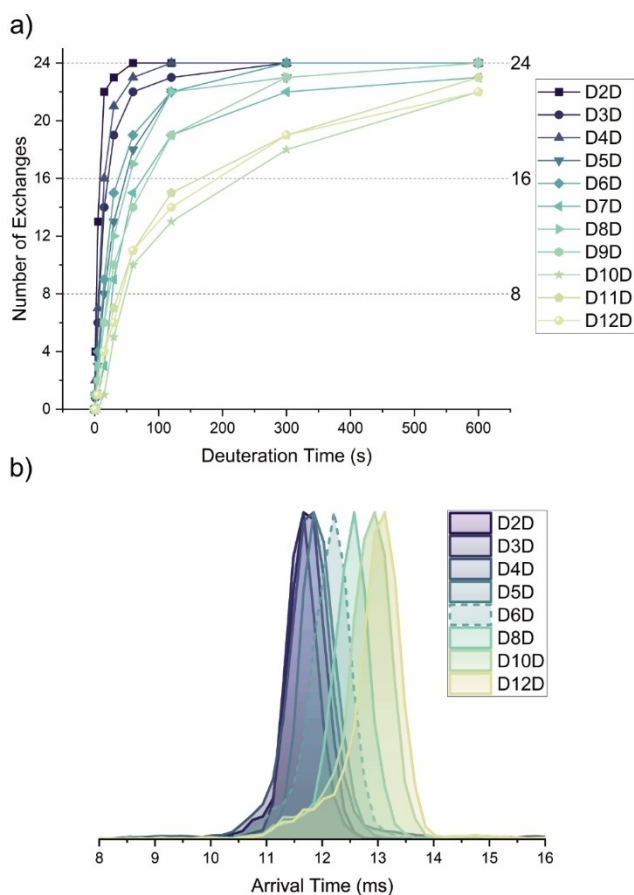


Figure 4. a) HDX for $[1_2\text{C}_n\text{D}_n]^{2+}$. The dashed lines represent the 8 NH and 16 OH which are exchangeable. The number of exchanges is consistent, but the rate decreases for longer guests; b) Arrival time distributions of $[1_2\text{C}_n\text{D}_n]^{2+}$ for $n=2-6,8,10,12$ $n=7,9,11$ omitted for clarity. Measurements performed on a Synapt G2-S with N_2 as buffer gas.

When considering space-filling models of both 1_2 and 2_2 (Figure S31), they show an almost non-porous structure and thus non-disrupted systems encapsulating the guests would have similar CCS, and hence arrival times. Consequently, short guests which are encapsulated without disrupting the hydrogen bonding seam should all have comparable arrival times in IMS. Measurements of the $[1_2\text{C}_n\text{D}_n]^{2+}$ ions show similar arrival times for $n \leq 5$ with gradual increases in arrival time beyond this guest length (Figure 4b). These results, like HDX, also support the idea of a completely intact hydrogen bonding seam for the shorter guests which is then disrupted by the medium to long guests increasing arrival times. Comparable IMS results were also obtained for 2_2 (Figure S32), but again shifted to the next larger guest in the series, consistent with the larger cavity. For 3 , a size increase was apparent for all guests with only slight increases seen for longer guests (Figure S33). In all cases, there is good agreement between the onset of size increases seen in IMS with the decreases in stability seen via CID.

The experimental results all correlate well to one another providing a consistent picture for all hosts. Computational modelling was then used to further explore the complexes

(Figure 5). Such large systems make full DFT calculation computationally expensive, so final structures were optimised using the HF-3c level of theory implemented in the ORCA software.^[18] HF-3c incorporates the D3 dispersion corrections and offers a nice balance between accuracy and cost while being suitable for the analysis of host-guest systems.^[33] The computational models of the different complexes provided structures and binding modes in line with all the observed results. As the charges on the guests are more localised on the inner nitrogen atoms, maximum cation- π interactions can be achieved by pointing these nitrogens into the resorcinarene cores (Figures 5a and S34). As 3 does not benefit from any interaction between cavitands, it can interact with the fully extended guests with no penalty resulting in acute angles between **D12D** and the upper rims of the resorcinarenes. Such an arrangement is not possible for the shorter **D5D** due to potential steric clashes of the two cavitands forcing a more head on arrangement with a larger binding angle. The angle between the guest and the second resorcinarene decreases with longer guests and this binding mode in addition to decreasing steric and Coulomb repulsion, can explain the stability trends seen via SY analysis (Figure 3b). The longer guests also account for the continual increase in arrival time seen in IMS (Figure S33), with the size convergence representing the point where the two resorcinarenes are parallel and pseudo-encapsulating the guests.

In 1_2 , the guests also maximise cation- π interactions by pointing their inner nitrogens towards the electron-rich resorcinarene cores. The intermolecular N-H...O hydrogen bonds between the strands prevent the simple translation of the two resorcinarenes (as with 3) so, to be able to maintain cation- π interactions, the two DABCONiums are effectively locked in position. Consequently, the carbon chain of the guest is forced to loop into a horseshoe-like arrangement (Figures 5b and S35). When the loop gets larger, it pushes against the strands of the host leading to a gradual weakening and eventual breaking of the H-bonds. Such weakening was first apparent with **D5D** which begins to strain the hydrogen bonds but allows the resorcinarene to reposition so that cation- π bonding is enhanced. The interplay between the weakening H-bonding and stronger cation- π interactions can account for the similar stabilities of **D2D–D5D**. Beyond **D5D**, longer guests continue to expand out of the cavity with the remaining H-bonds on the capsule effectively acting as a hinge to allow the portal to open further. This accounts for the observed stability trend seen in the SY plots as the hydrogen bonding on the strands near the guest loop continues to weaken when the loop grows. It would also decrease the HDX rate as the exchange begins to require a rearrangement which becomes more extreme with longer guests. Furthermore, as the strand is pushed away and the guests begin to expand outside the cavity, the CCS of the ion increases which contributes to the longer arrival times seen in IMS. IMS also has the benefit of being able to link computationally generated model compounds to experimental results via the calculation of both experimental CCS values ($^{TW}\text{CCS}_{\text{N}_2}$) from the arrival times via a calibrant and theoretical CCS values ($^{TM}\text{CCS}_{\text{N}_2}$) of computational

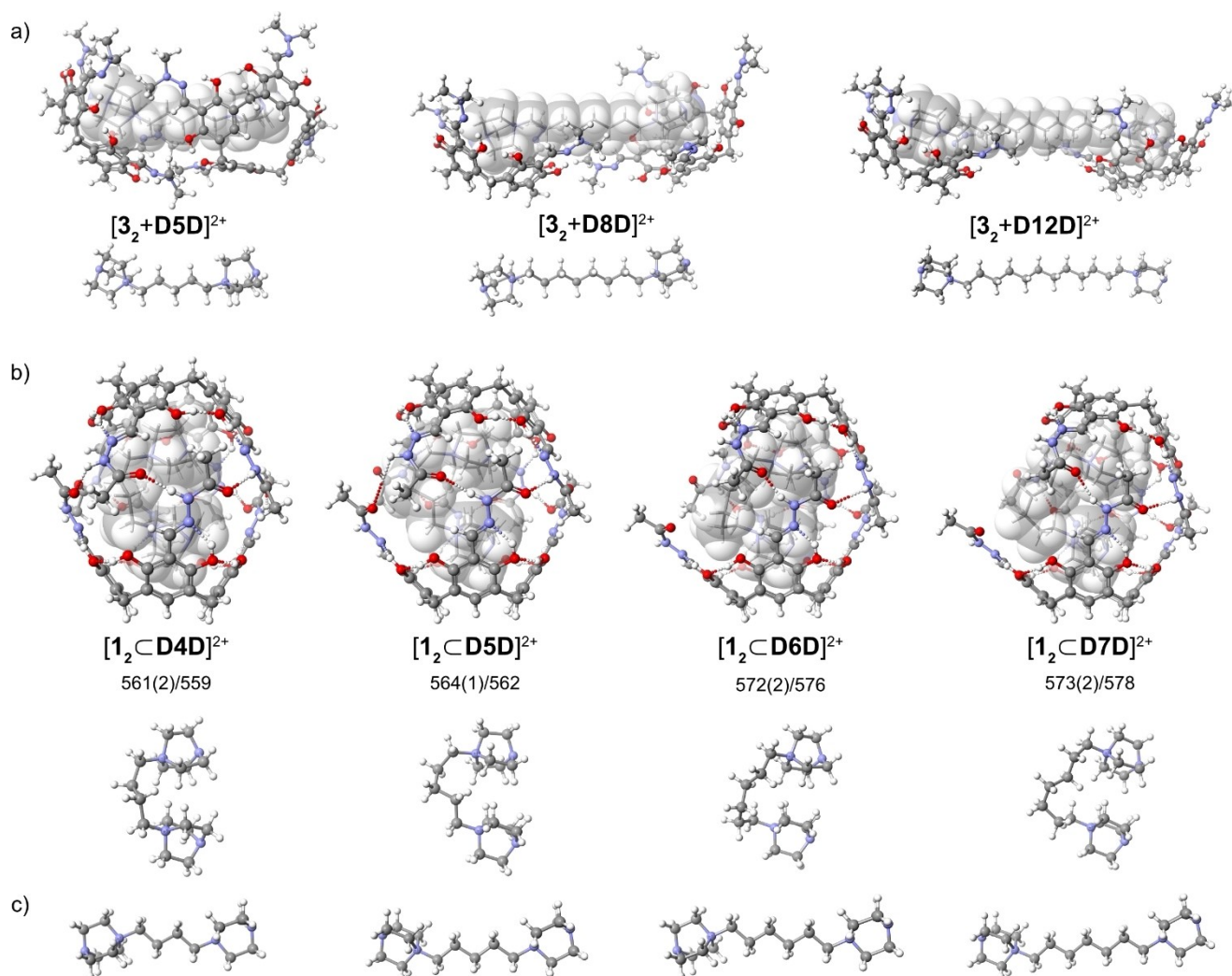


Figure 5. a) HF-3c optimised structures of $[3_2 + DnD]^{2+}$ with $n = 5, 8, 12$ (left to right). b) HF-3c optimised structures of $[1_2 \subset DnD]^{2+}$ with $n = 4, 5, 6, 7$ (left to right), experimental ${}^{\text{TM}}\text{CCS}_{\text{N}_2}$ values from CCS calibration (with standard deviation in parentheses) and theoretical ${}^{\text{TM}}\text{CCS}_{\text{N}_2}$ values (as noted in the supplementary material) are given below the $[1_2 \subset DnD]^{2+}$ structures. The bound guest is shown in space-filling mode in the host-guest structures and also shown without host underneath the respective host-guest structures. The *i-Bu* groups of the hosts have been omitted for clarity c) HF-3c optimised structures of free $D4$ – $D7$ (left to right) for comparison. The geometries of the bound guests within 1_2 deviates significantly from those of the free guests.

models of 1_2 (Figure 5b and Table S3) which in this case have good agreement with one another.^[34] Taken together, the theoretical and experimental studies provide consistent results and strongly support the proposed binding mode of the DnD guests. These surprising binding modes represent a large deviation from the guest's preferred geometry (up to 16 Å, Figure 5c, Table S4) against a Coulomb barrier and require rearrangement of the host to accommodate. Such a strained conformation persists in the gas-phase due to the strengthening of the non-covalent interactions that hold it together.

Conclusions

In conclusion, we have shown the ability of ESI to generate host-guest complexes which cannot be observed in solution. This is possible as the shrinking charged droplets formed during

ESI offer an environment where concentration increases, and ion pairing is obviated representing supramolecular chemistry occurring under conditions violating electroneutrality and reveals the intriguing chemistry that can result.

Using this strategy, guests too long for the cavity can be encapsulated in hydrogen-bonded resorcinarene capsules producing unusual conformations. The structures are assigned in the gas-phase with three structure-indicative MS techniques, CID, IMS and HDX which show decreasing stability above certain guest lengths and indicate guest expansion outside of the cavity for longer guests. The experimental results are coherent with one another and have been validated by computational modelling which reveals guests distorting into a horse-shoe arrangement upon encapsulation. This requires a large deviation of the guests from their ideal geometry in addition to distortions of the host, producing "spring-loaded" capsules with conformations that would be difficult to predict.

These complexes survive in the gas-phase, overcoming steric strain and the charge repulsion between the two DABCONium moieties, due to the strengthening of the non-covalent interactions in the absence of solvent enabling investigation with MS. The ability of MS to unravel the conformation of these complexes is important as MS is uniquely positioned to study the chemistry occurring in these charged droplets. We envisage that many unique binding motifs can be generated in this manner which can be studied by MS.

Supporting Information

The authors have cited additional references within the Supporting Information.^[35]

Acknowledgements

We thank the European Union through the NOAH project (H2020-MSCA-ITN project Ref. [76]5297) and FU Berlin for funding. Support for measurements by the BioSupraMol core facility at FU Berlin is gratefully acknowledged. Fei Jia is acknowledged for providing some of the guests used for initial measurements. We are grateful to Janos Wasternack for the NaBARF salt and to Sebastian Müller for synthesising it and acknowledge the members of the Szumna group and IChO staff for their support during the secondment of DLS in Warsaw. Thank you to Marek Szymański for help with the synthesis of 2. Open Access funding enabled and organized by Projekt DEAL.

Conflict of Interests

The authors declare no conflict of interest.

Data Availability Statement

The data that support the findings of this study are available from the corresponding author upon reasonable request.

Keywords: charged droplets · electrospray ionisation · host-guest systems · mass spectrometry · resorcinarenes

- [1] a) M. Wilm, *Mol. Cell. Proteomics* **2011**, *10*, M111.009407; b) P. Kebarle, L. Tang, *Anal. Chem.* **1993**, *65*, A972–A986; c) J. B. Fenn, *Angew. Chem. Int. Ed.* **2003**, *42*, 3871–3894; d) G. L. Glish, R. W. Vachet, *Nat. Rev. Drug Discovery* **2003**, *2*, 140–150.
 [2] a) X. Yan, R. M. Bain, R. G. Cooks, *Angew. Chem. Int. Ed.* **2016**, *55*, 12960–12972; b) M. Giroto, E. Moyano, D. I. Campbell, R. G. Cooks, *Chem. Sci.* **2011**, *2*, 501–510.
 [3] N. K. Beyeh, M. Kogej, A. Åhman, K. Rissanen, C. A. Schalley, *Angew. Chem. Int. Ed.* **2006**, *45*, 5214–5218.
 [4] a) J. Seo, S. Warnke, K. Pagel, M. T. Bowers, G. von Helden, *Nat. Chem.* **2017**, *9*, 1263–1268; b) S. Vandenbussche, G. Vandenbussche, J. Reisse, K. Bartik, *Eur. J. Org. Chem.* **2006**, *2006*, 3069–3073; c) D. P. Weimann, C. A. Schalley, *Supramol. Chem.* **2008**, *20*, 117–128.
 [5] S. C. Nanita, R. G. Cooks, *Angew. Chem. Int. Ed.* **2006**, *45*, 554–569.

- [6] J. Mehara, J. Roithová, *Chem. Sci.* **2020**, *11*, 11960–11972.
 [7] L. Cera, C. A. Schalley, *Chem. Soc. Rev.* **2014**, *43*, 1800–1812.
 [8] a) H.-J. Schneider, U. Schneider, *J. Incl. Phenomena Mol. Rec.* **1994**, *19*, 67–83; b) K. Kobayashi, M. Yamanaka, *Chem. Soc. Rev.* **2015**, *44*, 449–466.
 [9] K. N. Rose, L. J. Barbour, G. W. Orr, J. L. Atwood, *Chem. Commun.* **1998**, 407–408.
 [10] a) C. Gaeta, C. Talotta, M. De Rosa, P. La Manna, A. Soriente, P. Neri, *Chem. Eur. J.* **2019**, *25*, 4899–4913; b) M. Yamanaka, A. Shivanyuk, J. Rebek, Jr., *J. Am. Chem. Soc.* **2004**, *126*, 2939–2943; c) S. Gambaro, M. De Rosa, A. Soriente, C. Talotta, G. Floresta, A. Rescifina, C. Gaeta, P. Neri, *Org. Chem. Front.* **2019**, *6*, 2339–2347.
 [11] a) T. Heinz, D. M. Rudkevich, J. Rebek, Jr., *Nature* **1998**, *394*, 764–766; b) H. Mansikkamäki, M. Nissinen, K. Rissanen, *Chem. Commun.* **2002**, 1902–1903.
 [12] a) W.-Y. Pei, G. Xu, J. Yang, H. Wu, B. Chen, W. Zhou, J.-F. Ma, *J. Am. Chem. Soc.* **2017**, *139*, 7648–7656; b) R. Pinalli, V. Cristini, V. Sottili, S. Geremia, M. Campagnolo, A. Caneschi, E. Dalcanale, *J. Am. Chem. Soc.* **2004**, *126*, 6516–6517.
 [13] a) M. Chwastek, P. Cmoch, A. Szumna, *Angew. Chem. Int. Ed.* **2021**, *60*, 4540–4544; b) M. Chwastek, P. Cmoch, A. Szumna, *J. Am. Chem. Soc.* **2022**, *144*, 5350–5358.
 [14] a) N. K. Beyeh, F. Pan, K. Rissanen, *Angew. Chem. Int. Ed.* **2015**, *54*, 7303–7307; b) O. Dumele, N. Trapp, F. Diederich, *Angew. Chem. Int. Ed.* **2015**, *54*, 12339–12344.
 [15] a) D. Ajami, J. Rebek, Jr., *J. Am. Chem. Soc.* **2006**, *128*, 5314–5315; b) D. Ajami, J. Rebek, Jr., *Angew. Chem. Int. Ed.* **2007**, *46*, 9283–9286.
 [16] S. S. Zhu, H. Staats, K. Brandhorst, J. Grunenberg, F. Gruppi, E. Dalcanale, A. Lützen, K. Rissanen, C. A. Schalley, *Angew. Chem. Int. Ed.* **2008**, *47*, 788–792.
 [17] a) M. Szymański, M. Wierzbiński, M. Gilski, H. Jędrzejewska, M. Szytko, P. Cmoch, A. Shkurenko, M. Jaskólski, A. Szumna, *Chem. Eur. J.* **2016**, *22*, 3148–3155; b) M. P. Szymański, J. S. Czajka, P. Cmoch, W. Iwanek, A. Szumna, *Supramol. Chem.* **2018**, *30*, 430–437.
 [18] a) R. Sure, S. Grimme, *J. Comput. Chem.* **2013**, *34*, 1672–1685; b) F. Neese, *WIREs Comput. Mol. Sci.* **2012**, *2*, 73–78; c) F. Neese, *WIREs Comput. Mol. Sci.* **2022**, *12*, e1606.
 [19] H. Mansikkamäki, C. A. Schalley, M. Nissinen, K. Rissanen, *New J. Chem.* **2005**, *29*, 116–127.
 [20] R. J. Hooley, S. M. Biros, J. Rebek, Jr., *Chem. Commun.* **2006**, 509–510.
 [21] B. Wüstenberg, A. Pfaltz, *Adv. Synth. Catal.* **2008**, *350*, 174–178.
 [22] P. Kebarle, U. H. Verkerk, *Mass Spectrom. Rev.* **2009**, *28*, 898–917.
 [23] a) L. Sleno, D. A. Volmer, *J. Mass Spectrom.* **2004**, *39*, 1091–1112; b) M. Rodgers, K. M. Ervin, P. B. Armentrout, *J. Chem. Phys.* **1997**, *106*, 4499–4508.
 [24] C. A. Schalley, C. Verhaelen, F.-G. Klärner, U. Hahn, F. Vögtle, *Angew. Chem. Int. Ed.* **2005**, *44*, 477–480.
 [25] T. Heravi, J. Shen, S. Johnson, M. C. Asplund, D. V. Dearden, *J. Phys. Chem. A* **2021**, *125*, 7803–7812.
 [26] a) M. W. Forbes, D. A. Volmer, G. J. Francis, D. K. Böhme, *J. Am. Soc. Mass Spectrom.* **2005**, *16*, 779–791; b) T. M. Kertesz, L. H. Hall, D. W. Hill, D. F. Grant, *J. Am. Soc. Mass Spectrom.* **2009**, *20*, 1759–1767; c) N. Geue, T. S. Bennett, A.-A.-M. Arama, L. A. I. Ramakers, G. F. S. Whitehead, G. A. Timco, P. B. Armentrout, E. J. L. McInnes, N. A. Burton, R. E. P. Winpenney, P. E. Barran, *J. Am. Chem. Soc.* **2022**, *144*, 22528–22539; d) F. Schwer, S. Zank, M. Freiberger, R. Kaur, S. Frühwald, C. C. Robertson, A. Görling, T. Drewello, D. M. Guldi, M. von Delius, *Organic Materials* **2022**, *4*, 7–17.
 [27] a) D. Ajami, J. Rebek, Jr., *J. Am. Chem. Soc.* **2006**, *128*, 15038–15039; b) D. Ajami, J. Rebek, Jr., *Nat. Chem.* **2009**, *1*, 87–90; c) F. U. Rahman, R. Wang, H. B. Zhang, O. Brea, F. Himo, J. Rebek Jr, Y. Yu, *Angew. Chem. Int. Ed.* **2022**, *61*, e202205534.
 [28] a) H. D. F. Winkler, E. V. Dzyuba, C. A. Schalley, *New J. Chem.* **2011**, *35*, 529–541; b) K. D. Rand, S. D. Pringle, J. P. Murphy, K. E. Fadgen, J. Brown, J. R. Engen, *Anal. Chem.* **2009**, *81*, 10019–10028; c) M. E. Hemling, J. J. Conboy, M. F. Bean, M. Mentzer, S. A. Carr, *J. Am. Soc. Mass Spectrom.* **1994**, *5*, 434–442; d) M. A. Freitas, C. L. Hendrickson, M. R. Emmett, A. G. Marschall, *Int. J. Mass Spectrom.* **1999**, *185/186/187*, 565–575.
 [29] H. D. F. Winkler, E. V. Dzyuba, J. A. W. Sklorz, N. K. Beyeh, K. Rissanen, C. A. Schalley, *Chem. Sci.* **2011**, *2*, 615–624.
 [30] a) A. B. Kanu, P. Dwivedi, M. Tam, L. Matz, H. H. Hill, *J. Mass Spectrom.* **2008**, *43*, 1–22; b) F. Lanucara, S. W. Holman, C. J. Gray, C. E. Eyers, *Nat. Chem.* **2014**, *6*, 281–294.
 [31] E. Christofi, P. Barran, *Chem. Rev.* **2023**, *123*, 2902–2949.
 [32] a) E. Kalenius, M. Groessl, K. Rissanen, *Nat. Chem. Rev.* **2019**, *3*, 4–14; b) A. Krueve, K. Caprice, R. Lavendomme, J. M. Wollschläger, S. Schoder,

- H. V. Schröder, J. R. Nitschke, F. B. Cougnon, C. A. Schalley, *Angew. Chem. Int. Ed.* **2019**, *58*, 11324–11328; c) E. Hanozin, B. Mignolet, J. Martens, G. Berden, D. Sluysmans, A. S. Duwez, J. F. Stoddart, G. Eppe, J. Oomens, E. De Pauw, D. Morsa, *Angew. Chem. Int. Ed.* **2021**, *60*, 10049–10055; d) S. Ibáñez, C. Vicent, E. Peris, *Angew. Chem. Int. Ed.* **2022**, *61*, e202112513; e) C.-W. Chu, D. L. Stares, C. A. Schalley, *Chem. Commun.* **2021**, *57*, 12317–12320; f) M. C. Pfrunder, D. L. Marshall, B. L. Poad, T. M. Fulloon, J. K. Clegg, S. J. Blanksby, J. C. McMurtrie, K. M. Mullen, *Angew. Chem. Int. Ed.* **2023**, *62*, e202302229.
- [33] a) S. Grimme, S. Ehrlich, L. Goerigk, *J. Comput. Chem.* **2011**, *32*, 1456–1465; b) V. K. Prasad, A. Otero-de-la-Roza, G. A. DiLabio, *J. Chem. Theory Comput.* **2022**, *18*, 2208–2232; c) R. Sure, S. Grimme, *J. Chem. Theory Comput.* **2015**, *11*, 3785–3801; d) J. G. Brandenburg, M. Hochheim, T. Bredow, S. Grimme, *J. Phys. Chem. Lett.* **2014**, *5*, 4275–4284; e) M. Bursch, J.-M. Mewes, A. Hansen, S. Grimme, *Angew. Chem. Int. Ed.* **2022**, *61*, e202205735.
- [34] U. Warzok, M. Marianski, W. Hoffmann, L. Turunen, K. Rissanen, K. Pagel, C. A. Schalley, *Chem. Sci.* **2018**, *9*, 8343–8351.
- [35] a) M. Grajda, M. Wierzbicki, P. Cmoch, A. Szumna, *J. Org. Chem.* **2013**, *78*, 11597–11601; b) F. Jia, Z. He, L.-P. Yang, Z.-S. Pan, M. Yi, R.-W. Jiang, W. Jiang, *Chem. Sci.* **2015**, *6*, 6731–6738; c) Z. He, G. Ye, W. Jiang, *Chem. Eur. J.* **2015**, *21*, 3005–3012; d) M. Gaedke, H. Hupatz, F. Witte, S. M. Rupf, C. Douglas, H. V. Schröder, L. Fischer, M. Malischewski, B. Paulus, C. A. Schalley, *Org. Chem. Front.* **2022**, *9*, 64–74; e) P. Mal, B. Breiner, K. Rissanen, J. R. Nitschke, *Science* **2009**, *324*, 1697–1699; f) A. Shivanyuk, J. Rebek, Jr., *Proc. Natl. Acad. Sci. USA* **2001**, *98*, 7662–7665; g) A. Scarso, L. Trembleau, J. Rebek, Jr., *Angew. Chem. Int. Ed.* **2003**, *42*, 5499–5502; h) M. F. Bush, Z. Hall, K. Giles, J. Hoyes, C. V. Robinson, B. T. Ruotolo, *Anal. Chem.* **2010**, *82*, 9557–9565; i) V. Shrivastav, M. Nahin, C. J. Hogan, C. Larriba-Andaluz, *J. Am. Soc. Mass Spectrom.* **2017**, *28*, 1540–1551; j) D. P. Weimann, H. D. F. Winkler, J. A. Falenski, B. Kokschi, C. A. Schalley, *Nat. Chem.* **2009**, *1*, 573–577; k) K. M. Ervin, P. B. Armentrout, *J. Chem. Phys.* **1985**, *83*, 166–189.

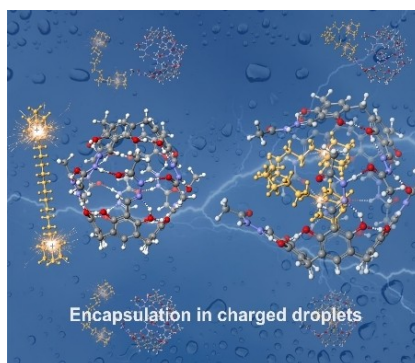
Manuscript received: July 3, 2023

Accepted manuscript online: September 19, 2023

Version of record online: ■■, ■■

RESEARCH ARTICLE

“Spring-loaded” resorcinarene capsules form in charged droplets. The complexes are not observed in solution and form during electrospray ionisation under conditions violating electroneutrality. The strained resorcinarene and dicationic guest complexes survive due to strengthening of non-covalent bonds in the gas-phase enabling structural assignment via different tandem mass spectrometry techniques.



D. L. Stares, Prof. A. Szumna,
Prof. Dr. C. A. Schalley**

1 – 9

**Encapsulation in Charged Droplets
Generates Distorted Host-Guest
Complexes**



Chemistry–A European Journal

Supporting Information

Encapsulation in Charged Droplets Generates Distorted Host-Guest Complexes

Daniel L. Stares, Agnieszka Szumna,* and Christoph A. Schalley*

Contents

Synthesis and Characterisation.....	1
General information	1
Synthesis and characterisation of acylhydrazone resorcinarene capsules.....	1
DnD (PF ₆) ₂ synthesis.....	7
Preparation of DnD (BArF) ₂	7
Encapsulation studies via NMR.....	9
Mass Spectrometry General	12
Collision Induced Dissociation and Survival Yield Curve.....	15
Ion Mobility mass spectrometry	19
HDX experiments	19
Computational Structures General	23
Computational structures of tertiary compound 3	23
Computational structures of H-bonded dimers 1₂ and 2₂	24
References	28

Synthesis and Characterisation

General information

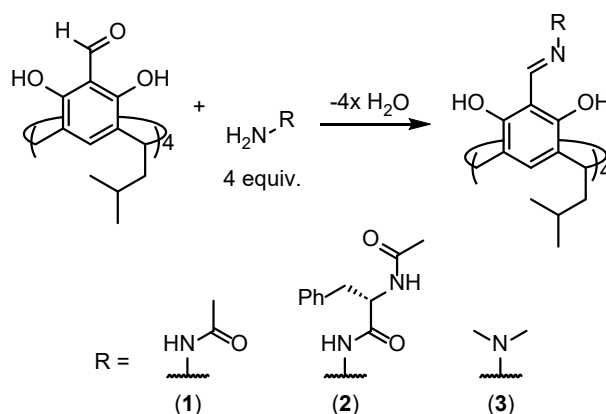
Reagents were purchased from chemical vendors and used without further purification. A Water's Synapt G2-S (Manchester, UK) was used for high resolution mass spectrometry (HRMS). ^1H , ^{13}C , ^{19}F NMR spectra were recorded on either a Varian 600 MHz, a JEOL ECZ 600 MHz or a Bruker AVANCE 700 MHz instrument with residual solvent signal as internal standard. Shifts are reported in ppm and assigned with s (singlet), d (doublet), t (triplet), m (multiplet). Hydrodynamic diameter was calculated by the Stokes-Einstein equation:

$$d = \frac{k_B T}{3\pi\eta D}$$

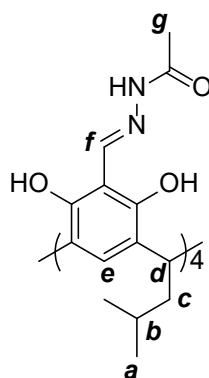
where k_B is Boltzmann's constant, T is temperature, η is solvent viscosity, D is diffusion

Synthesis and characterisation of acylhydrazone resorcinarene capsules.

Acylhydrazone cavitands were synthesised according to the following procedure based on a previous literature procedure.^[1]



Scheme 1: General reaction scheme to generate acylhydrazone resorcinarene capsules.



Acetylhydrazoneresorcinarene (**1**)

Tetraformylresorcin[4]arene (200 mg, 0.24 mmol, 1 equiv.) and acethydrazide (90 mg, 1.25 mmol, 5 equiv.) were dissolved in chloroform (10 mL) and stirred in a sealed pressure vial at 70°C for 18 hrs. The solvent was evaporated and the solid washed with CH₃OH (3 x 25 mL).

Yield: 92%

¹H NMR (600 MHz, CDCl₃): δ-12.93 (s, **OH**, 1H), 10.98 (s, **NH**, 1H), 8.76 (s, **OH**, 1H), 8.37 (s, **f**, 1H), 7.12 (s, **e**, 1H), 4.45 (t, **d**, 2H), 2.07-1.97 (m, **c**, 2H), 1.47 (q, **b**, 1H), 0.97 (d, **a**, 6H).

¹³C NMR (151 MHz, CDCl₃): δ-167.83, 152.43, 152.24, 147.34, 126.34, 124.30, 123.60, 107.06, 41.88, 30.46, 26.26, 23.02, 22.78, 21.98.

DOSY (600 MHz, CDCl₃, 298K): 4.20 x 10⁻¹⁰ m²s⁻¹; hydrodynamic diameter: ~19.3 Å

HRMS-ESI: *m/z* for C₅₆H₇₃O₁₂N₈⁺ ([M+H]⁺) *calc.* 1049.5348 *found.* 1049.5336

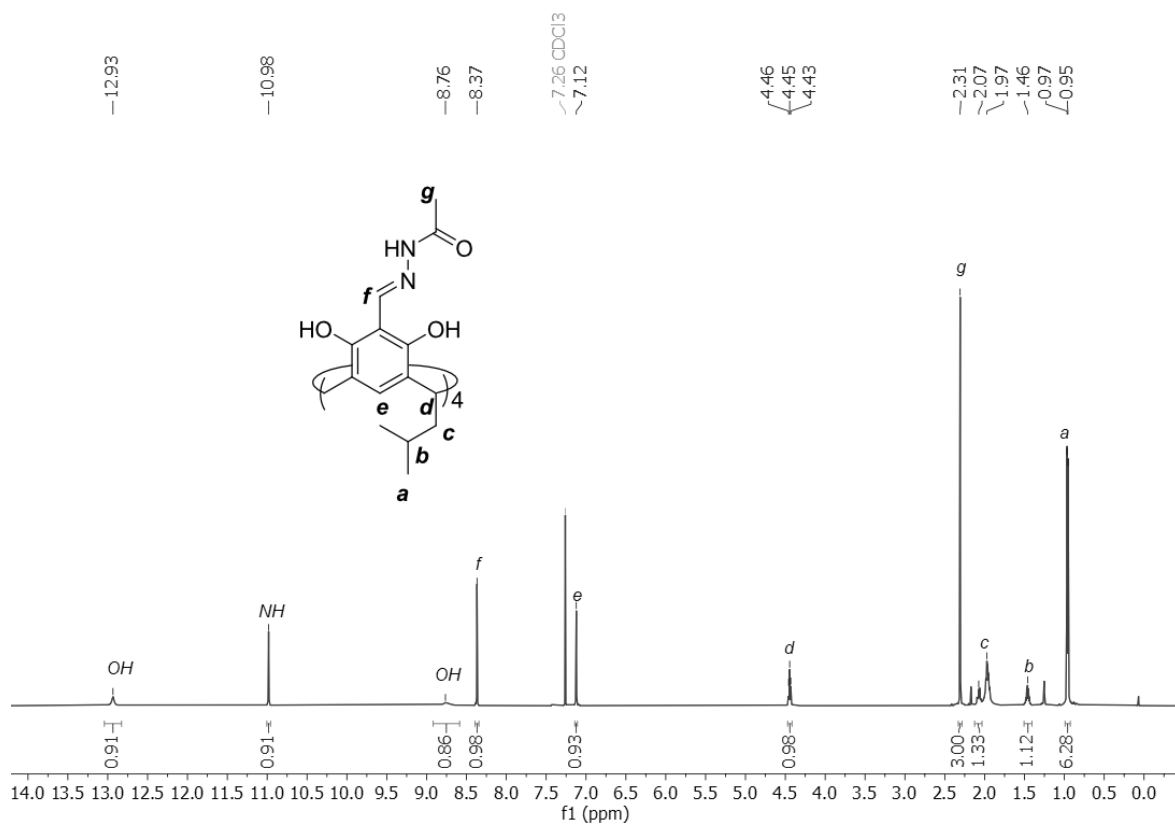


Figure S1: ^1H NMR of compound **1** (600 MHz, CDCl_3 , 298 K)

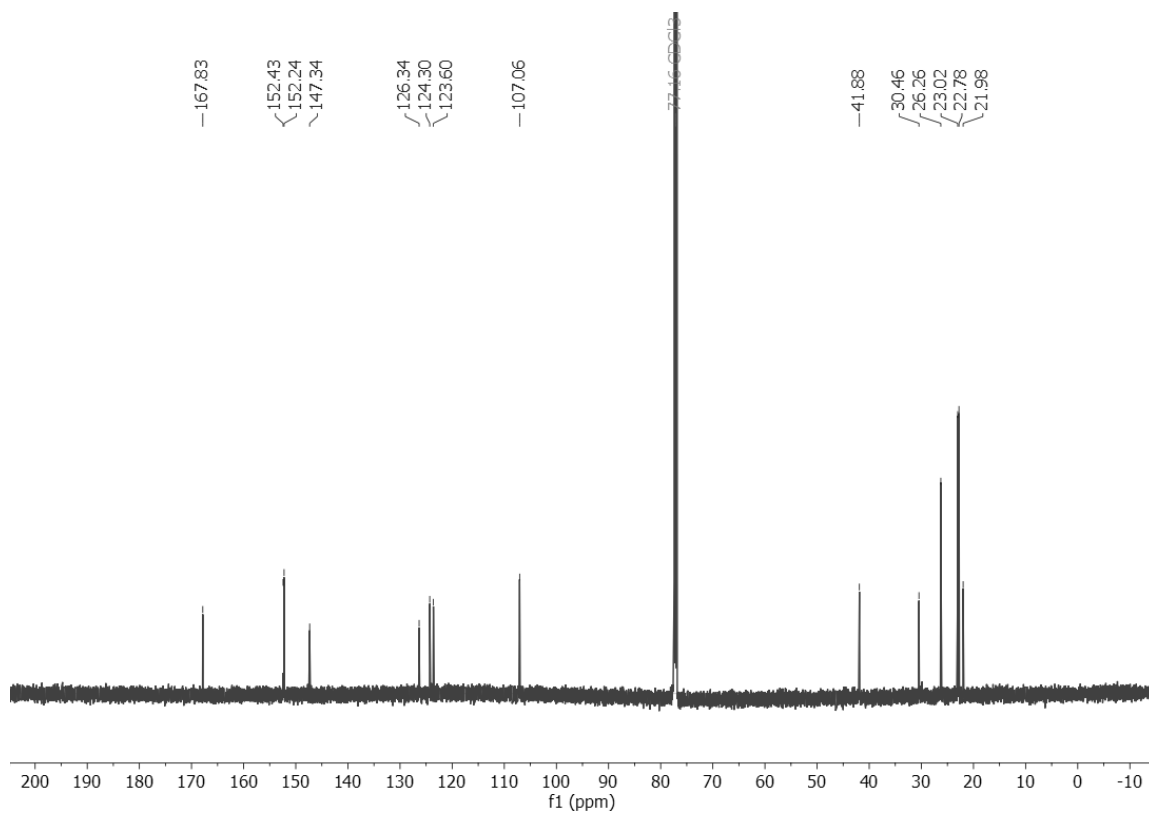


Figure S2: ^{13}C NMR of compound **1** (151 MHz, CDCl_3 , 298 K)

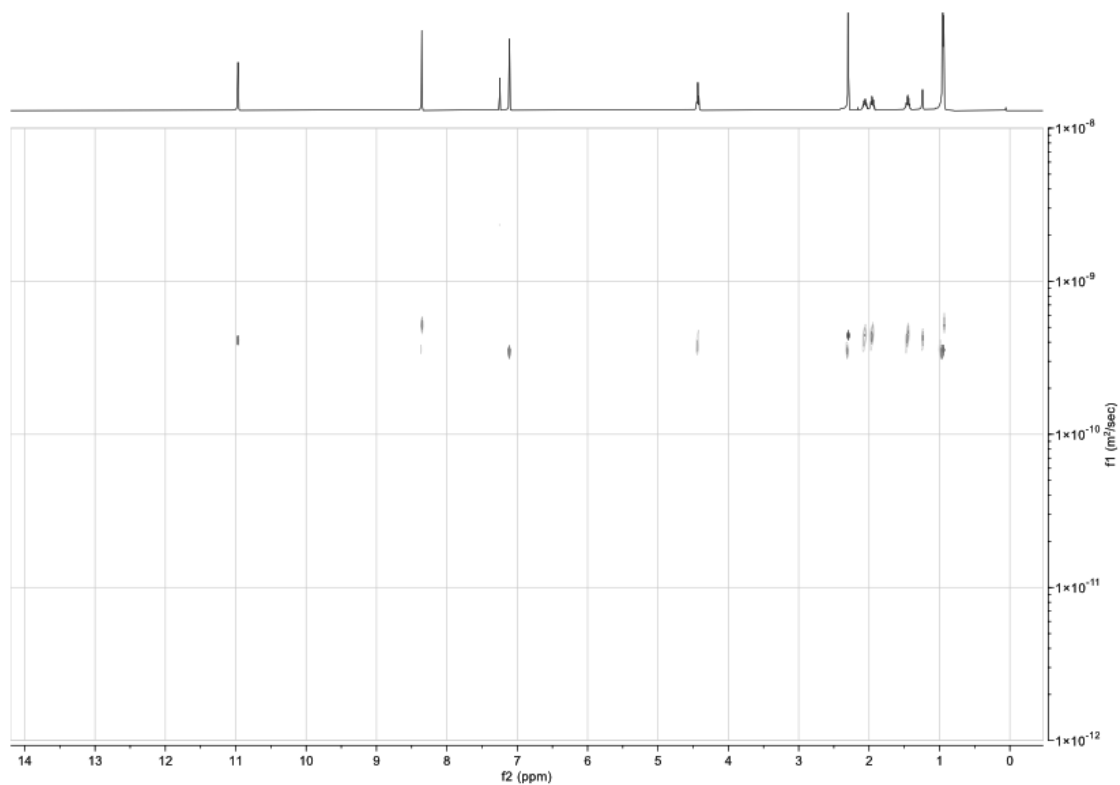


Figure S3: DOSY spectrum of compound **1** (600 MHz, CDCl₃, 298 K). The diffusion coefficient is consistent with a dimer.

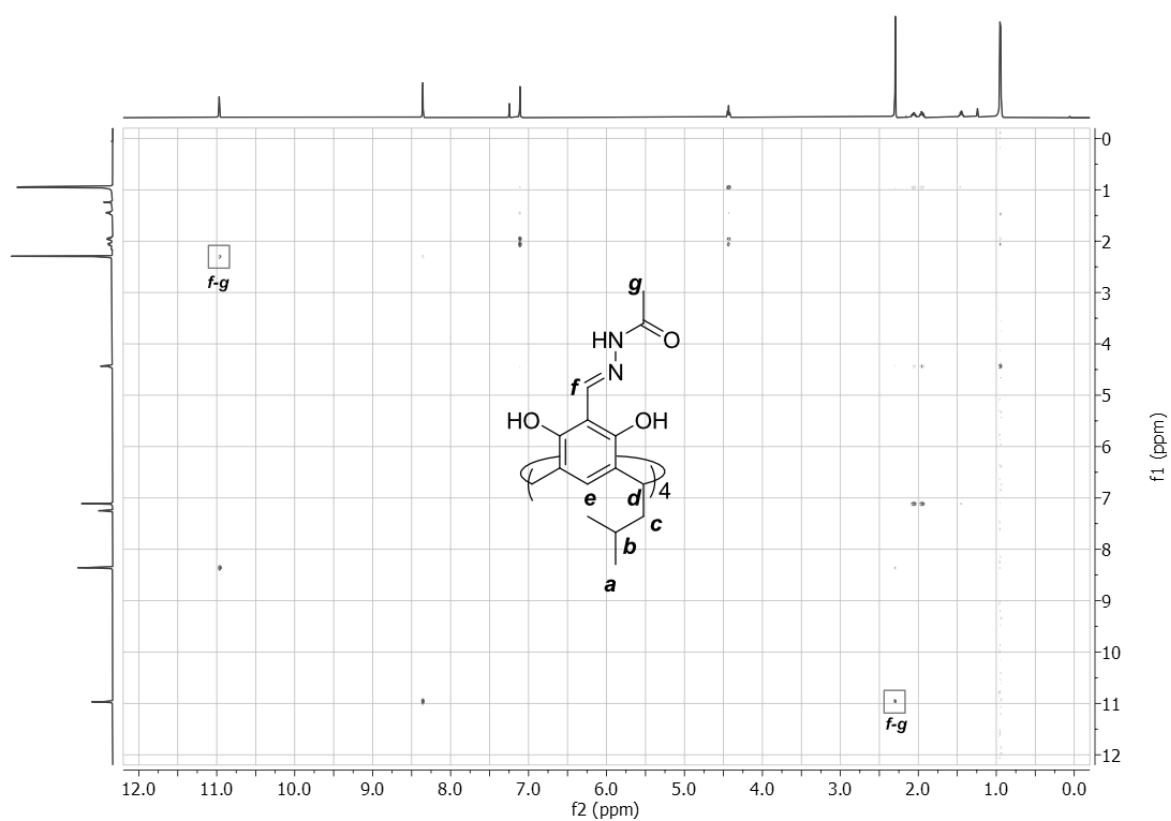


Figure S4: ROESY spectrum of **1** (600 MHz, CDCl₃, 298 K). The signal which supports dimerisation is enclosed with a box.

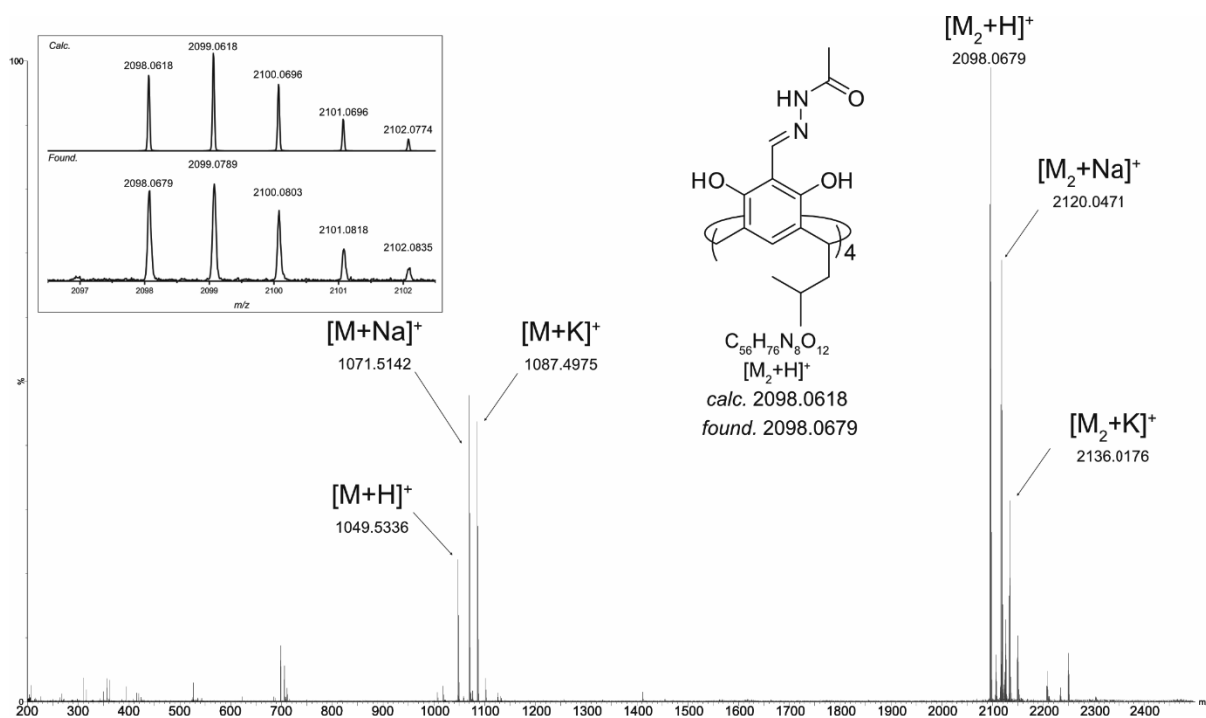
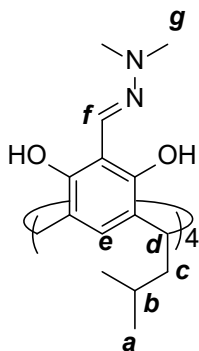


Figure S5: Full range HRMS of compound **1**



N,N-Dimethylhydrazoneeresorcinarene (3)

Tetraformylresorcinarene (50 mg, 0.061 mmol, 1 eq) and N,N-dimethylhydrazine (253 mg, 200 μ L, 0.91 mmol, 15 equiv.) were dissolved in CH_3OH (20 mL) and the reaction mixture was stirred at room temperature for 48hrs. The solution was filtered and the precipitate washed with CH_3OH (3x25mL)

Yield: 89%

1H NMR (700 MHz, $CDCl_3$): δ -13.46 (s, **OH**, 1H), 8.53 (s, **OH**, 1H), 7.89 (s, **f**, 1H), 7.16 (s, **e**, 1H), 4.54 (t, **d**, 2H), 2.86 (s, **g**, 6H), 2.07-1.97 (m, **c**, 2H), 1.51 (q, **b**, 1H), 0.99 (d, **a**, 6H).

^{13}C NMR (176 MHz, $CDCl_3$): δ -151.73, 150.68, 136.38, 123.92, 123.81, 123.61, 108.38, 43.19, 42.66, 30.64, 26.27, 23.02.

HRMS-ESI: m/z for $C_{56}H_{81}O_8N_8^+$ ($[M+H]^+$) *calc.* 993.6177 *found.* 993.6167

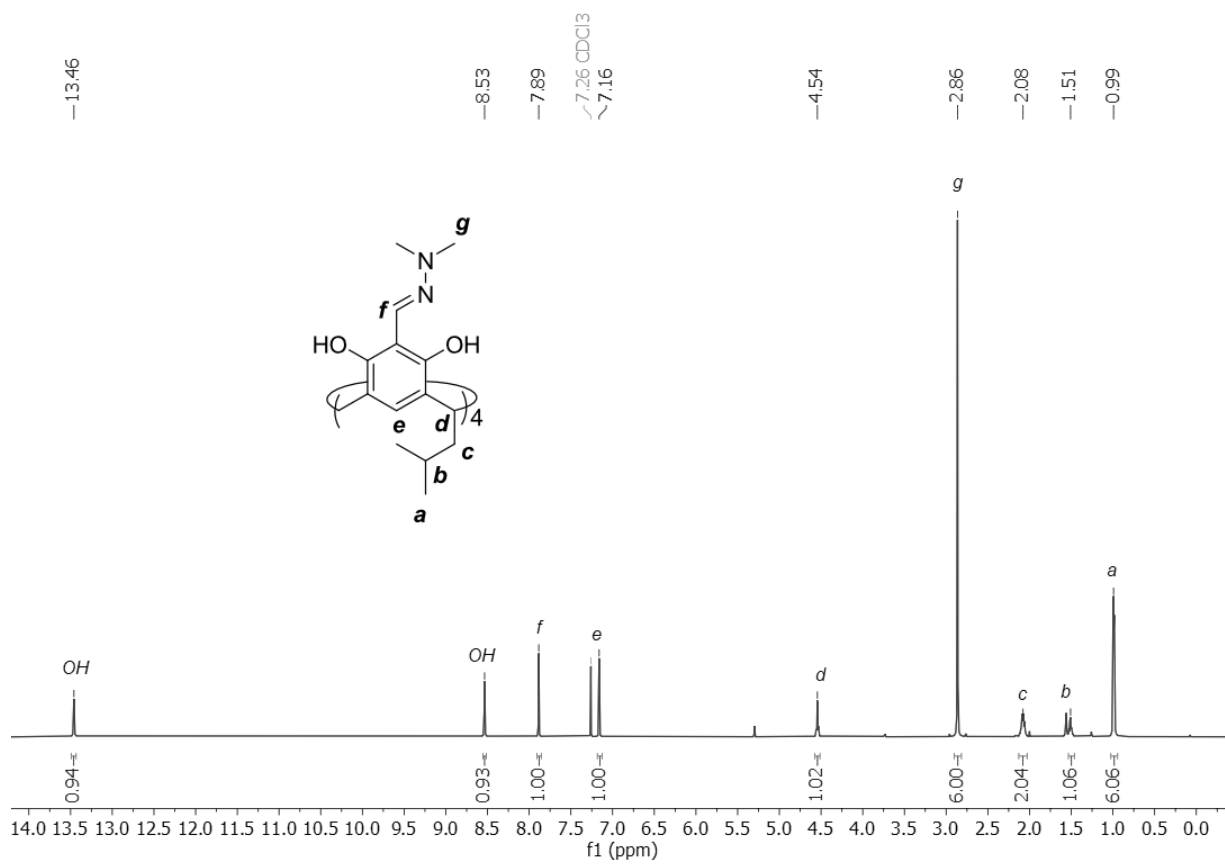


Figure S6: ^1H NMR of compound **3** (700 MHz, CDCl_3 , 298 K)

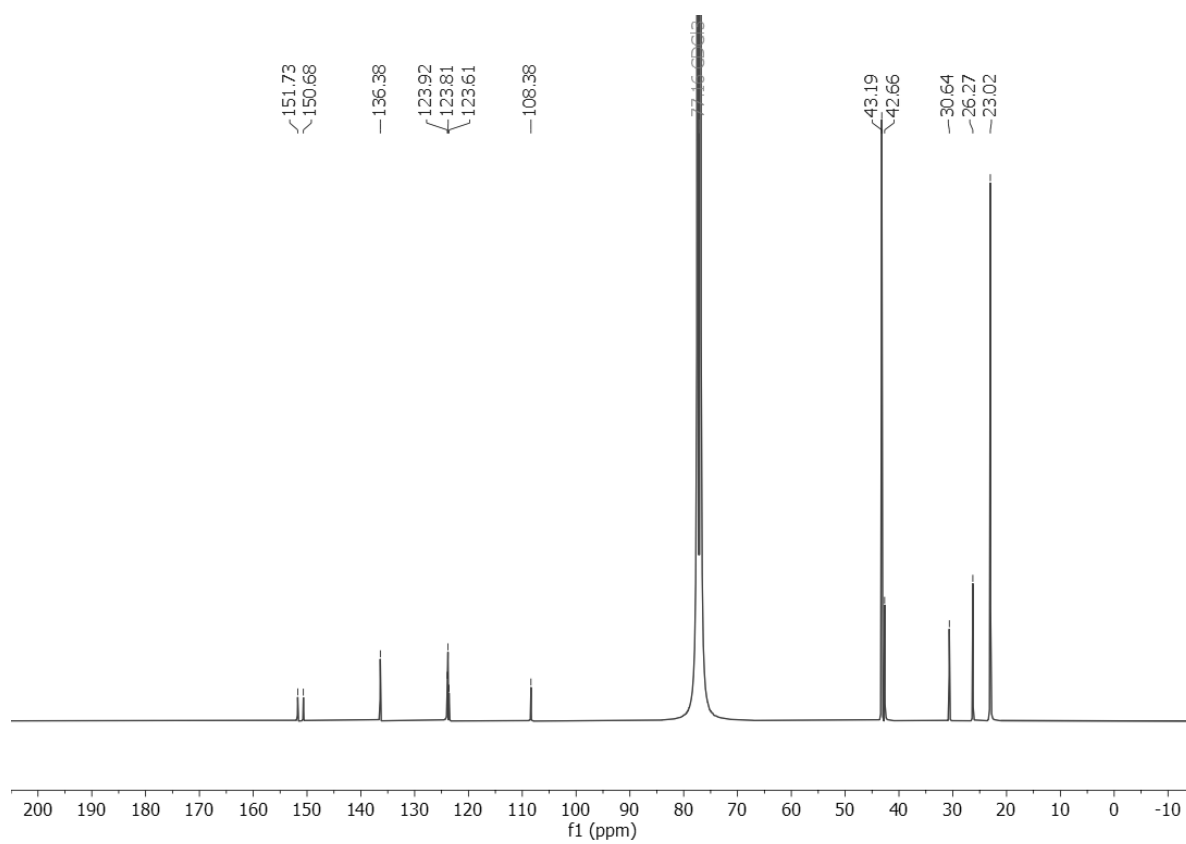


Figure S7: ^{13}C NMR of compound **3** (176 MHz, CDCl_3 , 298 K)

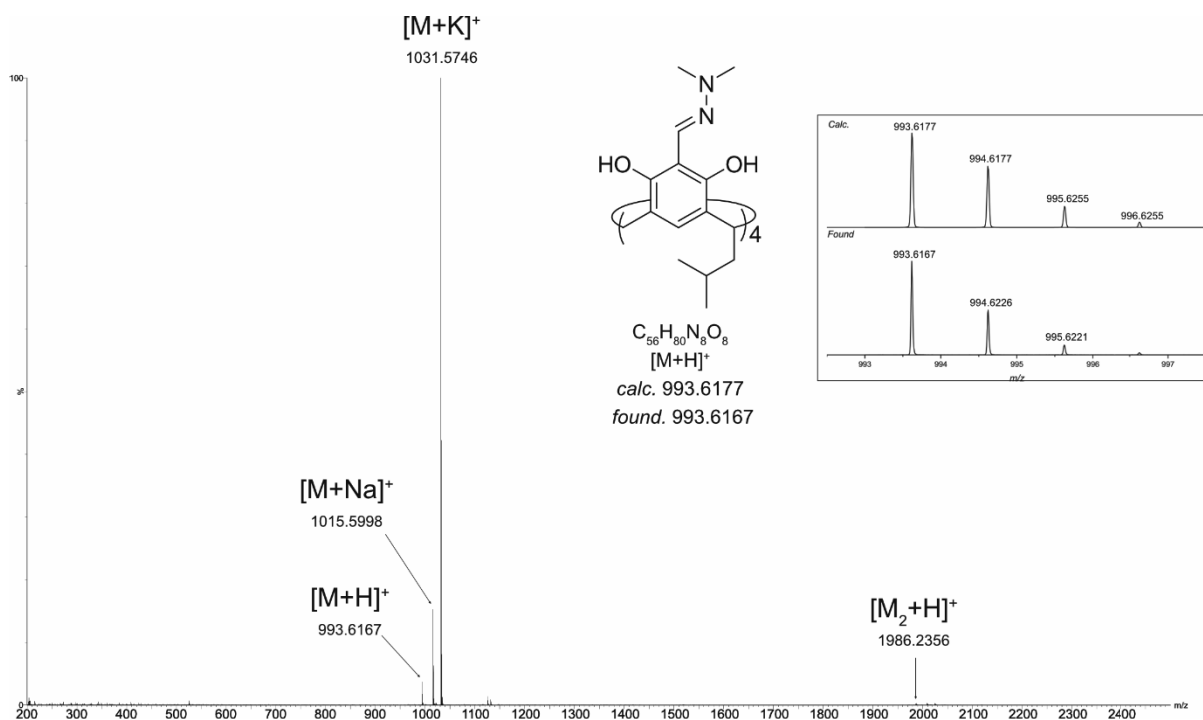


Figure S8: HRMS of compound **3**

DnD(PF₆)₂ synthesis

α,ω -alkylbisDABCONium (**DnD**) (PF₆)₂ guests were synthesised according to a literature procedure.^[2]

1,4'-Diazabicyclo[2.2.2] (DABCO) (8 equiv.) was dissolved in CH₃CN (25 mL). The dibromoalkane (1 equiv.) in CH₃CN (5 mL) was added dropwise and the solution stirred overnight at RT. The solvent was removed and the residue washed several times with diethylether and acetone. The remaining residue was dissolved in deionised water and then saturated aqueous NH₄PF₆ (5 mL) was added. The solution was allowed to stir for 3 hours, the precipitate was filtered and washed several times with deionised H₂O. The precipitate was dried to afford the **DnD**(PF₆)₂ as a colourless solid.

Preparation of DnD(BArF)₂.

Counterion exchange to BArF was adapted from previous procedure.^[3] **DnD**Br₂ was dissolved in CH₃OH. NaBArF (2 equiv.) was added and the solution was stirred for 3 hours at room temperature. The solvent was removed via rotary evaporation and the resulting product was dissolved in dichloromethane, washed with H₂O and dried with MgSO₄. The solvent was removed via rotary evaporation to yield the product as a slightly yellow solid.

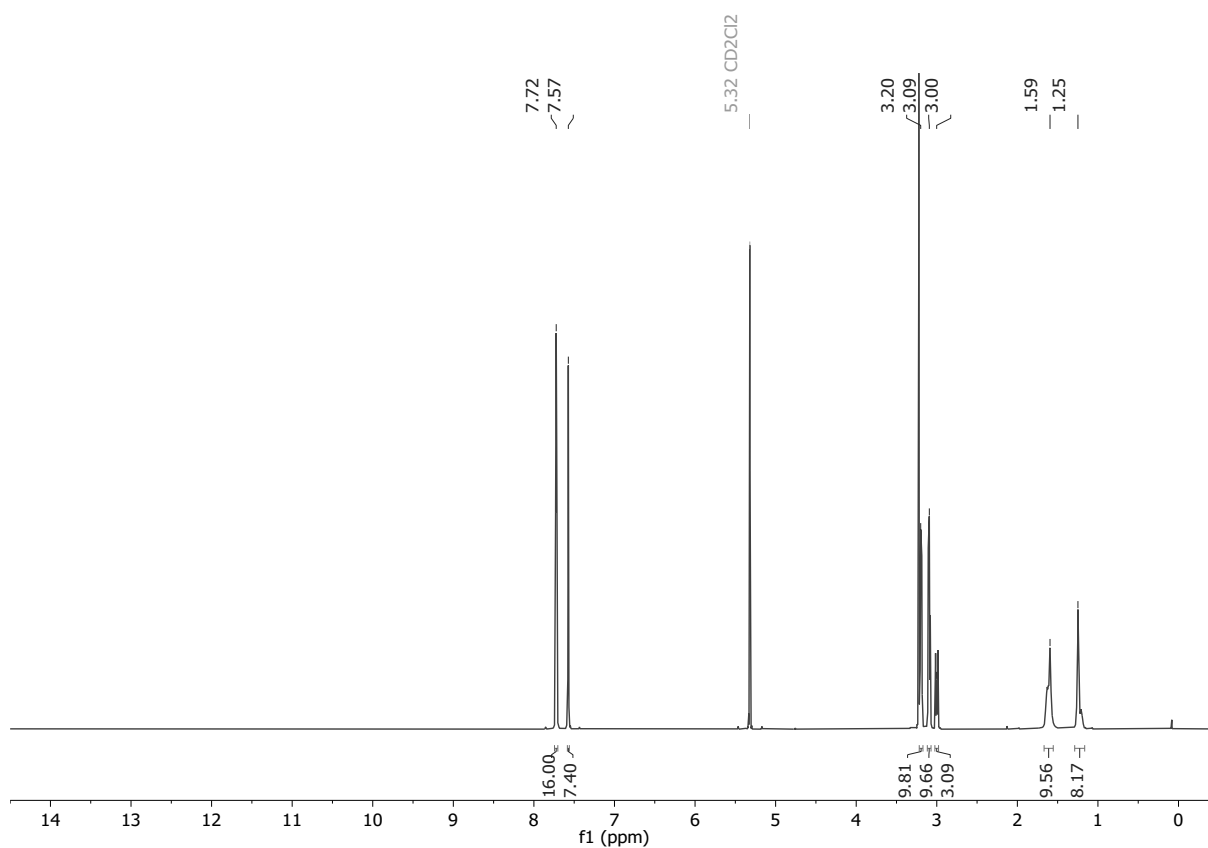


Figure S9: ¹H NMR of compound **D9D(BArF)₂** (600 MHz, CD₂Cl₂, 298 K)

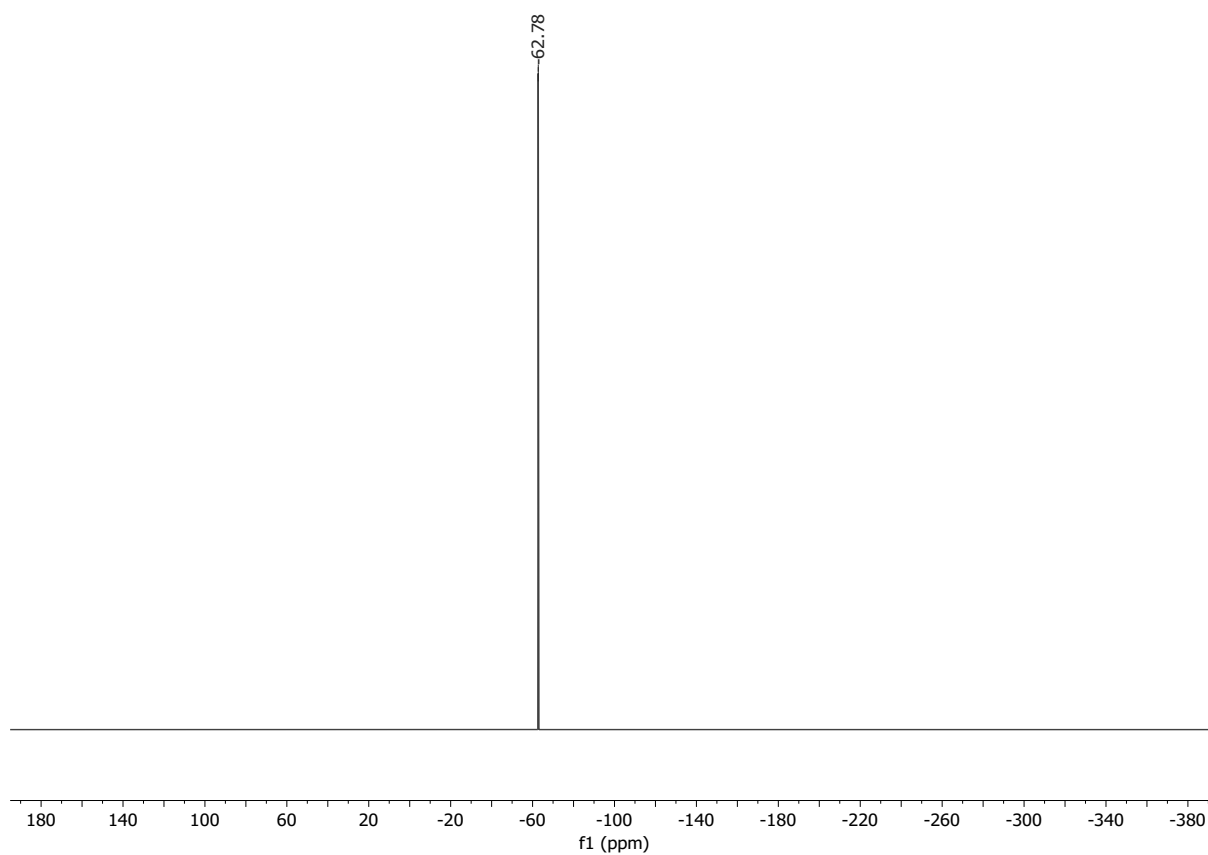


Figure S10: ¹⁹F NMR of compound **D9D(BArF)₂** (565 MHz, CD₂Cl₂, 298 K)

Encapsulation studies via NMR

NMR analysis was complicated due to the differing solubilities of the hosts and **DnD**(PF₆)₂ in the concentrations required for NMR and restriction to solvents which are not competitive for hydrogen bonding. Several different solvents were tested (CDCl₃, CD₂Cl₂, C₂D₄Cl₂ and C₂D₂Cl₄) but unfortunately no single solvent was found to be able to dissolve both host and guest. Therefore, a mixture of 4:1 CDCl₃ and CD₃CN was used to study the complex in solution. Although, CD₃CN is competitive for hydrogen bonds, it would not be expected to disrupt dimerization in these systems which have been shown to tolerate even comparatively high amounts of the more competitive CH₃OH. Encapsulation of a guest into a resorcinarene capsule would be expected to produce a clear upfield shift in the guest signals due to the anisotropy of the aromatic rings of the resorcinarene core leading to a shielding environment.^[4] When measurements were made with **D5D**(PF₆)₂ and **1₂** no shifts of either the host or guest could be detected (Figure S11). One explanation is that ion-pairing of the **D5D**(PF₆)₂ is preventing encapsulation. Measurements were also completed with tetrakis(3,5-bis(trifluoromethyl)phenyl)borate (BarF) **DnD** salts. BARF is a very weakly coordinating counterion and also increases the solubility of the guests in non-polar solvents.^[5] This meant that for longer guests (n ≥ 9), a single solvent (DCM) could be used to dissolve both host and guests. Even with these changes, no interaction between guest and **1₂** could be seen (Figure S12). This did not change when waiting several days (Figure S13), nor when measuring with different guests (Figure S14).

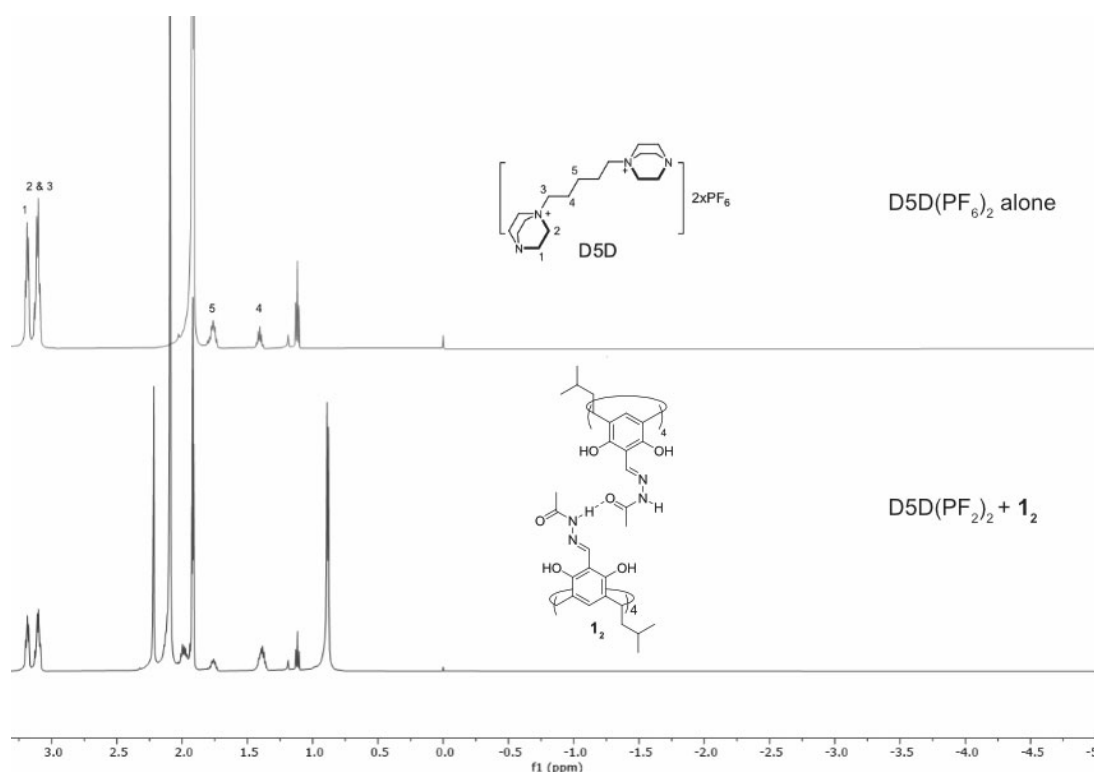


Figure S11: ^1H NMR of $\text{D5D}(\text{PF}_6)_2$ (top); $\text{D5D}(\text{PF}_6)_2 + \mathbf{1}_2$ (bottom) (600 MHz; $\text{CDCl}_3:\text{CD}_3\text{CN}$; 4:1, 298 K). Encapsulation of the guest would produce upfield shifts of guest signal (up to -5ppm) which were not seen indicating no interaction between host and guest.

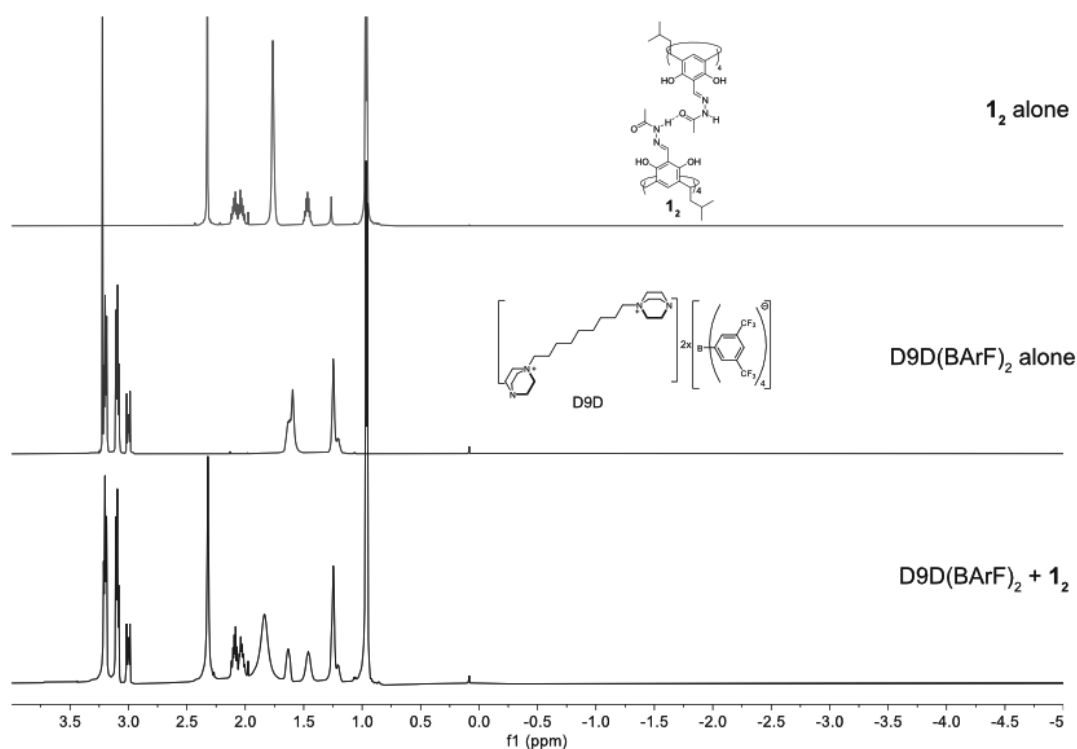


Figure S12: ^1H NMR of $\mathbf{1}_2$ (top); $\text{D9D}(\text{BArF})_2$ (middle); $\text{D9D}(\text{BArF})_2 + \mathbf{1}_2$ (bottom) (600 MHz; CD_2Cl_2 , 298 K). Encapsulation of the guest would produce upfield shifts of guest signal (up to -5ppm) which were not seen indicating no interaction between host and guest.

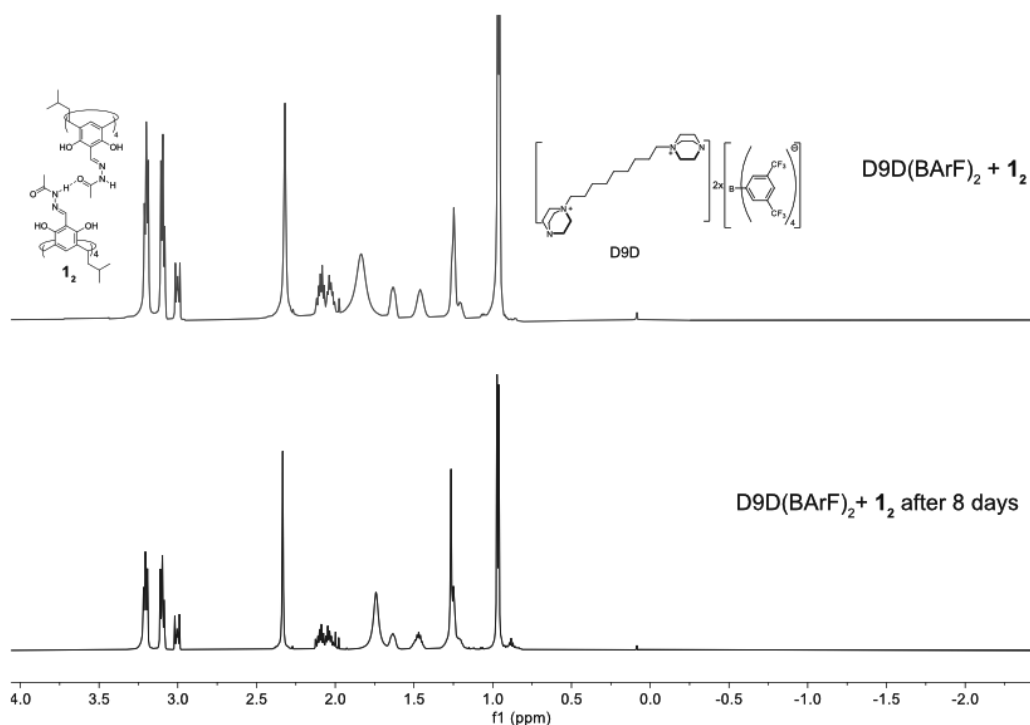


Figure S13: ^1H NMR of $\text{D9D}(\text{BArF})_2 + \mathbf{1}_2$ (top); $\text{D9D}(\text{BArF})_2 + \mathbf{1}_2$ after 8 days (bottom) (600 MHz; CD_2Cl_2 , 298 K). Encapsulation of the guest would produce upfield shifts of guest signal (up to -5ppm) which were not seen indicating no interaction between host and guest even after 8 days.

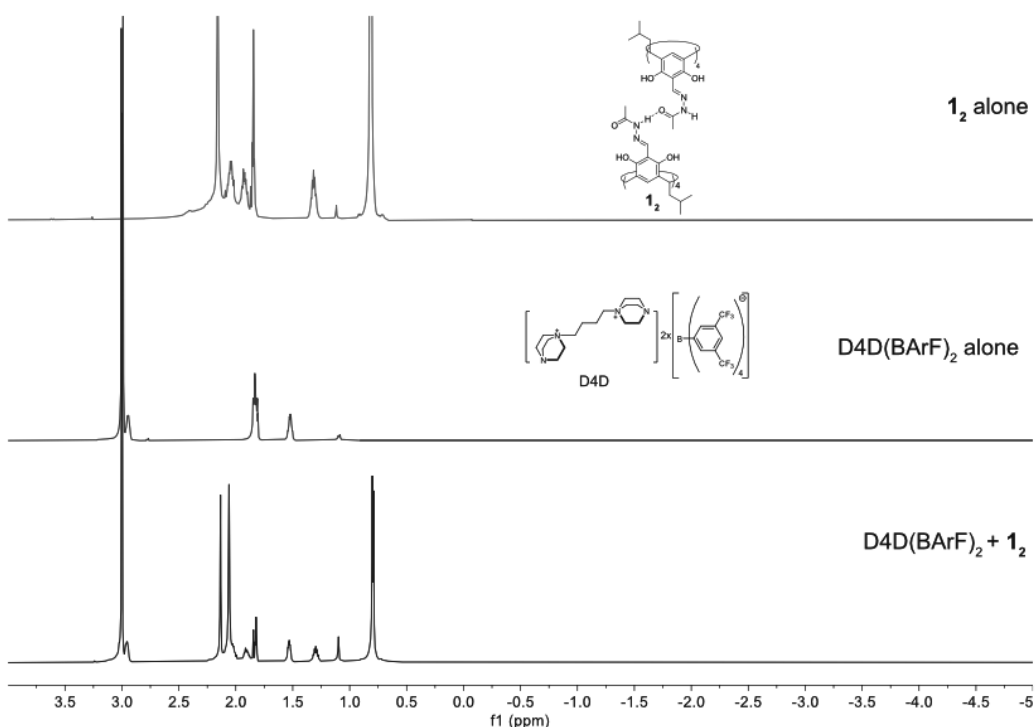


Figure S14: ^1H NMR of $\mathbf{1}_2$ (top); $\text{D4D}(\text{BArF})_2$ (middle); $\text{D4D}(\text{BArF})_2 + \mathbf{1}_2$ (bottom) (600 MHz; $\text{CDCl}_3:\text{CD}_3\text{CN}$; 4:1, 298 K). Encapsulation of the guest would produce upfield shifts of guest signal (up to -5ppm) which were not seen indicating no interaction between host and guest.

Mass Spectrometry

Collision-induced dissociation (CID) and ion-mobility mass spectrometry (IMS) were performed on a Waters Synapt G2-S traveling wave ion-mobility mass spectrometer Q-TOF (Manchester, UK) equipped with a Z-spray electrospray ionization source. Host-guest solutions were prepared as 5 μM of dimer, assuming complete dimerization (i.e. 10 μM of monomer), **DnD**(PF₆)₂ salts were used as guest and were prepared as 1 mM samples in CH₃CN, a final guest concentration of 5 μM was achieved via dilution with DCM. Thus, a typical sample would consist of 5 μM host Dimer, 5 μM **DnD**(PF₆)₂ in 199:1 DCM:CH₃CN, unless otherwise stated.

Samples were injected with a flow rate of 2 $\mu\text{L}/\text{min}$. A capillary voltage of 2.50 kV was used with the sample cone and source offset both set to 40 eV. The source and desolvation temperatures were both set to 40°C.

The drift cell was operated with N₂ as the drift gas and was turned on 45 minutes prior to measuring to allow the pressures to settle. TMCCS_{N₂} were determined with a polyalanine calibrant solution and performed in triplicate with different wave height and velocities according to a literature procedure.^[6] Theoretical TMCCS_{N₂} values were calculated using the trajectory method implemented in IMoS software (Larriba Lab).^[7] Arrival time distributions (ATD) were fitted with a modified gaussian equation in Origin pro 2020 (OriginLab corporation) corporation to determine precise arrival times.

Collision-induced dissociation (CID) was performed in the transfer cell with N₂ as the collision gas.

Hydrogen/deuterium exchange (HDX)^[8] experiments were performed in the hexapole of a Varian Ionspec FTICR-MS equipped with a 7 Tesla superconducting magnet and a Z-spray ESI source. The deuterating agent was CH₃OD (euristope 99% D) and was introduced via a solenoid pulsed valve. Reaction intervals are indicated in the respective spectra.

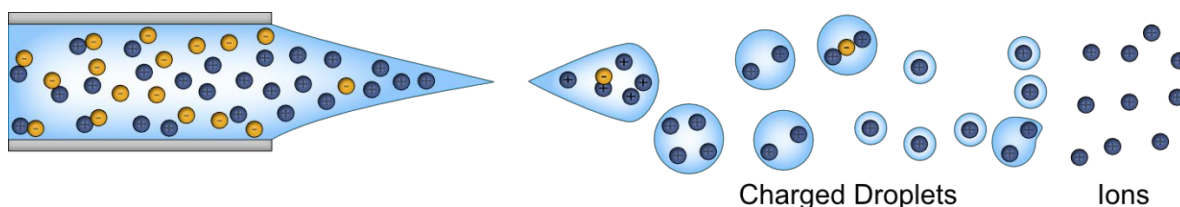


Figure S15: ESI process in positive mode. The charged droplets present an environment where the counterions of the guest are stripped away and allow interaction between host and the naked cation which facilitates encapsulation.

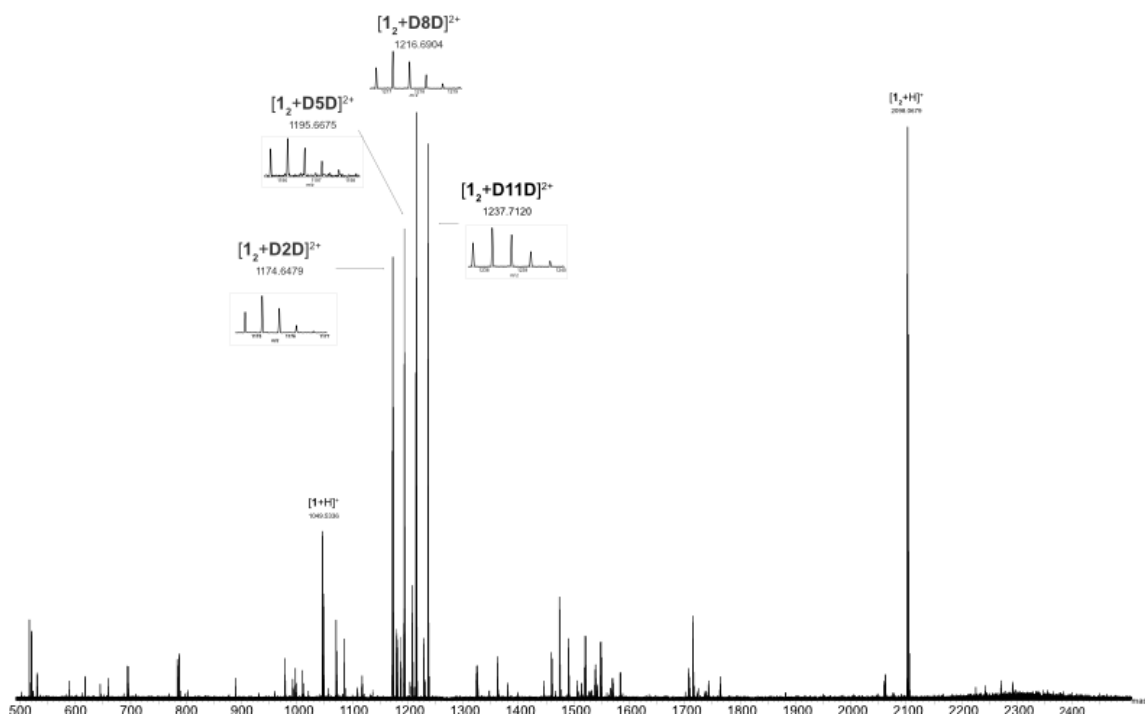


Figure S16: Spectrum of mixture of **1₂** with **D2D(PF₆)₂**, **D5D(PF₆)₂**, **D8D(PF₆)₂**, **D11D(PF₆)₂** (5 μM in 199:1 DCM:CH₃CN).

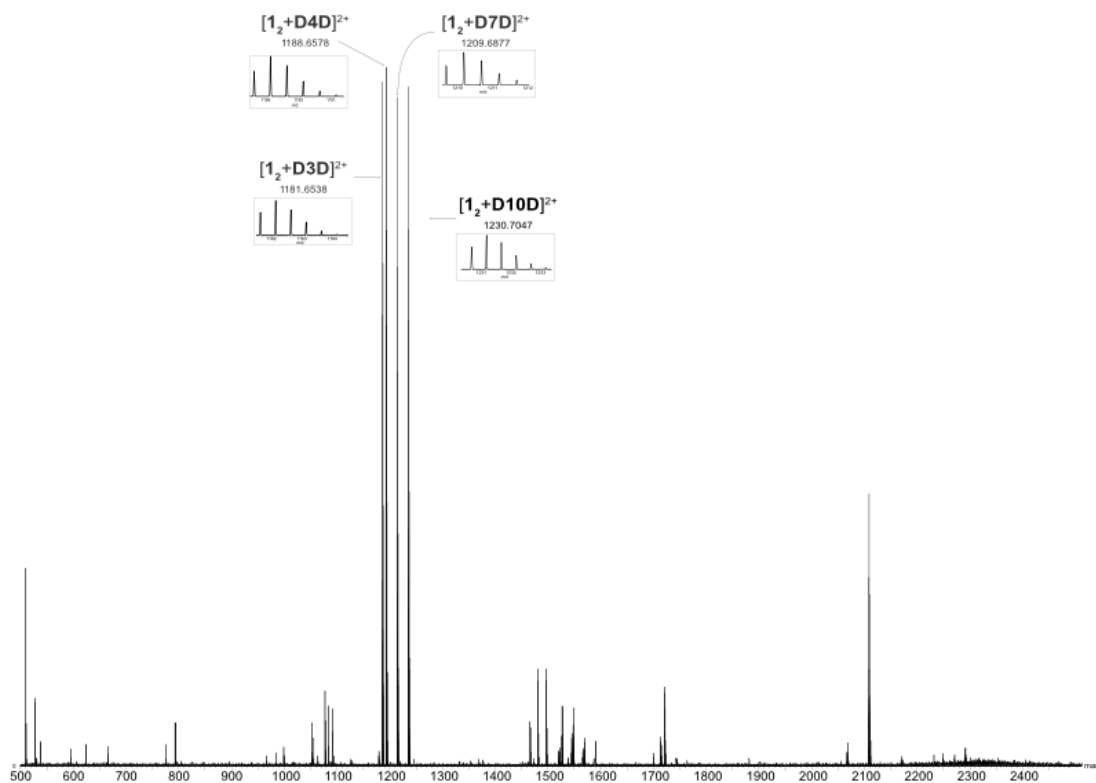


Figure S17: Spectrum of mixture of **1₂** with **D3D(PF₆)₂**, **D4D(PF₆)₂**, **D7D(PF₆)₂**, **D10D(PF₆)₂** (5 μM in 199:1 DCM:CH₃CN).

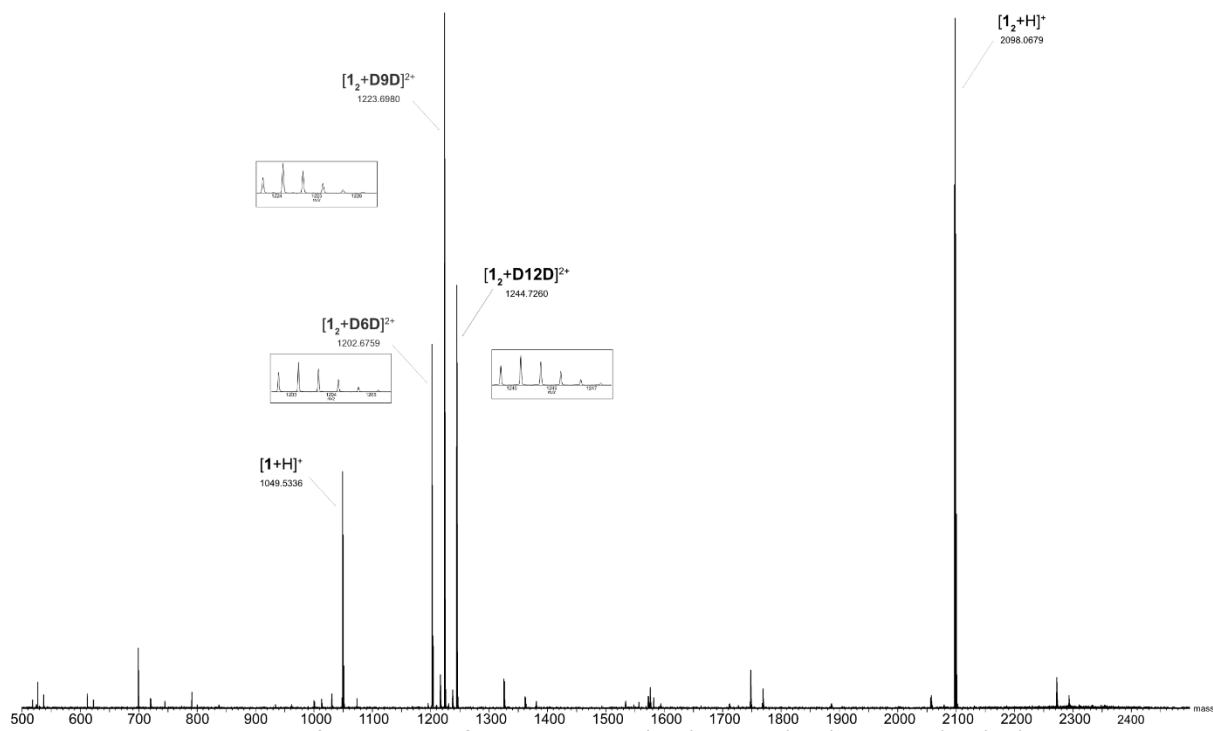


Figure S18: Spectrum of mixture of 1_2 with $D6D(PF_6)_2$, $D9D(PF_6)_2$, $D12D(PF_6)_2$ ($5 \mu M$ in 199:1 DCM:CH₃CN).

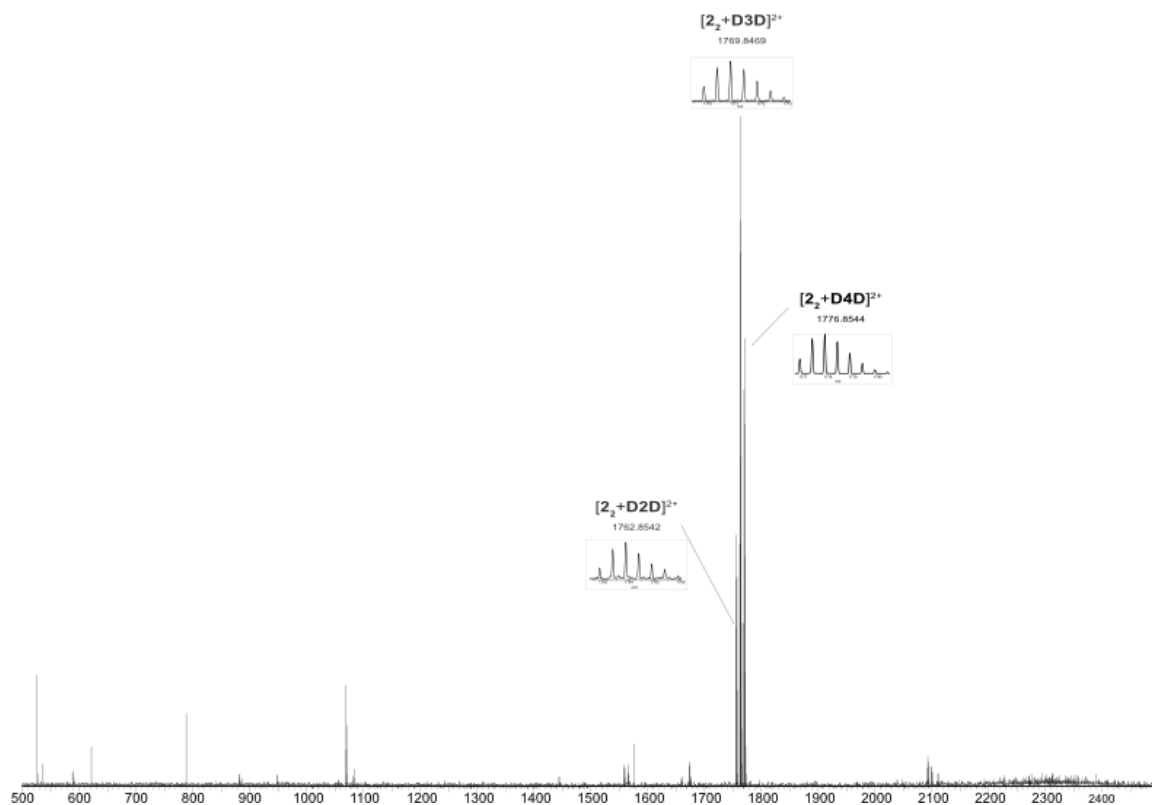


Figure S19: ESI MS of mixture of 2_2 with $D2D(PF_6)_2$, $D3D(PF_6)_2$, $D4D(PF_6)_2$ ($5 \mu M$ in 199:1 DCM:CH₃CN).

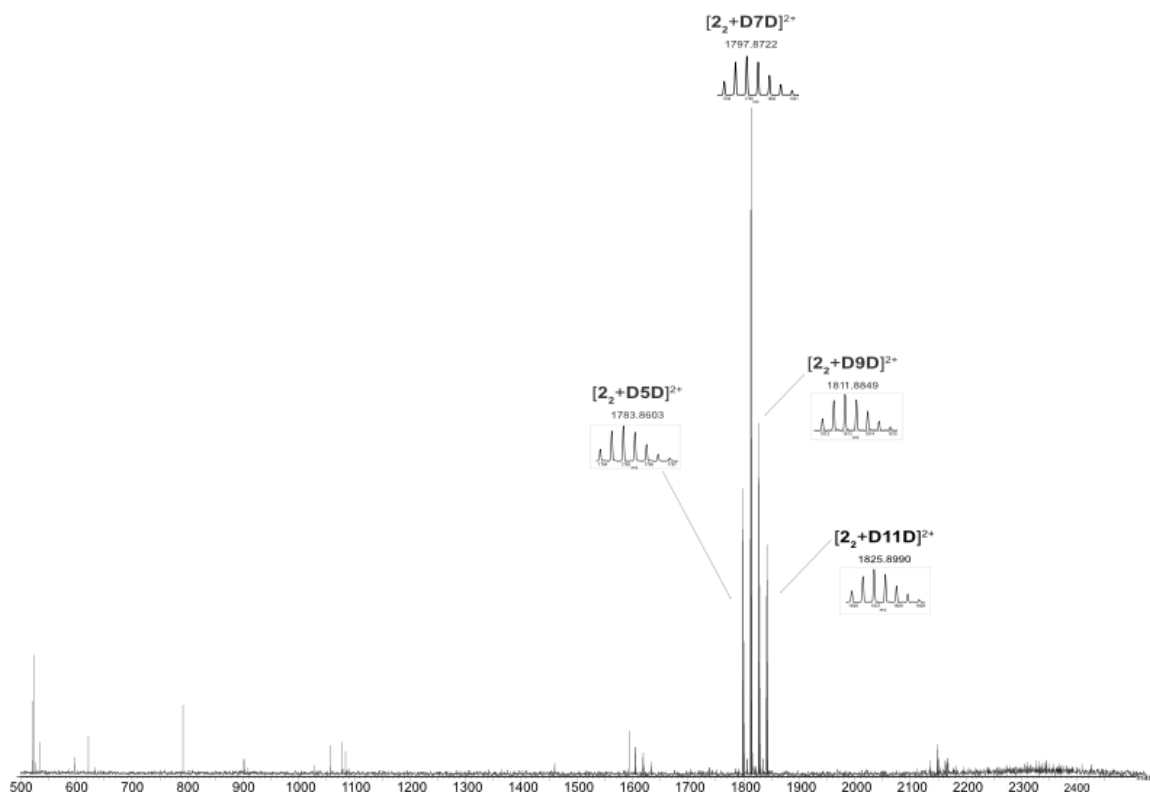


Figure S20: ESI MS of mixture of 2_2 with $D5D(PF_6)_2$, $D7D(PF_6)_2$, $D9D(PF_6)_2$, $D11D(PF_6)_2$ (5 μ M in 199:1 DCM:CH₃CN).

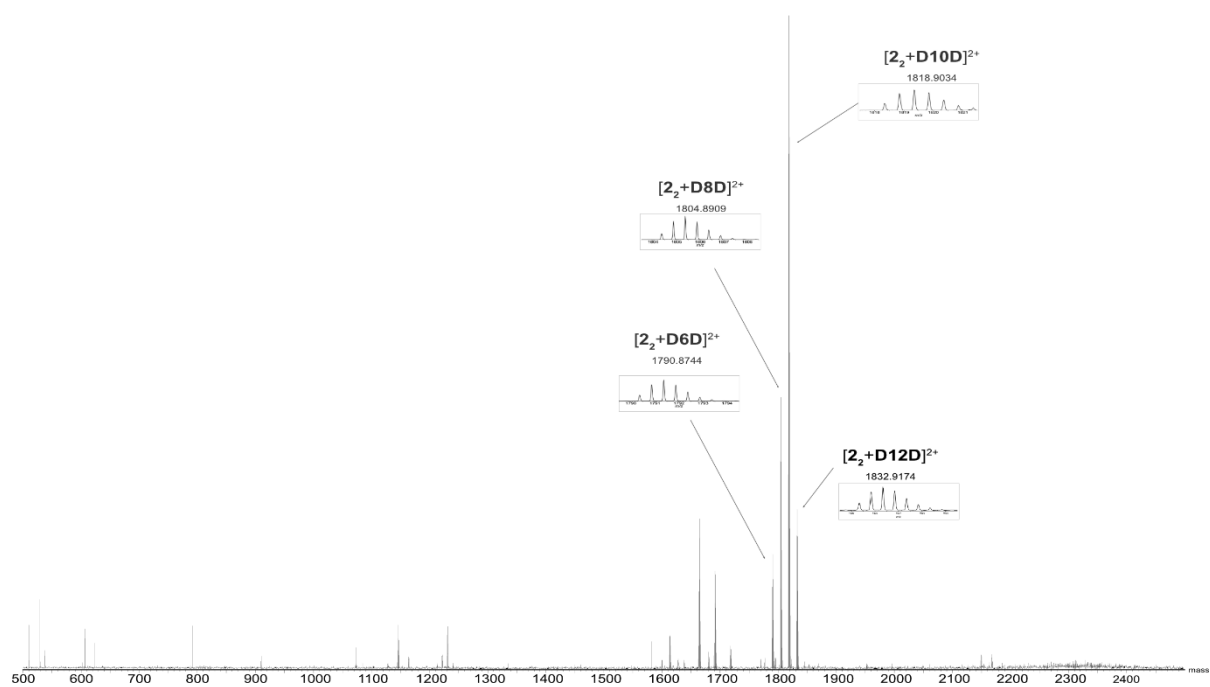


Figure S21: ESI MS of mixture of 2_2 with $D6D(PF_6)_2$, $D8D(PF_6)_2$, $D10D(PF_6)_2$, $D12D(PF_6)_2$ (5 μ M in 199:1 DCM:CH₃CN).

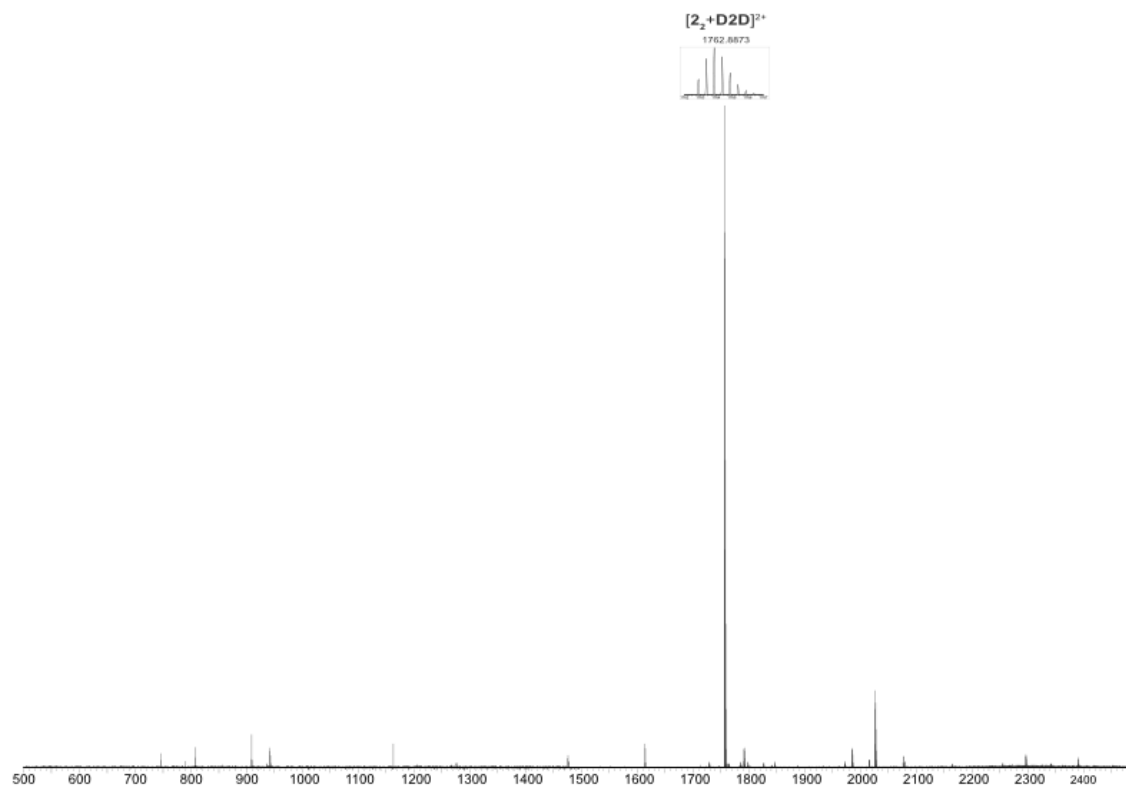


Figure S22: ESI MS of 2_2 with $D2D(PF_6)_2$ (50 μ M in CH_3CN)

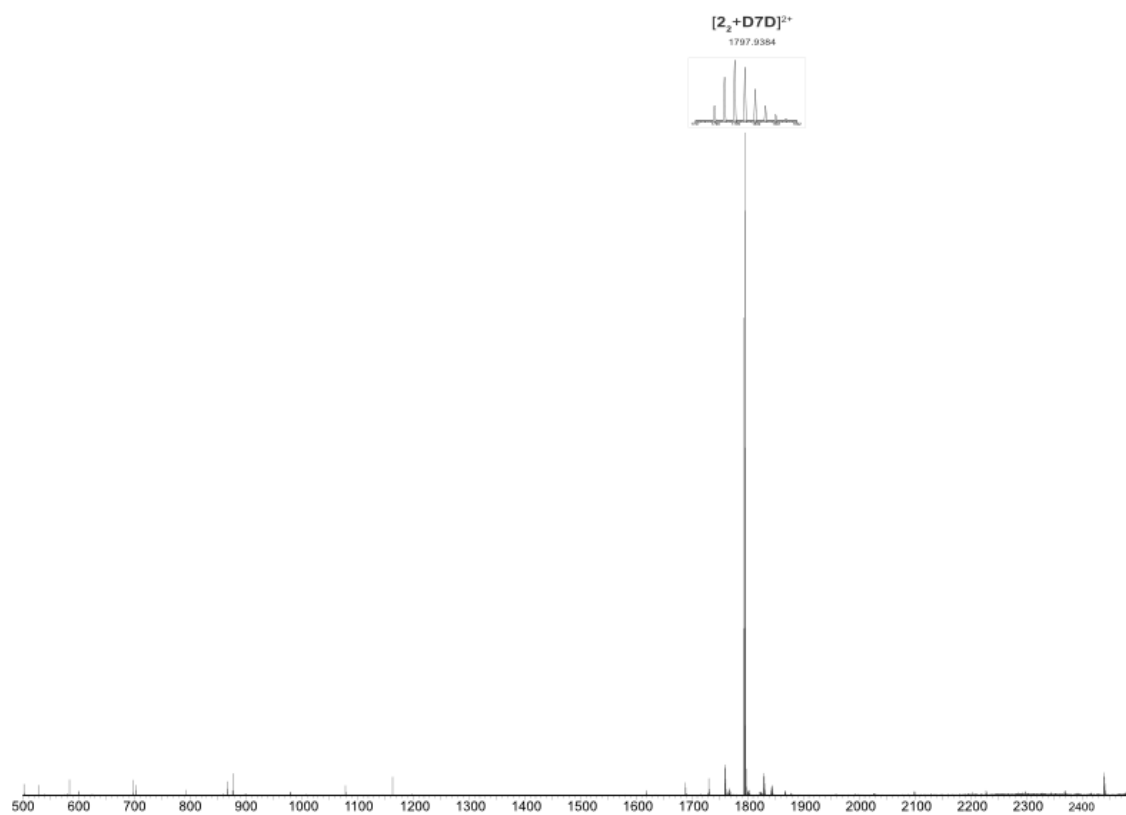


Figure S23: ESI MS of 2_2 with $D7D(PF_6)_2$ (50 μ M in CH_3CN)

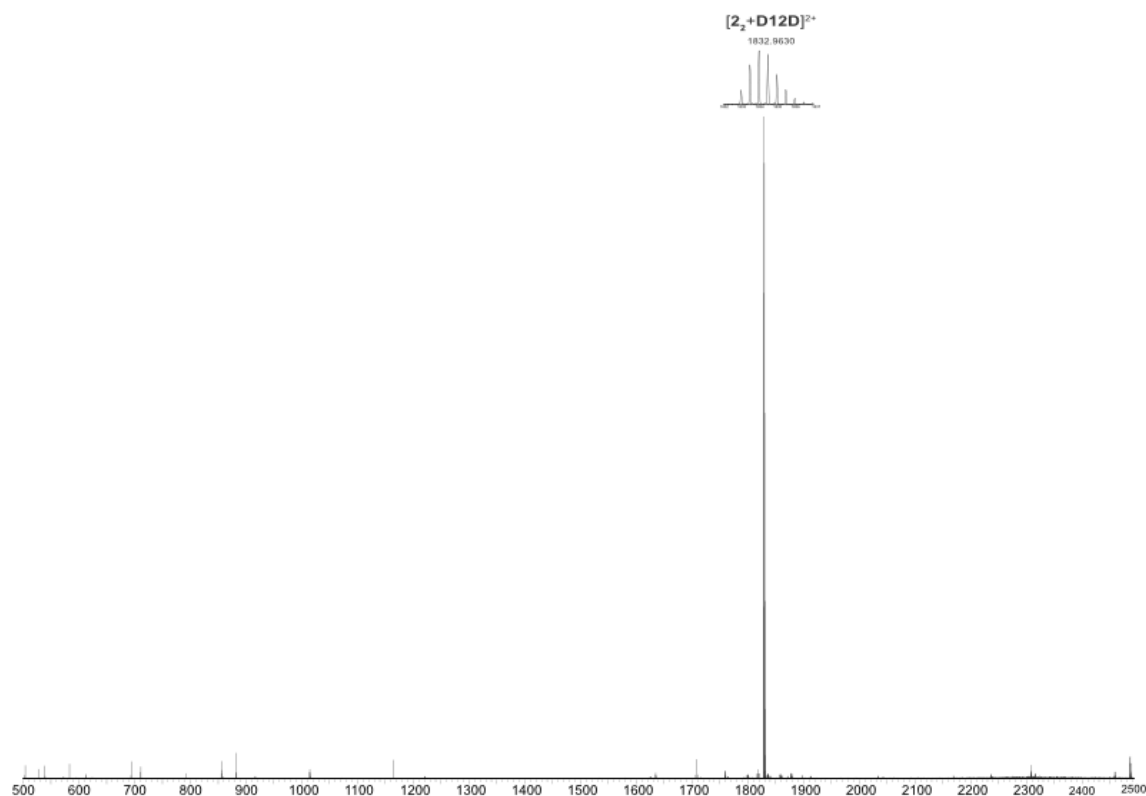


Figure S24: ESI MS of **2₂** with **D12D(PF₆)₂** (50 μM in CH₃CN)

Survival Yield Curves

Data for the survival yield (SY) curves was obtained by taking measurements with increasing CID voltage with 1 volt increments until the parent ion was fragmented completely. Data was exported and processed in Origin pro 2020 (OriginLab corporation). To obtain the 50% SY voltage (SY_{50%}) the relative parent ion intensity was plotted against collision voltage and the curves were fit with a sigmoidal Gaussian with the equation:

$$y = \frac{a}{(1 + e^{(-k*(x-SY_{50\%})})})}$$

Where a is the upper asymptote, k is steepest gradient, x is the collision voltage, SY_{50%} is the inflection point. Measurements were corrected for the degrees of freedom (DOF) to account for the different kinetic shifts of the ions by applying the following corrections:

$$\frac{DOF_{ref}}{DOF_{ion}}$$

DOF_{ref} was assigned to the lightest ion in a respective host (i.e [M₂+D2D]²⁺) and the different guest within the same host (DOF_{ion}) corrected to that.^[9] Collision voltage was converted to E_{lab} by the following equation:

$$E_{lab} = z U$$

Where z is charge of the ion and U the collision voltage applied. This was further converted to the centre of mass energy (E_{com}) by the following equation:

$$E_{com} = \frac{m_n}{m_n + m_{ion}} E_{lab}$$

where m_n is the mass of the collision gas and m_{ion} is the mass of the ion under investigation.^[10]

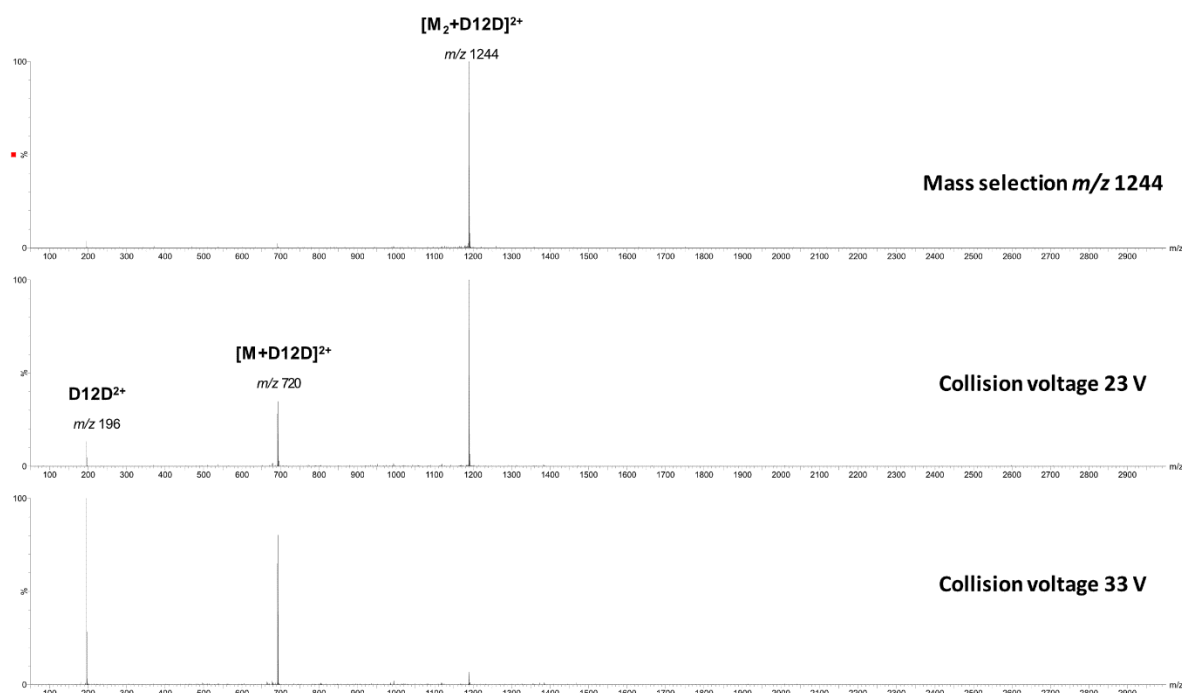


Figure S25: CID spectra of $[1_2 + D_{12}D]^{2+}$ with loss of one resorcinarene to form $[1 + D_{12}D]^{2+}$ before further dissociation to form the free guest $D_{12}D^{2+}$. The same fragmentation pathway was seen for guests with $n \geq 4$ in all hosts.

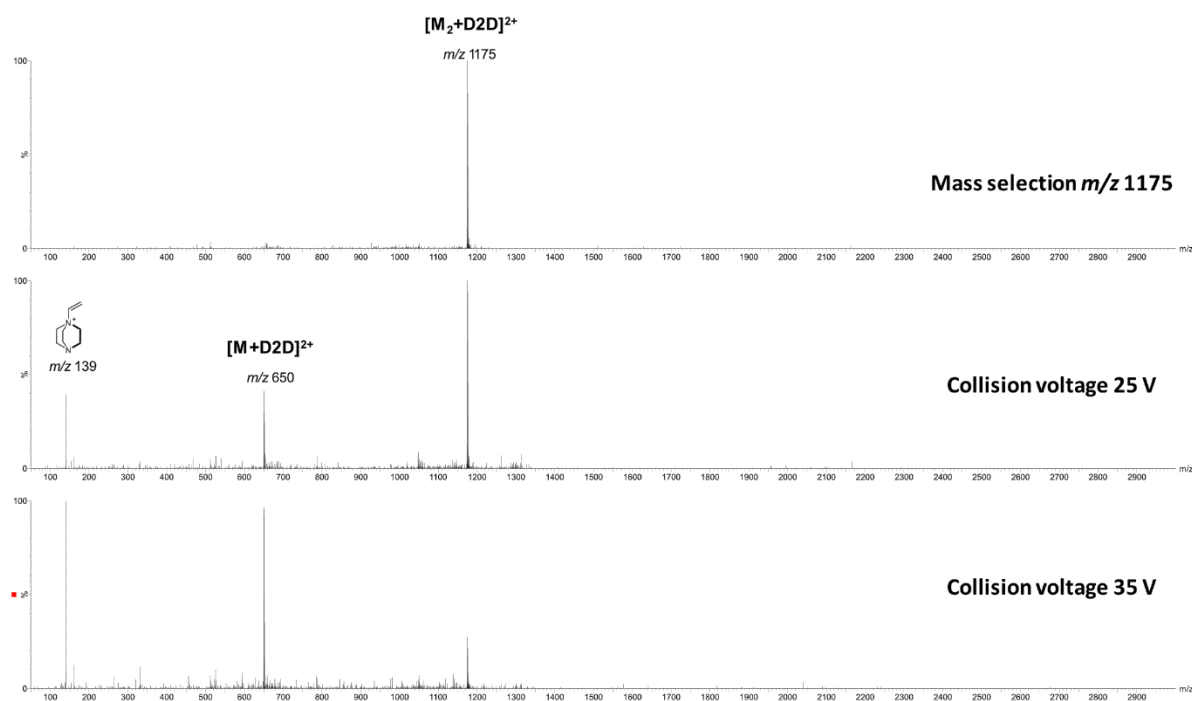


Figure S26: CID spectra of $[1_2 + D_2D]^{2+}$ where the free guest is not observed due to guest decomposition. This was also observed for $n=2$ & 3.

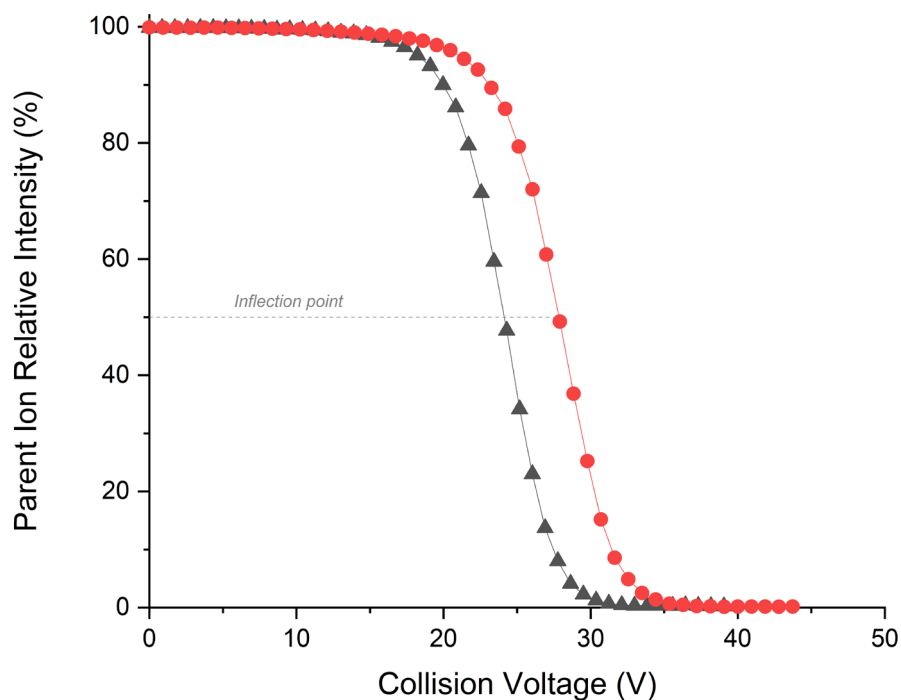


Figure S27: Typical SY plots which can be used to provide a relative ranking of gas phase stability. The inflection point represents the voltage at which 50% of the parent ion remains and is used for relative rankings ($SY_{50\%}$)

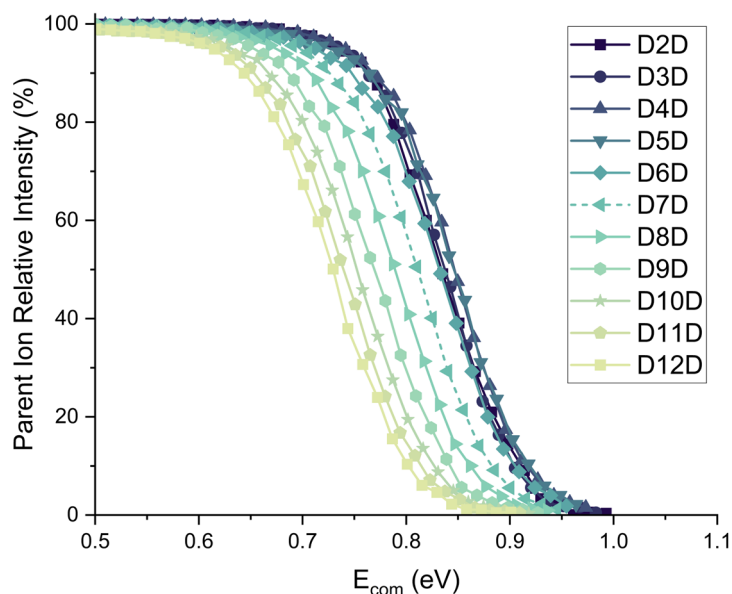


Figure S28: SY curves of $[2_2+DnD]^{2+}$

Table S1: Collected $SY_{50\%}$ of $[M_2+DnD]^{2+}$ of the various hosts. Most stable ion marked in green.

Host	D2D	D3D	D4D	D5D	D6D	D7D	D8D	D9D	D10D	D11D	D12D
1_2	0.706	0.708	0.714	0.704	0.679	0.646	0.625	0.600	0.583	0.572	0.557
2_2	0.828	0.831	0.840	0.844	0.819	0.794	0.770	0.748	0.730	0.714	0.701
3_2	NA	NA	NA	0.419	0.435	0.447	0.459	0.471	0.476	0.476	0.474

HDX experiments

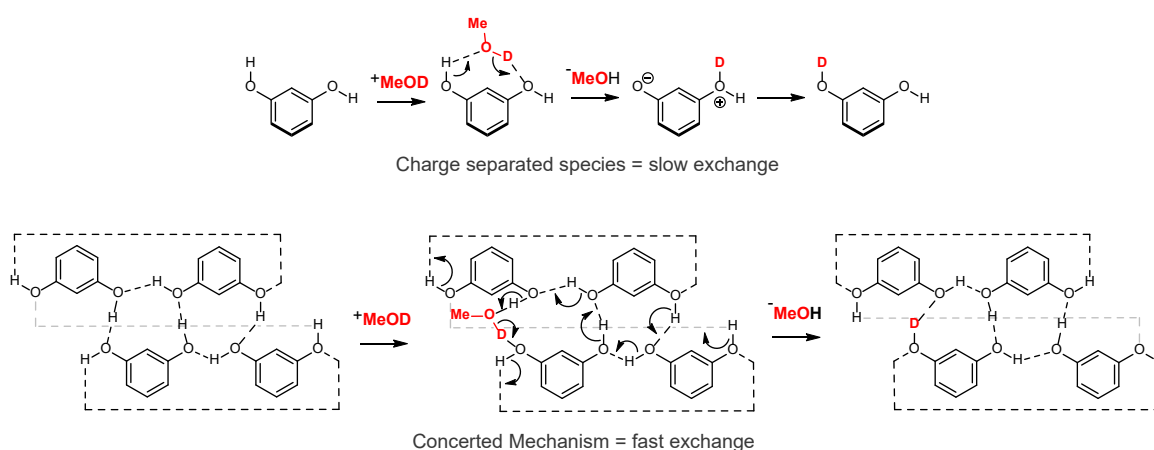


Figure S29: Principles of HDX. A non-continuous network exchanges via a relay mechanism with an unfavourable charge separated species (top). A continuous network can incorporate a CH_3OD and exchange via a Grotthius-like concerted mechanism (bottom).

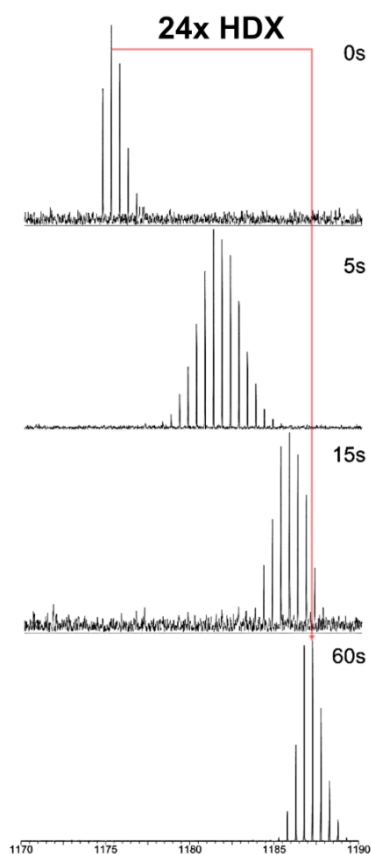


Figure S30: HDX spectra of $[\mathbf{1}_2+\mathbf{D}_2\mathbf{D}]^{2+}$. The number of exchanges can be determined at the different reaction intervals. This was repeated for the different guests to generate the plot seen in Figure 4.

Ion Mobility mass spectrometry

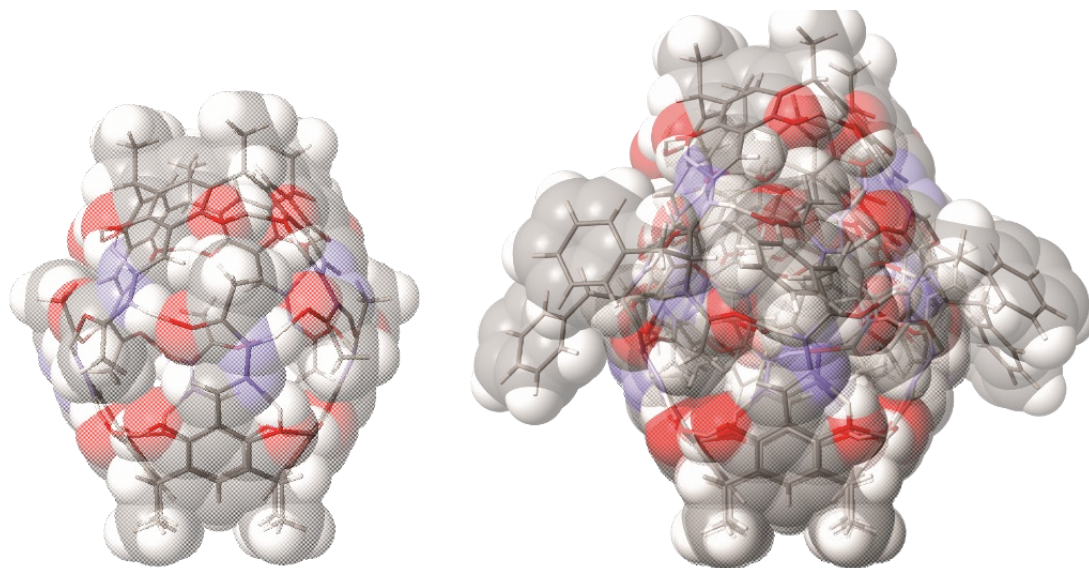


Figure S31: Space filling model of $\mathbf{1}_2$ (left) and $\mathbf{2}_2$ (right). The overall structures are non-porous so the likelihood of penetration of N_2 used as drift gas into the cavity is only small.

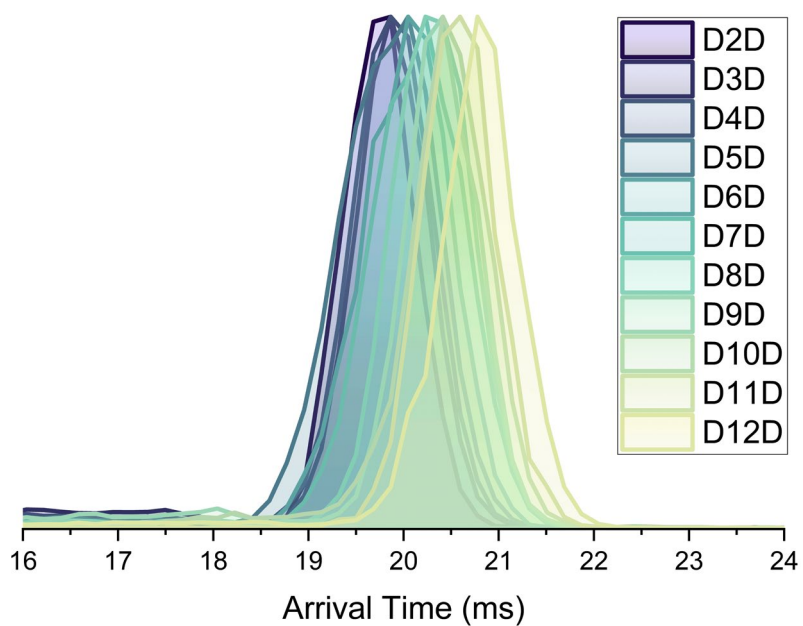


Figure S32: ATD curves of $[\mathbf{2}_2 + \text{D}_n\text{D}]^{2+}$. An increase in drift time is seen from D7D onwards. The increase is relatively smaller than that seen for $\mathbf{1}_2$ and $\mathbf{3}_2$ due to the overall larger size of the $\mathbf{2}_2$.

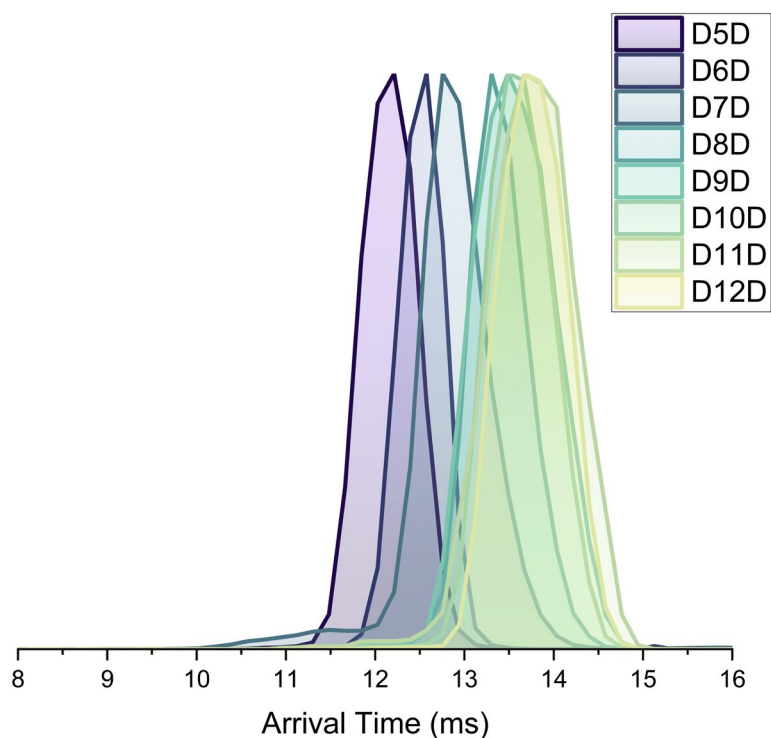


Figure S33: ATD curves of $[3_2+\text{DnD}]^{2+}$. Clear arrival time increase seen from **D5D** onwards but decreases in magnitude from **D8D** onwards.

Table S2: Collected arrival time (ms) of $[\text{M}_2+\text{DnD}]^{2+}$ of the various hosts with the $^{\text{TW}}\text{CCS}_{\text{N}_2}$ (\AA^2) calculated via polyaniline calibrant shown in paratheses. ATDs were fit with a modified Gaussian equation to determine arrival time.

Host	D2D	D3D	D4D	D5D	D6D	D7D	D8D	D9D	D10D	D11D	D12D
1₂	11.70 (557)	11.78 (559)	11.76 (559)	11.74 (557)	12.14 (568)	12.14 (568)	12.50 (577)	12.67 (580)	12.82 (585)	12.96 (598)	13.02 (599)
2₂	19.94 (740)	19.84 (738)	19.84 (738)	19.82 (738)	19.92 (740)	20.16 (745)	20.26 (746)	20.26 (746)	20.46 (750)	20.44 (749)	20.80 (756)
3₂	NA	NA	NA	12.12 (570)	12.51 (579)	12.63 (582)	13.15 (594)	13.55 (605)	13.44 (602)	13.73 (609)	13.76 (609)

For **1₂**, the CCS calibration was performed in triplicate with different wave heights and velocities using polyaniline as a standard. These values were then compared to theoretical values determined for computational structures (Table S3).

Table S3: $^{\text{TW}}\text{CCS}_{\text{N}_2}$ (average of 3 measurements with standard deviation in parenthesis) and $^{\text{TM}}\text{CCS}_{\text{N}_2}$ values calculated for $[1_2+\text{DnD}]^{2+}$ (\AA^2)

	D2D	D3D	D4D	D5D	D6D	D7D	D8D	D9D	D10D	D11D	D12D
$^{\text{TW}}\text{CCS}_{\text{N}_2}$	555 (2)	559 (3)	561 (2)	564 (1)	572 (2)	573 (1)	579 (2)	585 (2)	589 (2)	596 (2)	602 (2)
$^{\text{TM}}\text{CCS}_{\text{N}_2}$	558	555	555	562	576	578	582	588	590	597	599

Computational Structures General

Computational structures were initially generated using Scigress Version FJ 2.9. 1 (Fujitsu Limited, Tokyo) and optimised at the MM3 level to ensure potential H-bonds were considered before further optimisation using HF-3c implemented in the ORCA software version 5.0.4.^[11] This method was developed by the Grimme group and incorporates the D3 dispersion correction and makes it well suited to large non-covalent systems.^[12] The phenyl of **2**₂ and *iBu* of all hosts were cut to reduce computational cost. For **1**₂ structures used for TMCCS_{N2} calculations, a multilevel approach was used where the HF-3c structures were imported into Scigress and the geometry locked, *iBu* groups were added and optimised at the PM6 level (PM6) level. *i*-Bu groups of all compounds are removed for clarity in figure throughout the main text and SI.

Computational structures of N,N-Dimethylhydrazoneresorcinarene, **3**.

As the charges for the **DnD** are localised more on the inner nitrogen, directly pointing the guest into the resorcinarene bowl does not result in the most favourable cation- π interactions. Instead, being positioned more parallel to the rim with the inner nitrogen pointing into the core of the bowl allows for stronger interactions between host and guest. This can be seen when inspecting computational structures of the [**3**₂+**D12D**]²⁺ and [**3**₂+**D5D**]²⁺ (Figure S24). For [**3**₂+**D12D**]²⁺, the length of the guest allows enough space for the second bowl to position itself in the better position without the shorter **D5D** guest, the two resorcinarene are too close together and thus have to adopt a less favourable more direct head on arrangement with the second resorcinarene. The angle between the guest and the upper rim of the second resorcinarene decreases as the greater length allows enough space for the second bowl to position itself in the better position without significant steric repulsion which can be seen in the structure of [**3**₂+**D12D**]²⁺. This can rationalise the trend seen in the SY curve of this compound with increasing stability with longer chain length. From a chain length of 10 onwards, no further increase in stability is seen. Conceivable this could be because at this distance, coulombic repulsion plays no major factor and the guests are long enough that there is enough space to fit both bowls with favourable arrangements. Guests shorter than **D5D** would likely result in too much steric clash to dimerise. Overall, the difference between the geometry of free and bound **DnD** guests binding with **3**₂ are only minimal (Table S4).

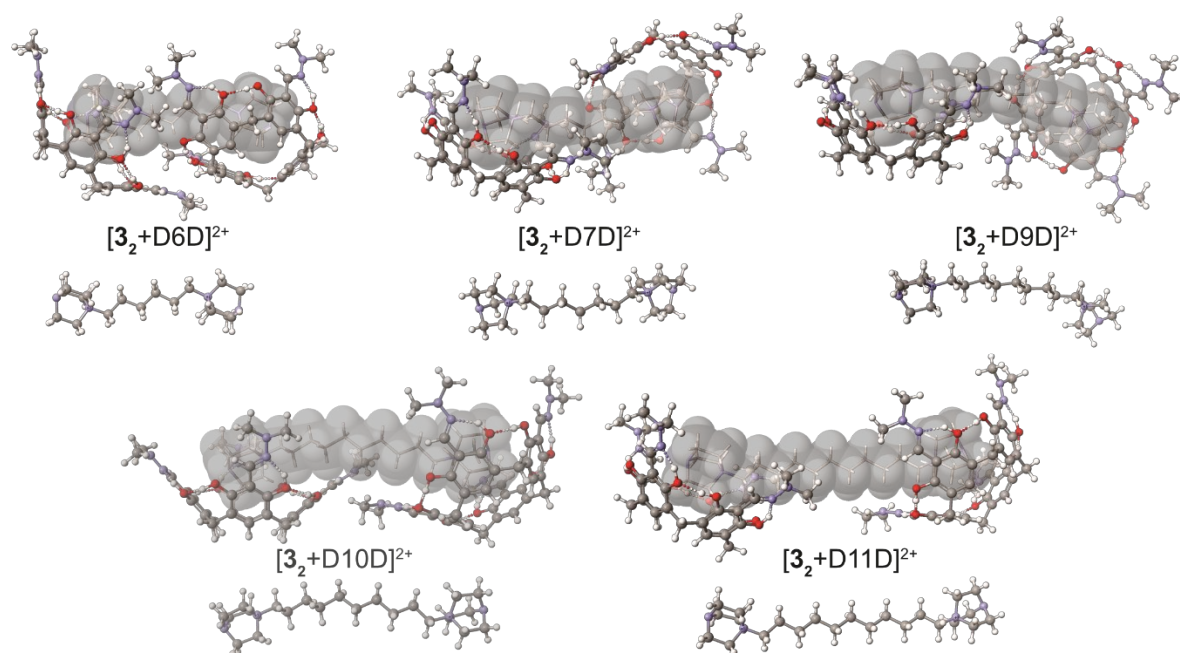


Figure S34: Computational structures of $[3_2+\text{DnD}]^{2+}$ for $n=6,7,9,10,11$. The bound guests are shown below without hosts for clarity.

Computational structures of H-bonded dimers 1_2 and 2_2

For 1_2 and 2_2 , the N-H \cdots O hydrogen bonding means that the two resorcinarenes cannot simply be moved away from one another so the two DABCONium moieties are effectively restrained. As a consequence of this, as the chain length of the **DnD** increases, it is forced to loop around into a horseshoe-like arrangement. The loops eventually become long enough that it impacts the wall of the capsule and will then push its way out by breaking a H-bond which allows the arm to move away. This also increases the flexibility to an extent that the resorcinarene can adjust its position to achieve better cation- π interactions. The calculated structures are entirely consistent with experimental results as the stability will decrease as the guest impacts the wall, this expansion is also seen in the arrival time via IMS and also leads to a decrease in the HDX rate. For 2_2 , the same trends are observed, but shifted to longer guests by one. The relative size difference that this produces in 2_2 is smaller than what is seen for 1_2 which accounts for the smaller increase in drift time for $[2_2\subset\text{DnD}]^{2+}$ compared to $[1_2\subset\text{DnD}]^{2+}$. For both 1_2 & 2_2 , large deviations from the free **DnD** are seen in order to be encapsulated.

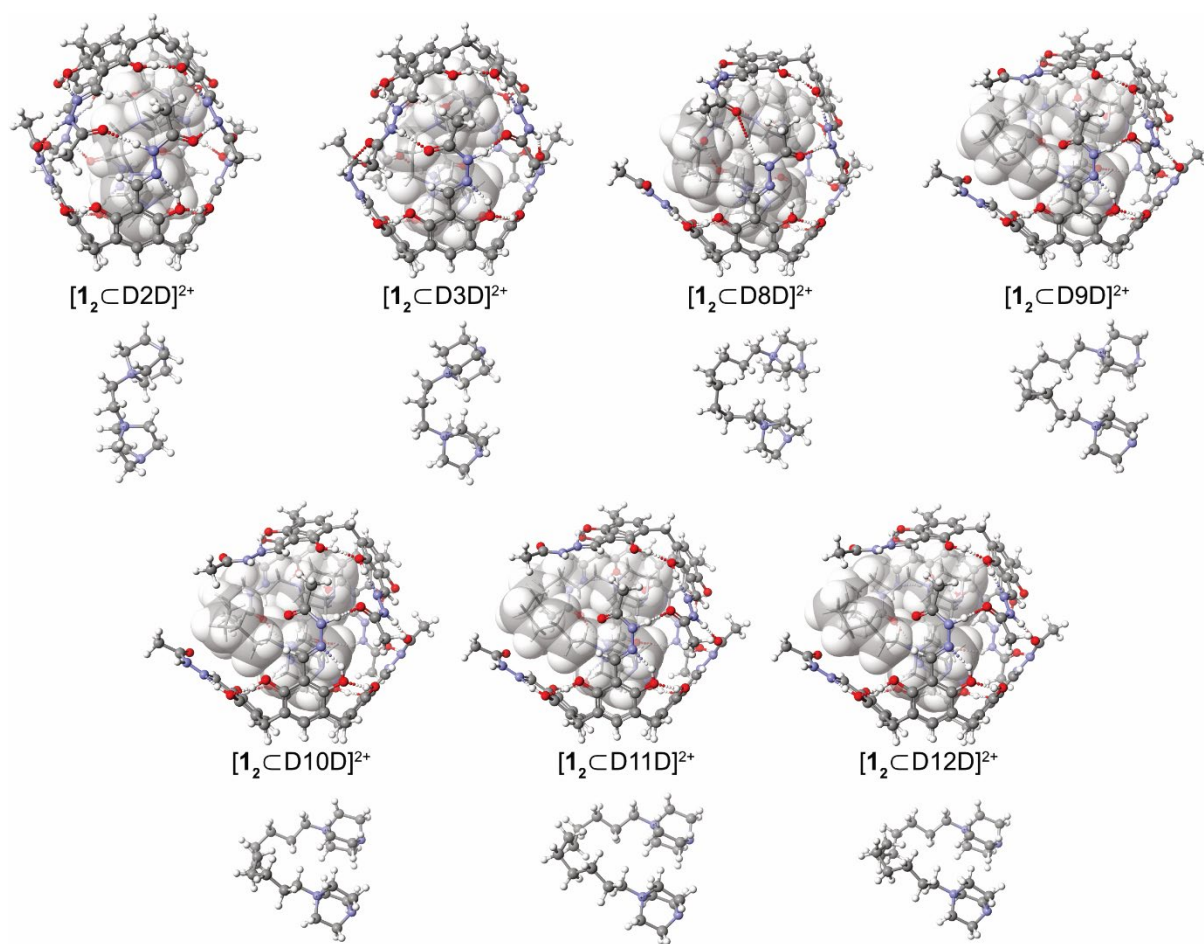


Figure S35: Computational structures of $[1_2C_nD_n]^{2+}$ for $n=2,3,8,9,11,12$. The bound guests are shown below without hosts for clarity.

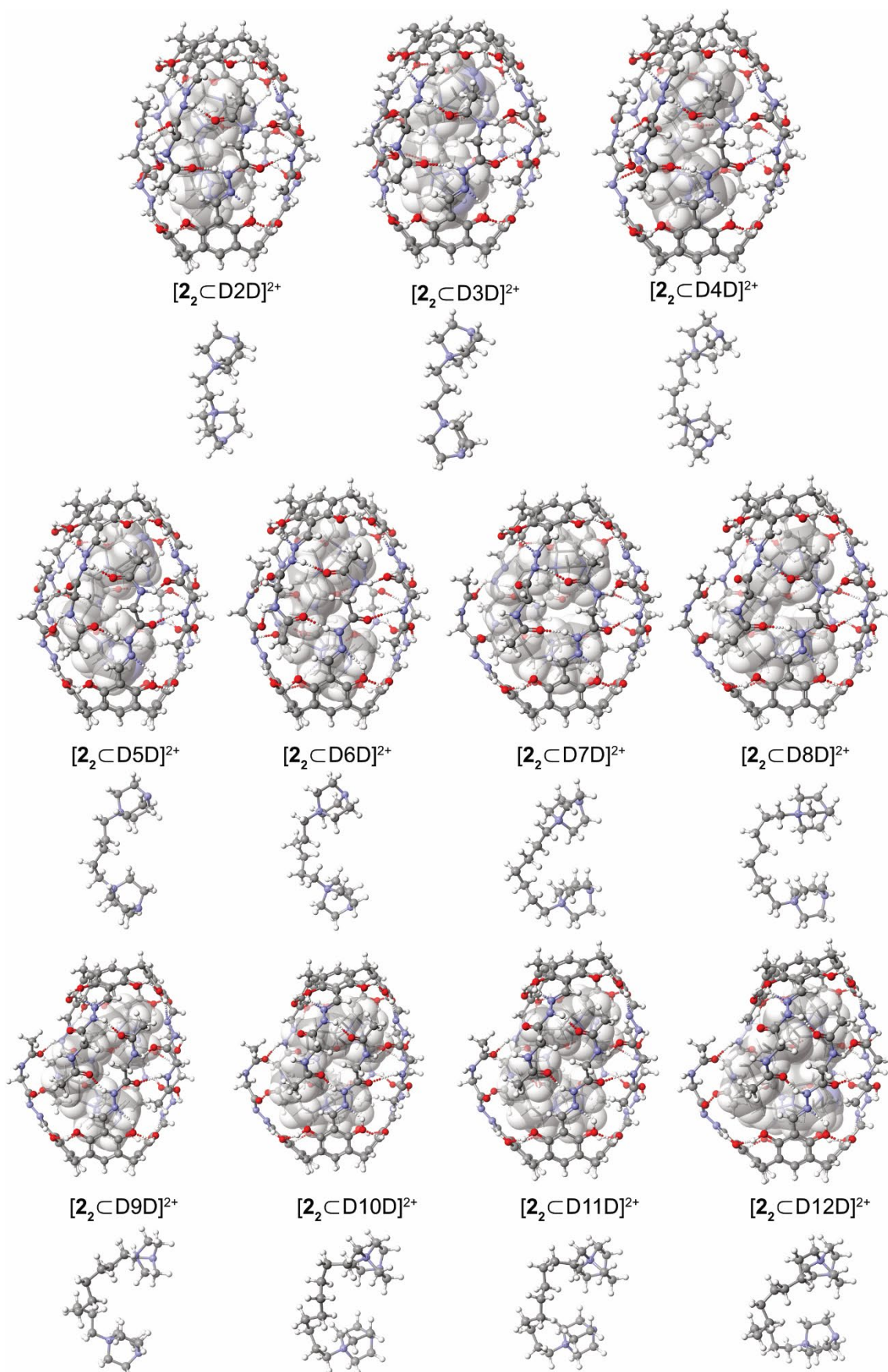


Figure S36: Computational structures of $[2_2CnDn]^{2+}$ for $n=2-12$ (left to right). The bound guests are shown below without host for clarity.

Table S4: Guest length (N(CH₂)₃-N(CH₂)₃) (Å) when 'free' and when encapsulated in **1₂**, **2₂**, **3₂**.

	D2D	D3D	D4D	D5D	D6D	D7D	D8D	D9D	D10D	D11D	D12D
Free	8.93	9.81	11.40	12.39	13.91	14.96	16.44	17.52	18.97	20.09	21.52
1 ₂	6.91	6.59	5.82	6.10	5.58	5.44	6.00	5.91	5.61	5.53	5.66
2 ₂	7.78	8.48	8.89	9.07	9.16	7.41	7.19	7.92	5.44	5.01	4.89
3 ₂	NA	NA	NA	12.32	13.65	14.19	16.32	16.83	18.37	20.13	21.37

References

- [1] a) M. Grajda, M. Wierzbicki, P. Cmoch, A. Szumna, *J. Org. Chem.* **2013**, *78*, 11597-11601; b) M. Szymański, M. Wierzbicki, M. Gilski, H. Jędrzejewska, M. Sztylko, P. Cmoch, A. Shkurenko, M. Jaskólski, A. Szumna, *Chem. Eur. J.* **2016**, *22*, 3148-3155.
- [2] a) F. Jia, Z. He, L.-P. Yang, Z.-S. Pan, M. Yi, R.-W. Jiang, W. Jiang, *Chem. Sci.* **2015**, *6*, 6731-6738; b) Z. He, G. Ye, W. Jiang, *Chem. Eur. J.* **2015**, *21*, 3005-3012.
- [3] M. Gaedke, H. Hupatz, F. Witte, S. M. Rupf, C. Douglas, H. V. Schröder, L. Fischer, M. Malischewski, B. Paulus, C. A. Schalley, *Org. Chem. Front.* **2022**, *9*, 64-74.
- [4] a) P. Mal, B. Breiner, K. Rissanen, J. R. Nitschke, *Science* **2009**, *324*, 1697-1699; b) A. Shivanyuk, J. Rebek, Jr., *Proc. Natl. Acad. Sci. USA* **2001**, *98*, 7662-7665; c) A. Scarso, L. Trembleau, J. Rebek, Jr., *Angew. Chem. Int. Ed.* **2003**, *42*, 5499-5502.
- [5] B. Wüstenberg, A. Pfaltz, *Adv. Synth. Catal.* **2008**, *350*, 174-178.
- [6] M. F. Bush, Z. Hall, K. Giles, J. Hoyes, C. V. Robinson, B. T. Ruotolo, *Anal. Chem.* **2010**, *82*, 9557-9565.
- [7] V. Shrivastav, M. Nahin, C. J. Hogan, C. Larriba-Andaluz, *J. Am. Soc. Mass Spectrom.* **2017**, *28*, 1540-1551.
- [8] D. P. Weimann, H. D. F. Winkler, J. A. Falenski, B. Kokschi, C. A. Schalley, *Nat. Chem.* **2009**, *1*, 573-577.
- [9] a) M. W. Forbes, D. A. Volmer, G. J. Francis, D. K. Böhme, *J. Am. Soc. Mass Spectrom.* **2005**, *16*, 779-791; b) T. M. Kertesz, L. H. Hall, D. W. Hill, D. F. Grant, *J. Am. Soc. Mass Spectrom.* **2009**, *20*, 1759-1767.
- [10] K. M. Ervin, P. B. Armentrout, *J. Chem. Phys.* **1985**, *83*, 166-189.
- [11] a) R. Sure, S. Grimme, *J. Comput. Chem.* **2013**, *34*, 1672-1685; b) F. Neese, *WIREs: Comput. Mol. Sci.* **2012**, *2*, 73-78; c) F. Neese, *WIREs: Comput. Mol. Sci.* **2022**, *12*, e1606.
- [12] E. Caldeweyher, J. G. Brandenburg, *J. Phys.: Condens. Matter* **2018**, *30*, 213001.

Bioderived Rotaxanes via Dynamic Covalent Boron Chemistry

Jingjing Yu¹, Marius Gaedke¹, Satyajit Das¹, Daniel L. Stares², Christoph A. Schalley², Fredrik Schaufelberger^{1*}

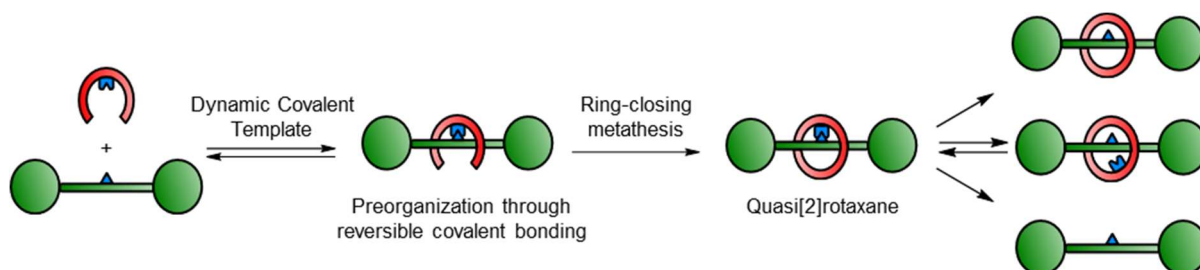
¹ KTH Royal Institute of Technology, Department of Chemistry, Teknikringen 30, 10044 Stockholm, Sweden

² Institut für Chemie und Biochemie, Freie Universität Berlin, Arnimallee 20, 14195 Berlin, Germany.

Keywords: Mechanical bonds, rotaxanes, dynamic covalent chemistry, boronic acids, self-assembly.

ABSTRACT

We report on the use of vicinal diols as a template for synthesis of mechanically interlocked molecules. Vicinal diols are prevalent in bio(macro)molecules such as carbohydrates, RNA as well as polyhydroxylated natural products, and a range of methods exists for recognition and selective binding to these motifs. Here we use dynamic covalent boron chemistry to reversibly attach a V-shaped boronic acid pincer ligand with two alkene-appended arms to a linear diol-containing thread. Following condensation of the pincer ligand with the thread, ring-closing metathesis establishes a quasi[1]rotaxane architecture along with a non-entangled isomer in a 1:2 ratio. Advanced NMR spectroscopy and mass spectrometry unambiguously assigned the isomers and revealed that the quasi[1]rotaxane was in equilibrium with its hydrolyzed free [2]rotaxane form. The boron handle could also be selectively oxidized to kinetically trap the rotaxane in place. This study demonstrates that prevalent biomolecular motifs can be used as templates for establishing mechanical bonds, meaning it might be possible to interlock unmodified native biomolecules and biopolymers for future biomedical applications.



INTRODUCTION

Mechanically interlocked molecules (MIMs) such as rotaxanes, catenanes and molecular knots have long been considered challenging synthetic targets, but recent synthetic advances are now allowing their properties to be explored in greater detail and their applications to be probed more systematically.^[1] One area that remains underdeveloped is the use of MIMs for biological applications.^[2] MIMs are attractive functional units for chemical biology due to their dynamic nature and stimuli-responsiveness, in addition to how they sterically protect delicate functional groups against degradation. However, the community has only begun to scratch the surface of this rich and interesting field.^[2a] From the sparse examples so far, MIMs have been used for small-molecule drug delivery^[3], to protect sensitive imaging agents from degradation^[4], for mechanical silencing of DNA duplex formation^[5], to aid substrate passage through cell membranes^[6], and for biosensing^[7].

There are nevertheless significant barriers to applying MIMs in biological contexts, with the most substantial being the synthetic difficulty of making biocompatible (and water-soluble) molecules. Most synthetic routes towards MIMs rely on non-covalent interactions to pre-organize the individual

component before establishing the mechanical bond.^[1a] However, this introduces extraneous functional groups (ligands for metals, H-bonds etc.) which are non-biogenic and cause problems in biological applications. A better approach would be to construct MIMs from biogenic building blocks, as such supramolecular assemblies would likely have higher biocompatibility.^[8] Unfortunately, accessing molecules such as rotaxanes using biomolecules as templates is extremely difficult, as the biological environment disrupts most pre-organizing interactions and renders template effects weaker and less directional.

We hypothesized that covalent rather than non-covalent templates would be favorable for constructing MIMs with biologically relevant templates.^[9] The robustness and directionality of covalent templates are higher than with non-covalent interactions, meaning mechanical bonds can be formed under more challenging conditions.^[10] The use of covalent bonds to preorganize different molecular components before interlocking was established as far back as the 1960s^[11] but most such strategies suffer limitations such as harsh cleavage conditions and complicated synthesis^[9]. Here we report a straightforward approach to make [2]rotaxanes from bioderived building blocks via covalent templates (Scheme 1). Key to this method is the use of dynamic covalent chemistry to pre-organize a bioderived thread and a V-shaped pincer receptor into a conformation that delivers a rotaxane upon ring closure and cleavage of the dynamic covalent linkage.^[12] Dynamic covalent bonds have “Goldilocks character” that make them uniquely suited as covalent templates, with the bonds being robust enough for efficient covalent template synthesis (under one set of conditions) but labile enough to later liberate the free MIM (under another set of conditions).^[13]

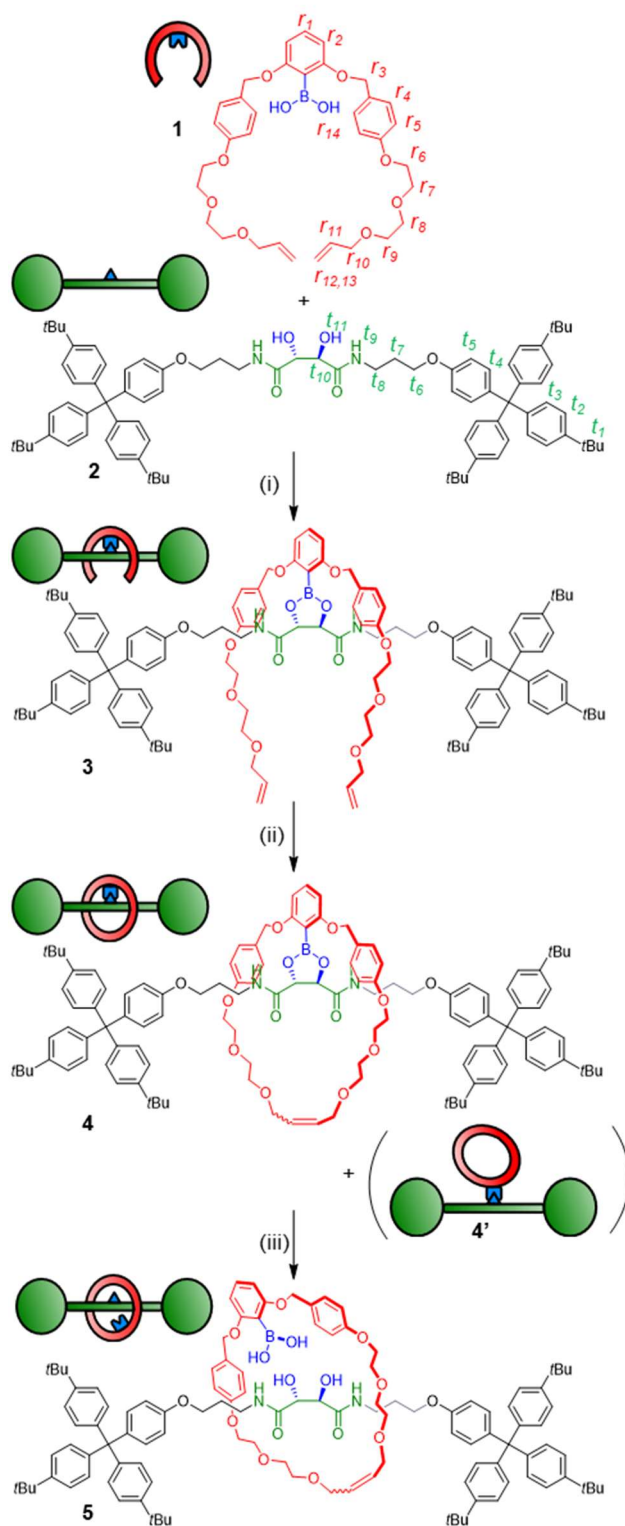
Boronic esters are classic examples of dynamic covalent bonds and form by exchange between vicinal diols and boronic acids.^[14] Reversible boronic acid complexation has been extensively used for biosensing^[15], catalysis^[16], self-healing materials^[17] and to solubilize polysaccharides^[18]. There is also ample precedence for the use of boron self-assembly to preorganize components towards macrocyclization^[19], though dynamic boron chemistry has not seen much use for MIM synthesis^[20]. Polyhydroxylated scaffolds and vicinal diols are furthermore ubiquitous in nature (RNA, carbohydrates, natural products etc.) and would hence provide versatile, naturally occurring templates for biocompatible rotaxanes.

This study establishes proof-of-concept for using dynamic boron chemistry and vicinal diol templates for [2]rotaxane synthesis. Our receptor uses a dynamic boron handle to reversibly bind to the hydroxyl groups, whilst apolar protruding side chains preorganize the receptor into a “clasp-type” conformation that encapsulates the top/bottom of the thread. This design causes clipping of the receptor onto the thread, and the dynamic covalent bond can then be readily broken or derivatized to free the quasi[1]rotaxane species and create true [2]rotaxanes.

RESULTS AND DISCUSSION

The V-shaped pincer ligand **1** bears a boronic acid moiety at its cleft and was synthesized in six steps as outlined in the Supporting information (Section S3). The ligand side chains were designed to feature benzyl-groups for increased dispersion interactions with the hydrophobic parts of the thread, to facilitate enclosure around rather than outside of the thread (*vide infra*).^[21] As thread, we synthesized model compound **2** in five steps starting from the natural product tartaric acid. To ensure a stable thread architecture and facilitate synthesis, we used amide bonds to connect the tartrate unit to the stoppers. The pincer ligand **1** and thread **2** were mixed in anhydrous toluene, leading to spontaneous self-assembly of the dynamic boronic ester species **3** in 67-89% conversion, as determined by ¹H-NMR analysis (Figure 1, Table S1).^[22] Pronounced ¹H-NMR spectral shifts for key resonances indicated successful complexation. For example, proton *t*₁₀ shifts strongly downfield ($\Delta\delta = 0.7$ ppm), while *t*₆ shifts upfield ($\Delta\delta = 0.2$ ppm), indicating boronic ester formation and the arms of the pincer shielding the thread via the desired clasp-type conformation. Protons *r*₁, *r*₂, *r*₄ and *r*₅ on the pincer also shifts noticeably, again indicating a more rigidified environment along with boronic ester formation. Aside from an upfield shift of 0.4 ppm, proton *r*₃ also changes splitting pattern from singlet to a doublet of doublets, due to the diastereotopic protons now residing in a conformationally restricted chiral environment imposed by the tartrate chiral centers. ¹¹B-NMR spectroscopy gave a shift of 28.9 ppm for **3**, which supports assignment of the boron moiety as a trigonal boronic ester (Spectrum S26).^[23] Reversibility of the linkage was confirmed by hydrolysing the complex back to **1** and **2** in water-saturated CDCl₃ (Figure S1-S2).

Scheme 1. Synthesis of a [2]rotaxane through a diol template.



^aReagents and conditions: (i) **1** (1 equiv.), **2** (1 equiv.), toluene, RT, 24 h; (ii) Hoveyda-Grubbs 2nd generation catalyst, CH₂Cl₂, RT, 24 h (16% yield over two steps); (iii) H₂O, CDCl₃, RT, 7 d (equilibrium yield 70%).

The covalently linked clasp-type receptor **3** is preorganized for rotaxane formation via ring-closing metathesis (RCM).^[24] While there is flexibility in the structure, that freedom of movement was deemed necessary for the arms to meet during ring closure as part of the RCM catalytic cycle (where an organometallic Ru complex is covalently attached to one chain terminus).^[25] Indeed, treatment of complex **3** with Grubbs-Hoveyda 2nd generation catalyst in CH₂Cl₂ led to efficient ring closure, as

evidenced by $^1\text{H-NMR}$ spectra of the crude mixture (Figure S3). The majority of the crude reaction appeared to be composed of two ring-closed species in 2:1 ratio (the remainder being unidentified oligo- and polymeric species). Analysis using electrospray ionization high resolution mass spectrometry (ESI-HRMS) indicated both species had the same molecular mass (observed mass m/z 1817.0221 for $[\text{C}_{116}\text{H}_{139}\text{N}_2\text{O}_{14}+\text{Na}]^+$, calculated m/z 1817.0253) as the desired quasi[1]rotaxane product **4**. This led us to believe that the two compounds were structural isomers **4** and **4'** (Scheme 1), stemming from ring closure around the thread (to generate the quasi[1]rotaxane **4**) and outside of the thread (to generate the non-interlocked conformer **4'**). Fortunately, separation of the two compounds using column chromatography was possible, and we could isolate the suspected quasi[1]rotaxane **4** in 16% yield over two steps (starting from free boronic acid **1** and thread **2**). The interlocked nature of **4** was clear already from its physical properties, as the compound was fully stable to chromatographic purification despite the hydrolytically sensitive boronic ester moiety.

$^1\text{H-NMR}$ analysis showed full consumption of the external alkene protons r_{12}/r_{13} from **3** and the characteristic change in both shift and splitting pattern (m to t) of the internal alkene proton r_{11} , corresponding to the ring-closed metathesis product (Figure 1).

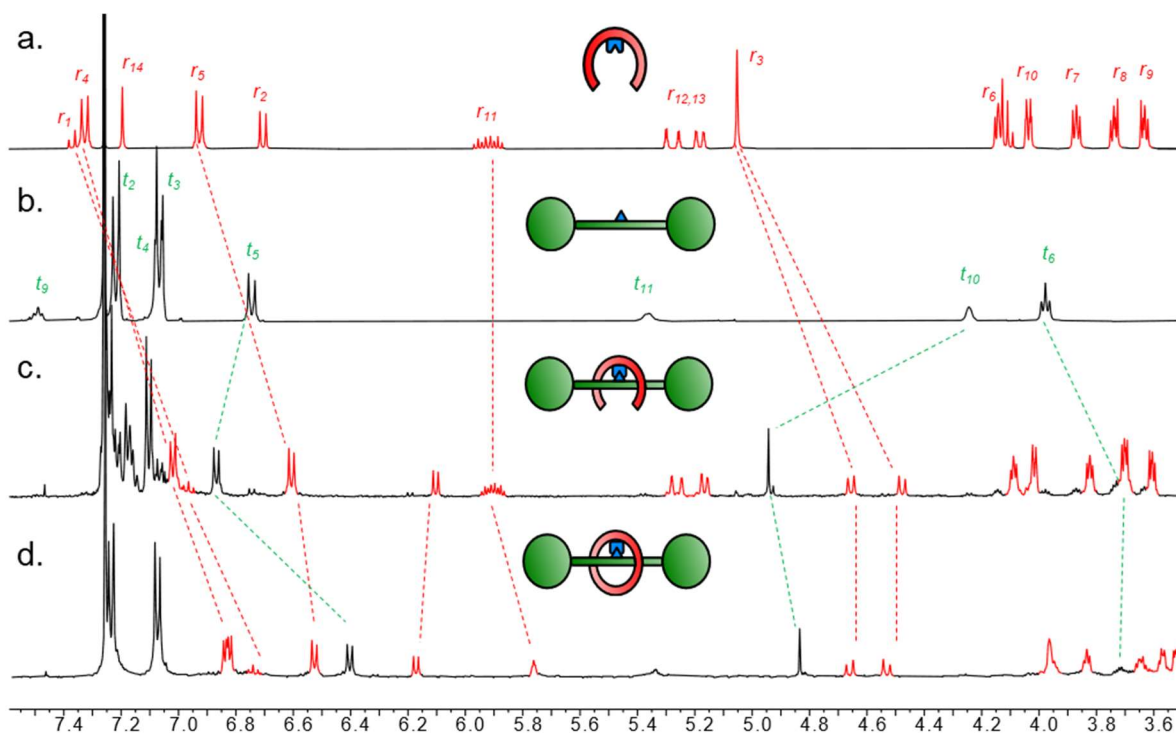


Figure 1. Partial $^1\text{H-NMR}$ spectra (500 MHz, CDCl_3 , 298 K) of a) boronic acid pincer ligand **1**; b) tartrate-derived thread **2**; c) boronic ester condensation product **3** (89% conversion); d) quasi[1]rotaxane **4**.

Large upfield shifts for peaks corresponding to protons on the arms of the pincer receptor (r_3 , r_4 , r_5) as well as the thread (t_5 , t_6) indicated the ring closing event produced a tight conformation with close association to the thread, in line with the expected quasi-interlocked conformation.

From this NMR analysis, we could now assign compound **4** as the minor product in the crude reaction mixture. A higher quantity of the suspected exo-macrocyclic conformer **4'** was, correspondingly, also observed. Attempts to isolate this molecule in pure form were fruitless, as **4'** hydrolyzed readily during chromatographic purification attempts or after being dissolved in wet organic solvents. Through rapid silica flash column chromatography we could isolate a mixture of **4'** together with the hydrolysis products, thread **2** and boronic-acid macrocycle **6** (Figure S5-S6).^[26] Interestingly, macrocycle **6** could not be synthesized by direct RCM of ligand **1**, as this only produced degradation products. This methodology is the only method we have been able to find to obtain **6** as a reference compound.

In contrast to some previously used covalent templates^[9], the boronic ester functionality is labile and requires only mild conditions to dissociate. Indeed, quasi[1]rotaxane **4** was found to slowly equilibrate to the free [2]rotaxane **5** when left in water-saturated CDCl_3 under ambient conditions. After several days, an equilibrium position of 70:30 between **5** and **4** was established (Figure 2). Considering the effective molarity between diol and boronic acid in **5**, the shift of the equilibrium position towards

hydrolysis product is somewhat unexpected and indicates that the boronic acid state is strongly favored over ester.

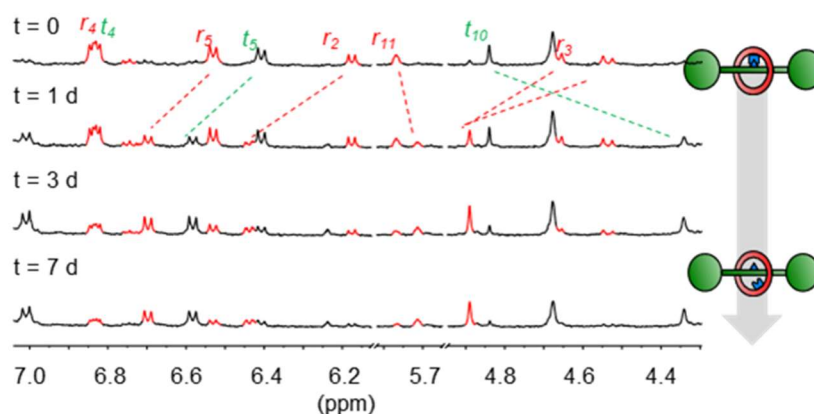


Figure 2. Partial $^1\text{H-NMR}$ spectra (500 MHz, CDCl_3 , 298 K) showing gradual hydrolysis of **4** into [2]rotaxane **5**.

In contrast, the non-interlocked nature of **4'** was obvious from its chemical stability. Upon being left in wet CDCl_3 for 24 h, **4'** had dissociated to free **2** and macrocycle **6**, with >95% conversion to these products being observed after 48 h (Figure S5). By condensing the free thread **2** and macrocycle **6** under similar conditions to formation of the condensation complex **3**, we could also regenerate **4'** *in situ* (Figure S6).

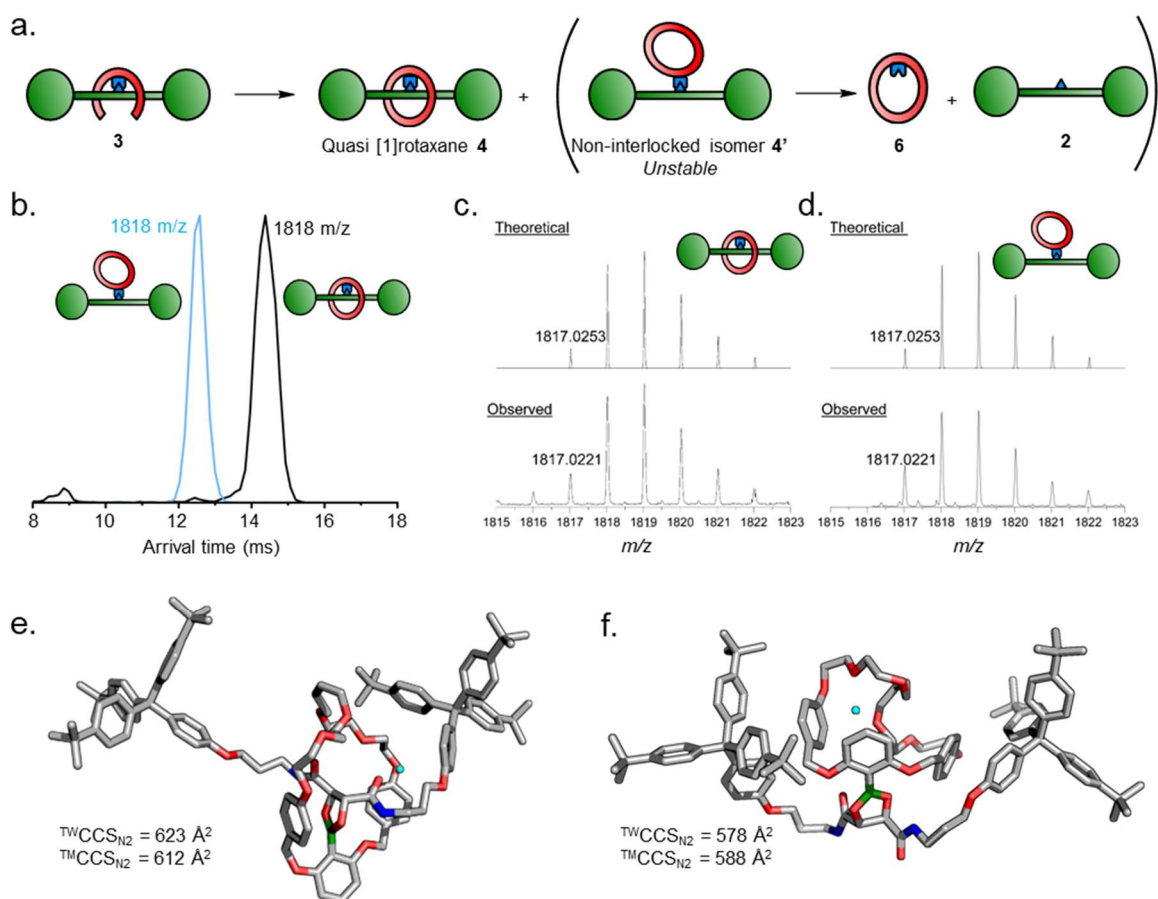


Figure 3. a) Scheme of ring-closing reaction to generate isomers **4** and **4'**, as well as the degradation of **4'** into macrocycle **6** and thread **2**. b) Overlapped TW-IMS measurements of **4** and **4'**. c) HRMS isotopic distribution for **4**. d) HRMS isotopic distribution for **4'**. e,f) HF-3c molecular models for e) $[\mathbf{4}\cdot\text{Na}]^+$ and f) $[\mathbf{4}'\cdot\text{Na}]^+$ used for calculation of theoretical collisional cross sections ($^{\text{TMCCSN}_2}$) and comparison with experimental collisional cross section values ($^{\text{TWCCSN}_2}$). Na^+ ion shown in cyan.

Isomers **4** and **4'** were also further analyzed via tandem mass spectrometry. The isolated samples were analyzed by traveling wave ion mobility mass spectrometry^[27] (TW-IMS), which showed different arrival times for **4** (14.4 ms) and **4'** (12.5 ms) (Figure 3b, Table S2).^[28] Experimental collision cross section ($^{TM}CCS_{N_2}$) values, determined via a polyalanine calibrant (full detail in supporting information), were calculated to be 623 ± 3 and 578 ± 4 Å², for **4** and **4'**, respectively. Theoretical collisional cross section ($^{TM}CCS_{N_2}$) of HF-3c optimised structures of **4** and **4'** (612 and 588 Å², respectively) were in good agreement with the experimental values (Figure 3e,f).^[29]

We further used collision induced dissociation (CID) mass spectrometry experiments to investigate the nature of the linkage between the ring and thread components in the RCM products by following the fragmentation of the hydrolysis products (Figure S9-10). Starting from compound **4'**, hydrolysis was induced by dissolving the sample in 4:1 MeCN/H₂O mixture and incubating for 1 h before measuring. We detected the hydrolysis complex [**4'**•2H₂O] (or [**2**•**6**]) in the MS and subsequently isolated this peak for fragmentation. This complex between free ring **6** and thread **2** dissociated readily under CID conditions, with essentially full dissociation already at 20 V, indicating that this species is held together only through weaker interactions such as H-bonds rather than a mechanical bond. By incubating **4** under the same hydrolysis conditions, free [2]rotaxane **5** was then observed in the mass spectrometer (m/z 1854) and was selected for fragmentation via CID. Much higher collision voltages (>70 V) were required to induce fragmentation of **5** which interestingly dissociated via a double condensation to reform the quasi[1]rotaxane **4**. Upon further increasing the collision voltage to 90 V, a second competing channel was also observed with dissociation of wheel and axle, likely by breaking one of the benzyl ether groups in the wheel. Even higher collision voltages were needed for fragmentation of **4** and **4'** where no specific thread/ring fragments were observed, as expected for entirely covalently linked molecules (Figure S11-S12). These measurements lend strong support to our interpretation that **5** is a mechanically interlocked molecule.

Quasi[1]rotaxane **4** is assembled through a boronic ester linkage. One advantage of boronic esters in organic chemistry is their versatility as synthetic handles. We hence tried exposing **4** to different derivatization conditions (Figure 4). As previously mentioned, free [2]rotaxane **5** is accessed through exposure to water-saturated CDCl₃ over extended time periods. Addition of strong acids (such as H₂SO₄ and HCl) mainly led to ring cleavage (likely via benzyl ether dissociation) and we could only observe small amounts of protodeboronylation rotaxane via ESI-HRMS (with only thread **2** isolable after workup). We then tried to oxidize the boronic ester with H₂O₂/NaOH to obtain a phenol, but this unexpectedly also led to cleavage of the macrocycle, liberating the free thread in 87% yield (Figure S7). Finally, we found that the phenol [2]rotaxane derivative could be accessed by omitting the base in the oxidation step. Dissolving compound **4** in a 1:1 THF/H₂O mixture with H₂O₂ for 1 h induced transformation to phenol rotaxane **7** in 67% isolated yield (Spectrum S41-S46, S9). This demonstrates we can selectively address the quasi[1]rotaxane scaffold in three different ways – macrocycle cleavage, thermodynamic ring-thread equilibration and derivatization of the macrocycle to obtain kinetically trapped [2]rotaxane **7**.

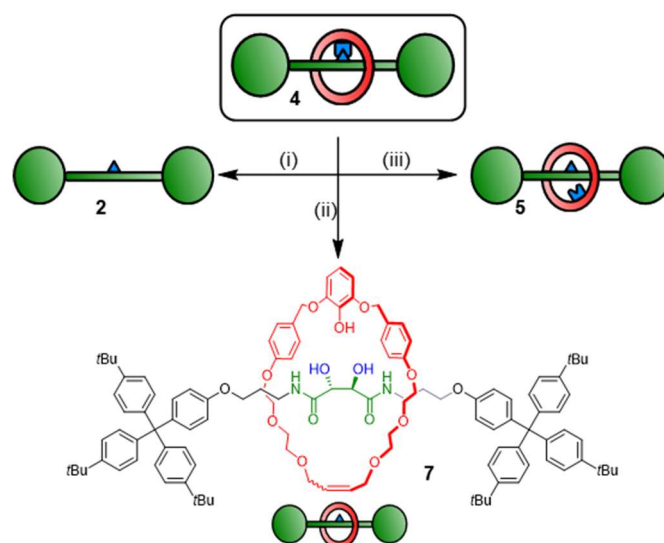


Figure 4. Derivatization of quasi[1]rotaxane **4**. Reagents and conditions: (i) H₂O₂, NaOH, THF/H₂O 1:1, RT, 1 h, 87%. (ii) H₂O₂, THF/H₂O 1:1, RT, 1 h, 67%. (iii) H₂O, CDCl₃, RT, 7 d (equilibrium yield 70%).

CONCLUSIONS

In summary, we have demonstrated that dynamic covalent bonds formed between boronic acids and vicinal diols can template rotaxane formation. The dynamic linkage brings the two components together in space, and by designing the boronic acid to be V-shaped we obtain preorganization for closure over the thread to obtain interlocked products. The isolated quasi[1]rotaxane is chemically stabilized from the mechanical bond, and could be derivatized in several ways through judicious choice of conditions. Though it is clear that the system can be optimized for both synthetic efficiency and compatibility with aqueous conditions, this nevertheless constitutes a proof-of-concept for the use of the biologically relevant vicinal diol motif as templates for mechanical bond formation. The use of dynamic covalent bonds for this purpose is critical, as bond cleavage in this system is facile and efficient, entirely circumventing the stabilizing “catenand effect” that has hindered template removal in previous examples of covalently templates MIMs.^[9] Future boron pincers need to improve condensation conditions for formation of the initial assembly, the selectivity of the ring closure in favor of more interlocked product and increase the water stability of the system. Still, this work will be useful as a starting point for using natural biomolecules as threads for rotaxanes. This would mean the mechanical bond could be incorporated in biomolecules such as carbohydrates, RNA and polyhydroxylated natural products to modulate physical properties and give useful functions. While this study still requires compounds soluble in organic solvents, we believe this class of molecules could have future impact as building blocks for rotaxane biosensors and therapeutics.^[2a]

ASSOCIATED CONTENT

Supporting Information. Experimental procedures, optimization data, NMR analysis and mass spectra (PDF). This material is available free of charge via the Internet.

AUTHOR INFORMATION

Corresponding Author

* Correspondence to: fresch@kth.se

Funding Sources

Swedish Research Council (2020-04225), Carl Tryggers Stiftelse (21:1584), Stiftelsen Olle Engkvist Byggmästare (215-0407), Magnus Bergvalls stiftelse, Wenner-Gren Stiftelserna (UPD2021-0106), and the H2020-MSCA-ITN project NOAH (765297).

Notes

The authors declare no competing financial interest.

ACKNOWLEDGMENT

FS gratefully acknowledges financial support from the Swedish Research Council (grant number 2020-04225), Carl Tryggers Stiftelse (21:1584), Stiftelsen Olle Engkvist Byggmästare (215-0407), Magnus Bergvalls stiftelse and the KTH Royal Institute of Technology. SD thanks Wenner-Gren Stiftelserna for an individual postdoctoral fellowship (UPD2021-0106). DLS thanks the European Union through the NOAH project (H2020-MSCA-ITN project Ref. 765297) and FU Berlin for funding. Support for measurements by the BioSupraMol core facility at FU Berlin is gratefully acknowledged.

ABBREVIATIONS

^{TW}CCS_{N2}, experimental collisional cross section; TMCCS_{N2}, theoretical experimental collisional cross section calculated using the trajectory method; CID, collision induced dissociation; ESI-HRMS, electrospray ionization high resolution mass spectrometry; MIM, mechanically interlocked molecule; RCM, ring closing metathesis; RT, room temperature; TW-IMS, travelling wave ion mobility mass spectrometry.

REFERENCES

- (1) (a) Bruns, C. J.; Stoddart, J. F. *The Nature of the Mechanical Bond: From Molecules to Machines*, Wiley-VCH, **2016**; b) van Dongen, S. F. M.; Cantekin, S.; Elemans, J. A. A. W.; Rowan, A. E.; Nolte, R. J. M. Functional interlocked systems. *Chem. Soc. Rev.* **2014**, *43*, 99–122; c) Erbas-Cakmak, S.; Leigh, D. A.; McTernan, C. T.; Nussbaumer, A. L. Artificial Molecular Machines. *Chem. Rev.* **2015**, *115*, 10081–10206; d) Ashbridge, Z.; Fielden, S. D. P.; Leigh, D. A.; Pirvu, L.; Schaufelberger, F.; Zhang, L. Knotting matters: orderly molecular entanglements. *Chem. Soc. Rev.* **2022**, *51*, 7779–7809; e) Heard, A.W.; Goldup, S.M. Simplicity in the design, operation, and applications of mechanically interlocked molecular machines. *ACS Cent. Sci.* **2020**, *6* 117–128.
- (2) a) Beeren, S.; McTernan, C. T.; Schaufelberger, F. The Mechanical Bond in Biological Systems. *Chem.* **2023**, *9*, 1378–1412; b) Pairault, N.; Barat, R.; Tranoy-Opalinski, I.; Renoux, B.; Thomas, M.; Papot, S. Rotaxane-based architectures for biological applications. *C. R. Chimie*, **2016**, *19*, 103–112; c) Riebe, J.; Niemeyer, J. Mechanically Interlocked Molecules for Biomedical Applications. *Eur. J. Org. Chem.* **2021**, 5106–5116; d) Lim, N. C. H.; Jackson, S. E. Molecular knots in biology and chemistry. *J. Phys.: Condens. Matter*, **2015**, *27*, 354101.
- (3) a) Kench, T.; Summers, P. A.; Kuimova, M. K.; Lewis, J. E. M.; Vilar, R. Rotaxanes as Cages to Control DNA Binding, Cytotoxicity, and Cellular Uptake of a Small Molecule. *Angew. Chem. Int. Ed.* **2021**, 10928–10934; b) Barat, R.; Legigan, T.; Tranoy-Opalinski, I.; Renoux, B.; Péraudeau, E.; Clarhaut, J.; Poinot, P.; Fernandes, A. E.; Aucagne, V.; Leigh, D. A.; Papot, S. A mechanically interlocked molecular system programmed for the delivery of an anticancer drug. *Chem. Sci.* **2015**, 2608–2613.
- (4) Baumes, J. M.; Gassensmith, J. J.; Giblin, J.; Lee, J.-J.; White, A. G.; Culligan, W. J.; Leevy, W. M.; Kuno, M.; Smith, B. D. Storable, thermally activated, near-infrared chemiluminescent dyes and dye-stained microparticles for optical imaging. *Nat. Chem.* **2010**, *2*, 1025–1030.
- (5) Acevedo-Jake, A.; Ball, A. T.; Gallii, M.; Kukwikila, M.; Denis, M.; Singleton, D. G.; Tavassoli, A.; Goldup, S. M. AT-CuAAC Synthesis of Mechanically Interlocked Oligonucleotides. *J. Am. Chem. Soc.* **2020**, 5985–5990.
- (6) Bao, X.; Isaacsohn, I.; Drew, A. F.; Smithrud, D. B. Determining the Intracellular Transport Mechanism of a Clef-[2]Rotaxane. *J. Am. Chem. Soc.* **2006**, *128*, 12229–12238.
- (7) a) Slack, C. C.; Finbloom, J. A.; Jeong, K.; Bruns, C. J.; Wemmer, D. E.; Pines, A.; Francis, M. B. Rotaxane probes for protease detection by ¹²⁹Xe hyperCEST NMR. *Chem. Commun.* **2017**, *53*, 1076–1079; b) Klass, S. H.; Truxal, A. E.; Fiala, T. A.; Kelly, J.; Nguyen, D.; Finbloom, J. A.; Wemmer, D. E.; Pines, A.; Francis, M. B. Rotaxane Probes for the Detection of Hydrogen Peroxide by ¹²⁹Xe HyperCEST NMR Spectroscopy. *Angew. Chem. Int. Ed.* **2019**, *58*, 9948–9953.
- (8) For examples of small-molecule MIMs with integrated biological functionalities, see a) Song, Y.; Schaufelberger, F.; Ashbridge, Z.; Pirvu, L.; Vitorica-Yrezabal, I. J.; Leigh, D. A. Effects of turn-structure on folding and entanglement in artificial molecular overhand knots. *Chem. Sci.* **2021**, *12*, 1826–1833; b) Schröder, H. V.; Zhang, Y.; Link, A. J. Dynamic covalent self-assembly of mechanically interlocked molecules solely made from peptides. *Nat. Chem.* **2021**, *13*, 850–857; c) Fernandes, A.; Viterisi, A.; Coutrot, F.; Potok, S.; Leigh, D. A.; Aucagne, V.; Papot, S. Rotaxane-Based Propeptides: Protection and Enzymatic Release of a Bioactive Pentapeptide. *Angew. Chem. Int. Ed.* **2009**, *48*, 6443–6447; d) Blankenship, J. W.; Dawson, P. E. Threading a peptide through a peptide: protein loops, rotaxanes, and knots. *Protein Sci.* **2007**, *16*, 1249–1256; e) Yamamoto, M.; Takeuchi, M.; Shinkai, S. Oligosaccharide binding to a boronic-acid-appended phenanthroline-Cu(I) complex which creates superstructural helicates and catenates. *Tetrahedron*, **2002**, *58*, 7251–7258; f) Echavarren, J.; Gall, M. A. Y.; Haertsch, A.; Leigh, D. A.; Spence, J. T. J.; Tetlow, D. J.; Tian, C. Sequence-Selective Decapeptide Synthesis by the Parallel Operation of Two Artificial Molecular Machines. *J. Am. Chem. Soc.* **2021**, *143*, 5158–5165; g) Coutrot, F.; Busseron, E. A New Glycorotaxane Molecular Machine Based on an Anilinium and a Triazolium Station. *Chem. Eur. J.* **2008**, *14*, 4784–4787.
- (9) Cornelissen, M. D.; Pilon, S.; van Maarseveen, J. H. Covalently Templated Syntheses of Mechanically Interlocked Molecules. *Synthesis*, **2021**, *53*, 4527–4548.
- (10) For examples of covalently templated MIMs, see a) Steemers, L.; Wanner, M. J.; Lutz, M.; Hiemstra, H.; van Maarseveen, J. H. Synthesis of spiro quasi[1]catenanes and quasi[1]rotaxanes via a templated backfolding strategy. *Nat. Commun.* **2017**, *8*, 15392; b) Schweez, C.; Shushkov, P.; Grimme, S.; Höger, S. Synthesis and Dynamics of Nanosized Phenylene–Ethynylene–Butadiynylene Rotaxanes and the Role of Shape Persistence. *Angew. Chem. Int. Ed.* **2016**, *55*, 3328–3333; c) Pilon, S.; Ingemann Jørgensen, S.; van Maarseveen, J. H. Covalent [2]Catenane and [2]Rotaxane Synthesis via a δ-Amino Acid Template. *ACS Org. Inorg. Au.* **2021**, *1*, 37–42; d) Steemers, L.; Wanner, M. J.; van Leeuwen, B. R. C.; Hiemstra, H.; van Maarseveen, J. H. Attempted [2]Catenane Synthesis via a Quasi[1]catenane by a Templated Backfolding Strategy. *Eur. J. Org. Chem.* **2018**, 874–878; e) Pilon, S.; Jørgensen, S. I.; van Maarseveen, J. H. [2]Catenane Synthesis via Covalent Templating. *Chem. Eur. J.* **2021**, *27*, 2310–2314; f) Bu, A.; Zhao, Y.; Xiao, H.; Tung, C.-H.; Wu, L.-Z.; Cong, H. A Conjugated Covalent Template Strategy for All-Benzene Catenane Synthesis. *Angew. Chem. Int. Ed.* **2022**, *61*, e202209449; g) Segawa, Y.; Kuwayama, M.; Hijikata, Y.; Fushimi, M.; Nishihara, T.; Pirillo, J.; Shirasaki, J.; Kubota, N.; Itami, K. All-benzene catenane and trefoil knot. *Science*, **2019**, *365*, 272–276; h) Ünsal, Ö.; Godt, A. Synthesis of a [2]catenane with functionalities and 87-membered rings. *Chem. Eur. J.* **1999**, *5*, 1728–1733; i) Kameta, N.; Hiratani, K.; Nagawa, Y. A novel synthesis of chiral rotaxanes via covalent bond formation. *Chem. Commun.* **2004**, *4*, 466–467.
- (11) Schill, G.; Lüttringhaus, A. The Preparation of Catena Compounds by Directed Synthesis. *Angew. Chem. Int. Ed. Engl.*, **1964**, *3*, 546–547.
- (12) a) Schaufelberger, F.; Timmer, B. J. J.; Ramström, O. *Principles of Dynamic Covalent Chemistry*, in “*Dynamic Covalent Chemistry: Principles, Reactions and Applications*” (eds. Zhang, W.; Jin, Y.), **2017**, Wiley-VCH; b) Jin, Y.; Yu, C.; Denman, R. J.; Zhang, W. Recent advances in dynamic covalent chemistry. *Chem. Soc. Rev.* **2013**, *42*, 6634–6654;
- (13) For a recent review on the topic see a) Yu, J.; Gaedke, M.; Schaufelberger, F. Dynamic Covalent Chemistry for Synthesis and Co-conformational Control of Mechanically Interlocked Molecules. *Eur. J. Org. Chem.* **2023**, *26*, e202201130. For examples of dynamic covalent chemistry for MIM synthesis, see b) Kawai, H.; Umehara, T.; Fujiwara, K.; Tsuji, T.; Suzuki, T. Dynamic covalently bonded rotaxanes cross-linked by imine bonds between the

- axle and ring: inverse temperature dependence of subunit mobility. *Angew. Chem. Int. Ed.* **2006**, *45*, 4281–4286; c) Hoshino, S.; Ono, K.; Kawai, H. Ring-Over-Ring Deslipping From Imine-Bridged Heterorotaxanes. *Front. Chem.* **2022**, *10*, 885939; d) Kandrnalova, M.; Kokan, Z.; Havel, V.; Nečas, M.; Šindelař, V. Hypervalent Iodine Based Reversible Covalent Bond in Rotaxane Synthesis. *Angew. Chem. Int. Ed.* **2019**, *58*, 18182–18185; e) Borodin, O.; Shchukin, Y.; Robertson, C. C.; Richter, S.; von Delius, M. Self-Assembly of Stimuli-Responsive [2]Rotaxanes by Amidinium Exchange. *J. Am. Chem. Soc.* **2021**, *143*, 16448–16457.
- (14) a) Peters, J. A. Interactions between boric acid derivatives and saccharides in aqueous media: Structures and stabilities of resulting esters. *Coord. Chem. Rev.* **2014**, *268*, 1–22; b) Springsteen, G.; Wang, B. A detailed examination of boronic acid–diol complexation. *Tetrahedron*, **2002**, *58*, 5291–5300; c) Sun, X.; Chapin, B. M.; Metola, P.; Collins, B.; Wang, B.; James, T. D.; Anslyn, E. V. The mechanisms of boronate ester formation and fluorescent turn-on in ortho-aminomethylphenylboronic acids. *Nat. Chem.* **2019**, *11*, 768–778; d) Bull, S. D.; Davidson, M. G.; Van den Elsen, J. M. H.; Fossey, J. S.; Jenkins, A. T. A.; Jiang, Y.-B. Kubo, Y.; Marken, F.; Sakurai, K.; Zhao, J.; James, T. D. Exploiting the reversible covalent bonding of boronic acids: recognition, sensing, and assembly. *Acc. Chem. Res.* **2013**, *46*, 312–326.
- (15) a) Davis, A. P. Biomimetic carbohydrate recognition. *Chem. Soc. Rev.* **2020**, *49*, 2531–2545; b) Williams, G. T.; Kedge, J. L.; Fossey, J. S. Molecular Boronic Acid-Based Saccharide Sensors. *ACS Sensors*, **2021**, *6*, 1508–1528.
- (16) a) McClary, C. A.; Taylor, M. S. Applications of organoboron compounds in carbohydrate chemistry and glycobiology: analysis, separation, protection, and activation. *Carbohydr. Res.* **2013**, *381*, 112–122; b) Estrada, C. D.; Ting Ang, H.; Vetter, K.-M.; Ponich, A. A.; Hall, D. G. Enantioselective Desymmetrization of 2-Aryl-1,3-propanediols by Direct O-Alkylation with a Rationally Designed Chiral Hemiboronic Acid Catalyst That Mitigates Substrate Conformational Poisoning. *J. Am. Chem. Soc.* **2021**, *143*, 4162–4167.
- (17) a) Röttger, M.; Domenech, T.; van der Weegen, R.; Breuillac, A.; Nicolaÿ, R.; Leibler, L. High-performance vitrimers from commodity thermoplastics through dioxaborolane metathesis. *Science*, **2017**, *356*, 62–65; b) Cromwell, O. R.; Chung, J.; Guan, Z. Malleable and Self-Healing Covalent Polymer Networks through Tunable Dynamic Boronic Ester Bonds. *J. Am. Chem. Soc.* **2015**, *137*, 6492–6495.
- (18) Hong, S. H.; Shin, M.; Park, E.; Ryu, J. H.; Burdick, J. A.; Lee, H. Alginate-Boronic Acid: pH-Triggered Bioinspired Glue for Hydrogel Assembly. *Adv. Funct. Mater.* **2020**, *30*, 1908497.
- (19) a) Stoltenberg, D., Lüthje, S., Winkelmann, O., Näther, C., Lüning, U. Tetraols as Templates for the Synthesis of Large endo-Functionalized Macrocycles. *Eur. J. Org. Chem.* **2011**, 5845–5859; b) Lüthje, S., Bornholdt, C., Lüning, U. Polyols as Templates for the Synthesis of Macrocycles from Boronic Acid Building Blocks. *Eur. J. Org. Chem.* **2006**, 909–915; c) Stoltenberg, D., Lüning, U. Macrocyclic synthesis by trimerization of boronic acids around a hexaol template, and recognition of polyols by resulting macrocyclic oligoboronic acids. *Org. Biomol. Chem.* **2013**, *11*, 5109–5116; d) Ono, K.; Onodera, S.; Kawai, H. Boroxine template for macrocyclization and postfunctionalization. *Chem. Commun.* **2022**, *58*, 12544–12547; e) Içli, B.; Christinat, N.; Tönnemann, J.; Schüttler, C.; Scopelliti, R.; Severin, K. Synthesis of Molecular Nanostructures by Multicomponent Condensation Reactions in a Ball Mill. *J. Am. Chem. Soc.* **2009**, *131*, 3154–3155.
- (20) For examples where boron is directly used for assembly, see a) Hicguet, M.; Mongin, O.; Roisnel, T.; Berrée, F.; Trolez, Y. Threading a linear molecule through a macrocycle thanks to boron. *ChemRxiv*, **2023**, 10.26434/chemrxiv-2023-707rs-v2; b) Zhang, G.; Presly, O.; White, F.; Oppel, I. M.; Mastalerz, M. A Shape-Persistent Quadruply Interlocked Giant Cage Catenane with Two Distinct Pores in the Solid State. *Angew. Chem. Int. Ed.* **2014**, *53*, 5126–5130. For other examples of boron-containing MIMs, see: c) Christinat, N.; Scopelliti, R.; Severin, K. Boron-based rotaxanes by multicomponent self-assembly. *Chem. Commun.* **2008**, 3660–3662; d) Koyama, Y.; Matsumura, T.; Yui, T.; Ishitani, O.; Takata, T. Fluorescence Control of Boron Enaminoketonate Using a Rotaxane Shuttle. *Org. Lett.* **2013**, *15*, 4686–4689; e) Rémy, M.; Nierengarten, I.; Park, B.; Holler, M.; Hahn, U.; Nierengarten, J.-F. Pentafluorophenyl Esters as Exchangeable Stoppers for the Construction of Photoactive [2]Rotaxanes. *Chem. Eur. J.* **2021**, *27*, 8492–8499; f) Kage, Y.; Shimizu, S.; Kociok-Kohn, G.; Furuta, H.; Pantoş, G. D. Subphthalocyanine-Stoppered [2]Rotaxanes. *Org. Lett.* **2020**, *22*, 1096–1101; g) Nisanci, B.; Sahinoglu, S.; Tuner, E.; Arik, M.; Kani, I.; Dastana, A.; Bozdemir, Ö. A. Synthesis of an F-BODIPY [2]catenane using the chemistry of bis(dipyrrinato)metal complexes. *Chem. Commun.* **2017**, *53*, 12418–12421; h) Nakamura, T.; Yamaguchi, G.; Nabeshima, T. Unidirectional Threading into a Bowl-Shaped Macrocyclic Trimer of Boron-Dipyrrin Complexes through Multipoint Recognition. *Angew. Chem. Int. Ed.* **2016**, *55*, 9606–9609.
- (21) Smith and co-workers have designed a range of fluorescent dyes with protective “arms” that resemble our condensation product, see: a) Li, D.-H.; Gamage, R. S.; Oliver, A. G.; Patel, N. L.; Usama, S. M.; Kalen, J. D.; Schnermann, M. J.; Smith, B. D. Doubly Strapped Zwitterionic NIR-I and NIR-II Heptamethine Cyanine Dyes for Bioconjugation and Fluorescence Imaging. *Angew. Chem. Int. Ed.* **2023**, *62*, e202305062; b) Li, D.-H.; Schreiber, C. L.; Smith, B. D. Sterically Shielded Heptamethine Cyanine Dyes for Bioconjugation and High Performance Near-Infrared Fluorescence Imaging. *Angew. Chem. Int. Ed.* **2020**, *59*, 12154–12161; c) Schreiber, C. L.; Li, D.-H.; Smith, B. D. High-Performance Near-Infrared Fluorescent Secondary Antibodies for Immunofluorescence. *Anal. Chem.* **2021**, *93*, 3643–3651; d) Li, D.-H.; Gamage, R. S.; Smith, B. D. Sterically Shielded Hydrophilic Analogs of Indocyanine Green. *J. Org. Chem.* **2022**, *87*, 11593–11601.
- (22) Condensation yield had a large variability under repeat conditions or even in glovebox settings. Attempts to increase condensation yield by switching solvents and concentrations failed, as did addition of a range of drying agents and use of a Dean-Stark apparatus. Instead of increased conversion to boronic ester, we observed boroxazine trimerization of the ligand under such conditions, indicating that the desired cleft-receptor **3** is likely a metastable reaction product.
- (23) Valenzuela, S. A.; Howard, J. R.; Park, H. M.; Darbha, S.; Anslyn, E. V. ¹¹B NMR Spectroscopy: Structural Analysis of the Acidity and Reactivity of Phenyl Boronic Acid–Diol Condensations. *J. Org. Chem.* **2022**, *87*, 15071–15076.
- (24) Guidry, E.N.; Cantrill, S.J.; Stoddart, J. F.; Grubbs, R. H. Magic ring catenation by olefin metathesis. *Org. Lett.* **2005**, *7*, 2129–2132.
- (25) Li, A.; Tan, Z.; Hu, Y.; Lu, Z.; Yuan, J.; Li, X.; Xie, J.; Zhang, J.; Zhu, K. Precise Control of Radial Catenane Synthesis via Clipping and Pumping. *J. Am. Chem. Soc.* **2022**, *144*, 2085–2089.

- (26) Taladhar, S. M.; D'Silva, C. The synthesis of 2-borono-1,3-xylyl crown ethers. *Tetrahedron Lett.* **1992**, 33, 265–268.
- (27) a) Kalenius, E.; Groessel, M.; Rissanen, K. Ion mobility–mass spectrometry of supramolecular complexes and assemblies. *Nat. Rev. Chem.* **2019**, 3, 4–14; b) Krüve, A.; Caprice, K.; Lavendomme, R.; Wollschläger, J. M.; Schoder, S.; Schröder, H. V.; Nitschke, J. R.; Coughon, F. B. L.; Schalley, C. A. Ion Mobility Mass Spectrometry for the Rapid Determination of the Topology of Interlocked and Knotted Molecules. *Angew. Chem. Int. Ed.* **2019**, 58, 11324–11328; c) Zimnicka M. M. Structural studies of supramolecular complexes and assemblies by ion mobility mass spectrometry. *Mass Spectrom. Rev.* **2023**, doi.org/10.1002/mas.21851.
- (28) Analysis of the crude reaction mixture also yielded a mixture of species with both arrival times, in line with expectations.
- (29) Sure, R.; Grimme, S. Corrected small basis set Hartree-Fock method for large systems. *J. Comput. Chem.* **2013**, 34, 1672–1685.

Bioderived Rotaxanes via Dynamic Covalent Boron Chemistry

Jingjing Yu¹, Marius Gaedke¹, Satyajit Das¹, Daniel L. Stares², Christoph A. Schalley²,
Fredrik Schaufelberger^{1*}

1. KTH Royal Institute of Technology, Department of Chemistry, Teknikringen 30, 10044
Stockholm, Sweden

2. Institut für Chemie und Biochemie, Freie Universität Berlin, Arnimallee 20, 14195 Berlin,
Germany.

*E-mail: fresch@kth.se

-Supporting Information-

Table of Contents

S1. Abbreviations	S3
S2. General experimental	S4
S3. Reaction schemes	S6
S4. Experimental procedures	S9
S5. Supplementary data	S16
S6. MS Spectra	S24
S7. NMR Spectra	S28
S8. Supplementary information references	S47

S1. ABBREVIATIONS

Abbreviations: COSY correlation spectroscopy; CID collision induced dissociation; DCM dichloromethane; DEPT distortionless enhancement by polarization transfer; DMF *N,N*-dimethylformamide; DIPEA *N,N*-diisopropylethylamine; DMSO dimethylsulfoxide; ESI electrospray ionization; HMBC heteronuclear multiple bond correlation; HRMS high resolution mass spectrometry; HSQC heteronuclear single quantum coherence spectroscopy; MeCN acetonitrile; NMR Nuclear magnetic resonance; RCM ring closing metathesis; RT room temperature; TFA trifluoroacetic acid; THF tetrahydrofuran; TLC thin layer chromatography; TMCCS_{N₂} theoretical experimental collisional cross section calculated using the trajectory method; ^{TW}CCS_{N₂} experimental collisional cross section; TW-IMS travelling wave ion mobility spectrometry

S2. GENERAL EXPERIMENTAL

Unless stated otherwise, reagents were obtained from commercial sources and used without purification. Reactions were carried out in anhydrous solvents and under an N₂ atmosphere. Anhydrous solvents were obtained by passing the solvent through an activated alumina column in a Glass Contour solvent dispensing system and stored over molecular sieves. Anhydrous THF was collected from redistillation with freshly-cut sodium wire and benzophenone indicator. Compounds **S1**,^[1] **S6**^[2], **S7**^[2], **S8**^[3], **S9**^[3] and **S10**^[4] were synthesized as previously described. ¹H NMR spectra were recorded on a Bruker Avance DMX 500 MHz NMR spectrometer and a Bruker Ascend 400 spectrometer (400 MHz). Chemical shifts are reported in parts per million (ppm) from high to low frequency using the residual solvent peak as the internal reference (CDCl₃ = 7.26 ppm). All ¹H resonances are reported to the nearest 0.01 ppm. The multiplicity of ¹H signals are indicated as: s = singlet; d = doublet; t = triplet; q = quartet; m = multiplet; br = broad; app = apparent; or combinations thereof. Coupling constants (*J*) are quoted in Hz and reported to the nearest 0.1 Hz. Where appropriate, averages of the signals from peaks displaying multiplicity were used to calculate the value of the coupling constant. ¹³C NMR spectra were recorded on the same spectrometers with the central resonance of the solvent peak as the internal reference (CDCl₃ = 77.16 ppm). All ¹³C resonances are reported to the nearest 0.01 ppm. For new compounds, DEPT, COSY, HSQC and HMBC experiments were used to aid spectral assignment. Fully characterized compounds were chromatographically homogeneous except where indicated otherwise in experimental descriptions. Computational models were optimized using HF-3c implemented in the ORCA software version 5.0.4.^[5-7]

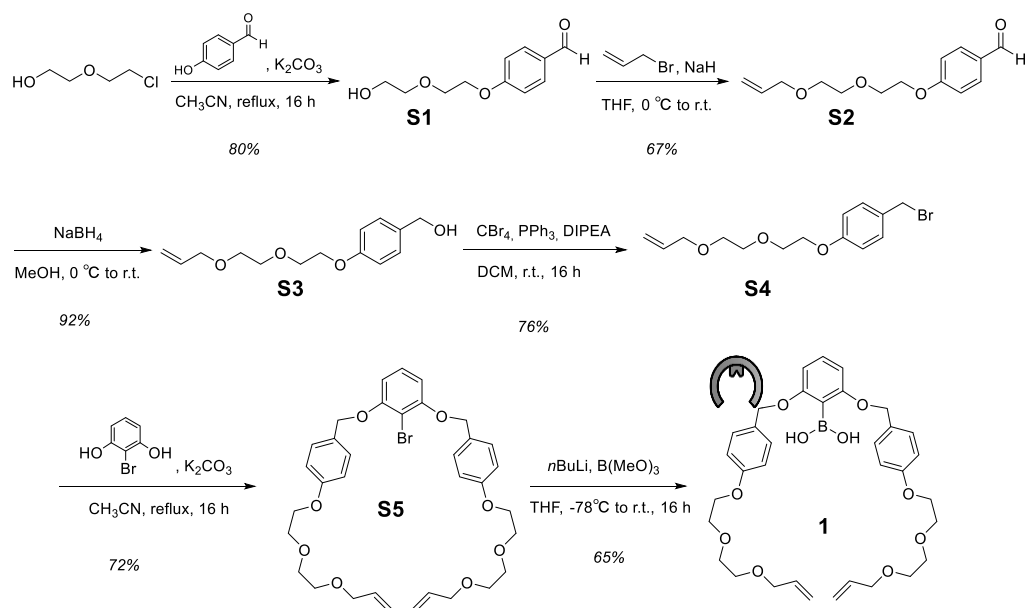
Flash column chromatography was carried out using Silica 60 Å (particle size 40–63 µm, Merck, Sweden) as the stationary phase. TLC was performed on precoated silica gel plates (0.25 mm thick, 60 F₂₅₄, Merck, Germany) and visualized using both short and long wave ultraviolet light in combination with standard laboratory stains (basic potassium permanganate, acidic ammonium molybdate). High-resolution mass spectrometry was performed on an LC-MS-QTOF 6530C instrument (Agilent).

TW-IMS and CID measurements: Ion mobility mass spectrometry measurements were performed on a Synapt G2-S traveling wave ion-mobility mass spectrometer Q-TOF (Waters) equipped with a Z-spray electrospray ionization source. Ion mobility samples were prepared with a final concentration of 25 µM in MeCN and were injected with a flow rate of 10 µL/min. Hydrolysis was initiated by preparing a 25 µM sample in 4:1 MeCN/H₂O. A capillary voltage of 3.75 kV was used with the sample cone and source offset both set to 25 eV. The source and desolvation temperatures were both set to 40°C. The drift cell was operated with N₂ as the

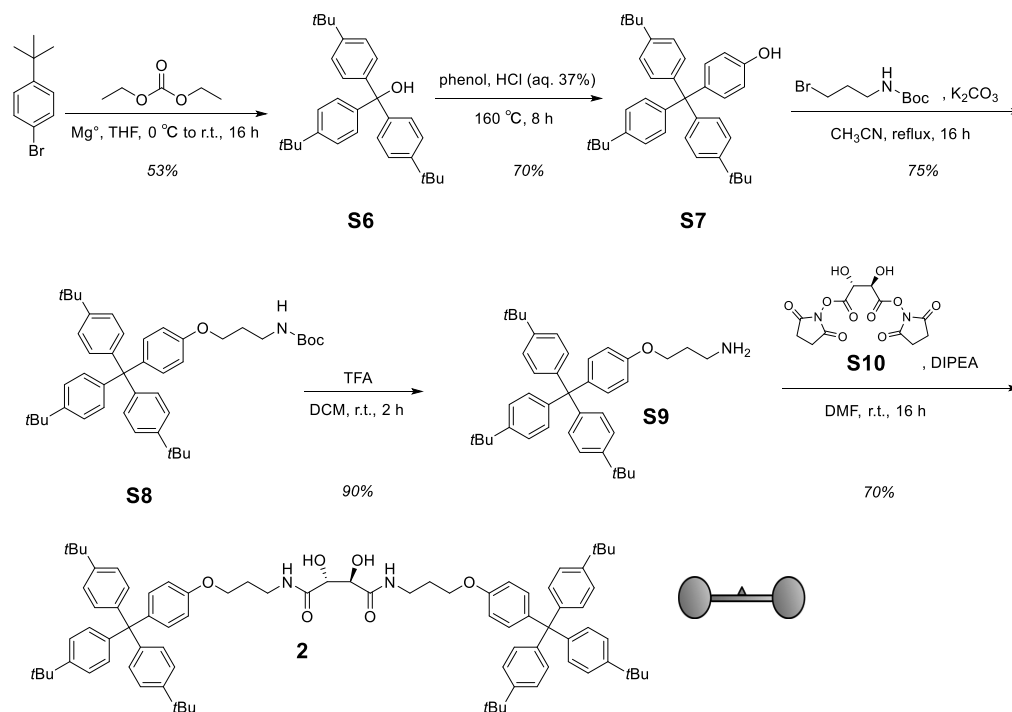
drift gas and was turned on 45 minutes prior to measuring to allow the pressures to settle. $^{TW}CCS_{N_2}$ were determined with a polyalanine calibrant solution and performed with 5 different wave height and velocities according to a literature procedure.^[8] Theoretical $^{TM}CCS_{N_2}$ values were calculated using the trajectory method implemented in IMoS software (Larriba Lab).^[9] Arrival time distributions were fit with a modified gaussian equation in Origin pro 2020 (OriginLab corporation) to determine precise arrival times. CID was performed in transfer cell with N_2 as collision gas.

S3. REACTION SCHEMES

3.1. Synthesis of tartrate diol thread and boronic open ring

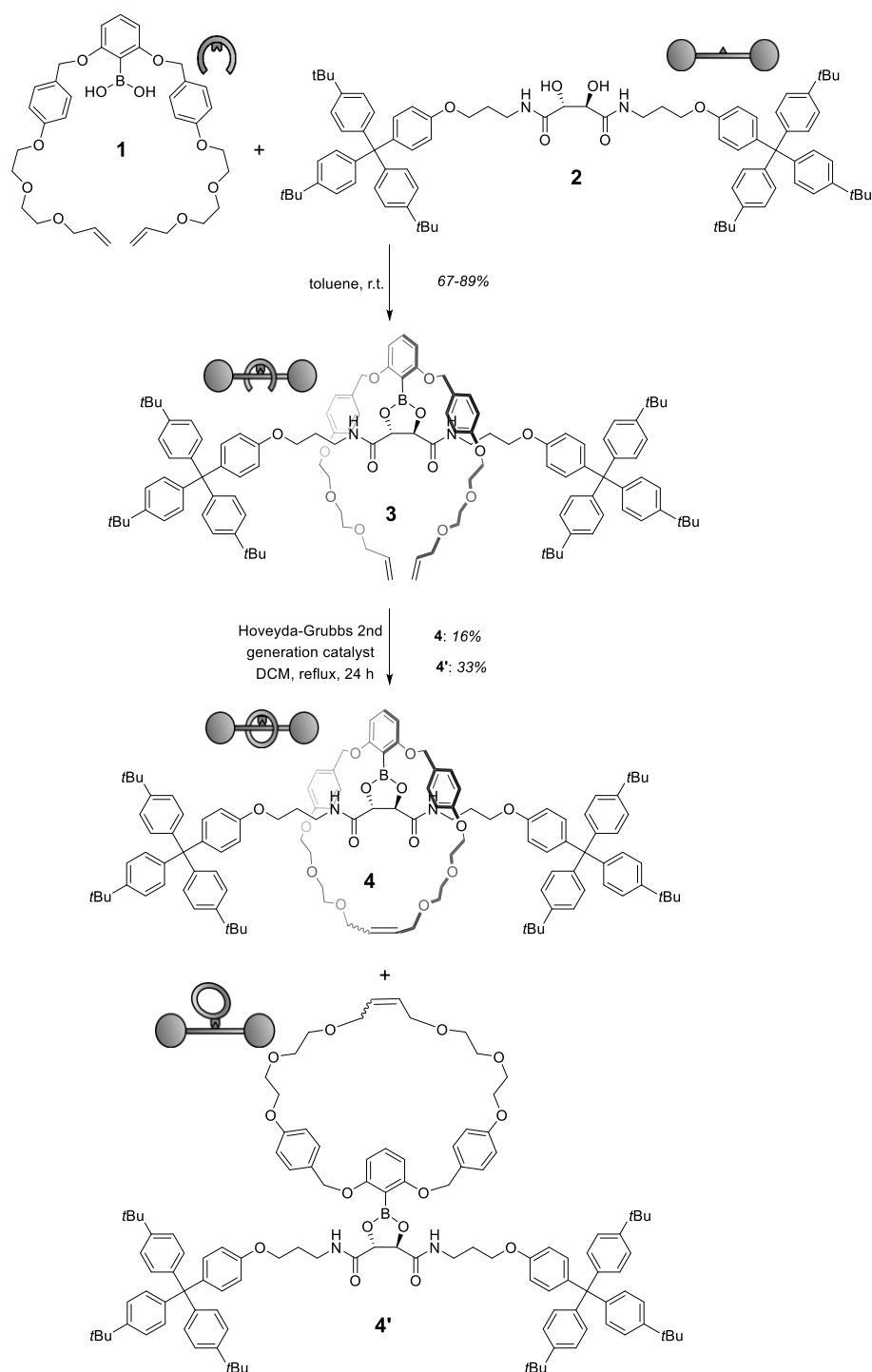


Scheme S1. Synthesis of boronic acid pincer ligand **1**.

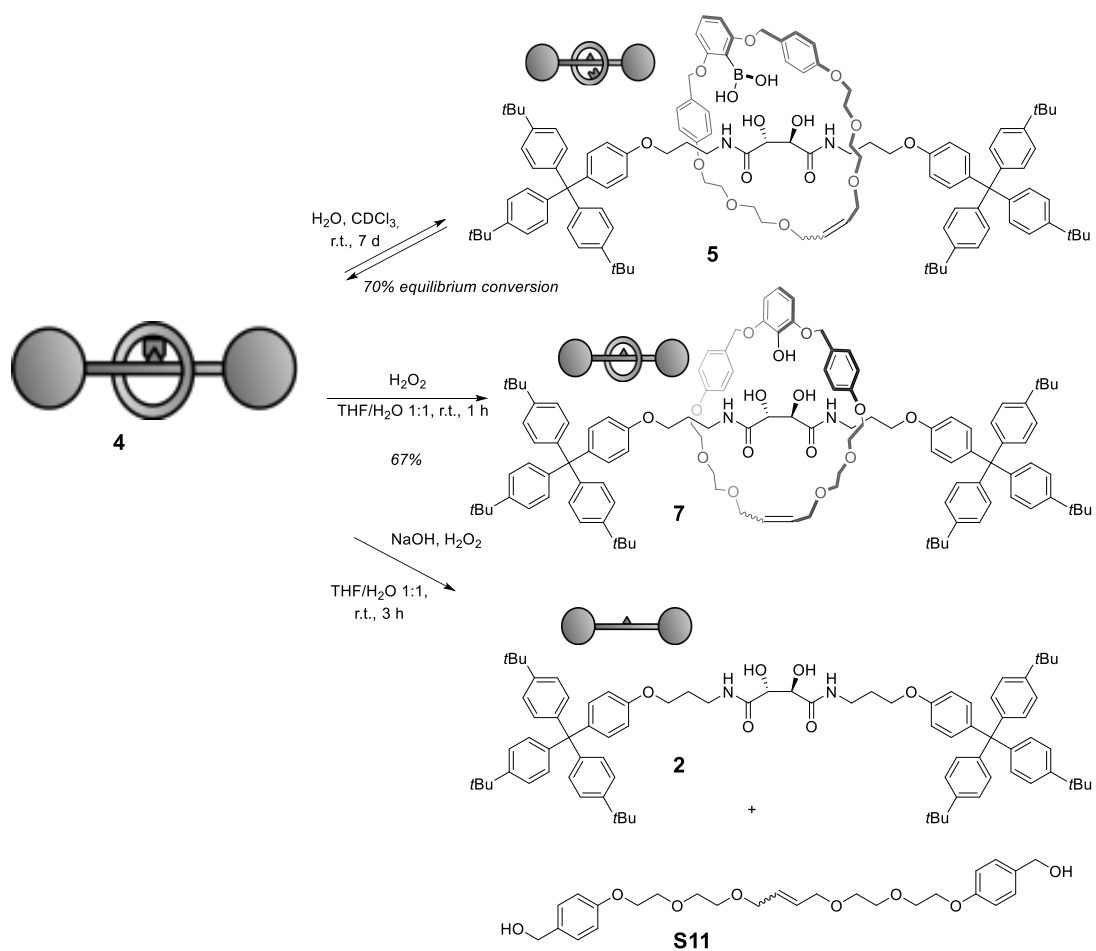


Scheme S2. Synthesis of tartrate diol thread **2**.

3.2. Synthesis of quasi[1]rotaxane and [2]rotaxane



Scheme S3. Synthesis of quasi[1]rotaxane **4** and isomer **4'**.

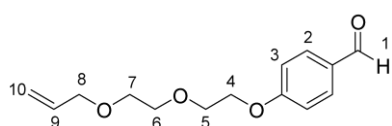


Scheme S4. Derivatization reactions of quasi[1]rotaxane **4**.

S4. EXPERIMENTAL PROCEDURES

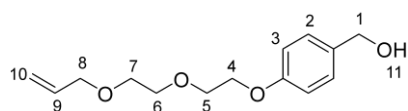
S4.1 Synthetic procedures and characterization details

S2



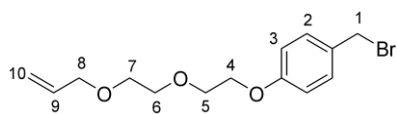
Sodium hydride (60% in mineral oil; 4.9 g, 122 mmol) was placed in a 200 mL, three-necked flask. The system was filled with dry nitrogen gas and cooled to 0 °C, after which THF (45 mL) was added. Compound **S1** (13 g, 50 mmol) was added dropwise to the suspension under stirring. After hydrogen gas evolution finished, allyl bromide (10.6 mL, 124 mmol) was added dropwise at 0 °C, and the mixture was stirred for 16 h at room temperature. Afterwards, the system was cooled to 0 °C and water (50 mL) was slowly added to quench the reaction. The mixture was transferred into a separating funnel and extracted repeatedly with ethyl acetate. The organic phase was washed with brine and dried over MgSO₄, filtered and concentrated. The residue was purified with column chromatography (silica gel; hexane/ethyl acetate, 2:1), to obtain compound **S2** (10 g, 67% yield) as a colorless oil. **¹H NMR** (500 MHz, CDCl₃): δ 9.88 (s, 1H, H₁), 7.82 (d, *J* = 8.5 Hz, 2H, H₂), 7.02 (d, *J* = 8.5 Hz, 2H, H₃), 5.84-5.98 (m, 1H, H₉), 5.27 (dd, *J* = 17.5 Hz, 2.0 Hz, 1H, H_{trans10}), 5.18 (dd, *J* = 10.5 Hz, 1.5 Hz, 1H, H_{cis10}), 4.16-4.27 (m, 2H, H₄), 4.03 (dt, *J* = 5.5 Hz, 1.5 Hz, 2H, H₈), 3.85-3.92 (m, 2H, H₅), 3.70-3.77 (m, 2H, H₆), 3.58-3.65 (m, 2H, H₇); **¹³C NMR** (126 MHz, CDCl₃): δ 190.92, 163.99, 134.78, 132.07, 130.20, 117.35, 115.02, 72.43, 71.10, 69.65, 69.58, 67.91; **HRMS** (ESI⁺) *m/z* calcd for C₁₄H₁₈O₄ [M+Na]⁺: 273.1103, found 273.1102 [M+Na]⁺.

S3



To a solution of compound **S2** (2.0 g, 8.0 mmol) in methanol was slowly added NaBH₄ (605 mg, 16 mmol) at 0 °C, after which the mixture was stirred for 1 h at room temperature. The reaction was quenched by slow addition of water while cooling the solution with an ice bath, and the reaction solution was extracted by DCM (3 × 50 mL), and washed with water. The organic layer was dried over MgSO₄, filtered and concentrated under reduced pressure. Compound **S3** was obtained as a colorless oil (1.84 g, 92% yield) without further purification. **¹H NMR** (500 MHz, CDCl₃): δ 7.28 (d, *J* = 8.5 Hz, 2H, H₂), 6.91 (d, *J* = 8.5 Hz, 2H, H₃), 5.84-6.00 (m, 1H, H₉), 5.28 (dd, *J* = 21.5 Hz, 2.0 Hz, 1H, H_{trans10}), 5.18 (dd, *J* = 12.5 Hz, 1.5 Hz, 2H, H_{cis10}), 4.61 (d, *J* = 5.6 Hz, 1H, H₁), 4.11-4.17 (m, 2H, H₄), 4.04 (dt, *J* = 7.0 Hz, 1.5 Hz, 2H, H₈), 3.83-3.90 (m, 2H, H₅), 3.69-3.77 (m, 2H, H₆), 3.59-3.66 (m, 2H, H₇); **¹³C NMR** (126 MHz, CDCl₃): δ 158.58, 134.86, 133.47, 128.73, 117.32, 114.86, 72.43, 71.03, 69.93, 69.60, 67.65, 65.19; **HRMS** (ESI⁺) *m/z* calcd for C₁₄H₂₀O₄ [M+Na]⁺: 275.1254, found 275.1265 [M+Na]⁺.

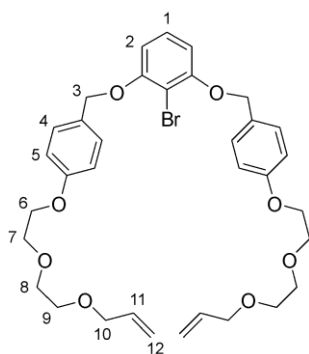
S4



To a mixture of compound **S3** (1.0 g, 3.97 mmol), carbon tetrabromide (1.580 g, 4.76 mmol) and DIPEA (880 μ L, 4.76 mmol) was injected anhydrous THF (100 mL), then triphenyl

phosphine (1.040 g, 3.970 mmol) dissolved in anhydrous THF (50 mL) was slowly injected into the mixture at 0 °C. The mixture was slowly warmed to room temperature and stirred overnight under N₂ atmosphere. Afterwards, the reaction was quenched by addition of water (200 mL), and the reaction solution was extracted with ethyl acetate (3 \times 100 mL) and washed with brine. The organic layer was dried over MgSO₄, filtered and concentrated under reduced pressure. The residue was purified with column chromatography (silica gel; hexane/ethyl acetate, 2:1), and compound **S4** was obtained as a colorless oil (947 mg, 76% yield). **¹H NMR** (500 MHz, CDCl₃): δ 7.31 (d, J = 8.5 Hz, 2H, H₂), 6.88 (d, J = 8.5 Hz, 2H, H₃), 5.85-5.98 (m, 1H, H₉), 5.28 (dd, J = 17.5 Hz, 1.5 Hz, 1H, H_{trans10}), 5.18 (dd, J = 10.5 Hz, 1.5 Hz, 1H, H_{cis10}), 4.5 (s, 2H, H₁), 4.10-4.16 (m, 2H, H₄), 4.03 (dt, J = 6.0 Hz, 1.5 Hz, 2H, H₈), 3.83-3.89 (m, 2H, H₅), 3.70-3.75 (m, 2H, H₆), 3.60-3.65 (m, 2H, H₇); **¹³C NMR** (126 MHz, CDCl₃): δ 159.04, 134.85, 130.54, 130.26, 117.32, 115.04, 72.44, 71.04, 69.84, 69.60, 67.66, 34.06; **HRMS** (ESI⁺) m/z calcd for C₁₄H₁₉BrO₃ [M+Na]⁺: 337.0410 and 339.0390, found 337.0419 and 339.0401 [M+Na]⁺.

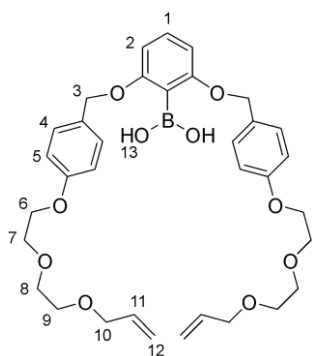
S5



To a solution of compound **S4** (1.0 g, 3.185 mmol), in acetonitrile (30 mL) was added 2-bromoresorcinol (249 mg, 1.327 mmol) and K₂CO₃ (1.0 g, 7.962 mmol). The mixture was heated to reflux and stirred under N₂ atmosphere overnight. Afterwards, the reaction solution was filtered and washed with acetone (100 mL), and the filtrate was concentrated under vacuum. The obtained residue was purified with column chromatography (silica gel; hexane/ethyl acetate, 2:1), The compound **S5** was obtained as a liquid oil (626

mg, 72% yield). **¹H NMR** (500 MHz, CDCl₃): δ 7.38 (d, J = 8.5 Hz, 4H, H₄), 7.14 (t, J = 8.4 Hz, 1H, H₁), 6.93 (d, J = 8.5 Hz, 4H, H₅), 6.60 (d, J = 8.5 Hz, 2H, H₂), 5.85-5.99 (m, 2H, H₁₁), 5.28 (dd, J = 17.5 Hz, 2.0 Hz, 2H, H_{trans12}), 5.18 (dd, J = 10.5 Hz, 1.5 Hz, 2H, H_{cis12}), 5.08 (s, 4H, H₃), 4.10-4.18 (m, 4H, H₆), 4.04 (dt, J = 6.0 Hz, 1.5 Hz, 4H, H₁₀), 3.83-3.90 (m, 4H, H₇), 3.70-3.77 (m, 4H, H₈), 3.59-3.66 (m, 4H, H₉); **¹³C NMR** (126 MHz, CDCl₃): δ 158.71, 156.62, 134.86, 129.05, 128.78, 128.75, 128.11, 117.34, 114.83, 107.04, 72.44, 71.03, 70.98, 69.92, 69.61, 67.61; **HRMS** (ESI⁺) m/z calcd for C₃₄H₄₁BrO₈ [M+Na]⁺: 679.1877 and 681.1857, found 679.1893 and 681.1881 [M+Na]⁺.

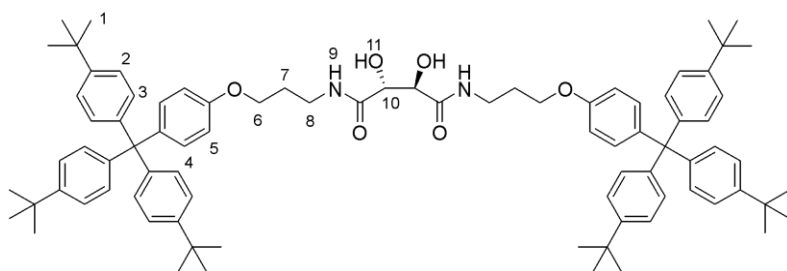
1



Compound **S5** (200 mg, 0.305 mmol) was dissolved in rigorously anhydrous tetrahydrofuran (5 mL, see general experimental for drying protocol) and cooled to $-78\text{ }^{\circ}\text{C}$. *n*-butyllithium (146 μL , 2.5 M in hexanes, 1.2 mmol) was added dropwise and the mixture was stirred at $-78\text{ }^{\circ}\text{C}$ for another 30 min. Anhydrous trimethyl borate (68 μL , 0.610 mmol) was added and the mixture stirred for 16 h while warming to room temperature. After quenching by addition of water and ethyl acetate (50 mL each), the layers were separated. The

aqueous layer was extracted with ethyl acetate (3 \times 30 mL) and the combined organic layers were washed with brine (30 mL), dried with MgSO_4 , filtered and concentrated. The remaining residue was purified with chromatography on silica gel (hexane/ethyl acetate 10:1 \rightarrow 2:1), and the product was obtained as a transparent oil (124 mg, 65 %). **$^1\text{H NMR}$** (500 MHz, CDCl_3): δ 7.36 (t, $J = 8.5$ Hz, 1H, H_1), 7.33 (d, $J = 8.5$ Hz, 4H, H_4), 7.20 (s, 2H, H_{13}), 6.93 (d, $J = 8.5$ Hz, 4H, H_5), 6.71 (d, $J = 8.5$ Hz, 2H, H_2), 5.85-5.98 (m, 2H, H_{11}), 5.28 (dd, $J = 21.5$ Hz, 2.0 Hz, 2H, $\text{H}_{\text{trans}12}$), 5.18 (dd, $J = 12.5$ Hz, 1.5 Hz, 2H, $\text{H}_{\text{cis}12}$), 5.05 (s, 4H, H_3), 4.12-4.17 (m, 4H, H_6), 4.04 (dt, $J = 6.0$ Hz, 1.5 Hz, 4H, H_{10}), 3.83-3.90 (m, 4H, H_7), 3.70-3.77 (m, 4H, H_8), 3.59-3.67 (m, 4H, H_9); **$^{13}\text{C NMR}$** (126 MHz, CDCl_3): δ 171.30, 164.97, 159.28, 134.87, 133.02, 129.68, 127.87, 117.34, 115.20, 106.01, 72.45, 71.22, 71.03, 69.86, 69.60, 67.64; **$^{11}\text{B NMR}$** (160 MHz, CDCl_3): δ 29.2; **HRMS** (ESI⁺) m/z calcd for $\text{C}_{34}\text{H}_{43}\text{BO}_{10}$ $[\text{M}+\text{Na}]^+$: 645.2841, found 645.2864 $[\text{M}+\text{Na}]^+$.

2

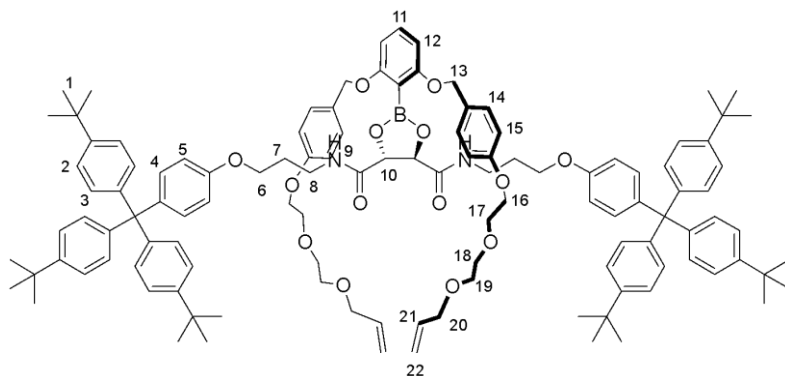


Compound **S10** (70 mg, 0.203 mmol) and compound **S9** (250 mg, 0.445 mmol) were dissolved in DMF (25 mL) and DIPEA (150 μL , 0.809 mmol)

was added. The mixture was stirred at room temperature for overnight, after which the reaction mixture was concentrated under vacuum. The residue was extracted with ethyl acetate and washed with brine, and the combined organic layers were dried with Na_2SO_4 , filtered and concentrated. The residue was purified with column chromatography (silica gel, hexane/ethyl acetate 1:1), and the product **2** was obtained as a white solid (175 mg, 70%). **$^1\text{H NMR}$** (500 MHz, CDCl_3): δ 7.49 (t, $J = 6.0$ Hz, 2H, H_9), 7.22 (d, $J = 10.5$ Hz, 12H, H_2), 7.06 (d, $J = 9.0$ Hz, 4H, H_4), 7.07 (d, $J = 10.5$ Hz, 12H, H_3), 6.74 (d, $J = 9.0$ Hz, 4H, H_5), 5.34-5.39 (m, 2H, H_{11}), 4.21-4.27 (m, 2H, H_{10}), 3.98 (t, $J = 5.5$ Hz, 4H, H_6), 3.38-3.51 (m, 4H, H_8), 1.89-2.00 (m, 4H,

H₇), 1.29 (s, 54H, H₁); ¹³C NMR (126 MHz, CDCl₃): δ 174.14, 156.45, 148.46, 144.24, 140.12, 132.47, 130.87, 124.19, 113.02, 70.29, 66.01, 63.20, 37.27, 34.43, 31.53, 28.94; HRMS (ESI⁺) *m/z* calcd for C₈₄H₁₀₄N₂O₆ [M+K]⁺: 1275.7526, found 1275.7536 [M+K]⁺.

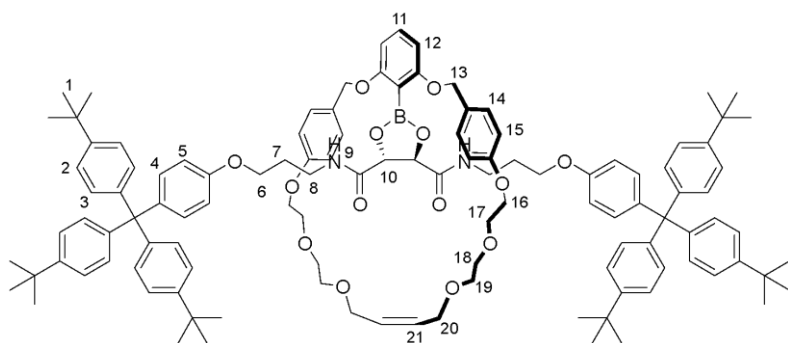
3



Compound **1** (15.0 mg, 0.024 mmol) and compound **2** (30 mg, 0.024 mmol) were dissolved in anhydrous toluene (2 mL) and stirred at room temperature for 24h, until the condensation equilibrium was reached.

Condensation was monitored by ¹H NMR analysis, through withdrawal of reaction aliquots and sampling into CDCl₃ (integrity of the compound was confirmed through secondary analysis with other NMR solvents). After equilibrium was reached, the solvent was removed under vacuum. The obtained crude residue was directly used in next step without further purification. Through analysis via ¹H NMR spectroscopy, these optimized conditions yielded conversions of 70-89% of **3**, with variability between experiments. ¹H NMR (500 MHz, CDCl₃): δ 7.23 (d, *J* = 8.5 Hz, 12H, H₂), 7.21 (d, *J* = 8.5 Hz, 4H, H₁₄), δ 7.10 (d, *J* = 8.5 Hz, 12H, H₃), 7.02 (d, *J* = 8.5 Hz, 4H, H₄), 7.02 (m, 2H, H₉), 6.96 (t, *J* = 8.5 Hz, 1H, H₁₁), 6.87 (d, *J* = 8.5 Hz, 4H, H₁₅), 6.61 (d, *J* = 8.5 Hz, 4H, H₅), 6.10 (d, *J* = 8.5 Hz, 2H, H₁₂), 5.85-5.96 (m, 2H, H₂₁), 5.26 (dd, *J* = 17.5 Hz, 2.0 Hz, 2H, H_{trans22}), 5.17 (dd, *J* = 10.5 Hz, 1.5 Hz, 2H, H_{cis22}), 4.94 (s, 2H, H₁₀), 4.66 (d, *J* = 10.5 Hz, 2H, H₁₃), 4.48 (d, *J* = 10.5 Hz, 2H, H₁₃), 4.09 (t, *J* = 4.5 Hz, 4H, H₁₆), 4.02 (dt, *J* = 5.5 Hz, 1.5 Hz, 4H, H₂₀), 3.82 (t, *J* = 4.5 Hz, 4H, H₁₇), 3.72-3.76 (m, 4H, H₆), 3.68-3.72 (m, 4H, H₁₈), 3.59-3.62 (m, 4H, H₁₉), 3.06-3.21 (m, 4H, H₈), 1.60-1.67 (m, 4H, H₇), 1.29 (s, 54H, H₁); ¹³C NMR (126 MHz, CDCl₃) δ 170.18, 164.41, 159.11, 156.62, 148.44, 144.33, 139.69, 138.00, 134.86, 132.37, 130.85, 129.57, 129.17, 125.44, 124.22, 117.31, 114.90, 113.08, 105.76, 79.14, 72.42, 71.03, 70.74, 69.85, 69.58, 67.68, 65.09, 63.18, 36.24, 34.44, 31.54, 29.85; ¹¹B NMR (160 MHz, CDCl₃): δ 28.9.

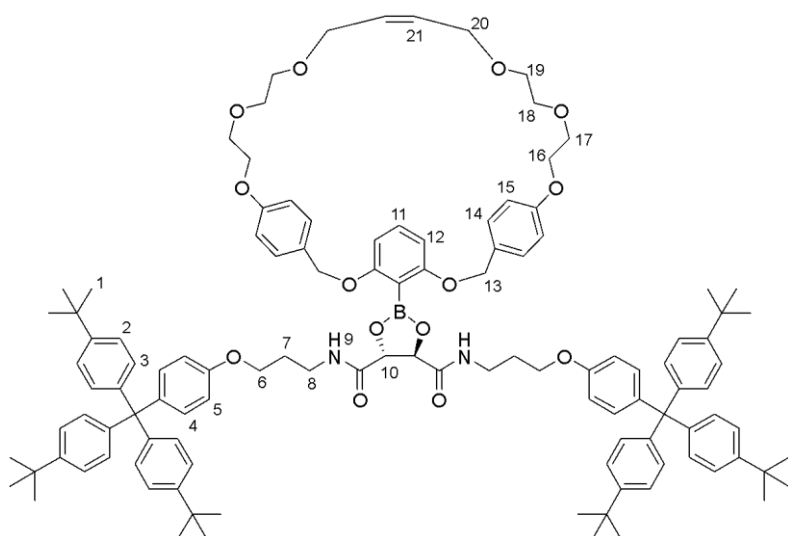
4



The crude mixture containing complex **3** (45 mg) from the protocol described above was redissolved into degassed DCM (20 mL). Hoveyda-Grubbs 2nd generation catalyst (10% mol, 1.5 mg) in

degassed DCM (5 mL) was then injected into the reaction solution. The mixture was stirred under refluxing conditions for 24 h, after which the reaction was quenched by addition of vinyl acetate (2 mL). The solution was concentrated under vacuum, and the crude directly purified by chromatography (silica gel, hexane/ethyl acetate 1:1). Quasi[1]rotaxane **4** was then obtained as transparent oil (7.0 mg, 16% over two steps). ¹H NMR (500 MHz, CDCl₃): δ 7.25 (m, 2H, H₉), 7.24 (d, *J* = 8.5 Hz, 14H, H₂), 7.08 (d, *J* = 8.5 Hz, 12H, H₃), 6.84 (d, *J* = 8.5 Hz, 4H, H₁₄), 6.82 (d, *J* = 9.0 Hz, 4H, H₄), 6.75 (t, *J* = 8.0 Hz, 1H, H₁₁), 6.53 (d, *J* = 8.5 Hz, 4H, H₁₅), 6.41 (d, *J* = 9.0 Hz, 4H, H₅), 6.18 (d, *J* = 8.0 Hz, 2H, H₁₂), 5.77 (t, *J* = 3.0 Hz, 2H, H₂₁), 4.84 (s, 2H, H₁₀), 4.67 (d, *J* = 11.5 Hz, 2H, H₁₃), 4.54 (d, *J* = 11.5 Hz, 2H, H₁₃), 4.06-4.17 (m, 4H, H₁₆), 3.93-4.06 (m, 4H, H₂₀), 3.84 (t, *J* = 5.0 Hz, 4H, H₁₇), 3.69-3.76 (m, 4H, H₆), 3.63-3.67 (m, 4H, H₁₈), 3.51-3.55 (m, 4H, H₁₉), 3.09-3.26 (m, 4H, H₈), 1.82-1.90 (m, 4H, H₇), 1.29 (s, 54H, H₁); ¹³C NMR (126 MHz, CDCl₃): δ 169.73, 162.58, 158.61, 156.28, 148.39, 144.39, 139.60, 132.06, 130.85, 129.97, 129.69, 129.38, 128.72, 124.19, 115.20, 114.52, 113.16, 108.15, 78.70, 71.59, 71.48, 70.94, 70.07, 69.64, 67.64, 66.60, 63.15, 37.58, 34.45, 31.57, 29.84; HRMS (ESI⁺) *m/z* calcd for C₁₁₆H₁₃₉BN₂O₁₄ [M+Na]⁺: 1818.0212, found 1818.0258 [M+Na]⁺.

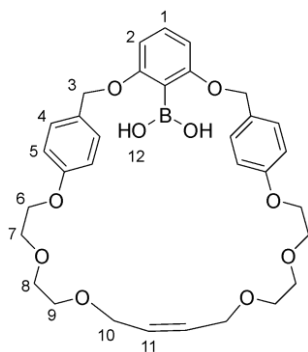
4'



Through the procedure described for synthesis of compound **4** above, the non-interlocked isomer **4'** was also obtained as a white solid (15 mg, 33% over two steps, could only be isolated with impurities in the form of hydrolysis products **2** and **6**). This compounds could also be obtained by direct

condensation of 1:1 ratio of macrocycle **6** and thread **2**. **¹H NMR** (500 MHz, CDCl₃): δ 7.48 (t, *J* = 6.0 Hz, 12H, H₉), 7.23 (d, *J* = 8.5 Hz, 12H, H₂), 7.07 (d, *J* = 8.5 Hz, 12H, H₃), 7.06 (d, *J* = 8.5 Hz, 4H, H₁₄), 7.03 (d, *J* = 9.0 Hz, 4H, H₄), 6.92 (t, *J* = 8.5 Hz, 1H, H₁₁), 6.79 (d, *J* = 8.5 Hz, 4H, H₁₅), 6.65 (d, *J* = 9.0 Hz, 4H, H₅), 6.19 (d, *J* = 8.5 Hz, 2H, H₂), 5.77 (t, *J* = 1.5 Hz, 2H, H₂₁), 5.06 (s, 2H, H₁₀), 4.94 (s, 4H, H₁₃), 4.02-4.07 (m, 2H, H₁₆), 3.97-4.01 (m, 4H, H₂₀), 3.93 (t, *J* = 6.0 Hz, 4H, H₆), 3.76-3.80 (m, 4H, H₁₇), 3.64-3.68 (m, 4H, H₁₈), 3.54-3.57 (m, 4H, H₁₉), 3.34-3.44 (m, 4H, H₈). 1.90-1.99 (m, 4H, H₇), 1.29 (s, 54H, H₁); **¹³C NMR** (126 MHz, CDCl₃): 170.43, 162.60, 158.50, 156.53, 148.43, 144.27, 139.81, 137.98, 132.36, 130.84, 129.64, 129.16, 128.35, 125.43, 124.18, 114.97, 113.03, 105.95, 79.33, 71.40, 71.05, 69.79, 69.66, 67.69, 65.07, 63.17, 36.88, 34.42, 31.53, 29.84; **HRMS** (ESI⁺) *m/z* calcd for C₁₁₆H₁₃₉BN₂O₁₄ [M+Na]⁺: 1818.0212, found 1818.0258 [M+Na]⁺.

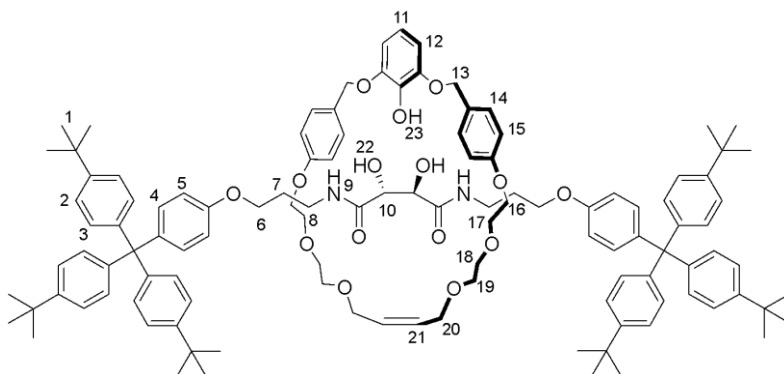
6



Through the procedure described for synthesis of compound **4** above, compound **6** was formed as a byproduct and could be separated out on the silica column as a transparent oil (3 mg, 23% over two steps). **¹H NMR** (500 MHz, CDCl₃): δ 7.36 (s, 2H, H₁₂), 7.22 (d, *J* = 8.5 Hz, 4H, H₄), 7.15 (t, *J* = 8.5 Hz, 1H, H₁), 6.86 (d, *J* = 8.5 Hz, 4H, H₅), 6.54 (d, *J* = 8.5 Hz, 2H, H₂), 5.77 (t, *J* = 1.5 Hz, H₁₁), 5.21 (s, 4H, H₃), 4.08-4.14 (m, 4H, H₆), 3.97-4.03 (m, 4H, H₁₀), 3.76-3.85 (m, 4H, H₇), 3.63-3.71 (m, 4H, H₈), 3.51-3.60 (m, 4H, H₉);

¹³C NMR (126 MHz, CDCl₃): δ 163.98, 158.90, 132.41, 129.73, 129.57, 129.22, 128.11, 115.16, 107.17, 71.44, 71.06, 70.57, 69.87, 69.65, 67.79; **HRMS** (ESI⁺) *m/z* calcd for C₃₂H₃₉BO₁₀ [M+Na]⁺: 617.2528, found 617.2584 [M+Na]⁺.

7



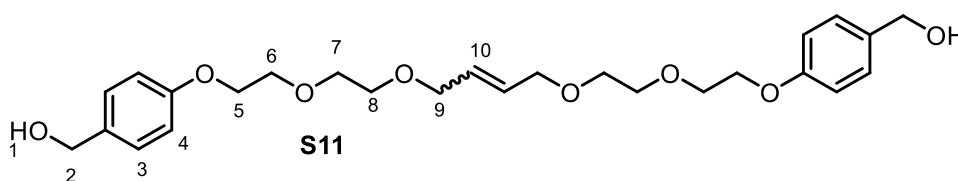
To a solution of compound **4** (1.8 mg, 0.001 mmol) in THF (200 μL) and water (200 μL) was added 30% H₂O₂ (aq, 2 μL), the mixture was stirred at room temperature for 3 h. After that, the reaction solution was extracted by ethyl acetate (50

ml x 3) and washed with brine. The combined organic layers were dried with Na₂SO₄, filtered and concentrated. The residue was purified with preparative silica gel TLC (DCM/MeOH 25:1) and the product was obtained as a white solid (1.2 mg, 67%). **¹H NMR** (500 MHz, CDCl₃): δ

7.76 (s, 1H, H₂₃), 7.23 (d, *J* = 8.5 Hz, 12H, H₂), 7.16-7.20 (m, 2H, H₉), 7.12 (d, *J* = 8.0 Hz, 4H, H₁₄), 7.09 (d, *J* = 8.5 Hz, 12H, H₃), 7.01 (d, *J* = 8.5 Hz, 4H, H₄), 6.64 (d, *J* = 8.0 Hz, 4H, H₁₅), 6.55 (d, *J* = 8.5 Hz, 4H, H₅), 6.40-6.47 (m, 3H, H₁₁, H₁₂), 5.72 (br, 2H, H₂₁), 4.98 (s, 4H, H₁₃), 4.26 (d, *J* = 7.5 Hz, 2H, H₁₀), 3.85-3.94 (m, 8H, H₁₆, H₂₀), 3.67 (t, *J* = 5.0 Hz, 4H, H₁₇), 3.54-3.62 (m, 8H, H₆, H₁₈), 3.45-3.50 (m, 4H, H₁₉), 3.07-3.24 (m, 4H, H₈), 1.63-1.65 (m, 4H, H₇), 1.29 (s, 54H, H₁); ¹³C NMR (126 MHz, CDCl₃): δ 175.59, 172.62, 158.58, 156.53, 148.43, 146.17, 144.35, 139.71, 137.28, 132.26, 130.86, 130.17, 129.67, 124.20, 118.83, 114.69, 113.16, 108.67, 71.63, 71.39, 71.35, 70.83, 69.82, 69.70, 67.47, 65.69, 63.20, 36.87, 34.44, 31.55, 29.85; HRMS (ESI⁺) *m/z* calcd for C₁₁₆H₁₄₂N₂O₁₅ [M+Na]⁺: 1827.0336, found 1827.0340 [M+Na]⁺.

Macrocycle cleavage from compound 4

To a solution compound **4** (2.0 mg, 0.001 mmol) in THF (150 μL) and water (150 μL) was added 2N NaOH aqueous solution (60 μL) and 30% H₂O₂ (aq, 100 μL), and the mixture was stirred at room temperature for 1 h. After that, the reaction solution was quenched by adding 2N HCl aq (60 μL), extracted with ethyl acetate (20 ml x 3) and washed with brine. The combined organic layers were dried with Na₂SO₄, filtered and concentrated. The residue was purified with preparative silica gel TLC (DCM/MeOH 25:1) and thread **2** was recycled as a white solid (1.2 mg, 87%). The cleaved ring residue could not be isolated, but was identified as **S11** from HRMS and NMR analysis of the crude mixture (which showed a 1:1 ratio between **S11** and thread **2**). ¹H NMR (500 MHz, CDCl₃) of **S11**: δ 7.28 (d, *J* = 8.0 Hz, 4H, H₃), 6.90 (d, *J* = 8.0 Hz, 4H, H₄), 5.79 (m, 2H, H₁₀), 4.61 (s, 4H, H₂), 4.13 (t, *J* = 4.5 Hz, 4H, H₅), 4.02 (m, 4H, H₉), 3.86 (m, 4H, H₆), 3.72 (m, 4H, H₇), 3.61 (m, 4H, H₈). HRMS (ESI⁺) *m/z* calcd for C₂₆H₃₆O₈ [M+Na]⁺: 499.2308, found 499.2303 [M+Na]⁺.



S5. SUPPLEMENTARY DATA

5.1. Screening of conditions for boronic ester condensation

Table S1. Condensation experiments between pincer ligand **1** and thread **2**.^a

Entry	Solvent	T (°C)	c (mM)	Desiccant	24 h conversion ^b	48 h conversion ^b
1	toluene	r.t.	10	/	67%	70%
2	1,4-dioxane	r.t.	10	/	59%	52%
3	DCM	r.t.	10	/	58%	60%
4	THF	r.t.	10	/	54%	56%
5	THF	r.t.	1	/	40%	48%
6	THF	r.t.	5	/	49%	55%
8	THF	r.t.	30	/	57%	57%
9	toluene	40	10	/	65%	63%
10	toluene	80	10	/	N/A ^c	N/A ^c
11	toluene	r.t.	10	Na ₂ SO ₄	61%	63%
12	toluene	r.t.	10	4Å MS	67%	64%

^a Conditions: **1** (0.002 mmol), **2** (0.002 mmol), solvent (200 µL), r.t. ^b Conversion obtained by ¹H NMR analysis of a reaction aliquot added into CDCl₃ (0.55 mL). ^c No complex **3** observed due to boroxazine formation.

5.2. Hydrolysis of condensation complex 3

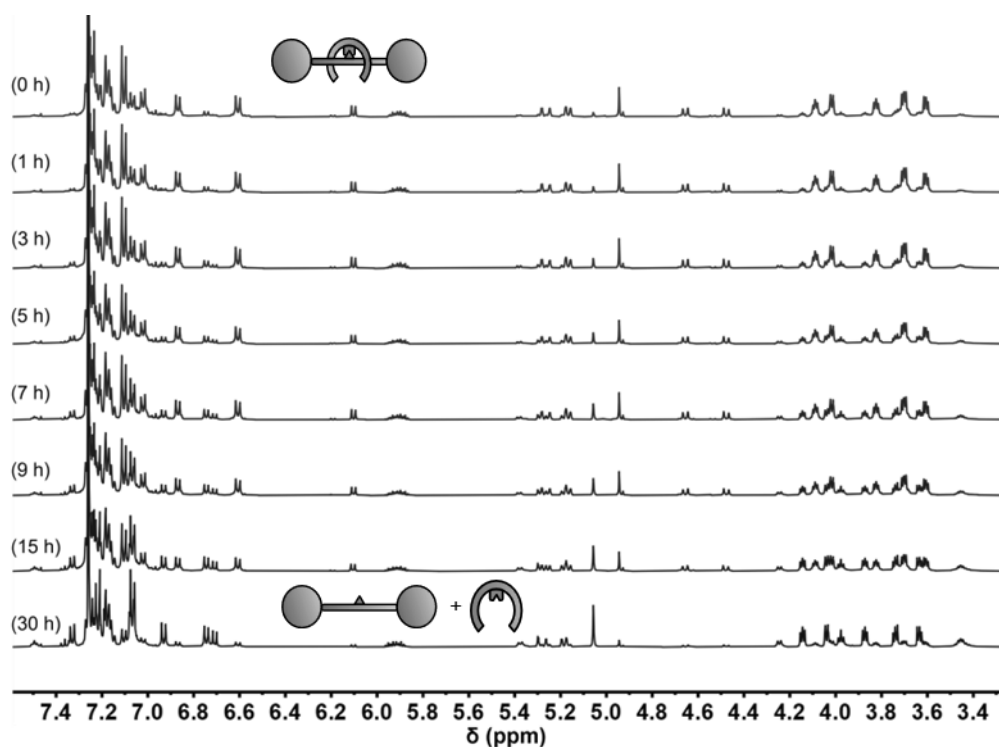


Figure S1. Partial ^1H NMR spectra (500 MHz, CDCl_3 , 298 K) of the gradual hydrolysis of condensation complex **3** when incubated in water-saturated CDCl_3 after the time indicated next to each spectrum.

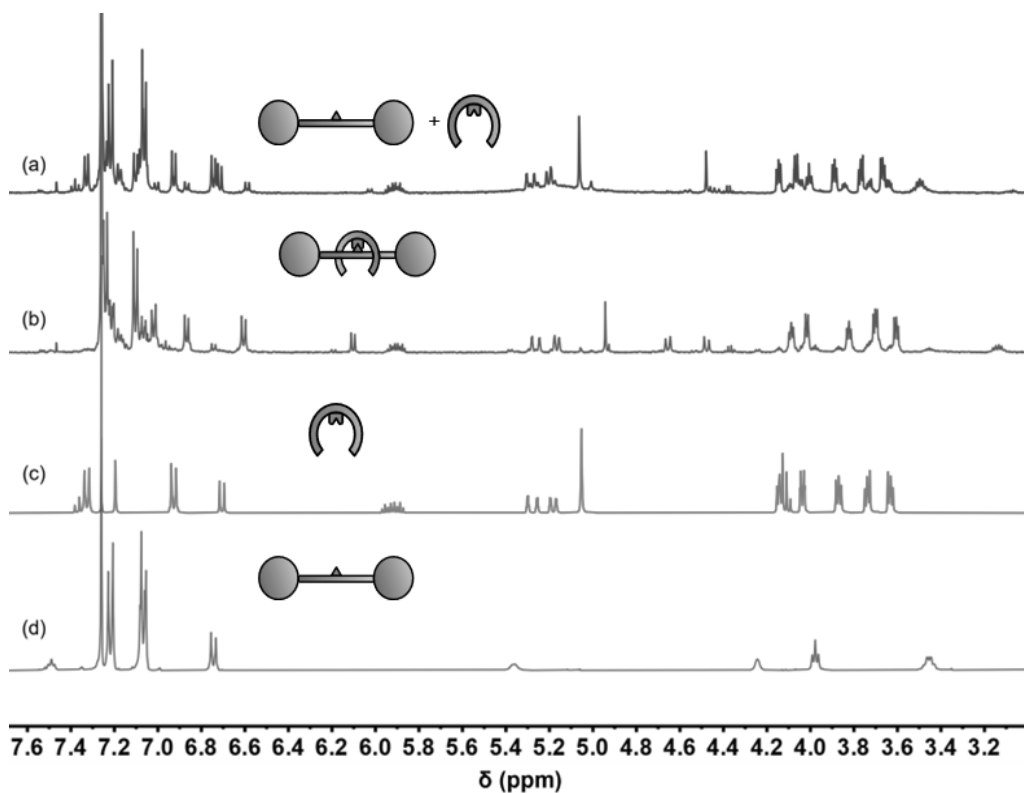


Figure S2. Partial ^1H NMR spectra (500 MHz, CDCl_3 , 298 K) showing (a) immediate hydrolysis of condensation complex **3** after adding 5 eq CF_3COOH (b) condensation complex **3** before hydrolysis (c) boronic acid pincer **1**, (d) diol thread **2**.

5.3. RCM crude mixture analysis

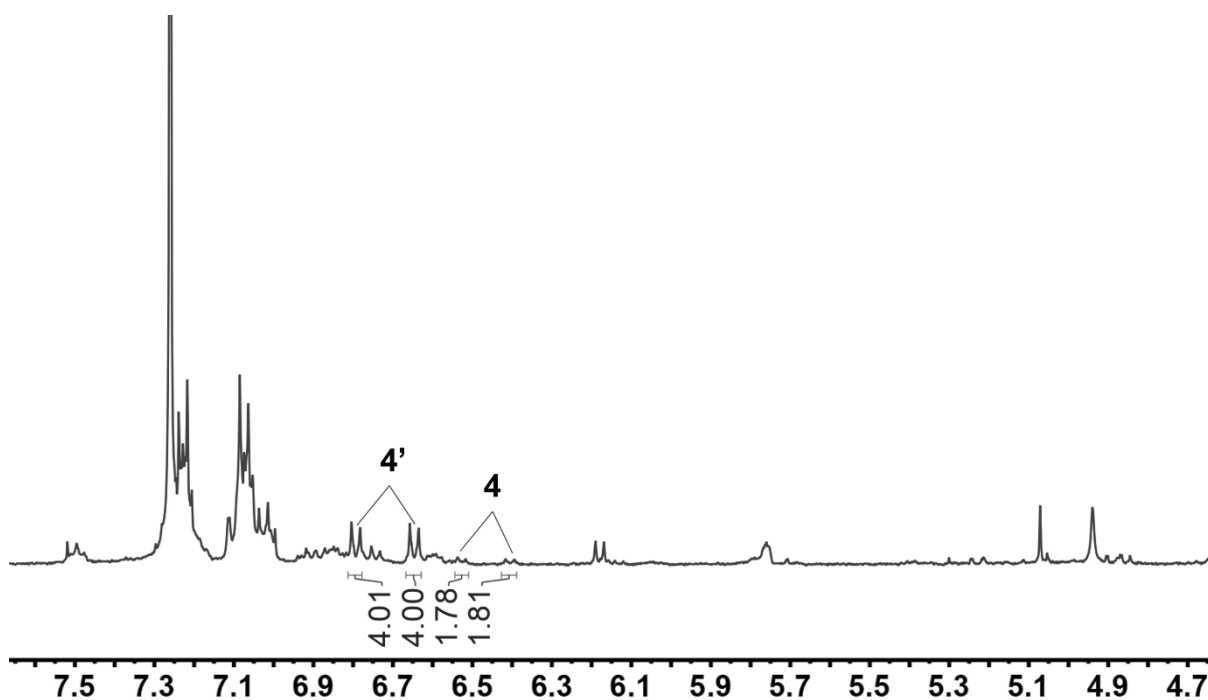


Figure S3. Partial ¹H NMR spectra (500 MHz, CDCl₃, 298 K) of crude reaction mixture after RCM on condensation complex **3**.

5.4. Hydrolysis of quasi[1]rotaxane **4**

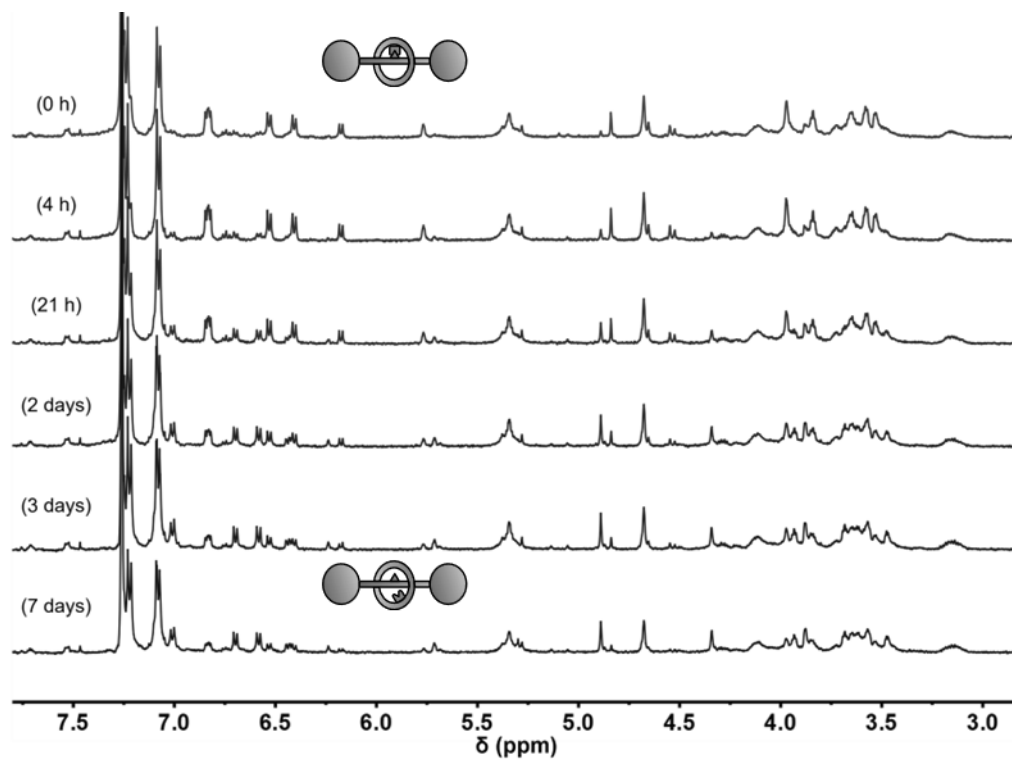


Figure S4. Partial ¹H NMR spectra (500 MHz, CDCl₃, 298 K) of the gradual hydrolysis of quasi[1]rotaxane **4** when incubated in water-saturated CDCl₃ after the time indicated next to each spectrum.

5.5. Hydrolysis of non-interlocked isomer 4'

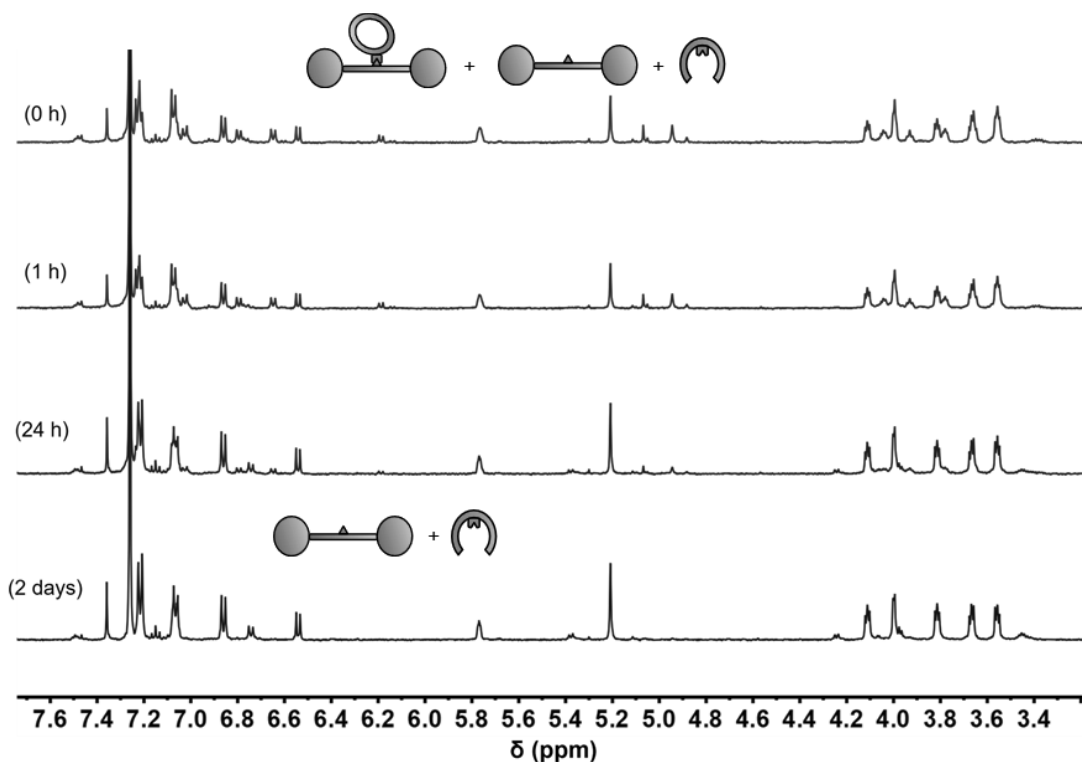


Figure S5. Partial ^1H NMR spectra (500 MHz, CDCl_3 , 298 K) of hydrolysis of the non-interlocked isomer **4'** (isolated as a mixture together with hydrolysis products **1** and **2**) after incubation in water-saturated CDCl_3 for the time indicated next to each spectrum.

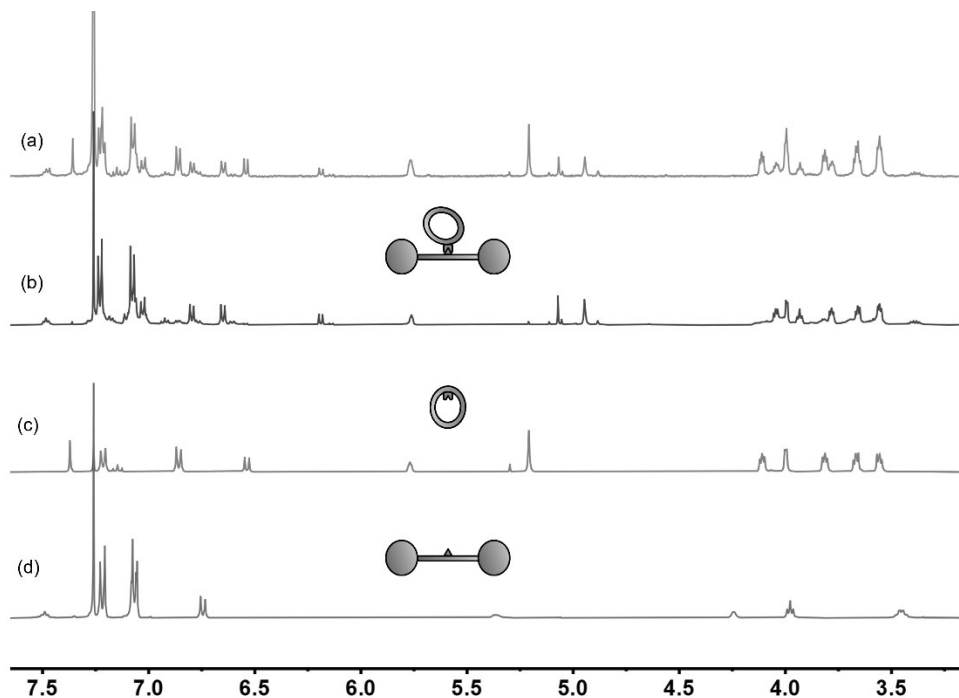


Figure S6. Partial ^1H NMR spectra (500 MHz, CDCl_3 , 298 K) of (a) the non-interlocked isomer **4'** (isolated as a mixture together with hydrolysis products **1** and **2**), (b) the non-interlocked isomer **4'** formed by condensation of **6** and **2** in anhydrous toluene for 24h, (c) boronic acid macrocycle **6**, and (d) thread **2**.

5.6. Macrocycle cleavage from compound 4

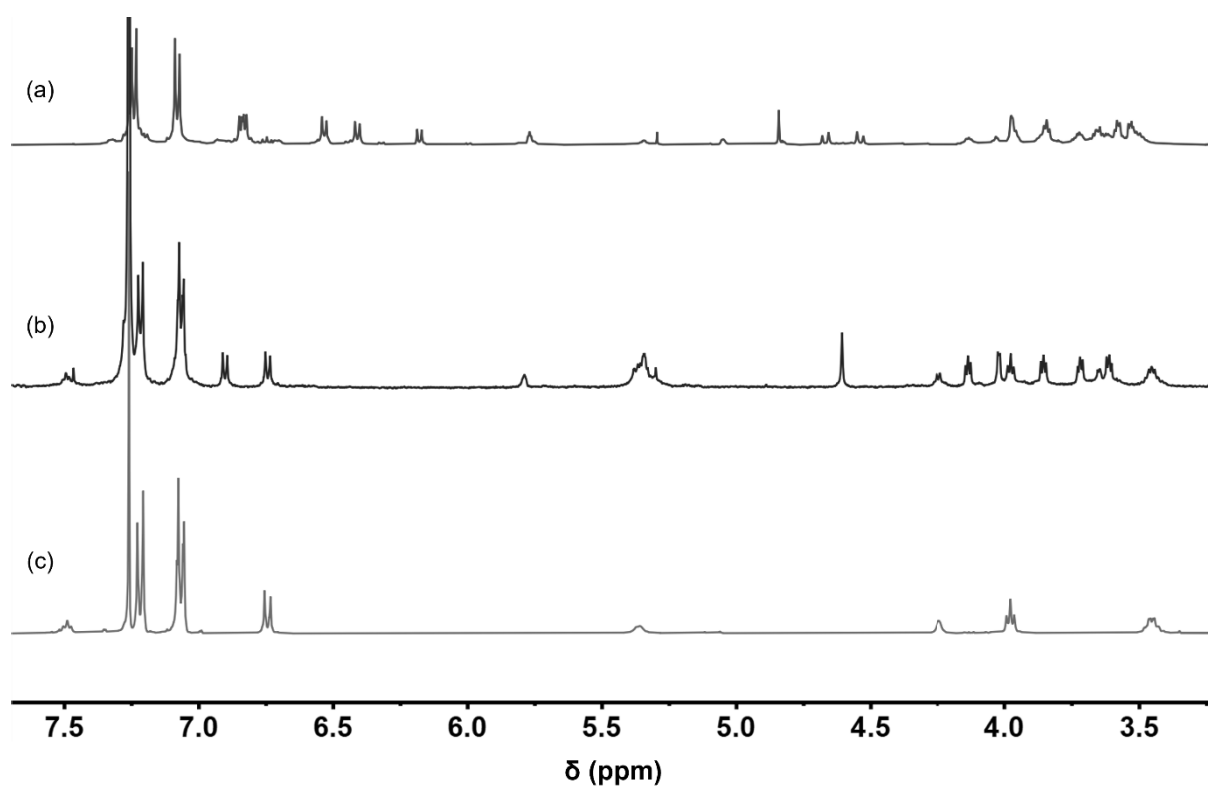


Figure S7. Partial ¹H NMR spectra (500 MHz, CDCl₃, 298 K) of (a) quasi[1]rotaxane **4**, (b) crude mixture obtained after treatment of **4** with NaOH and H₂O₂, (c) diol thread **2**.

5.7. TW-IMS measurements

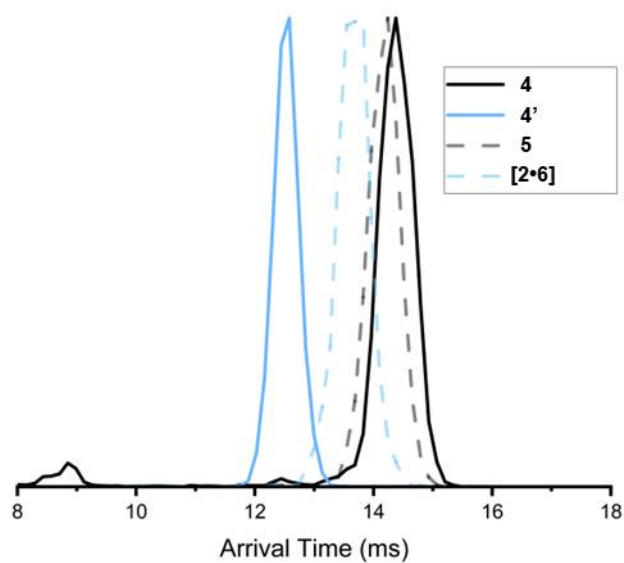


Figure S8. TW-IMS spectra showing arrival times of the four main species **4**, **4'**, **5** and **[2•6]**. See general experimental section for measurement details.

Table S2. Summary of TW-IMS arrival times.

Compound	Arrival time (ms)
4	14.4
4'	14.3
5	12.5
[2•6]	13.7

5.8. CID measurements

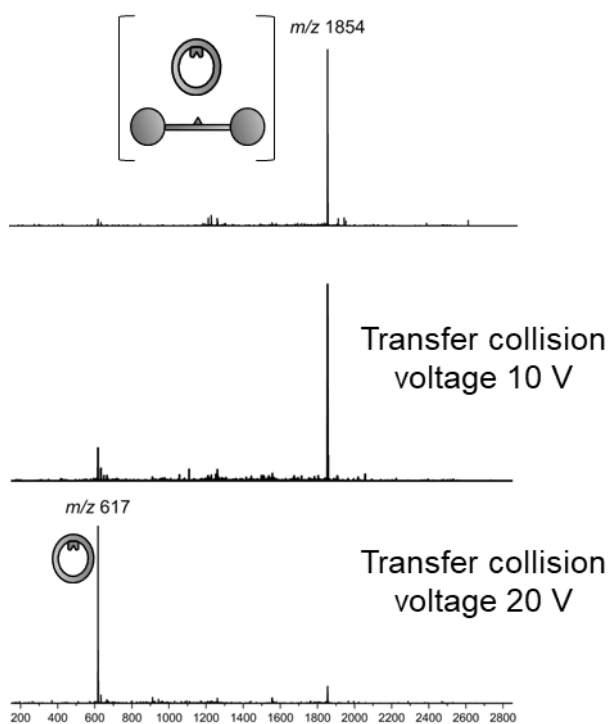


Figure S9. MS/MS (+ESI) spectra of [2•6], with mass selection m/z 1854 (top) and after application of transfer collision voltages of 10 V (middle) and 20 V (bottom) to fragment the parent ion.

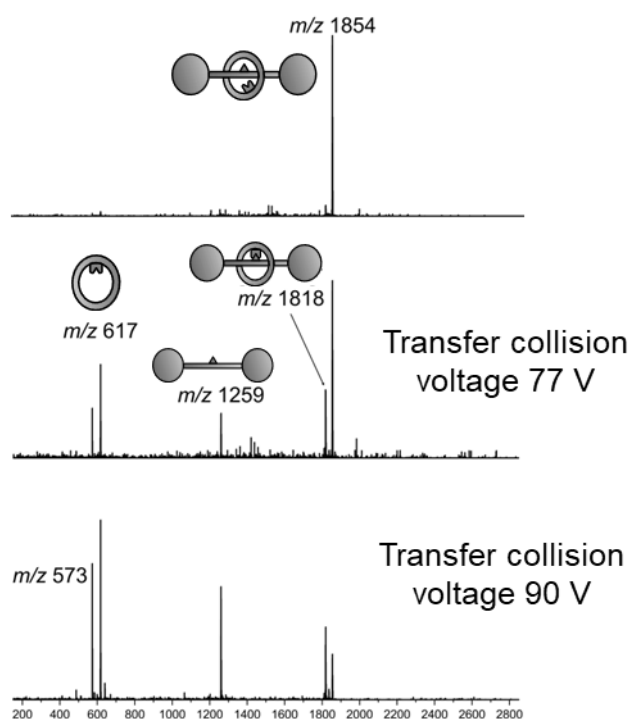


Figure S10. MS/MS (+ESI) spectra of [5], with mass selection m/z 1854 (top) and after application of transfer collision voltages of 77 V (middle) and 90 V (bottom) to fragment the parent ion.

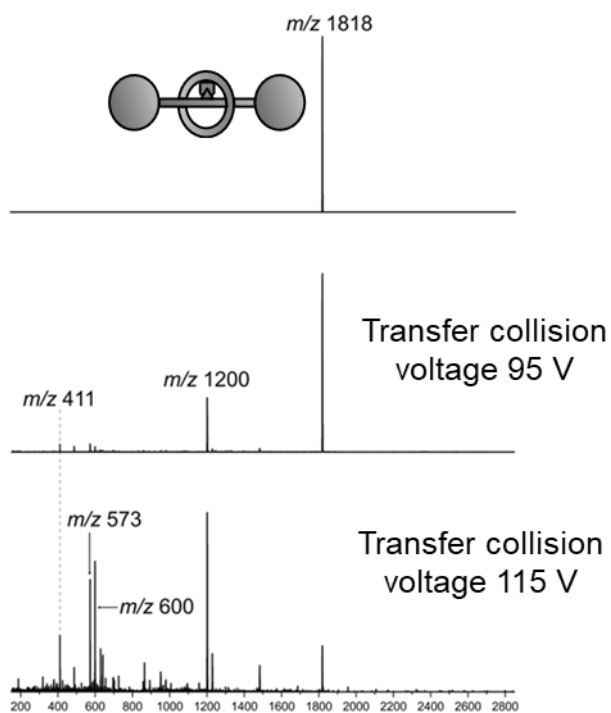


Figure S11. MS/MS (+ESI) spectra of [4], with mass selection m/z 1854 (top) and after application of transfer collision voltages of 95 V (middle) and 115 V (bottom) to fragment the parent ion.

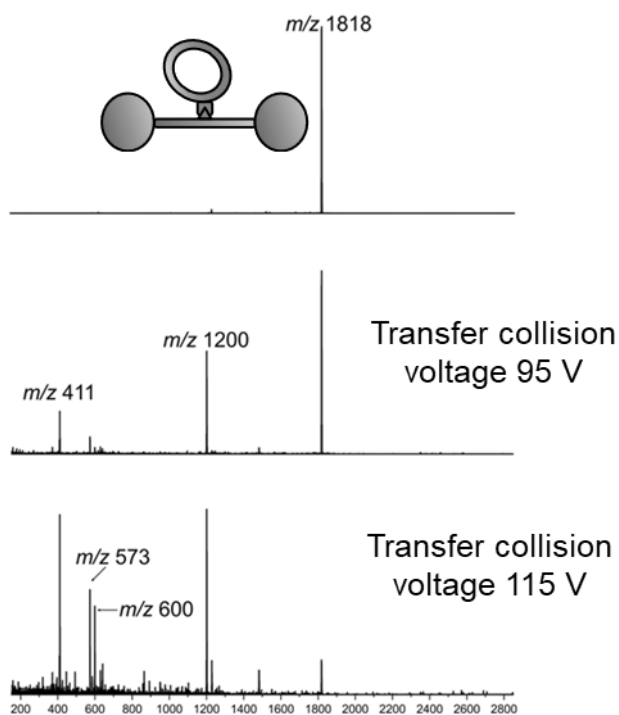
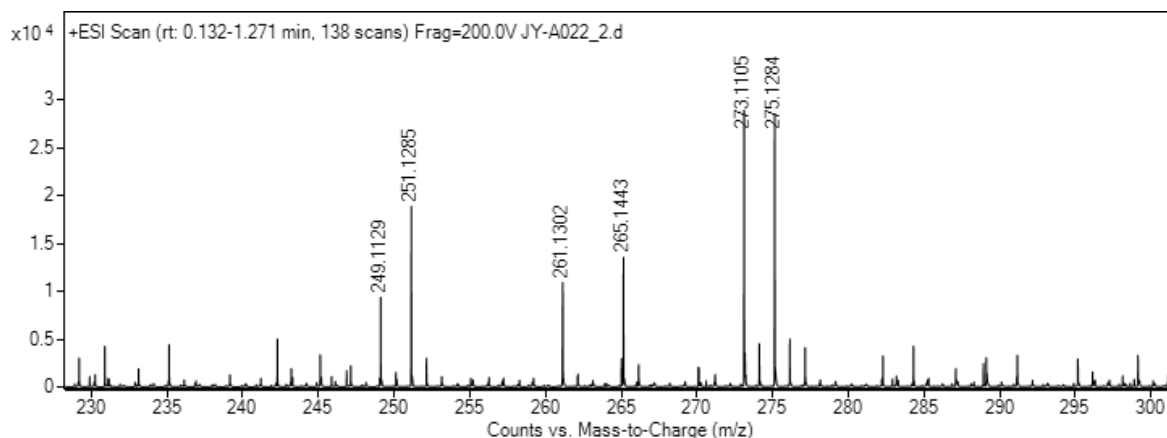
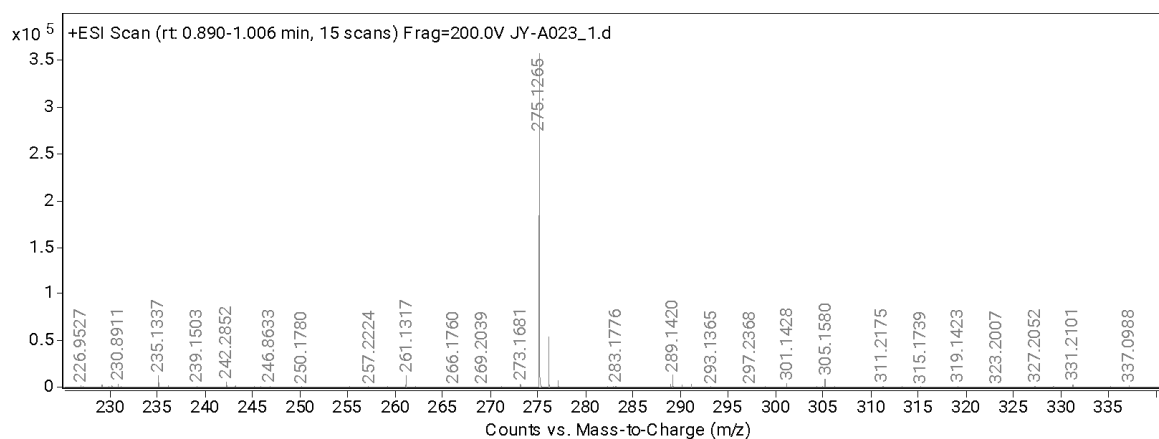


Figure S15. MS/MS (+ESI) spectra of [4'], with mass selection m/z 1854 (top) and after application of transfer collision voltages of 95 V (middle) and 115 V (bottom) to fragment the parent ion.

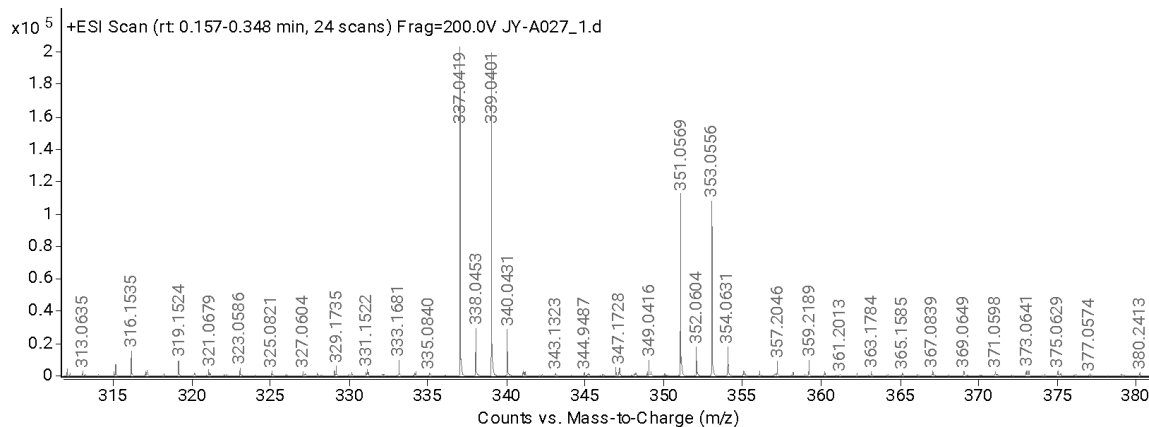
S6. MASS SPECTRA



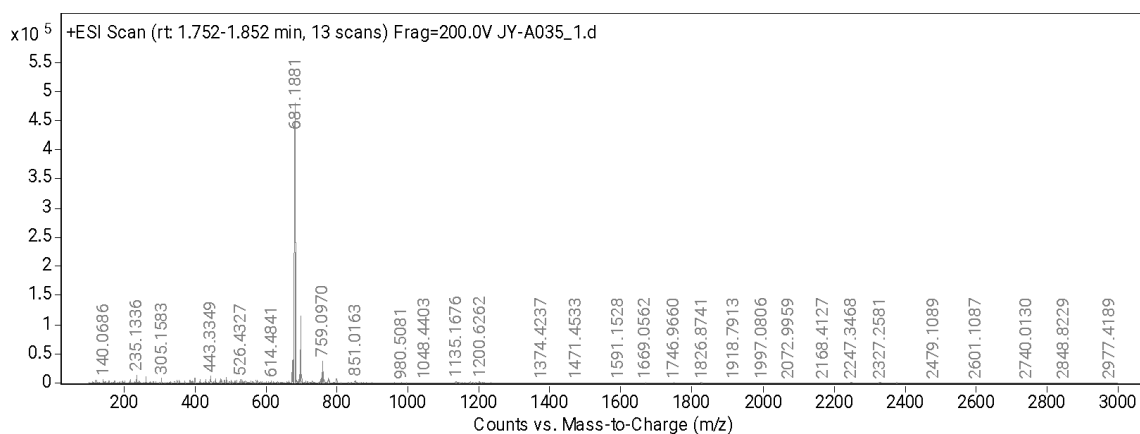
Spectrum S1. High-resolution ESI-MS (positive mode) of **S2**.



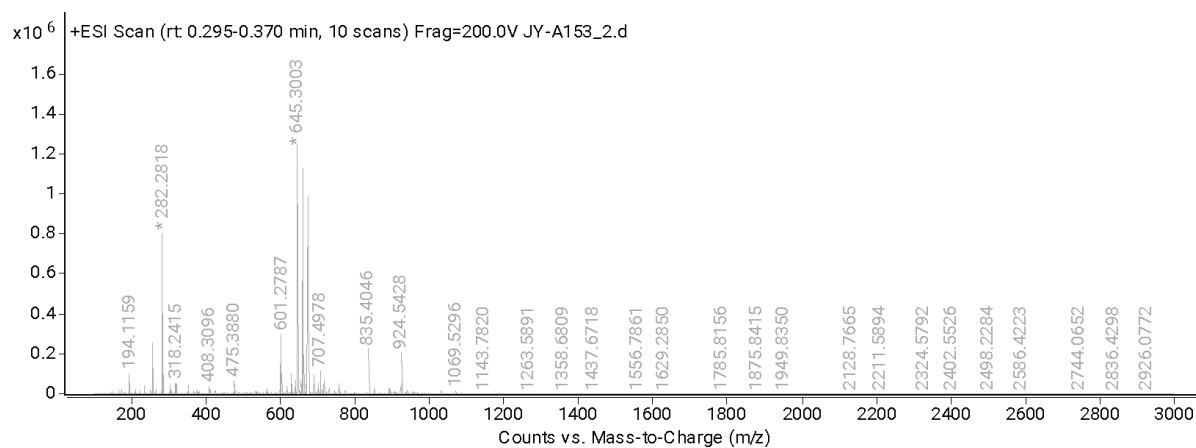
Spectrum S2. High-resolution ESI-MS (positive mode) of **S3**.



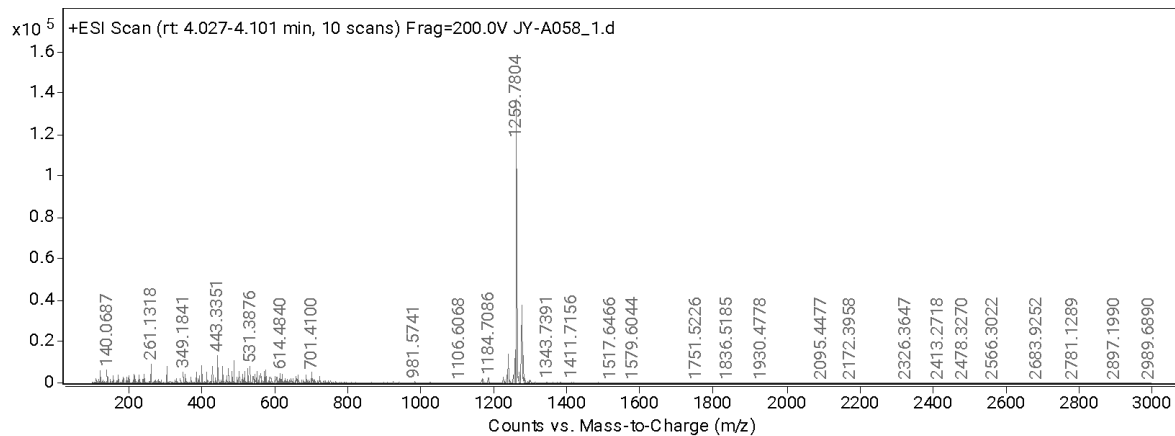
Spectrum S3. High-resolution ESI-MS (positive mode) of **S4**.



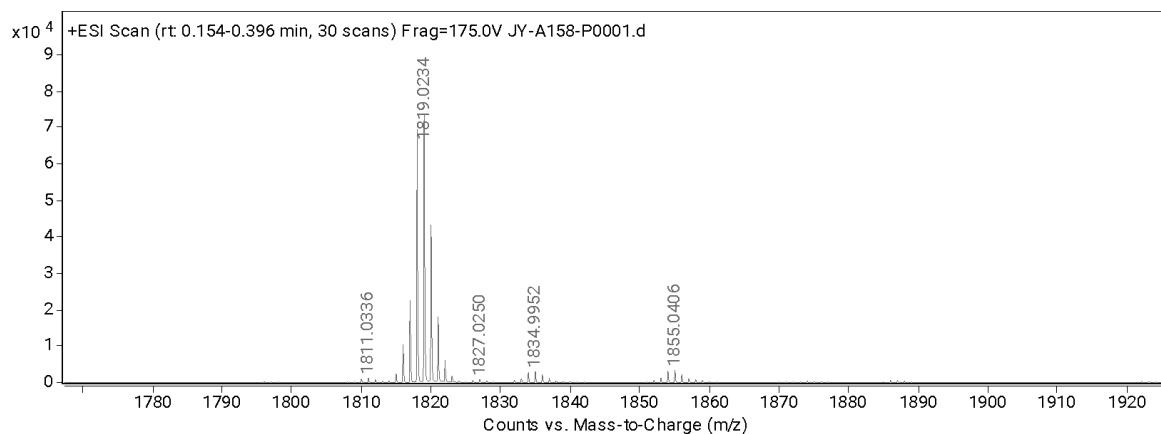
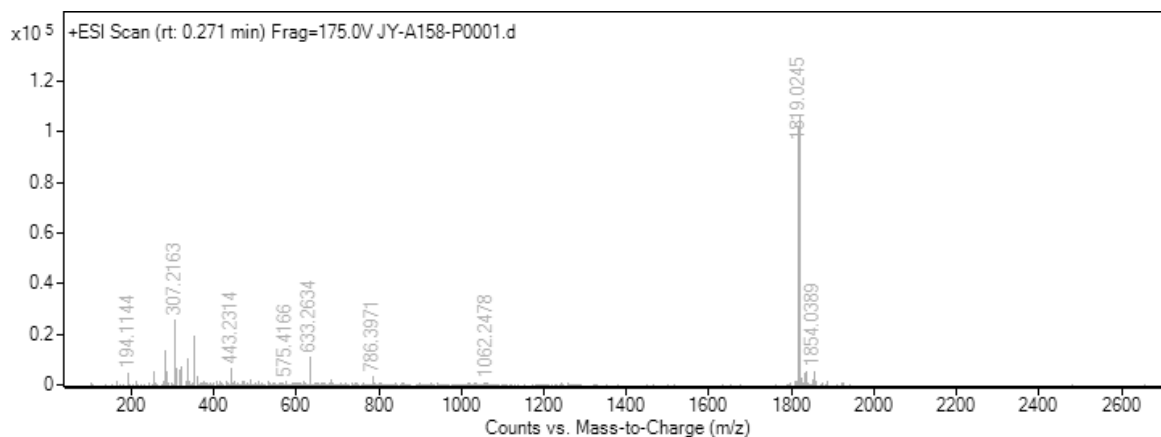
Spectrum S4. High-resolution ESI-MS (positive mode) of **S5**.



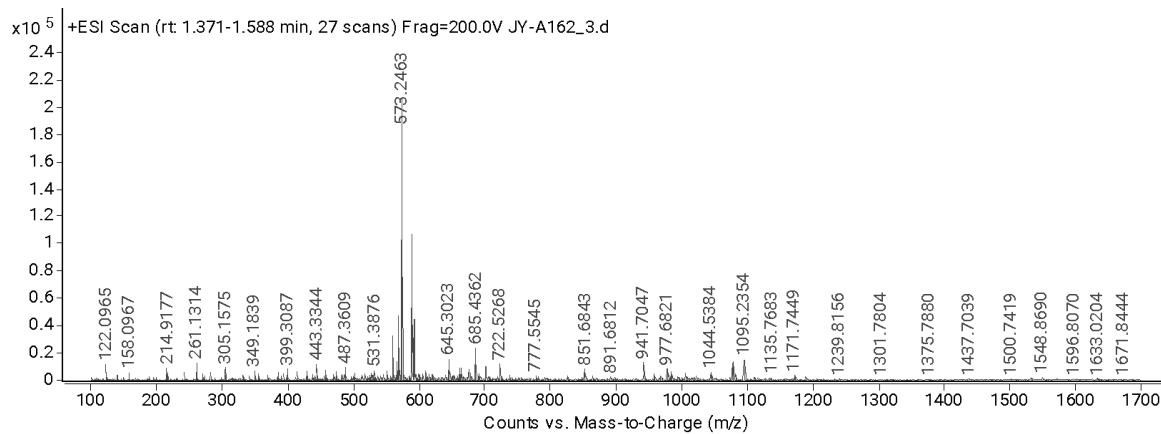
Spectrum S5. High-resolution ESI-MS (positive mode) of **1**.



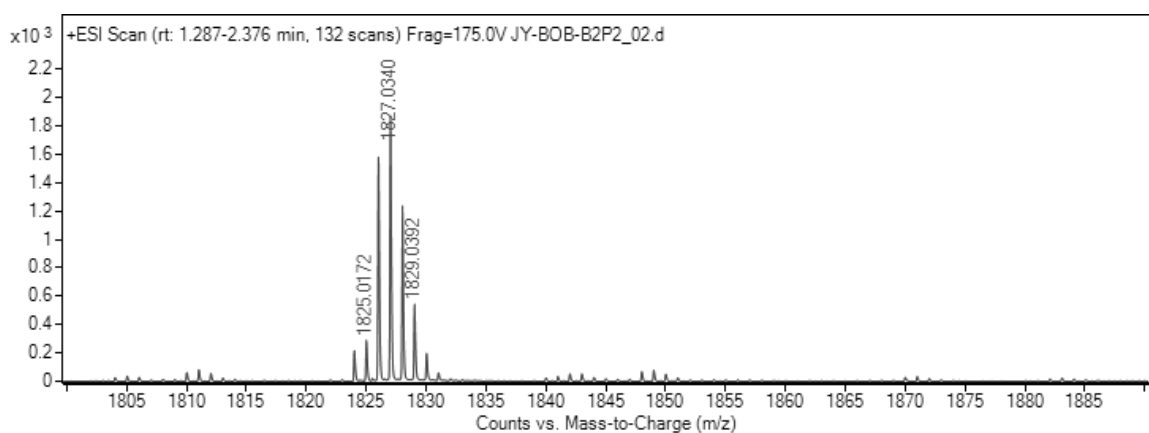
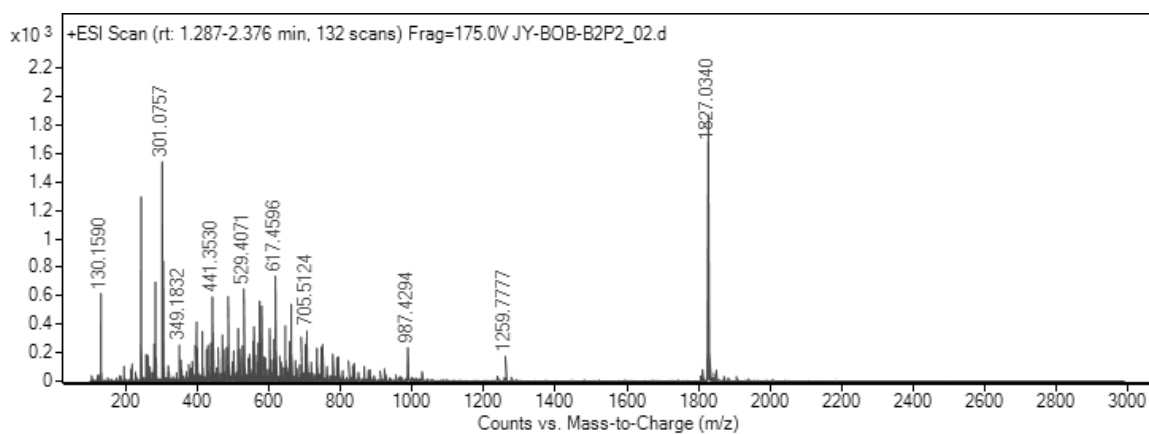
Spectrum S6. High-resolution ESI-MS (positive mode) of **2**.



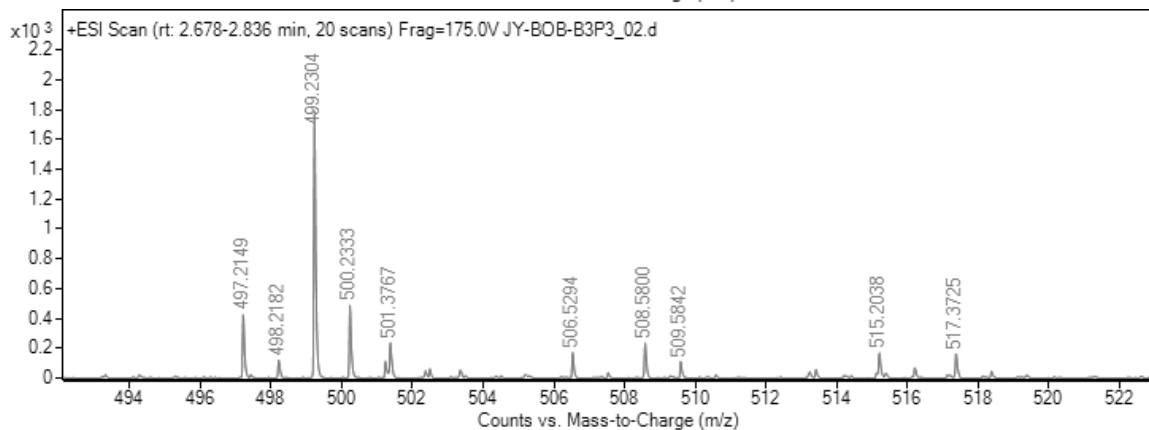
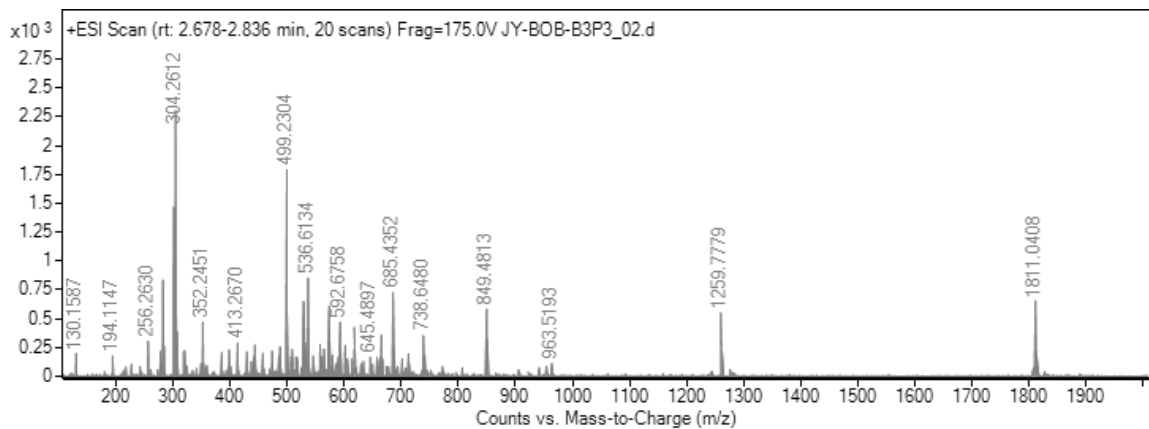
Spectrum S7. High-resolution ESI-MS (positive mode) of **4** (top: full spectrum; bottom: zoom).



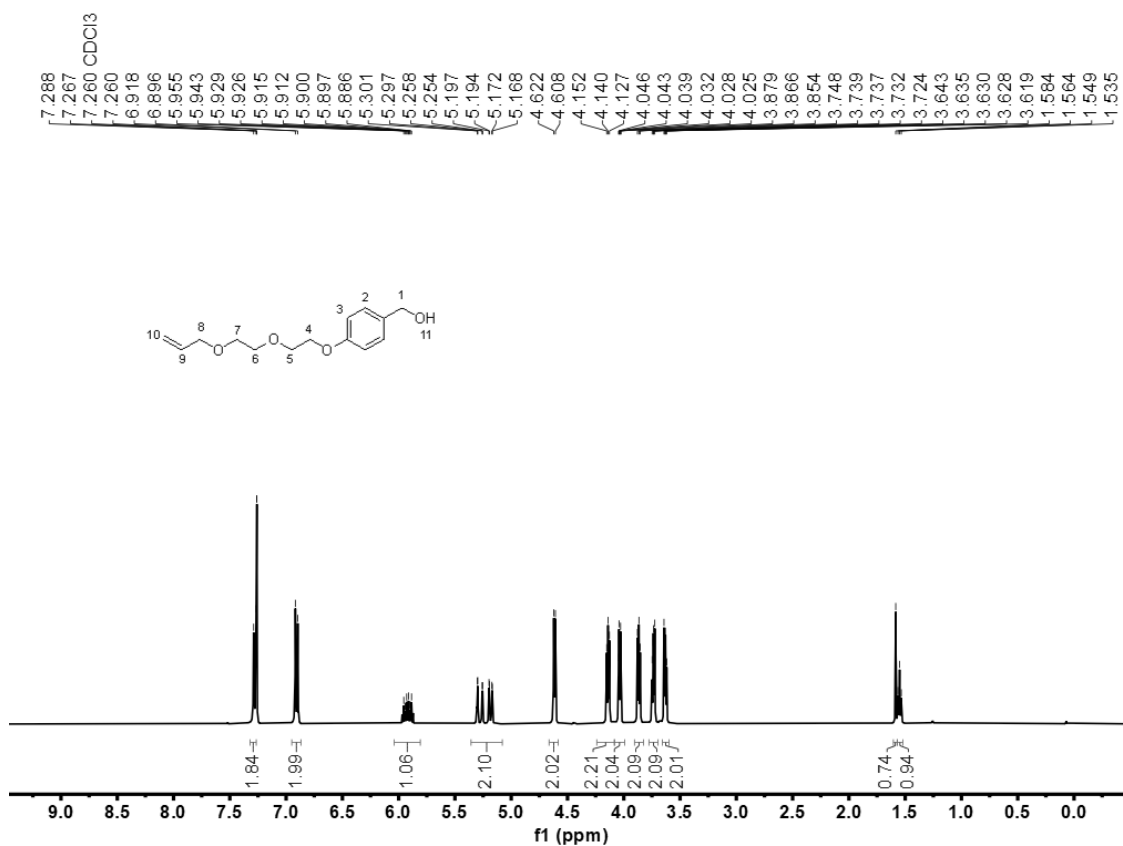
Spectrum S8. High-resolution ESI-MS (positive mode) of **6**.



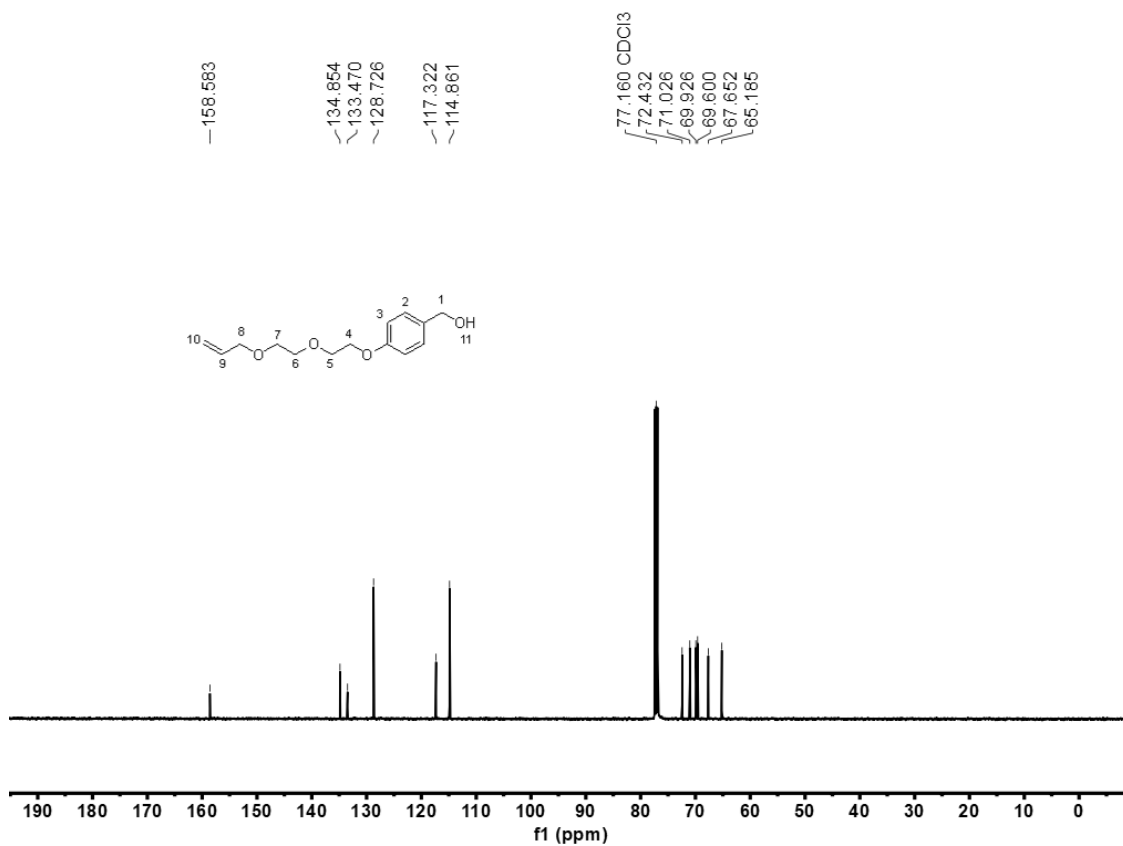
Spectrum S9. High-resolution ESI-MS (positive mode) of **7** (top: full spectrum; bottom: zoom).



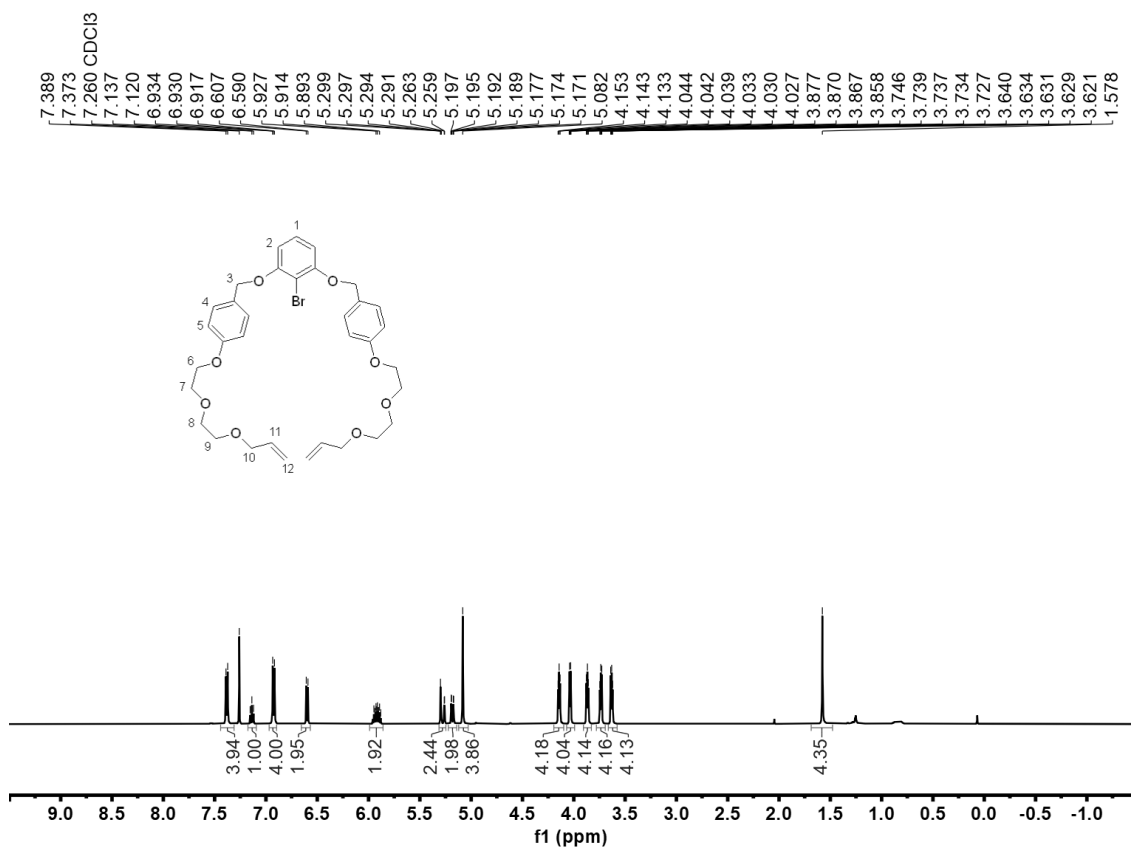
Spectrum S10. High-resolution ESI-MS (positive mode) of ring residue **S11** (top: full spectrum; bottom: zoom).



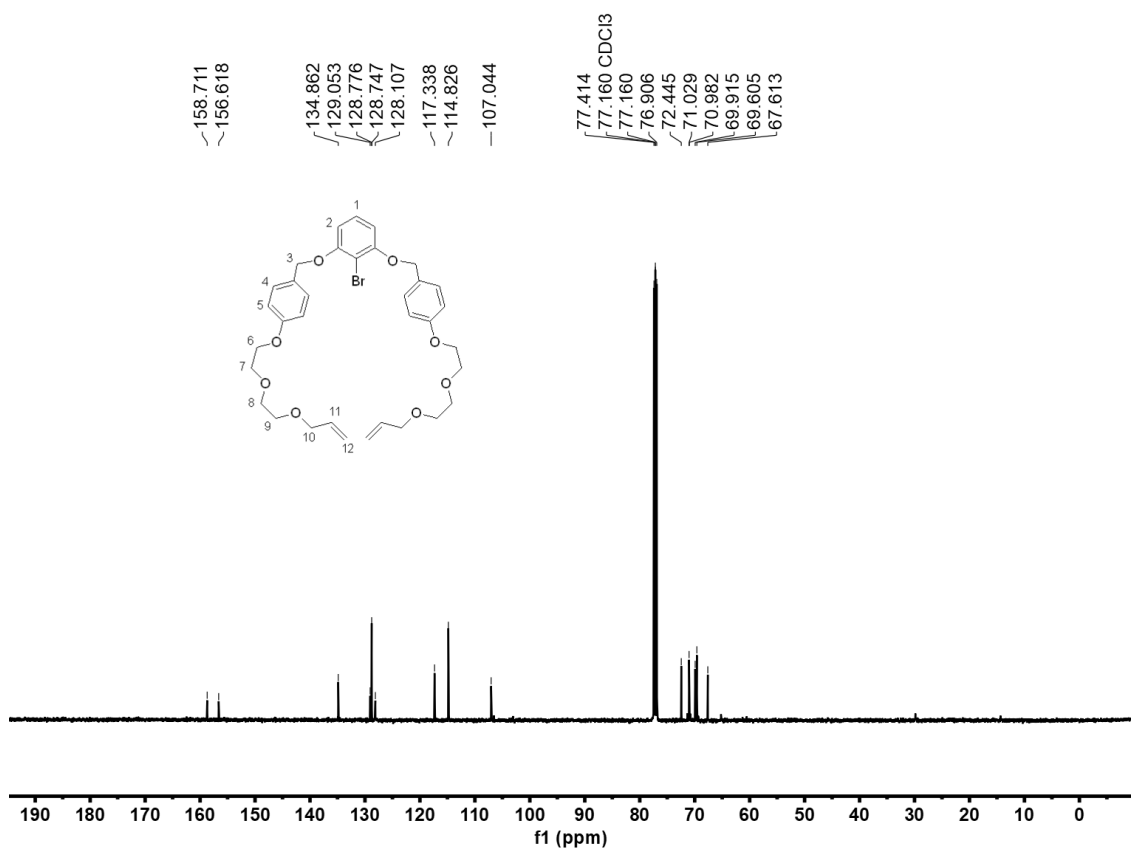
Spectrum S13. ¹H NMR spectrum (500 MHz, CDCl₃, 298 K) of S3.



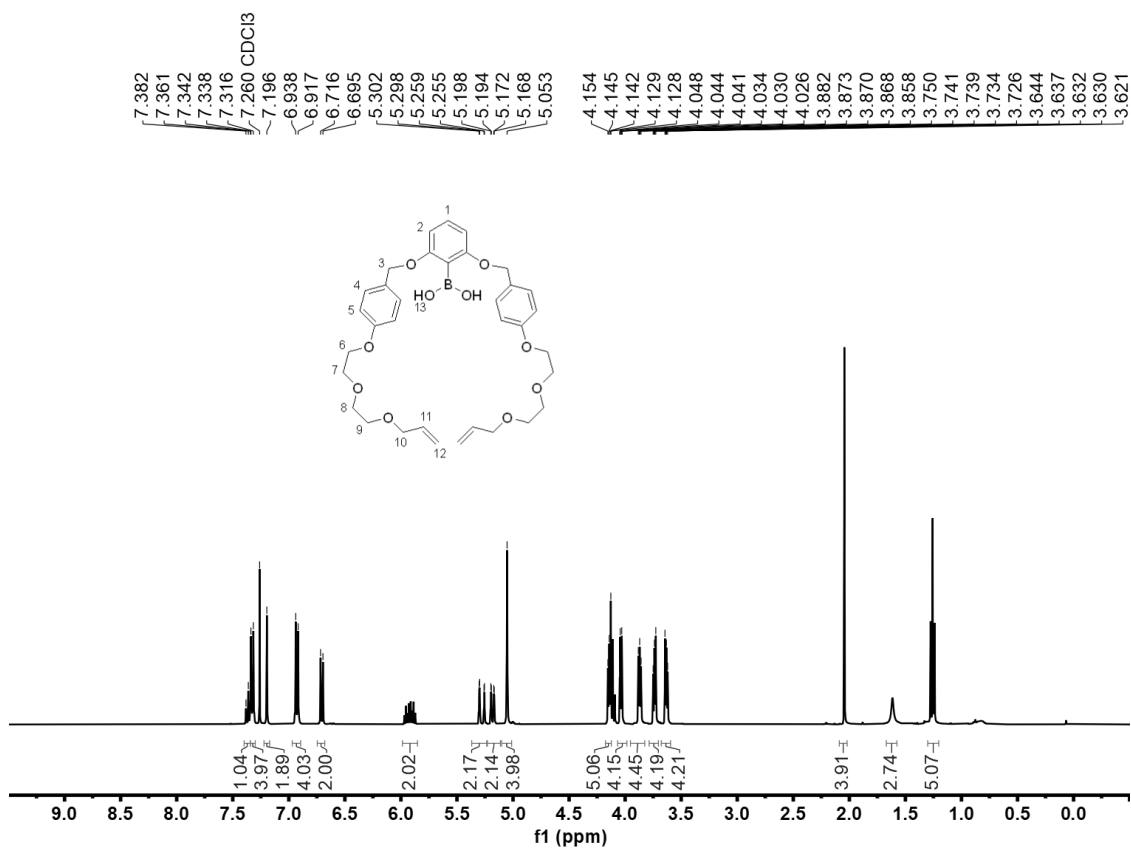
Spectrum S14. ¹³C NMR spectrum (126 MHz, CDCl₃, 298 K) of S3.



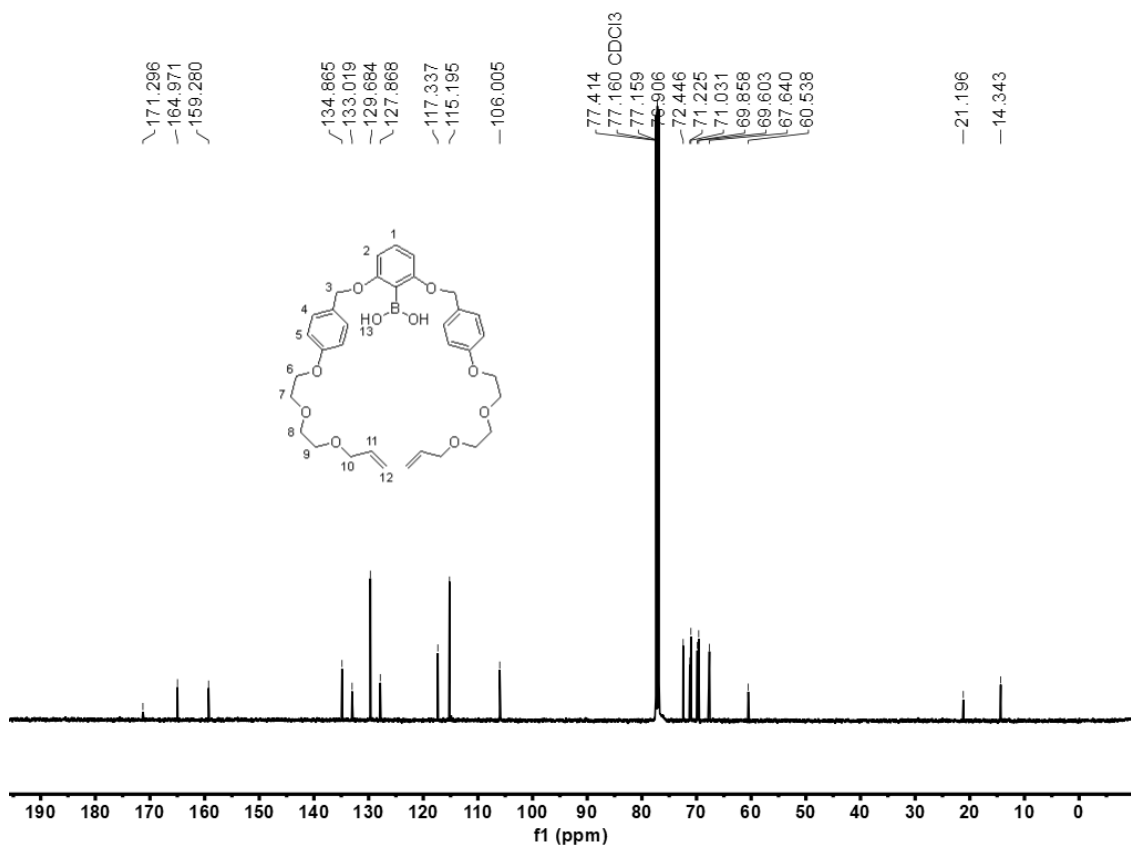
Spectrum S17. ¹H NMR spectrum (500 MHz, CDCl₃, 298 K) of S5.



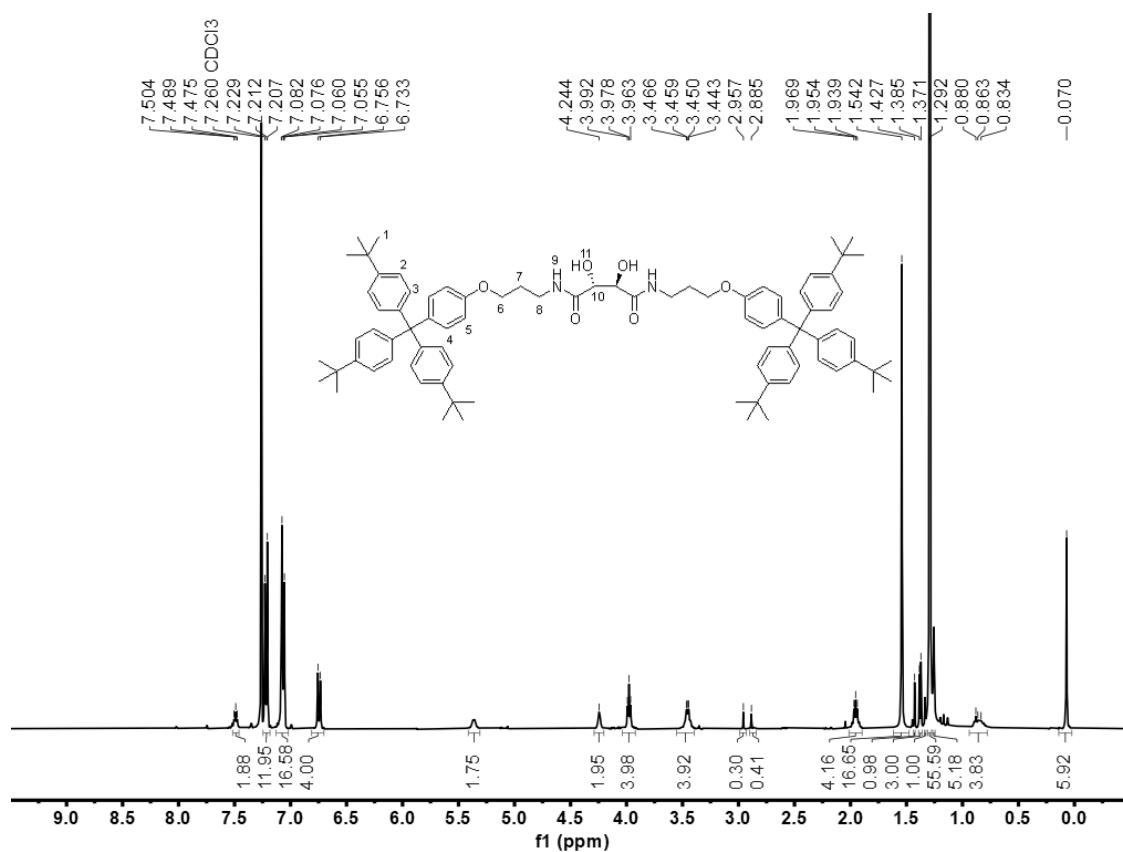
Spectrum S18. ¹³C NMR spectrum (126 MHz, CDCl₃, 298 K) of S5.



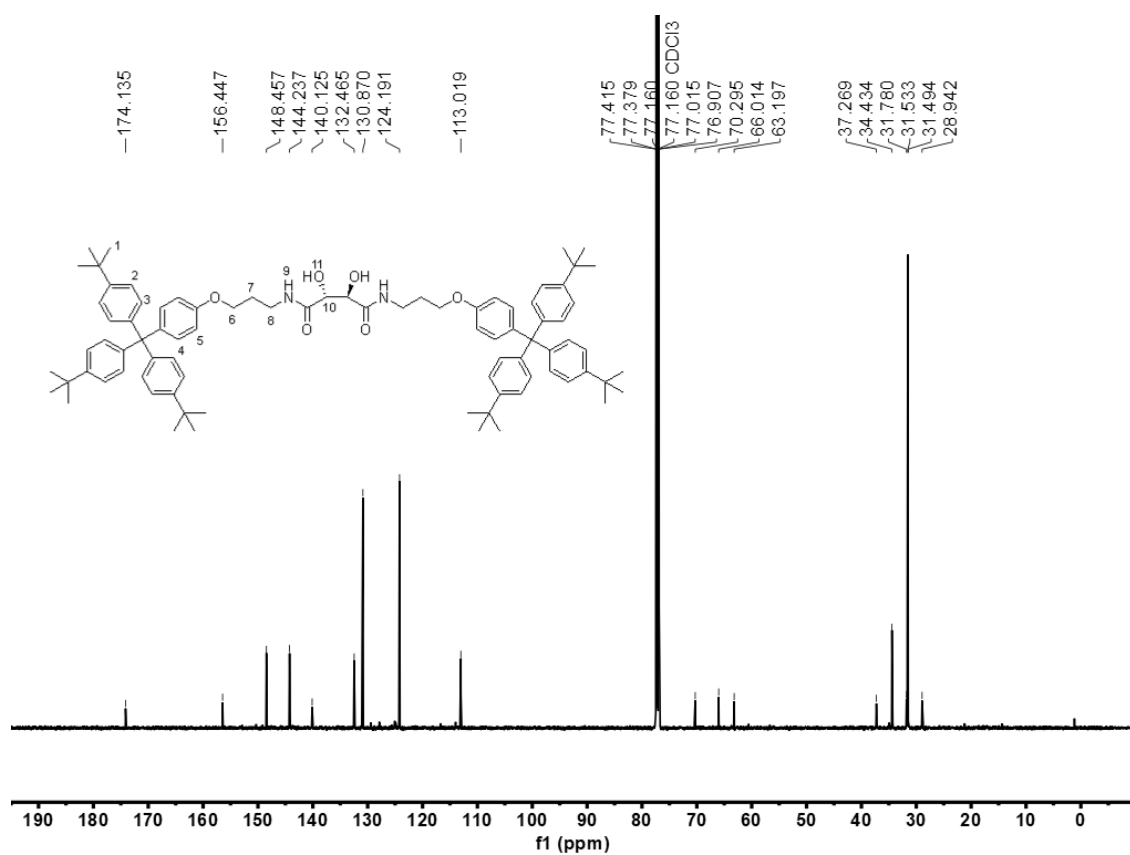
Spectrum S19. ¹H NMR spectrum (500 MHz, CDCl₃, 298 K) of 1.



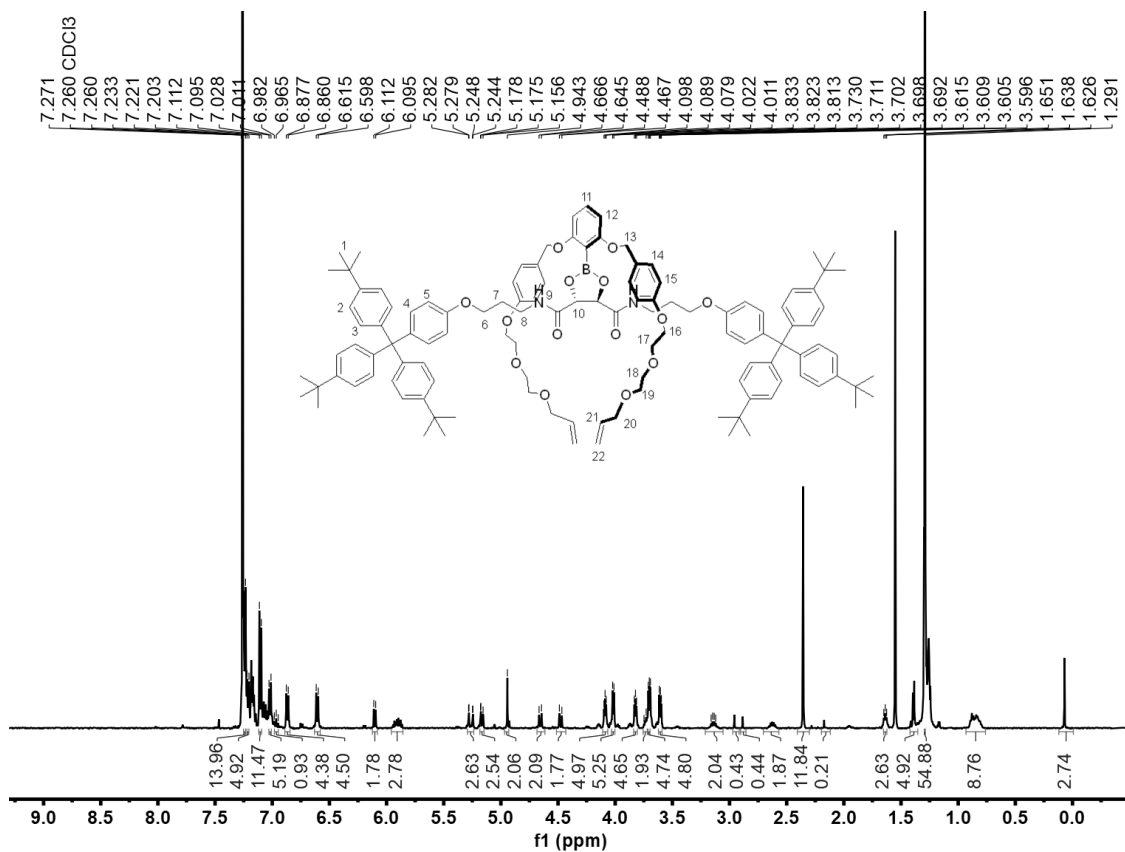
Spectrum S20. ¹³C NMR spectrum (126 MHz, CDCl₃, 298 K) of 1.



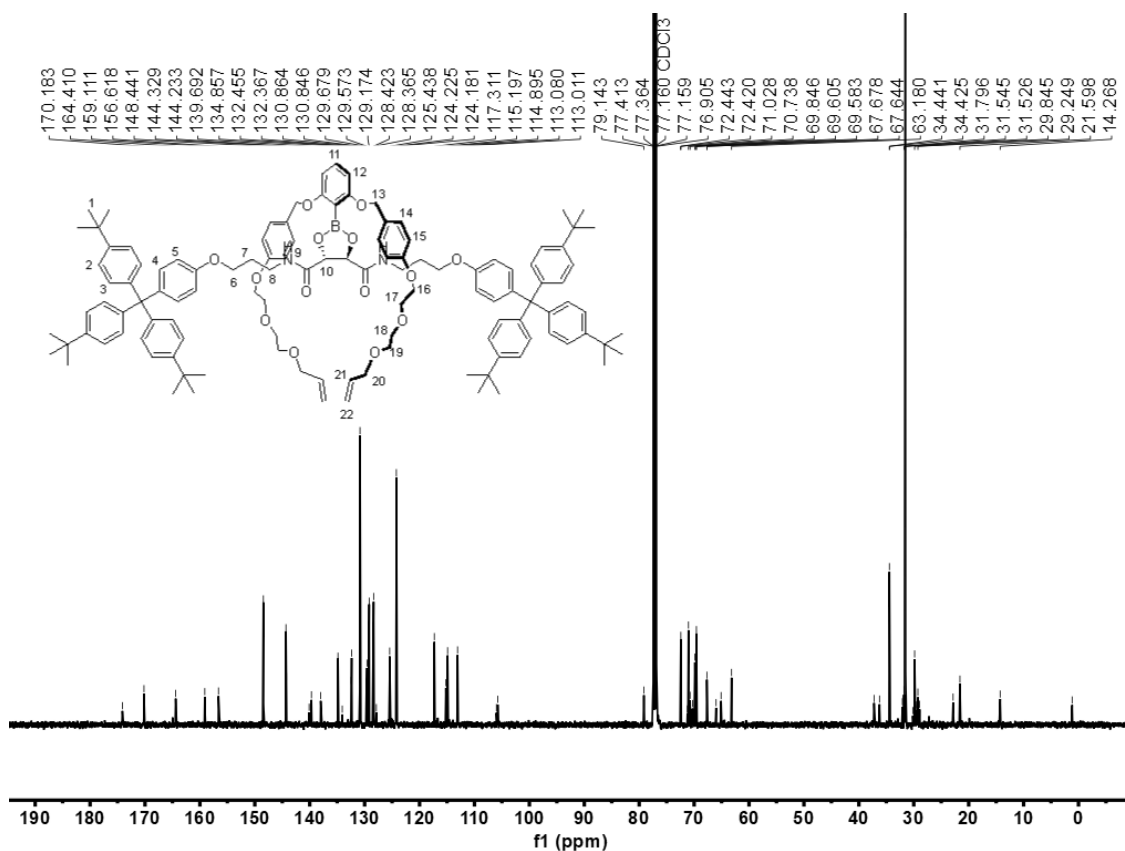
Spectrum S22. ¹H NMR spectrum (500 MHz, CDCl₃, 298 K) of **2**.



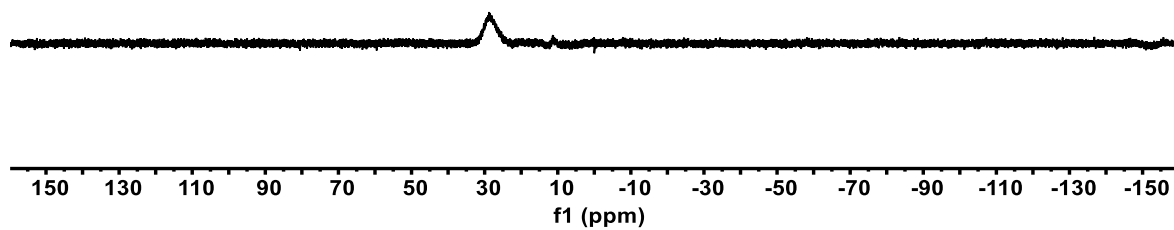
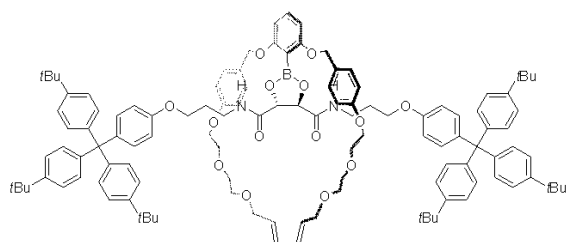
Spectrum S23. ¹³C NMR spectrum (126 MHz, CDCl₃, 298 K) of **2**.



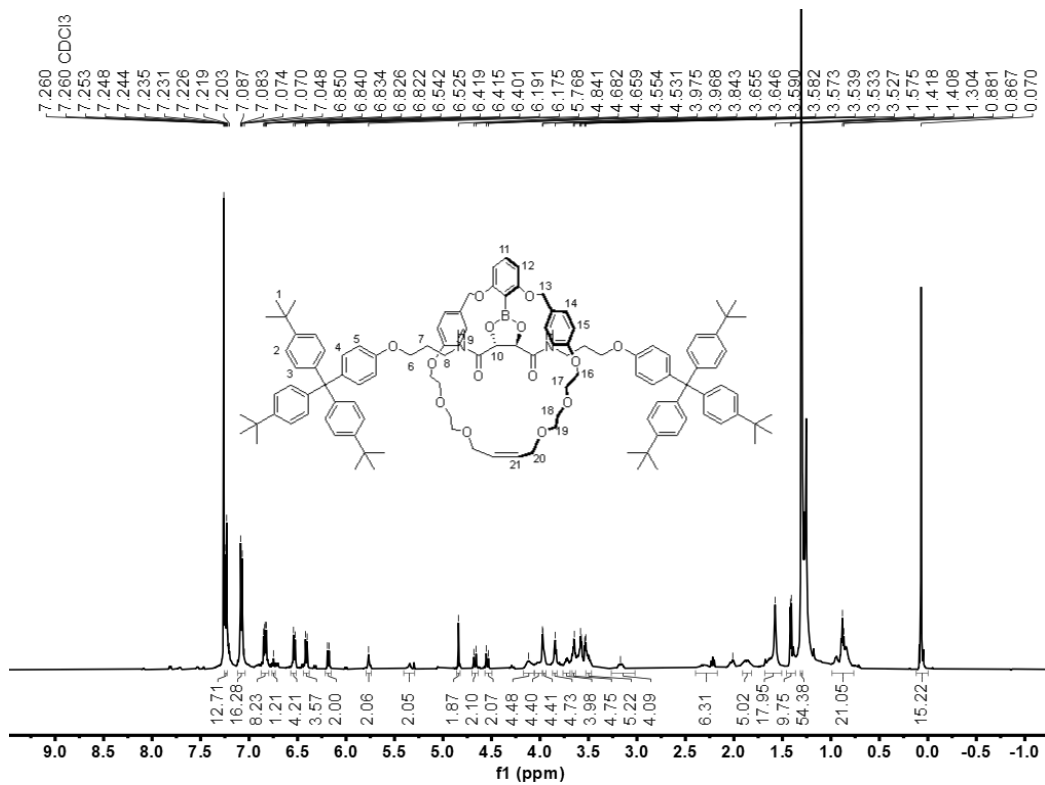
Spectrum S24. ¹H NMR spectrum (500 MHz, CDCl₃, 298 K) of 3.



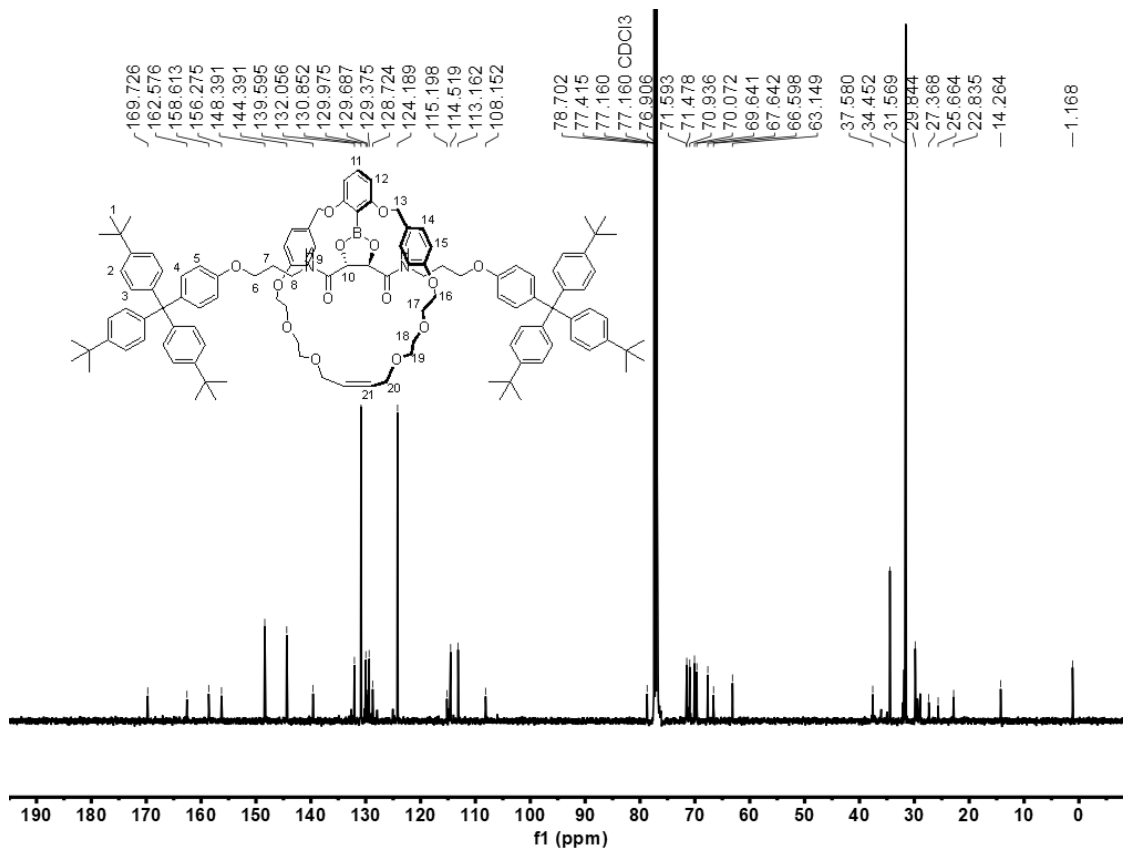
Spectrum S25. ¹³C NMR spectrum (126 MHz, CDCl₃, 298 K) of 3.



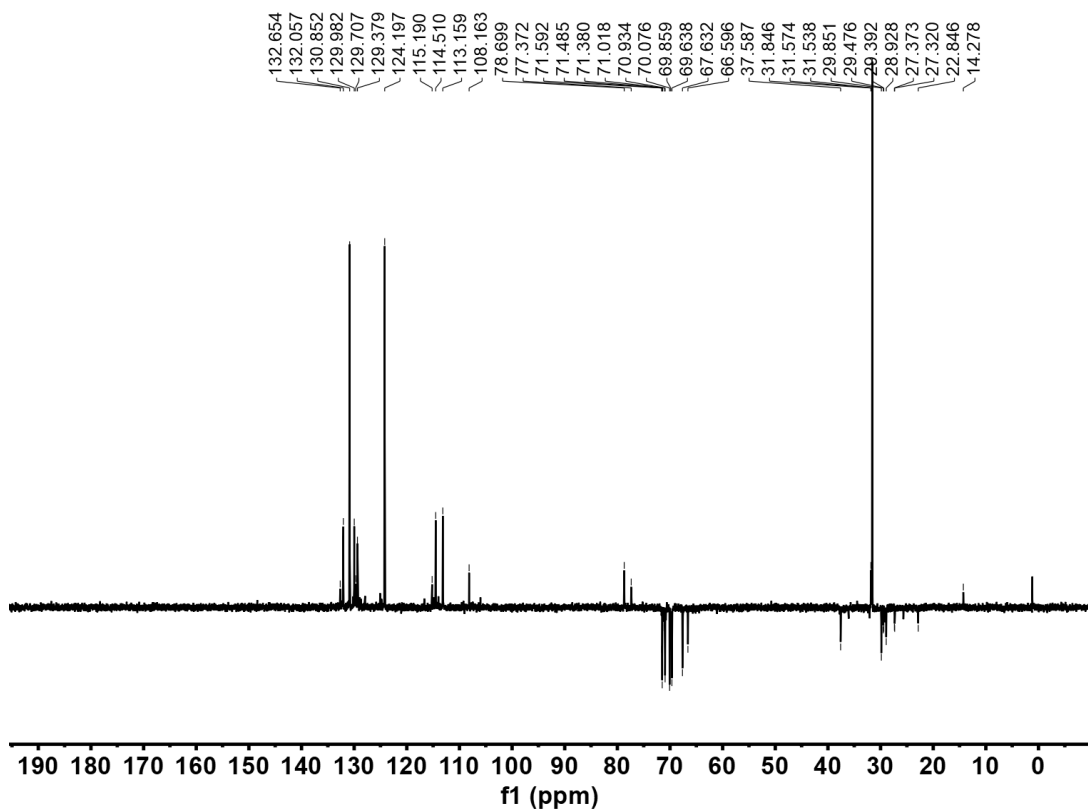
Spectrum S26. ^{11}B NMR spectrum (160 MHz, CDCl_3 , 298 K) of **3**.



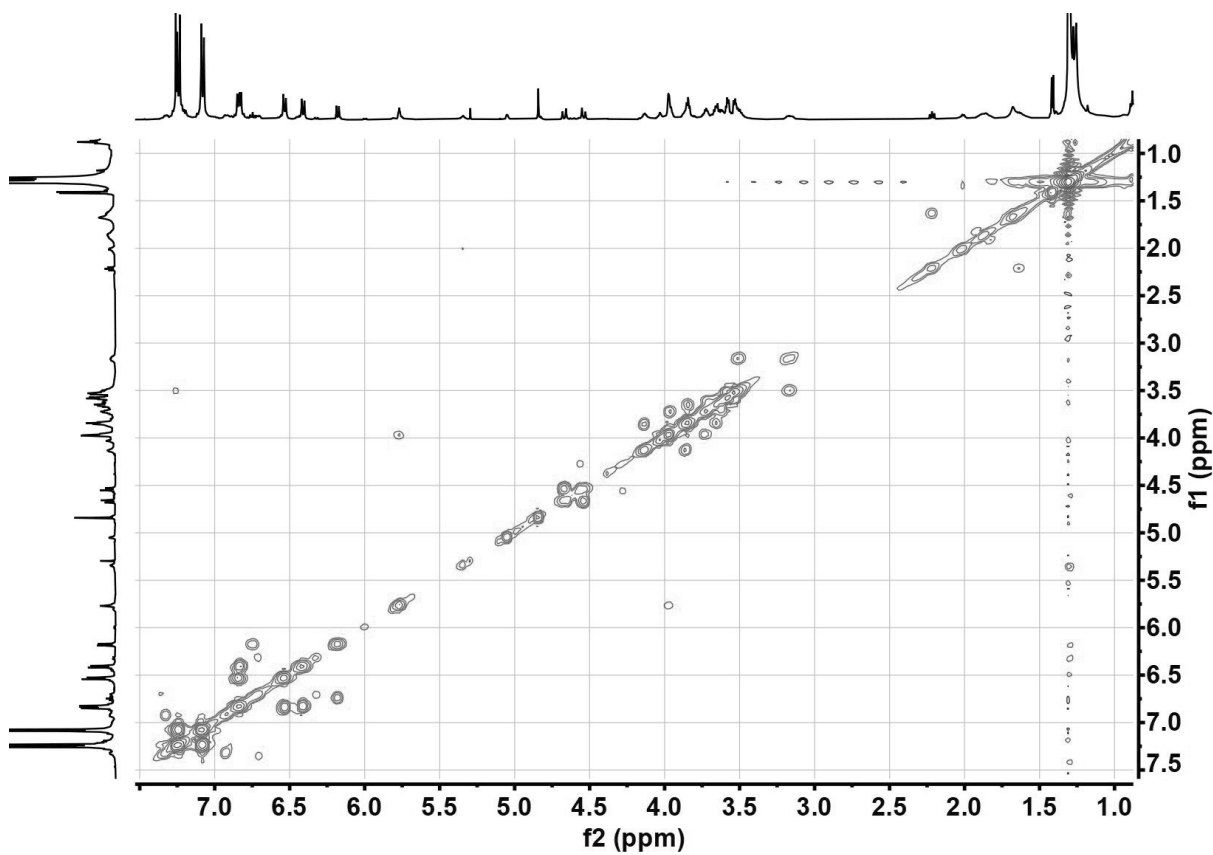
Spectrum S27. ¹H NMR spectrum (500 MHz, CDCl₃, 298 K) of **4**.



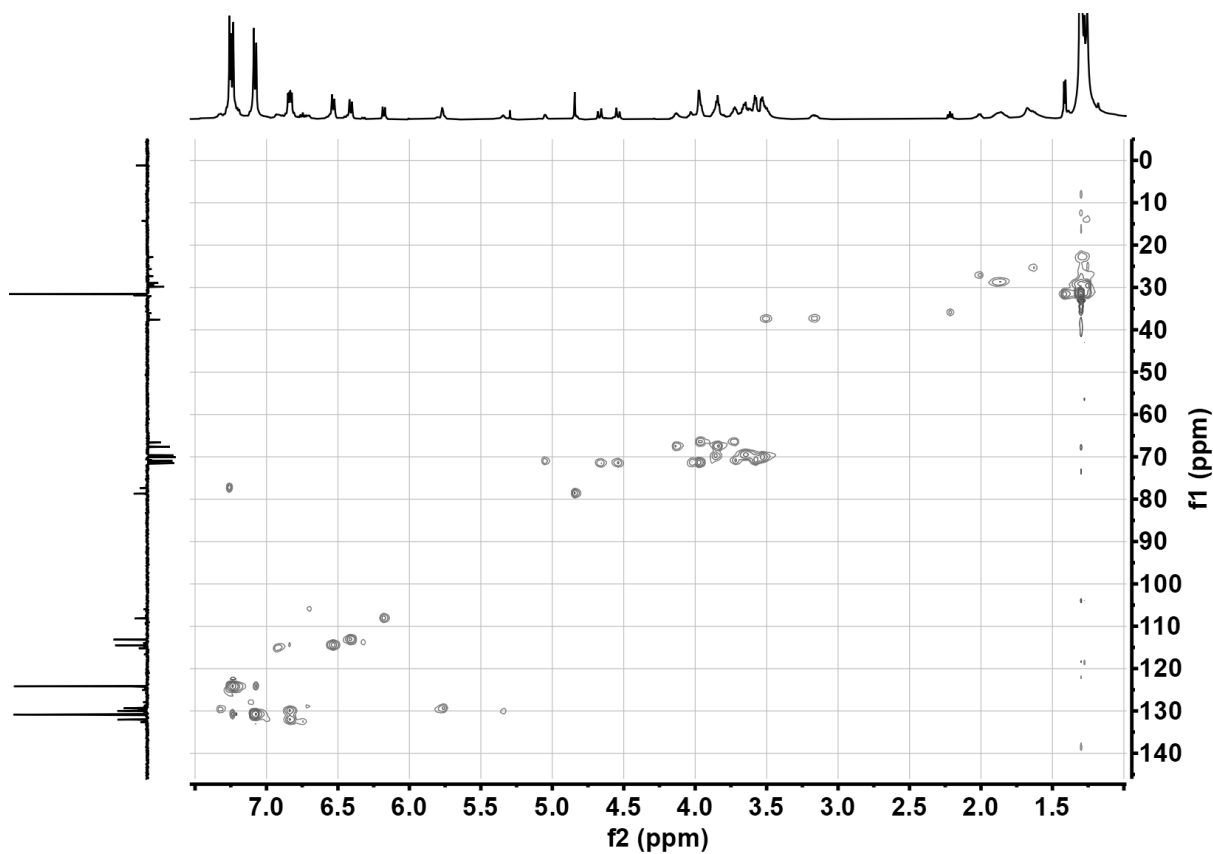
Spectrum S28. ¹³C NMR spectrum (126 MHz, CDCl₃, 298 K) of **4**.



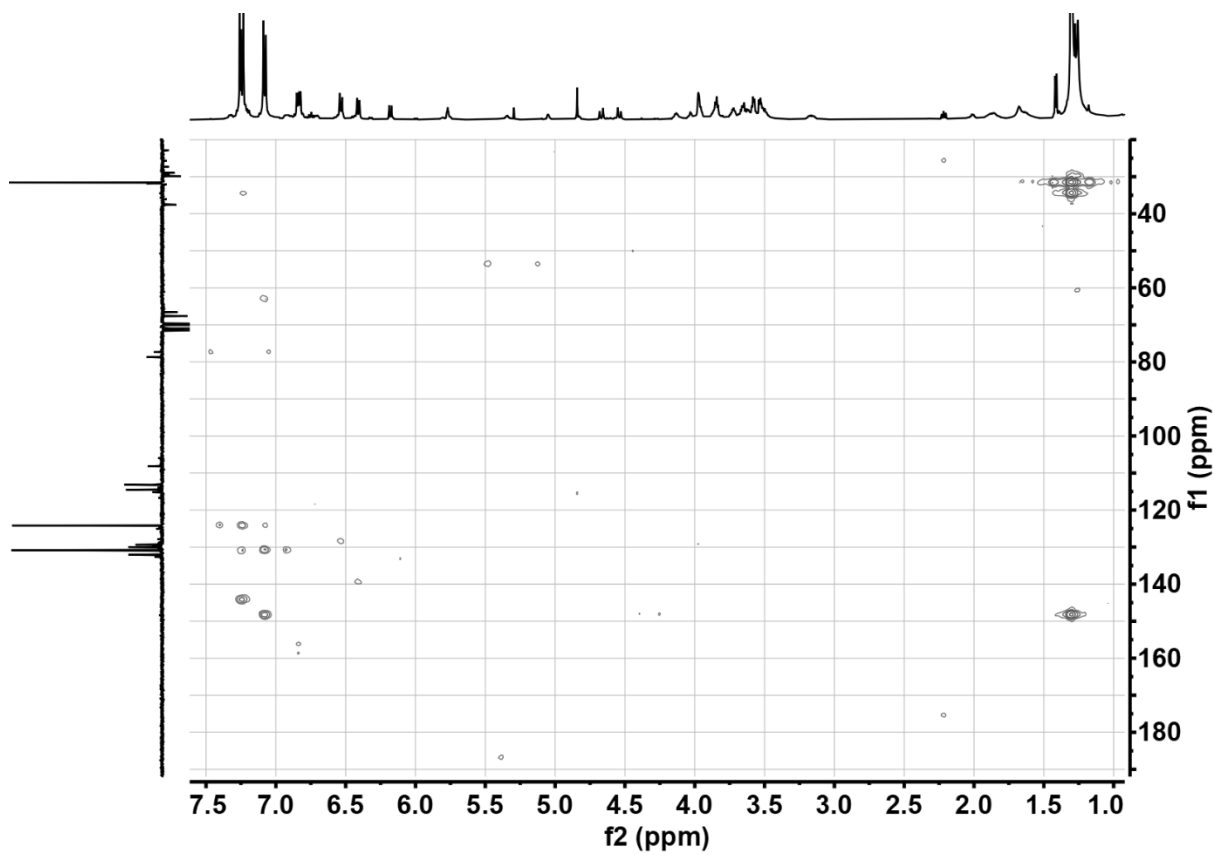
Spectrum S29. DEPT135 spectrum (126 MHz, CDCl₃, 298 K) of 4



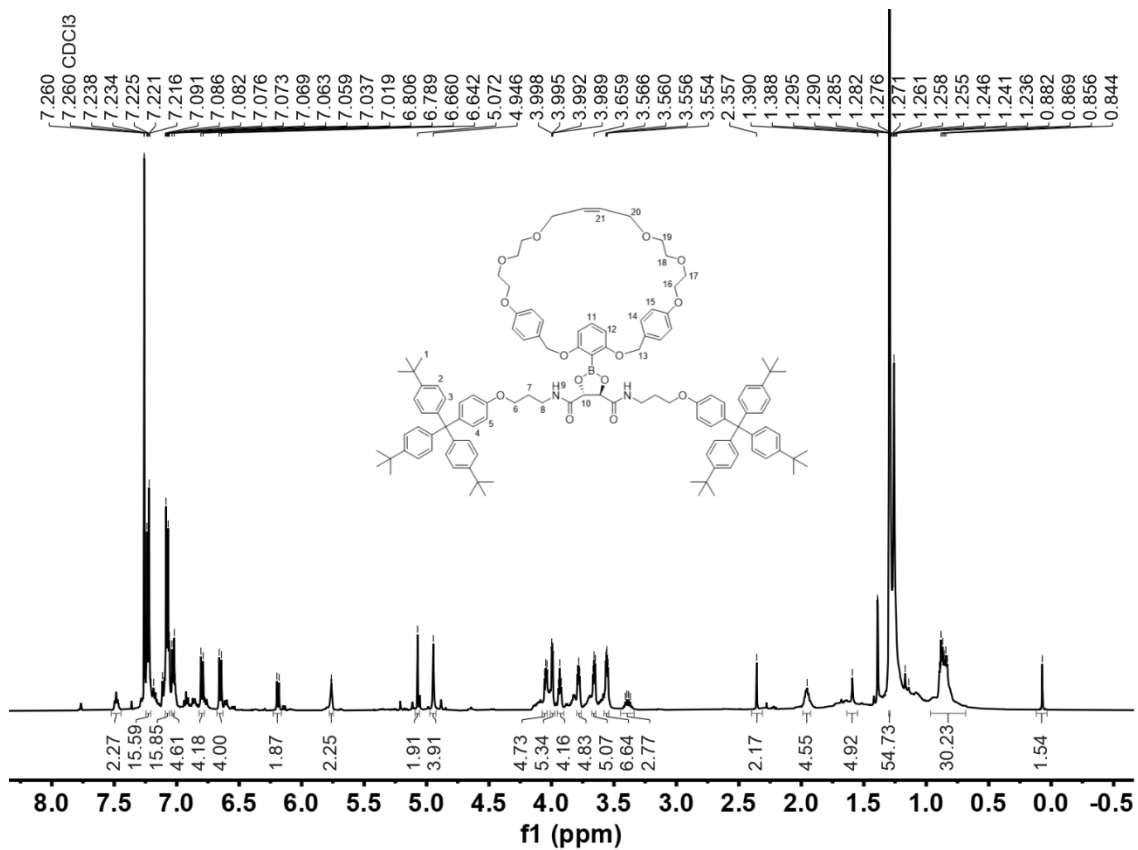
Spectrum S30. ¹H-¹H COSY spectrum (500 MHz, CDCl₃, 298 K) of 4.



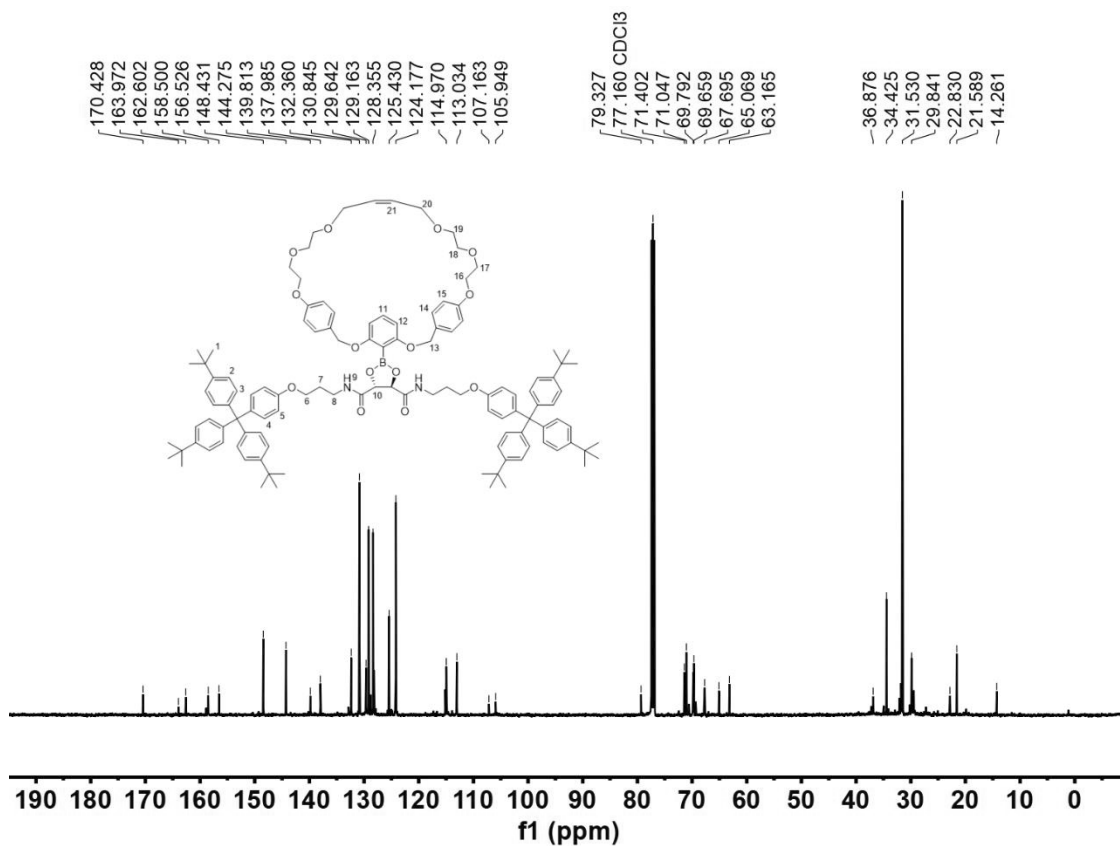
Spectrum S31. ^1H - ^{13}C HSQC spectrum (500 MHz, CDCl_3 , 298 K) of 4.



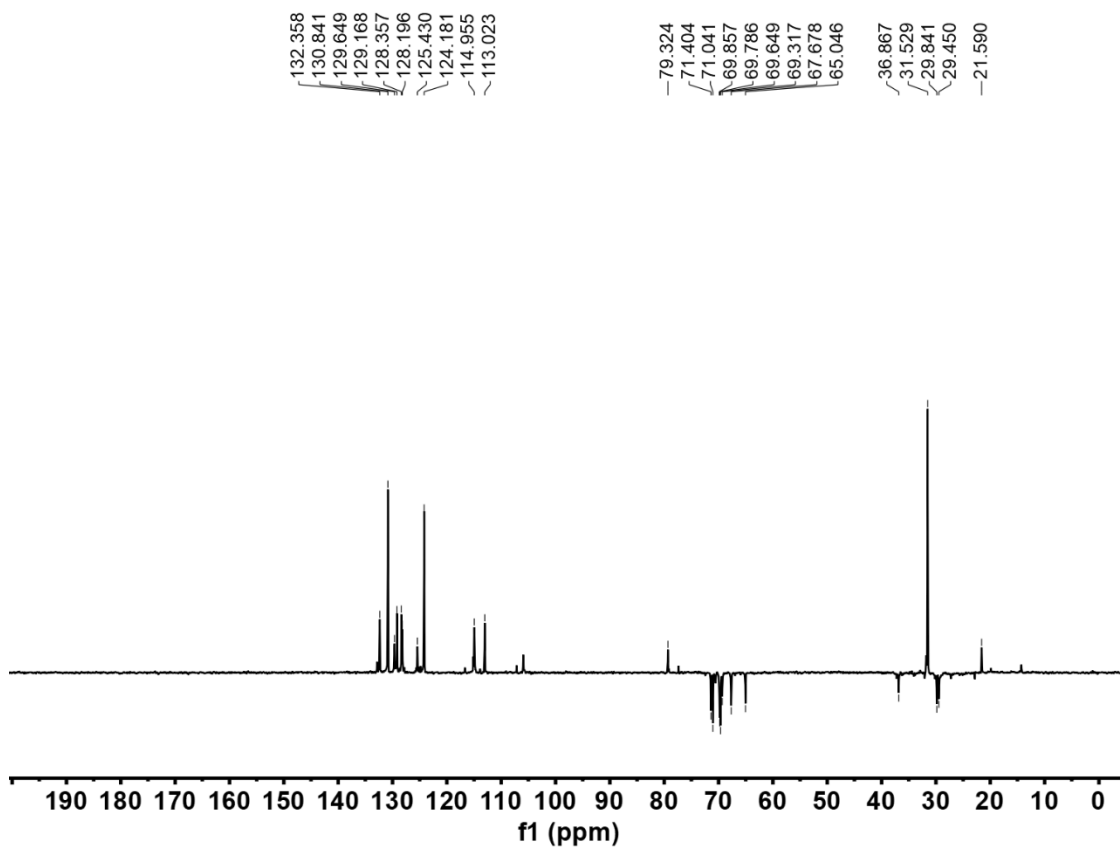
Spectrum S32. ^1H - ^{13}C HMBC spectrum (500 MHz, CDCl_3 , 298 K) of 4.



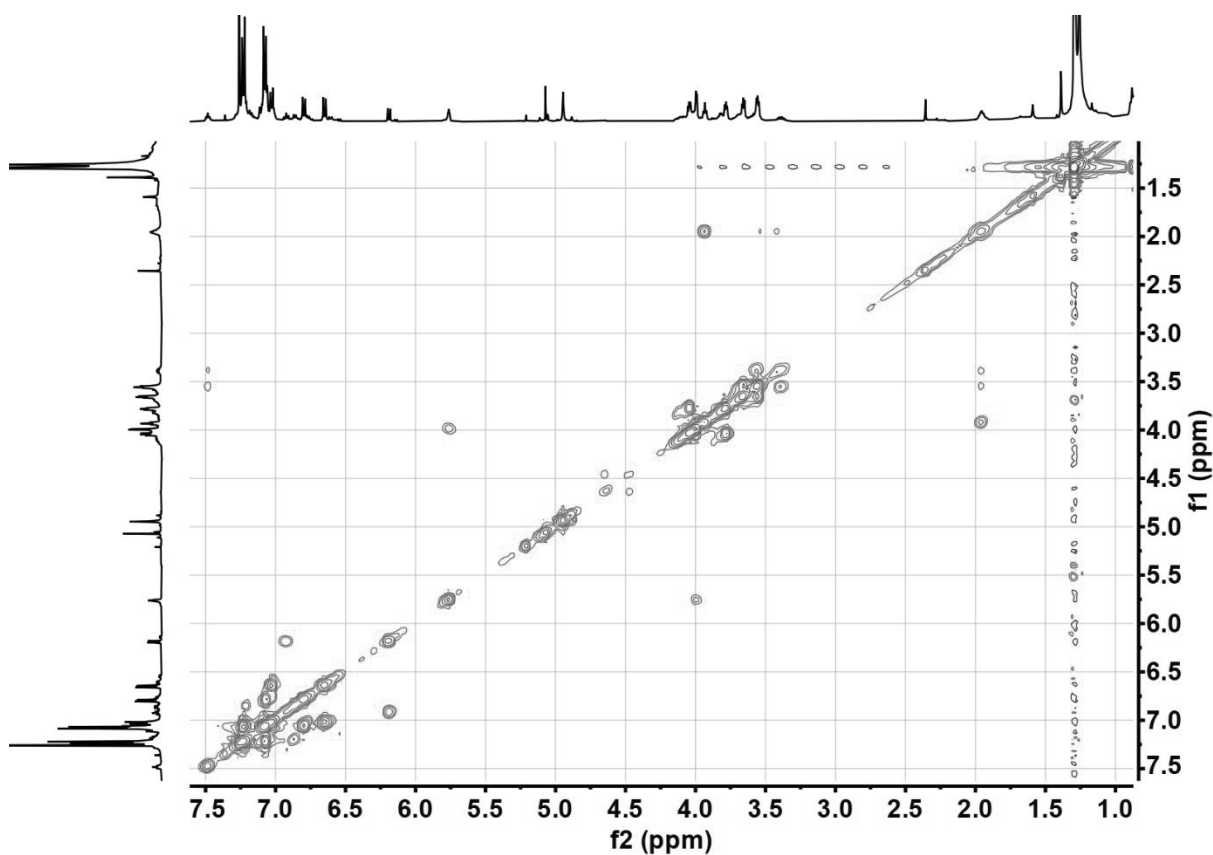
Spectrum S33. ¹H NMR spectrum (500 MHz, CDCl₃, 298 K) of 4'.



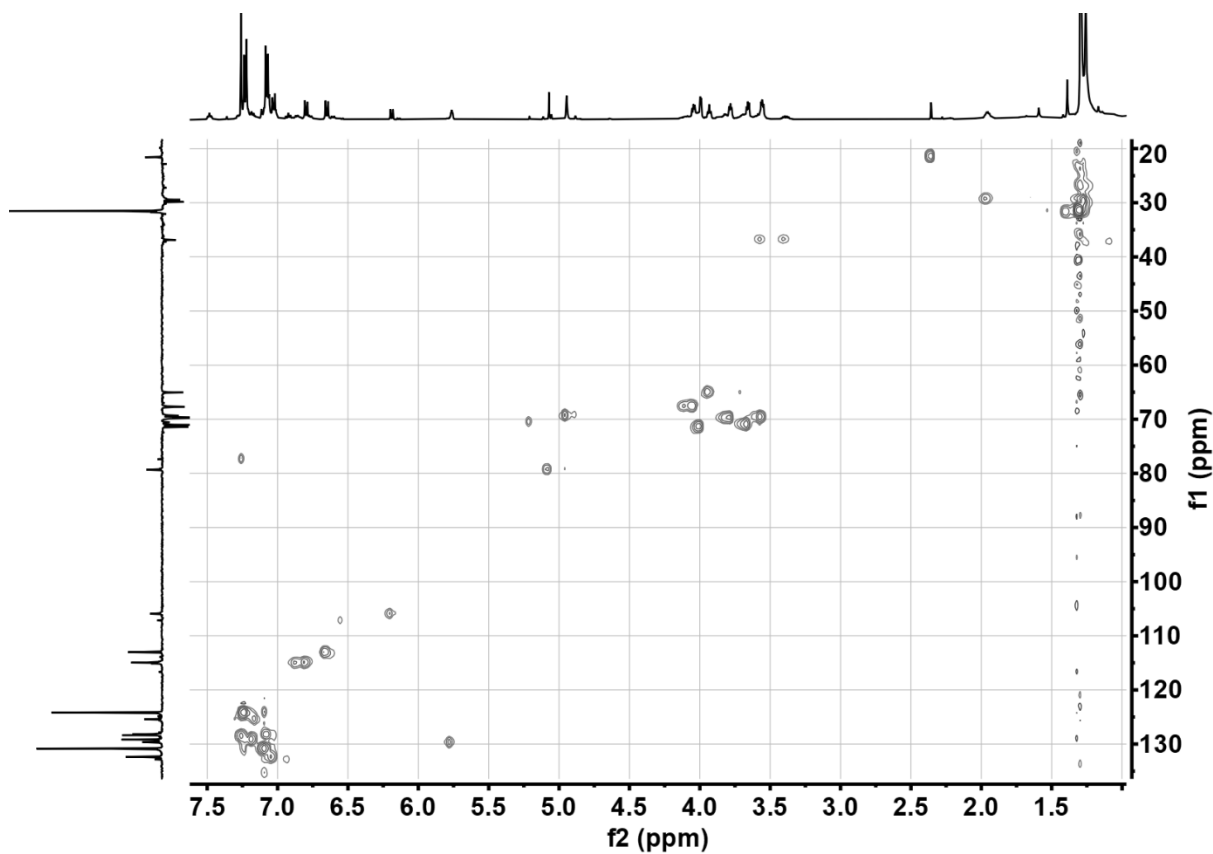
Spectrum S34. ¹³C NMR spectrum (126 MHz, CDCl₃, 298 K) of 4'.



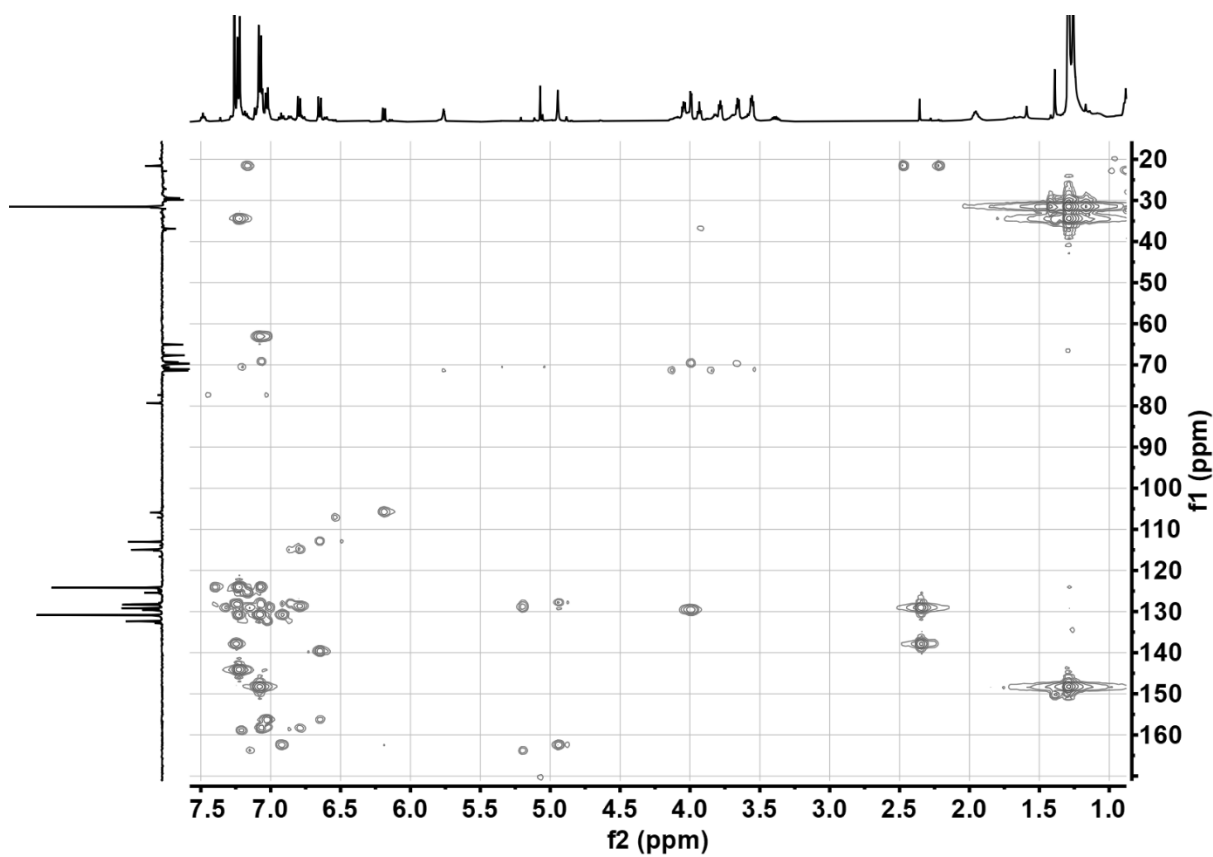
Spectrum S35. DEPT135 spectrum (126 MHz, CDCl_3 , 298 K) of **4'**



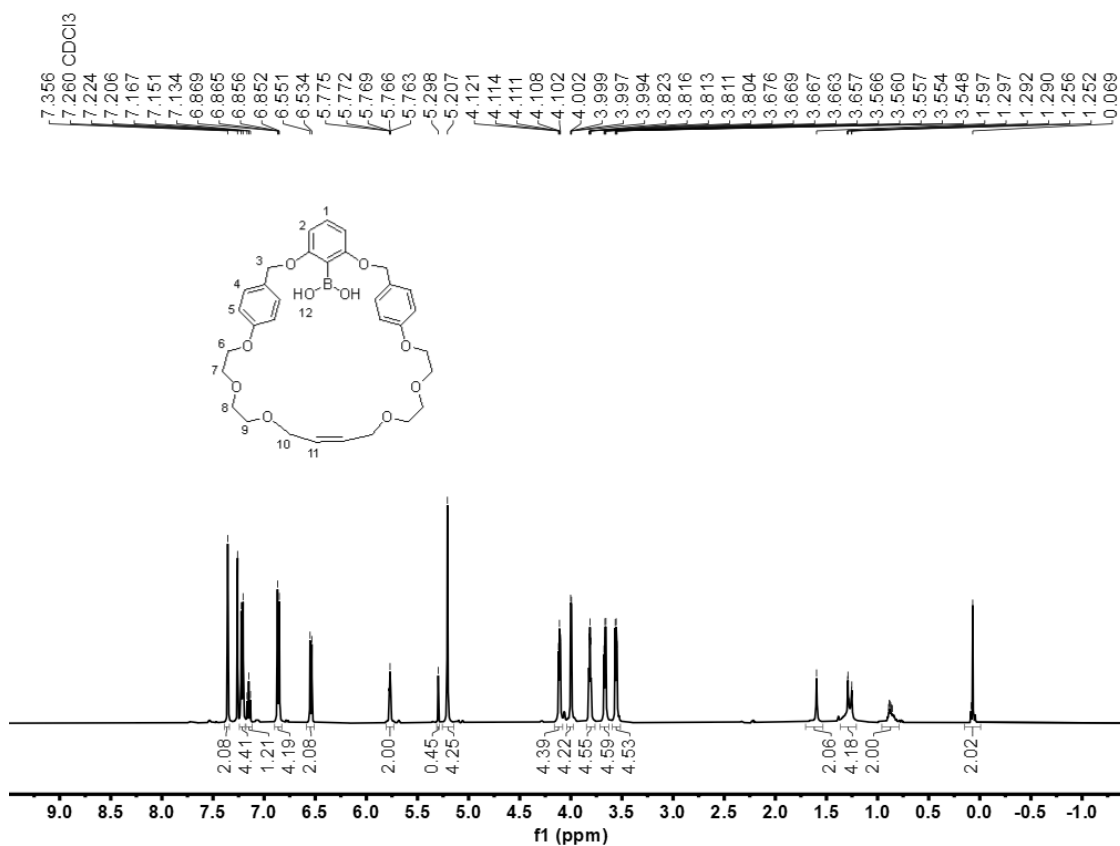
Spectrum S36. ^1H - ^1H COSY spectrum (500 MHz, CDCl_3 , 298 K) of **4'**



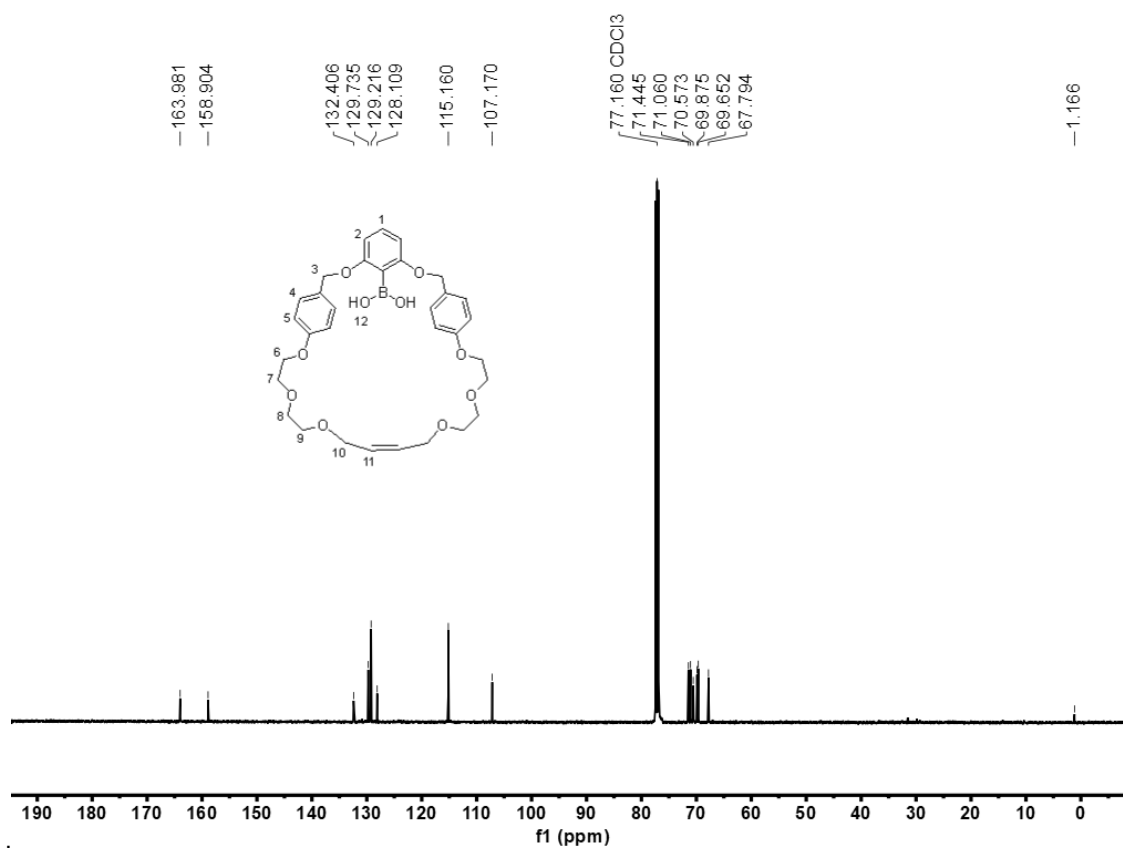
Spectrum S37. ^1H - ^{13}C HSQC spectrum (500 MHz, CDCl_3 , 298 K) of **4'**.



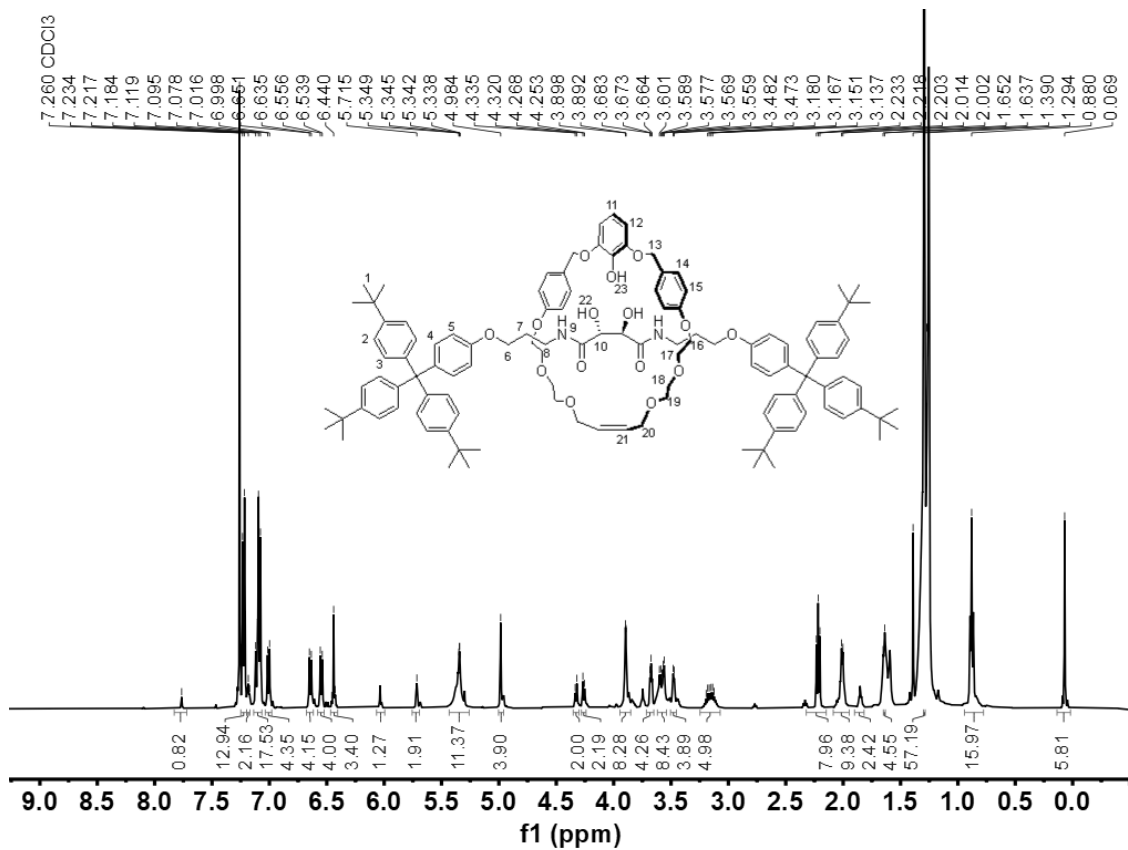
Spectrum S38. ^1H - ^{13}C HMBC spectrum (500 MHz, CDCl_3 , 298 K) of **4'**.



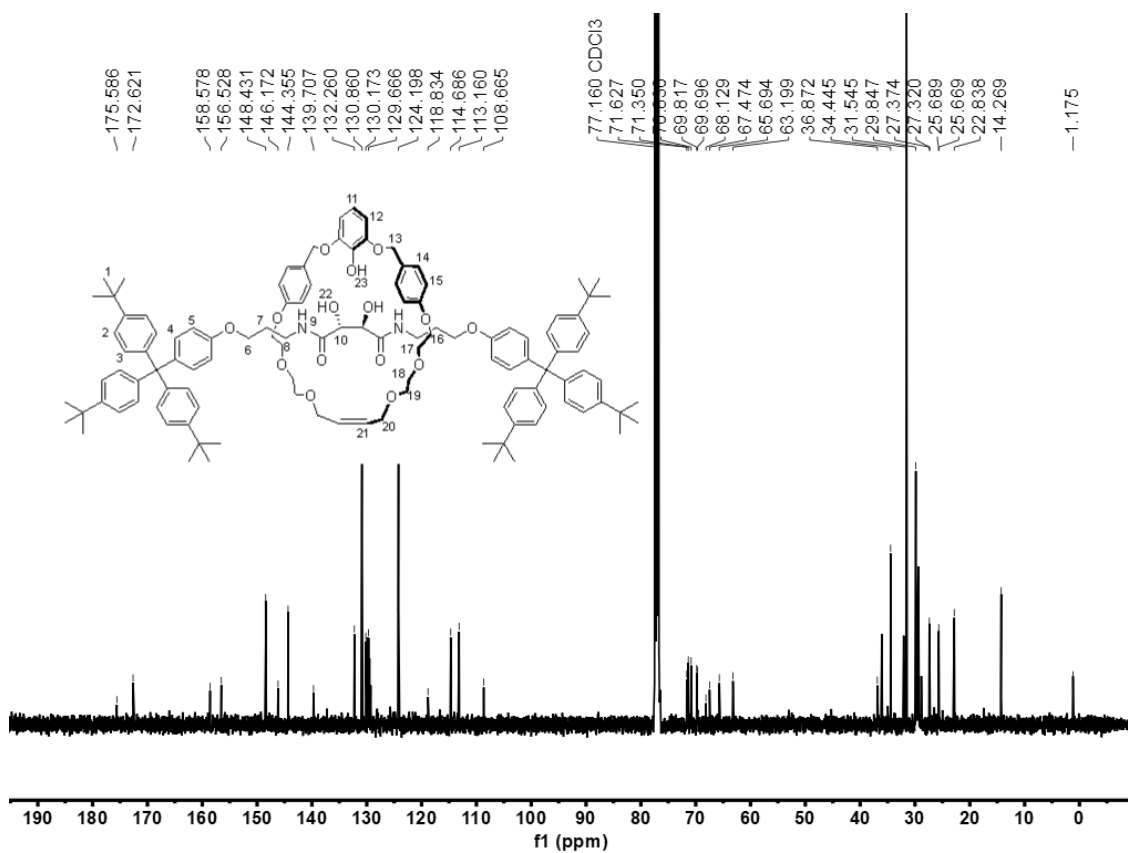
Spectrum S39. ¹H NMR spectrum (500 MHz, CDCl₃, 298 K) of 6.



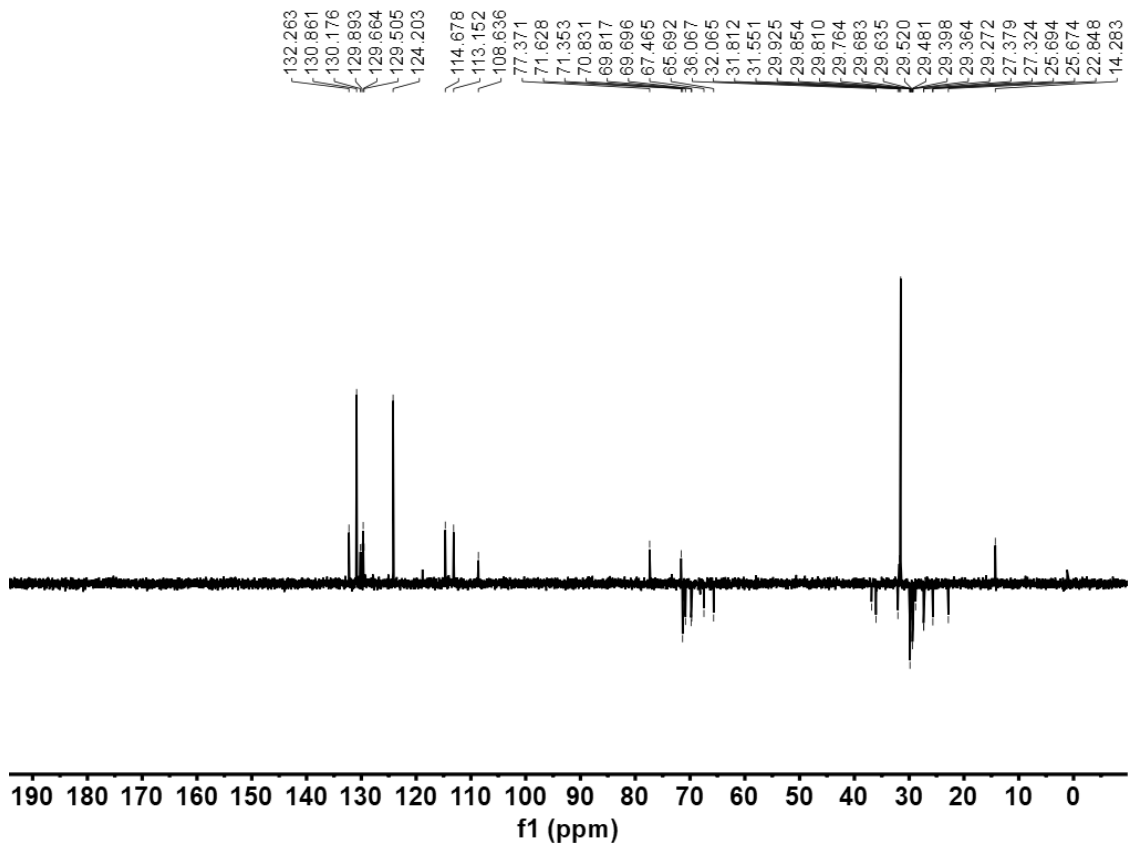
Spectrum S40. ¹³C NMR spectrum (126 MHz, CDCl₃, 298 K) of 6.



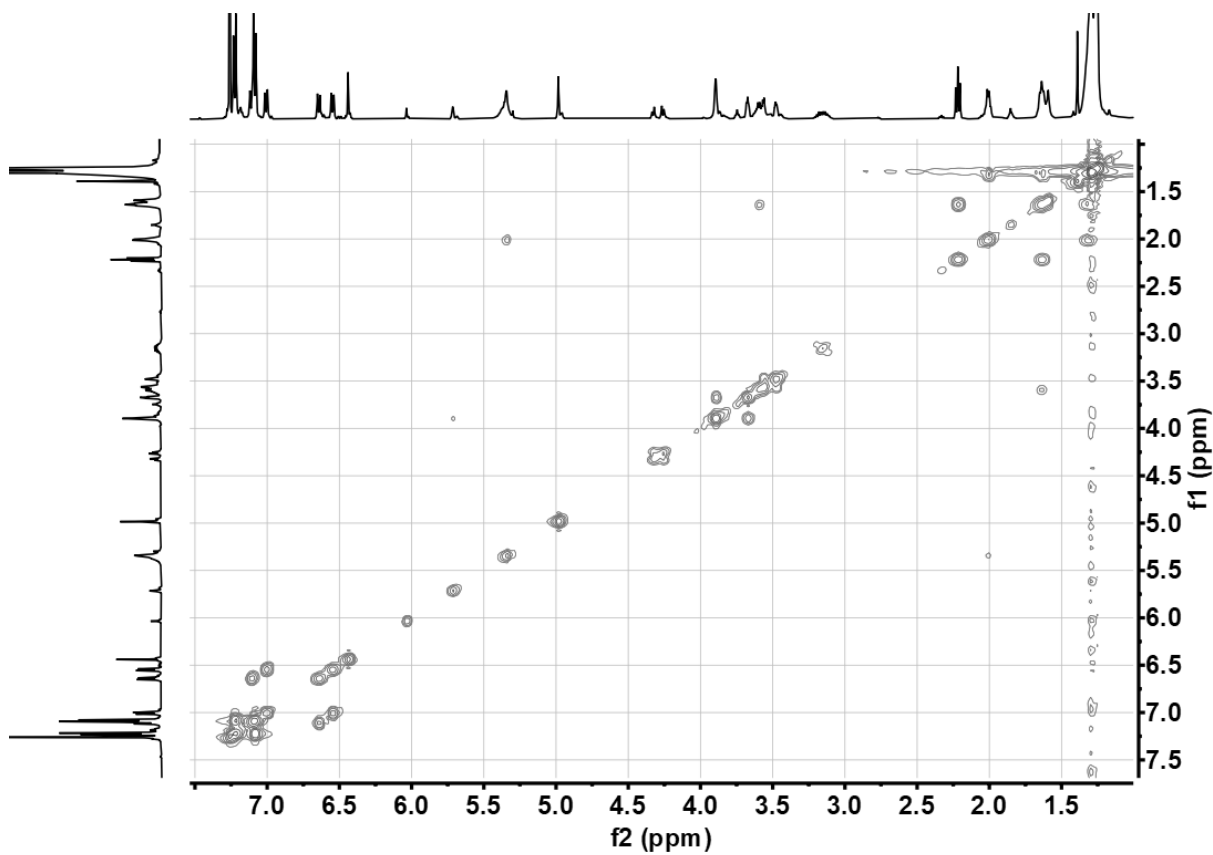
Spectrum S41. ¹H NMR spectrum (500 MHz, CDCl₃, 298 K) of 7.



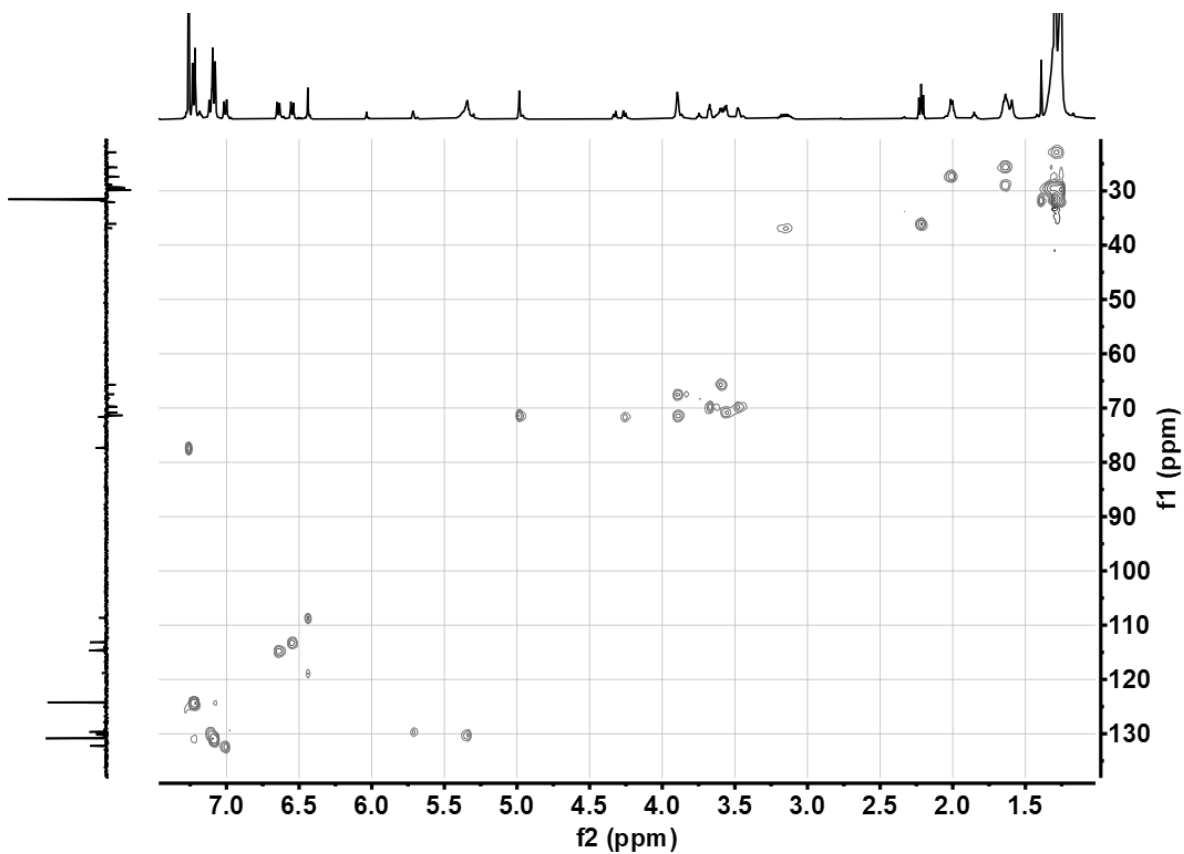
Spectrum S42. ¹³C NMR spectrum (126 MHz, CDCl₃, 298 K) of 7.



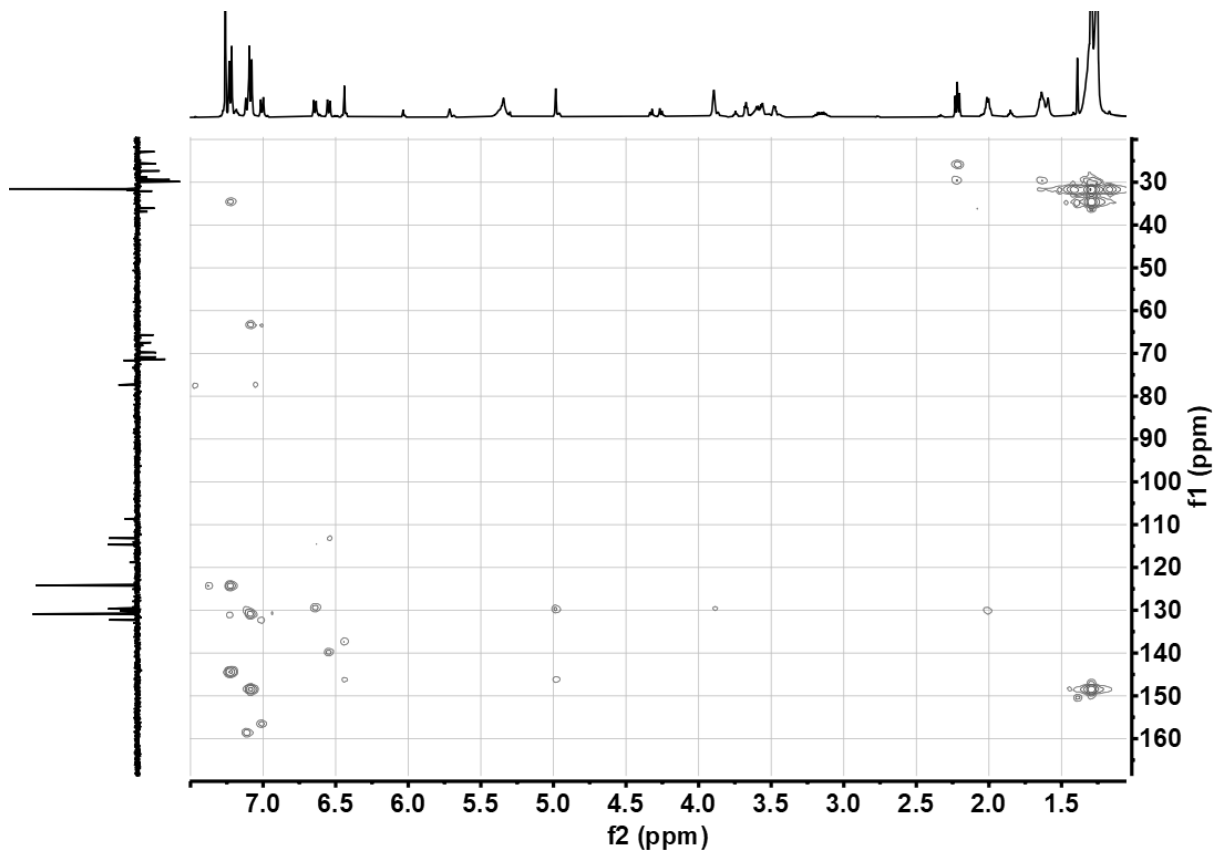
Spectrum S43. DEPT135 spectrum (126 MHz, CDCl₃, 298 K) of 7



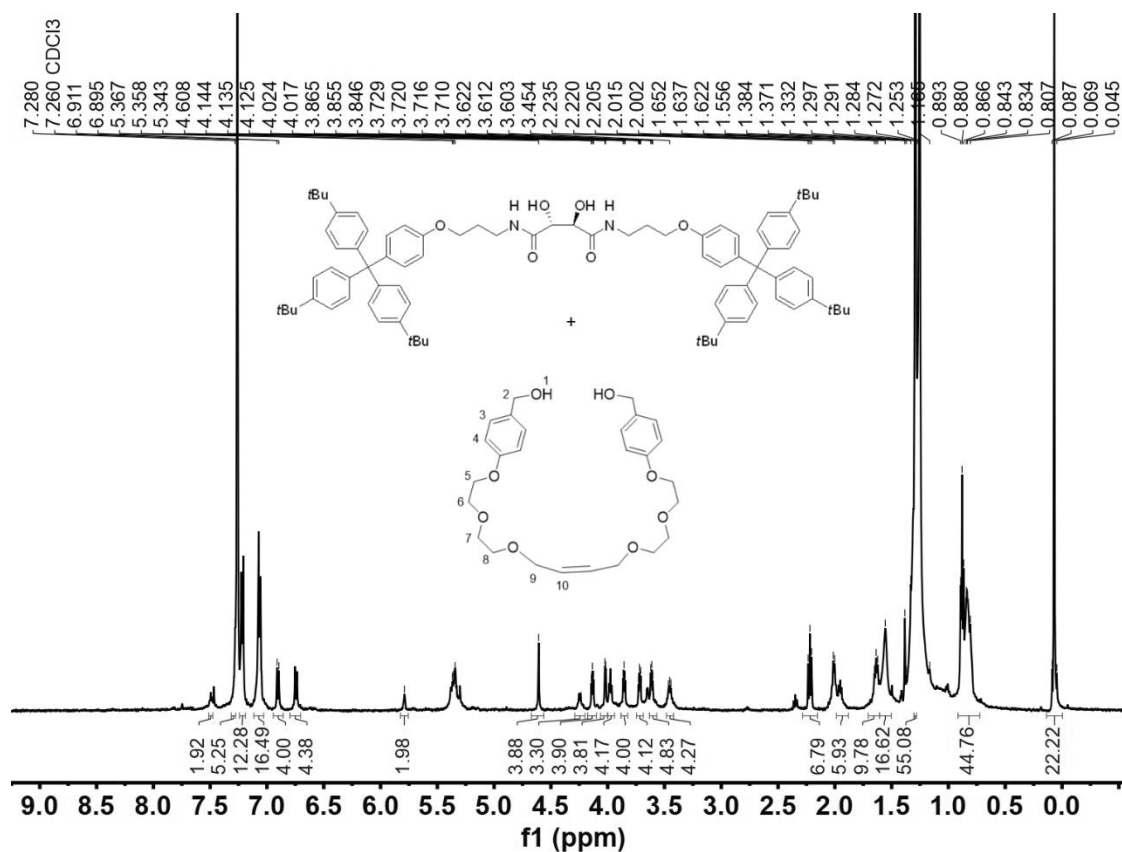
Spectrum S44. ¹H-¹H COSY spectrum (500 MHz, CDCl₃, 298 K) of 7.



Spectrum S45. ^1H - ^{13}C HSQC spectrum (500 MHz, CDCl_3 , 298 K) of **7**.



Spectrum S46. ^1H - ^{13}C HMBC spectrum (500 MHz, CDCl_3 , 298 K) of **7**.



Spectrum S47. ¹H NMR spectrum (500 MHz, CDCl₃, 298 K) of crude S11.

S8. REFERENCES

- [1] S. Sarkar, P. Sarkar, P. Ghosh, *Org. Lett.* **2018**, *20*, 6725–6729.
- [2] S. Hoekman, M. O. Kitching, D. A. Leigh, M. Papmeyer, D. Roke, *J. Am. Chem. Soc.* **2015**, *137*, 7656–7659.
- [3] J. Beswick, V. Blanco, G. De Bo, D. A. Leigh, U. Lewandowska, B. Lewandowski, K. Mishiro, *Chem. Sci.* **2015**, *6*, 140–143.
- [4] S. Shinkaruk, B. Bennetau, P. Babin, J.-M. Schmitter, V. Lamothe, C. Bennetau-Pelissero, M. C. Urdaci, *Bioorg. Med. Chem.* **2008**, *16*, 9383–9391.
- [5] R. Sure, S. Grimme, *J. Comput. Chem.* **2013**, *34*, 1672–1685.
- [6] F. Neese, *WIREs: Comput. Mol. Sci.* **2012**, *2*, 73–78.
- [7] F. Neese, *WIREs: Comput. Mol. Sci.* **2022**, *12*, e1606.
- [6] M. F. Bush, Z. Hall, K. Giles, J. Hoyes, C. V. Robinson, B. T. Ruotolo, *Anal. Chem.* **2010**, *82*, 9557–9565.
- [7] V. Shrivastav, M. Nahin, C. J. Hogan, C. Larriba-Andaluz, *J. Am. Soc. Mass Spectrom.* **2017**, *28*, 1540–1551.